

© Copyright 2025

Naghmeh M. Mojb

# Evaluation of Intra-Build Interactions on Fracture-Critical Properties of PBF-EB Ti6Al4V

Naghmeh M. Mojob

A dissertation  
submitted in partial fulfillment of the  
requirements for the degree of

Doctor of Philosophy

University of Washington  
2025

Reading Committee:  
Ramulu Mamidala, Co-Chair  
Dwayne Arola, Co-Chair  
Junlan Wang

Program Authorized to Offer Degree:  
Department of Mechanical Engineering

University of Washington

**Abstract**

**Evaluation of Intra-Build Interactions on Fracture-Critical Properties  
of PBF-EB Ti6Al4V**

Naghme M. Mojb

Co-Chairs of the Supervisory Committee:

Ramulu Mamidala

Department of Mechanical Engineering

Dwayne Arola

Department of Materials Science and Engineering

The increasing adoption of metal Additive Manufacturing in high-performance industries, particularly aerospace, necessitates a comprehensive understanding of fracture-critical properties to ensure structural reliability. However, property variability remains a significant barrier to the qualification and certification of AM components. Additionally, standard post-processing treatments have proven inadequate in consistently enhancing the fracture-critical properties of AM titanium alloys, necessitating modifications to advance the state-of-the-art in post-processing. This study investigates the intra-build variability – the part-to-part variations – of electron beam powder bed fusion Ti6Al4V, focusing on fracture toughness and high cycle fatigue performance, while also evaluating the effectiveness of an optimized low-

temperature/high-pressure hot isostatic pressing treatment currently developed in AMS7028 in improving damage tolerance. A systematic design of experiments approach was employed to evaluate the influence of common design parameters – including sample orientation, geometry, and spatial location– on microstructural evolution, defect distribution, and mechanical behavior. Seven builds comprised of over 270+ compact tensile and 155+ high cycle fatigue samples were printed representative of the PBF-EB build space, followed by microstructural characterization, X-ray microcomputed tomography, surface roughness analysis, and fracture toughness and high cycle fatigue testing per ASTM E399 and ASTM E466, respectively.

The average fracture toughness in the as-built condition was  $65\pm 6$  MPa $\sqrt{\text{m}}$ , with preferential crack growth direction the dominant factor influence damage tolerance, resulting in orientation-dependent crack propagation mechanisms contributing significantly to property scatter. Additionally, the spatial location and geometry effects demonstrated strong correlations with microstructural variations, influencing the fracture resistance. Thicker samples exhibited higher fracture toughness, further emphasizing the critical role of part design in mechanical performance. The application of modified low-temperature/high-pressure hot isostatic pressing process effectively enhanced fracture toughness to  $74\pm 4$  MPa $\sqrt{\text{m}}$  by reducing internal defects and increasing ductility while preserving the microstructure and yield strength. However, crack propagation dependent on build direction and location-dependent properties remained, highlight the persistent influence of the as-fabricated microstructure.

High cycle fatigue behavior was primarily governed by surface and subsurface defects, with as-built surface roughness contributing to the largest variation in fatigue life. While HIP treatment alone was insufficient to enhance fatigue performance, combining LTHIP, machining, and shot peening significantly improved fatigue strength up to 400 MPa, surpassing cast Ti6Al4V properties. Despite these improvements, intra-build design parameters continued to impact fatigue scatter, with 6mm samples exhibiting 50 – 60 % reduction in fatigue life compared to the 9mm samples due to increased sensitivity to defects.

This research provides crucial insight into the interplay between part design, build design, microstructure, and fracture-critical properties in PBF-EB Ti6Al4V. The findings highlight the need for intentional build strategies, where sample orientation, geometry, and spatial location influenced should be considered when adopting PBF-EB components in load-bearing applications. Furthermore, by implementing traceability of design parameters and PBF-EB-

specific post-processing, consistent and repeatable mechanical performance can be achieved. By demonstrating that PBF-EB Ti6Al4V can achieve fracture toughness and fatigue strength comparable to cast and wrought alloys under optimized condition, this study aids in advancing the metal AM for safety-critical applications in aerospace and beyond.

# Acknowledgements

I would like to express my heartfelt gratitude to all those who have supported me throughout my PhD journey.

First and foremost, I would like to thank my advisors, Professor Ramulu Mamidala and Professor Dwayne Arola, for their guidance and support. Your insights and expertise have been invaluable to my research, and I am deeply grateful for the opportunity to learn from you.

I would also like to extend my sincere appreciation to the Mechanical Engineering Department staff, including Wanwisa Kisalang, Bill Kuykendall, and Corey Clay. Your unwavering support has been essential in helping me navigate my PhD. Thank you for always being there to lend a hand and for creating such a welcoming environment.

I am thankful to the students and mentors who have helped along the way.

I owe a debt of gratitude to my family and friends for their unwavering support and encouragement. Thank you for believing in me and providing the emotional support that helped me persevere through the challenges of graduate school.

Lastly, I would like to acknowledge the funding and resources provided by Boeing, which made this research possible.

Thank you all for being a part of this journey.

# Table of Contents

<b>Acknowledgements .....</b>	<b>vi</b>
<b>List of Figures.....</b>	<b>5</b>
<b>List of Tables.....</b>	<b>12</b>
<b>List of Abbreviations.....</b>	<b>14</b>
<b>1 Introduction .....</b>	<b>16</b>
<b>2 Background and Literature Review .....</b>	<b>19</b>
<b>2.1 Metal AM Process .....</b>	<b>19</b>
<b>2.2 Process-Induced Attributes .....</b>	<b>24</b>
2.2.1 Microstructure.....	25
2.2.2 Internal Defects .....	28
2.2.3 Residual Stresses .....	30
2.2.4 Surface Roughness .....	30
<b>2.3 Failure in Metals .....</b>	<b>32</b>
<b>2.4 Mechanical and Fracture-Critical Properties.....</b>	<b>33</b>
2.4.1 Tensile Behavior.....	33
2.4.2 Fracture Toughness .....	39
2.4.3 Fatigue Performance.....	47
<b>3 Research Goals and Objectives.....</b>	<b>62</b>
<b>4 Experimental Methods and Procedures .....</b>	<b>64</b>
<b>4.1 Feedstock .....</b>	<b>64</b>
<b>4.2 Sample Fabrication.....</b>	<b>66</b>
<b>4.3 Design of Experiments .....</b>	<b>67</b>
4.3.1 Tensile Properties .....	69
4.3.2 Fracture Toughness .....	69
4.3.3 High Cycle Fatigue .....	73

<b>4.4</b>	<b>Analysis Procedure .....</b>	<b>79</b>
4.4.1	Surface Roughness .....	79
4.4.2	Internal Defect Analysis .....	79
4.4.3	Microstructure .....	81
<b>4.5</b>	<b>Post-Processing .....</b>	<b>82</b>
4.5.1	Hot Isostatic Pressing .....	82
4.5.2	Surface Treatment .....	83
<b>4.6</b>	<b>Experimental Testing .....</b>	<b>84</b>
4.6.1	Mechanical Properties .....	84
4.6.2	Fracture Toughness Testing .....	84
4.6.3	High Cycle Fatigue Testing .....	87
<b>4.7</b>	<b>Fractography .....</b>	<b>88</b>
<b>5</b>	<b><i>Fracture Toughness: As-Built Condition.....</i></b>	<b>89</b>
<b>5.1</b>	<b>Introduction .....</b>	<b>89</b>
<b>5.2</b>	<b>Results.....</b>	<b>91</b>
5.2.1	Microstructure .....	91
5.2.2	Porosity analysis .....	93
5.2.3	Surface Roughness .....	96
5.2.4	Tensile Properties .....	98
5.2.5	Fracture Toughness .....	99
5.2.6	Fractography .....	103
<b>6</b>	<b><i>Fracture Toughness: Hot Isostatic Pressing Effects.....</i></b>	<b>106</b>
<b>6.1</b>	<b>Introduction .....</b>	<b>106</b>
<b>6.2</b>	<b>Results.....</b>	<b>108</b>
6.2.1	Microstructure .....	108
6.2.2	Internal Defect analysis.....	113
6.2.3	Tensile Properties .....	115
6.2.4	Fracture Toughness .....	117
6.2.5	Fractography .....	120
6.2.6	Effect of Build Design .....	125
<b>7</b>	<b><i>Fatigue Performance: As-Built and Post-processing effects .....</i></b>	<b>128</b>

<b>7.1</b>	<b>Introduction .....</b>	<b>128</b>
<b>7.2</b>	<b>Results.....</b>	<b>128</b>
7.2.1	Surface Roughness .....	128
7.2.2	Internal Defect Analysis .....	132
7.2.3	Tensile Properties .....	134
7.2.4	High Cycle Fatigue .....	135
7.2.5	Fractography .....	138
7.2.6	Fatigue Life Variation.....	148
<b>8</b>	<b>Discussion .....</b>	<b>157</b>
<b>8.1</b>	<b>Fracture Toughness .....</b>	<b>158</b>
8.1.1	Anisotropy .....	158
8.1.2	Intra-Build Variation .....	160
8.1.3	Hot Isostatic Pressing .....	166
<b>8.2</b>	<b>High Cycle Fatigue .....</b>	<b>170</b>
8.2.1	Anisotropy .....	170
8.2.2	Intra-Build Variation .....	170
8.2.3	Post-Processing.....	172
<b>9</b>	<b>Conclusion .....</b>	<b>179</b>
<b>9.1</b>	<b>Fracture Toughness .....</b>	<b>179</b>
<b>9.2</b>	<b>High Cycle Fatigue .....</b>	<b>180</b>
<b>9.3</b>	<b>Future Work .....</b>	<b>183</b>
	<b>References .....</b>	<b>184</b>
	<b>Appendix .....</b>	<b>210</b>
<b>A-</b>	<b>Experimental Properties .....</b>	<b>211</b>
	Hardness .....	211
	Tensile Properties.....	218
	Fracture Toughness Data .....	220
<b>B –</b>	<b>Statistical Analysis .....</b>	<b>229</b>
	As-Built Fracture Toughness DOE Tables and ANOVA Results.....	229
	Intra-Build Fracture Toughness RSM ANOVA.....	233

HIP Fracture Toughness ANOVA .....	237
Tukey Ad-Hoc Results .....	240
<b>C - High Cycle Fatigue Data .....</b>	<b>244</b>
Murakami Defect Area .....	251
<b>D – Microstructure .....</b>	<b>252</b>
Statistics .....	298
<b>E - Surface Roughness .....</b>	<b>300</b>
<b>F - Fractography.....</b>	<b>325</b>
Fracture Toughness .....	325
High Cycle Fatigue.....	350
<b><i>Curriculum Vitae (CV)</i>.....</b>	<b>363</b>

# List of Figures

Figure 2-1: The metal AM process from start to finish. ....	20
Figure 2-2: (a) The metal AM line-by-line scanning strategy in a single layer <sup>32</sup> , (b) Thermal profile experienced a single layer in metal AM of Ti6Al4V <sup>33</sup> .....	21
Figure 2-3: Ti6Al4V microstructure formation process, dictated by cooling rate <sup>34</sup> .....	21
Figure 2-4: The PBF-EB internal schematic and the layerwise PBF additive process <sup>38</sup> .....	22
Figure 2-5: EBSD maps of the typical microstructure of PBF-EB Ti6Al4V exhibiting columnar prior $\beta$ -grain formed along the build direction with a basketweave $\alpha+\beta$ , and $\alpha$ colony microstructure <sup>71</sup> .....	26
Figure 2-6: SEM images of PBF-EB microstructure. <sup>72</sup> .....	27
Figure 2-7: SEM images of PBF-LB microstructure. <sup>72</sup> .....	27
Figure 2-8: High magnification images of (a) LOF and (b) porosity defect. The LOF defect forms between two layers and contains unmelted or partially melted powder particles. <sup>78</sup> .....	29
Figure 2-9: The rough surface exterior of PBF-EB components composed of partially melted powder particles <sup>95</sup> .....	31
Figure 2-10: The types and percentage of aircraft component failures <sup>18</sup> .....	32
Figure 2-11: The sample orientation nomenclature with respect to the build orientation <sup>129</sup> .....	37
Figure 2-12: Schematic of CT specimens orientation designation, with respect to the build and raster direction <sup>138</sup> .....	40
Figure 2-13: The Fatigue performance of PBF-EB in the as-built and post-processed condition. <sup>26, 41, 175,178,179</sup> .....	48
Figure 2-14: The machining effects on PBF-EB fatigue performance <sup>26</sup> .....	49
Figure 2-15: The HCF performance of PBF-EB Ti6Al4V compared to conventional alloys <sup>26</sup> ...	50
Figure 2-16: Orientation effects on fatigue performance <sup>47, 171,175</sup> .....	53
Figure 2-17: Comparison of surface treatment methods on PBF-EB fatigue performance <sup>41, 175,217,218</sup> .....	57
Figure 4-1: SEM micrograph of Ti6Al4V unused powder obtained from AP&C. ....	64
Figure 4-2: The nomenclature adopted to evaluate the PBF-EB build space denoting the two spatial parameters: radial distance and height. ....	68
Figure 4-3: The orientation designation for tensile samples.....	69

Figure 4-4: (a) Fracture toughness orientation designation, shown with respect to the build direction and recoater path. (b) ASTM E399 CT fracture toughness specimen size, units in mm. .... 70

Figure 4-5: Fracture toughness build layout for ZX-oriented samples. Shown are the front, top and isometric views, respectively. Radial distance (R), height (H), and thickness (T) are three factors evaluated in this study and are defined as illustrated. .... 72

Figure 4-6: Fracture toughness build layout for XZ- and XY-oriented samples. Shown are the front, top and isometric views, respectively. Radial distance (R), height (H), and thickness (T) are three factors evaluated in this study and are defined as illustrated. .... 72

Figure 4-7: The orientation designation for fatigue samples ..... 73

Figure 4-8: The sequence of post-processing for each set of samples investigated in Phase I.... 74

Figure 4-9: The build layout of the as-fabricated HCF samples and final dimensions ..... 75

Figure 4-10: The sequence of post-processing for each set of samples investigated in Phase II. 77

Figure 4-11: The final dimensions for the 6- and 9-mm samples post-machining per ASTM E466. Dimensions are in mm. .... 77

Figure 4-12: PBF-EB build layout for the horizontally oriented high cycle fatigue (HCF) specimens. Shown are the front, side, and top views, respectively. Radial distance (R), height (H), and thickness (T) are three factors evaluated in this study and are defined as illustrated. .... 78

Figure 4-13: LTHIP treatment cycle provided for reference ..... 83

Figure 4-14: Load vs. Crack Mouth Opening Displacement (CMOD) Curve for sample specimen. The blue line is the linear-elastic portion, and the fracture toughness is obtained from the dashed-pink 95% secant line per ASTM E399. .... 86

Figure 5-1: PBF-EB Ti6Al4V microstructure of the machined (a) ZX and (b) XY oriented samples. Columnar prior- $\beta$  grain formed along the build direction, comprised of an  $\alpha+\beta$  basketweave microstructure within the grain. (b) The dark color identifies the acicular  $\alpha$  grains and the  $\beta$ -rib in white after etching..... 91

Figure 5-2: (a) Box plot of the ZX, XZ, and XY fracture toughness values, overlaid with model significance and Tukey test indicating significance. (b) the four-way DOE table and (c) results. (d) the plot of prediction equations obtained from the ANOVA model..... 92

Figure 5-3: High magnification images of porosity and LOF defect. The arrows denote spherical gas pores. The outlined region indicates the LOF defect formed between two layers and contained unmelted and partially melted powder particles. .... 94

Figure 5-4: The  $\mu$ CT reconstruction of the As-Built and LTHIP samples. The LTHIP process showed a significant reduction in porosity and defect size..... 95

Figure 5-5: Graphs representing the defect characteristics obtained from  $\mu$ CT analysis. (a) The defect diameter is plotted versus the defect sphericity. (b) A positive linear relationship between mean diameter and thickness and height exists. (c) the DOE table evaluated and the resulting (d) ANOVA table. .... 96

Figure 5-6: The 2D surface roughness profile in each sample. Note the difference in scale. .... 97

Figure 5-7: The stress-strain curve as a function of surface and build orientation..... 98

Figure 5-8: The RSM four-way ANOVA (a) DOE table and (b) significance test evaluating the effect of orientation and the intra-build design parameters. .... 100

Figure 5-9: The RSM ANOVA significance test for the intra-build parameters in the ZX As-Built, ZX Machined, XZ Machined, and XY Machined condition. (b)The contribution of each factor in the model, and (c) the resulting equation for the given model. .... 101

Figure 5-10: The RSM prediction curves in the ZX, XZ, and XY orientation. Each factor is individually plotted while keeping the other two factors constant. .... 102

Figure 5-11: Fracture surface of the ZX, XZ, and XY orientations. (a) The samples exhibited thumbnail precrack and shear lips along the edges, notably the ZX samples. (b) The crack path through the microstructure is shown. (c) The fracture micromechanisms are provided, with quasi-brittle facets (black arrows) observed on all three orientations. Porosity (white arrows) and tearing ridges (grey arrows) are identified. The transparent arrows identify regions roughly 50  $\mu$ m apart. .... 104

Figure 6-1: Key microstructural features such as prior  $\beta$  grains, the  $\alpha$ -grain boundary, and the basketweave structure, with respect to the build orientation. .... 109

Figure 6-2: Microstructure of the LTHIP ZX, XZ, XY oriented samples..... 110

Figure 6-3: Summary of the microstructural characteristics of PBF-EB Ti6Al4V, as a function of orientation and metal condition ..... 112

Figure 6-4: The  $\mu$ CT reconstruction of the As-Built and LTHIP samples. The LTHIP process showed a significant reduction in porosity and defect size..... 114

Figure 6-5: The two types of internal defects (porosity and LOF) commonly found in metal AM, ..... 114

Figure 6-6: The defect diameter trends versus the defect sphericity in the untreated and LTHIP conditions. (b) The defect diameter distribution in the untreated and LTHIP conditions, with the darkest regions indicating the largest concentration of defects. .... 115

Figure 6-7: The stress-strain response of the PBF-EB Ti6Al4V as a function of metal condition and sample orientation ..... 116

Figure 6-8: The load (P) vs. the crack mouth opening displacement (CMOD) graph for select 9 mm samples in all three orientations in the untreated and LTHIP condition. .... 118

Figure 6-9: The average fracture toughness as a function of orientation and metal condition... 119

Figure 6-10: The fracture surface of the sample specimens in the ZX, XZ, and XY orientations. (a) thumbnail pre-crack is observed, followed by the crack propagation region and shear lips along the edges of the samples. (b) A 3D fracture surface map highlights orientation-dependent fracture surfaces. (c) The crack path through the microstructure is provided. (d) notable micro-mechanisms of failure were observed using SEM and are provided. Where the black arrows are regions of flat featureless quasi-brittle features, the clear arrows signify approximately 50 $\mu$ m and correspond to the prior  $\beta$  grain. Porosity and LOF were not observed on the fracture surface..... 121

Figure 6-11: Common defects found on the fracture surface of the AB surface and after LTHIP treatment. .... 123

Figure 6-12: The contribution of intra-build design factors in the untreated and LTHIP metal 125

Figure 6-13: The relationship between fracture toughness and the intra-build design parameters as a function of metal condition in the ZX orientation ..... 126

Figure 7-1: The 2D surface roughness profile in each sample. Note the difference in scale. .... 130

Figure 7-2: The 3D reconstruction of the surface and the internal view of the As-Built and HIP samples. Porosity and LOF defects are observed in the As-Built condition, while surface machining has removed any existing surface defects. Porosity and LOF defects are not observed in the HIP bulk material, however, surface porosity was observed..... 133

Figure 7-3: The overall defect diameter trends in the as-built and HIP samples. (a) the defect diameter vs. sphericity, where the largest defects are those with the least spherical shapes..... 134

Figure 7-4: Fatigue stress-life curve of the PBF-EB Ti6Al4V in the Vertical orientation as a function of surface and metal condition, where the data was used to obtain the Basquin curve.136

Figure 7-5: The fatigue life of as-built PBF-EB Ti6Al4V specimens, in the horizontal and vertical orientations..... 138

Figure 7-6: SEM Fractography of the common defects found on the As-Built and STHIP samples including (a) gas porosity, (b) LOF, and (c) surface defects. .... 138

Figure 7-7: The rough surface exterior of PBF-EB components composed of partially melted 139

Figure 7-8: Fractography of the striations on the (a) As-Built and the (b) As-Built + STHIP samples. The images were obtained close to the crack nucleation sites. .... 140

Figure 7-9: Fractography of the samples after fatigue failure. The arrows indicate the location of crack initiation in the (a) As-Built and the (b) As-Built + STHIP samples. Multiple crack initiation regions were often observed on samples. .... 140

Figure 7-10: The fracture surface of the horizontal machined HCF samples. (a) The fracture surface of the horizontally oriented samples in the untreated condition is shown, highlighting the region of crack initiation and propagation. (b) a higher magnification of the porosity and LOF defects. The clear arrow points out the source of crack initiation, with the solid white arrow the LOF defect and the black/clear arrow porosity defects..... 141

Figure 7-11: The fatigue striations of the horizontal machined and Machined+LTHIP HCF samples..... 142

Figure 7-12: The fracture surface of the horizontal machined HCF samples. The clear arrow points out the source of crack initiation, with the solid white arrow the LOF defect and the black/clear arrow porosity defects. (a) higher magnification image of the source of crack initiation. (b) the low magnification and (c) high magnification images of the microcrack formed perpendicular to the crack growth direction and parallel to the build direction. .... 143

Figure 7-13: Optical fractography of the (a) Vertical and (b) Horizontal orientation. The arrows indicate the location of crack initiation. Multiple crack initiation regions were often observed on samples, as seen on the (b). (c) sharp surface notches formed from subsurface defects deforming during the LTHIP process. .... 144

Figure 7-14: SEM fractography of the LTHIP+SP samples after fatigue failure. (a) the crack origin due to internal defects with crack propagating radially out. And (b) the striations observed near the crack initiation region. .... 145

Figure 7-15: Optical fractography of the samples after fatigue failure. The arrows indicate the location of crack initiation. .... 146

Figure 7-16: SEM fractography of the Machined samples after fatigue failure, where a smaller crack propagated from the external surface while it was not the main crack nucleation. Porosity and LOF defects observed on the fracture surface located randomly.....	146
Figure 7-17: SEM fractography of the crack nucleation sites on the (a) LTHIP, (b) Machined, (c) SP samples, where the critical defect is outlined and calculated after fatigue failure. ....	147
Figure 7-18: The predicted versus the experimental fatigue life ( $R=0.1$ ), where the predicted values are calculated using the Basquin equation. ....	148
Figure 7-19: The ratio between the stress amplitude and the Theoretical Fatigue Stress versus the experimental fatigue life. The predicted values obtained using Equation 7-2.....	149
Figure 7-20: The ratio between the stress amplitude and the Ideal Fatigue Stress versus the experimental fatigue life. The predicted values are obtained using Equation 7-3.....	150
Figure 7-21: The relationship between the (a) average surface roughness ( $R_a$ ) and (b) 10-point roughness ( $R_z$ ) with respect to cycles to failure in the STHIP condition. ....	151
Figure 7-22: The relationship between the (a) average surface roughness ( $R_a$ ) and (b) 10-point roughness ( $R_z$ ) with respect to cycles to failure in the Machined + LTHIP condition. ....	152
Figure 7-23: The relationship between the (a) average surface roughness ( $R_a$ ) and (b) 10-point roughness ( $R_z$ ) with respect to cycles to failure in the Machined+LTHIP+SP condition. ....	153
Figure 7-24: The relationship between the max valley depth ( $R_v$ ) with respect to cycles to failure. ....	153
Figure 7-25: The regression equation comprised of the metal quality, surface roughness, and internal defects. ....	154
Figure 8-1: The average fracture toughness values in the ZX, XY, and XY orientation .....	159
Figure 8-2: The microstructural characteristics $\alpha$ -lath size and the $\beta$ vol.% in the ZX, XZ, and XY. (***) denotes statistical significance of ( $p<0.001$ ). ....	160
Figure 8-3: $\alpha$ -lath variation as a function of sample height for each orientation.....	161
Figure 8-4: The RSM prediction curves for fracture toughness and a-lath thickness, in the ZX, XZ, and XY orientation. Each factor is individually plotted while keeping the other two factors constant. ....	162
Figure 8-5: The RSM prediction curves for fracture toughness and a-lath thickness, in the ZX, XZ, and XY orientation. Each factor is individually plotted while keeping the other two factors constant. ....	163

Figure 8-6: The RSM prediction curves for fracture toughness and $\alpha$ -lath thickness, in the ZX, XZ, and XY orientation. Each factor is individually plotted while keeping the other two factors constant. ....	163
Figure 8-7: The 9mm thick fracture toughness and $\alpha$ -lath values at three intra-build locations in the PBF-EB build chamber for each crack orientation. ....	164
Figure 8-8: The comparison of $\alpha$ -lath size and the $\beta$ vol.% in the untreated and LTHIP condition. ....	166
Figure 8-9: The average fracture toughness in the untreated and LTHIP condition .....	167
Figure 8-10: The $\alpha$ -lath thickness of the ZX, XY, and XY in the LTHIP condition, where the XY orientation is statistically significant compared to the ZX and XZ orientations. (***) denotes statistical significance of ( $p < 0.001$ ) .....	169
Figure 8-11: The trends in microstructure and fracture toughness as a function of sample thickness and height.....	169
Figure 8-12: The fatigue life of as-built PBF-EB Ti6Al4V specimens in the untreated horizontal orientation .....	171
Figure 8-13: Summary of crack nucleation source of each sample, respective to the metal and surface condition. ....	173
Figure 8-14: The fatigue life of as-built PBF-EB Ti6Al4V specimens in the untreated horizontal orientation (purple circle marker) and the LTHIP vertical (red triangle marker) as a function of the intra-build design parameters (thickness, height, and radial distance). ....	175

# List of Tables

Table 2-1: Comparison of metal AM processes <sup>16, 31, 38,52,53</sup> .....	24
Table 2-2: The defect types, causes and characteristics in metal AM .....	25
Table 2-3: Summary of tensile values of metal AM, wrought, and cast Ti6Al4V alloy .....	35
Table 2-4: Summary of Ti6Al4V PBF-EB fracture toughness values, with average PBF-LB, wrought, and cast properties for comparison .....	42
Table 4-1: Unused Titanium Grade 5 (Ti6Al4V) powder composition as provided by the manufacturer. ....	65
Table 4-2: The reuse cycle and powder lot used to manufacture the specimens .....	65
Table 4-3: General powder chemistry for PBF-EB Ti6Al4V powder with reuse <sup>10,227</sup> .....	66
Table 4-4: Build parameters as defined in melt theme .....	66
Table 4-5: Overview of Fracture Toughness specimen size and location .....	71
Table 4-6: Sample DOE table to evaluate Fracture Toughness. Each row represents the parameter set utilized for a given sample. Refer to Appendix for each respective DOE table used. ....	71
Table 4-7: Summary of the number of samples manufactured in each condition .....	73
Table 4-8: Summary of samples evaluated in Phase I .....	76
Table 4-9: The intra-build design factors and levels in the vertical and horizontal orientation ...	78
Table 4-10: Scan Parameters for the 9-mm Fracture Toughness specimens .....	80
Table 4-11: Scan Parameters for 9mm High Cycle Fatigue Samples.....	80
Table 4-12: Summary of the sample type, condition, and orientation evaluated by $\mu$ CT .....	81
Table 4-13: Machining Parameters.....	83
Table 4-14: Stress Levels tested for each material condition .....	88
Table 5-1: CT samples surface roughness characteristics in each condition.....	98
Table 5-2: Summary of the tensile properties.....	99
Table 5-3: Summary of fracture toughness values obtained for each orientation. ....	103
Table 6-1: The microstructure factors of each orientation and material condition.....	113
Table 6-2: Tensile mechanical properties of each orientation and material condition. ....	116
Table 6-3: Summary of fracture toughness values obtained for each thickness.....	119
Table 6-4: The ANOVA results of the DOE model in the LTHIP condition .....	125
Table 7-1: Surface roughness characteristics in each condition .....	131

Table 7-2: Mechanical properties in each condition..... 135  
Table 7-3: Experimental and theoretical fatigue limit in each condition..... 155

# List of Abbreviations

AM – additive manufacturing  
PBF – Powder Bed Fusion  
PBF-EB – Electron Beam Powder Bed Fusion  
PBF- LB – Laser powder bed fusion  
DED – Direct Energy Deposition  
SEM – Scanning Electron Microscope  
 $\mu$ CT –X-ray Micro-computed Tomography  
DOE – Design of Experiments  
CT – Compact tension fracture toughness specimen  
CoV – Coefficient of Variation  
ANOVA – Analysis of Variance  
CMOD – Crack mouth opening displacement  
 $K_{Ic}$  – Plane strain fracture toughness  
 $K_Q$  – Conditional fracture toughness  
 $P_{max}$  – Max Load  
 $P_Q$  - Conditional Load value at secant  
 $\sigma_{ys}$  – Yield Strength  
a – crack length  
W – sample width  
LOF – lack of fusion  
RSM – Response Surface Methodology  
HCF – High cycle fatigue  
SIF – Stress intensity factor  
YS – Yield Strength  
UTS – Ultimate Tensile Strength  
EF – Elongation at Failure  
HIP – Hot Isostatic Pressing  
LTHIP – Low-Temperature High Pressure HIP  
STHIP – Standard Temperature HIP  
SP – Shot Peen  
V – Vertical  
H – Horizontal

$R_a$  – Average surface roughness  
 $R_z$  - Ten-point height  
 $R_q$  - root mean square  
 $R_t$  - maximum valley to peak height  
 $R_{sk}$  - skewness  
 $R_{Ku}$  - kurtosis  
 $R_v$  - maximum valley depth  
 $S_a$  – Average areal roughness  
 $S_z$  - Ten-point height  
 $S_q$  - root mean square  
 $S_t$  - maximum valley to peak height  
 $S_{sk}$  - skewness  
 $S_{Ku}$  - kurtosis  
 $S_v$  - maximum valley depth

# 1 Introduction

Critical components with complex geometries have long been manufactured using conventional techniques such as casting or forging, powering the Industrial Revolution and beyond. However, further topological complexities (*e.g.*, topology-optimized parts) require a paradigm shift. Metal additive manufacturing (AM) techniques offer a technologically viable pathway to realizing this paradigm shift in manufacturing parts with intricate geometries using metals <sup>1,2</sup>. Due to the stringent demands placed on damage tolerance by regulatory bodies demanding rigorous examination, the adoption of AM in service components has been slow. Key roadblocks to metal AM certification have been identified by various groups, including researchers, government agencies, and standard organizations <sup>3-5</sup>. One topic that continues to arise as a major hurdle in metal AM is the property variability that generates from the start to the end of the fabrication process <sup>3</sup>. As researchers investigate the mechanical properties from subsequent builds <sup>6,7</sup>, powder reuse <sup>8-12</sup>, and different machine generations <sup>13,14</sup>, there exists a gap in understanding the contribution of the Electron Beam Powder Bed Fusion (PBF-EB) process-induced features on property variability. Therefore, the objective of this research is to investigate the part-to-part variability in the PBF-EB fabricated Ti6Al4V within the build chamber, termed the intra-build variability. To do so, this study has performed extensive and systematic fracture toughness and high cycle fatigue testing, focusing on the influence of intra-build design parameters on the fracture-critical properties. In doing so, we obtained a comprehensive understanding of the variability within the build space due to the printing process; a topic necessary in advancing adoption of AM for safety-critical applications. The scientific rationales for investigating the fracture and fatigue properties of PBF-EB Ti6Al4V are first introduced, followed by the general structure of the dissertation. The introduction is further substantiated by a comprehensive background provided in the following chapter, imparting further insight into the state of the art.

Damage tolerant structures are designed to sustain loads even in the presence of existing damage, such as cracks or defects, to prevent catastrophic failure. These designs are crucial in aerospace applications, where safety and reliability are paramount. By focusing on damage tolerance, metal AM components that meet the stringent requirements of aerospace industry can be adopted. Current shortcomings of metal AM include porosity, surface roughness, and anisotropy <sup>15,16</sup>, which directly map to damage tolerance and the survivability of deployed products

<sup>17</sup>. The common shortcomings which influence the tensile behavior of PBF-EB Ti6Al4V result in a large range of data reported for fracture toughness and can be detrimental to fatigue performance. As a result, experimental testing is used to investigate these fundamental mechanical properties. Since metals are inherently imperfect, it is difficult to ascertain the ability of a material to resist an applied load in the presence existing damage with tensile testing alone. In contrast, fracture toughness is the critical mechanical property that quantifies a materials resistance to crack propagation under applied load, playing a vital role in determining its reliability and performance in structural applications. For titanium alloys such as Ti6Al4V, High Cycle Fatigue (HCF) is also especially critical as metal AM processes become widespread in demanding aerospace applications where 55% of failures are due to repetitive loading <sup>18</sup>. Since the deployment ability of PBF-EB Ti6Al4V is dependent on fracture toughness and fatigue performance, it has attracted a large focus in metal AM research <sup>19-21</sup>. However, the limited build design information and minimal number of samples make it difficult to qualify and certify metal AM properties for damage-tolerant designs.

The scatter in metal AM properties is further fueled by the AM process, where the build design contributes to variation in mechanical properties <sup>13,22-24</sup>. While these investigations have evaluated the quality of the metal, Best Practices developed based on the intra-build design effects are vital for adoption of end-use components. In lieu of standards-driven Protocols, AM samples are often subjected to post-processing to obtain optimal properties, where defect removal and microstructure coarsening produce a broad range of mechanical properties <sup>25-27</sup>. Furthermore, post-processing may complicate understanding the foundational impact of the layer-by-layer manufacturing process on property variation, making it difficult to uncover. Not to mention the increase in cost and manufacturing lead-time.

On the other hand, subjecting materials to AM-optimized post-processing treatments could prove useful in enhancing performance. ASTM F2924 provides guidelines for post-processing of metal AM Ti6Al4V to reduce internal defects and enhance mechanical properties<sup>28</sup>. While foundational for metal AM, advancements in HIP optimization for PBF-LB Ti6Al4V has led to development of AMS7028 <sup>29</sup>. However, its suitability for PBF-EB Ti6Al4V remains uncertain, necessitating further research to confirm application for critical applications. Therefore, the primary goal for fabricating stress-critical components should be understanding the source of variation due to the fabrication process. Especially in fabrication of metal AM components, where

the line-by-line movement of the beam establishes a unique microstructure which continues to grow with the addition of each layer. As a result, the final component design and build orientation dictate the microstructure and subsequent mechanical properties, where traceability of the design and fabrication process is vital from start to finish. To further understand how each of these intra-build design parameters influence PBF-EB Ti6Al4V performance, it is crucial to approach the experiment systematically which allows for the statistical interpretation of the data. However, the ability of the PBF-EB metal to mitigate catastrophic failure depends on understanding the influence of build design on fracture resistance and cyclic behavior, inspiring an experimental approach. Hence, both experimental evaluation of the fracture critical properties and the factors influencing the metal quality and performance due the printing process are vital to the fabrication of repeatable and reliable mechanical properties.

This thesis is organized as follows. Chapter two provides a comprehensive review of the current literature inspiring this research, followed by the motivation and objectives of this study in chapter three. Chapter four provides the experimental methods used to achieve the goals of this research. In the fifth chapter, the results from fracture toughness testing are used to investigate the untreated PBF-EB Ti6Al4V resistance to crack growth. The microstructure and internal defects were used to interpret the variation in fracture toughness as a function of the build design parameters. The spatial location and geometry were found to significantly influence fracture toughness variation. The sixth chapter explores the impact of intra-build design parameters in crack growth resistance after being subjected to post-processing. A modified hot isostatic pressing treatment was used to limit change in microstructure while reducing internal defects.  $\mu$ CT analysis was used to evaluate the effectiveness of HIP, where samples were scanned before testing. The results provided evidence for the efficacy of post-processing PBF-EB Ti6Al4V. In the seventh chapter, HCF testing in various surface conditions were investigated. The results focused on the different features associated with generating and propagating fatigue cracks resulting in failure. In addition to HCF testing,  $\mu$ CT and mechanical properties were incorporated to predict the fatigue performance. The eighth chapter provides a discussion of the PBF-EB fracture-critical properties, pathways towards enhancing the fracture-critical properties, and the influence of build design parameters. Our study paved the way for implementing standards-driven build design and fabrication of PBF-EB Ti6Al4V components. Finally, the ninth chapter summarize and concludes all of the work, providing recommendations for the future work.

## 2 Background and Literature Review

Metal Additive Manufacturing, also known as 3D printing, has revolutionized the fabrication of unique, lightweight, and complex components, especially for high-performance applications. Despite the design freedom it offers, the widespread adoption of metal AM for critical-safe applications is hindered by challenges related to structural integrity and durability. This literature review explores various aspects of metal AM, including the printing processes, microstructure, and mechanical performance. Furthermore, the review examines factors influencing property variability and factors hindering certification, establishing the critical need for foundational research on the sources of variability in the PBF-EB process. While a variety of metals are available for metal AM, this chapter focuses mainly on titanium alloys, specifically Ti6Al4V which makes up over 50% of titanium alloys used in aerospace structures<sup>30</sup>.

### 2.1 Metal AM Process

Metal additive manufacturing processes, such as binder jetting, material extrusion, powder bed fusion (PBF), and direct energy deposition (DED), each have unique fabrication process that influence the microstructure and mechanical behavior of final components. Each of these emerging metal 3D printing techniques employ their own energy source, feedstock state, and material feeding process<sup>15,16,31</sup>. As a result, the raw material application, support structure, and process parameters affect part complexity, surface roughness, microstructure, and mechanical properties, as highlighted in Figure 2-1. PBF and DED are considered direct manufacturing techniques, resulting in consistent components with superior dimensional accuracy and mechanical properties. In contrast, indirect manufacturing techniques (material extrusion and binder jet) require further post processing to achieve the final component<sup>31</sup>. Due to the focus on technologies prevalent for industrial applications, this document reviews PBF and DED processes.

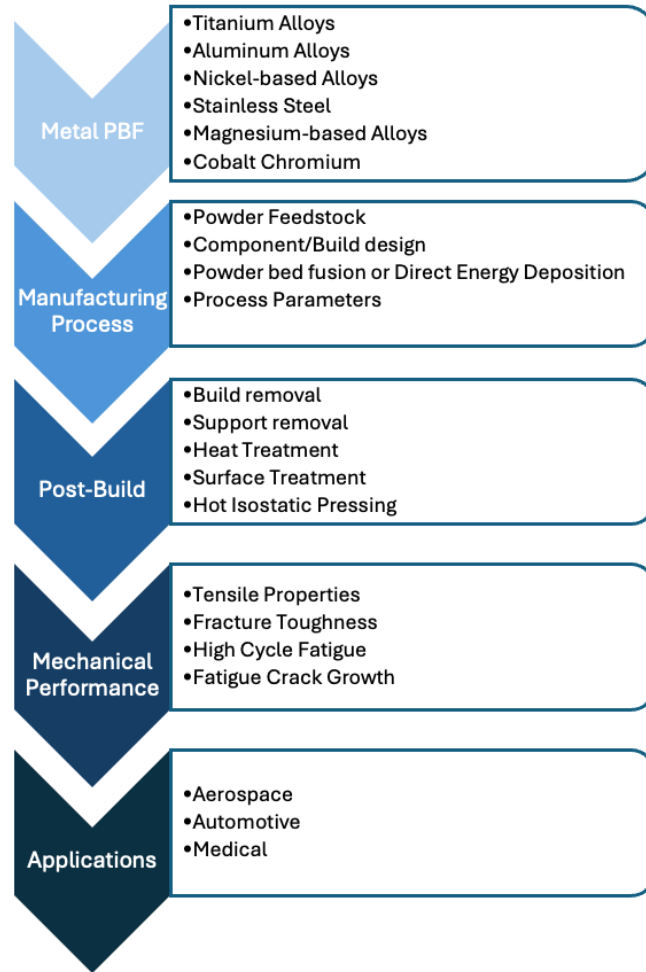


Figure 2-1: The metal AM process from start to finish.

The PBF printing process is extensively explored for engineered components, making it a promising alternative to conventional manufacturing. In PBF, a layer of powder with a predetermined thickness is distributed on the powder bed from the hopper(s) and selectively melted using the respective heat sources (laser or electron beam) <sup>16</sup>. During the melting of a single layer, the outer edges or contour are melted initially, and the inside region is melted in a line-by-line fashion, referred to as hatching, as indicated in Figure 2-2a. Once the specified regions in the layer is melted, the build platform lowers, a new layer of powder applied, and the specified regions melted as the process continues until the component is fully fabricated. As each new layer is applied, the previously melted regions undergo rapid cooling and heating, experiencing complex thermal cycling, as seen in Figure 2-2b. This repetitive thermal cycling influences the resulting microstructure as observed in Figure 2-3. As a result, heat accumulation and cooling rate depend on the geometry of the samples, spatial location, and support structure utilized. Once the build is

complete, the unmelted powder particles are removed, sifted, and often reused for subsequent builds.

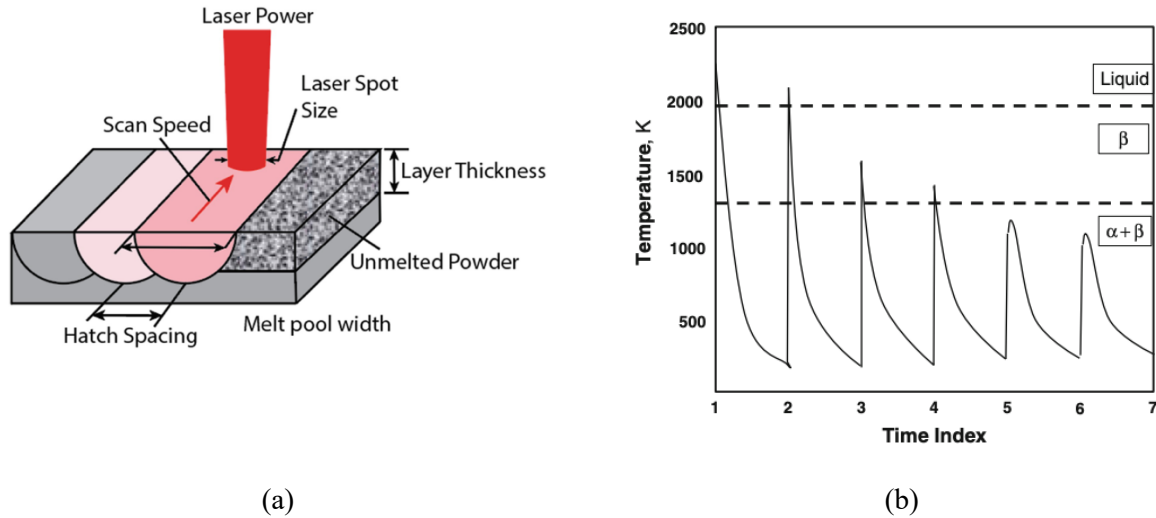


Figure 2-2: (a) The metal AM line-by-line scanning strategy in a single layer <sup>32</sup>, (b) Thermal profile experienced a single layer in metal AM of Ti6Al4V <sup>33</sup>

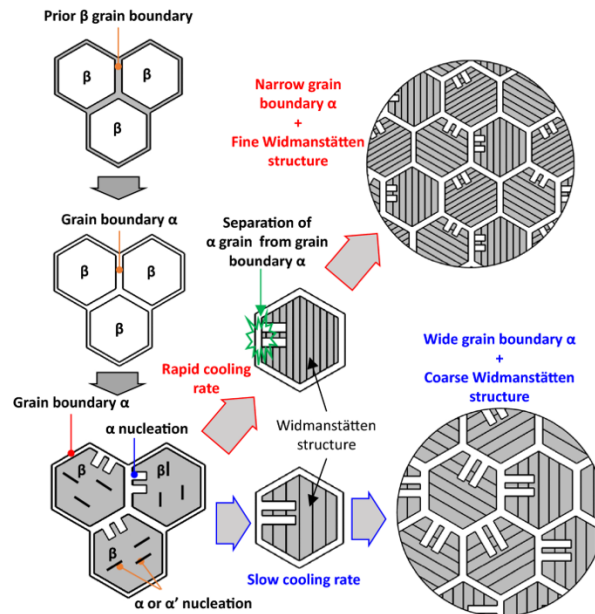


Figure 2-3: Ti6Al4V microstructure formation process, dictated by cooling rate<sup>34</sup>

Electron beam melting PBF (PBF-EB) melts a layer of powder through the acceleration of electrons emitted from a tungsten filament (in A2X system) using the electromagnetic coils, shown in Figure 2-4. This process sinters and subsequently melts predetermined regions in the powder bed using the electron beam <sup>35-37</sup>. The electrons are focused and deflected by the electromagnetic

lenses along the column, which can result in high processing temperatures (300 – 1100°C)<sup>38</sup> and several kilowatts of power output, much higher than the laser energy output of laser-based PBF (PBF-LB) systems (200-1000W)<sup>39</sup>. The temperature and power control unique to this melting process not only stabilizes the powder bed but optimizes the energy input for processing different metal alloys, making it preferable for materials prone to cracking (e.g., Nickel-based alloys) and reflective alloys such as copper<sup>40</sup>. To enable fast printing without interacting with its surroundings, the system operates under a vacuum environment (10<sup>4</sup> – 10<sup>5</sup> mbar), when coupled with the high temperature, limit contamination and oxidation, preferable when manufacturing metals prone to oxygen pickup such as titanium and aluminum alloys. The high build temperature of the PBF-EB process yields properties comparable to wrought alloys with negligible residual stresses<sup>41</sup>, high elongation<sup>42</sup>, and promising fracture toughness<sup>13,43</sup>. However, the larger powder size used in the PBF-EB process requires a layer thickness between 50 and 150µm and focal spot size between 140 to 250µm, often yielding components with poor surface quality. However, due to the rough surface and desired properties, there is a growing interest in the tribological properties of the samples for medical use, with recent research on the wear of the PBF-EB surface<sup>44,45</sup>, where Soria et al.<sup>45</sup> demonstrated the frictional dissipated energy is dominated by the microstructure.

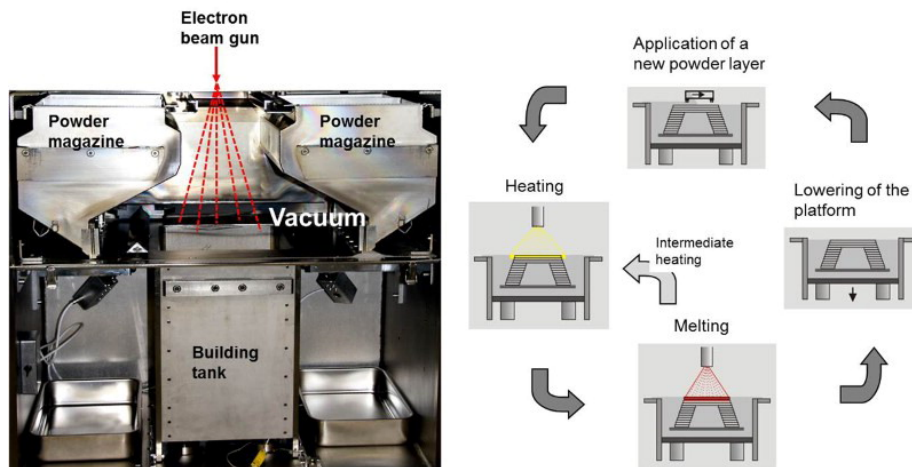


Figure 2-4: The PBF-EB internal schematic and the layerwise PBF additive process<sup>38</sup>

In contrast to PBF-EB, laser powder bed fusion (PBF-LB) uses a high-intensity laser beam to fabricate components. The smaller layer thickness (20 to 200µm), focal spot size (50 to 180µm), and powder size (~30µm) yield parts with improved surface finish and dimensional accuracy compared to PBF-EB<sup>16,31</sup>. However, PBF-LB fabricate components at very low temperature, which leads to residual stress build up due to the rapid cooling rate with the application of each

layer. To limit part distortion during printing, parts are printed directly onto the build platform, requiring post-machining. The residual stresses in the part can lead to premature build failure in higher strength alloys such as titanium or Inconel and reduced fatigue<sup>46,47</sup> and fracture toughness properties<sup>48-50</sup>, where a stress-relief operation is often performed. However, the overall faster manufacturing turnaround and lower machine costs have made it a very popular metal AM method. Recent research on PBF-LB utilizes a machine learning approach for predicting metal performance<sup>51</sup>, where data-driven explicit models were developed to predict mechanical properties with respect to the process parameters.

The quality of the metal components manufactured by DED depends on the type of heat source, build environment, deposition parameters, and the powder feedstock. The DED process focuses a heat source (laser, electron beam, or electric arc) to melt the feedstock material (powder or wire) onto a substrate<sup>52</sup>. In contrast to the PBF processes, the flexibility of the DED platform is not restricted by size, making it popular in fabricating large-scale components or in repair of low quantity parts<sup>53</sup>. For example, some DED technologies fabricate components in atmosphere-controlled environment or vacuum, while other systems use an inert gas shroud to limit contamination and oxidation. This allows simultaneous printing or multiple axis deposition to fabricate complex components, in a large work envelope. However, the larger layer thickness (250 to 500  $\mu\text{m}$ ), fast printing speed (0.5 – 10kg/hr.), and large spot size (0.3 to 3mm) result in components with residual stresses, shrinkage, poor dimensional accuracy and low density, where secondary post-processing is often required to obtain engineered components<sup>52,53</sup>. Recent research in DED manufacturing has developed an increased efficiency in manufacturing large-size lattice structures, where Xu et al.<sup>54</sup> developed parallel multi-arc method to fabricate components with reduced distortion in a shorter time. Fabricating multi-material components is also another popular area of investigation, where metal-ceramic composites can introduce new exciting materials for structural applications<sup>55</sup>. However, to fabricate complex multi-material components with acceptable mechanical properties, a comprehensive experimentation is critical.

In summary, PBF and DED are the two commonly used metal AM technologies capable of fabricating complex engineered components, summarized in Table 2-1. Understanding the printing process and the resulting structure and mechanical properties is essential for producing high-quality parts.

Table 2-1: Comparison of metal AM processes <sup>16, 31, 38, 52, 53</sup>

<b>AM Process</b>	<b>PBF</b>		<b>DED</b>		
<b>Heat Source</b>	<b>Electron</b>	<b>Laser</b>	<b>Electric Arc</b>	<b>Electron Beam</b>	<b>Laser</b>
<b>Power (W)</b>	50 – 7000	200 – 1000	1000 – 3000	500 – 2000	100 – 3000
<b>Speed (mm/s)</b>	10-1000	10-1000	5 – 15	1 – 10	5 – 20
<b>Dimensional Accuracy (mm)</b>	0.04 – 0. 2	0.04 – 0. 2		1 – 1.5	0.5 – 1
<b>Surface Roughness (µm)</b>	10 - 50	5 - 20		8 – 15	4 – 10
<b>Materials</b>	Titanium, Cobalt Chromium, Magnesium, Inconel	Aluminum, Titanium, Stainless Steel, Inconel	Aluminum, Titanium, Stainless Steel, Inconel	Titanium, Stainless Steel, Inconel	Aluminum, Titanium, Stainless Steel, Inconel
<b>Advantages</b>	Negligible Residual Stresses, lamellar microstructure, vacuum, rapid print speed	Fine lamellar microstructure, better surface roughness, improved dimensional accuracy, higher metal density	Used in repair or hybrid systems large build platform,		
<b>Disadvantages</b>	Poor surface finish, long cooldown period	High residual stresses, post-processing required to remove parts from platform,	Poor dimensional accuracy, poor surface finish,		

## 2.2 Process-Induced Attributes

Rapid solidification due to the hatching melting process results in a fine microstructure similar to a quenching treatment. With the addition of each layer, the previously deposited layers undergo repetitive heating and cooling, resulting in complex thermal cycling that must be considered when evaluating the microstructure and residual stresses. Additionally, process parameters dictate the quality of the metal. Specifically, the scan speed and beam direction dictate the shape and size of the melt pool and solidification rate, influencing the resulting meso-structure: grain orientation, grain size <sup>56-58</sup>, defect formation <sup>59-61</sup>, and surface roughness <sup>62-64</sup>. These factors together yield components with unique microstructure and mechanical properties which differ from traditionally manufactured components. The following sections will provide an overview of the AM process-induced features including microstructure, flaws, residual stresses, and surface roughness.

Table 2-2: The defect types, causes and characteristics in metal AM

<b>Defect Type</b>	<b>Cause</b>	<b>Characteristics</b>
Gas porosity	Gas entrapment/ vaporization, or excessive energy	Spherical gas pores
Lack of fusion	Insufficient energy or scan parameters	Large, flat, and irregularly shaped, often found between layers
Unmelted powder	Insufficient energy or hatch parameters	Partially or incomplete melted powder
keyholing	Excessive energy	Large and round shape
Cracks/Delamination	Residual stresses	discontinuity in material
Surface roughness		partially fused particles, unmelted/surface discontinuities

### 2.2.1 Microstructure

The microstructure of metal AM alloys depends on process parameters, thermal cycling, geometry, and sample orientation. In both the PBF and DED printed alloys, a columnar grain structure is often observed due to the repeated thermal cycling<sup>65</sup> and the continued growth of grains from previous layers as seen in Figure 2-5. This grain structure influences anisotropic mechanical properties<sup>66-68</sup>, making post-processing often desired. Therefore, researchers have rigorously investigated process parameters to optimize the metal AM microstructure, shown in Figure 2-6. Kumar et al.<sup>69</sup> changed the checkerboard microstructure in PBF-LB changed to a more globular and equiaxed microstructure as scan rotation changed from 90° to 67°. Liu et al.<sup>70</sup> further explored the transition mechanism from columnar grains to equiaxed structures, demonstrating the transition is controlled by undercooling when changing from a spot strategy to line melt. However, the anisotropy in microstructure and the subsequent mechanical properties continues to prevail.

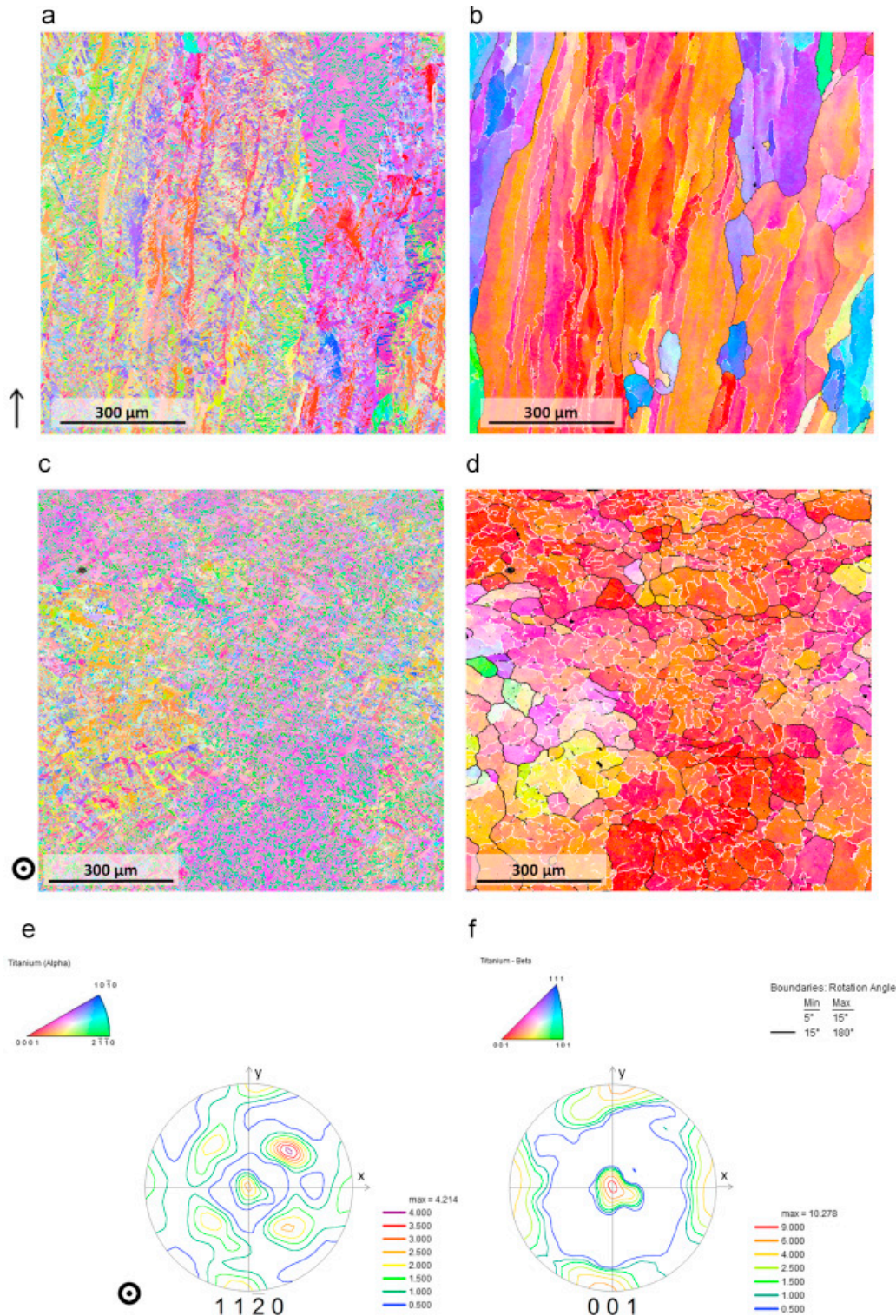


Figure 2-5: EBSD maps of the typical microstructure of PBF-EB Ti6Al4V exhibiting columnar prior  $\beta$ -grain formed along the build direction with a basketweave  $\alpha+\beta$ , and  $\alpha$  colony microstructure<sup>71</sup>

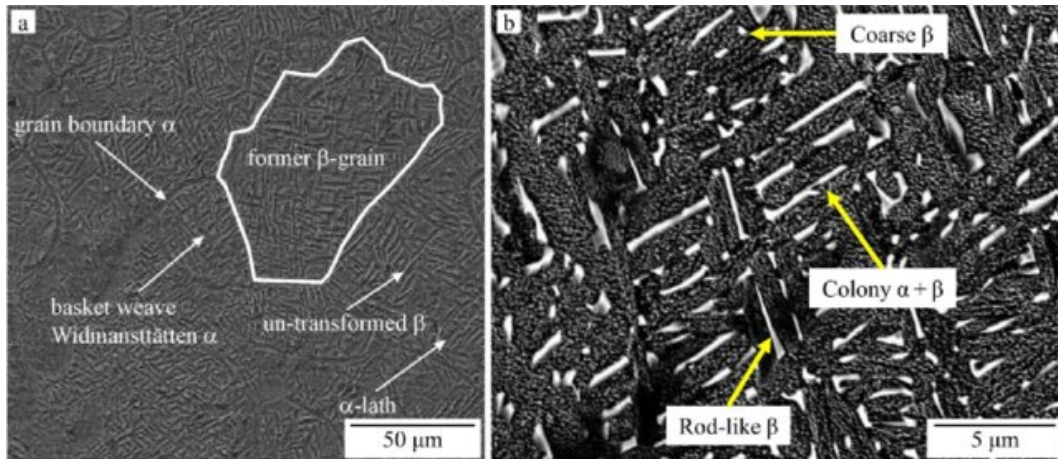


Figure 2-6: SEM images of PBF-EB microstructure.<sup>72</sup>

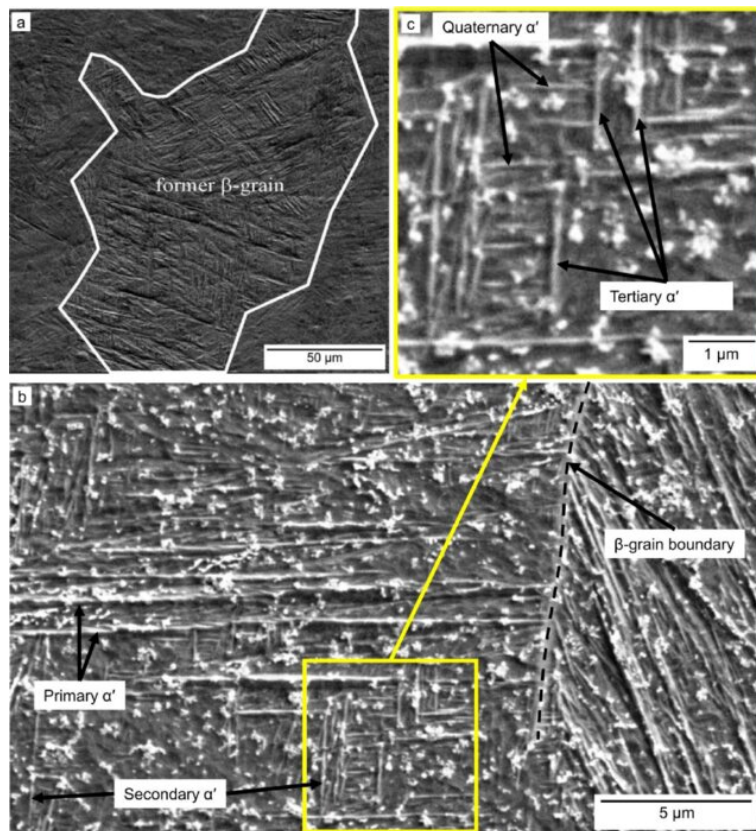


Figure 2-7: SEM images of PBF-LB microstructure.<sup>72</sup>

While a variety of alloys have been explored for metal AM, this review will mainly focus on the behavior of titanium alloys. The rapid solidification of the metal AM process results in a component with a fine microstructure, often containing fine martensitic  $\alpha'$  phase shown in Figure 2-6 and Figure 2-7. Due to the elevated build temperature in the PBF-EB process, the microstructure is further transformed into a more ductile  $\alpha+\beta$  basketweave microstructure, within

the columnar prior- $\beta$  grains<sup>38</sup>. Studies have reported that the columnar grains may have a more significant effect on anisotropy than the weak  $\alpha$  phase texture, with the mechanical properties are dictated by the prior- $\beta$  grains and basketweave microstructure  $\alpha+\beta$ <sup>73</sup>. Post processing treatments can further be employed to alter the component microstructure to obtain desired properties<sup>74</sup>. Stress relieving between 480 - 650°C can transform the fine martensite  $\alpha'$  towards  $\alpha$ , while a higher temperature annealing (705 – 975°C) can promote formation of  $\beta$  precipitates along the  $\alpha$ -laths and coarsening of the  $\alpha$ -laths<sup>75</sup>. Alternatively, heat treatments above the  $\beta$ -transus temperature of 950°C can alter the microstructure through recrystallization, globularization, and prior- $\beta$  grain growth, removing the anisotropic grains formed during the AM fabrication process. The influence of microstructure of the metal AM properties will be further explored in the following mechanical property sections.

### *2.2.2 Internal Defects*

Process parameters also influence the formation of internal defects, which ultimately affect the quality of metal AM components. Flaws includes gas porosity, lack of fusion (LOF), inclusions, and keyholing. These flaws reduce metal density and act as a source of crack initiation under loading. The larger track size of the DED process and lower input energy can lead to partially unmelted regions<sup>76</sup>. Therefore, optimizing process parameters is critical to achieve full dense components by altering the layer thickness and scan strategy. This is especially critical as there is a direct link between the energy input and defect formation. Insufficient energy can result in partially molten areas and LOF defects shown in Figure 2-8, which are often found between or across multiple layers and exhibit an irregular shape with sharp corners. Conversely, excess energy input leads to an unstable melt pool, causing spatter and constituent vaporization, resulting in trapped gas particles and keyhole defects<sup>77</sup>.

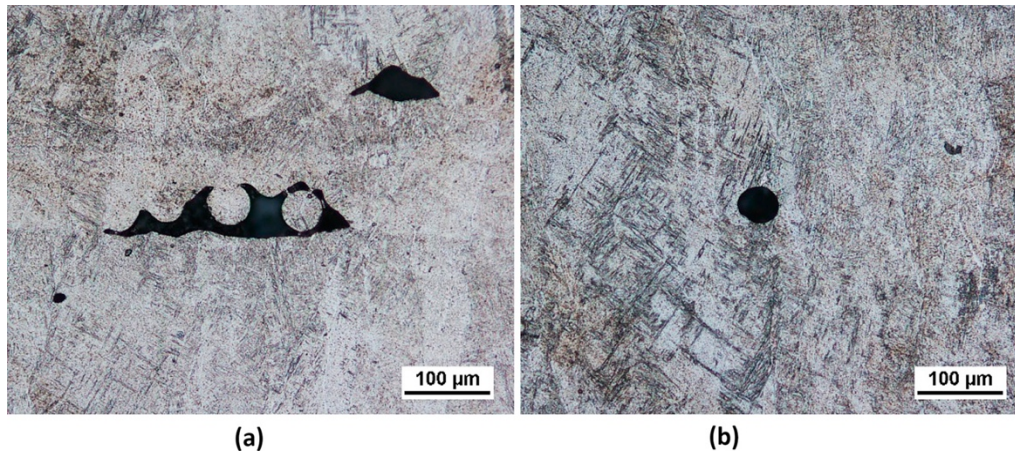


Figure 2-8: High magnification images of (a) LOF and (b) porosity defect. The LOF defect forms between two layers and contains unmelted or partially melted powder particles. <sup>78</sup>

Flaws may act as crack initiation sites under loading, which is detrimental to fatigue behavior. However, not all flaws are created equal. The shape, size, and location (relative to the external surface or other defects) influence the mechanical properties, where in-depth investigations on effects of defects are vital <sup>79–81</sup>. The three defect characteristics of interest are sphericity, aspect ratio, and size. Sphericity measures how spherical the defect is and is calculated as the ratio of the sphere and flaw's surface area, shown in Figure 2-8. Aspect ratio is the ratio between the smallest and largest dimension of the bounding box the defect encompasses. And the defect size is the largest diameter of the flaw. These characteristics help differentiate between near-spherical gas pores and the flat, irregularly shaped LOF defects. The porosity diameter has been correlated to the melt pool size, with the PBF-LB exhibiting smaller average diameters than PBF-EB, while hatch spacing dictates the LOF size. Tamas-Williams et al. <sup>59</sup> observed LOF defects often form roughly 0.5 mm from the sample surface, coinciding with the external contour and internal hatching scan overlap in the PBF-EB process. Changing the laser scan orientation or hatching overlap between adjacent melt-pools has been successful in reducing large LOF defects <sup>69</sup>. Powder feedstock also influences porosity in samples <sup>82</sup>. While optimizing process parameters is the first essential step in fabricating PBF-EB components, using appropriate feedstock is crucial for achieving desired mechanical properties.

### 2.2.3 Residual Stresses

The rapid localized heating and fast cooling experienced with the addition of each layer result in localized heat accumulation, leading to formation of high thermal stresses. With the fast solidification rate, these thermal stresses turn into residual stresses, which can lead to geometric distortion and premature build failure<sup>83</sup>. The elevated build temperature of the PBF-EB process acts as a stress-relief process, making residual stresses negligible. However, the lower process temperature of the PBF-LB and DED processes yields components with residual stresses along the build direction, sometimes 50-80% of the yield strength of the alloy, with the highest concentration near the part-platform interface<sup>84,85</sup>. The surface and subsurface residual stresses act as sources of crack initiation, ultimately leading to cracking, warping, and potential build failure. To diminish the tensile residual stresses, post-processing is often implemented. Heat treatment can significantly improve the mechanical properties of PBF-LB and DED samples<sup>67,86,87</sup>. However, post-processing can be time-consuming and costly, motivating process parameter optimization. Ali et al.<sup>88</sup> demonstrated the magnitude of residual stresses is related to the length of the scan line, where long uninterrupted lines of laser travel are undesired. Through alternating the scan strategy to 90°C and optimizing the layer height, residual stress build up were shown to be reduced. In another study, Ali et al.<sup>89</sup> significantly reduced the tensile residual stresses formed during fabrication of PBF-LB Ti6Al4V by preheating the build platform. They found that preheating the build temperature to 570°C resulted in enhanced the strength and ductility of the metal through decomposition of fine microstructure. While several methods are available in mitigating the residual stresses, the influence on mechanical properties need to be considered.

### 2.2.4 Surface Roughness

The poor surface finish of metal AM parts depends on the layer-by-layer process, which creates staircase effect, partially melted powder particles, or unmelted regions, shown in Figure 2-9. The surface finish depends on the AM technique, with DED samples exhibiting the best surface finish (4-15  $\mu\text{m}$ ) compared to PBF-LB (7-15  $\mu\text{m}$ ) and PBF-EB (25  $\mu\text{m}$ )<sup>62,63,90</sup>. The process parameters, powder feedstock, build orientation, and geometry which influence microstructure, defects, and residual stresses, also impact the surface finish of AM components. One of the largest sources of variation in surface roughness is related to build orientation. Components with a downward or angles surface exhibit the roughest surface finish, while upwards facing surfaces

have the best finish <sup>91</sup>. While studies have reported the rough finish promoting bone-growth in biomedical applications <sup>92,93</sup>, the surface defects can be detrimental in load-bearing applications <sup>26,94</sup>. The as-built surface acts as dominant source of crack nucleation under fatigue loading, making post-processing applications vital for achieving long lasting AM parts.

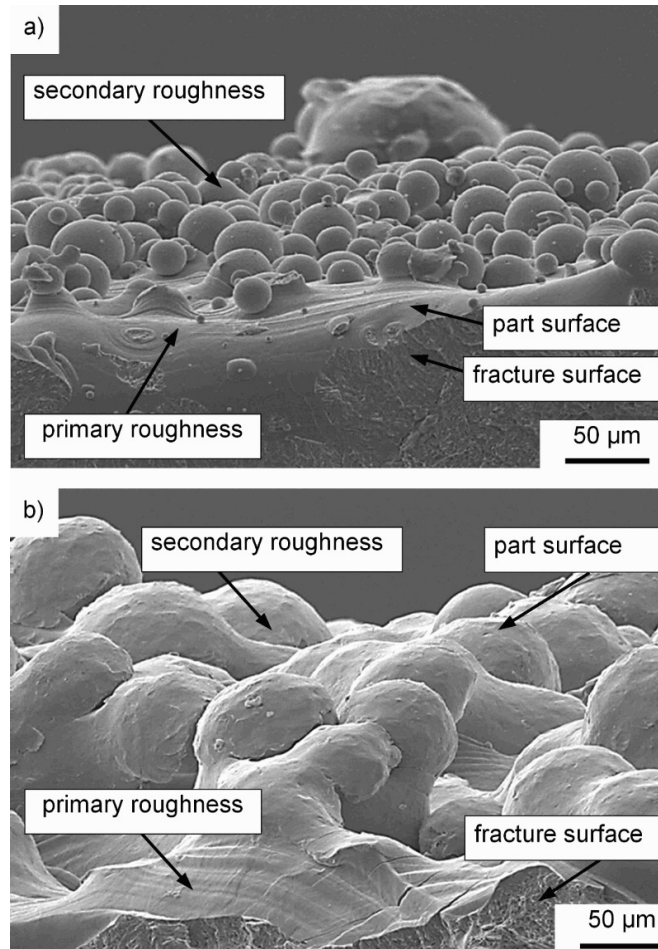


Figure 2-9: The rough surface exterior of PBF-EB components composed of partially melted powder particles <sup>95</sup>

In summary, the process-induced features form due to the metal AM fabrication process and can significantly influence the quality and performance. As a result, understanding the impact of process parameters and thermal cycling on the microstructure, flaws, residual stresses, and surface roughness is essential for optimizing the quality and performance of metal AM components.

## 2.3 Failure in Metals

In manufacturing, a “failure” typically occurs when a part does not meet its intended function due to defects, such as those discussed in the previous section. Cracks may arise from imperfections in the metal that cannot withstand localized stresses, leading to crack initiation and growth. Such defects typically exhibit a much larger size than anticipated in the components’ factor of safety, leading to premature failure even when the applied loading is lower than the materials’ tensile strength. Figure 2-10 provides a summary of the typical failure types in aircraft components, with fatigue failure making up the majority of failure. This becomes a concern especially under fatigue loading, where cyclic loading experienced by the component can result in catastrophic fracture.

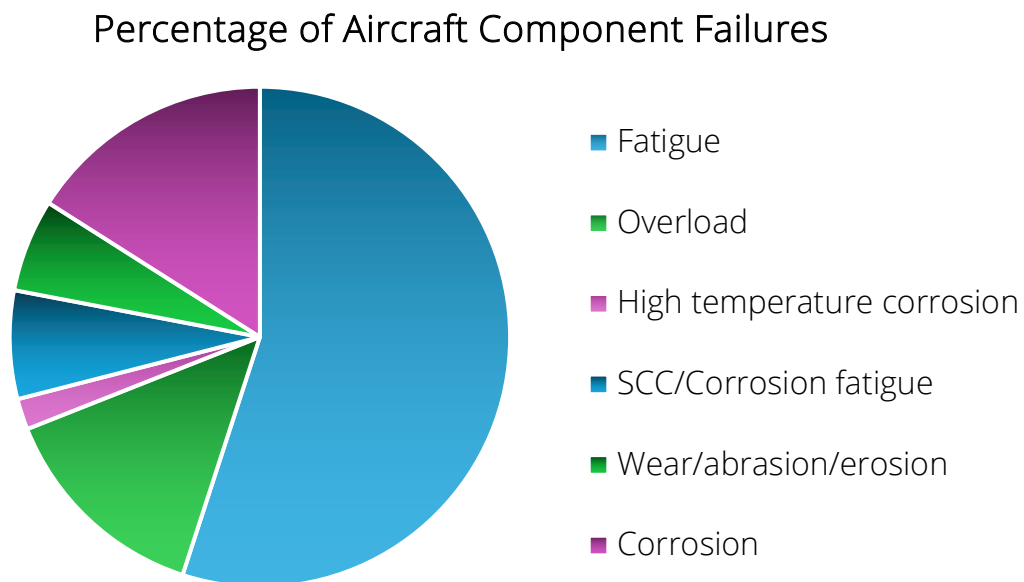


Figure 2-10: The types and percentage of aircraft component failures <sup>18</sup>

Process-induced defects often reduce mechanical properties and cause premature failure. Internal defects and microstructural imperfections may cause microcracks under applied loading, which continue to grow until reaching a critical size, resulting in failure. In contrast, surface roughness irregularities result in a much larger stress concentration, where internal defects would need to be 4-10x the size to have the same influence <sup>96,97</sup>. While defects, internal or external, are often responsible for the crack nucleation, small crack growth is governed by the microstructure <sup>98</sup>. Specifically, the strength of a material is influenced by how easily dislocation motion and slip occur. Dislocations under applied loading result in plastic deformation, which is often responsible

for work hardening. As the crack grows larger, crack propagation depends on the material. Therefore, as components experience loading, many different aspects influence the mechanical behavior and can be a source of property variation.

Fracture mechanics provides a methodology to evaluate behavior of imperfect components, helping to understand and prevent structural failures by providing a "flaw tolerance limit". In cracked components, the critical stress level is described by the stress intensity factors (SIF), which depend on the size of the crack and components' geometry <sup>99</sup>. In conventional alloys, minute variations in composition, microstructure, and residual stresses can adversely affect resistance to fracture. This issue is exacerbated in metal AM due to the layer-by-layer fabrication process, where post-processing is often necessary to achieve properties comparable to traditionally manufactured alloys.

The microscopic events within the plastic zone size, such as microstructure, determine the damage tolerance. Differences in grain size, orientation, and colony structure influence crack growth behavior <sup>98</sup>. In addition to these intrinsic features (microstructure, defects, and plastic zone formation), extrinsic features such as material structure can increase crack growth resistance without affecting strength. As such, it is important to understand how each of the process induced-features influence mechanical properties, and the overall process-structure-property relationship which ultimately effect metal AM component in engineered applications.

## 2.4 Mechanical and Fracture-Critical Properties

To be able to best use metal AM components, it's not just key to understand their respective process and process-induced features. One of the key things that is being more concentrated on is developing a comprehensive understanding of the process-structure-property relationships. In doing so, we can't just look at the metal microstructure, defects, and process separately, but how they are all intertwined together. Therefore, to aid in understanding how each influences the overall component behavior, an overview of mechanical properties and the complexity in achieving parts with a high strength, while maintaining superior fracture resistance can be achieved.

### 2.4.1 Tensile Behavior

The high strength-to-weight ratio that makes titanium Ti6Al4V alloy the "workhorse" of the aerospace industry in conventional manufacturing <sup>100</sup> also inspires AM research <sup>19,20</sup>. While the

structural properties of titanium make it a popular alloy, its high cost and reactivity result in usage in niche applications. The features that contribute to property variation in conventionally produced metals (e.g. surface roughness, internal defects, chemical composition, and microstructure) can be further exasperated by the layerwise manufacturing process. In essence, the properties of AM-produced parts can differ significantly from their conventionally manufactured counterparts due to anisotropy<sup>23,101,102</sup>, surface finish<sup>103,104</sup>, and porosity<sup>22,23,105,106</sup>. The following section provides an overview of how each of these factors influence the tensile properties and contributes to the variation observed in current literature.

The fine microstructure produced by the metal AM process typically results in high static strength and low ductility, following the Hall-Petch relationship<sup>56,107,108</sup>. Table 2-3 provides a summary of select tensile properties reported for AM Ti6Al4V, fabricated by PBF-EB, PBF-LB, and DED, compared to wrought and cast alloys. As seen, the yield strength (YS) and ultimate tensile strength (UTS) are comparable to, and in some cases even exceed, traditionally manufactured Ti6Al4V. However, ductility or elongation at failure (EF) is significantly lower, especially in the PBF-LB samples. The fast-cooling rate in the PBF-LB process yields a higher strength but brittle alloy. In contrast, the slower cooling rate in the DED process and higher build temperatures of the PBF-EB process yields alloys with comparable YS, UTS, and EF to wrought. The higher ductility is due to the transformation of the fine  $\alpha'$  martensite to a lamellar  $\alpha+\beta$  microstructure<sup>56</sup>. However, in some cases, ductility as low as 2% was reported in the DED process, where oxygen contamination contributed to the increase in strength and drop in ductility<sup>109</sup>. Schur et al.<sup>42</sup> reported similar finding in the PBF-EB process, where an increase in YS and over 50% decrease in ductility was observed with increase in oxygen content with powder reuse. Therefore, the chemical composition of alloys contributes to variation in properties, especially in reactive titanium alloys that are susceptible to oxidation.

Yield strength, ultimate tensile strength, and elongation at failure often exhibit anisotropic behavior, regardless of the metal AM process, as observed in Table 2-3. Figure 2-11 defines the sample orientation with respect to build direction. The YS and UTS properties are often higher on samples fabricated along the build direction (Z), with the most significant influence observed in metal ductility. Columnar grains typically cause the anisotropic tensile properties<sup>110-112</sup>; but, additional AM process-induced features can contribute to the scatter in the tensile properties. The

AM technology, powder feedstock, process parameters, and post-processing can influence the anisotropy observed.

Table 2-3: Summary of tensile values of metal AM, wrought, and cast Ti6Al4V alloy

Machine Type	Raw Material	Metal Condition	Orientation	Yield Strength (MPa)	Ultimate Tensile Strength (MPa)	Elongation (%)	Ref.
<b>PBF-EB</b>							
Arcam A1	Grade 5	As-Built	XY	783 ± 15	833 ± 22	2.7 ± 0.4	41
			Z	812 ± 12	851 ± 19	3.6 ± 0.9	
Arcam A2	Grade 23 (ELI)	As-Built	Z	928 ± 13.3	1,011 ± 14.8	13.6 ± 1.4	113
		HIP	Z	813 ± 14.3	908 ± 3.2	17.7 ± 0.9	
Arcam A2X	Grade 23 (ELI)	As-Built	XY	851.8 ± 5.8	964 ± 0.3	16.3 ± 0.8	114
Arcam A2X	Virgin, Grade 5	As-Built	XY	739 ± 2.7	857 ± 10.4	9.28 ± 1.06	115
			Z	733 ± 20.7	859 ± 20.5	12.2 ± 0.42	
	Reused (x10), Grade 5		XY	837 ± 2.6	940 ± 7.6	6.91 ± 0.27	
			Z	838 ± 9.5	924 ± 16.6	9.71 ± 0.46	
	Reused (x30), Grade 5		XY	1050 ± 5.3	1120 ± 8.7	3.53 ± 0.26	
			Z	1000 ± 18.5	1130 ± 188.6	7.34 ± 0.33	
Arcam Q10	50% reused powder, Grade 5	As-Built	XY	973	1032	15	116
			Z	1051	1116	12	
Aged		XY	1039	1294	10		
		Z	1001	1073	11		
Arcam A2	50% reused powder, Grade 5	As-Built	XY	1006	1066	15	116
Z			1001	1073	11		
Arcam Q20+	Compliant Grade 5	As-Built	Z	930 ± 9	1015 ± 5	13.4 ± 1.7	12
		Machined	Z	973 ± 15	1053 ± 3	13.4 ± 0.9	
	Non-Compliant Grade 5	As-Built	Z	913 ± 18	981 ± 26	4.7 ± 2.0	
		Machined	Z	973 ± 20	1045 ± 12	7.8 ± 2.1	
Arcam Q10	Grade 23, 50% reuse	1110C/2h/WQ Machined	Z	932 ± 80	1200 ± 50	1.8 ± 1.5	117
		1110C/2h/AC Machined	Z	847 ± 90	998 ± 90	13 ± 7	
<b>PBF-LB</b>							
EOS 270	Grade 23	Machined	Z	1143 ± 30	1219 ± 20	4.9 ± 0.6	106
			XY	1195 ± 19	1269 ± 9	5 ± 0.5	
SLM 250HL	Grade 5	Machined + SR	Z	961	1032	2.7	105
Realizer SLM 100	Grade 23	Machined	Z	1150	1250	4	118
			XY	1100	1150	4	
		Machined + HIP	Z	850	900	12	
<b>DED</b>							

DED-LB	Grade 5	Machined	Z (top)	945 ± 13	1041 ± 12	14.5 ± 1.2	111
			Z (bottom)	970 ± 17	1087 ± 8	13.6 ± 0.5	
			XY	960 ± 26	1063 ± 20	10.9 ± 1.4	
DED-LB	Grade 5	Annealed + Machined	Z	950 ± 2	1025 ± 2	5 ± 1	119
			XY	950 ± 2	1025 ± 10	12 ± 1	
		HIP + Machined	XY	850 ± 2	920 ± 1	17 ± 2	
DED-LB	Grade 5	Machined	Z	976 ± 35			120
			XY	924 ± 25			
		HIP	Z	909 ± 15			
			XY	879 ± 30			
EBAM	Grade 5	HIP	Z	791 ± 20			
			XY	785 ± 35			
<i>Wrought</i>	Grade 5	Annealed	Z	836 ± 9	942 ± 8	12.5 ± 1.2	121
			XY	832 ± 10	933 ± 7	13 ± 1.5	
<i>Cast</i>	Grade 5			896	1000	8	122,123

The PBF-EB process often produces parts with high surface roughness and internal defects (e.g., spherical gas porosity and irregularly shaped lack of fusion (LOF)), both of which act as crack initiation sites, reducing the tensile strength and elongation<sup>106,124–126</sup>. Machining the PBF-EB surface increased YS, UTS, and EF by 15%, 18%, and 20%, respectively. Thus, machining is often recommended, especially in PBF-EB samples. Removing the rough surface shift the source of crack initiation from the surface to internal defects<sup>101,127,128</sup>. A direct correlation was observed between the LOF pore area and EF, specifically causing scatter and reduced properties in the vertical orientation, where EF decreased with increasing pore size<sup>42</sup>. While similar trends were not observed in the horizontal orientation, minimizing LOF formation is vital for repeatable and reliable mechanical properties.

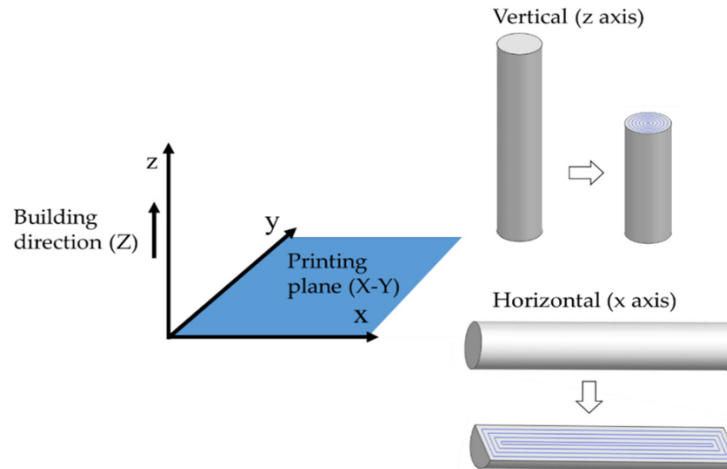


Figure 2-11: The sample orientation nomenclature with respect to the build orientation <sup>129</sup>

Even with optimal parameters, the complex thermal cycling of the PBF process contributes to property variability. Repeated heating and cooling during melting of neighboring and subsequent layers form a graded microstructure due to the reduced cooling rate <sup>114,130</sup>. Yadollahi et al. <sup>131</sup> found that the time between printing each layer in PBF-LB influences the microstructure and the resulting the mechanical properties. Additionally, changes in sample volume <sup>132,133</sup>, orientation <sup>127</sup>, and support structure <sup>134</sup> further influence the thermal gradient and cooling rate within the sample, ultimately determining the local microstructure and mechanical behavior. For example, Zhao et al. <sup>118</sup> investigated the tensile properties of PBF-EB Ti6Al4V with different thicknesses, showing a 60% decrease in  $\alpha$ -lamellae size as thickness decreased from 7 to 1.2 mm, resulting in a drop in elongation from 14% to 3% due to the finer microstructure. In the same study, the PBF-LB samples also exhibited finer  $\alpha'$  grains in the thinnest samples; however, the large density of internal defects overshadowed any mechanical property variation resulting from microstructure. Similar geometry-dependent mechanical properties have been demonstrated, where a decrease in sample thickness resulted in an increase in strength and hardness, following the Hall-Petch relationship expected with decreasing  $\alpha$ -lath thickness <sup>135,136</sup>. For this reason, engineers need to fabricate test samples according to the final engineered component when validating mechanical properties.

The thermal gradient within each sample is further exasperated as a different temperature and cooling rate throughout the build space. Landau et al. <sup>137</sup> demonstrated that the center of the build space experiences a slower in cooling rate resulting in  $\sim 70^\circ\text{C}$  difference in temperature between the center and the edges of the PBF-EB Q20+ build space. The increased conductivity of

the build plate used in older PBF-EB generations also influence cooling rate, resulting in a finer microstructure in samples at the start of the build and towards the edges of the build space compared to the coarser microstructure towards the end of the build space<sup>22,23, 127,138</sup>. As such, Derimow et al.<sup>139</sup> revealed a decrease in YS with increasing build height in samples up to 35mm. Similarly, Hrabe et al.<sup>140,141</sup> revealed a 3% and 30% drop in YS and EF, respectively, as samples were placed closer to the edges of the build space<sup>23</sup>. Other studies on build variation found the change in properties was also attributed to the 3x increase in internal voids in samples built closer to the edge of the build space, in addition to the change in microstructure.

While these studies have been foundational in understanding the variation in mechanical properties with changes in design parameters, they evaluated the influence of each parameter individually. As a result, there is a lack of holistic understanding of how the parameters influence property variability and interaction with each other. In contrast, our previous study by Ghods et al.<sup>127</sup> evaluated the part-to-part variation with respect to sample geometry and location, using a multi-factor approach to maintain traceability and pinpoint the sources of variation. The investigation revealed that sample geometry and location each significantly influence the property variation, where an increase in defects resulted in a 30% drop in EF and a 5% increase in YS due to the finer microstructure.

To improve tensile properties and reduce scatter in mechanical properties, various treatments have been performed in PBF and DED Ti6Al4V. These treatments include machining<sup>26,42</sup>, annealing<sup>87,117</sup>, Hot isostatic pressing<sup>117,142,143</sup> and tool-less surface treatments (i.e., cavitation, shot, or laser peen)<sup>144,145</sup>. Removing the rough PBF-EB surface finish resulted in a 16% increase in YS and 30% increase in ductility<sup>42</sup>. Annealing treatments are often performed on the PBF-LB alloys to mitigate the residual stresses and improve ductility. However, even with a stress relief process, the ductility of the PBF-LB alloys remains below those of PBF-EB and wrought alloys, where multiple processes are required. While stress relieving has not resulted in a change in the PBF-EB mechanical properties due to the high build temperature and slow post-print cooling, sub- $\beta$  treatments have promoted recrystallization of columnar grain to a preferred equiaxed, resulting in an increase in fracture resistance<sup>146</sup>. Ter Haar et al.<sup>147</sup> evaluated a duplex heat treatment process to obtain EF as high as 20% by transforming the microstructure into a bimodal structure containing equiaxed primary  $\alpha$  phase and a secondary lamellar  $\alpha+\beta$  structure. However, the internal pores and defects remained within the metal.

HIP is a post-processing treatment often used in the aerospace industry to reduce internal defects and residual stress and improve mechanical properties in conventional alloys<sup>148</sup>. While the HIP process reduces internal defects and increases ductility, the coarse microstructure leads to a decrease in tensile properties<sup>149,150</sup>. Similarly, Keist et al.<sup>120</sup> demonstrated a decrease in strength overall from the coarsening of the  $\alpha$ -lath structure without changes to the anisotropic mechanical properties after HIP application of DED Ti6Al4V. Therefore, is there an increasing interest in performing HIP treatments that deviate from the standard recommended 920-950°C/100MPa/2hrs<sup>149,150</sup>. Ahlfors et al.<sup>151</sup> evaluated multiple HIP processes, founding the highest strength in PBF-EB properties at 800°C, due to the limited coarsening of the finer  $\alpha$ -lath microstructure. A super- $\beta$  HIP treatment (1030°C/175MPa/2hrs.) performed by Zhang et al.<sup>74</sup> demonstrated enhanced YS and UTS, and significant improvement in EF compared to samples heat treated at the same temperature. While the columnar grains remained in the SR samples, the transformation to equiaxed grains in the HIP samples resulted in the isotropic strength and ductility. Overall, post-processing metal AM components is beneficial. However, further attention is needed on evaluating modified HIP treatments that reduce internal defects while refining the microstructure to obtain superior strength and ductility.

#### *2.4.2 Fracture Toughness*

While the tensile properties of metal AM have been heavily investigated, information about fracture is comparatively scarce. This is surprising because fracture toughness is a key property needed for selecting appropriate materials for use in engineered components. For the adoption of AM components, material reliability and structural integrity are essential to ascertain their performance for long-term use. The diverse processing conditions contribute to variation in tensile properties also influences fracture toughness<sup>17</sup>. Intensive effort is needed to understand the processing conditions that result in repeatable and reliable mechanical performance. The combination of microstructure and residual stresses from the metal AM process considerably reduces ductility, resulting in a decrease in fracture resistance. By altering the chemical composition and fabrication process, microstructural changes enhance fracture toughness. However, build orientation shown in Figure 2-12 and process parameters result in defects which contribute to scatter in properties. Using optimal process parameters and secondary heat treatment

can minimize defects. Furthermore, the increase in ductility and decrease of internal defects after HIP treatment have shown promising results in enhancing fracture toughness of metal AM.

The typical fracture toughness for wrought Ti6Al4V ranges from 30 –100 MPa√m, depending on microstructure, orientation, and heat treatment<sup>98,121</sup>. The fracture toughness of PBF-EB and DED is comparable to wrought alloys and double those of PBF-LB<sup>68,152</sup>, summarized in Table 2-4. The residual stresses coupled with the fine martensitic microstructure in as-fabricated PBF-LB alloys contribute to lower fracture toughness properties. The higher fracture toughness of PBF-EB and DED in the as-built condition is a product of the preferred  $\alpha+\beta$  basketweave microstructure. A stress relief application in PBF-LB yield a metal with comparable toughness to PBF-EB and DED, with the refinement of  $\alpha'$  structure into the more stable  $\alpha+\beta$  preferred in-service conditions<sup>94</sup>. Kumar et al.<sup>153</sup> reported superior fracture toughness up to 106 MPa√m (40-100% increase) with a duplex heat treatment because of the  $\alpha'$  decomposition to  $\alpha+\beta$  basketweave structure in PBF-LB Ti6Al4V and a ~10-20% decrease in YS. In contrast, a duplex heat treatment of PBF-EB Ti6Al4V performed by Dzugan et al.<sup>154</sup> resulted in a smaller 9% increase from 63 to 70 MPa√m, where annealing altered the size and morphology of the  $\alpha$  phase, where the overall coarsening of the  $\alpha$ -lamellae contributed to the 6% decrease in YS. The combination of increased ductility and the lamellar structure after annealing often leads to some of the highest fracture toughness in metals but at a cost to tensile strength<sup>155</sup>. Similar to conventional alloys, the metal AM process history and heat-treatments have a complex influence on microstructure, making it challenging to achieve both high strength and fracture toughness.

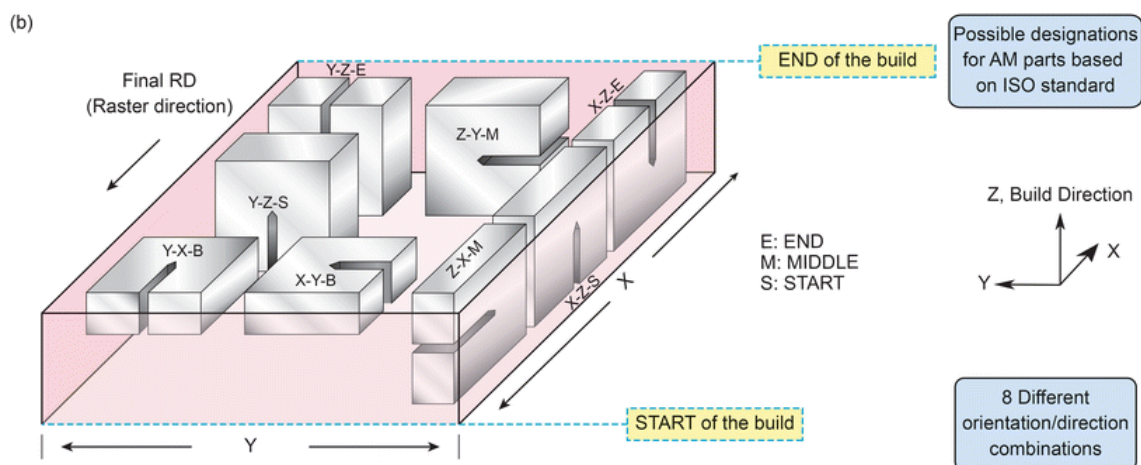


Figure 2-12: Schematic of CT specimens orientation designation, with respect to the build and raster direction<sup>138</sup>

Even though acceptable fracture toughness has been reported in metal AM alloys, a large range of values in the as-built condition (45 – 110 MPa√m) and post-processed condition (61 to 119 MPa√m) hinder adoption in engineered applications. One potential source of variation in properties is ascribed to the process-induced anisotropy<sup>41, 138,156</sup>. In wrought alloys, the rolling direction results in anisotropic fracture toughness. In contrast, the columnar prior  $\beta$  grains are one of the main contributors to anisotropy in metal AM fracture toughness. Seifi et al.<sup>13</sup> and Dzukan et al.<sup>154</sup> reported the ~15% difference in fracture toughness in the different orientations was influenced by the columnar grain structure in PBF-EB Ti6Al4V. An increase in crack path tortuosity was observed as the crack propagated through the grains, in contrast to the easier crack path along the brittle  $\alpha$ -grain boundary ( $\alpha$ -GB). The crack tortuosity observed in AM alloys leads to extrinsic toughening from the meso-structure, where a substantial increase in fracture toughness was achieved by Paul et al.,<sup>157</sup> exceeding conventional alloys. While improving ductility can aid in increasing fracture toughness, controlling the meso-structure for enhanced properties should also be considered. Kumar et al.<sup>153</sup> evaluated the relationship between microstructure and anisotropic fracture toughness in PBF-LB Ti6Al4V, investigating the influence of process parameters and orientation-dependent properties. Near-isotropic fracture toughness values in both the as-built (48 – 54 MPa√m) and stress-relieved condition (~95 MPa√m) were obtained by changing the scan direction in PBF-LB from 90° to 67°, changing the columnar grain structure to a more equiaxed one<sup>153</sup>. However, the orientation-dependent EF and fracture toughness was not fully removed due to additional process-induced features. This orientation-dependent behavior is critical for the design and application of AM components, as it can influence performance under load.

Table 2-4: Summary of Ti6Al4V PBF-EB fracture toughness values, with average PBF-LB, wrought, and cast properties for comparison

Machine Type	Condition	Post Processing	Powder	Specimen Type	Orientation	Thickness (mm)	Fracture Toughness, K <sub>Q</sub> (MPa√m)	Ref.
<b>PBF-EB</b>								
Arcam A1	As-Built			CT	XY ZX	40	110 ± 8.9 102 ± 7.2	41
Arcam A2	Annealed, milled HIP, milled	710C for 2h, argon cooled HIP at 920C @100 MPa for 2hr, cooling not reported		CT	ZX ZX	25	106.5 ± 3.5 119	94
Arcam*	As-Built HIP			CT	XY ZX XY ZX		96.9 78.1 99 83.1	156
Arcam A2	As-built (ELI)		recycled ELI powder	3PB	LT (XY) LS (XZ) TL (YX) SL (ZX)	9 10 9 10	68, 80 76 67 65	138
Arcam A2	As-Built (ELI) HIP	950C @ 100MPa for 3 hrs., furnace cooled		3PB	XY ZX XY ZX	10	60.2 ± 13.9 80.4 ± 14.8 61 67.7 ± 9.2	13
Arcam A2X	As-Built (ELI) HIP	950C @ 100MPa for 3 hrs., furnace cooled		3PB	XY ZX XY ZX	10	82 97 ± 7.2 84 92 ± 6.9	
Arcam A2X	As-Built Annealed HIP	1035C for 30min, water quench. 390C for 240min, air cooled 920C at 100MPa for 2h, rapid quench	reused powder, 6X	CT (data from middle specimen)	XZ ZX XZ ZX XZ ZX	4	59.2 ± 2.0 68.8 ± 1.2 65.5 ± 2.0 74.7 ± 2.7 61.1 ± 4.7 61.6 ± 2.0	154
<b>Laser (PBF-LB)</b>								
EOS M280	Annealed HIP	710C for 2h, argon cooled HIP at 920C @100 MPa for 2hr, cooling not reported		CT	ZX ZX	25	49.5 ± 1.5* 93.5 ± 0.5	94
EOS M280	SR	670C/5h	14	CT	XY XZ	16	40.3 ± 3.4% 45.6 ± 4.3%	152

					ZX		38.1 ± 1.6%	
					O/45		38.9 ± 6.3%	
	HIP	920C/2h/100MPa	15		XY	16	64.9 ± 1.6%	
				XZ	67.3 ± 5.3%			
				ZX	59.4 ± 0.2%			
				O/45	63.6 ± 0.5%			
<b>EOS M280</b>	Stress-Relieved			CT	YXZ	6.5	80 ± 4	158
					ZXY		85 ± 4	
<b>Wire Arc</b>	AB			CT	XZ	5	73.9	50
					ZX		81.8	
					XZ	19	74.3	
					ZX		82.1	
<b>Hybrid Wrought + DED</b>	AB				ZX	20	65.3	159
	SR	solid solution 1000C and age 540			CT	ZX	20	
<b>Wrought</b>	Air-cooled						44 - 66	121
<b>Cast</b>	Annealed						77 ± 12.5	121

\*machine generation and thickness not provided

\*\*K<sub>q</sub> values reported

\*\*\*K<sub>c</sub> values reported

In addition to microstructure, it is important to consider additional micro-mechanism influencing fracture behavior, such as residual stresses and porosity. For example, an inverse relationship between fracture toughness and residual stresses in PBF-LB Ti6Al4V has been observed. In addition to the decrease in fracture resistance in the presence of residual stresses, Cain et al.<sup>48</sup> also observed residual stresses contributing to orientation dependent fracture toughness. Anisotropic fracture toughness can similarly be influenced by porosity, where Muro-Barrios et al.<sup>80</sup> reported a correlation in toughness to the size, location, and type of defect. The small spherical pores located just above or below the crack path resulted in a tortuous crack path or dissipating energy by creating smaller clusters of cracks, increasing toughness. However, the larger LOF defects decreased crack path resistance by acting as elongated cracks in the metal and promoting rapid crack growth. Altogether, the process-induced microstructure, residual stresses, and porosity contribute to variation in mechanical properties, making reproducibility and repeatability difficult. However, through comprehensive understanding and control of process parameters, enhanced fracture toughness of metal AM alloys can be achieved. Furthermore, the orientation and location of internal defects can further exacerbate the anisotropic properties, where LOF defects oriented parallel to the crack path significantly reduce the resistance to crack growth. However, the spherical gas pores located above or below the crack path may result in a more tortuous crack path

by dissipating energy through crack deflection. Conway et al.<sup>160</sup> implemented architected porosity where internal pores are intentionally designed to produce a weak interface which delayed fracture by aiding in arresting and deflecting the crack path, resulting in a fourfold increase in fracture toughness, depending on the material. Therefore, a complex relationship exists regarding the process-induced defects and microstructure, which make predicting fracture toughness of metal AM difficult.

An improvement in fracture toughness with increased density, where an increase from 95 to 99% contributed to an increase from 45 to 60 MPa $\sqrt{m}$  in powder metallurgical Ti6Al4V<sup>155</sup>. The highest fracture toughness in metals where pores were isolated and randomly scattered. For randomly and far apart pores, there is less likelihood of pore interaction, making the crack growth harder and increasing resistance. The increase in density in the metal is also recommended in enhancing the tensile behavior, which would also have an expected improvement in fatigue strength. A relationship between pore volume fraction and fracture toughness of PBF-EB Ti6Al4V was observed, where a ~30% decrease in fracture toughness resulted from an increase in pore vol.% from 0.002% to 0.02%<sup>13</sup>. The increase in pore vol.% was suggested to be a result of the hatching pattern, with a large concentration of defects located along the external edge of the samples, where a notch would exhibit the highest stresses and decrease in resistance. The study also found the PBF-EB machine generation influenced the size of defects, where a ~25% difference in fracture toughness was observed between the A2 and A2X systems<sup>13,59</sup>. In addition to the density of internal defects, pore size also plays a role in fracture toughness. Even though toughness was found to be less sensitive to porosity than tensile properties in a study by Araujo et al., an increase in homogenization temperature resulted in a threefold increase in internal gas pores, reducing fracture toughness by 30%<sup>86</sup>.

The diverse processing condition that contributes to variation in tensile properties also influences fracture toughness<sup>17</sup>, where intensive effort is needed to understand the process-structure-property relationships. Seifi et al.<sup>13,154</sup> and Dzukan et al.<sup>154</sup> demonstrated an 15-30% fracture toughness variation due to the local microstructure throughout individual samples influenced by the cooling rate and temperature gradient. Therefore, it is not only the influence of the columnar grains and internal defects which needs to be considered, but the effect of the metal AM process on the overall fracture resistance. Specifically, this key finding necessitates further investigation of specimen geometry and spatial location is essential. Additionally, variation in

fracture toughness due to machine generation<sup>138</sup> and powder feedstock<sup>41</sup>, may further result in scatter in fracture toughness properties. Despite the extensive research on the fracture toughness of metal AM in various orientations, there is a gap in knowledge about the process-induced variability affecting crack growth resistance, potentially compromising its long-term reliability and durability, especially in PBF-EB Ti6Al4V. This gap is one of the primary motivations of this research.

A HIP post-processing treatment has been implemented in metal AM to achieve nearly-dense metals, through application of elevated temperature and high pressure. Greitemeier et al.<sup>94</sup> observed a twofold increase in fracture toughness of PBF-LB Ti6AL4V, from a 49.5 MPa√m in the annealed condition to 93.5 MPa√m in the HIP condition, while only a 10% increase in PBF-EB Ti6Al4V processed due to the existing  $\alpha+\beta$  lamellar microstructure. Similarly, Zhang et al.<sup>161</sup> reported comparable fracture toughness after a heat treatment and HIP process, where porosity was found to have negligible effects on the PBF-LB Ti6Al4V while the grain size and phase fraction had a more significant role on metal ductility and the resulting fracture toughness. Other investigations performing standard HIP treatment (920-950°C/100MPa/2h) for PBF-EB Ti6AL4V has resulted in defect-free components, but contradicting enhancement of fracture toughness is reported<sup>13, 154, 156,161,162</sup>. Seifi et al.<sup>13</sup> reported the coarsening microstructure and the change in texture compete with the reduction in defects which did not always result in higher toughness. The coarser microstructure resulted from the increase in  $\alpha$ -lath thickness, reducing the alloy's strength which would result in higher fracture toughness<sup>15</sup>. The coarsening of the microstructure has two effects on metal AM fracture toughness: the decrease in crack growth resistance due to the easy fracture path and the heightening of anisotropy due to the preferential crack growth along the columnar  $\beta$  grains. Alternatively, Dzugan et al.<sup>154</sup> attributed the reduction in fracture toughness after HIP to the higher strength and the less resistant recrystallized microstructure. One limitation of the current HIP treatments employed is the processing metal per the ASTM standard for conventional alloys. Tarik et al.<sup>163</sup> investigated the effect of two HIP treatments (730 and 950C @ 101MPa/2h) on PBF-LB CpTi, where the fracture toughness tripled in the samples treated to the lower temperature, while the higher temperature resulted in only a 30% increase in toughness due to the drastic microstructure coarsening. While ASTM F2924<sup>28</sup> provides guidelines for post-processing of metal AM Ti6Al4V, advancements in HIP optimization for PBF-LB Ti6Al4V has led to development of AMS7028<sup>29</sup>. However, its suitability for PBF-EB Ti6Al4V remains

uncertain, necessitating further research to confirm application for critical applications. Therefore, investigation of HIP treatments which differ from the standard recommendation are crucial in finding optimal process conditions for the desired engineered application. Moreover, due to the unique microstructure formed between each different metal AM process, AM process-specific treatments need to be studied.

Although there has been an uptake on experimental testing of AM fracture toughness, modeling could be a cost-effective approach which can create better comparison between all these competing factors. Experimental testing, printing, and microstructural analysis are time consuming and expensive, where numerical modeling can be used to find structure-property relationships and further advance our knowledge and adoption of AM Ti6Al4V. An extended finite element method (XFEM) was used to simulate crack propagation method in compact tension models<sup>164</sup>. Prediction of fracture toughness using machine learning<sup>165</sup>. Anisotropic variability in PBF-LB was explored, providing further statistical analysis for A and B-basis qualification, with the A-basis providing a confidence level between 95-99% and B-basis providing 90-95% confidence level for material strength during aircraft design<sup>166</sup>. Watring et al.<sup>167</sup> characterize pores to predict fracture-related properties using machine learning to build neural networks which predict fracture toughness based on porosity. Kumar et al. 2019<sup>168</sup> used XFEM to predict crack growth behavior in presence of microstructural defects. For accurate prediction of the fracture resistance and crack growth behavior, representative data of the microstructure, internal defect, and fracture toughness is necessary. Furthermore, the fracture toughness variation due to the intra-build design parameters such as part design and spatial location needs to be considered for accurate model creation. Through the mapping of the build space using a multi-factor approach, design engineers can confidently optimize for ideal mechanical properties for production components.

In summary, fracture toughness evaluation of metal AM is a complex area of research that encompasses various process-induced and post-processing effects. Key studies have highlighted the importance of microstructure, process parameters, and build orientation in determining fracture resistance. These insights are essential to advancing the reliability of AM technologies in safety-critical applications.

### 2.4.3 Fatigue Performance

Fatigue properties are one of the more meaningful properties, as it accounts for the majority of component failure. Fatigue life is defined as the number of cycles that a component can survive under cyclic loading. The fatigue limit is the level of stress the component can undergo which failure will not occur, often measured by high cycle fatigue (HCF). The process-induced features which influence tensile, and fracture properties can be particularly detrimental to fatigue performance of metal AM alloys<sup>26,27,169–171</sup>. Furthermore, in metal AM, there are four types of features which can significantly reduce the fatigue performance including surface roughness, subsurface and internal defects, build orientation, and residual stresses. However, it is also important to consider the loading applied as there is a shift in crack nucleation location from surface and subsurface defects under high stresses compared to internal crack initiation at lower applied loads<sup>172</sup>.

#### 2.4.3.1 Influence of Surface Roughness

The fatigue performance and variability of Ti6Al4V as a function of the metal AM process has been heavily investigated experimentally, where the lifespan of as-fabricated titanium (~75-300MPa) is considerably inferior compared to that of wrought alloys (~600 MPa)<sup>98</sup>. Many studies have shown the poor fatigue behavior shown in Figure 2-13 of metal AM components is a result surface defects behaving as crack initiation sites as a result of the inherent poor surface finish<sup>26,27,104,118,173–175</sup>. Le et al.<sup>176</sup> reported a 37-85% probability of defect formation on the AM surface, where not only is there an increased likelihood of crack initiation from the surface but multiple crack initiation sites. The numerical fatigue property is in agreement with published experiment values, where the rough surfaces act as the source of crack initiation<sup>41,177</sup>. Multiple cracks initiate from the surface, independently growing and ultimately coalescing until sample fails abruptly<sup>171</sup>. The interaction between multiple cracks contributes significantly to the reduced fatigue resistance in the AB PBF-EB and PBF-LB components.

As the surface roughness improves in Figure 2-14, an increase in the metal AM fatigue behavior is observed in PBF and DED Ti6Al4V<sup>26,27,118,171,173–175</sup>. However, the improvement in behavior is directly correlated to the final surface finish, where a range of improvement is reported depending on the amount of material removed and the AM process. Childerhouse et al.<sup>173</sup> explored the influence of machining depth of cut of PBF-EB fatigue strength and observed that while a

superior surface finish was obtained with only 0.5 mm material removed, the number of cycles remained the same. In contrast, with 1 mm of material removed, the number of cycles doubled compared to the AB metal. The shallow machining proves to be insufficient in removing surface defects and brings subsurface spores to the surface, acting as crack initiation sites<sup>173</sup>. The notable increase in the fatigue behavior is a result of the shift in crack initiation shifts from surface defects to subsurface defects.

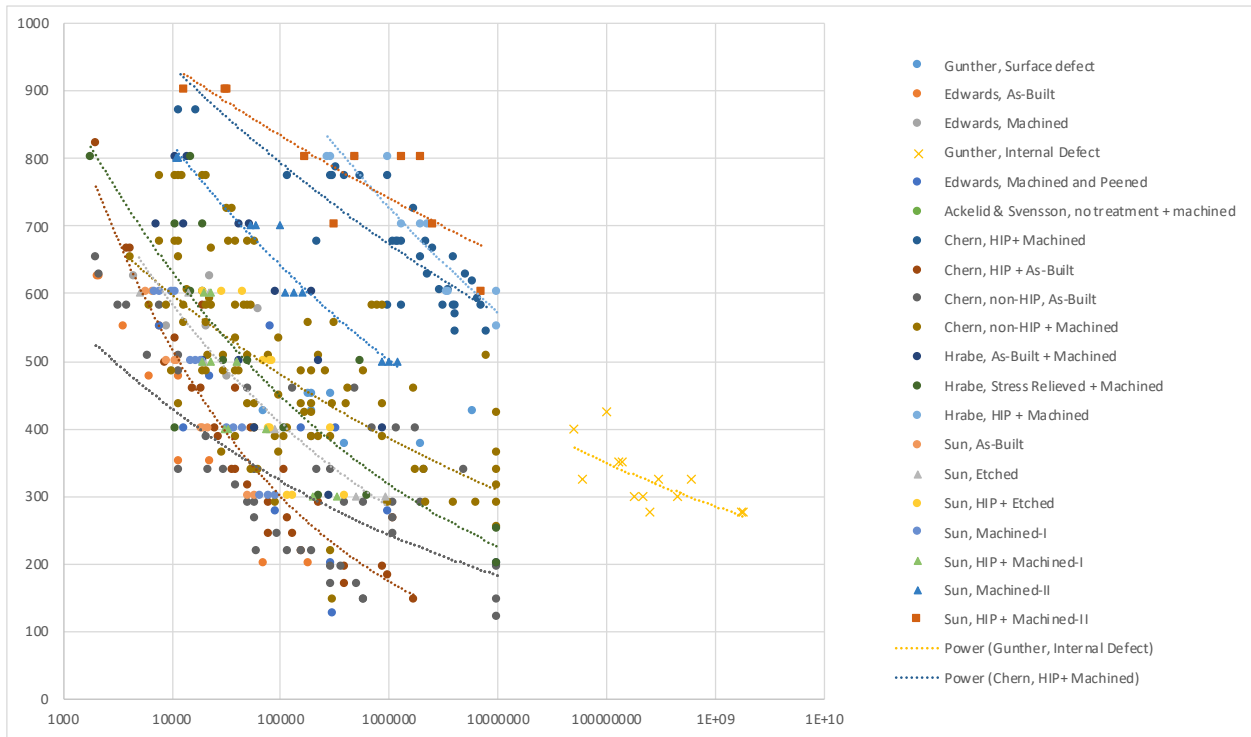


Figure 2-13: The Fatigue performance of PBF-EB in the as-built and post-processed condition.<sup>26, 41, 175,178,179</sup>

The tensile residual stresses formed on the free-surface of PBF and DED alloys can be critical for fatigue crack initiation, reducing the overall performance<sup>83,180</sup>. Leuders et al.<sup>181</sup> observed that while subsurface pores may contribute to crack initiation, fatigue crack propagation was significantly reduced because of residual stresses. Through process optimization<sup>89</sup> and post-processing<sup>179,182,183</sup>, a reduction in residual stresses and improved microstructure is used to enhance the metal AM fatigue behavior. While a stress relief has resulted in improved fatigue crack growth rate, the overall fatigue performance does not always improve.

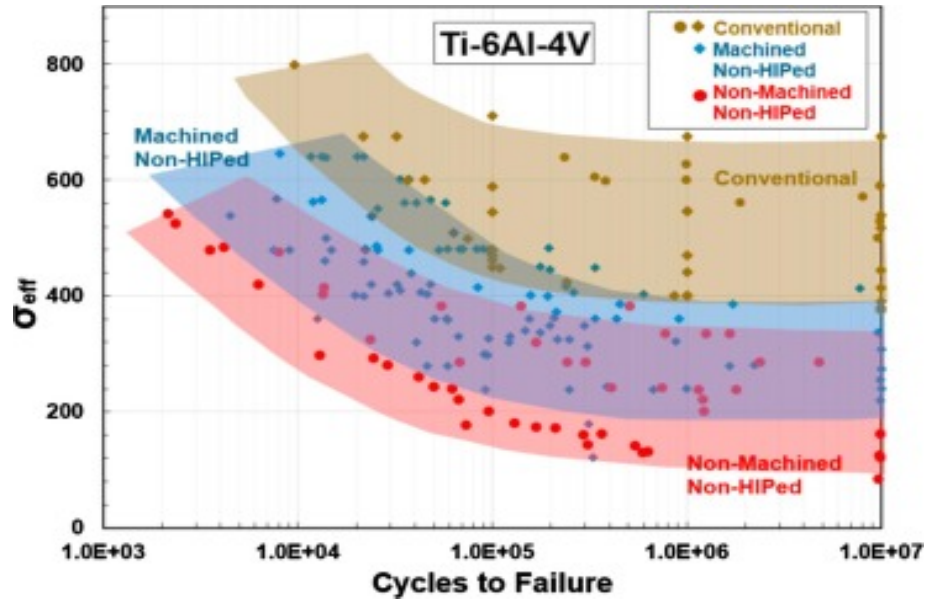


Figure 2-14: The machining effects on PBF-EB fatigue performance<sup>26</sup>

#### 2.4.3.2 Influence of Defects

With the removal of the rough surface and reduction of tensile residual stresses, defects become even more critical at higher stresses in very high cycle fatigue region, shown in Figure 2-13. The internal defects can further influence the load-carrying capacity of the metal, leading to variation in HCF performance. As such several studies have observed a decrease in fatigue performance with an increase in porosity<sup>184,185</sup>. However, the pore volume alone was not sufficient in predicting the fatigue performance, as seen Figure 2-15. The density, distribution, orientation, morphology, size, and location of the internal defects contribute to scatter in fatigue properties<sup>59, 81,186,187</sup>. Vansickle et al.<sup>188</sup> observed fatigue cracks typically propagated towards clusters of pores near the crack tip, leading to premature failure. Therefore, there is great interest in exploring the role of porosity on fatigue life. The shape and morphology of defects has been one of the main topics of study. While NDT evaluation can obtain key information regarding internal defects, further analysis is required to understand and predict the influence of defects on fatigue. Extreme Value Statistics have been shown to be a successful method of determining the critical defect size in metal AM alloys<sup>189</sup>.

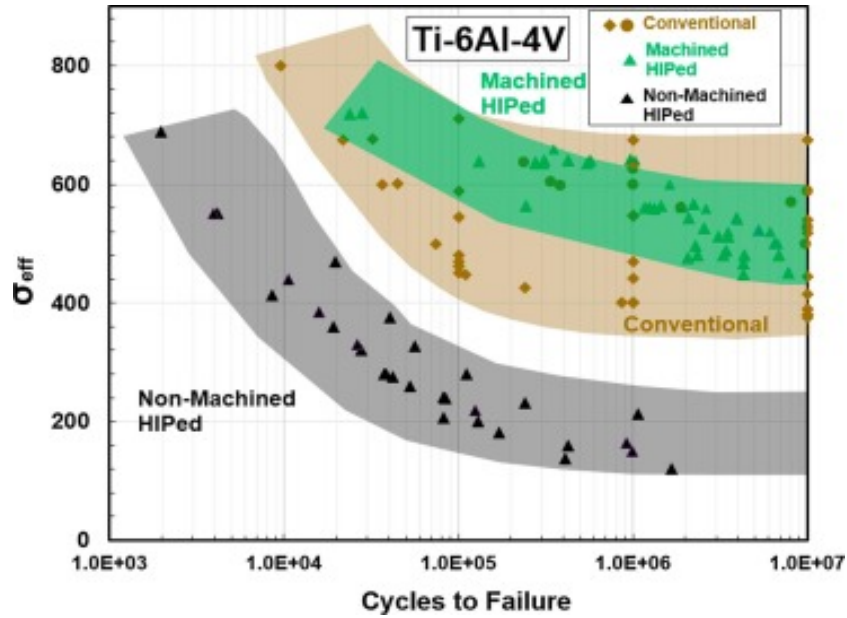


Figure 2-15: The HCF performance of PBF-EB Ti6Al4V compared to conventional alloys<sup>26</sup>

Moreso, the shape of the LOF defects also plays a critical role in fatigue behavior, where lower aspect ratio and irregularly shaped LOF defects are far more detrimental for fatigue behavior compared to rounder equiaxed LOF defects<sup>190</sup>. Crack initiation due to gas porosity in PBF-LB alloys are comparable to wrought alloys, but a significant decrease from 650MPa to 400MPa in fatigue life is observed when LOF defects are present<sup>190,191</sup>. Additionally, the sphericity of the defect contributed to the stress concentration induced with pancake shaped defect resulting in a larger source of stress concentrations than spherical pores<sup>192</sup>. Through implementing conical and cylindrical defects in the center of PBF-EB fatigue samples, Gong et al.<sup>193</sup> demonstrated that crack initiation persisted from the surface discontinuities and subsurface defects, however the presence of internal defects decreased the fatigue limit from 500 to 350 MPa. As the location of LOF defects move closer to the sample surface, the endurance limit decreased by 250 MPa, with little influence from location of gas pores<sup>176</sup>. Therefore, there has been a special attention in identifying the role of critical defect size which is most likely to trigger crack nucleation. Murakami et al.<sup>79,194</sup> has extensively explored the role and effect of defect size of AM fatigue life variation and proposed the use of the  $\sqrt{\text{area}}$  parameter to predict the fatigue life of the component. Tamas-Williams et al.<sup>59</sup> observed an increase in fatigue life where cracks initiated from gas pores compared to those from LOF defects. The high aspect ratio and irregular shape of LOF defects results in an increase in stress concentration, making them more critical than gas pores. With the reduction of LOF

defects, the spherical gas porosity overshadows microstructural-initiating cracks, such that microstructure does not have as much of an influence on the fatigue behavior as the internal defects. While characterizing the defect size is often used in understanding the fatigue behavior, the defect location and morphology are vital in predicting fatigue performance.

The location of internal defects within the bulk material also plays a significant role, where a decrease fatigue life in metal AM alloys is observed as the void location moves from the surface, subsurface, or internal. So not all porosity location can be treated similarly, where subsurface pores are far more detrimental to fatigue behavior due to their higher stress concentration, which makes them much more critical than internal defects<sup>81</sup>. While the location of gas porosity defects alloys do not significantly influence fatigue properties, the location of LOF defects contribute to a range of properties from 200 – 550 MPa, where an increase in fatigue behavior is observed and the location of LOF is closer to the surface<sup>191</sup>. Sarkar et al.<sup>195</sup> observed the subsurface defects, and micro-notches as the primary crack initiation in the laser re-melted and electro-polished samples, resulting in fatigue properties below wrought. Similarly, early fatigue failure in PBF-EB samples has been attributed to the presence of subsurface defects, where the distance from the surface was more detrimental compared to the aspect ratio<sup>196–198</sup>. Ghods et al.<sup>169</sup> observed a large concentration of porosity roughly 0.7 mm from the PBF-EB surface, which coincided with the contour-hatching overlap of the PBF-EB process. Fleishel et al.<sup>199</sup> demonstrated a correlation between the PBF-EB process parameters and fatigue life, where offset values which deviated from typical values generated voids. Roirand et al.<sup>200</sup> observed similar correlation in laser scan strategy and porosity formation, where insufficient overlap of scan strategy resulted in an increase in number of pores and decreased the fatigue crack resistance in PBF-LB Ti6Al4V. A variation in defect distribution formed as a result of PBF-LB build pattern, beam travel direction, location of specimen on build platform, and proximity of samples to each other, which would further influence scatter in fatigue limit. Choosing the optimal process parameters are essential in limiting formation of detrimental subsurface defects, thus improving fatigue properties. Developing a foundational understanding that links the AM process parameters to the fatigue performance assures the qualification and certification of high-performing PBF-EB components.

### 2.4.3.3 Anisotropy

Similar to tensile and fracture toughness properties, orientation-dependent AM fatigue properties have been observed, as seen in Figure 2-16. As the angle between the loading direction and the build orientation changes, changes in fatigue behavior have been observed<sup>101,197,201</sup>. Three things happen as the build orientation changes: 1) there is a change in the surface finish, 2) the orientation of LOF defects, 3) the temperature gradient forms as the heat was dissipated along the build direction producing columnar grains. The surface roughness of samples increases significantly depending on orientation, where Rogers et al.<sup>91</sup> reported 35% lower fatigue properties in samples built in angles between 0°-30° due to the partial solidification from the support structures and the higher downward-facing roughness compared to samples built between 50°-90° from the build platform. Pegues et al.<sup>202</sup> observed a significant drop in fatigue behavior with an increase in the PBF-LB sample surface area, due to the increase in surface roughness and surface defects in the 45° oriented samples. The significantly rougher downward surface is due to the gravitational forces during meltpool solidification and the contact with unmolten powder particles. However, with post-machining, the influence of the rough surface finish can be mitigated.

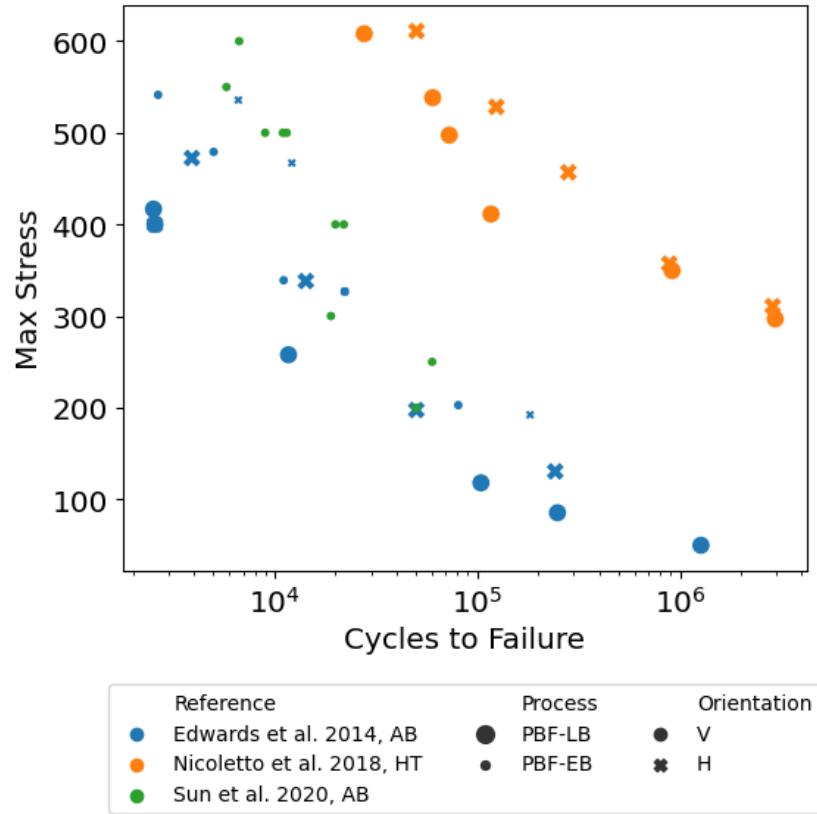


Figure 2-16: Orientation effects on fatigue performance<sup>47, 171, 175</sup>

Second, the orientation of LOF defects can become roughly perpendicular to the loading direction, significantly influencing fatigue behavior by decreasing the load carrying capacity. Chastand et al.<sup>105</sup> also observed that the anisotropy in the fatigue behavior was highly dependent on subsurface LOF zones, where failure in the vertically oriented samples originated from defects in contrast to the microstructural features in the horizontal orientation. However, with surface machining and removal of subsurface LOF defects, fatigue anisotropy of PBF-EB Ti6Al4V can be reduced<sup>26</sup>. Shrestha et al.<sup>203</sup> observed that while vertical samples had lower fatigue life than horizontal samples, the diagonally built samples had a significantly lower fatigue life. The reason for this was the LOF orientation of defects aligned with the plane of maximum shear stress, resulting in the lower fatigue properties. Lastly, the columnar grain can dictate crack propagation path, where there is an increase in crack growth rate as crack travels along the columnar grains. Lueders et al.<sup>204</sup> demonstrated that there is an increase in the stress intensity factor when the crack propagates along the grain boundary, and therefore crack growth is faster when oriented parallel

to the columnar grains. Therefore, there are multiple material features which contribute to the orientation-dependent properties, each with a different effect.

The anisotropic microstructure alone does not fully account for the orientation-dependent fatigue properties where the surface and internal defects ultimately determine the fatigue behavior. One reason for this is the crack initiation is driven by the internal defects such as surface, LOF or porosity. And in high cycle fatigue, crack initiation is often the longest portion of the failure, where LOF defects significantly contribute to early-stage fatigue crack initiation and scatter with limited influence on the crack growth rate<sup>181</sup>. However, LOF defects can contribute to scatter in properties due to multiple crack initiation sites and minor acceleration of the crack growth rate near present defects<sup>188,205</sup>. In contrast, the fatigue crack growth rate is lower for crack initiating from internal defects compared to LOF defects<sup>96</sup>. So while internal defects are detrimental to fatigue behavior, their location is what influences the fatigue crack growth rate. Given this, it's the microstructure which ultimately dictates the crack growth rate and the columnar grain structure acting as a preferential path<sup>188,204</sup>. However, microstructural anisotropy has less influence on crack initiation in the presence of defects, inspiring a larger focus on creating fully dense metals.

In the absence of defect, the microstructure can play a significant role in fatigue crack growth. Vansickle et al.<sup>188</sup> observed a preferential fatigue crack path along the fine martensitic  $\alpha'$  grains, which deflected when reaching a prior  $\beta$  grain boundary. The study indicated the significant influence of the microstructure on the plastic zone size surrounding the crack tip because of the high strain regions due to the fine  $\alpha'$  laths. The faster cooling rate in PBF-LB develops a very fine microstructure, which shows higher yield and fatigue strength. The finer microstructure increases the number of grain boundaries, thus increasing resistance to crack growth. In contrast, the coarse  $\alpha$ -laths in the PBF-EB which are preferred for higher fracture toughness yield a low strength material and endurance limit. In addition to the grain size, the structure can play an extrinsic role in mechanical properties. Razavi et al.<sup>206</sup> demonstrated enhanced fatigue behavior and notch sensitivity due to the fine basketweave and columnar grains in DED compared to forged Ti6Al4V samples. The basketweave structure often causes a zigzag crack path deflection, specifically observed in the small crack region<sup>207</sup>. As such, careful attention needs to be paid when designing materials with high strength and damage tolerance.

#### 2.4.3.4 Influence of Part Design

While similar columnar grains exist in metal AM components, the difference in cooling rate and process temperature leads to difference in fatigue limit between the different process. Samples built at double the interlayer speed (time between a previous layer is subsequently melted) exhibited a coarser microstructure due to the increase in heat accumulation and thus a slower cooling rate which increased the LOF formation and overall led to a decrease in fatigue resistance<sup>208</sup>. Additionally, the heat dissipating with different cooling rates as a function of sample design can further influence the final microstructure; the variation in microstructure would then lead to variation in tensile and effect the fatigue properties. As a result, choices in component design such as geometry, size, and part spacing are an important consideration in fabricating repeatable components. Shrestha et al.<sup>209</sup> reported higher fatigue resistance in PBF-LB SS17-4 samples machined from a square rod (12x12mm) due to the increase in heat accumulation compared to those machined from near-net specimen (AB gage diameter 8mm). Furthermore, Zhao et al.<sup>118</sup> compared the mechanical properties of between PBF-EB and PBF-LB samples and observed part size had a significant influence on microstructure in both PBF-EB and PBF-LB samples, with a near doubling in  $\alpha$ -lath thickness with increase in sample thickness from 1.2 mm to 7 mm. Even though the specimen size influenced the metal AM microstructure, size-dependent fatigue properties were only observed in the PBF-EB samples due to the large scatter of internal defects in the PBF-LB samples. In addition to microstructure, the surface condition is influenced by change in geometry, resulting in fatigue variation. Razavi et al.<sup>210</sup> observed a 20MPa decrease in PBF-EB Ti6Al4V fatigue strength with decreasing thickness from 5- to 1-mm due to the increase in surface roughness with decrease in thickness. Le et al.<sup>191</sup> attributed the similar fatigue properties of two different thicknesses due to the probabilistic nature of defect location as volume changes, where the defect location overshadowed any differences in microstructure. Despite the significant influence of specimen design on fatigue properties, further experimentation is necessary to fully understand the role of specimen design on the variation of the process-induced features and the proceeding properties.

#### 2.4.3.5 Influence of Build Design

In addition to variation with changes to the sample design, the build design has also been a source of scatter in fatigue performance. Soltani-Tehrani et al.<sup>211</sup> observed SS17-4 PBF-LB fatigue samples manufactured with unused powder exhibited considerable location-dependent

fatigue behavior, with superior performance in samples built towards the front of the build space compared to those printed along the back. They also found the highest fatigue life resulted from samples built closer to the powder bin, with more uniform powder packing as the recoater moved away the larger powder particles along the build platform. Tiferet et al. <sup>24</sup> similarly observed location dependent fatigue properties, however a large scatter in the fatigue behavior due to internal defects and limited samples necessitate further evaluation of the intra-build (variation inside the build space) effects on fatigue. While extensive work has been done to evaluate the influence of geometry, Ghods et al. <sup>169</sup> has holistically investigated the role of location on HCF, finding an increase in LOF defect formation with decrease in sample thickness, and as samples were printed towards the edges of the build space, resulting in 37% decrease in fatigue performance of PBF-EB Ti6Al4V. These sources of variability highlight the importance of understanding spatial effects and developing standardized approaches to understand AM part quality. However, as the study was only limited to the vertical orientation, the change in crack growth behavior with build orientation requires evaluation in the horizontal orientation. As such, a holistic assessment of the influence and interaction of the build and specimen design is what is motivating this study.

#### *2.4.3.6 Post-Processing*

Despite the significant efforts to optimize process-parameters to fabricate fully-dense components, post-processing is often implemented in achieved functional parts, summarized in Figure 2-17. Heat treatments and HIP are two of the post-treatment executed. Shui et al. <sup>212</sup> performed both a HT and HIP at 920°C, and observed the fatigue life in the HT condition was comparable to as-fabricated due to the remaining small defects. Furthermore, in PBF-LB samples, annealing increased the pore size due to entrapped gas and powder particles, while expansion was not observed in the HIP samples <sup>213</sup>. Even more important, annealing resulted in directional expansion, with internal defects oriented perpendicular to the loading direction grew larger resulting in a larger stress concentration than in the as-fabricated condition. In contrast, HIP has four distinct benefits in fatigue performance. First, while not all pores close, the defect size is reduced, therefore reduced the number of defects above the critical threshold needed to initiate a crack. Second, HIP can refine the local microstructure surrounding defects, which limits cracks initiation <sup>214</sup>. Third, HIP changes the defect shape, where studies report fatigue life is AM after HIP is controlled by crack initiation from microstructure as opposed to build defects. Kaletsch et al. <sup>187</sup> found a larger number of irregularly shaped defects which are more critical in fatigue

performance compared to more uniform shape after the HIP. Additionally, HIP application increased ductility and fatigue resistance, in addition to mitigating the location-dependent fatigue behavior<sup>24</sup>. Fourth, HIP acts as a stress relief application, decomposing any of the brittle  $\alpha'$  microstructure and internal residual stresses. However, HIP alone has not resulted in enhanced fatigue performance. Sub  $\beta$ -transus temperature treatment promotes coarsening of the  $\alpha$ -phase and  $\beta$ -phase vol.% growth<sup>215,216</sup>. However, as the temperature increases closer to the  $\beta$ -transus temperature, the columnar  $\beta$  grains increase in size combined with significant increase in the  $\alpha$ -grain boundary, significantly degrading fatigue performance<sup>149</sup>. Galarraga et al.<sup>117</sup> observed that while HIP is useful in densification of the metal, the increase in columnar grain width,  $\alpha$ -lath thickness,  $\beta$ -vol.%, decrease in dislocation density aid in contributing to the overall increase in ductility, which is preferred for improving fatigue resistance.

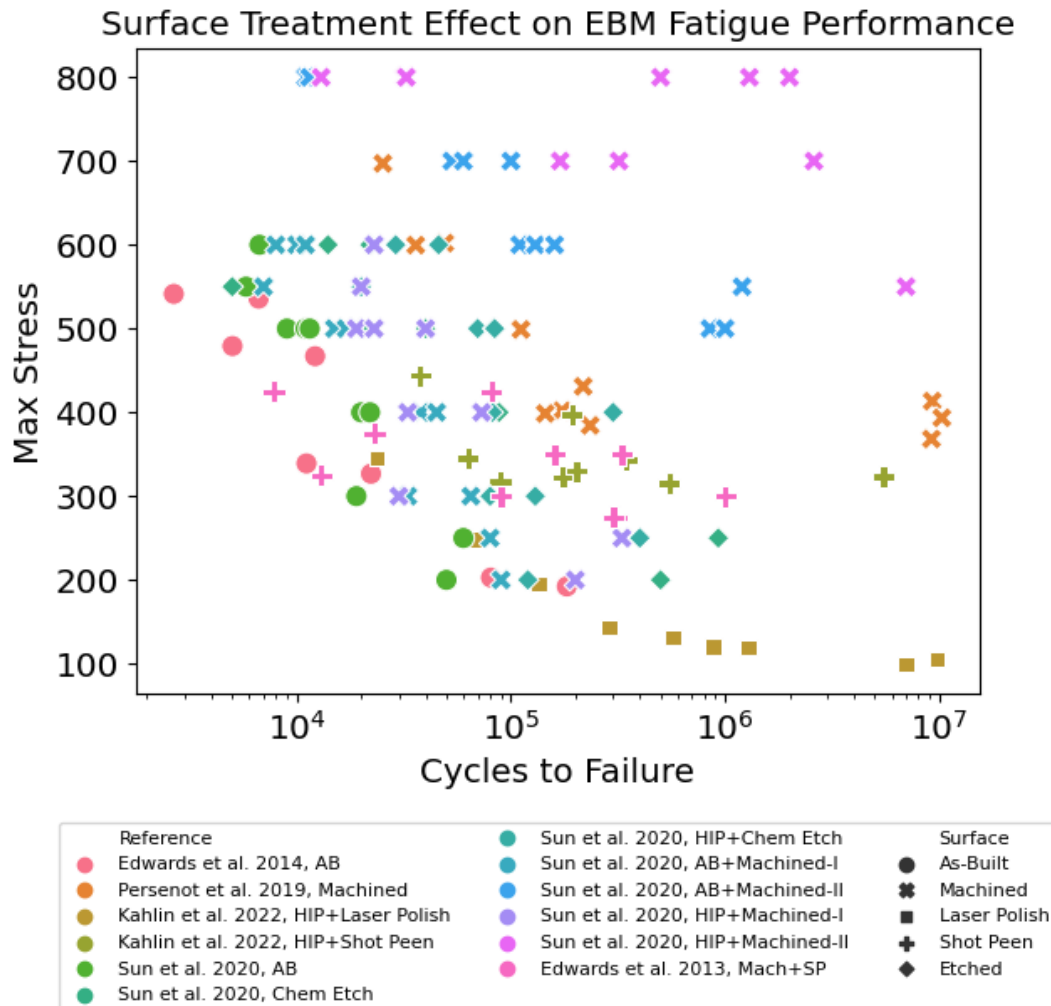


Figure 2-17: Comparison of surface treatment methods on PBF-EB fatigue performance<sup>41,175,217,218</sup>

One of the largest limitations of the HIP treatment utilized is the application of the standard process meant for wrought Ti6Al4V. While the current HIP results in a denser metal, the coarsening in microstructure is detrimental to crack growth rate and overall fatigue life. Verma et al.<sup>164</sup> found the microstructure evolution of metal AM components after HIP influence mechanical properties differently than conventionally manufactured parts, such that modification of the standard HIP process is imperative for advancing the state-of-the-art in post-processing PBF-EB Ti6Al4V. In contrast to the standard HIP, to obtain a finer microstructure, a lower temperature and higher-pressure HIP (LTHIP) has been recommended<sup>219</sup>. Moran et al.<sup>184</sup> performed an extensive study evaluating the application of standard, low temperature, and high-pressure HIP on fatigue performance of Ti6Al4V. They observed that not only does the LTHIP treatment significantly outperform the other two temperatures, but even with a larger defect density, the refined microstructure was crucial in the fatigue crack resistance. Furthermore, this study was essential in highlighting the final post-HIP metal is dependent on the metals initial condition. LTHIP has proved to be far superior and recommended for fatigue critical applications of metal AM components.

While HIP has been successful in reducing the influence of subsurface defects on fatigue, it alone is not sufficient in obtaining enhanced fatigue performance. Through application of a HIP and machining process, PBF-EB fatigue strengths of up to 500 MPa have been achieved<sup>26, 94, 118, 179, 220</sup>. With HIP and machining, the PBF-EB Ti6Al4V outperformed the samples in machined state at the higher number of cycles, where crack initiation is driven by internal defects<sup>220</sup>. Sun et al.<sup>175</sup> demonstrated optimal PBF-EB Ti6Al4V fatigue limit through a combination of HIP and precision machining. However, machining is very limiting due to the complex designs of metal AM components. Chemical polishing successfully improved the surface finish of PBF-EB alloys, however an improvement in fatigue strength was not obtained<sup>27</sup>. A cavitation, laser, and shot peen process was performed on PBF-EB and PBF-LB Ti6Al4V only resulted in fatigue increase of up to 300 – 350 MPa<sup>221</sup>. With an application of a grinding or machining process prior to peening, fatigue strength of 450 MPa were achieved<sup>221, 222</sup>. While toolless surface treatments are an attractive option for metal AM structures for not only improving the surface finish but the induced compressive residual stresses are not sufficient in improving the fatigue behavior. Additionally, contamination from the peening media can occur where the media stuck in the unmelted regions of metal AM structures act as subsurface inclusions and potential crack initiation sites<sup>223</sup>. Through

performing a polishing process prior to laser shock peening, fatigue strength of up to 700 MPa was achieved, where the combination of compressive residual stresses and alpha phase grain refinements reduced surface sensitivity and increased the fatigue crack resistance <sup>144</sup>.

Fatigue models incorporating both the surface finish and the critical defect size have been better able to predict the fatigue behavior of metal AM alloys. Derrick et al. <sup>224</sup> utilized component hardness, defect size, build orientation, and surface characteristics to analyze and develop approximation equations for metal with hardness HV<500. While the model was able to predict fatigue strength at lower life, which is limited by the Murakami model <sup>79</sup>, the dataset was separated based on surface condition. Mian et al. <sup>225</sup> modeled the fatigue strength using including surface and internal defects characteristics and found surface was more crucial, determining the fatigue strength (surface:150MPa and internal:350MPa) compared to internal defects. Similarly, Sanaei et al. <sup>189</sup> incorporated the average surface roughness parameter ( $R_a$ ) to account for the variation in fatigue behavior of PBF-LB titanium. Due to the significant influence of the surface finish on fatigue performance, the surface roughness characteristics are necessary for an accurate fatigue model. Lee et al. <sup>226</sup> investigated the effect of the as-fabricated and semi-polished PBF-LB samples on surface roughness and observed subsurface defects hidden under the partially melted powder particles were not detected using optical measurements. Not only did these subsurface defects act as crack initiation site in the semi-polished samples, but the average roughness parameters did not accurately represent the actual surface quality. Rather, the depth of the deepest valley ( $R_v$ ) was more accurate in predicting the fatigue behavior of as-fabricated samples. Rogers et al. <sup>91</sup> observed that different surface roughness parameters are suited when correlating surface roughness and fatigue life, where in upward surface  $R_v$  is suitable, while in downward its depth of highest peak ( $R_p$ ). Therefore, an accurate fatigue model encompassing the complete variation due to the complex manufacturing process and unique build choices is complex.

For the adoption of AM components, material reliability and structural integrity are essential to ascertain their performance in realistic loading scenarios. While the tensile property research has been necessary for creating a foundational understanding of how PBF-EB Ti6Al4V, fracture-critical behavior is necessary for understanding the structural integrity. In general, the fracture resistance and fatigue behavior of metal alloys is dependent on the surface finish, microstructure, and internal defects, where the wide range of variability due to the build space poses a risk in applications where material performance must be predictable and reliable. Hence,

the motivation leading to this research study. This research is needed to address the variability and reliability concerns associated with metal AM, specifically in terms of fracture toughness and high cycle fatigue in PBF-EB Ti6Al4V. By improving understanding of the foundational aspects of the AM process, microstructure, and post-processing impacts the structural integrity and durability, this research will provide insight needed to advance AM into a viable option for high-performance, safety-critical applications.

## **Summary**

Metal additive manufacturing has revolutionized modern manufacturing by enabling fabrication of complex and lightweight components, with reduced material usage. These benefits have inspired utilization of AM in industries such as aerospace. PBF processes are at the forefront of AM manufacturing, especially PBF-EB for its ability to fabricate highly reactive metals such as Ti6Al4V in a vacuum environment at elevated build temperatures. However, adoption of PBF-EB components in load-bearing application hinges on addressing critical challenges related to damage tolerance and reliability, especially in high-performance application where structural integrity is vital. However, various factors such as process parameters, build orientation, sample geometry, and post-processing significantly affect the microstructure, and consequently the mechanical properties of AM parts. Furthermore, the unique hatching and layerwise manufacturing process introduces unique challenges, making damage tolerance essential in design of metal AM parts for structural applications.

Damage tolerance, which include mechanical properties such as fracture toughness and fatigue strength, is essential for ensuring quality and longevity of AM components. The layer-by-layer manufacturing process of AM introduces inherent complexities, including columnar grains, poor surface finish, residual stresses, and process-induced defects. These issues significantly influence mechanical properties and lead to part-to-part variability. Design parameters such as sample geometry and build design play a critical role in the reproducibility of metal AM components. For instance, thickness-dependent variation in tensile and fatigue properties due to the underlying microstructural variation have been observed, where a reduction in gauge size corresponded to reduction in fatigue performance. Furthermore, the spatial location of a component within the build chamber significantly affects its thermal history and cooling rates, introducing variability in microstructure, residual stresses, and defect distribution. These findings

underscore the complex relationship between the build design parameters and the resulting mechanical properties of PBF-EB, highlighting the need for a comprehensive understanding of these interactions to ensure repeatable and reliable mechanical properties.

To establish repeatable components used in critical applications, it is necessary to establish rigorous process control. Furthermore, robust defect detection methods and post-processing treatments need to be investigated to examine and mitigate flaws. In all, certification of AM components demands a thorough understanding of the process-structure-property relationships to develop and predict reliable performance models which meet industry standards.

Ensuring repeatability and reliability also requires robust quality assurance frameworks through incorporating standardized testing protocols to evaluate mechanical properties, focusing on damage tolerance. This allows for certifications where detailed documentation and validation of the manufacturing process to the final components, highlight the need for systematic research into how the overall process influences property variability. However, one of the limitations barring from adoption is the limited availability of material, process, and testing standards specific to metal AM products. Therefore, not only is comprehensive testing required for evaluating the metal AM performance, but systematic evaluations that guarantees identifying and understanding the variations due to the build space parameters. Through consistent evaluation of mechanical properties, repeatable and reliable AM parts can be manufactured. It also provides key information needed to create regulatory requirements and standards that ensure quality components.

This research focuses on fabricating Ti6Al4V using PBF-EB, to deepen the understanding of the relationship between build design parameters, microstructure, and damage tolerant properties. By systematically investigating fracture toughness and high cycles fatigue, this study aims to address the key gaps in knowledge regarding process-induced variability. The findings will provide key insight into producing reliable, components with consistent quality, enabling broader industrial adoption of metal AM for safety-critical applications.

### 3 Research Goals and Objectives

The motivation for this study stems from several critical limitations and opportunities in the field of metal additive manufacturing. The adoption of metal AM for damage tolerant applications is limited by the inconsistencies in the mechanical properties across builds, largely due to process induced variability. Understanding these variations is essential to unlocking the full potential of AM in demanding industries such as aerospace. While the metal AM literature has extensively studied processes such as PBF-LB, comparatively less research focuses on PBF-EB.

This study provides an opportunity to advance the understanding of PBF-EB-specific phenomena and their effect on the fracture-critical properties. Titanium alloy Ti6Al4V is widely used in PBF-EB due to its exceptional strength-to-weight ratio. However, the fracture-critical properties, particularly fracture toughness and fatigue behavior of Ti6Al4V, is susceptible to the microstructural characteristics and defects introduced during the AM process. Recent studies have discovered Ti6Al4V tensile property variation resulting from the build design parameters; however, the influence of intra-build design parameters on the fatigue and fracture of PBF-EB Ti6Al4V has not been widely reported. To do so, an investigation of the part-to-part variability within the PBF-EB build chamber is necessary. Utilizing the entire build space reflects production at-scale, often performed to produce higher quantity of components with reduced manufacturing time and part cost. Assessing the fracture-critical property variation within the build space is the key to enabling the adoption of PBF-EB Ti6Al4V components. To do so, a comprehensive and holistic approach to evaluating the process-structure-property relationships need to be considered. However, there is limited information on the influence of build design factors on the fracture-critical properties.

This research aims to bridge the gap between the PBF-EB process and the Ti6Al4V fracture-critical properties, focusing on quantifying the variability. Research into the sources of mechanical variability is essential to fabricating reliable and repeatable engineered components. Focusing on the intra-build design parameters is a novel approach for several reasons. First, there's a lack of standards-driven build design requirements. Secondly, the variation throughout the build space can be accurately used for prediction and numerical modeling. Thirdly, by identifying the root cause of variability in PBF-EB Ti6Al4V, this research can provide the knowledge needed to meet stringent demands and increase confidence in AM technologies. Furthermore, while post-

processing methods such as HIP and heat treatment are commonly implemented to improve properties, PBF-EB-specific post-processing is vital for enhanced performance. An investigation of optimizing post-processing for property enhancement and reduction in variability is evaluated.

Based on this motivation, the following research objectives can be established. A qualitative and quantitative analysis of the PBF-EB Ti6Al4V metal quality, focusing on the fracture toughness and fatigue performance. A systematic and in-depth investigation of the common design factors (e.g., sample orientation, geometry, and spatial location) influencing property variability. As a result, the relationship between mechanical behavior and process-induced features will be obtained by characterizing the surface roughness, microstructure and defects. Additionally, defect mitigation, microstructural evolution, and mechanical properties are assessed and optimized for enhanced fracture toughness and fatigue performance through post-processing application.

To achieve the following goals of this research, these three objectives will be pursued:

- **Aim 1:** To investigate the influence of build design parameters (e.g., geometry, orientation, spatial position) on the microstructure, defects, and fracture toughness behavior of PBF-EB Ti6Al4V
- **Aim 2:** To explore the effect of a modified HIP treatment on internal defects, microstructure, and fracture toughness properties.
- **Aim 3:** To assess the effect of post processing on the high cycle fatigue performance.

## 4 Experimental Methods and Procedures

The goal of this work is to evaluate the quality and durability of PBF-EB Ti6Al4V, focusing on the fracture toughness and high cycle fatigue properties. To obtain an overall understanding of the mechanical properties, samples in the as-built, surface treated, and heat-treated condition are explored. The following section provides in-depth information regarding the parameters of interest, testing methodology, and the post-processing treatment evaluated.

### 4.1 Feedstock

The specimen produced in the following study were printed using recycled Grade 5 Titanium alloy (Ti6Al4V) acquired from the GE subsidiary Advanced Powders & Coatings. A typical SEM micrograph and particle size distribution of the unused titanium powder, corresponding to Batch P1143, is shown in Figure 4-1. The powder size distribution was 45 – 106  $\mu\text{m}$ , flow rate per ASTM B213 is 26s/50g, and apparent and tap density per ASTM B212 and B527 were 2.49g/cc and 2.8g/cc, respectively in the unused powder. The flow rate, tap and apparent density were all within the permissible limits. The chemical composition of the unused powder is provided by the manufacturer, found in Table 4-1.

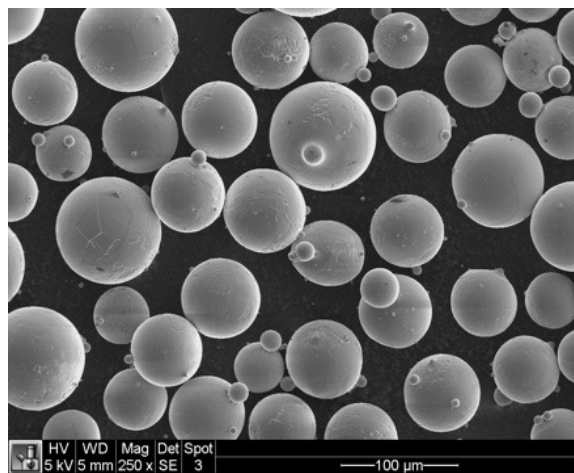


Figure 4-1: SEM micrograph of Ti6Al4V unused powder obtained from AP&C.

Table 4-1: Unused Titanium Grade 5 (Ti6Al4V) powder composition as provided by the manufacturer.

Element	Required		Measured	Testing method
	ASTM F2924	UAC065-170510		
Carbon (C)	< 0.08	< 0.08	0.02	ASTM E1941
Oxygen (O)	< 0.20	0.11-0.20	0.14	ASTM E1409
Nitrogen (N)	< 0.05	< 0.05	0.02	ASTM E1409
Hydrogen (H)	< 0.015	< 0.015	0.002	ASTM E1447
Iron (Fe)	< 0.30	< 0.30	0.20	ASTM E2371
Aluminum (Al)	5.50-6.75	6-6.75	6.37	ASTM E2371
Vanadium (V)	3.50-4.50	3.50-4.50	4.01	ASTM E2371
Yttrium (Y)	< 0.005	< 0.005	< 0.001	ASTM E2371
Others	< 0.40	< 0.40	< 0.40	ASTM E2371
Titanium (Ti)	Balance	Balance	Balance	ASTM E2371

Table 4-2 provides the powder lot number and reuse cycles of the powder used to fabricate the samples. One set of samples was produced using Batch P1303, fabricated alongside the powder reuse DOE investigation of <sup>10</sup>. The original build started with 100kg of unused powder, where the remaining powder from each subsequent build was recycled through the Powder Recover System, sieved, and mixed with powder left in the hoppers for the subsequent build. The powder utilized had undergone seven reuse cycles by Ghods et al.<sup>127</sup> prior to builds 8&9 highlighted in Table 4-2. The chemical composition of the Ti6Al4V powder in the unused and 10<sup>th</sup> build cycle condition from the study is provided in Table 4-3 as reference <sup>10,227</sup>. Another 100kg of powder (Lot P1143) was obtained to fabricate samples to evaluate the intra-build effect on the fracture-critical properties. The powder was recycled similar to the reuse DOE, where no additional powder was added to the builds. The second batch of powder had undergone four reuse cycles by Ghods et al.<sup>127,169</sup> prior to the five builds performed for this study. While there is a positive linear relationship between oxygen wt.% content and powder reuse, the PBF-EB Ti6Al4V powder remains compliant for up to 11 reuse cycles <sup>10</sup>, such that the builds manufactured in this investigation remained below this limit.

Table 4-2: The reuse cycle and powder lot used to manufacture the specimens

Powder Lot	Reuse Cycle
Batch P1303	7 – 9
Batch P1143	5, 6, 8 – 10

Build	O (wt.%)	N (wt.%)	H (wt.%)	Al (wt.%)	V (wt.%)	Fe (wt.%)
1 (unused)	0.142	0.024	0.0014	5.41	3.43	0.21
10	0.189	0.026	0.0010	5.50	3.26	0.25

## 4.2 Sample Fabrication

The specimens in this study were manufactured using GE Additive (ARCAM) A2X Electron Beam System (Mölnadal, Sweden). ARCAM PBF-EB Version 5.0.64 control software and layer thickness of 50  $\mu\text{m}$  were utilized for this study. *Manufacturer recommended build parameters* in Table 4-4 were used, including standard preheating and melting strategies. Once the build was complete, the machine requires a cooldown period until it reaches a safe temperature for the build to be removed.

Table 4-4: Build parameters as defined in melt theme

Build Temperature	650-680°C
Beam Speed	4530 mm/s
Beam Current	15 mA
Max Current	20 mA
Focus Offset	25 mA
Speed Function	45
Snake	True
Line Order	1
Randomized Hatch	False
Line Offset	0.2 mm
Hatch Depth	0.05 mm
Speed Factor	1.5 mm
Exponent Factor	0.51/mm

Upon reaching room temperature, the sintered block is removed and placed into the Powder Recovery System to remove the printed part from the unmelted powder particles, in addition to separating any metallic impurities. The powder in the hoppers was removed using a dedicated vacuum and combined with the unsintered powder particles obtained from the sintered block separated using the PRS. The unmelted powder particles are then placed into a vibratory sieve to

separate any lumps of powder and impurities above 125  $\mu\text{m}$ . The combined powder volume was mixed manually by hand for 15 minutes and sieved through a 120  $\mu\text{m}$  mesh size to ensure thorough mixing and to remove large particles. If a subsequent build is to be performed, the powder is placed back into the hoppers. If not, the powder is then stored safely to reduce contamination and oxygen pickup for future builds. The powder history is recorded and maintained to insure traceability.

### 4.3 Design of Experiments

Fabrication of PBF-EB components requires multiple process steps (e.g., component design, powder and support removal, post-processing, etc.) until the final product is achieved. Each of these steps may affect the quality of the final product, inspiring extensive research into each of these manufacturing steps. However, examining of each of these steps is time and cost-extensive. As a result, many studies focus on how optimizing process parameters, or a post-processing application can enhance the PBF-EB mechanical properties. But, to fully understand the influence of the PBF-EB process on the fracture-critical properties, holistically evaluating the build design parameters need to be explored. Of all the factors, this study explores the common engineering design considerations such as sample orientation, geometry, and location within the build space. These terms, referred to as the intra-build design parameters (parameters within the build chamber), were selected and their effect on manufactured components examined. The following section initially defines these intra-build design parameters, and the overall approach adopted. The section then further provides details into the experimental design utilized to fabricate the samples necessary to evaluate the fracture-critical properties.

The common design choices made when fabricating PBF-EB include the sample design, where samples are located within the build space, and the orientation at which the component are manufactured within the build space. These three parameters were identified as the three most critical design choices made by engineers to manufacturing PBF-EB parts. The part design parameter investigated in this study captures any variation due to sample geometry through evaluating the influence of thickness on mechanical properties. The thickness of each specimen corresponds to the thinnest area of the specimen. Radial distance and height are the two spatial location factors representing the placement in the build chamber, shown in Figure 4-2. The radial distance is measured from the center of the build plate to the center axis of the sample and the height is from the build plate to the center of the sample. Radial distance was chosen as the spatial

parameter to reflect the tracking of the electron beam during the printing process. Lastly, the sample orientation with respect to the build direction is explored, as seen in Figure 4-3. These factors permit evaluation of the build space reflecting choices made by design engineers. The following sections provides further details regarding the specific design of experiment adopted to evaluate the fracture-critical properties.

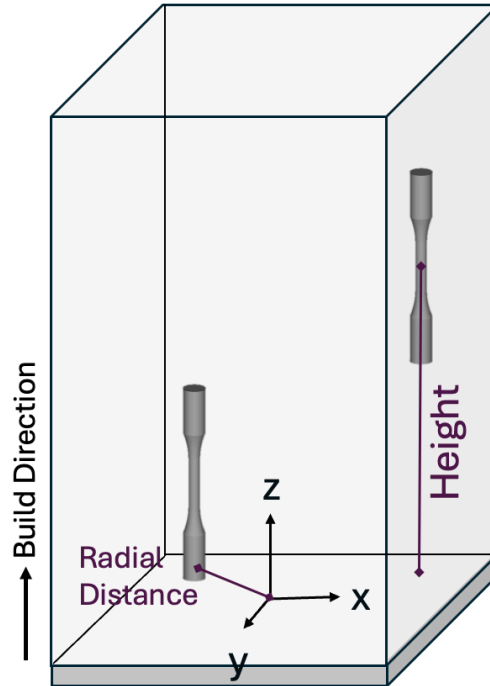


Figure 4-2: The nomenclature adopted to evaluate the PBF-EB build space denoting the two spatial parameters: radial distance and height.

To systematically investigate the effects of the selected design parameters, a Design of Experiments (DOE) approach was adopted. A DOE allows for a structured way to plan, conduct, and analyze the experiments efficiently, in addition to identifying the variation within the data. Utilizing a DOE also allowed adoption of a consistent design between the builds to control the variables of interest, provide a method to statistically analyze the results, reduced testing time, and enable prediction and optimization of mechanical properties. To do so, a multi-factor DOE approach was utilized in this study. When possible, a full factorial build design was adopted, with 3-levels for each factor, to investigate every combination of factors using ANOVA or regression

statistics. The following section provides further detail regarding the DOE adopted to evaluate the fracture-critical properties.

### 4.3.1 Tensile Properties

Several studies have been conducted on the effect of build design parameters on the tensile properties, focusing on either individual parameters<sup>22,23,210</sup> or on influence and interaction of multiple design parameters<sup>127</sup>. These studies were crucial in paving the way to understanding the mechanical behavior of PBF-EB Ti6Al4V. Since the studies focused on the tensile properties, the main focus of this study was on the fracture toughness and high cycle fatigue variation, to further push forward the knowledge of PBF-EB damage tolerance. However, tensile specimens were fabricated alongside the fracture toughness and HCF samples, to validate the properties and to place this work within the broader research.

The tensile samples were fabricated in both the horizontal and vertical orientations, shown in Figure 4-3. Due to the variation reported by Ghods et al.<sup>127</sup>, samples were placed in the center and in the outer regions of the build space, to obtain an approximate range of possible tensile properties.

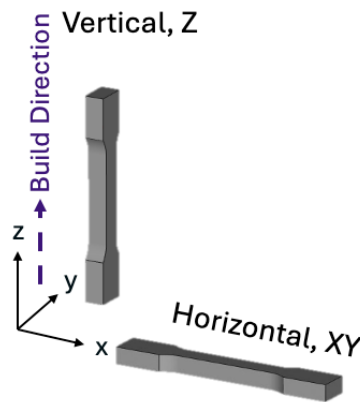


Figure 4-3: The orientation designation for tensile samples

### 4.3.2 Fracture Toughness

The build layout was designed using a multi-factorial approach and the final data evaluated using Response Surface Methodology (RSM) from the Design Expert software (“Stat-Ease,” Minneapolis, MN, USA). The design of experiment (DOE) enables a systematic method for

evaluating the variation in the dataset and property mapping of the build space. The factorial design evaluated the influence and interaction of the design parameters (crack orientation, geometry, spatial location, and post-processing) on fracture toughness. Fracture toughness samples were designed to meet the dimensional requirements to obtain valid plane-strain  $K_{Ic}$  values per ASTM E399, shown in Figure 4-4<sup>228</sup>. Each sample has two-letter designations with respect to the build direction (Z) and recoater direction (X) shown in Figure 4-4a. In the fracture toughness samples, *the first letter designates the direction normal to the crack plane and the second designates the direction of crack propagation per the coordinate system shown in Figure 4-2*. The latter two letters denote the direction of crack plane. While the influence of the crack plane is on interest due to the complex AM microstructure and crack growth relationship, the first two letters are used in this document, aligned with the requirements of ASTM E399.

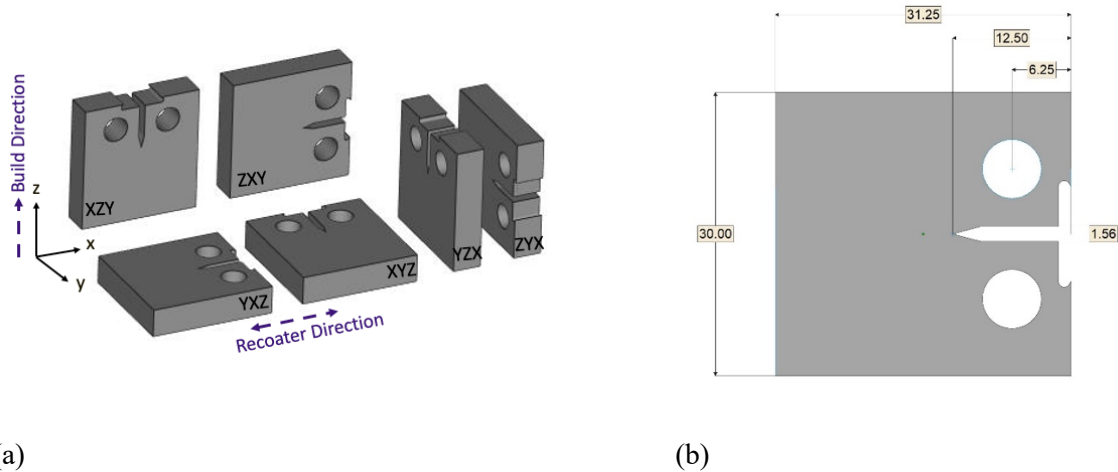


Figure 4-4: (a) Fracture toughness orientation designation, shown with respect to the build direction and recoater path. (b) ASTM E399 CT fracture toughness specimen size, units in mm.

The discrete levels of interest for the orientations designated by Figure 4-4 for the discrete design parameters provided in Table 4-5. The data was analyzed using a factorial three-way Analysis of Variance (ANOVA) to determine the effect of independent variables (intra-build design parameters) on the response (fracture toughness), along with the interactions between parameters. The impact of multiple independent factors can be evaluated using a factorial ANOVA and the statistical significance between the means of each of the levels deemed significant with a  $p\text{-value} \leq 0.05$ . The build layouts are provided in Figure 4-5 and Figure 4-6, and the build space parameters and respective levels are in Table 4-5. In this work, T designates the thickness, R designates the radial distance, and H designates the height.

Table 4-5: Overview of Fracture Toughness specimen size and location

Orientation	ZX	XZ	XY
Parameter	Levels		
Thickness (T, mm)	6, 9	6, 9,12	6, 9,12
Radial Distance (R, mm)	35, 65, 95	35, 65, 95	35, 65, 95
Height (H, mm)	56, 156, 256	56, 156, 256	56, 156, 256

Table 4-6: Sample DOE table to evaluate Fracture Toughness. Each row represents the parameter set utilized for a given sample. Refer to Appendix for each respective DOE table used.

Run	Thickness	Radial Distance	Height	Orientation
1	12	35	256	ZX
2	6	95	56	ZX
3	6	65	56	ZX
4	6	35	256	XZ
5	6	35	256	XZ
6	6	65	56	XZ
7	9	35	256	XY
8	12	95	56	XZ
9	6	95	156	XZ
10	9	35	56	ZX
11	6	35	56	XY
12	6	95	256	XY
13	12	65	56	XY
14	9	35	256	XY
15	6	35	56	ZX
16	12	95	56	XZ
17	9	35	56	XZ
18	12	95	156	ZX
19	6	65	156	XY
20	12	95	256	XY
21	6	35	56	XY
22	6	95	256	ZX
23	6	35	156	ZX
24	9	95	56	XY
25	12	35	156	XZ
26	9	65	256	XZ

Fracture toughness samples were designed to meet the dimensional requirements to obtain valid plane-strain  $K_{Ic}$  values per ASTM E399, shown in Figure 4-4<sup>228</sup>. Each sample has two-letter designations with respect to the build direction (Z) and recoater direction (X) shown in Figure

4-4a. In the fracture toughness samples, *the first letter designates the direction normal to the crack plane and the second designates the direction of crack propagation per the coordinate system shown in Figure 4-2.*

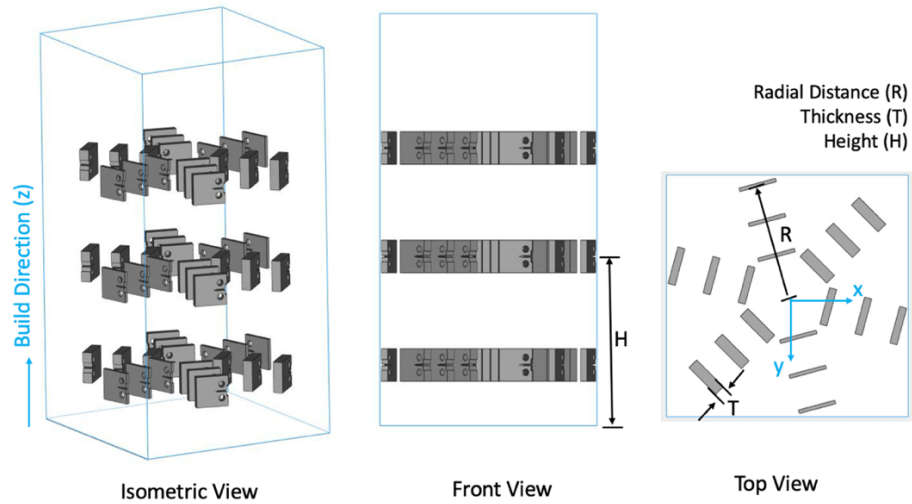


Figure 4-5: Fracture toughness build layout for ZX-oriented samples. Shown are the front, top and isometric views, respectively. Radial distance (R), height (H), and thickness (T) are three factors evaluated in this study and are defined as illustrated.

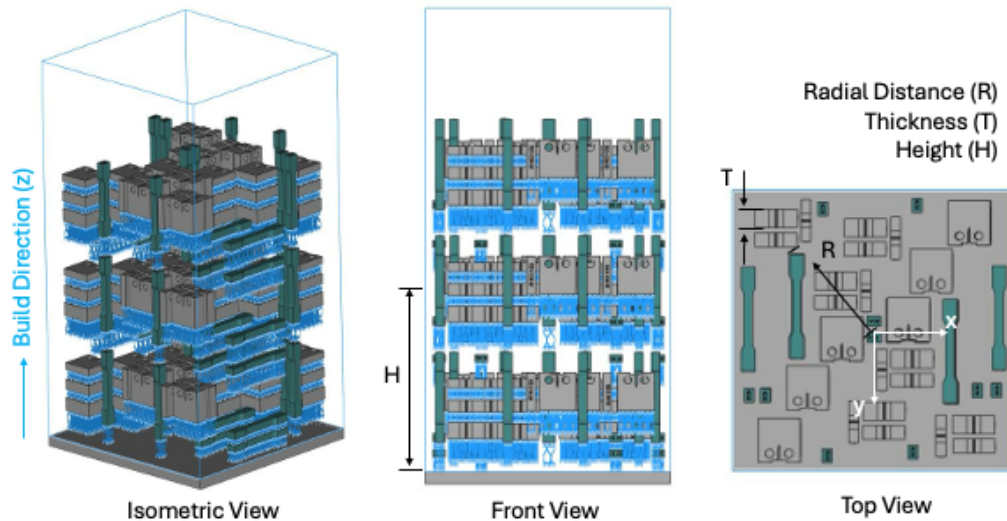


Figure 4-6: Fracture toughness build layout for XZ- and XY-oriented samples. Shown are the front, top and isometric views, respectively. Radial distance (R), height (H), and thickness (T) are three factors evaluated in this study and are defined as illustrated.

Four builds were performed using the same build design parameters to obtain enough samples to evaluate the influence of the intra-build design parameters, post-processing, and the crack orientation. The sequence of builds, post-processing performed, and the total number of samples is provided in Table 4-7. The initial build evaluated the as-fabricated condition in the ZX orientation. The subsequent build evaluated influence of surface finish on the fracture toughness in the ZX orientation, where the free surface was machined. The third build was composed of samples in all three orientations (ZX, XY and XZ). All samples underwent a machining process. The XZ and XY samples were tested in the machined condition to investigate the influence of crack orientation. The ZX samples underwent an additional LTHIP treatment. Lastly, a final build partial build was performed to evaluate the LTHIP treatment effect on the XZ and XY oriented samples.

Table 4-7: Summary of the number of samples manufactured in each condition

Build Sequence	Orientation	Metal Condition	Number of Samples
1	ZX	As-Fabricated	54
2	ZX	Machined	27
3	ZX	LTHIP + Machined	36
	XY, XZ	Machined	54
4	XY, XZ	LTHIP + Machined	36

### 4.3.3 High Cycle Fatigue

Initially, the effect of post-processing on the PBF-EB Ti6Al4V fatigue behavior is explored. The two orientations explored in the HCF study are the vertical and horizontal orientation, shown in Figure 4-7. In the second phase of the fatigue study, the effect of intra-build parameters on untreated and post-processed fatigue PBF-EB Ti6Al4V samples is evaluated.

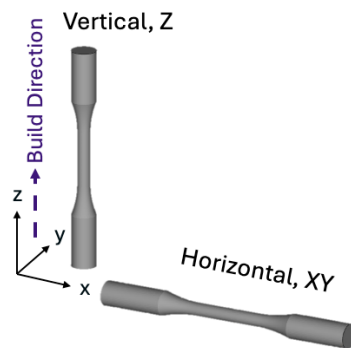
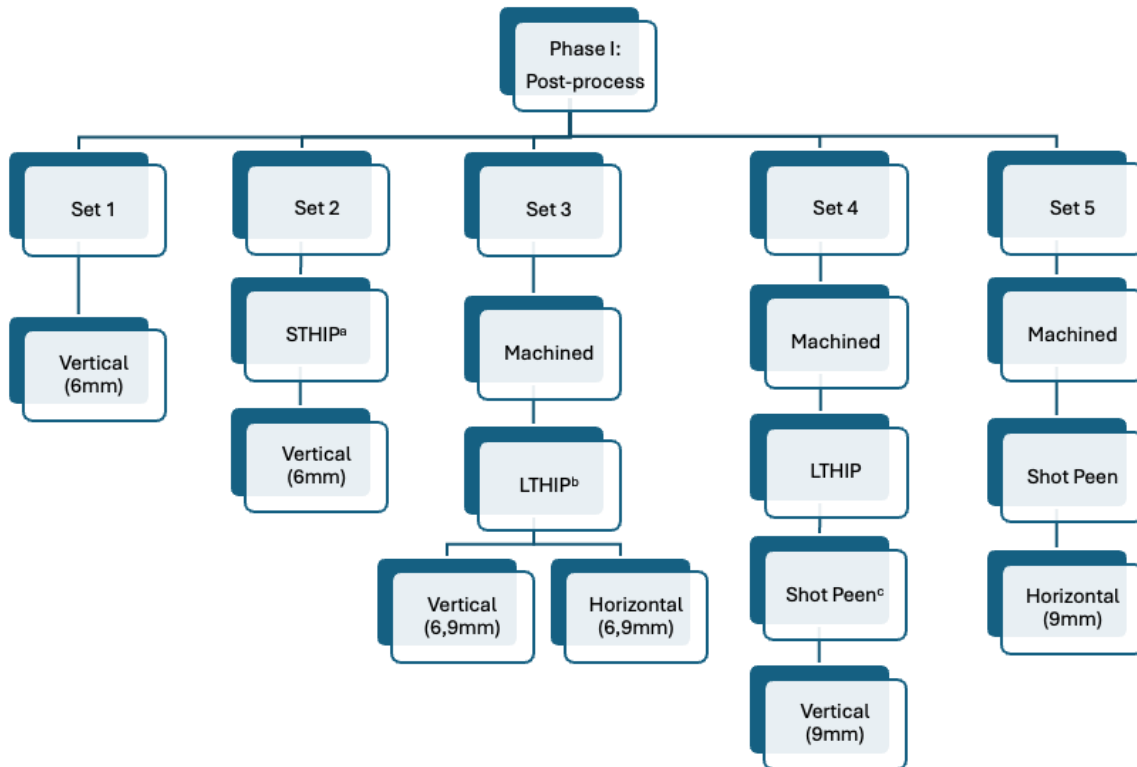


Figure 4-7: The orientation designation for fatigue samples

#### 4.3.3.1 Phase I:

Four post-processing treatments are explored in the following study: machining, standard HIP (STHIP), low temperature HIP (LTHIP), and shot peening (SP). The samples were manufactured in five sets and followed the processing order highlighted in Figure 4-8. Additional information regarding the post-processing parameters adopted can be found in Post-Processing Section.



a- 920°C/100 MPa for 120 min

b- 815°C/190 MPa for 165 min

c- CW35 shot peen media/.006-.01A intensity

Figure 4-8: The sequence of post-processing for each set of samples investigated in Phase I.

The third through fifth set of samples were manufactured concurrently with DOE of Phase II. The build layout and sample dimensions are provided in the following section. The second set of samples underwent machining and a subsequent low-temperature HIP (LTHIP) treatment. The third set of samples included a total of 82 of samples in the horizontal and vertical orientation with the gage diameter of 6mm and 9mm. The fourth set of samples underwent the processing in the following order: machining, LTHIP and shot peen. The samples were fabricated in of the vertical

orientation with a 9mm gauge diameter. A final set of samples fabricated in horizontal (H) orientation with a 9mm gauge diameter underwent machining and a post-shot peen process.

summarizes the treatment, orientation, powder reuse cycle, and the number of samples evaluated in the following study. A total of four builds were performed to obtain the samples investigated in this study. The powder used ranged from build 7 to 10 reuse cycles. An initial subset (qty 8) of reference samples were tested in the untreated and unmachined state, obtained from the first build. The second and third builds contained twenty (20) samples were fabricated in two builds (for a total 40) with the build layout and dimensions shown in Figure 4-9 in the vertical (V) orientation. These second set of specimens underwent a standard hot isostatic pressing (STHIP) treatment to explore the influence of post-processing on PBF-EB Ti6Al4V fatigue behavior. The specimens underwent an STHIP treatment solely, with no addition surface or post-processing treatments. The gage diameter of the cylindrical specimens' post treated was measured to be between 6.0 to 6.8 mm.

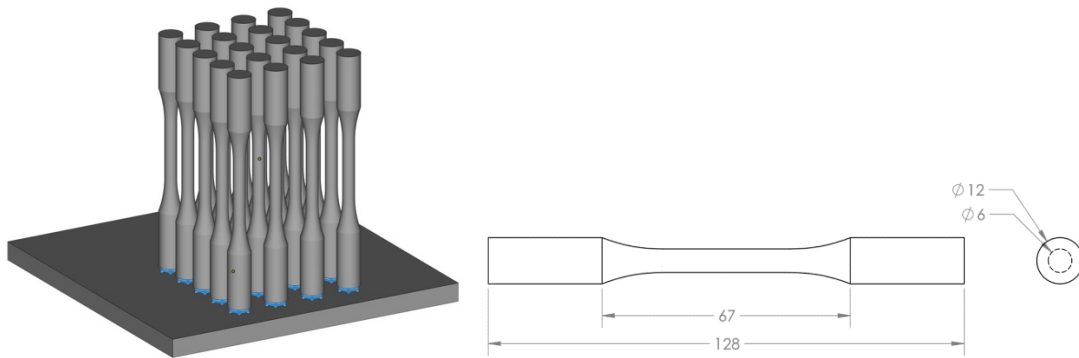


Figure 4-9: The build layout of the as-fabricated HCF samples and final dimensions

The third through fifth set of samples were manufactured concurrently with DOE of Phase II. The build layout and sample dimensions are provided in the following section. The second set of samples underwent machining and a subsequent low-temperature HIP (LTHIP) treatment. The third set of samples included a total of 82 of samples in the horizontal and vertical orientation with the gage diameter of 6mm and 9mm. The fourth set of samples underwent the processing in the following order: machining, LTHIP and shot peen. The samples were fabricated in of the vertical orientation with a 9mm gauge diameter. A final set of samples fabricated in horizontal (H) orientation with a 9mm gauge diameter underwent machining and a post-shot peen process.

Table 4-8: Summary of samples evaluated in Phase I

Set	Treatment	Orientation	Number of Samples	Powder Reuse #
1	As-Built	V	8	7
2	STHIP	V	36	8, 9
3	Machined + LTHIP	V, H	82	10
4	Machined + LTHIP + Shot Peen	V	10	10
5	Machined + Shot Peen	H	12	10

#### 4.3.3.2 Phase II:

The source of variation due to the build space parameters is of interest. The influence of the intra-build design parameters was previously explored in the vertical orientation. However, the influence of the intra-build design parameters in the horizontal orientation has not been widely explored. In addition, how the post-processing changes the scatter due to the intra-build design parameters has not been widely explored. The build design implemented in the following phase remained consistent with the multi-factor DOE adopted in the fracture toughness section. A partial-factorial build design was adopted, with 3-levels for each factor, to investigate every combination of factors using regression statistics. The part design parameter investigated in this study captures any variation due to sample geometry through evaluating the influence of thickness on mechanical properties. The thickness of each specimen corresponds to the thinnest area of the gauge section. Radial distance and height are the two spatial location factors representing the placement in the build chamber. The radial distance is measured from the center of the build plate to the center axis of the sample and the height is from the build plate to the center of the sample. Radial distance was chosen as the spatial parameter to reflect the tracking of the electron beam during the printing process. Lastly, the sample orientation with respect to the build direction is explored, as seen in Figure 4-3. These factors permit evaluation of the build space reflecting choices made by design engineers.

The sequence of post-processing of the samples in Phase II is provided in Figure 4-10 for each respective thickness and orientation. The influence of thickness is one of the intra-build design parameters explored, where cylindrical samples of 7 mm and 10 mm were fabricated and machined to the final dimensions shown in Figure 4-11.

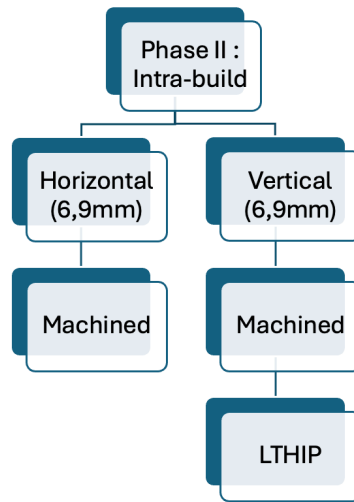


Figure 4-10: The sequence of post-processing for each set of samples investigated in Phase II.

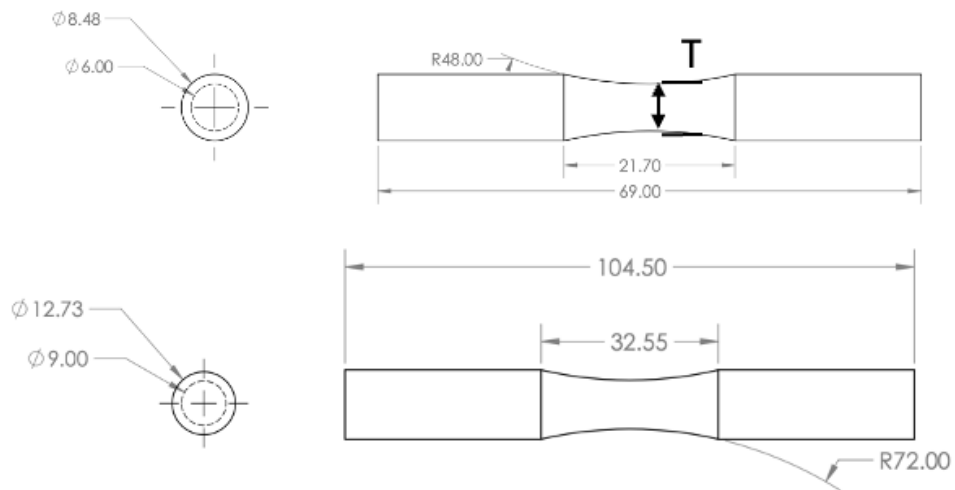


Figure 4-11: The final dimensions for the 6- and 9-mm samples post-machining per ASTM E466. Dimensions are in mm.

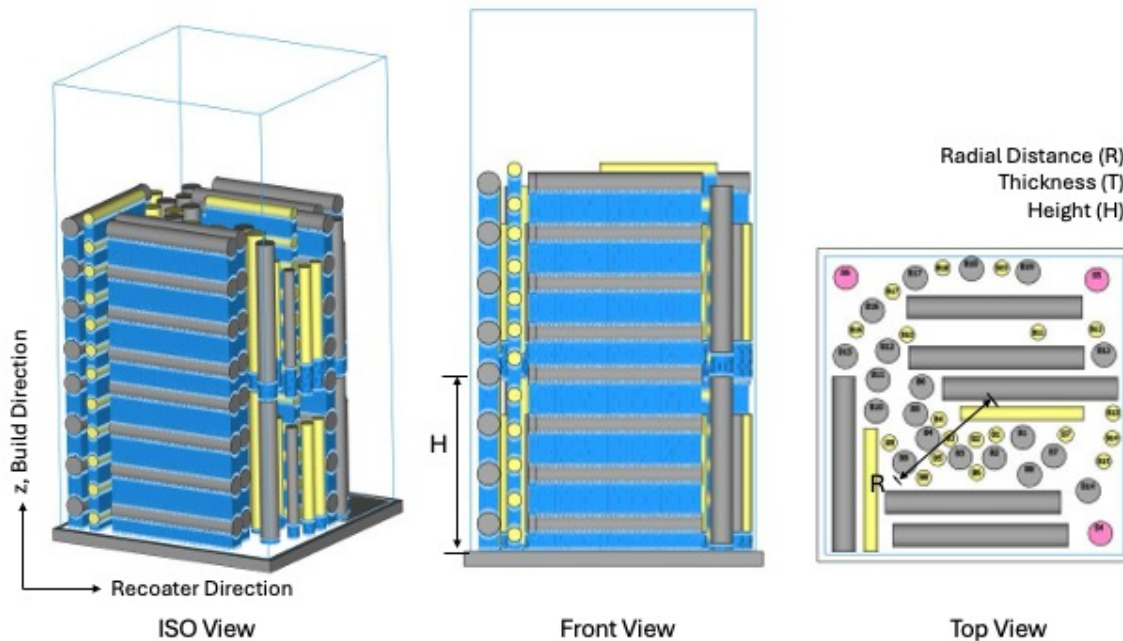


Figure 4-12: PBF-EB build layout for the horizontally oriented high cycle fatigue (HCF) specimens. Shown are the front, side, and top views, respectively. Radial distance (R), height (H), and thickness (T) are three factors evaluated in this study and are defined as illustrated.

Table 4-9: The intra-build design factors and levels in the vertical and horizontal orientation

Parameters	Levels	
	Vertical	Horizontal
Orientation	Vertical	Horizontal
Thickness (T, mm)	6, 9	6, 9
Radial Distance (R, mm)	35, 65, 95	35, 65, 95
Height (H, mm)	56, 156	5, 17, 48, 80, 143, 174, 206
Total Number of Samples	66	34

One build was performed to fabricate samples in both the horizontal and vertical orientation, with the build layout provide in Figure 4-12. The two orientations were printed together to maintain a consist heating during the fabrication process, limit rapid cooling, and limit swelling of layers, in addition to reduce fabrication time. The intra-build design parameters (thickness, radial distance, and height) in Table 4-9 remained consistent with the fracture toughness DOE of the previous section. The vertical samples were printed per the design parameters originally adopted by Ghods et al.<sup>169</sup> to allow for comparison of the intra-build design parameters in the untreated and HIP condition. However, to fabricate samples in the horizontal

orientation, changes needed to be made to accommodate the number of samples necessary for fatigue testing. The specimen thickness and radial distance remained consistent with the DOE designed in the previous section, but the sample height ranged from 5 mm to 250 mm, shown in Table 4-9. The total number of samples fabricated and tested in also provided in Table 4-9.

## 4.4 Analysis Procedure

### 4.4.1 Surface Roughness

The surface quality of the As-Built, Machined, and Shot Peened samples were characterized prior to testing using the contact type profilometer MarSurf XR20 (Mahr Inc., RI, USA) equipped with a 2.5 $\mu$ m conical diamond tip with a 5nm resolution. Optical profilometer VR-3100 (Keyence Corporation, Itasca, IL) captured the 2D and 3D surface profiles and topography. The parameters associated with the 2D and 3D topography is given in Appendix E - Surface Roughness. The average surface roughness ( $R_a$ ), ten-point height ( $R_z$ ), root mean square ( $R_q$ ), maximum valley to peak height ( $R_t$ ), skewness ( $R_{sk}$ ), kurtosis ( $R_{Ku}$ ), and maximum valley depth ( $R_v$ ) were obtained.  $R_a$  is the average of each height and depth of the surface roughness profile,  $R_z$  is the average of the five highest peaks and valleys,  $R_q$  is the square root of the sum of squares of each height and depth from the mean line,  $R_{sk}$  is an indicator of the surface from symmetry, and  $R_{Ku}$  indicates the sharpness of peaks. The 3D areal parameters are average roughness ( $S_a$ ), ten-point height ( $S_z$ ), maximum valley to peak ( $S_t$ ), skewness ( $S_{sk}$ ), kurtosis ( $S_{Ku}$ ), and maximum valley depth ( $S_v$ ). The values were obtained along the gauge section of the HCF specimens and the area along the notch in the CT samples.

### 4.4.2 Internal Defect Analysis

X-ray microcomputed tomography ( $\mu$ CT) is a non-destructive analysis method that is especially useful in imaging internal defects. During the  $\mu$ CT process, an object is irradiated with X-rays to create a cross-sectional view of the object from the absorbed X-rays. The part repeatedly rotates to obtain images of the entire structure. The images are consolidated to form a 3D volume comprised of voxels. Each voxel represents a different material density which can be used for various measurement and qualification analyses such as defects, surface roughness, and dimensional measurements.

$\mu$ CT was used to obtain defect distributions of select fracture toughness and fatigue specimens prior to testing using a commercial system (X5000, North Star Imaging, Rogers, MN, USA). The scan parameters for the fracture toughness and fatigue samples are provided in Table 4-10 and Table 4-11, respectively. Seven (7) gain maps were obtained for accurate greyscale variations of the projections with a 0.127 mm brass filter. High-resolution scans are critical in capturing small porosity defects. The projection of each scan was reconstructed using propriety software provided by the manufacturer of the  $\mu$ CT system. Appropriate beam hardening corrections are applied during the reconstruction to reduce process-induced artifacts. The reconstructed volume is imported as an image stack into Volume Graphics VGStudio Max 3.1 (Volume Graphics Inc., Charlotte, NC) for defect analysis and to obtain key defect characteristics (i.e., diameter, sphericity, location).

Table 4-10: Scan Parameters for the 9-mm Fracture Toughness specimens

<b>Scan Parameter</b>	<b>6 mm</b>	<b>9 mm</b>
Voltage	210 kV	210 kV
Current	80 $\mu$ A	90 $\mu$ A
Geometric Zoom	x11.67	x11.67
Projections	2400	2400
Frame Average	2	2
Frames per second	2	2
Gain Maps	7	7
Voxel Size	16.75 $\mu$ m	15.44 $\mu$ m
Filter	.005 in brass	.005 in brass

Table 4-11: Scan Parameters for 9mm High Cycle Fatigue Samples

<b>Scan Parameter</b>	<b>9 mm</b>
Voltage	215 kV
Current	60 $\mu$ A
Geometric Zoom	x15.91
Projections	3600
Frame Average	2
Frames per second	1
Gain Maps	7
Voxel Size	15.7 $\mu$ m
Filter	.005 in brass

The background and material boundary were differentiated by the difference in grey value between the material and defects. Gaussian filter was applied to improve differentiation between the material and defects. After evaluating various surface determination methods, the Automatic Surface Determination yielded the most accurate representation of defects. Edge-preserving filters were applied to reduce computation time without affecting volumetric porosity. Internal defect characteristics are determined using the VGDefx algorithm, with the option to exclude ring and streak artifacts that may have developed due to beam hardening. The low-probability pores were ignored using a high-adaptive noise filter according to their grey threshold values.

A comprehensive analysis of the distribution of defects in PBF-EB Ti6Al4V metal was previously performed by Ghods et al. <sup>169</sup>. Therefore, to reduce cost of analysis, a subset of each sample type and thickness was analyzed, per Table 4-12. To reduce scan time, two samples were evaluated at a time such that a smaller geometric zoon was necessary to fully capture the sample gauge section.

Table 4-12: Summary of the sample type, condition, and orientation evaluated by  $\mu$ CT

Type	Metal Condition	Orientation	Number of Samples
Fracture Toughness	Untreated	ZX	14
		XY	9
	LTHIP	ZX	4
		XY	4
High Cycle Fatigue	Untreated	H.	4
	STHIP	V	2
	LTHIP	V	4

#### 4.4.3 Microstructure

CT specimens of each thickness in 3-5 build locations were selected for microstructure analysis after testing. Specimens were cut and mounted in a conductive graphite-based powder with a Buehler Pneument I mounting press. Each specimen is polished using Silicon Carbide paper through increasing mesh numbers ranging from #240 to #800. A secondary finer polishing step is performed using felt pads and DiaLube diamond suspension of 9  $\mu$ m, and a subsequent attack polish. Between each polishing step, specimens are ultrasonically cleaned with deionized water. A final etch is performed using Kroll's Reagent (2%HF, 6% HNO<sub>3</sub>, and 92% water) for 3-4s to obtain the microstructural morphology.

After etching, the specimens are examined using an optical and scanning electron microscope (SEM). The area along the crack path is also imaged to obtain information regarding the crack path preference through the microstructure. The average  $\alpha$ -lath,  $\alpha$ -grain boundary, phase volume fraction and prior  $\beta$  grain width are all obtained from minimum three SEM images per sample. The  $\alpha$ -lath measured according to Searles et al.<sup>229</sup>, where the lath is defined as the shortest distance between two adjacent  $\beta$  ribs. The measurement process is previously provided in<sup>43</sup>. The  $\alpha$ -grain boundary and  $\beta$  grain width were obtained from 5 measurements using a commercial software (NIH ImageJ, Bethesda, MD, USA). The volume phase fraction was obtained by performing a thresholding technique on a grayscale image, then segmenting, and measuring the total area of the  $\beta$  phase.

## 4.5 Post-Processing

### 4.5.1 Hot Isostatic Pressing

The influence of hot isostatic pressing (HIP) was evaluated in the following study. An initial set of samples underwent the standard recommended HIP (STHIP) 920°C at 100 MPa for 120 min at a commercial HIP facility. An alternative modified HIP treatment was performed at a lower temperature HIP (LTHIP) with high pressure at 815°C at 190 MPa for 165 min. Utilizing temperature further below the  $\beta$ -transus (980 °C) for Ti6Al4V alloys has shown a decrease in microstructure coarsening, while the increase in pressure aids in mitigating internal defects<sup>151</sup>. The LTHIP treatments were performed by Quintus Technologies and the treatment cycle provided below.

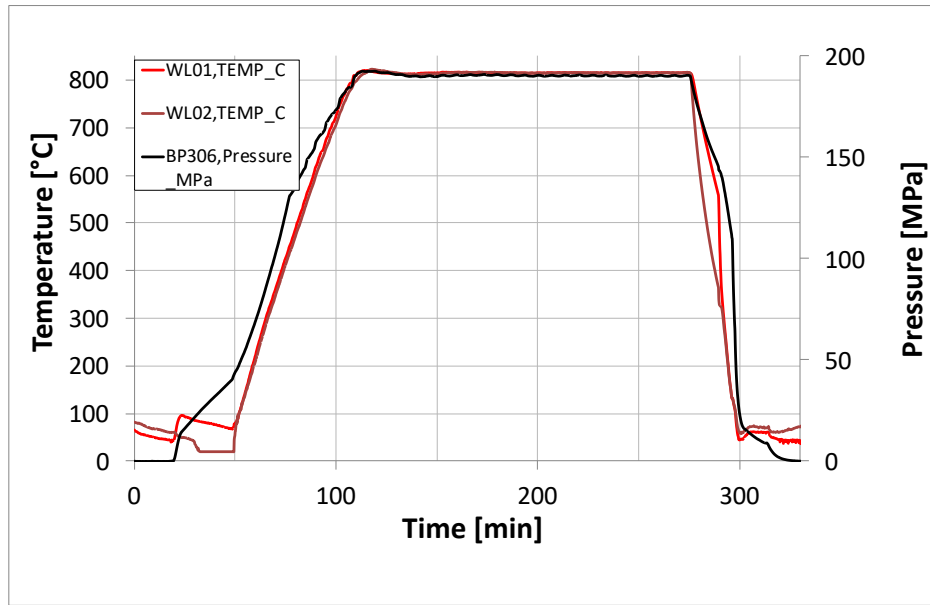


Figure 4-13: LTHIP treatment cycle provided for reference

#### 4.5.2 Surface Treatment

Surface treatments were explored to evaluate influence of the surface finish on the fracture toughness and fatigue properties. The fracture toughness samples were dry milled in-house on a Computer Numerical Control (CNC) with the machining parameters of Table 4-13. The samples were dry milled with three single depth of cut of a full depth passes to achieve the dimensions in Figure 4-4, in compliance with requirements of ASTM E399<sup>228</sup>.

Table 4-13: Machining Parameters

Cutting Tool	Carbide End Mill
Tool Diameter (in)	0.5
Cutting Speed (in/min)	3
Spindle Speed (rpm)	500

The DOE HCF specimens were printed as cylinders and machined to size, per the dimensional requirements of ASTM E466<sup>230</sup>. Samples were machined by a local machining vendor (Ballard Machine Works, Seattle, WA) prior to any other surface treatments via a turning process with appropriate parameters for titanium to avoid residual stresses buildup. A minimum of 1 mm was removed from the external diameter to insure sufficient removal of the PBF-EB surface and subsurface defects. The subset of DOE HCF samples were shot peened by a local

vendor (ASKO Processing, Seattle, WA) per MIL-S-13165. A CW35 shot peen media was used at a .006-.01A intensity along the sample gauge section.

## 4.6 Experimental Testing

### 4.6.1 Mechanical Properties

Tensile samples were designed and tested per ASTM E08 requirements<sup>231</sup>. Samples were printed throughout the build space alongside the CT samples in both horizontal and vertical orientations. Samples were tested in the post-machined condition where approximately 0.4 mm was removed from each surface. Scatter and crack initiation due to the rough surface is reduced by machining the surface.

Tensile tests were performed using a commercial universal testing system (Instron: Model 5585 H; Norwood, MA) under displacement control loading at a strain rate of  $0.05 \text{ s}^{-1}$ . Stress-strain response curves were generated from the load displacement data, which were used to calculate the elastic modulus, yield strength, ultimate tensile strength, % elongation, and the strain hardening exponent.

The Vickers hardness values were obtained using a LM247AT micro-indenter and AMH43 software (LECO Corp., MI) according to ASTM E92<sup>232</sup>. A minimum of five indentations were performed on each sample with a load of 100-gram force for 13 seconds. Per ASTM E92, each indentation location was verified before and after indentation with a distance greater than  $2.5d$  ( $d$  = Indentation Diagonal) between indents.

### 4.6.2 Fracture Toughness Testing

The specimens were printed with dimensions and crack orientation, as shown in Figure 4-4, using straight-through wide-notch compact tension (CT) specimens per ASTM E399<sup>228</sup>. Per the standard, to limit plasticity at the crack tip, the thickness must be between 6- and 12 mm for our specimen with a width of 25 mm, per Eq. 4.1. However, as plane-strain  $K_{Ic}$  values are not guaranteed, approximate fracture toughness values are used for the initial design. Three orientations (ZX, XZ, and XY) were explored in this study to understand the influence of crack orientation with respect to the build and loading directions. Two-letter designations are used in this study and shown with respect to the build orientation and recoater direction, where the first

letter designates the direction normal to the crack plane and the second designates the direction of crack propagation, as shown in Figure 4-4.

The precracking and testing of the 6- and 9-mm samples was performed on a commercial universal testing system with a 20 kN (Instron Model 8511) and on a 100 kN (Instron Model 85215 Nordwood, MA) capacity for 12mm thick samples. Initially, a sharp precrack is generated from the existing notch via cyclic loading at a frequency of 10 Hz and a stress ratio of 0.1, in accordance with ASTM E399. The load used for fatigue precracking was calculated using literature plane-strain fracture toughness values for Ti6Al4V <sup>98</sup>. A fatigue precrack length of approximately 12 mm was formed as designated by Eq. 4.2 to ensure the material behaves under linear-elastic conditions during testing.

The fracture toughness test was performed under quasi-static linear-elastic conditions using the plane-strain method to determine the apparent fracture toughness. The cracking was performed at a constant rate of 0.08 – 0.15 kN/s while the crack mouth opening displacement (CMOD) was monitored and recorded using a displacement gauge, resulting in the load-displacement curves in Figure 4-14. The specimens were tested under rising conditions of  $\Delta K$  until complete fracture. All tests were performed at room temperature in compliance with the ASTM E399 <sup>228</sup>.

$$2 < \frac{W}{B} < 4 \quad \text{Eq 4.1}$$

$$0.45W \leq a \leq 0.55W \quad \text{Eq 4.2}$$

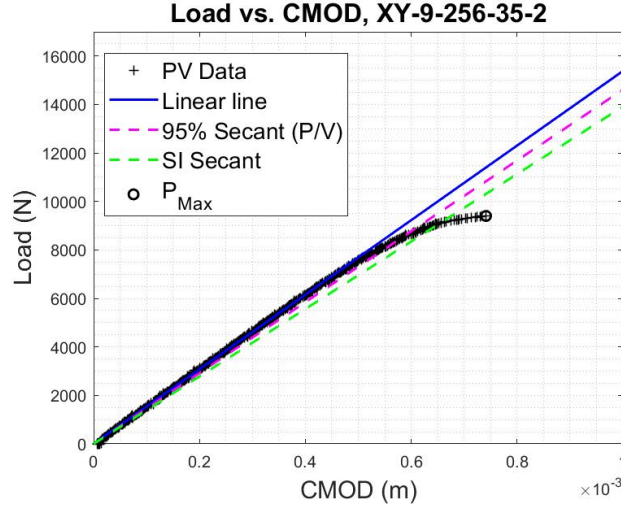


Figure 4-14: Load vs. Crack Mouth Opening Displacement (CMOD) Curve for sample specimen. The blue line is the linear-elastic portion, and the fracture toughness is obtained from the dashed-pink 95% secant line per ASTM E399.

Upon completion of the test, the conditional fracture toughness  $K_Q$  is obtained per the following steps. The force at a 5% secant offset ( $P_Q$ ), which corresponds to about 2% crack extension in the specimen, is obtained from the initial linear slope of the recorded applied load and CMOD. An example is shown for selected specimens in Figure 4-14. The conditional fracture toughness  $K_Q$  is calculated using the value of  $P_Q$  using Eq. 4.3, where  $f(a/W)$  of Eq. 4.4 is the size correction factor,  $a$  is the crack size,  $W$  is the frontal width, and  $P$  is the applied load.

$$K = \frac{P}{T\sqrt{W}} f\left(\frac{a}{W}\right) \quad \text{Eq 4.3}$$

$$f\left(\frac{a}{W}\right) = \frac{(2 + \frac{a}{W}) \left[ 0.886 + 4.64 \frac{a}{W} - 13.32 \left(\frac{a}{W}\right)^2 + 14.72 \left(\frac{a}{W}\right)^3 - 5.6 \left(\frac{a}{W}\right)^4 \right]}{\left(1 - \frac{a}{W}\right)^{3/2}} \quad \text{Eq 4.4}$$

The validity of each test was confirmed using Eq 4.5 and Eq 4.6, where  $\sigma_{ys}$  is the yield strength and  $P_{max}$  the maximum load from the load-displacement curve. For values that meet both validity equations, the stress intensity value  $K_Q$  has met plane-strain conditions and can be designated as  $K_{Ic}$  and considered a material property.

$$W - a \geq 2.5 \left( \frac{K_Q}{\sigma_{ys}} \right)^2 \quad \text{Eq 4.5}$$

$$\frac{P_{max}}{P_Q} \leq 1.10 \quad \text{Eq 4.6}$$

Valid plane strain fracture toughness values were investigated for accurate determination of the influence of intra-build design parameters on the fracture behavior. To determine the effect of the build space and the interactions between each of the parameters (orientation, thickness, radial distance, and height) on fracture toughness, an Analysis of Variance (ANOVA) is used. ANOVA is a statistical method which compares the difference between the factor mean versus the group mean. It is a powerful tool as it can compare multiple independent factors (such as the intra-build parameters explored in this study) and allows for comparison of multiple independent factors and the interactions between factors. For a parameter or interaction to be deemed significant, a *p-value*  $\leq 0.05$  is required. While ANOVA statistics finds the significance of the model and its factors, it lacks information on where the differences lie. Therefore, a pairwise comparison was performed between each factor level using a Tukey post-hoc test to evaluate where the differences between each factor level lies. Stat-Ease (Design Expert, Minneapolis, MN, USA) was used for the ANOVA statistics and IBM SPSS Statistics software (Chicago, IL, USA) to perform the ad-hoc comparison tests. The data investigated in included in Appendix A - Experimental Properties.

#### 4.6.3 High Cycle Fatigue Testing

Uniaxial tension-tension high cycle fatigue (HCF) testing is to be conducted per ASTM E466<sup>230</sup>. The fatigue tests on the Phase I of the STHIP was performed on an Instron hydraulic testing system (Instron Model 8511, Norwood, MA) with a 20kN capacity under constant amplitude with a load ratio (R) of 0.1 at 10 Hz. The remainder of the samples were tested on an Instron hydraulic system (Instron model 8520, Norwood, MA) with a 100kN capacity under constant amplitude with a load ratio (R) of 0.1 at 15 Hz. The total number of cycles is recorded until failure or an endurance limit of  $10^7$  cycles is reached. Minimum of three stress levels between 200 – 800 MPa were selected for each set of experiments, with the specific stress levels provided in Table 4-14. The stress and cycles to failures were plotted onto a Stress-life diagrams, with the Basquin power-law relationship used for fitting, where

$$S = AN_f^B \quad \text{Eq 4.7}$$

*S* is the stress level (max stress, stress amplitude, or effective stress), *A* and *B* are the stress-life constant and exponent, and *N<sub>f</sub>* is the number of cycles to failure. Multiple linear regression was performed using IBM SPSS Statistics software (Chicago, IL, USA) to evaluate the stress-life

distribution and the relationship with respect to the intra-build design parameters for each metal condition.

Table 4-14: Stress Levels tested for each material condition

Condition	Orientation	Stress Levels
Machined	Horizontal	400, 550, 700
STHIP	Vertical	200, 300, 400, 600
Machined + LTHIP	Vertical	300, 400, 600, 800
Machined + LTHIP	Horizontal	400, 550, 700
Machined + LTHIP + SP	Vertical	500, 600, 800

## 4.7 Fractography

Nikon SMZ1000 (Nikon Metrology Inc., MI, USA) optical microscope and FEI Sirion XL30 (Amsterdam, Netherlands) scanning electron microscopy (SEM) was used to observe the fracture surface. In the fracture toughness samples, the crack length prior to final fracture and mechanisms associated with crack growth were identified. The macroscopic characteristics of the fracture surface and determination of crack length were performed using the optical microscope. The SEM was utilized to obtain finer details of the fracture surface and observe anomalies influencing fracture toughness properties.

Microscopy was used in the HCF samples to assess the regions of crack initiation, crack propagation and the area of final rupture of the HCF specimens. The SEM was utilized to obtain finer details of the fracture surfaces, obtain quantitative measurement of crack initiation features, and observe possible anomalies leading to variation in properties.

# 5 Fracture Toughness: As-Built Condition

## 5.1 Introduction

Metal additive manufacturing (AM) is promising for its ability to create intricate and low-waste products. However, understanding the mechanical performance of metal AM components is essential for adoption in stress-critical applications and is an area of growing interest <sup>15, 19,233</sup>. Electron Beam Melting (PBF-EB) and Laser Powder Bed Fusion (PBF-LB) are two popular metal AM processes manufacturing nearly dense parts. PBF-EB is favored for its fast printing speeds, vacuum-inert atmosphere, and high build temperatures that enable printing with minimal support structures and components with negligible residual stresses <sup>15,16</sup>. PBF-LB components exhibit finer resolution, a better surface finish and reduced powder degradation.

In conventionally manufactured alloys, minute composition, microstructure, and process variations contribute to scatter in mechanical properties <sup>98</sup>. The layer-by-layer AM process yields a different set of issues not previously accounted for in conventional manufacturing processes where build orientation, geometry, printing parameters, powder, and microstructural differences contribute to additional scatter in mechanical properties <sup>15, 19, 127, 220,234,235</sup>. Bertsch et al. <sup>234</sup> investigated the property variation in PBF-EB and PBF-LB Ti6Al4V and observed that defect density can influence mechanical property, but the microstructure and phase distribution of the Ti6Al4V that ultimately dictated the mechanical performance. Moreover, the rough surface can reduce the PBF-EB tensile properties by 10% and over 50% under cyclic conditions <sup>220,235</sup>. The As-Built surface of metal AM components depends on the build orientation, geometry, powder size, and process parameters <sup>16,38</sup>. The rough PBF-EB surfaces can exhibit staircase effects, partially fused powder particles from the layer-by-layer process, and partially unmelted areas due to the line-by-line scanning strategy or inadequate process parameters. The feedstock powder shape and size also influence the surface roughness, with PBF-EB components reporting surface roughness values double ( $\sim 28 \mu\text{m Ra}$ ) those of PBF-LB parts ( $\sim 15 \mu\text{m Ra}$ ) due to a larger powder size distribution. While it is important to understand the overall mechanical properties, a holistic approach investigating the contribution of microstructure, surface condition, and porosity on mechanical properties is vital.

Furthermore, the fracture-critical properties are necessary for adoption of metal AM components. Fracture toughness, or the material's resistance to fracture, represents the alloy's quality, reliability, and durability, an essential material property for fracture prevention of engineered components. While there is a growing interest in metal AM fracture resistance, the limited PBF-EB data hinders comparison between the studies and impedes the adoption of metal AM components. The PBF-EB Ti6Al4V  $K_{Ic}$  fracture toughness values are in the promising range of 60 - 100 MPa $\sqrt{m}$ , comparable to wrought and cast alloys<sup>13, 41, 94, 154</sup>. The fine martensitic PBF-LB microstructure and large residual stresses reduce crack growth resistance and toughness (16 – 60 MPa $\sqrt{m}$ ) compared to their PBF-EB counterparts<sup>49, 153, 158, 161, 236</sup>. Orientation-dependent fracture toughness properties have also been observed in both PBF-EB and PBF-LB components<sup>13, 41, 154, 158, 236</sup>. A comprehensive study on the PBF-EB process-structure-property relationships, focusing on reproducibility, will bring metal AM closer to use in load-bearing applications. Although elevated PBF-EB build temperatures are preferred for maintaining part shape and reducing residual stresses, a thermal gradient exists as new layers are added and lower layers cool. Additionally, specimens can undergo different temperature cycles depending on location, with the largest concentration of heat in the center of the build<sup>137</sup>. This contributes to a coarser microstructure in metals in the center of the build space than those close to the edges, resulting in location-dependent tensile properties<sup>22, 23, 127</sup>. Microstructure directly influences fracture toughness such that microstructural characterization of the entire PBF-EB build space is necessary to produce repeatable components.

The contribution of porosity, microstructure, surface condition, and orientation on fracture resistance must be explored to push the barriers limiting metal AM adoption. To further develop quality and reliable metal AM components, the build design influences on fracture property variability is key. In this study, we investigated the effects of build space parameters and part design and their interaction on the fracture toughness of PBF-EB Ti6Al4V. Statistical analysis was performed to understand the influence and interaction of the most critical features influencing fracture resistance. This study reports foundational knowledge of the property variability due to build space and provides general guidelines for design engineers in producing acceptable and repeatable components.

## 5.2 Results

### 5.2.1 Microstructure

The typical microstructure imaged using SEM is shown in Figure 5-1. The rapid heating and cooling with the addition of each layer creates columnar  $\beta$  grains with large aspect ratios parallel to the build direction, as seen in Figure 5-1a. The prolonged high build temperature of the PBF-EB process is akin to stress relief and anneal process below the  $\beta$ -transus temperature, transforming the initial  $\alpha'$ -martensite into  $\alpha+\beta$  basketweave within the columnar  $\beta$  grain. The  $\beta$  volume fraction of ZX, XZ, and XY samples is 11%, 11.5, and 12%, respectively. The average prior  $\beta$  width grain size measured approximately 42, 39, and 39  $\mu\text{m}$  in the ZX, XZ, and XY samples, respectively. Statistical significance from the intra-build design parameters was not observed to influence the  $\beta$  phase fraction and grain width and additional samples are recommended.

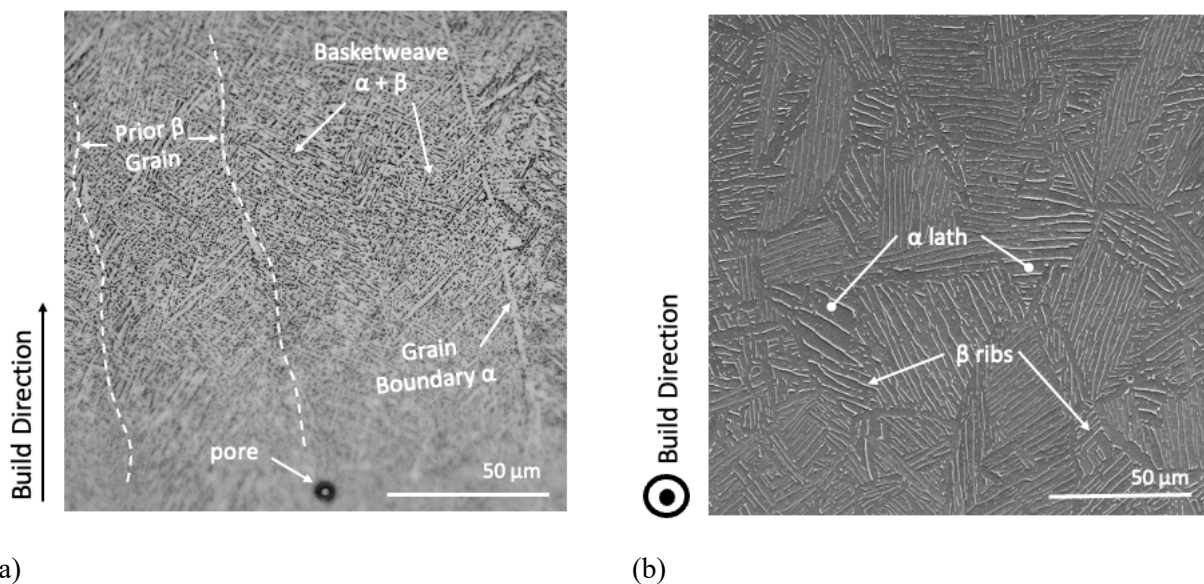
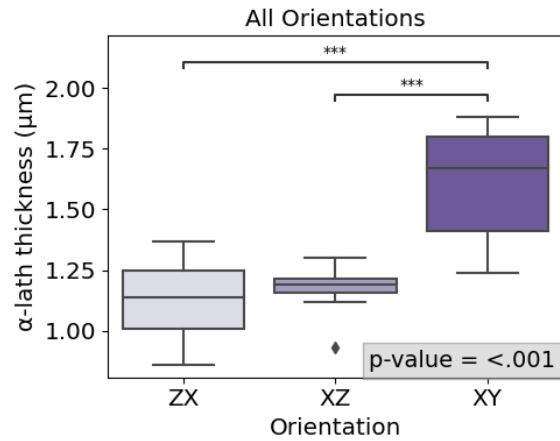


Figure 5-1: PBF-EB Ti6Al4V microstructure of the machined (a) ZX and (b) XY oriented samples. Columnar prior- $\beta$  grain formed along the build direction, comprised of an  $\alpha+\beta$  basketweave microstructure within the grain. (b) The dark color identifies the acicular  $\alpha$  grains and the  $\beta$ -rib in white after etching.

A box plot of the  $\alpha$ -lath thickness for the three orientation is provided in Figure 5-2a. The box plots represent the median, upper, and lower interquartile range. The outliers are represented by the individual data points. As evident from Figure 5-2a, the ZX and XZ samples reported similar  $\alpha$ -lath thicknesses between 1-1.2  $\mu\text{m}$ , and the XY samples reported a 30% larger thickness,

between 1.3-1.8  $\mu\text{m}$ . A factorial ANOVA on the data resulted in significant p-values, indicating that orientation had the largest influence (67% contribution) on the  $\alpha$ -lath thickness, followed by the intra-build parameters. A pair-wise Tukey test was performed and shown in Figure 5-2a. The bars connecting two groups with a (\*\*\*) indicates the XY orientation is statistically different from the ZX and XZ orientations.



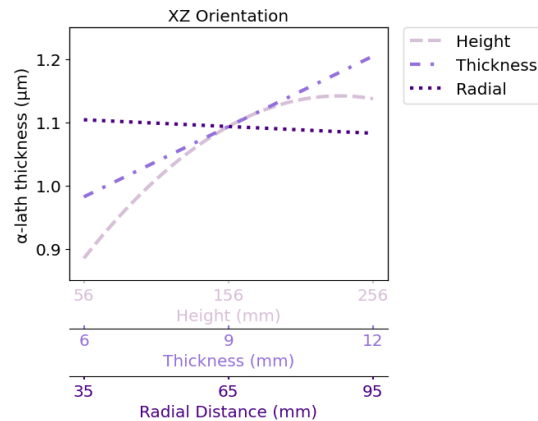
	Factor 1	Factor 2	Factor 3	Factor 4	Response 1
<b>Sample</b>	A: Thickness	B: Height	C: Radial Distance	D: Orientation	a-lath thickness (um)
1	12	156	65	ZX	1.23
2	6	256	95	ZX	0.988
3	12	56	95	ZX	0.97
4	12	156	65	XZ	1.17
5	9	156	95	ZX	1.1
6	12	156	35	XY	1.76
7	12	56	35	XY	1.33
8	12	256	95	XZ	1.21
9	12	256	35	ZX	1.26
10	9	156	35	ZX	1.1
11	12	56	35	ZX	1.03
12	12	256	95	ZX	1.29
13	9	56	35	ZX	1.05
14	9	256	35	ZX	1.13
15	12	256	95	XY	1.76
16	9	256	95	ZX	1.23
17	12	56	35	XZ	1.07

(a)

Source	Sum of Squares	% Contribution	df	Mean Square	F-value	p-value
<b>Model</b>	0.7782		6	0.1297	19.38	< 0.0001
<b>Thickness</b>	0.0530	8.2	1	0.0530	7.92	< 0.05
<b>Height</b>	0.1336	20.7	1	0.1336	19.97	< 0.05
<b>Radial Distance</b>	0.0013	0.2	1	0.0013	0.1959	0.6675
<b>Orient</b>	0.4346	67.3	2	0.2173	32.48	< 0.0001
<b>HP</b>	0.0235	3.6	1	0.0235	3.51	0.0904

Equation: ZX a-lath = 0.4138 + 0.0370\*B + .00383\*H - 0.000355\*R - .0000082\*H<sup>2</sup>  
 XZ a-lath = 0.385 + 0.0370\*B + .00383\*H - 0.000355\*R - .0000082\*H<sup>2</sup>  
 XY a-lath = 0.848 + 0.0370\*B + .00383\*H - 0.000355\*R - .0000082\*H<sup>2</sup>

(b)



(c)

(d)

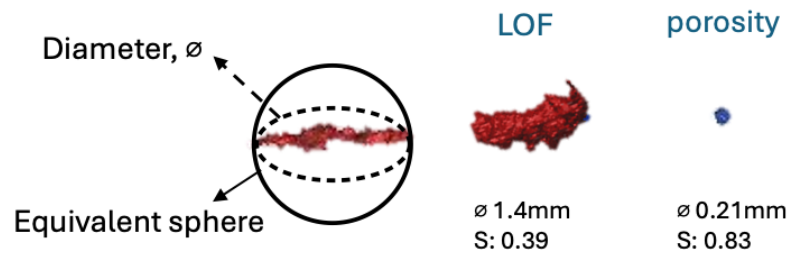
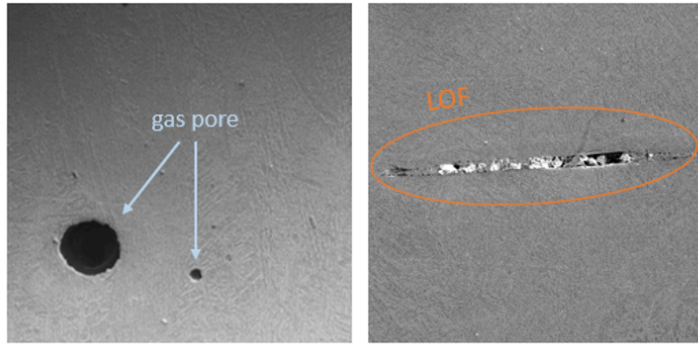
Figure 5-2: (a) Box plot of the ZX, XZ, and XY fracture toughness values, overlaid with model significance and Tukey test indicating significance. (b) the four-way DOE table and (c) results. (d) the plot of prediction equations obtained from the ANOVA model.

Height had the second largest impact (21%) on  $\alpha$ -lath thickness, with  $\sim 20\%$  increase in lath size with increasing height, as seen in Figure 5-2c. The Tukey pair-wise comparison test for height found the lowest height level was significantly different from the middle and high height levels, which is contributing to the curvature observed in the Height factor Figure 5-2c. The largest change in lath thickness occurred between the low and mid height levels, such that samples closest to the

build plate exhibited a finer microstructure. The positive linear relationship between  $\alpha$ -lath and geometry resulted in a ~10% increase with increasing thickness, shown in Figure 5-2d for the XZ orientation. The microstructural trends were observed for all three orientations, and the XY and ZX orientation provided in Appendix D - Statistics. Additionally, a small decrease in  $\alpha$ -lath thickness was observed with increasing radial distance, however the parameter was not found to be significant. The resulting model equation can be used to make predictions of the  $\alpha$ -lath thicknesses for the given intra-build design parameters, as shown in Figure 5-2b for each orientation.

### *5.2.2 Porosity analysis*

For this study, defect diameters above 50  $\mu\text{m}$  were analyzed, with an interest on the defect diameter and shape seen in Figure 5-3 and Figure 5-4. The diameter of the pores is defined as the maximum possible diameter of the defect, and sphericity is the measure of how likely an object resembles a sphere and is found as the ratio of the surface area of a circumscribed sphere with the same volume to the surface area of the defect. A defect with sphericity close to one (1) is nearly spherical and defects with lower sphericity close to zero (0) tend to have higher aspect ratios and irregular or non-spherical shapes, such as the flat and irregularly shaped LOF defects. It can be seen from Figure 5-5a defect diameter distribution with the majority of defect diameter  $< 0.4$  mm and sphericity  $> 0.4$  mm, where the largest defect diameters also correspond to the lowest sphericity.



$$\text{Sphericity, } S = \frac{\text{surface area of equivalent sphere}}{\text{surface area of particle}}$$

Figure 5-3: High magnification images of porosity and LOF defect. The arrows denote spherical gas pores. The outlined region indicates the LOF defect formed between two layers and contained unmelted and partially melted powder particles.

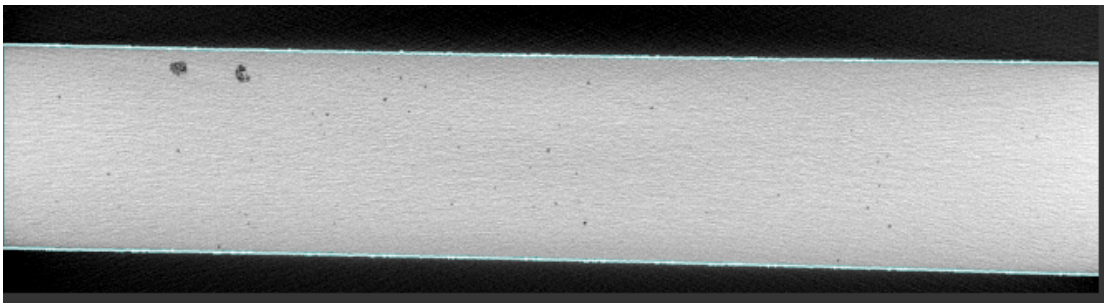
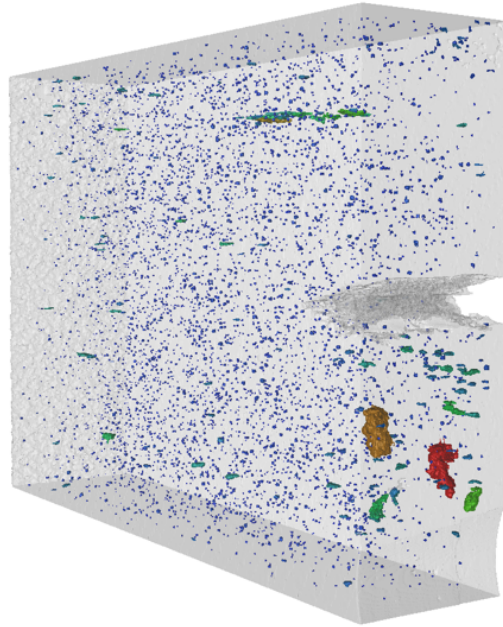
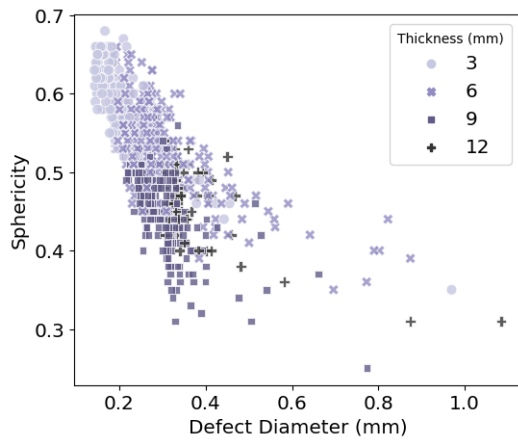
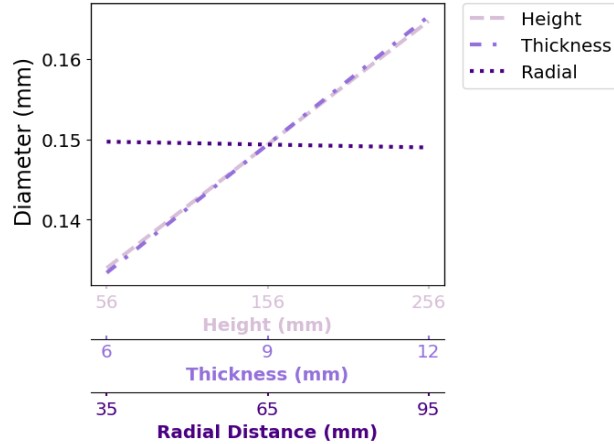


Figure 5-4: The  $\mu$ CT reconstruction of the As-Built and LTHIP samples. The LTHIP process showed a significant reduction in porosity and defect size.

The influence of the intra-build design parameters on the average defect diameter was further evaluated. Thickness and height were found to significantly influence the change in defect size. The positive regression relationship between thickness and height on average diameter is shown in Figure 5-5b, where an increase in defect size is observed.



(a)



(b)

	Factor 1	Factor 2	Factor 3	Response 3
Samples	A: Thickness	B: Height	C: Radial	Mean Diameter
1	12	156	65	0.175
2	6	256	95	0.156
3	6	56	95	0.123
4	12	156	95	0.1845
5	9	156	95	0.143
6	6	56	35	0.134
7	6	256	35	0.114
8	9	156	35	0.151
9	9	156	65	0.143
10	12	256	95	0.176
11	9	56	35	0.117
12	12	56	65	0.155
12	9	56	95	0.122
14	9	256	95	0.158

(c)

Source	Sum of Squares	% Cont.	df	Mean Square	F-value	p-value
Model	0.0042		3	0.0014	8.98	0.0045
A-Thickness	0.0017	53%	1	0.0017	11.15	0.0087
B-Height	0.0015	47%	1	0.0015	9.56	0.0129
C-Radial	8.688E-07		1	8.688E-07	0.0056	0.9419
Equation: Mean Dia. = 0.0787 + .00533*A +.00015*B - .000012*C						

(d)

Figure 5-5: Graphs representing the defect characteristics obtained from  $\mu$ CT analysis. (a) The defect diameter is plotted versus the defect sphericity. (b) A positive linear relationship between mean diameter and thickness and height exists. (c) the DOE table evaluated and the resulting (d) ANOVA table.

### 5.2.3 Surface Roughness

The 3D surface morphology and line roughness profile are provided in Figure 5-6 as a function of surface condition. Additional data regarding the surface morphology and parameters in provided in Appendix E - Surface Roughness. The topography was obtained to better understand the features influencing mechanical properties. The roughness profiles were obtained from a line scan and provides a 2D view of the surface. The As-Built surface exhibited the largest peaks and valleys compared to the other surface conditions. The rough surface of the CT samples exhibits the partially fused powder particles evident in the As-Built condition which was removed with machining. However quantitative analysis was required to fully understand the influence of surface roughness.

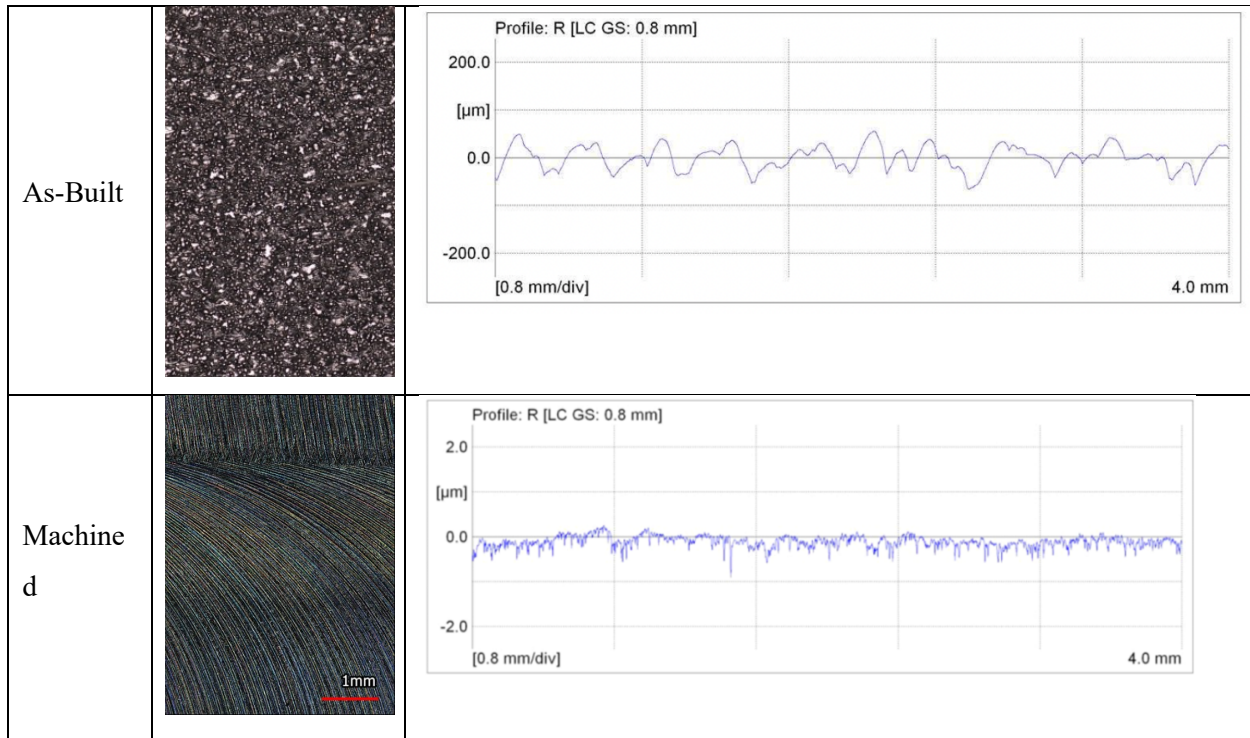


Figure 5-6: The 2D surface roughness profile in each sample. Note the difference in scale.

Table 5-1 summarizes the surface roughness parameters including: the average surface roughness values ( $R_a$ ), ten-point height ( $R_z$ ), root mean square ( $R_q$ ), maximum valley to peak height ( $R_t$ ), skewness ( $R_{sk}$ ), kurtosis ( $R_{Ku}$ ), and maximum valley depth ( $R_v$ ). The surface roughness characteristics were obtained as a function of surface and metal condition. The PBF-EB surface decreased from  $\sim 20 \mu\text{m}$  in the as-built to  $0.2 - 1 \mu\text{m}$  with machining 1 mm from the external surface. While many PBF-EB studies report the  $R_a$  and  $R_z$  values, the other surface parameters have been shown to be beneficial in understanding the mechanical properties. The maximum peak to valley, root mean square, and maximum valley depth were all shown to decrease significantly with machining. The decrease in  $R_q$ ,  $R_t$ , and  $R_v$  indicate a decrease of features which may act as surface notches. The negative  $R_{sk}$  values indicate the surface is made up of valleys primarily, where the machined samples had the lowest skewness. The decrease in average and range of skewness implies the surface symmetry decreased with machining.

Table 5-1: CT samples surface roughness characteristics in each condition

Parameter	As-Built	Machined
R <sub>a</sub> (μm)	24.4 ± 5.6	0.15 ± 0.10
R <sub>z</sub> (μm)	168.5 ± 48.5	0.68 ± 0.08
R <sub>q</sub> (μm)	25.3 ± 2.5	0.17 ± 0.01
R <sub>t</sub> (μm)	107.6 ± 14.3	11.69 ± 1.48
R <sub>sk</sub> (μm)	-0.1 ± 0.10	-1.48 ± 0.11
R <sub>ku</sub> (μm)	2.9 ± 0.43	2.79 ± 0.63
R <sub>v</sub> (μm)	56.5 ± 7.8	5.64 ± 0.59

### 5.2.4 Tensile Properties

Figure 5-7 shows the stress-strain curves as a function of surface condition and orientation. The stress-strain responses were constructed by calculating the stress based on the instantaneous area and strain from the change in area. Because of machining and orientation, three experimental observations are implied in Figure 5-7. First, the yield strength as a function of surface condition increases, which is attributed to the improvement in the surface quality. Second, the area under the stress-strain curve, denoting the toughness, increases with machining. Lastly, the horizontal and vertically oriented samples exhibit similar tensile behavior.

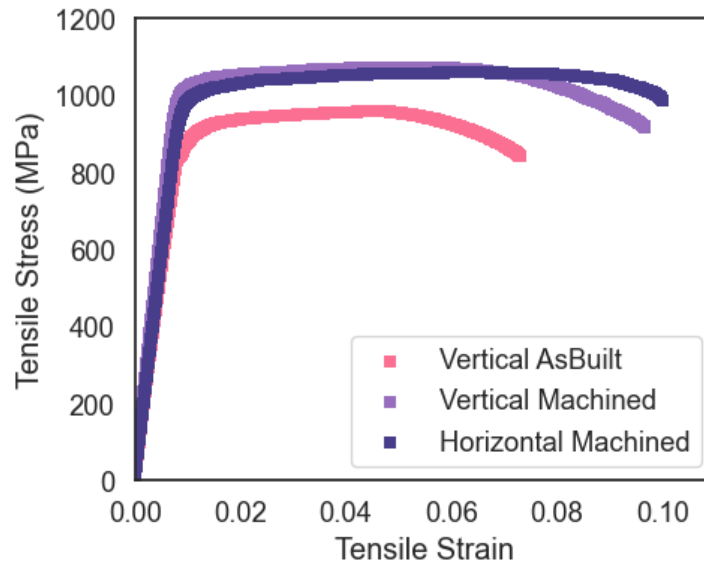


Figure 5-7: The stress-strain curve as a function of surface and build orientation

Table 5-2 summarizes the tensile properties, including the yield strength, ultimate tensile strength, elongation at failure, and strain hardening. The properties were obtained as a function of the surface condition and orientation. The YS and UTS increased significantly with machining. With an improvement in the surface quality, stress induced due to surface and subsurface defects

is removed, resulting in an increase in properties. Similar trends were observed in <sup>42</sup>. Furthermore, the EF remains comparable between the two metal types and orientations. EF is typically affected by internal porosity, where the similar bulk properties would yield similar ductility. The YS, UTS, and EF are comparable to the study by <sup>12</sup>, where an increase in YS and UTS was observed after machining, while the EF remained the same.

Table 5-2: Summary of the tensile properties

Type	Orientation	Yield Strength (MPa)	Ultimate Tensile Strength (UTS)	Elongation % (EF)
As-Fabricated	Vertical	840	960	9
Machined	Vertical	975	1122	10
	Horizontal	972	1100	10

### 5.2.5 Fracture Toughness

Response surface methodology (RSM) was used to evaluate the influence and interaction of the intra-build design parameters (orientation, thickness, radial distance, and height) on fracture toughness. The DOE table and ANOVA results includes the term examined in the model, including the main factors and significant interactions effects. The model and the intra-build design parameters were found to be significant ( $p \leq 0.05$ ), and the ANOVA tables provided in Figure 5-8. The four-way ANOVA model was performed to evaluate the influence of orientation, and the intra-build design parameters. The model was significant, with orientation, height, and radial distance having the largest influence on fracture toughness variation. XY samples reported higher fracture toughness values than the ZX and XZ oriented samples. When the sample orientation was considered, the fracture toughness variation decreased from 10% to roughly 8%. The influence of surface condition in the ZX orientation using a one-way ANOVA was not found to be significant, with roughly 3% variation between the unmachined and machined samples.

	Factor 1	Factor 2	Factor 3	Factor 4	Response 1
Sample	A: thickness	B: height	C: radial distance	D: Orientation	Fracture toughness
1	9	56	95	ZX	56.7
2	6	156	65	ZX	63.7
3	12	56	65	XZ	61
4	6	56	95	XZ	54.8
5	9	156	35	ZX	68.3
6	9	256	95	XY	70
7	6	56	35	XY	66
8	12	56	35	XY	68
9	9	56	35	ZX	66
10	6	56	65	ZX	56.5
11	12	156	95	XZ	61
12	6	256	35	XY	71
13	9	256	65	XZ	71
14	9	256	65	XZ	69
15	6	256	95	ZX	69.6
16	6	156	35	XZ	63.8
17	9	156	65	XY	67
18	12	56	95	XY	64
19	9	156	65	XY	70
20	6	256	35	XZ	75
21	6	56	95	XY	63
22	6	156	95	XY	64
23	9	156	65	ZX	61.4
24	12	256	65	XY	74
25	9	156	35	XY	69
26	9	156	95	XZ	60

(a)

Source	Sum of Squares	% Contribution	df	Mean Square	F-value	p-value
<b>Model</b>	615.79		7	87.97	19.03	< 0.0001
<b>Thickness</b>	18.43	3.2	1	18.43	3.99	0.0612
<b>Height</b>	336.31	58.6	1	336.31	72.75	< 0.0001
<b>Radial distance</b>	98.50	17.2	1	98.50	21.31	<0.001
<b>Orientation</b>	88.35	15.4	2	44.18	9.56	<0.05
<b>ZX FT = 58.029 + 0.395*T + 0.059*H – 0.0838*R</b>						
<b>XX FT = 56.273 + 0.395 *T + 0.624*H – 0.0838*R</b>						
<b>XY FT = 65.148 + 0.395 *T + 0.031*H – 0.0838*R</b>						

(b)

Figure 5-8: The RSM four-way ANOVA (a) DOE table and (b) significance test evaluating the effect of orientation and the intra-build design parameters.

The relationship between each factor (thickness, radial distance, and height) and fracture toughness in each orientation was further evaluated using a three-way ANOVA, results provided in Figure 5-9a and the contribution of each factor in Figure 5-9b. The factor plots in Figure 5-10 show the relationship between the response (fracture toughness) and the different levels of a given factor, while keeping the other two factors constant at the mid-level. A linear relationship was observed for parameters where only the specific parameter influences fracture toughness. A non-linear

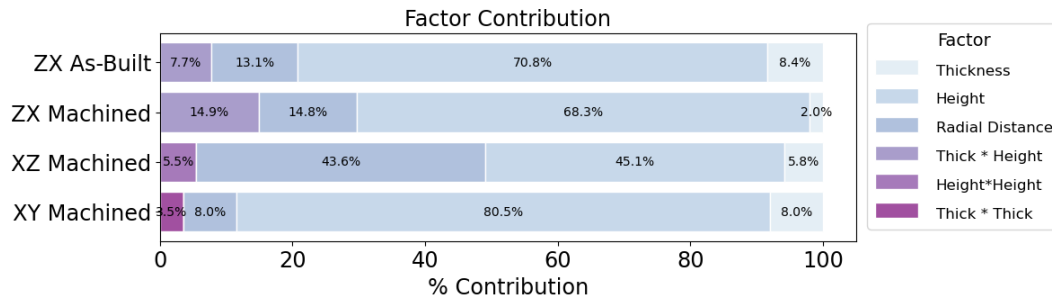
relationship is presented for samples where both the specified parameters and the interaction between the other parameters exist.

ZX As-Built							ZX Machined						
Source	Sum of Squares	df	Mean Square	F-value	p-value		Source	Sum of Squares	df	Mean Square	F-value	p-value	
Model	491.27	4	122.82	13.98	< 0.0001	significant	Model	343.38	4	85.84	20.14	< 0.0001	significant
A-thickness	42.53	1	42.53	4.84	0.0419		A-thickness	9.15	1	9.15	2.15	0.1737	
B-height	358.70	1	358.70	40.84	< 0.0001		B-height	315.44	1	315.44	74.00	< 0.0001	
C-radial	66.35	1	66.35	7.55	0.0137		C-radial	68.51	1	68.51	16.07	0.0025	
AB	38.92	1	38.92	4.43	0.0505		AB	68.97	1	68.97	16.18	0.0024	
Residual	149.32	17	8.78				Residual	42.62	10	4.26			
Lack of Fit	92.32	11	8.39	0.8835	0.5948	not significant	Cor Total	386.00	14				
Pure Error	57.00	6	9.50										
Cor Total	640.59	21											

XZ Machined							XY Machined						
Source	Sum of Squares	df	Mean Square	F-value	p-value		Source	Sum of Squares	df	Mean Square	F-value	p-value	
Model	488.74	4	122.18	21.87	< 0.0001	significant	Model	442.37	4	110.59	22.27	< 0.0001	significant
A-thickness	33.34	1	33.34	5.97	0.0274		A-thickness	33.53	1	33.53	6.75	0.0164	
B-height	256.96	1	256.96	45.99	< 0.0001		B-height	336.61	1	336.61	67.78	< 0.0001	
C-radial	248.54	1	248.54	44.48	< 0.0001		C-radial	33.53	1	33.53	6.75	0.0164	
B <sup>2</sup>	31.36	1	31.36	5.61	0.0317		A <sup>2</sup>	14.50	1	14.50	2.92	0.1016	
Residual	83.81	15	5.59				Residual	109.26	22	4.97			
Lack of Fit	56.81	12	4.73	0.5260	0.8167	not significant	Lack of Fit	104.76	21	4.99	1.11	0.6470	not significant
Pure Error	27.00	3	9.00				Pure Error	4.50	1	4.50			
Cor Total	572.55	19					Cor Total	551.63	26				

(a)



(b)

$$ZX FT = 44.725 + 2.640 * T + 0.131 * H - 0.077 * R - 0.010 * T * H$$

$$XZ FT = 66.328 + 0.561 * T - 0.042 * H - 0.137 * R + 0.0002 * H^2$$

$$XY FT = 74.984 - 2.570 * T + 0.044 * H - 0.047 * R + 0.169 * T^2$$

(c)

Figure 5-9: The RSM ANOVA significance test for the intra-build parameters in the ZX As-Built, ZX Machined, XZ Machined, and XY Machined condition. (b)The contribution of each factor in the model, and (c) the resulting equation for the given model.

As it can be seen, the intra-build design parameters have a similar effect on the fracture toughness behavior, regardless of orientation. The sample height within the build space was observed in Figure 5-9 and Figure 5-10 to have the strongest influence on fracture toughness (45 – 80% contribution), with fracture toughness increase with increasing height from the build plate. Radial distance had the second largest effect (8 – 44% contribution), exhibiting a negative correlation to fracture toughness, with a decrease in fracture toughness in samples located closer to the edges of the build space. Lastly, a positive relationship between fracture toughness and thickness was observed in all three orientations. The thickness parameter contributed to roughly 2 – 8% of variation in the model. Due to the limited number of valid  $K_{Ic}$  values in the ZX Machined orientation, thickness was not found to be significant, and additional samples are recommended in the future.

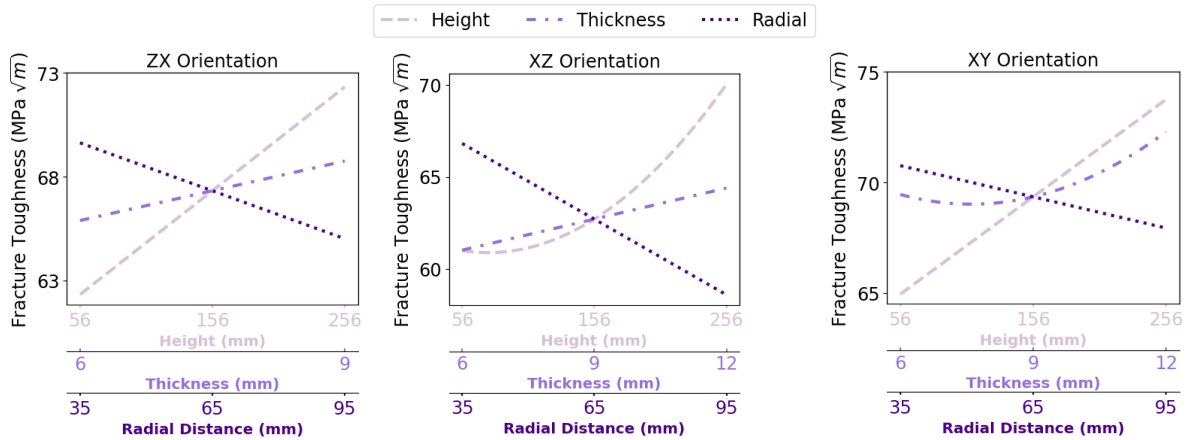


Figure 5-10: The RSM prediction curves in the ZX, XZ, and XY orientation. Each factor is individually plotted while keeping the other two factors constant.

The average PBF-EB Ti6Al4V fracture toughness and the Coefficient of Variation (CoV) are provided in Table 5-3 for each orientation and surface condition. The CoV was calculated to better understand the repeatability and variability of the results. The valid  $K_{Ic}$  plane-strain fracture toughness values reported an average fracture toughness of 65 MPa√m with less than 10% variation in overall properties, comparable to conventionally manufactured alloys<sup>98</sup>.

Table 5-3: Summary of fracture toughness values obtained for each orientation.

Condition	Orientation	$K_{Ic}$ ( $\sqrt{m}$ )	(MPa CoV	$K_{Ic, 95CI}$ ( $\sqrt{m}$ )	(MPa Ref
All	All	$65.5 \pm 5.9$	9.12	$65.5 \pm 1.2$	
As-Built	ZX	$67.3 \pm 6.8$	10.21	$67.3 \pm 3.3$	
Machined	ZX	$63.2 \pm 4.9$	7.83	$63.2 \pm 2.7$	
	XZ	$64.3 \pm 5.2$	8.22	$63.3 \pm 1.9$	
	XY	$67.0 \pm 5.4$	8.12	$67.0 \pm 2.0$	
Wrought, air-cooled		44 - 66			237
Cast, annealed		$77 \pm 12.5$			98

### 5.2.6 Fractography

The fracture surfaces of selected specimens were analyzed using an optical microscope to evaluate the macro and micro-mechanisms of fracture behavior. The pre-crack, crack propagation, and area of final fracture are provided in Figure 5-11. Macroscopically, the fracture surface consisted of flat fracture center and angled shear lips along the edges. Porosity and LOF defects were visible on the fracture surfaces, most notable on the fracture surfaces of the ZX oriented samples as seen in Figure 5-11c. Porosity and defects made up roughly 0.2% of the XZ and XY fracture surface, while 1.3% of the ZX fracture surface.

High magnification images of the fracture surfaces were obtained using scanning electron microscopy to evaluate the microscopic fracture features. In the unstable crack growth region following the precrack, ductile and brittle failure micro-mechanisms were observed on the fracture surface as seen in Figure 5-11c. Ductile dimpling due to micro-void coalescence comprises much of the fracture surface. However, smooth flat quasi-cleaved facets were found in all three orientations. Secondary small cracks were observed on all the samples normal to the crack growth direction on the fracture surface. Similar shallow cracks were shown to be initiated from the prior- $\beta$  grain boundary when observed from the side of the samples.

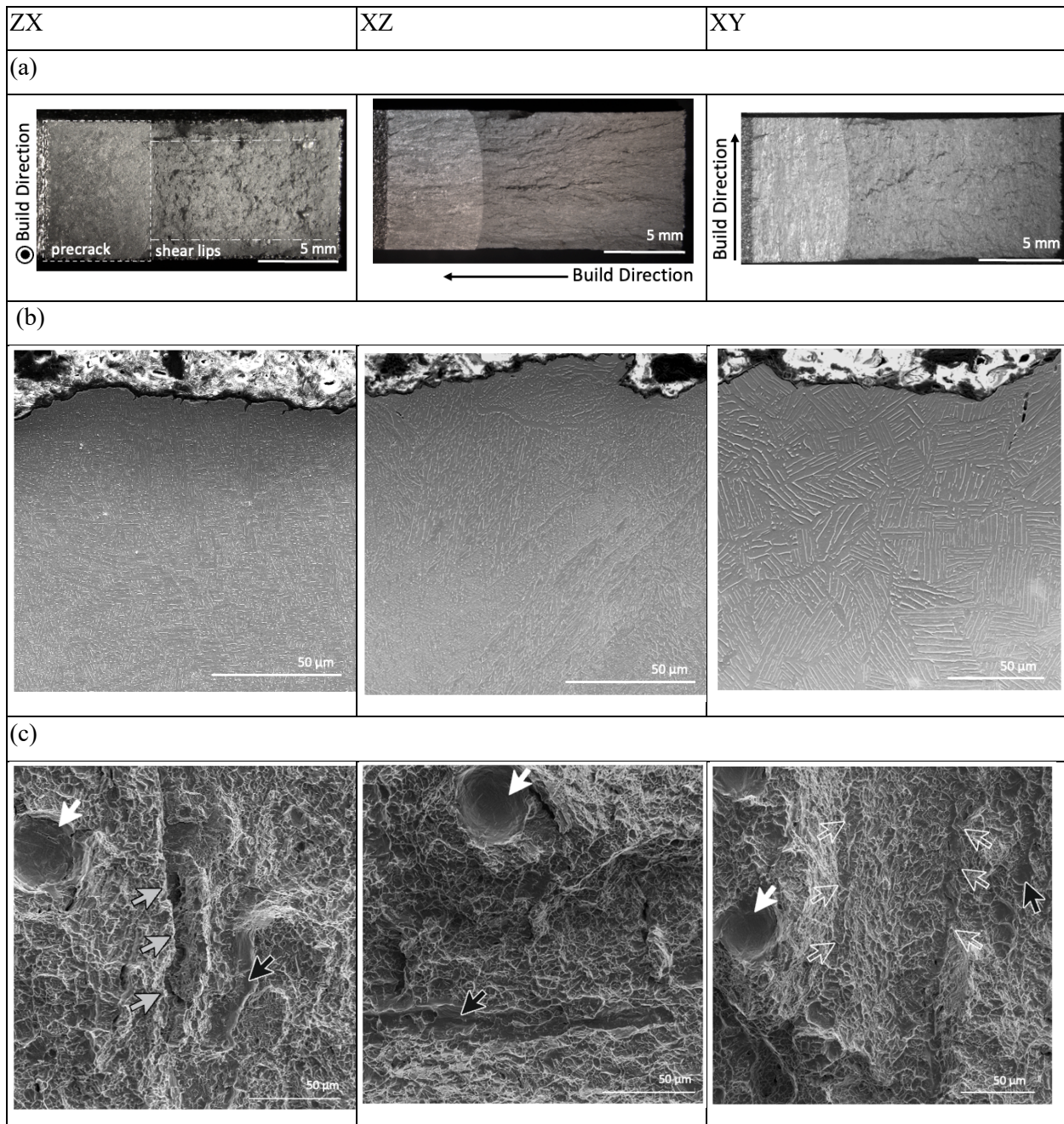


Figure 5-11: Fracture surface of the ZX, XZ, and XY orientations. (a) The samples exhibited thumbnail precrack and shear lips along the edges, notably the ZX samples. (b) The crack path through the microstructure is shown. (c) The fracture micromechanisms are provided, with quasi-brittle facets (black arrows) observed on all three orientations. Porosity (white arrows) and tearing ridges (grey arrows) are identified. The transparent arrows identify regions roughly 50  $\mu\text{m}$  apart.

While the samples had similar fracture features, orientation-dependent fracture mechanisms were noted. The ZX oriented samples exhibited the largest shear lip area ranging from 12 – 30% of the fracture surface and the roughest surface compared to the XZ and XY orientations.

High magnification imaging showed ductile dimpling on the majority of the ZX fracture surface, alongside a few flat features likely formed due to failure along the slip planes. In addition, the fracture surface existed on multiple planes, where defects were found on the bottom of the facets.

The XZ samples also exhibited a rough fracture surface but were unique to the long ridges that radiated from the pre-crack regions in the crack growth direction. A smaller shear lip area of 9-20% of the fracture surface is observed on the XZ compared to the ZX samples. Microscopically, the samples were composed of ductile dimpling surrounded by several flat facets, seen in Figure 5-11c. Large dimples existed along the crack growth direction, spaced at roughly 50  $\mu\text{m}$  increments, aligned with the build direction, and similar in size to the columnar  $\beta$  grain average width.

The XY fracture surface had the smoothest and flattest fracture surface compared to the other orientations. The samples also had the smallest shear lip area, ranging between 8 – 15%, with many of the samples only forming a shear lip along one free surface. Microscopically, the samples exhibit a mixture of ductile and quasi-brittle fracture mechanisms, with increased areas of quasi-cleaved facets present compared to the ZX and XZ orientations. A notable feature of the XY oriented samples is 50  $\mu\text{m}$  thick features on the fracture surface. The edges of these features were distinguished by elongated dimples coalescing and cleavage facets initiating possibly from the  $\alpha$ -enriched grain boundary.

# 6 Fracture Toughness: Hot Isostatic Pressing Effects

## 6.1 Introduction

Recent advances in additive manufacturing (AM) of metals highlights the imperative need for post-processing to remedy the inherent shortcomings, especially in production environments <sup>74, 120, 142, 238</sup>. In critical applications such as aerospace structures, the mechanical performance (*e.g.*, fracture toughness) is at the cornerstone of the design and analysis of engineered components and products <sup>98</sup>. Common shortcomings of metal AM include porosity, surface roughness, and anisotropy <sup>19, 239</sup>, which directly map to the survivability of deployed products. However, post-processing treatments for PBF-EB Ti6Al4V remains suboptimal, particularly in balancing defect reduction without microstructure coarsening <sup>150</sup>. The latter dictates the tensile properties resulting in a decrease in strength <sup>220, 240, 241</sup>, where the cost and time increase may not justify the treatment process. To address post-processing deficiencies in PBF-LB Ti6Al4V, AMS7028, a standardized hot isostatic pressing (HIP) specification, has been introduced <sup>29</sup>. This standard aims to enhance mechanical properties by optimizing HIP parameters for defect reduction while mitigating microstructural coarsening. However, a comparable standardized HIP process for PBF-EB Ti6Al4V is still lacking. Therefore, the motivation for this research is to explore an optimized post-process treatment resulting in enhanced properties that transcend the state-of-the-art.

Another critical challenge in PBF-EB is the intra-build variation- the spatial difference in microstructure, defects, and mechanical properties within a single build. Unlike conventional manufacturing, where homogeneity is more easily controlled, PBF-EB components exhibit thermal gradients and localized variations due to the prolonged beam exposure at elevated temperatures during the layer-by-layer process. Li et al. <sup>242</sup> observed deterioration of the mechanical properties along the build direction resulting from the thermal gradient within sample. Landau et al. <sup>137</sup> further observed a decreased cooling rate and temperature gradient of nearly 70 °C contribute across the build space, which can lead to a difference in microstructure in samples along the edges of the build space <sup>23, 127</sup>, thus directly impacting tensile strength, ductility, and fatigue life <sup>22, 23, 127, 140, 141, 211</sup>. Derimow et al. <sup>139</sup> investigated the effect of build height in PBF-EB Ti6Al4V and found a strong correlation influencing mechanical performance. Furthermore, our previous study <sup>43</sup> quantified spatial differences in fracture toughness behavior, emphasizing the

need to track intra-build parameters to fabricate repeatable and reliable components. Thus, the build space design must be fully considered and tracked for consistent mechanical behavior. At the same time, investigating the tensile response has been important for creating a foundational understanding. However, the PBF-EB Ti6Al4V fracture resistance behavior is vital for appraising its structural integrity, where material reliability and structural integrity are key for adoption of AM components and ascertaining their performance in realistic loading scenarios. The diverse processing conditions contributing to variation in PBF-EB tensile properties also influence fracture toughness, where intensive effort is needed to understand the process-structure-property relationships.

To improve mechanical properties and reduce scatter, a variety of heat treatments have been employed in PBF-EB Ti6Al4V including stress relieving<sup>71,94</sup>, duplex heat treatments<sup>117,243</sup>, and hot isostatic pressing<sup>117,142</sup>. The subtransus heat treatments resulted in a moderate change in the mechanical properties of PBF-EB Ti6Al4V due to the already high build temperature and slow post-printing cooling. Whereas the supertransus treatments have promoted recrystallization of the columnar grain into a preferred equiaxed structure<sup>117</sup>. However, the internal pores and defects remained within the metal. Hot isostatic pressing (HIP) is a thermo-mechanical treatment often used in the aerospace industry to reduce internal defects and residual stress and improve mechanical properties<sup>148</sup>. However, the standard HIP (STHIP) process produces a coarse microstructure, greatly reducing mechanical properties<sup>149,150</sup>. Limited data is available of PBF-EB-specific treatments to improve fracture resistance despite the growing interest in evaluating the fracture toughness properties of AM metal alloys<sup>154,244</sup>. Seifi et al. and Dzugan et al. investigated the fracture toughness properties of PBF-EB Ti6Al4V using STHIP treatment (920-950°C/100MPa/2h)<sup>13,154</sup>. The STHIP-treated samples were defect-free, but the expected increase in fracture toughness did not materialize. Seifi et al.<sup>13</sup> observed that the coarsening microstructure and the change in texture compete with the reduction in defects, which does not always result in higher toughness. Dzugan et al.<sup>154</sup> attributed the decrease in fracture toughness after STHIP to the higher strength and the less resistant recrystallized microstructure. Therefore, modification of the STHIP process is imperative for advancing the state-of-the-art in post-processing PBF-EB Ti6Al4V, *i.e.*, the primary motivation for this research study.

Given the shortcomings of the standard PBF-EB post-processing, this study seeks to investigate an optimized HIP treatments that enhances fracture resistance while minimizing

microstructural degradation. A systematic approach is adopted including micro-computed tomography for defect analysis, microstructural characterizations, and statistical evaluation of the intra-build design parameters (e.g., crack orientation, location, and thickness) to quantify the fracture toughness variation. By modifying the HIP process to balance defect reduction with microstructural changes, this research aims to advance post-processing strategies for PBF-E Ti6Al4V, aligning them industry standards such as AMS7028 while addressing the unique challenges of PBF-EB. The overarching goal of this research is to establish robust process-structure-property relationship for PBF-EB Ti6Al4V, providing insight into the microstructure-fracture resistance interactions and crack-growth mechanisms with different orientations. The primary novelty is not only the overall effectiveness of the treatment, but the design of the experiment is utilized to enable mapping and predicting the fracture toughness properties of PBF-EB Ti6Al4V. The findings will provide critical guidance for the design and qualification of PBF-EB components for structurally demanding applications, ensuring their reliability and long-term performance.

## 6.2 Results

### 6.2.1 Microstructure

Figure 6-1 shows the typical microstructure of the PBF-EB Ti6Al4V as a function of build orientation. The micrographs were obtained from SEM imaging, with the key characteristics ( $\alpha$ -enriched grain boundaries,  $\alpha$ -colonies, and basketweave microstructure) obtained from thresholding image analysis. The micrographs in Figure 6-1 implies the following observations. First, the  $\beta$  grain in Figure 6-1(a) is notable as the columnar grains formed along the build direction. The preferred epitaxial growth of the  $\beta$  grains is due to the repetitive melting and cooling of the with the addition of each layer <sup>16</sup>. Secondly, the initial  $\alpha'$ -martensite transforms into  $\alpha + \beta$  basketweave structure with the rapid cooling ( $10^3$ - $10^5$  K/s) to the build temperature of roughly 650°C of the PBF-EB process. The elevated temperatures of the PBF-EB process transform the acicular  $\alpha'$  martensite into a more ductile  $\alpha$ -phase with improved metal ductility and fracture resistance, akin to heat treatments below the  $\beta$ -transus temperature <sup>100</sup>. Lastly, a long, often uninterrupted  $\alpha$ -enriched grain boundary ( $\alpha$ -GB) is observed at the grain boundary.

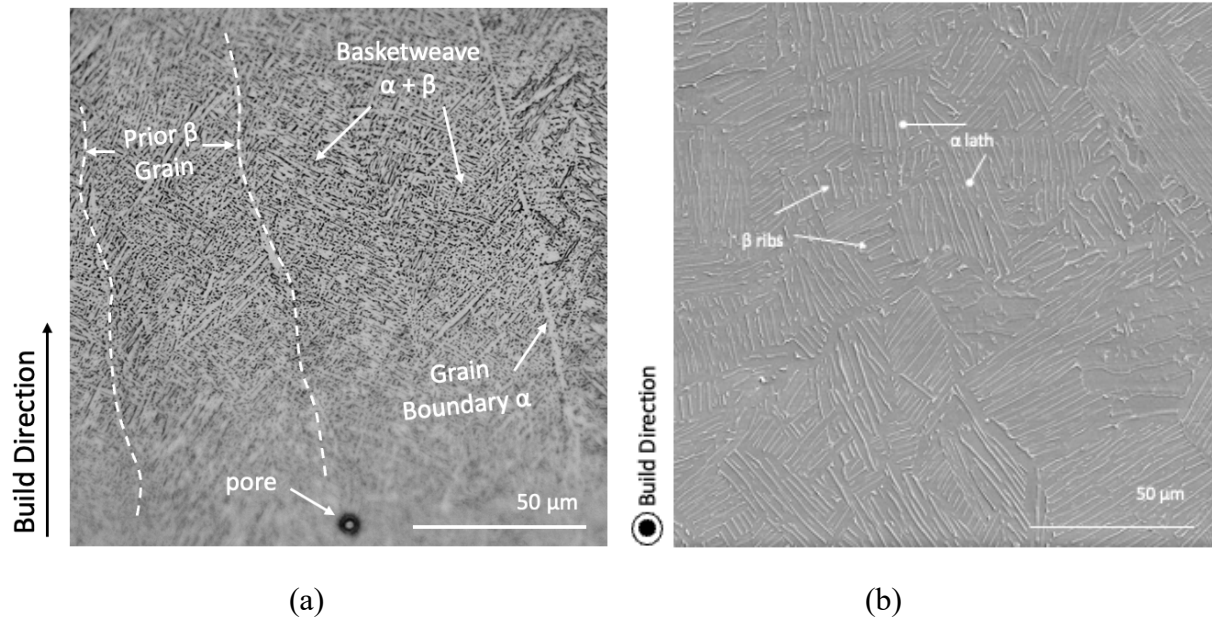


Figure 6-1: Key microstructural features such as prior  $\beta$  grains, the  $\alpha$ -grain boundary, and the basketweave structure, with respect to the build orientation.

Figure 6-2 shows the microstructure of the untreated and LTHIP PBF-EB Ti6Al4V as a function of crack orientation. High-magnification images of the microstructural features were obtained below the crack path and provided further insight into the effect of post-processing in each orientation. First, the existing basketweave microstructure remained after post-processing. Second, the  $\alpha$  needles increased in thickness, while the  $\beta$  ribs have become better defined. Even though a lower temperature HIP process was performed, coarsening of the microstructure was noted, as seen in Figure 6-3. While an increase in  $\alpha$ -lath thickness improves ductility and crack growth resistance, the increase in the  $\alpha$ -grain boundary thickness seen in Figure 6-3 can harm mechanical properties. Lastly, the direction-dependent columnar grains remain, outlined by the  $\alpha$ -GB.

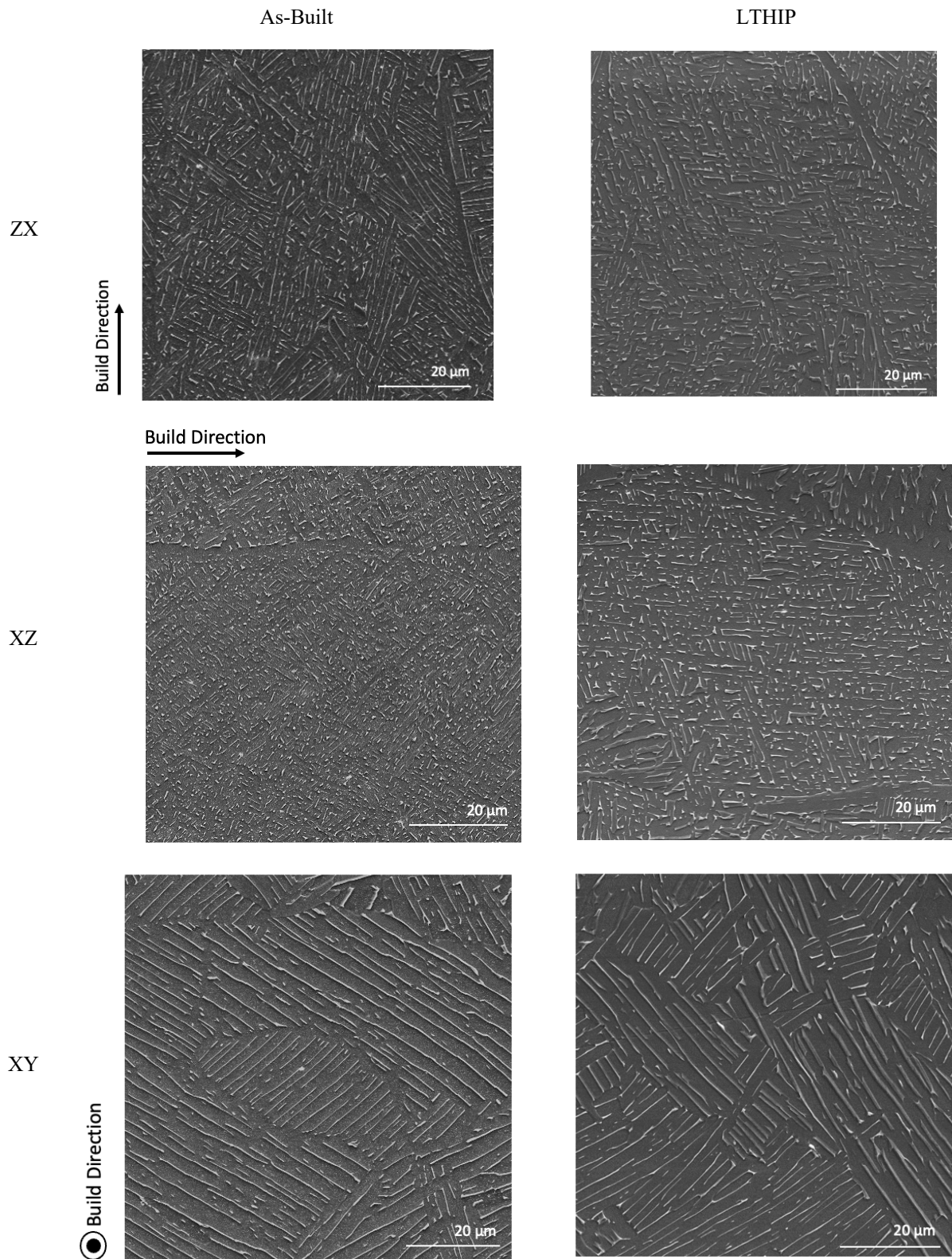


Figure 6-2: Microstructure of the LTHIP ZX, XZ, XY oriented samples.

Table 6-1 summarizes the key characteristics obtained from the micrographs of Figure 6-3. The  $\alpha$ -lath,  $\alpha$ -GB thickness, prior  $\beta$  width, and  $\beta$  vol.% were obtained as a function of post-processing. The  $\alpha$ -lath thickness increased as a function of metal condition, with up to a 20% increase attributed to the LTHIP process temperature. This increase is not, however, as notable as the 150% increase in  $\alpha$ -lath thickness Changyong et al.<sup>240</sup> reported after a STHIP treatment, where a significant coarsening is observed with the 920 °C HIP temperature. The prior  $\beta$  grain width remained similar after post-processing, and comparable to other published works of Zhai et al.<sup>14</sup>. The processing temperature was 150°C below the  $\beta$  transus (995±20 °C) with a furnace cooling process, where grain transformation from the columnar to equiaxed would not occur. The  $\beta$  vol.% increased by 2% from the untreated condition, comparable to studies by Jaber et al and Katzarov et al.<sup>245,246</sup>. Takajo et al.<sup>247</sup> demonstrated during the PBF-EB fabrication process; the metal is preheated to 700°C briefly before cooling down to 650°C, which is insufficient time for the vanadium to diffuse and stabilize the  $\beta$  phase. With a post-processing treatment above 600°C, the diffusional redistribution of vanadium contributed to the increase in the  $\beta$  phase. The increase in lamellar- $\alpha$  and the  $\alpha$ -GB thickness have been correlated to an increase in fracture resistance<sup>13,127</sup>. While a direct relationship between strength and fracture toughness does not exist, grain refinement, which increases strength, can limit crack growth resistance. Pairing the increase in the softer  $\beta$  phase with the increase in  $\alpha$ -lath thickness would result in a favorable increase in metal ductility and improve resistance to plastic deformation.

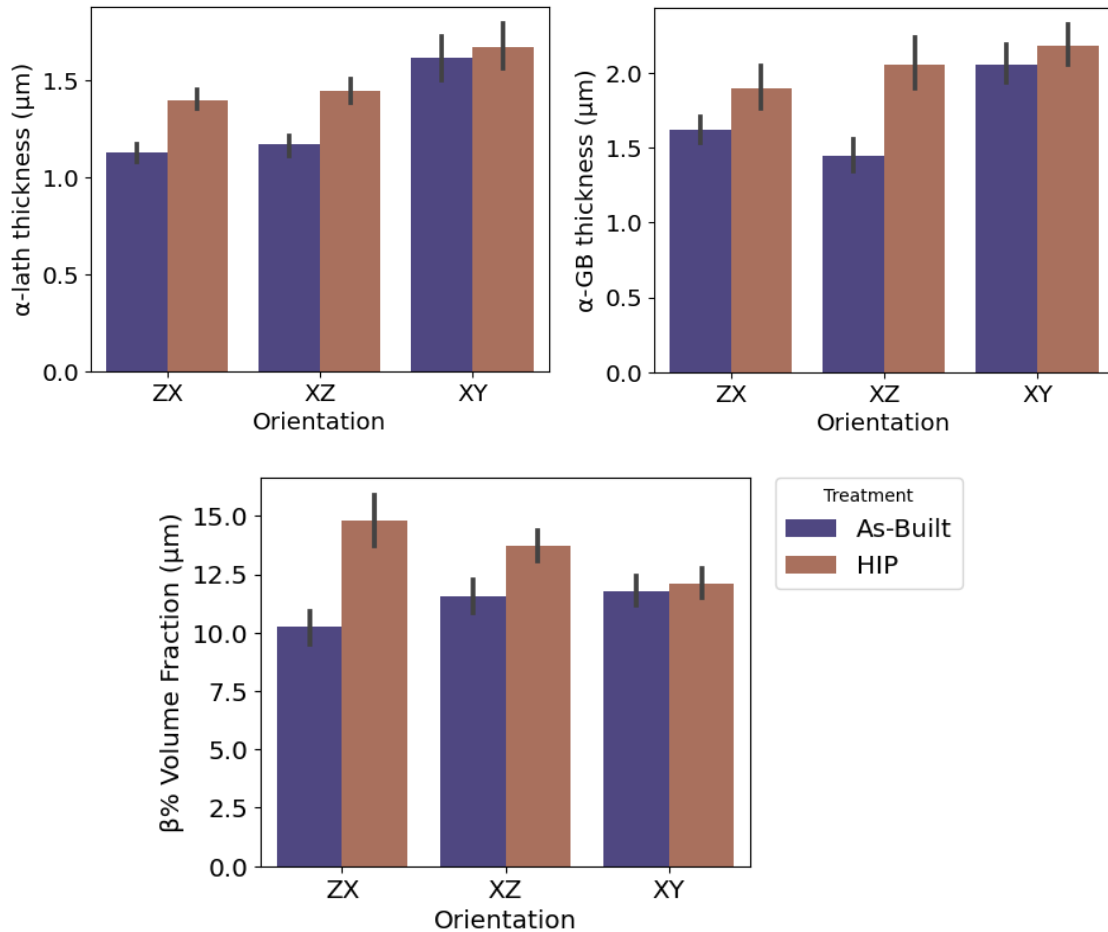


Figure 6-3: Summary of the microstructural characteristics of PBF-EB Ti6Al4V, as a function of orientation and metal condition

Table 6-1 also summarizes the key microstructure features for each sample orientation. The 30% increase in  $\alpha$ -lath thickness as a function of sample orientation was due to the melt area of each sample during printing where the XZ/ZX samples had a much smaller melt area than the XY samples. Similar orientation-dependent microstructure has been previously reported by Ghods et al.<sup>127</sup>, with a 25% increase in  $\alpha$ -lath thickness in the horizontal orientation. Orientation-dependent columnar grains remained unchanged after the LTHIP process. A change in prior  $\beta$  grain width as a function of orientation was not observed, as the LTHIP treatment remained below the  $\beta$  transus temperature. Abu-Issa et al.<sup>149</sup> observed similar trends in columnar grains after HIP below the  $\beta$  transus temperature.

Table 6-1: The microstructure factors of each orientation and material condition.

Type	Orientation	$\alpha$ -lath thickness ( $\mu\text{m}$ )	$\alpha$ -grain boundary thickness ( $\mu\text{m}$ )	$\beta$ width ( $\mu\text{m}$ )	$\beta$ vol.%
Machined	ZX	$1.1 \pm 0.1$	$1.6 \pm 0.6$	$42 \pm 17$	$11 \pm 2$
	XZ	$1.2 \pm 0.1$	$1.4 \pm 0.5$	$39 \pm 10$	$12 \pm 1$
	XY	$1.6 \pm 0.2$	$2.1 \pm 0.7$	$39 \pm 11$	$12 \pm 1$
Machined + LTHIP	ZX	$1.4 \pm 0.1$	$1.9 \pm 0.7$	$41 \pm 15$	$15 \pm 2$
	XZ	$1.4 \pm 0.1$	$2.0 \pm 0.7$	$50 \pm 17$	$14 \pm 1$
	XY	$1.7 \pm 0.2$	$2.2 \pm 0.6$	$43 \pm 21$	$12 \pm 1$

### 6.2.2 Internal Defect analysis

Figure 6-4 shows the reconstruction of the select fracture toughness samples in the as-built and LTHIP conditions. The reconstruction was constructed with the 2D images layered to create a 3D body. The  $\mu\text{CT}$  images in Figure 6-4 highlight three observations. First, most defects in the as-built condition are the spherical gas porosity, with diameters below colored in blue. Second, the LTHIP application successfully reduced the number of defects, resulting in a nearly defect-free metal. Lastly, while large and irregularly shaped lack-of-fusion (LOF) defects of Figure 6-5 were not observed after LTHIP, a small number of spherical pores remained. Wang et al.<sup>76</sup> observed gas entrapped within the powder can become entrapped during the melting process and cannot be entirely removed during HIP, where porosity can collapse or shrink during the HIP process. While a difference in grey-threshold indicated presence of internal defects, inspection of defects in the LTHIP samples did not find any distinct internal defects within the reconstructed volume.

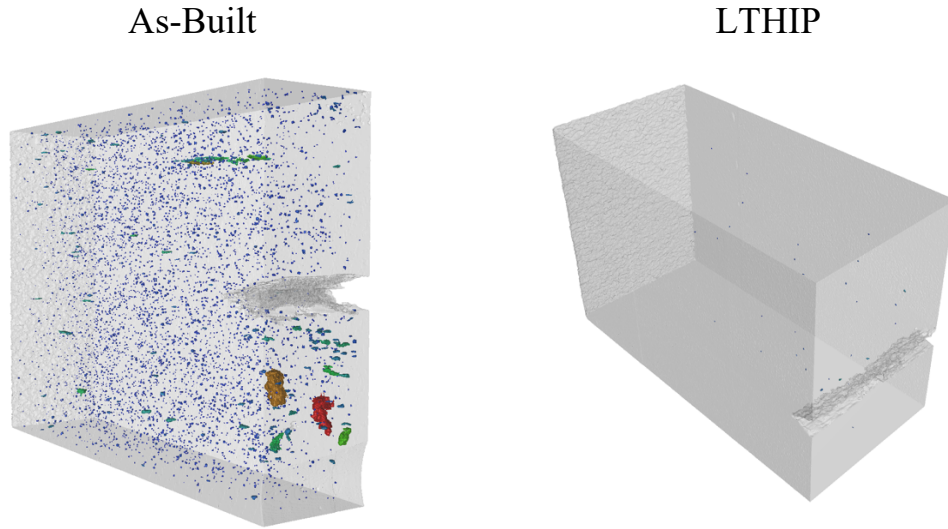


Figure 6-4: The  $\mu$ CT reconstruction of the As-Built and LTHIP samples. The LTHIP process showed a significant reduction in porosity and defect size.

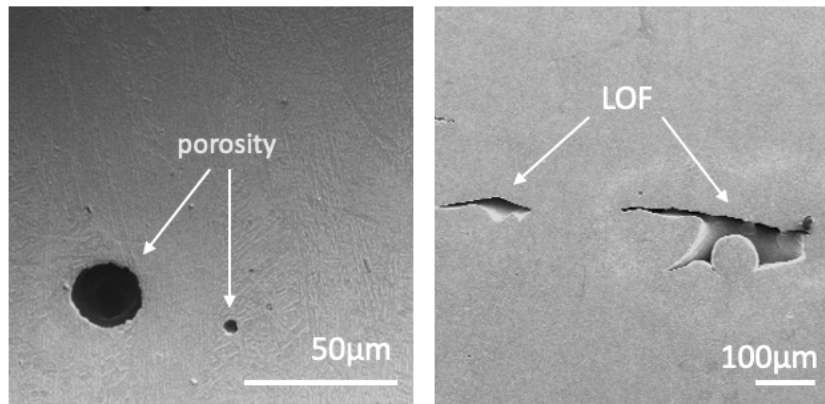


Figure 6-5: The two types of internal defects (porosity and LOF) commonly found in metal AM,

Figure 6-6 summarizes the key defect characteristics as a function of diameter and sphericity in the as-built and LTHIP conditions. A histogram of the defect diameters as a function of the metal condition is also included, where the darkest regions consist of a larger number of defects at that diameter. The following can be observed from the following figures. First, as the defect diameter increases, the sphericity increases in both metal conditions. This is consistent with findings by Tammam-Williams et al. <sup>248</sup>, where the largest defects are often LOF defects with low aspect ratio. Second, the decrease in median diameter from 0.15mm to <0.10mm is attributed to the high-pressure LTHIP application. The largest diameters decreased from ~0.8 mm to 0.3 mm

after LTHIP. This decline demonstrated the closure of the significant LOF defects commonly found in untreated metal. As the defects were reduced to below the resolution of the scan, finer resolution scans are necessary to capture internal defects after LTHIP accurately. However, the LTHIP treatment was shown to be beneficial in reducing the number and size of defects within the samples, especially the more critical LOF defects as shown in Figure 6-4 and Figure 6-6.

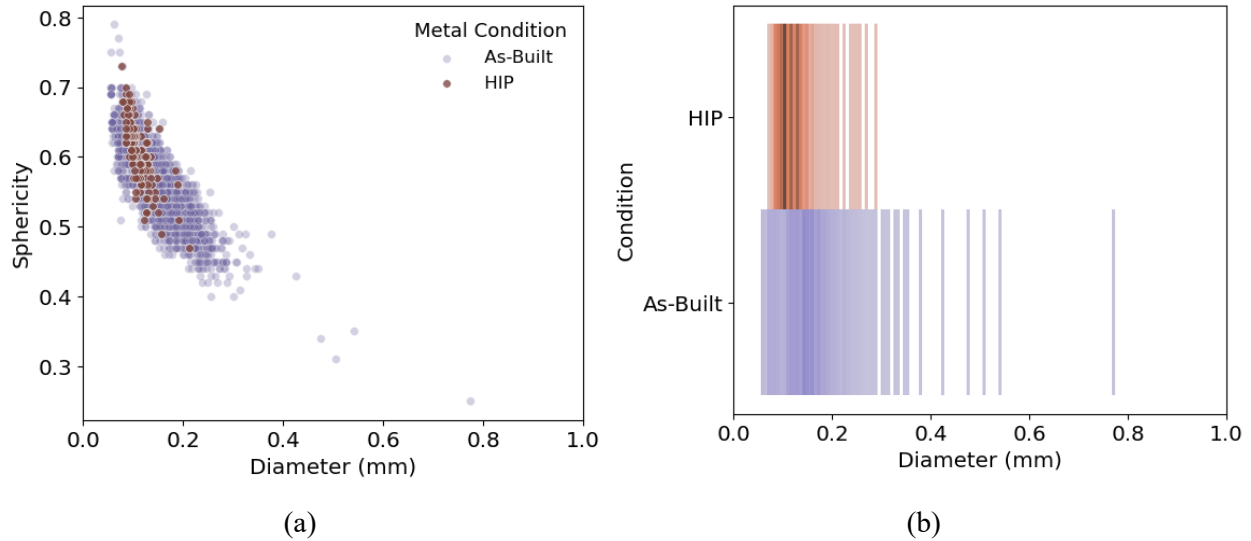


Figure 6-6: The defect diameter trends versus the defect sphericity in the untreated and LTHIP conditions. (b) The defect diameter distribution in the untreated and LTHIP conditions, with the darkest regions indicating the largest concentration of defects.

### 6.2.3 Tensile Properties

Figure 6-7 shows the stress-strain curves as a function of metal condition and orientation. The stress-strain responses were constructed by calculating the stress based on the instantaneous area and strain from the change in area. Because of post-processing and orientation, three experimental observations are implied in Figure 6-7. First, yield strength as a function of metal condition is in a similar range, which is attributed to the low temperature post-processing treatment. Second, there is a notable difference in the area under the stress-strain curve, denoting the metal toughness with the LTHIP application. Increasing toughness is desired, enhancing the material's deformability and improving a metal's fracture resistance. Lastly, the stress-strain curve in each orientation after LTHIP becomes comparable.

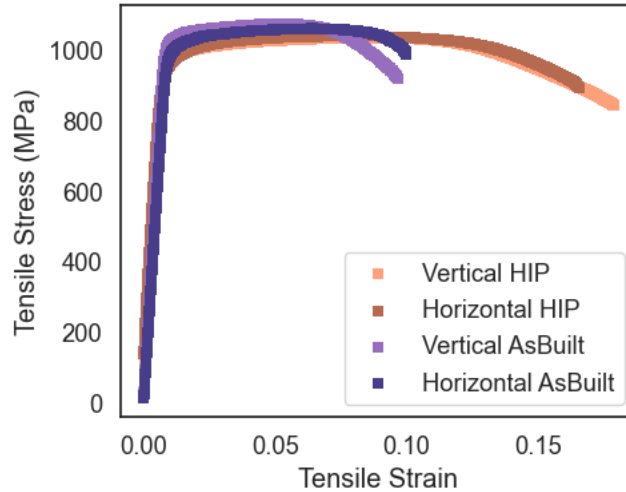


Figure 6-7: The stress-strain response of the PBF-EB Ti6Al4V as a function of metal condition and sample orientation

Table 6-2: Tensile mechanical properties of each orientation and material condition.

Type	Orientation	Yield Strength (MPa)	Ultimate Tensile Strength (UTS)	Elongation (%)	Strain Hardening	Hardness (HV)
As-Built*	Vertical	975 ± 29	1111 ± 36	9.6 ± 3.1	0.05	350 ± 18
	Horizontal	997 ± 56	1124 ± 46	8.8 ± 2.9	0.05	350 ± 30
LTHIP	Vertical	967 ± 9	1028 ± 9	16.9 ± 1.9	0.08	327 ± 10
	Horizontal	938 ± 7	1023 ± 13	13.4 ± 2.1	0.07	326 ± 27
% Change with LTHIP	Vertical	-0.8 %	-7.5 %	76.0 %	60 %	-6.6 %
	Horizontal	-5.9 %	-9 %	52.3 %	40 %	-6.9 %
Published	Vertical	868 ± 2.9	942 ± 2.6	12.9 ± 0.8		
STHIP	Horizontal	866 ± 6.4	959 ± 8.2	13.6 ± 0.6		

\*The As-Built values are obtained from previous DOE study

Table 6-2 summarizes the tensile properties, strain hardening exponent, and hardness values, including the % change in properties after LTHIP. The properties were obtained as a function of the build orientation and metal condition. The metal ductility exhibited the largest change after post processing. The PBF-EB Ti6Al4V ductility has been shown to be directly related to internal defects, where a drastic increase in %el was a result of defect removal<sup>249</sup>. The YS and UTS decreased as a function of post-processing. The ~5% decrease is attributed to the increase in grain size, following the Hall-Petch relationship<sup>250</sup> and the elimination of internal defects. While there is a decrease in strength after the LTHIP treatment, the YS, UTS, and %el are all higher than

the reported tensile properties after STHIP of Franchitti et al. <sup>220</sup>. A 7% decrease in hardness is also observed with the LTHIP application, aligned with the decrease in yield strength. Similar study by Tahri et al. <sup>251</sup> reported 285 HV after STHIP treatment. Strain hardening increased as function post-processing condition, which is attributed to the application of high pressure (200 MPa) during the HIP process. The high-pressure process plastically deforms the metal, leading to a decrease in dislocation density and transformation of the dislocation patterns<sup>240</sup>. Such increase in work hardening aids in the metal ability to limit dislocations and increase energy required for deformation. Overall, the LTHIP treatment proved to be successful in increasing ductility while maintaining the favorable high strength of PBF-EB Ti6Al4V compared to the STHIP treatment.

#### 6.2.4 Fracture Toughness

Figure 6-8 shows the load-CMOD curves as a function of condition and crack orientation. The load-CMOD response was constructed from the applied load based on the sample area and the crack length measurements. It is important to note that the load-CMOD data provided are all for samples in the 9-mm thickness and with the same pre-crack length for each orientation. The fracture behavior in Figure 6-8 exhibits three experimental observations. First, the crack orientation has a significant influence on the metal's capacity for deformation, captured by the area under the curve. Samples with a larger area under the load-displacement curve require more energy to deform, resulting in higher fracture toughness values. Second, the LTHIP treatment influenced fracture resistance, with an increase in energy absorption with post processing. Thirdly, not all three orientations experienced the same increase in fracture resistance as a function of post-processing, with the ZX orientation exhibiting the largest change in energy absorption.

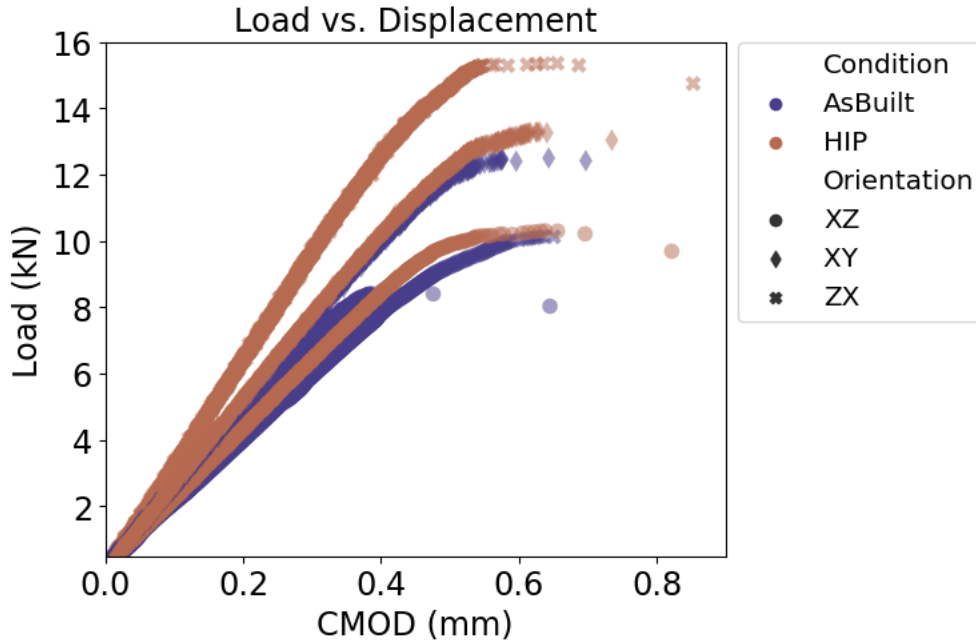


Figure 6-8: The load (P) vs. the crack mouth opening displacement (CMOD) graph for select 9 mm samples in all three orientations in the untreated and LTHIP condition.

Table 6-3 includes the average fracture toughness values, Coefficient of Variation (CoV), and % change in each metal condition as a function of crack orientation. The low-temperature, high-pressure LTHIP treatment was found to have significant effect on plane-strain fracture toughness, with an increase in average  $K_{Ic}$  from  $\sim 65$  to  $\sim 74$   $\text{MPa}\sqrt{\text{m}}$ , higher than wrought annealed and cast alloys<sup>98</sup>. The CoV decreased by 4% with the reduction of internal defects and dislocations after LTHIP. A lower CoV means less variation in the fracture toughness results and overall improved repeatability, making it promising for adoption. For the LTHIP samples, thickness and crack length dependent  $K_Q$  values are reported, where the  $K_{Ic}/K_Q$  ratio is within 2 – 6%<sup>228</sup>. The ratio less than 10% implies that while larger sample size is recommended for future experiments, the values are within acceptable range of variation.

Table 6-3: Summary of fracture toughness values obtained for each thickness

Type	Orientation	$K_Q$ (MPa $\sqrt{m}$ )	$K_{Ic}$ (MPa $\sqrt{m}$ )	CoV	% change
As-built	ZX		$63.2 \pm 4.9$	7.8	
	XZ		$63.3 \pm 5.2$	8.2	
	XY		$67.0 \pm 5.4$	8.1	
LTHIP	ZX	$78.9 \pm 3.8$	$77.6 \pm 3.7$	4.7	22.7 %
	XZ	$71.3 \pm 3.7$	$70.6 \pm 2.7$	3.8	11.5 %
	XY	$77.4 \pm 5.0$	$75.1 \pm 3.7$	4.9	12.0 %
Published	ZX <sup>13</sup>	$92 \pm 6.9$			
	XY	84			
STHIP	ZX <sup>154</sup>	$61.6 \pm 2.0$			
	XZ	$61.1 \pm 4.7$			
Wrought, air-cooled <sup>252</sup>			67.5		
Cast, annealed <sup>121</sup>		$77 \pm 12.5$			

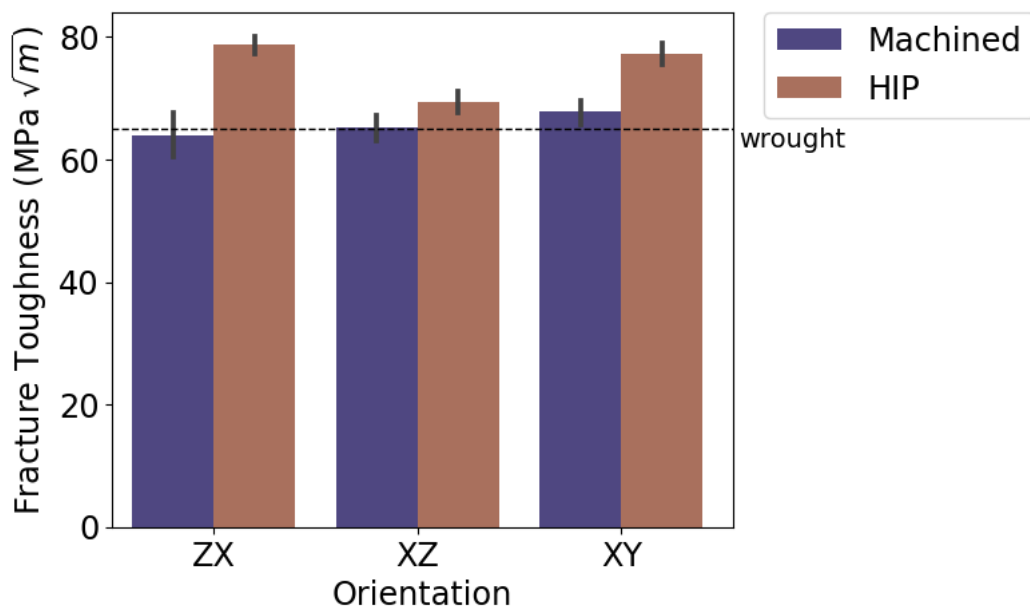


Figure 6-9: The average fracture toughness as a function of orientation and metal condition

Figure 6-9 summarizes the average fracture toughness values as a function of post-processing. The largest increase in fracture toughness was observed in the ZX orientation, where the  $K_{Ic}$  values are ~23% higher after LTHIP. In contrast, the XZ and XY orientation reported ~12% increase in fracture toughness after post-treatment. The overall improvement in fracture resistance with LTHIP can be attributed to the combined changes in mechanical behavior, defects, and

microstructure. The ductility and strain hardening exponent considerably improved with post-processing, requiring more energy to deform the sample. Additionally, the LTHIP process eliminated majority of defects, as seen in Figure 6-6, where crack growth resistance improved as spherical pores, and the large and irregularly shaped LOF defects were minimized. The LTHIP application in this study resulted in 12% higher fracture toughness than what Dzugan et al. reported using a standard HIP treatment. Similar studies of processing PBF-EB Ti6Al4V using STHIP treatment process has led to significant grain coarsening, mitigating any benefits STHIP had on defect closure of the samples <sup>13,50</sup>. This means that while the STHIP treatment was shown to successfully reduce internal defects, the influence of a lower processing temperature on PBF-EB Ti6Al4V can be more influential in enhancing fracture resistance while maintain YS and UTS.

### *6.2.5 Fractography*

Figure 6-10 provides the fracture surfaces of select LTHIP specimens in the ZX, XZ and XY orientations. The macro and micro-mechanisms of fracture behavior in the pre-crack, crack propagation, and fracture region were evaluated using optical microscope, Keyence, and scanning electron microscopes. Macroscopically, the fracture surface exhibited a thumbnail pre-crack, brittle fracture surface in the center, with shear lips along the free surface. The shear lip area remained consistent with each thickness and measured as follows in the LTHIP condition: 16.5%, 19.7%, and 23.3% is the XY, XZ, and ZX orientation respectively. The shear lip area increased by 5% in the XY orientation, 4% in the XZ, and only 2% in the ZX orientation compared to the untreated samples. Shear lips forms when the specimen undergoes a state of stress triaxiality where the center regions grows faster than the free surface.

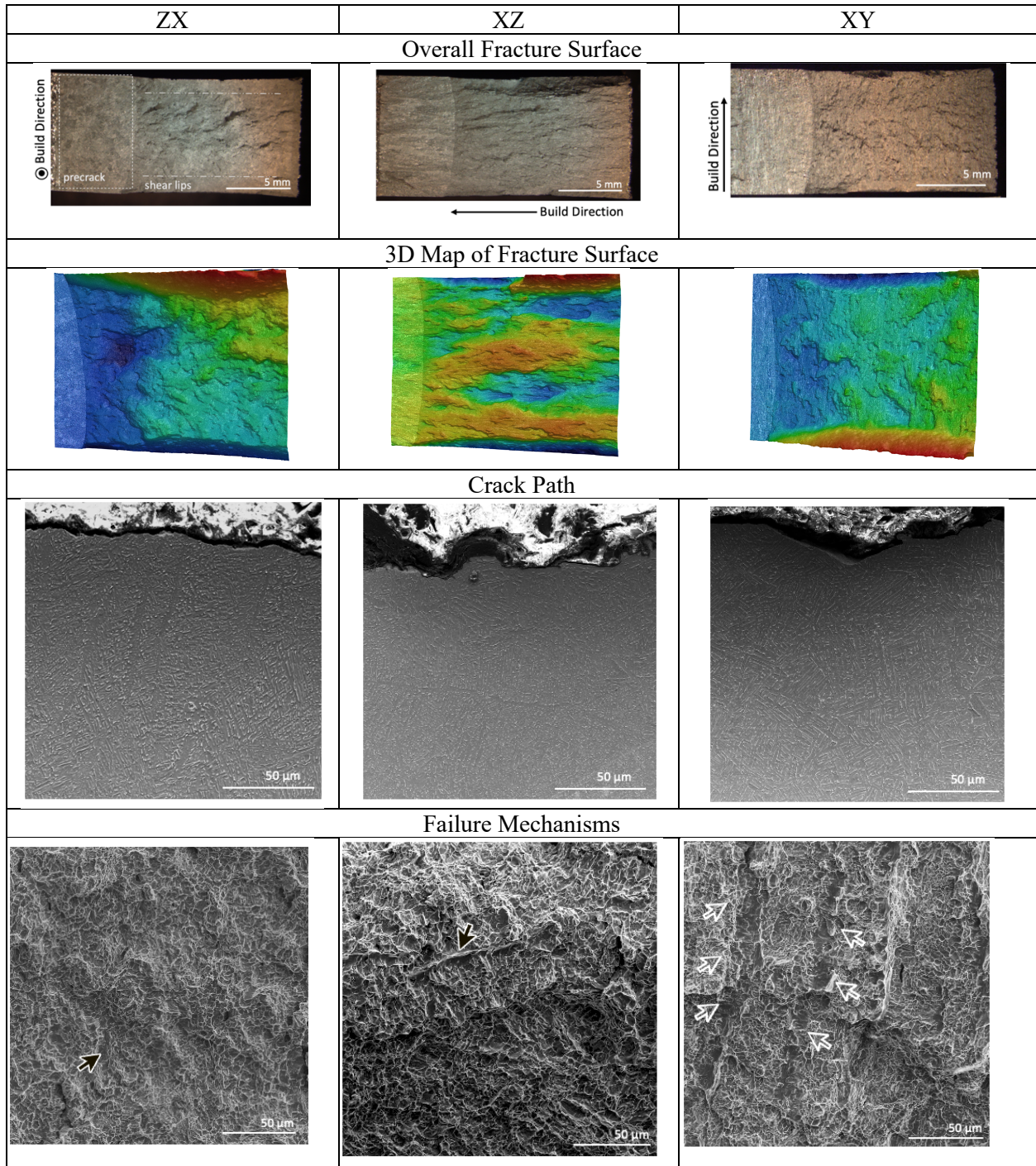


Figure 6-10: The fracture surface of the sample specimens in the ZX, XZ, and XY orientations. (a) thumbnail pre-crack is observed, followed by the crack propagation region and shear lips along the edges of the samples. (b) A 3D fracture surface map highlights orientation-dependent fracture surfaces. (c) The crack path through the microstructure is provided. (d) notable micro-mechanisms of failure were observed using SEM and are provided. Where the black arrows are regions of flat featureless quasi-brittle features, the clear arrows signify approximately 50 $\mu$ m and correspond to the prior  $\beta$  grain. Porosity and LOF were not observed on the fracture surface.

Microscopic features on the fracture surface were obtained using high magnification SEM micrography. Fatigue striations were found in the pre-crack region of the fracture surface of Figure 6-11, providing evidence of fatigue crack growth from the notch as required per ASTM E399. Crack propagation mechanisms ahead of the crack tip are shown in Figure 6-10. Unstable crack growth starts to occur as the crack extends past the pre-crack region. In the unstable crack growth region, both ductile and brittle micro-mechanisms of failure were observed. Ductile dimpling due to micro-void coalescence compromise much of the fracture surface with sporadic smooth flat features evident. The occasional quasi-cleaved facets formed from failure along slip planes. Shallow secondary cracks perpendicular to the crack growth direction were observed on all the fracture surfaces. The shallow micro-cracks were similarly observed when imaged from the side of the samples. Notably, the micro-cracks were located between two columnar grains, as the crack deflected towards the brittle  $\alpha$ -GB, shown in Figure 6-10. Porosity and LOF defects were visible on the untreated sample surface of Figure 6-11 but not on the fracture surface of the LTHIP samples. However, spherical features similar to porosity were observed on the LTHIP fracture surface, with evidence of dimpling suggesting that the surfaces had bonded together during post-processing.

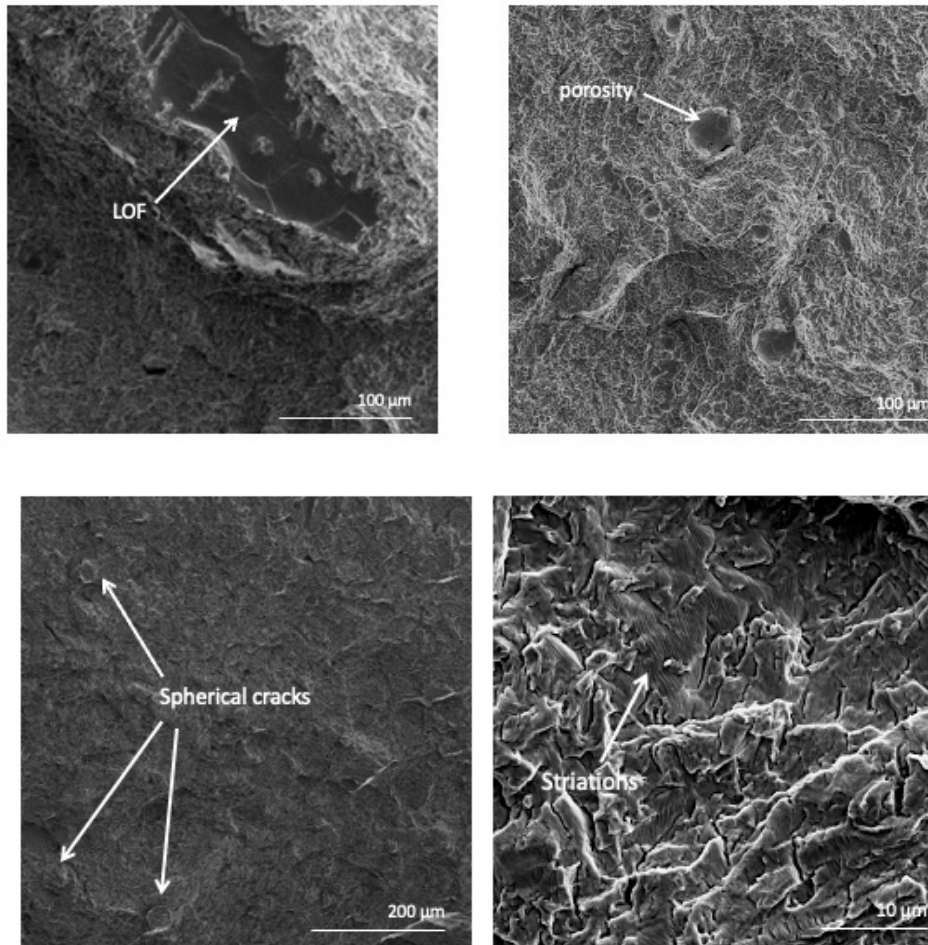


Figure 6-11: Common defects found on the fracture surface of the AB surface and after LTHIP treatment.

While the samples had similar fracture features, orientation-dependent fracture mechanisms were noted. Figure 6-10 highlights the following three observations. First, the ZX oriented samples exhibited the largest shear lip area in all thicknesses and the roughest surface, followed by XZ and XY orientations. The ZX oriented fracture surface in Figure 6-10 revealed a rougher surface finish, which supports the more tortuous crack path as travels through the prior- $\beta$  grains. The XZ samples also exhibited long ridges that radiated from the pre-crack regions in the crack growth direction. The XY fracture surface had the smoothest and flattest fracture surface compared to the other two orientations. The samples also had the smallest shear lip area, with many of the samples only forming a shear lip along one free surface. In contrast, the XZ orientation which had the lowest fracture toughness, exhibited a much smoother fracture surface.

Second, there was distinct difference in crack path preference through the microstructure between the three orientations. The metal AM microstructure exhibits anisotropic grains due to the repetitive rapid heating and cooling which promotes growth of the columnar grain with each added layer. Microscopic images of the ZX orientation showed the crack path travelled through basketweave microstructure in the columnar prior- $\beta$  grain. In contrast, the XY and XZ exhibited transgranular and intergranular crack path where the crack traveled both through and along the prior- $\beta$  grains. There is an increase in crack tortuosity as the crack propagates through the prior  $\beta$  grain through the  $\alpha + \beta$  basketweave microstructure thus increasing crack resistance, crack with preferential growth along the prior- $\beta$  grain would yield decreased fracture resistance. However, it would be expected that the XY and XZ orientations would therefore yield similar fracture toughness values, which was not the case. One possibility for the XY orientation reporting higher fracture toughness could be due to the increase in grain boundaries in the crack path. As the crack propagates in the XY samples, it comes upon many more columnar grains. More energy is needed to deflect or go through the grain itself, thus increasing the crack growth resistance. As a result, crack path preference due to the crack orientation contributed significantly to variation in the fracture toughness.

Lastly, while an overall increase in fracture toughness was observed in the three orientations, the increase was not uniform. The ZX and XY orientations reported comparable fracture toughness values after LTHIP, with the XZ orientation the lowest fracture toughness. The microstructure and internal defects most likely contributed to this difference. With the coarsening of the  $\alpha$ -phase, the crack growth resistance in the XZ orientation would decrease, limiting increase in the fracture toughness. Additionally, the closure of the LOF defects further contributes to the orientation-specific increase after LTHIP. While some small pores were observed in the alloy after post-processing, the large and irregularly shaped LOF defects were removed. While reduction in porosity probably contributed to some increase in fracture toughness in the XZ and XY orientation, LOF defect removal would have the most significant effect on the ZX orientation. In the ZX orientation, the LOF defects would be oriented perpendicular to the load direction, acting as a large stress concentration. As a result, the largest increase (16%) in fracture toughness after post-processing was the ZX orientation.

### 6.2.6 Effect of Build Design

Table 6-4 provides the four-way ANOVA statistics results, including the significance value of each intra-build design factor and its contribution to overall variation in the model. First, the model found the build design factors (crack-orientation, sample thickness, and spatial location) to be significant using a four-way ANOVA statistical analysis of the LTHIP Ti6Al4V metal. Second, crack orientation had the most significant contribution (~50%) to the variation in the LTHIP metal. The crack path interaction with the columnar grains has the largest effect on the orientation-dependent fracture toughness. Lastly, the build design parameters accounted for the remaining variation in the model, with height (37%) and thickness (12%) design parameters having the largest influence.

Table 6-4: The ANOVA results of the DOE model in the LTHIP condition

Source	Contribution	Sum of Squares	df	Mean Square	F-value	p-value
<b>Model</b>		509.54	6	84.92	117.63	< 0.0001
Thickness	12.4 %	62.41	1	62.41	86.45	< 0.0001
Radial Distance	0.7 %	3.51	1	3.51	4.86	0.0388
Height	37.0 %	185.61	1	185.61	257.10	< 0.0001
Orientation	49.1 %	246.24	2	123.12	170.54	< 0.0001
Height <sup>2</sup>	0.6 %	3.44	1	3.44	4.76	0.0406

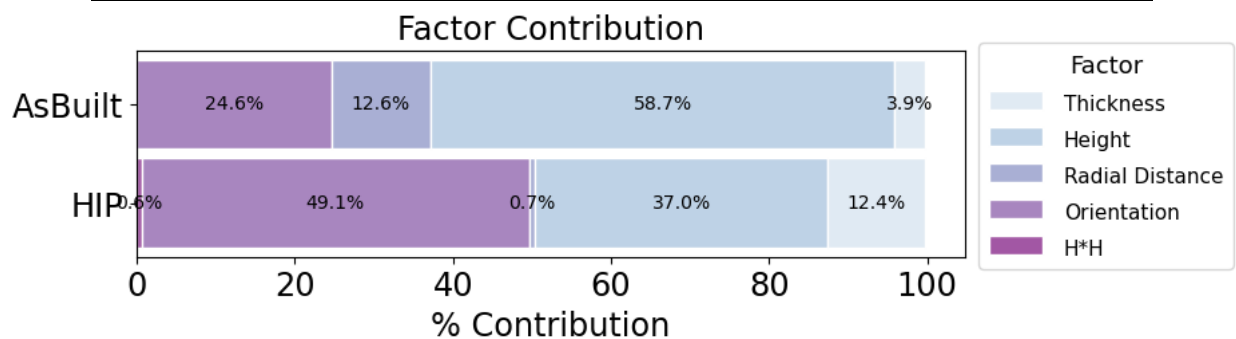


Figure 6-12: The contribution of intra-build design factors in the untreated and LTHIP metal

The contribution of each factor on fracture toughness in the untreated metal was previously examined in <sup>43</sup> and is compared to the LTHIP metal in Figure 6-12. The relationship between fracture toughness and each build design parameter in the ZX orientation is provided in Figure 6-13, for each metal condition. Figure 6-12 and Figure 6-13 provide the three following observations. First, height and orientation were the two largest contributors to fracture toughness variation in both the untreated and the LTHIP metal. Second, the effect of radial distance was

reduced from ~13% to <1% in the LTHIP condition. Lastly, the build design parameters had similar effects on fracture toughness in the untreated and the post-processed condition.

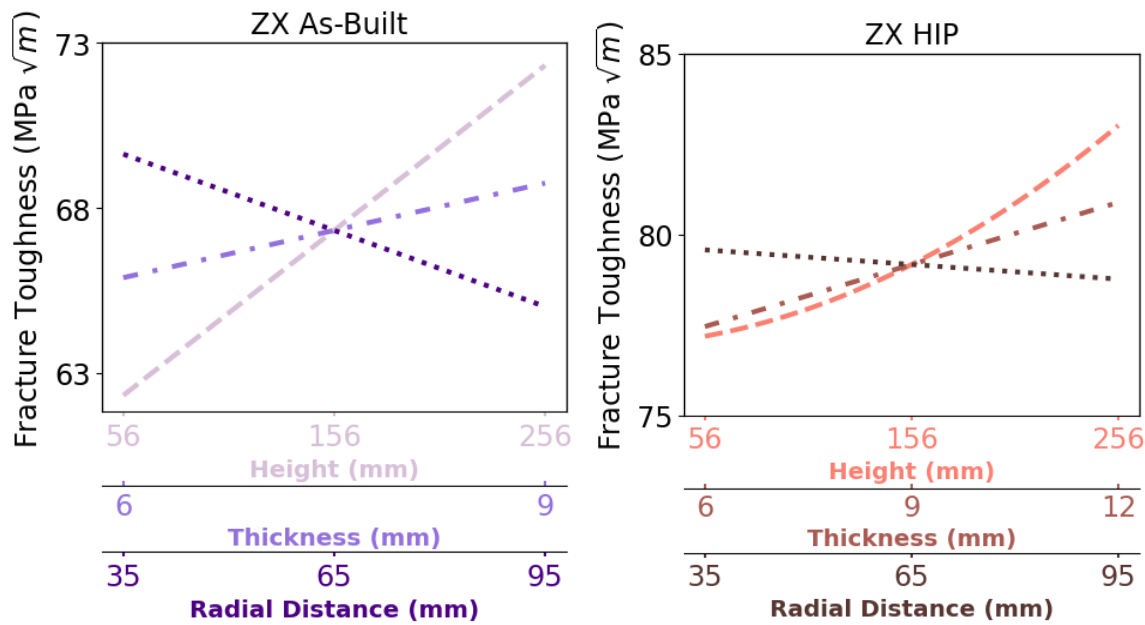


Figure 6-13: The relationship between fracture toughness and the intra-build design parameters as a function of metal condition in the ZX orientation

The intra-build design parameters were found to significantly influence the grain size in both the untreated samples previously, <sup>43</sup>. While the low-temperature HIP treatment improved fracture resistance, the fundamental microstructure and anisotropy remained, contributing to orientation-dependent and scatter in the fracture toughness properties. The ANOVA analysis showed trends due the intra-build design parameters were similar in both the untreated and post-processed condition. In essence, while LTHIP increased the fracture toughness, the intra-build design parameters left a lasting mark on the microstructure which was not changed with LTHIP. The complex thermal gradient from the decrease in cooling rate with the addition of each layer and prolonged PBF-EB cooldown to contribute to variation in the microstructure. This thermal gradient also influences the mechanical properties. Therefore, macro- and microstructure both play critical roles in crack growth behavior. As a result, while the LTHIP process was shown to be promising treatment in enhancing the fracture resistance of PBF-EB Ti6Al4V, the PBF-EB manufacturing process resulted in build dependent fracture toughness properties. The build orientation was shown to dictate the crack growth behavior should be the initial design consideration when manufacturing for end-use production. Furthermore, the following study also

shows engineers should consider the influence of geometry and build design for fabricating repeatable and reliable components.

# 7 Fatigue Performance: As-Built and Post-processing effects

## 7.1 Introduction

For the adoption of AM components, material reliability and structural integrity are essential to ascertain their performance in realistic loading scenarios. While the tensile property research has been necessary for creating a foundational understanding of how PBF-EB Ti6Al4V, fatigue behavior is necessary for understanding the structural integrity. In general, the fatigue behavior of metal alloys is dependent on the surface finish and internal defects, where the wide range of variability due to the build space poses a risk in applications where material performance must be predictable and reliable. Hence, the motivation leading to this research study. This research is needed to address the variability and reliability concerns associated with metal AM, specifically in terms of high cycle fatigue in PBF-EB Ti6Al4V. By improving understanding of the foundational aspects of the AM process, build design, and post-processing impacts the structural integrity and durability, this research will provide insight needed to advance AM into a viable option for high-performance, safety-critical applications.

## 7.2 Results

The results section is organized to establish the essential findings for understanding the fatigue behavior of PBF-EB Ti6Al4V in different metal and surface conditions. The metal quality, surface characteristics, mechanical properties, and the high cycle fatigue properties are reported and discussed. In addition to evaluating the influence of post-processing, the sources of variation due to the build design are explored and discussed. The final section utilizes a fracture-mechanics based approach to aid in predicting the overall fatigue behavior.

### 7.2.1 *Surface Roughness*

The 3D surface morphology is provided in Figure 7-1 as a function of metal and surface condition. The topography was obtained to better understand the features influencing mechanical properties. The rough surface and partially fused powder particles evident in the As-Built condition was removed with machining. Small defects were observed in the machined samples that underwent a

LTHIP treatment. Lastly, SP samples exhibited a deformed surface due to the shot peening process. However quantitative analysis was required to fully understand the influence of surface roughness.

Figure 7-1 shows the roughness profile as a function of metal condition. The roughness profiles were obtained from a line scan and provides a 2D view of the surface. The As-Built surface exhibited the largest peaks and valleys compared to the other surface conditions. The overall roughness improved with machining, with recurring valleys representative of the machining process. However, after a subsequent LTHIP treatment, very sharp deep valleys formed on the surface. The sharp valleys were not observed on the Machined + SP samples, with the surface exhibiting wave-like features.

Table 7-1 summarizes the surface roughness parameters including: the average surface roughness values ( $R_a$ ), ten-point height ( $R_z$ ), root mean square ( $R_q$ ), maximum valley to peak height ( $R_t$ ), skewness ( $R_{sk}$ ), kurtosis ( $R_{Ku}$ ), and maximum valley depth ( $R_v$ ). The surface roughness characteristics were obtained as a function of surface and metal condition. The PBF-EB surface decreased from  $\sim 20 \mu\text{m}$  in the as-built to  $0.2 - 1 \mu\text{m}$  with machining 2 mm from the external surface. While many PBF-EB studies report the  $R_a$  and  $R_z$  values, the other surface parameters have been shown to be beneficial in predicting the fatigue properties. The maximum peak to valley, root mean square, and maximum valley depth were all shown to decrease significantly with machining. The samples that were machined were fabricated as cylinders with an extra 2 mm, where both the surface and subsurface defects would be removed with machining.

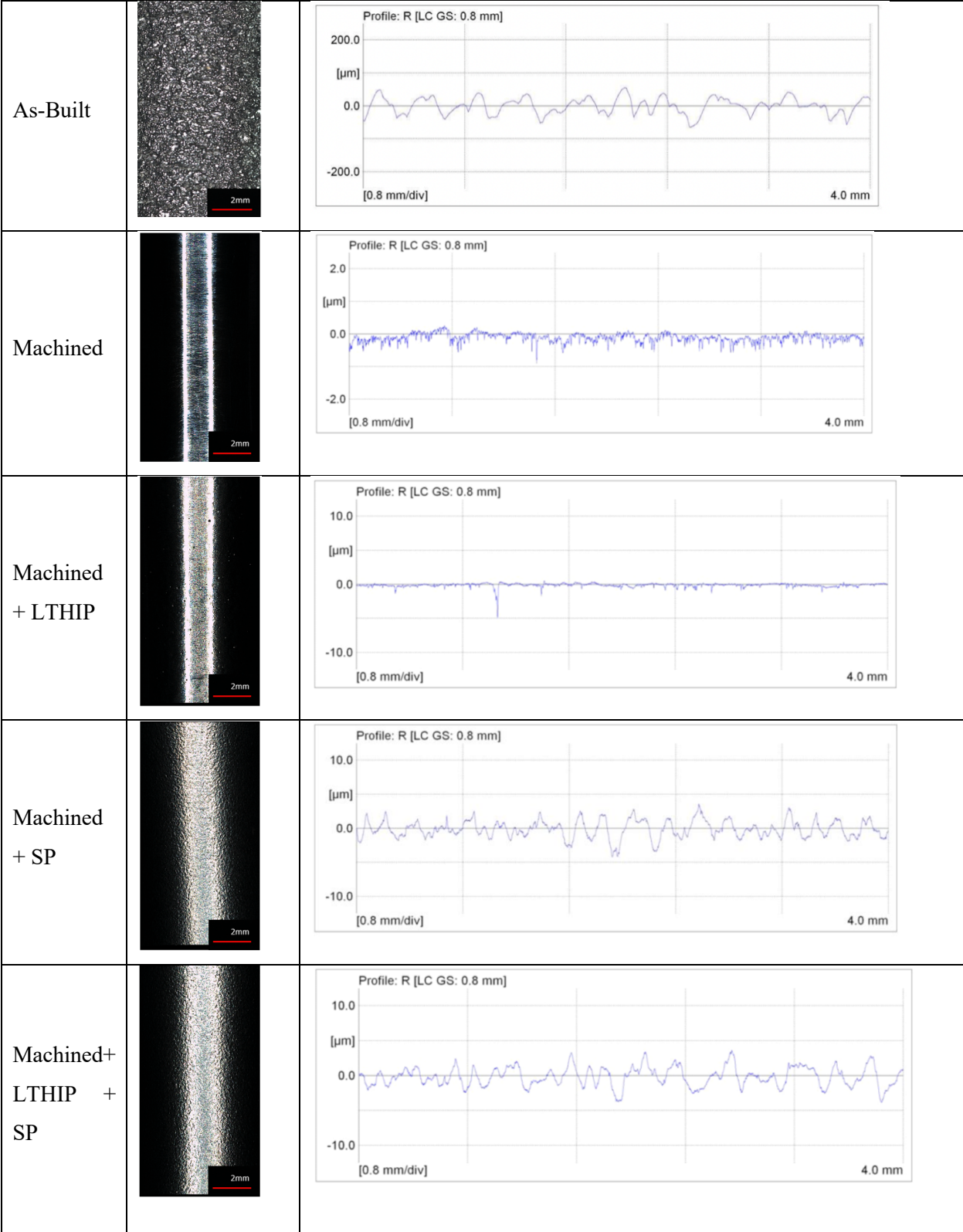


Figure 7-1: The 2D surface roughness profile in each sample. Note the difference in scale.

The decrease in  $R_q$ ,  $R_t$ , and  $R_v$  indicate a decrease of features which may act as surface notches. The negative  $R_{sk}$  values indicate the surface is made up of valleys primarily, where the machined and machined + LTHIP samples had the lowest skewness, with an increase in skewness after the LTHIP treatment. However, it is important to note the significant increase in the scatter in data after the LTHIP treatment indicating a large range of valleys adorning the surface. Lastly, while shot peening increased the  $R_a$  and  $R_z$  values, the skewness and the standard deviation decreased compared to the machined and Machined+LTHIP samples. The decrease in average and range of skewness implies the surface symmetry increased with shot peening.

The Arola-Ramulu (AR) Model<sup>253</sup> (Eq. 7-1) was developed to estimate the stress concentration factor using the surface roughness parameters. The AR Model calculates the stress concentration factor  $K_t$  using multiple surface characteristics and the effective profile valley radius ( $\rho$ ). The correction factor  $n$  accounts for any material dependencies on load type, where  $n = 2$  for uniform tension, and  $n = 1$  for shear loads. Mojib et al.<sup>254</sup> previously found the AR Model can be used to determine the stress concentration of the as-fabricated surface, reporting between 3 and 6. However, as the surface roughness parameters decrease with surface treatment, the stress concentration factor would also decrease for a given surface defect.

$$\overline{K}_t = 1 + n \left( \frac{R_a}{\rho} \right) \left( \frac{R_t}{R_z} \right) \quad \text{Equation 7-1}$$

Table 7-1: Surface roughness characteristics in each condition

Parameter	As-Built	STHIP	Machined	Machined + LTHIP	Machined + SP	Machined + LTHIP + SP
$R_a$ ( $\mu\text{m}$ )	$24.4 \pm 5.6$	$21.2 \pm 2.83$	$0.15 \pm 0.10$	$0.22 \pm 0.10$	$1.15 \pm 0.13$	$0.97 \pm 0.14$
$R_z$ ( $\mu\text{m}$ )	$168.5 \pm 48.5$	$101.9 \pm 12.0$	$0.68 \pm 0.08$	$1.94 \pm 0.58$	$6.28 \pm 1.05$	$5.42 \pm 0.71$
$R_q$ ( $\mu\text{m}$ )	$25.3 \pm 2.5$	$25.9 \pm 4.7$	$0.17 \pm 0.01$	$0.32 \pm 0.10$	$1.46 \pm 0.18$	$1.22 \pm 0.164$
$R_t$ ( $\mu\text{m}$ )	$107.6 \pm 14.3$	$122.6 \pm 19.8$	$11.69 \pm 1.48$	$10.17 \pm 2.37$	$7.92 \pm 0.86$	$10.78 \pm 3.42$
$R_{sk}$ ( $\mu\text{m}$ )	$-0.1 \pm 0.10$	$0.05 \pm 0.24$	$-1.48 \pm 0.11$	$-2.66 \pm 2.48$	$-0.26 \pm 0.19$	$-0.39 \pm 0.31$
$R_{ku}$ ( $\mu\text{m}$ )	$2.9 \pm 0.43$	$2.5 \pm 0.18$	$2.79 \pm 0.63$	$3.20 \pm 0.39$	$3.17 \pm 0.19$	$2.89 \pm 0.20$
$R_v$ ( $\mu\text{m}$ )	$56.5 \pm 7.8$	$57.4 \pm 16.3$	$5.64 \pm 0.59$	$3.12 \pm 0.59$	$2.98 \pm 0.31$	$3.89 \pm 1.11$

### 7.2.2 Internal Defect Analysis

Figure 7-2 shows the  $\mu$ CT reconstruction of the HCF PBF-EB Ti6Al4V samples in the *Machined* and *LTHIP* condition prior to testing. Non-destructive testing permits evaluation of the metal quality without destroying the samples. The reconstructed samples show three key features of the PBF-EB metal in the untreated and post-processed condition. The untreated metal in horizontal orientation in Figure 7-2 shows the presence of randomly spaced spherical porosity due to trapped gas and irregularly shaped LOF defects which often formed due to insufficient consolidation between two layers. The shape and high aspect ratio of the LOF defects was distinct from the spherical gas pores, which when perpendicular to the build direction can be detrimental to mechanical performance. The large and irregular shape of LOF defects lead to high local stresses under cyclic loading, in addition to reducing the load-bearing area of the sample. Together, the large source of stress concentration in the metal leads to premature failure under cyclic loading. Porosity or LOF defects were not observed in the LTHIP metal shown in Figure 7-2, where a uniform metal was observed. Lastly, small spherical defects were observed on the LTHIP sample's free surface corresponding to the sharp valleys recorded during surface profilometry. However, similar surface defects were not observed on the Machined surface.

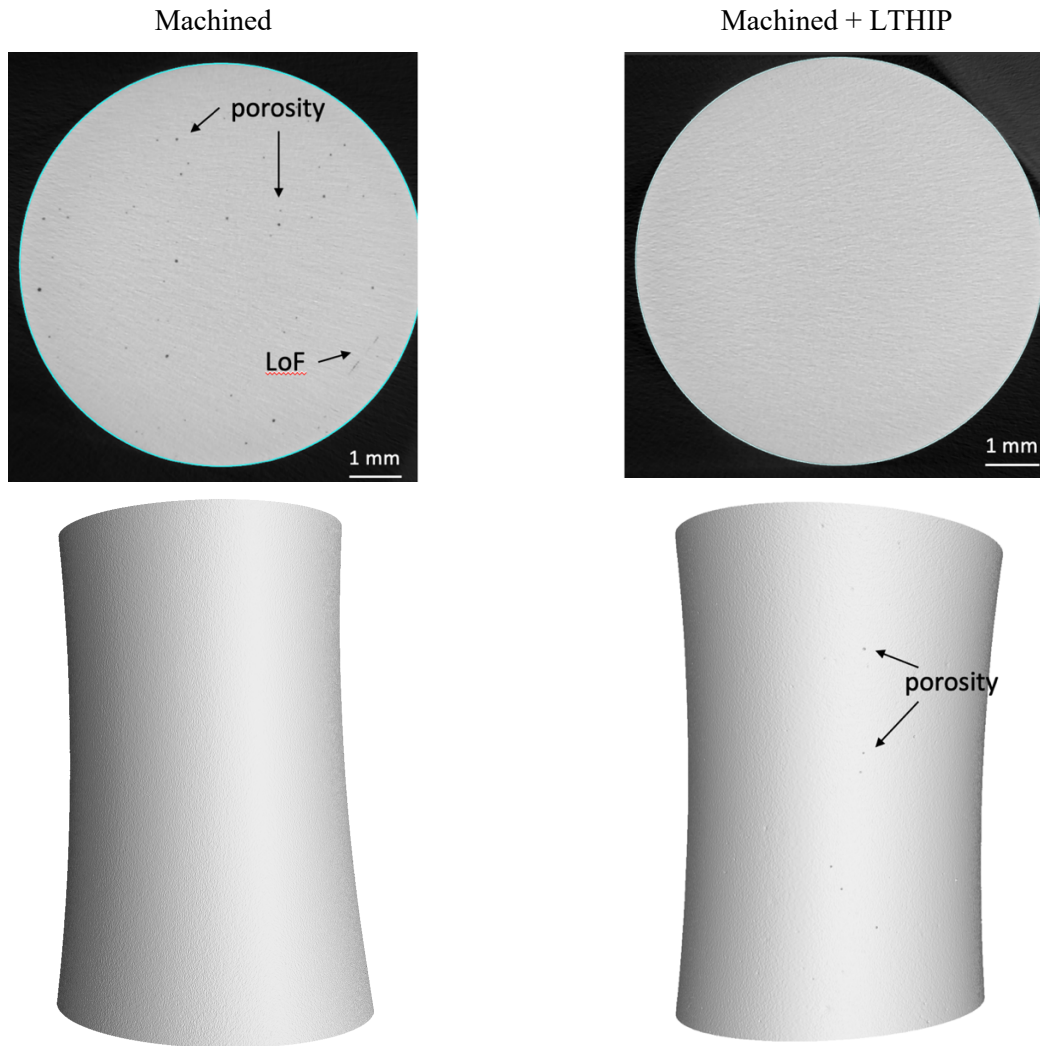


Figure 7-2: The 3D reconstruction of the surface and the internal view of the As-Built and HIP samples. Porosity and LOF defects are observed in the As-Built condition, while surface machining has removed any existing surface defects. Porosity and LOF defects are not observed in the HIP bulk material, however, surface porosity was observed.

Figure 7-3 summarizes the defect trends as a function of diameter and sphericity in the as-printed and LTHIP condition. The defect diameter was calculated based on a sphere of the same volume while the sphericity was the ratio of the 3D objects surface area to the surface area of a sphere of the same volume. For spherical pores, sphericity will be closer to 1, however, as the object becomes more irregular, its surface area will increase resulting in a lower sphericity. The defect size and shape trends in Figure 7-3 indicate the three following observations. First, the defect size ranged from 50  $\mu\text{m}$  to 600  $\mu\text{m}$ , with most defects below 250  $\mu\text{m}$  and above 0.5

sphericity. While defects smaller than 50  $\mu\text{m}$  could be present, the scan was limited by the resolution size. It has been shown that although small gas porosity defects exist, the initiating defects will most likely be large irregularly shaped defects<sup>80,128</sup>. The diameter and shape of the defects were of utmost interest and are provided in Figure 7-3. Second, the defects with the largest diameter had the lowest sphericity, corresponding to the irregularly shaped LOF defects. Lastly, with the LTHIP treatment, the number of the defects decreased drastically, with the full removal of the irregularly shaped LOF defects. While post-analysis inspection of the reconstruction did not observe defects in the LTHIP metal, the  $\mu\text{CT}$  thresholding did pick up on high probability regions of internal defects where the metal may not have fully closed. However, those defects were not observed with manual inspection of the data. Furthermore, it is important to note that the software is unable to recognize surface defects due to software limitations. As such, any defects attached to the surface were excluded in the  $\mu\text{CT}$  data analysis.

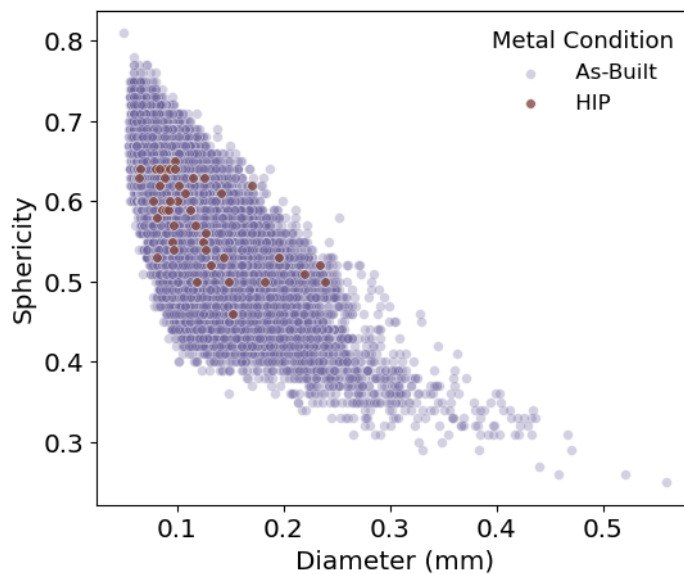


Figure 7-3: The overall defect diameter trends in the as-built and HIP samples. (a) the defect diameter vs. sphericity, where the largest defects are those with the least spherical shapes.

### 7.2.3 Tensile Properties

Table 7-2 summarizes the static mechanical properties in each metal condition, surface, and orientation, including the yield strength (YS), ultimate tensile strength (UTS), elongation (%el), strain hardening, and hardness. The As-Built, Machined, and LTHIP values are reported from the previous chapter, and compared to the tensile properties after STHIP treatment. While the YS and UTS remained similar, a 50% increase in ductility was observed with STHIP

application. The unchanged strength was comparable to findings by <sup>255</sup>, but lower than properties reported by <sup>105</sup> which was associated with the as-fabricated surface finish. The small difference in strength was due to the surface defects acting as a source of crack initiation. However, the significant increase in ductility was due to the increase in metal density. There was a strong correlation between internal defects and ductility, with a decrease in ductility with increase in pore size and volume <sup>127</sup>. As a result, while a change in YS and UTS was not observed, the closure of internal defects after STHIP contributed to the increase in ductility.

The YS, UTS, strain hardening, and hardness increased by 15%, 20%, 25%, and 23% with the removal of the as-fabricated surface. Similar increase was reported by Schur et al. <sup>42</sup>, which was due to the removal of the irregular surface defects formed during the printing process. However, with an application of STHIP and machining, studies have found a drop in tensile properties, where the microstructural coarsening often outweighs the benefits of the improved ductility <sup>26</sup>. In contrast, with the application of LTHIP and machining, the YS and UTS of the PBF-EB Ti6Al4V remained comparable to wrought alloys <sup>121</sup>, in addition to the slight improvement in strain hardening and %elongation. The increase in strain hardening and improved ductility was attributed to the closure of internal defects with the high-pressure HIP process. While the process temperature below B-transus limit microstructural changes <sup>117</sup>. As a result, the LTHIP treatment was successful in increasing the metal ductility while maintaining the favorable high strength of the PBF-EB Ti6Al4V.

Table 7-2: Mechanical properties in each condition

Type	Orientation	Yield Strength (MPa)	Ultimate Tensile Strength (UTS)	Elongation (%)	Strain Hardening
As-Built	Vertical	840	960	9	0.03
STHIP	Vertical	852 ± 8	922 ± 9	15.3 ± 1.9	0.04
Machined	Vertical	975	1122	10	0.05
	Horizontal	972	1100	10	0.05
Machined +	Vertical	967 ± 9	1028 ± 9	16.9 ± 1.9	0.08
LTHIP	Horizontal	938 ± 7	1023 ± 13	13.4 ± 2.1	0.07

#### 7.2.4 High Cycle Fatigue

The following section will discuss the various factors influencing PBF-EB fatigue performance. Experimental analysis of PBF-EB in the as-fabricated, surface-treated, and heat-

treated condition are evaluated. Additionally, a modified LTHIP treatment is explored. Lastly, the section will include a discussion of additional source of variation in PBF-EB HCF.

#### 7.2.4.1 Overall Post-Processing

Figure 7-4 shows the stress-life curves of untreated and post-processed PBF-EB Ti6Al4V as a function of surface and metal condition. The stress-life curves were determined through fitting the experimental data to the Basquin equation for each metal condition and overlaid on published fatigue behavior of AM, wrought, and cast Grade 5 Ti6Al4V<sup>98, 121,169</sup>. The fatigue life curves Figure 7-4 implies three experimental observations. First, the AB PBF-EB fatigue behavior was significantly low, exhibiting fatigue life 30% below those of wrought and cast Ti6Al4V properties. Alternatively, through removal and refinement of the as-printed surface, fatigue life comparable to wrought and cast alloys was achieved.

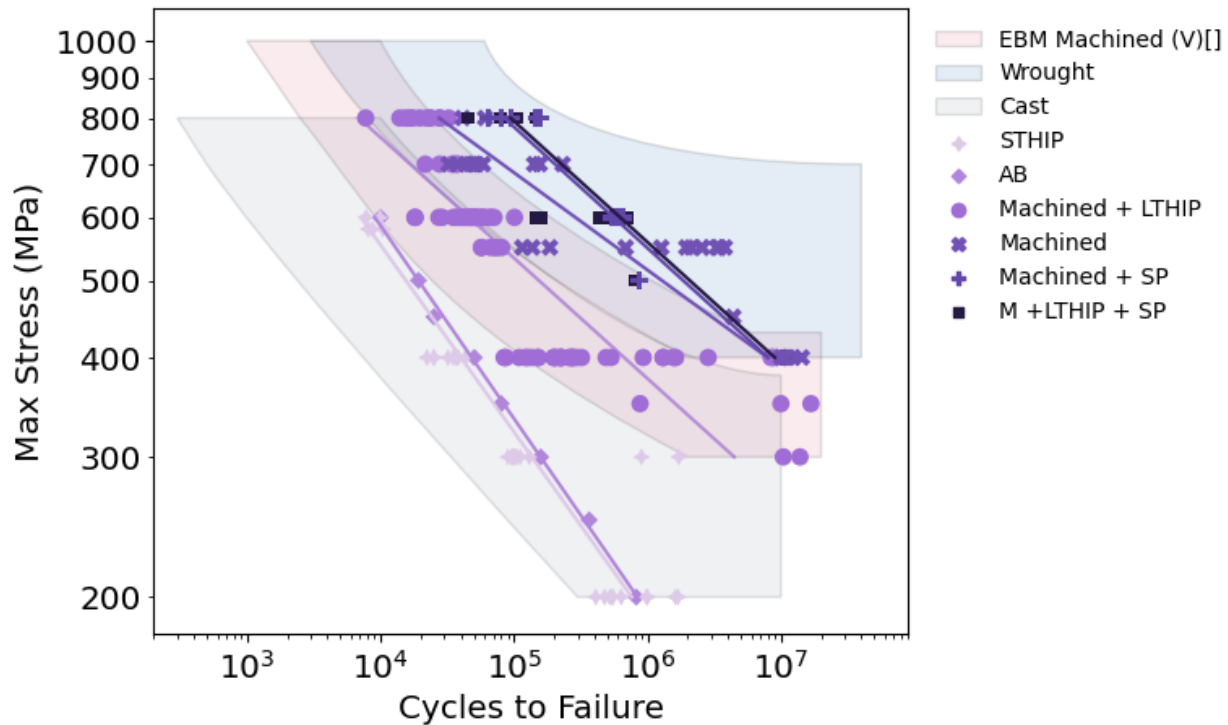


Figure 7-4: Fatigue stress-life curve of the PBF-EB Ti6Al4V in the Vertical orientation as a function of surface and metal condition, where the data was used to obtain the Basquin curve.

#### 7.2.4.2 HIP Effects

The following sections will provide further insight on the advantages and the limitations of the STHIP and LTHIP process. The samples which underwent STHIP only exhibited the same fatigue behavior as the As-Built samples. With the STHIP treatment, the fatigue limit was roughly

200MPa, and comparable to the untreated condition. Comparing the LTHIP + Machined to the Machined-only samples also exhibits a difference in fatigue strength. The fatigue limit decreased from ~400MPa to 300MPa with an application of the LTHIP treatment.

#### *7.2.4.3 Machining Effects*

Post-processing significantly enhanced the PBF-EB fatigue life but heavily depended on the surface condition. Fatigue limit increased from 200 MPa in the AB condition to 400 MPa with the machining application. Machining had the largest increase in fatigue behavior, with the removal of the rough as-built surface. A difference in fatigue performance is observed in the machined samples, depending on the metal condition, for example, if the metal underwent an LTHIP condition.

#### *7.2.4.4 Shot Peening Effects*

Shot peening had the most significant enhancement in fatigue strength, yielding endurance limit up to 400 MPa. Not only did the shot peened samples outperform the as-built and LTHIP samples, a reduction in scatter in properties is observed. Furthermore, the SP+LTHIP samples and the SP-only samples performed similarly, exceeding fatigue strengths compared to the machined-only samples. In essence, regardless of presence of internal defects, the as-printed surface remained detrimental to the fatigue life of PBF-EB Ti6Al4V.

#### *7.2.4.5 Anisotropy*

While the surface finish had the most significant influence on the fatigue behavior of PBF-EB Ti6Al4V, further investigation was necessary for understanding factors influencing scatter in the fatigue behavior. The influence of the print orientation on the fatigue behavior of the PBF-EB Ti6Al4V is shown in Figure 7-5. Overall, the horizontal orientation survived longer than the vertical orientation, with the largest variation in the untreated condition. With an additional application of shot peening, the orientation-dependent fatigue behavior was nearly eliminated. Effectively, the comparable fatigue properties in the two orientations after the shot peening application means that with surface and heat treatment, the largest sources of variation (surface finish, orientation, internal defects) could be reduced. The remaining variation in the properties of the PBF-EB manufactured Ti6Al4V samples pointed toward the underlying effects of the manufacturing process.

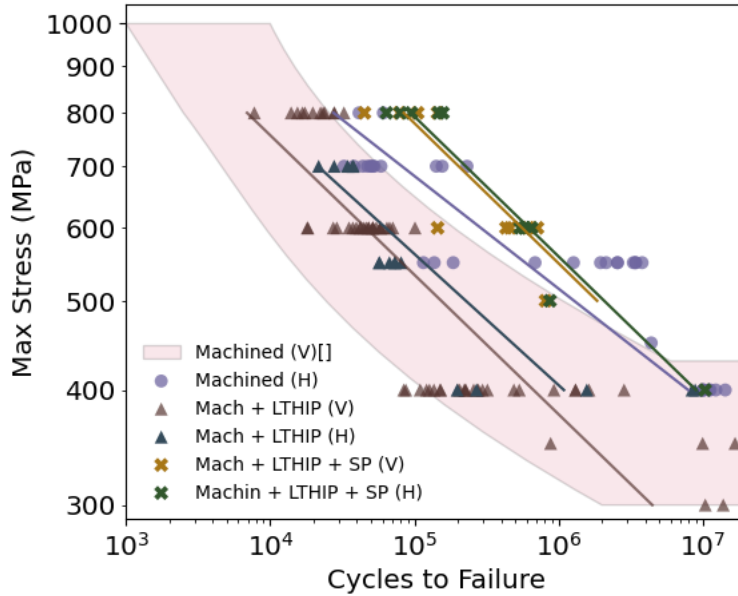


Figure 7-5: The fatigue life of as-built PBF-EB Ti6Al4V specimens, in the horizontal and vertical orientations

### 7.2.5 Fractography

Fractography of the fractured samples provides insight into the defects leading to failure. In the As-Built samples, the common defects including porosity and LOF defects are observed, as shown in Figure 7-6. The internal defects were not commonly observed after the STHIP treatment. However, the rough surface finish was observed in both the As-Built and STHIP condition, as shown in Figure 7-6 and Figure 7-7.

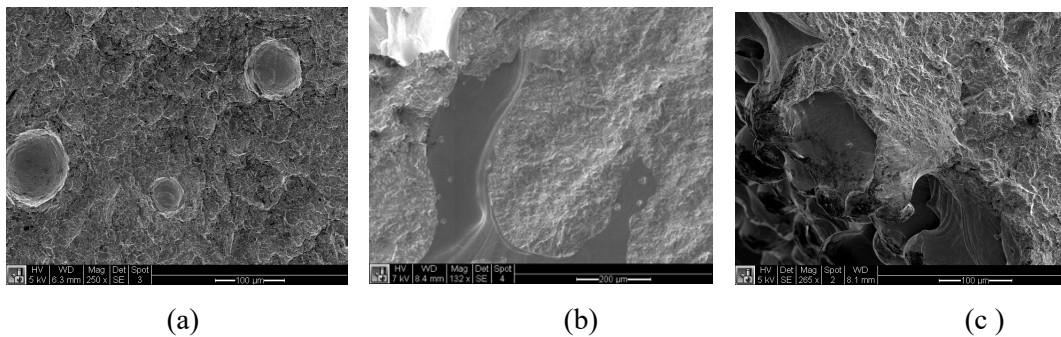


Figure 7-6: SEM Fractography of the common defects found on the As-Built and STHIP samples including (a) gas porosity, (b) LOF, and (c) surface defects.

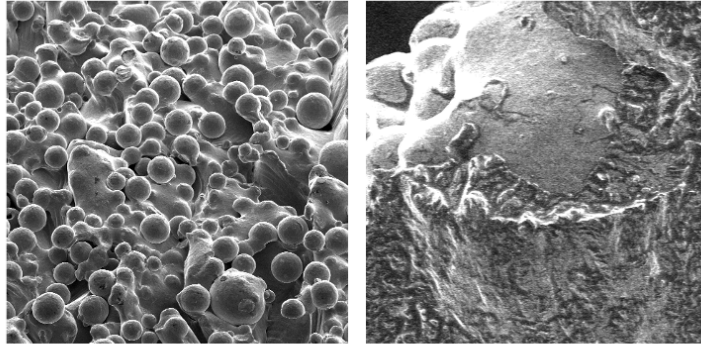
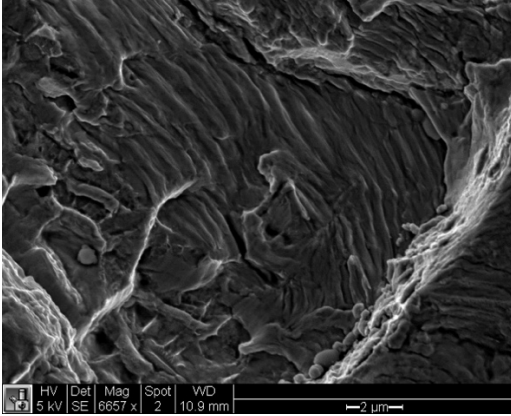
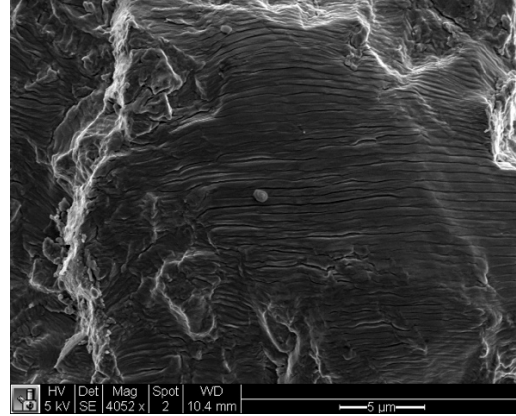


Figure 7-7: The rough surface exterior of PBF-EB components composed of partially melted

Fractography was performed after sample fracture using optical and scanning electron microscopes. A typical fatigue fracture surface exhibits three distinct regions: the source of crack initiation, the area of crack propagation and the area of final fracture. Typically, lines are found radiating away from the crack initiation source until it reached a flat fracture region as the crack grows, until the final fracture, where shear lips and ductile dimpling are observed. In the initial regions of crack initiation, fatigue striations, which are evidence of fatigue failure are often observed. These striations were observed in both the As-Built and STHIP samples shown in Figure 7-8. The samples in this study exhibited the three typical fatigue nucleation sources: surface, subsurface, and internal defects. The following section is organized by the surface condition of the fatigue samples. Additional features of interest regarding the specimen surface and internal defect are provided and discussed.



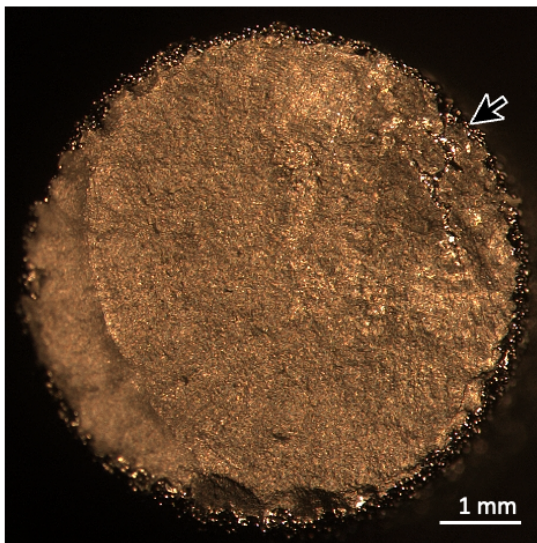
(a)



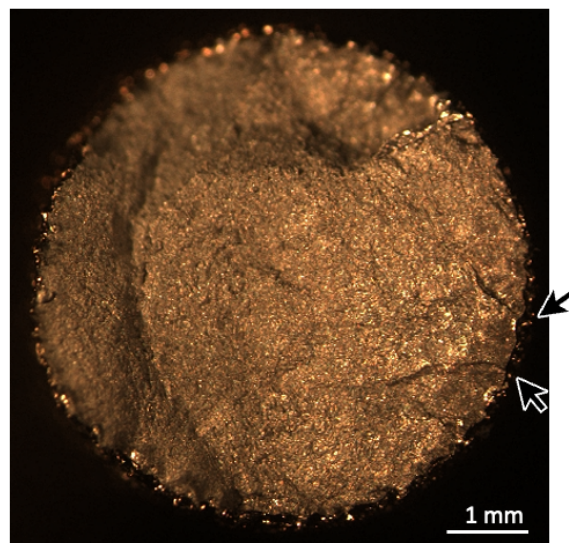
(b)

Figure 7-8: Fractography of the striations on the (a) As-Built and the (b) As-Built + STHIP samples. The images were obtained close to the crack nucleation sites.

Figure 7-9 provides the optical and SEM fractography of the As-Built and STHIP samples with the as-fabricated surface. While spherical gas porosity and LOF defects were only observed on the fracture surface of the untreated sample, fatigue cracks nucleated from the external surface in both the untreated and STHIP samples. The irregular external surface comprised of partially molten powder particle and sharp notch-like features formed during the PBF-EB process, resulting in multiple crack initiation sites in the samples.



(a)



(b)

Figure 7-9: Fractography of the samples after fatigue failure. The arrows indicate the location of crack initiation in the (a) As-Built and the (b) As-Built + STHIP samples. Multiple crack initiation regions were often observed on samples.

The fracture surface after fatigue failure of the horizontally oriented samples in the machined condition is provided in Figure 7-10. Three observations can be made regarding the figure. First, there is a fisheye or circular crack pattern which appears when the crack nucleates from an internal defect. Additionally, the internal circular crack growth is more often observed during high cycle fatigue. Secondly, there are additional sources of cracks nucleating from the surface, as denoted by the black arrow. Lastly, porosity and LOF defects are observed on the fracture surface, with the LOF defects exhibiting a long and thin shape.

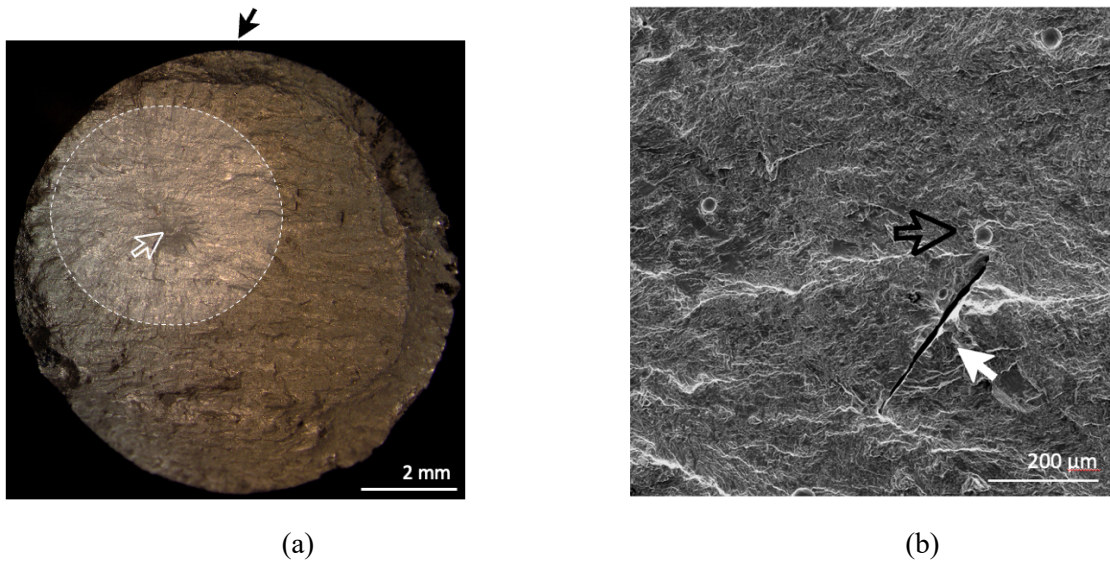
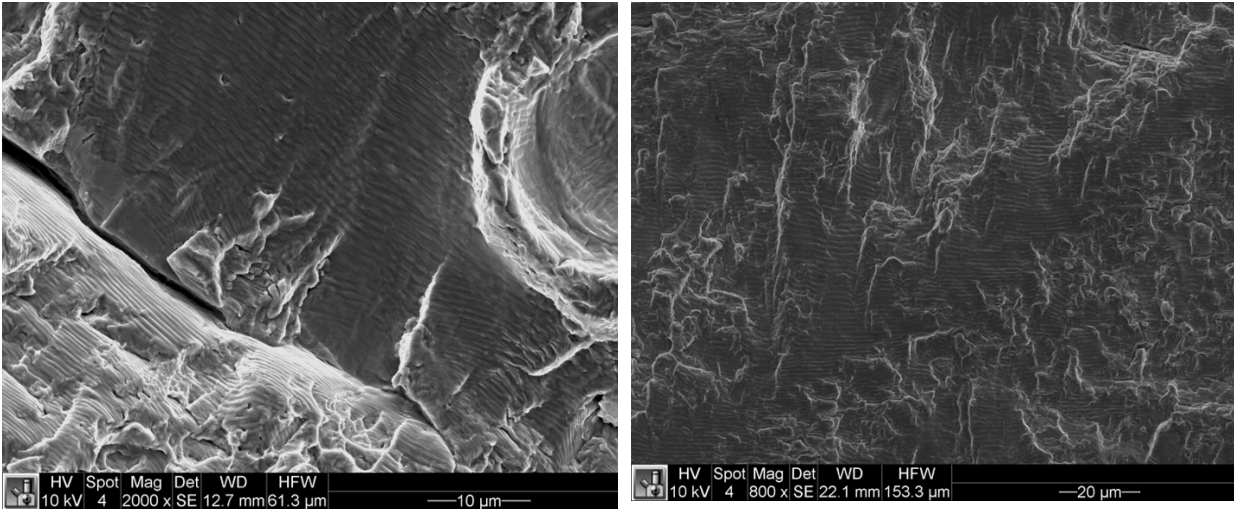


Figure 7-10: The fracture surface of the horizontal machined HCF samples. (a) The fracture surface of the horizontally oriented samples in the untreated condition is shown, highlighting the region of crack initiation and propagation. (b) a higher magnification of the porosity and LOF defects. The clear arrow points out the source of crack initiation, with the solid white arrow the LOF defect and the black/clear arrow porosity defects.

Evidence of fatigue was observed on the Horizontal orientation, in both the machined and Machined+LTHIP condition, as seen in Figure 7-11. The fatigue striations are marks on the fracture surface resulting from the incremental growth of the fatigue crack. The fatigue striations observed in the horizontal orientation are evidence of fatigue crack growth.

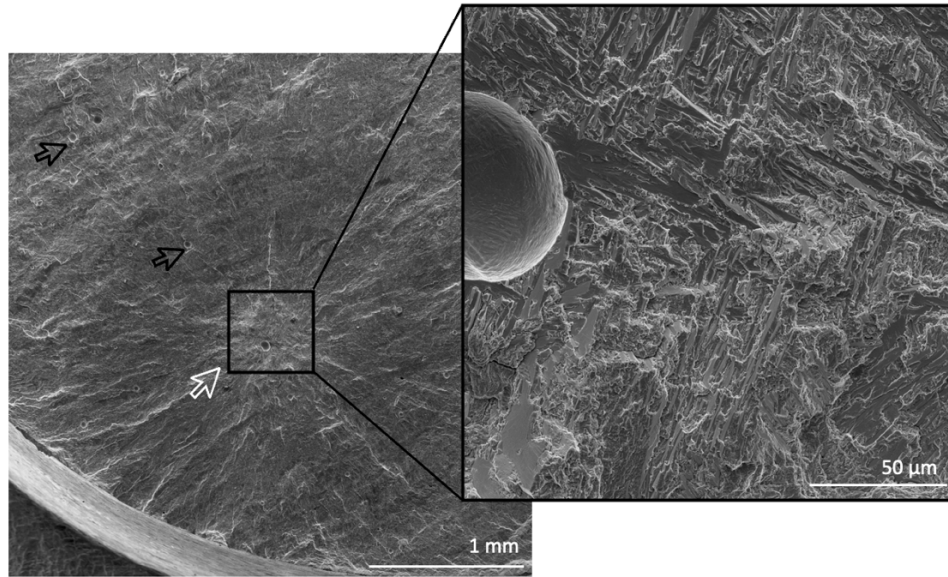


Horizontal Machined

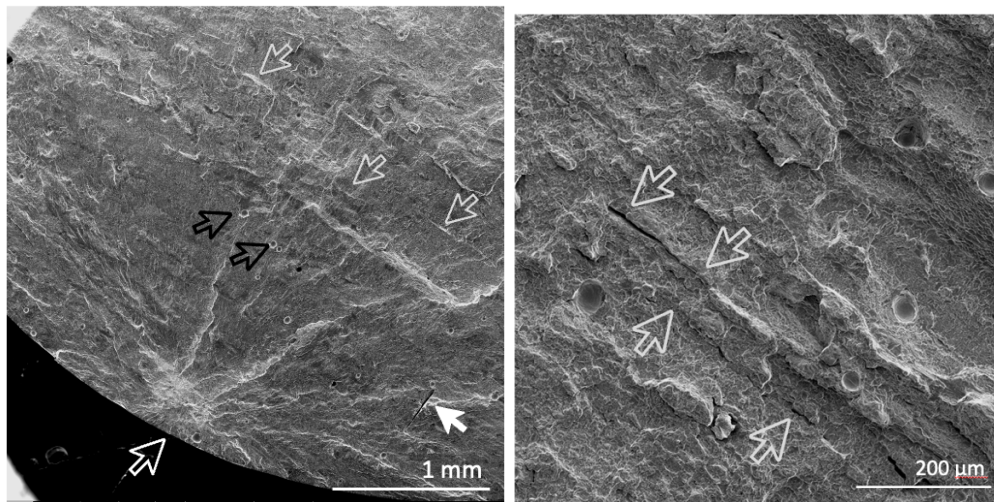
Horizontal Machined + LTHIP

Figure 7-11: The fatigue striations of the horizontal machined and Machined+LTHIP HCF samples.

Figure 7-12 shows fracture surfaces of machined samples. Internal porosity and LOF defects were observed on the fracture surface of the horizontal HCF samples. With the removal of the rough surface exterior, cracks nucleated from surface, subsurface, and internal defects, highly depending on the applied load. Porosity and LOF defects were the main sources of internal crack initiation, with located randomly on the fracture surface of the horizontally orientated samples. As the maximum applied stress decreases, cracks often nucleated from internal defects, such as the penny-shaped region seen in Figure 7-12. The fracture surface exhibited cracks radiating from the crack initiation region as cracks propagated outward. In addition to the crack radiating, an additional set of cracks running parallel to each other were observed roughly 50  $\mu\text{m}$  intervals, irrespective of the crack propagation direction.



(a)



(b)

(c)

Figure 7-12: The fracture surface of the horizontal machined HCF samples. The clear arrow points out the source of crack initiation, with the solid white arrow the LOF defect and the black/clear arrow porosity defects. (a) higher magnification image of the source of crack initiation. (b) the low magnification and (c) high magnification images of the microcrack formed perpendicular to the crack growth direction and parallel to the build direction.

Figure 7-13 shows the fracture surface of samples with a LTHIP treatment as a function of build orientation. The LTHIP treatment was successful in removing internal defects, where porosity and LOF defects were not observed on the fracture surface. The subsurface defects located 200 $\mu$ m from the surface with  $\mu$ CT were similarly observed with high-magnification imaging and

profilometry. The sharp notch-like defects on the surface of the samples were a result of the high-pressure LTHIP process deforming preexisting subsurface defects below the external surface.

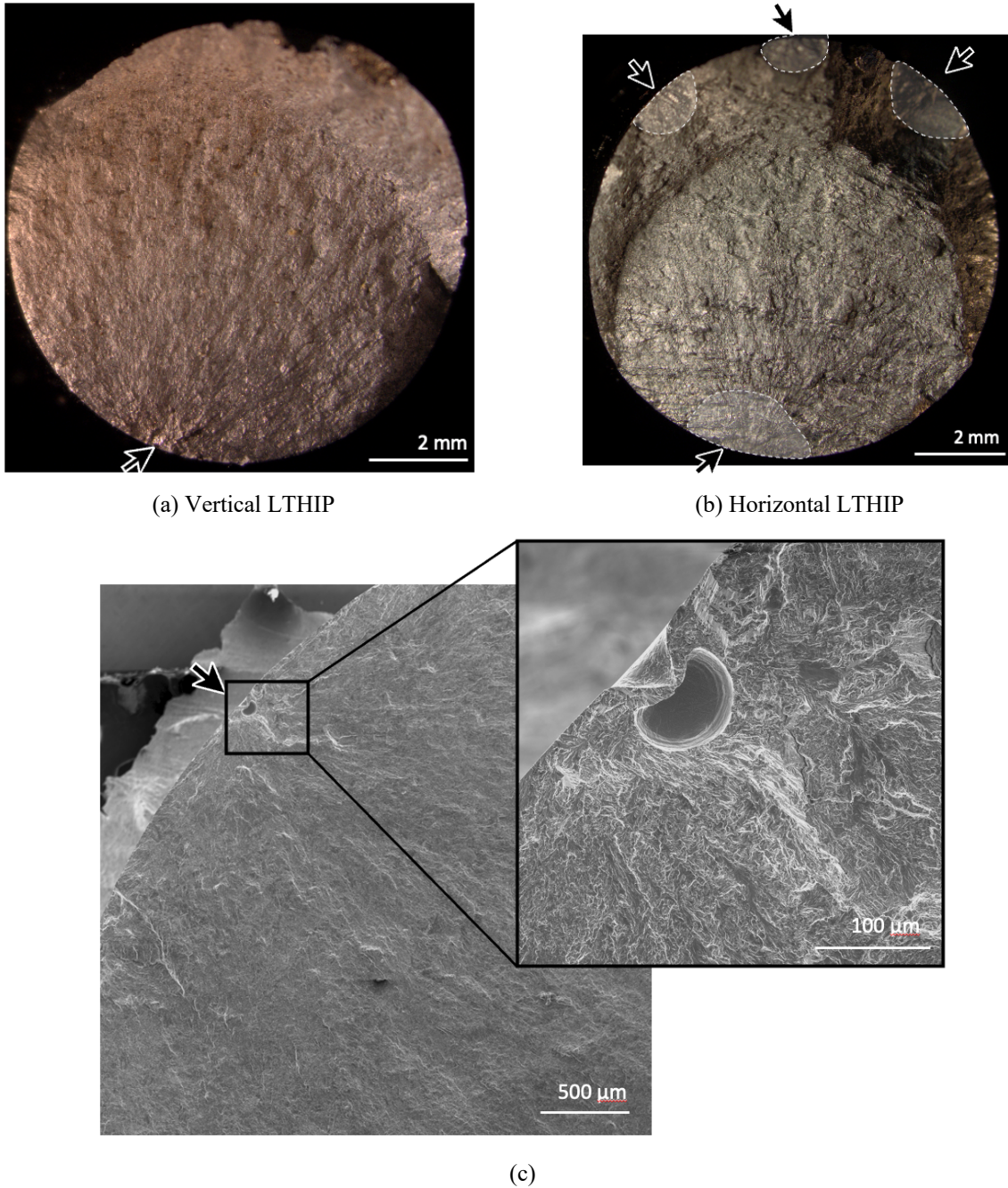
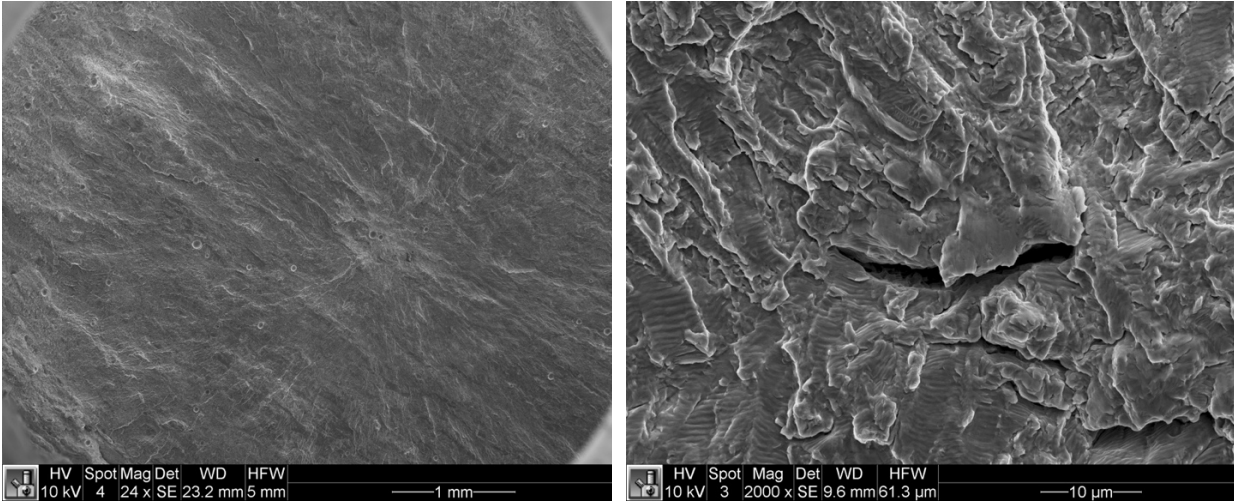


Figure 7-13: Optical fractography of the (a) Vertical and (b) Horizontal orientation. The arrows indicate the location of crack initiation. Multiple crack initiation regions were often observed on samples, as seen on the (b). (c) sharp surface notches formed from subsurface defects deforming during the LTHIP process.

High magnification images of the source of crack nucleation in the shot peened samples is shown in Figure 7-14. Internal defects contributed to the internal crack initiation observed in the Machined+Shot peened samples. Cracks are observed to radiate outward as the crack propagated and grew larger until fracture occurred. Fatigue striations were observed on the fracture surface of the shot peened samples, evidence of fatigue crack growth, shown in Figure 7-14.

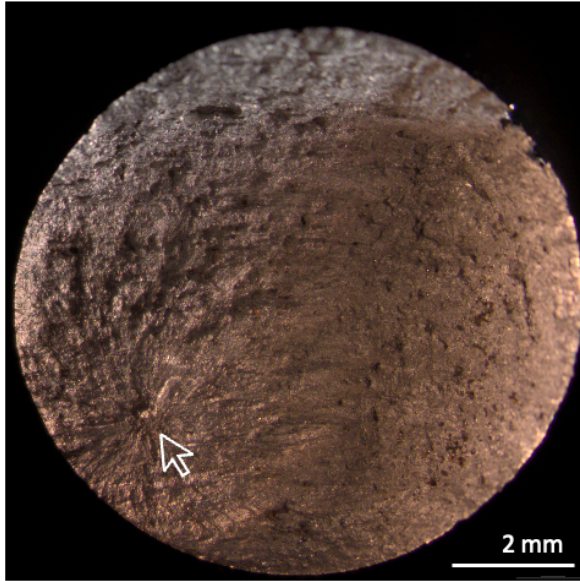


(a) Horizontal Machined + SP

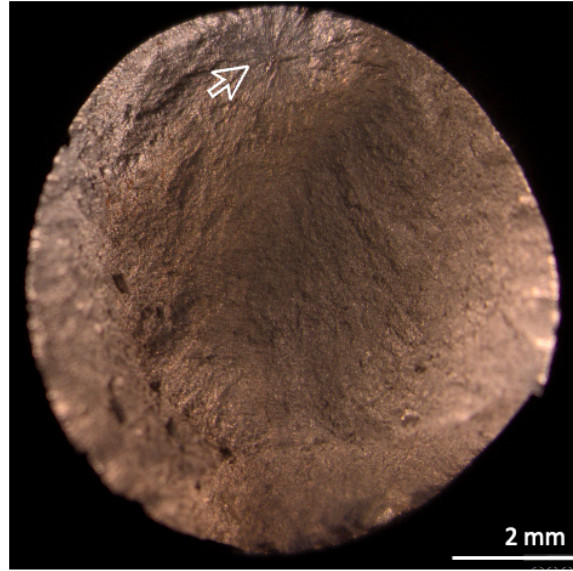
(b) Horizontal Machined + SP Striations

Figure 7-14: SEM fractography of the LTHIP+SP samples after fatigue failure. (a) the crack origin due to internal defects with crack propagating radially out. And (b) the striations observed near the crack initiation region.

Figure 7-15 shows low magnification fatigue fracture surfaces of the shot peened samples. While LOF and porosity defects were only observed on the Machined + SP samples, the samples in both conditions often failed due to subsurface and internal features. The cracks running parallel found in the horizontal orientation of Figure 7-12 were also observed in the horizontally oriented SP samples. These features were not observed on the vertical shot peened samples.



(a) Horizontal LTHIP + SP



(b) Vertical LTHIP + SP

Figure 7-15: Optical fractography of the samples after fatigue failure. The arrows indicate the location of crack initiation.

The location of crack initiation was compiled for all the samples after final fracture. Many samples exhibited multiple regions of crack initiation, such as the sample shown in Figure 7-16. The source of crack initiation which exhibited the largest crack growth region was used to compile the crack nucleation site which resulted in the largest influence on fatigue failure.

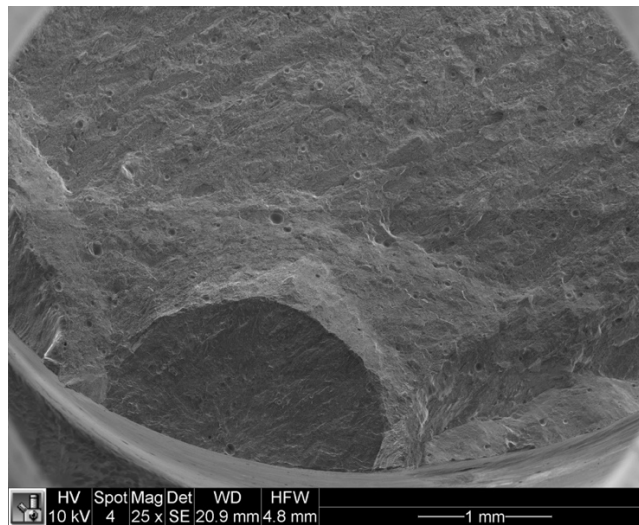
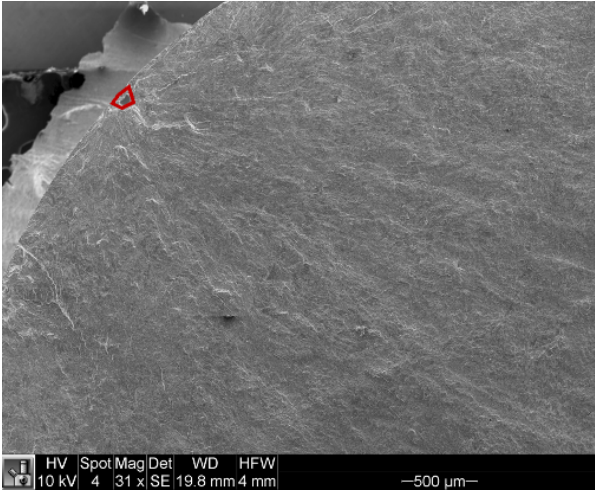
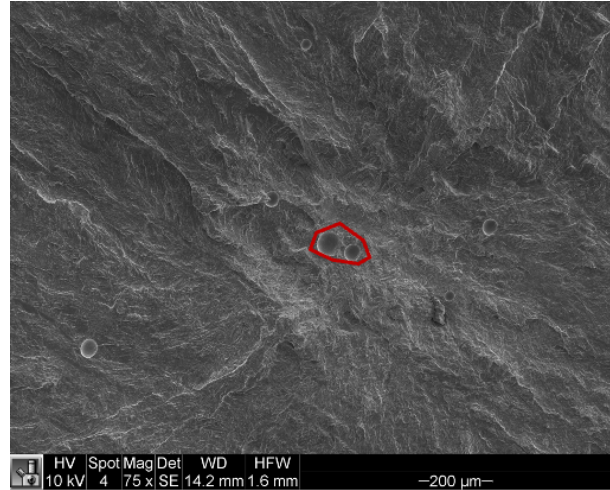


Figure 7-16: SEM fractography of the Machined samples after fatigue failure, where a smaller crack propagated from the external surface while it was not the main crack nucleation. Porosity and LOF defects observed on the fracture surface located randomly.

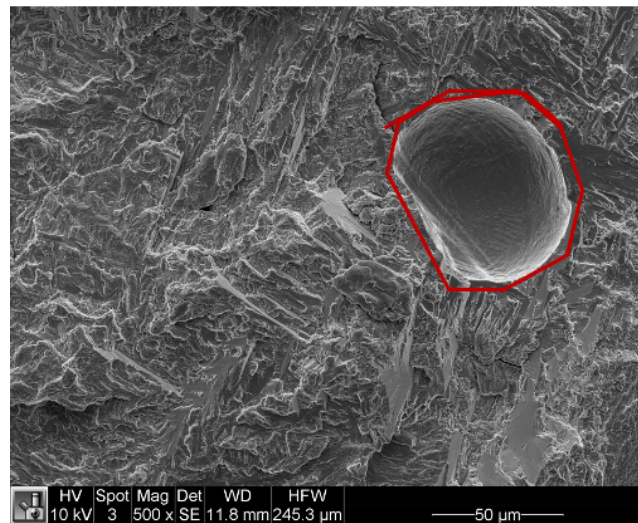
The critical defect size of select samples was images and calculated according to the  $\sqrt{Area}$  parameter model originally developed by Murakami et al. <sup>256</sup> The  $\sqrt{Area}$  is the equivalent defect size and the results are provided Appendix C - Murakami Defect Area.



(a) Machined + LTHIP



(b) Machined



(c) Machined + SP

Figure 7-17: SEM fractography of the crack nucleation sites on the (a) LTHIP, (b) Machined, (c) SP samples, where the critical defect is outlined and calculated after fatigue failure.

### 7.2.6 Fatigue Life Variation

To better understand the variation in the fatigue life of PBF-EB Ti6Al4V. Plotting the experimental fatigue cycles versus the predicted cycles as calculated from the Basquin equation is plotted in Figure 7-18. All samples were tested at R=0.1. However, a large variation in fatigue performance exists, where the Basquin equation by itself is not able to accurately predict the fatigue behavior, compared to the experimental results.

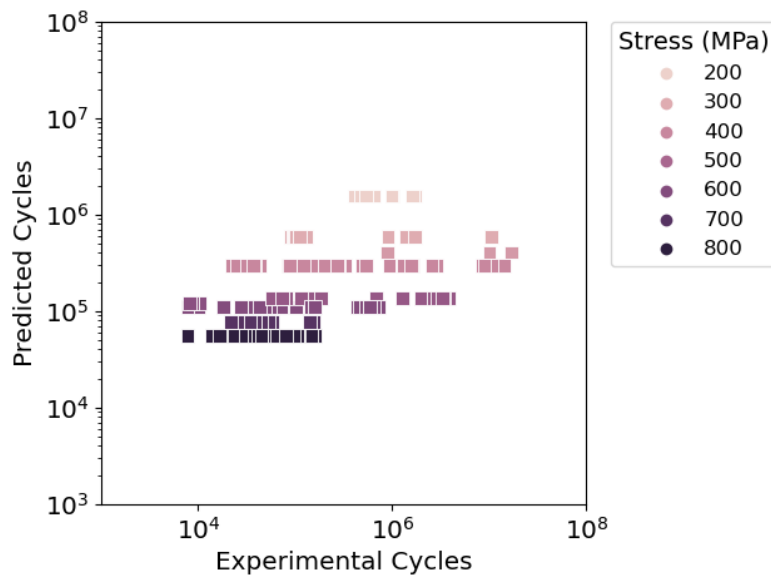


Figure 7-18: The predicted versus the experimental fatigue life (R=0.1), where the predicted values are calculated using the Basquin equation.

To better predict the fatigue behavior of the PBF-EB Ti6Al4V, a *Theoretical Fatigue Stress Limit* was established by Murakami et al.<sup>256</sup>. A correlation between the *Theoretical Fatigue Stress Limit* of Equation 7-2 and hardness in steels has shown to be applicable to wrought titanium alloys<sup>256</sup>, for hardness up to 400 HV

$$\sigma_w = 1.6 HV \pm 0.1HV \quad \text{Equation 7-2}$$

where *HV* is the Vickers hardness and  $\sigma_w$  is the ideal fatigue limit. The following equation was compared to the experimental findings of this study. The theoretical fatigue limit is calculated using Equation 7-1 and summarized in Table 7-3. However, comparing the ratio between the stress amplitude and the calculated theoretical fatigue life fall short of the experimental results, where a

ratio of 1.0 is desired. As such, using the hardness values alone is underestimated the fatigue behavior of PBF-EB Ti6Al4V.

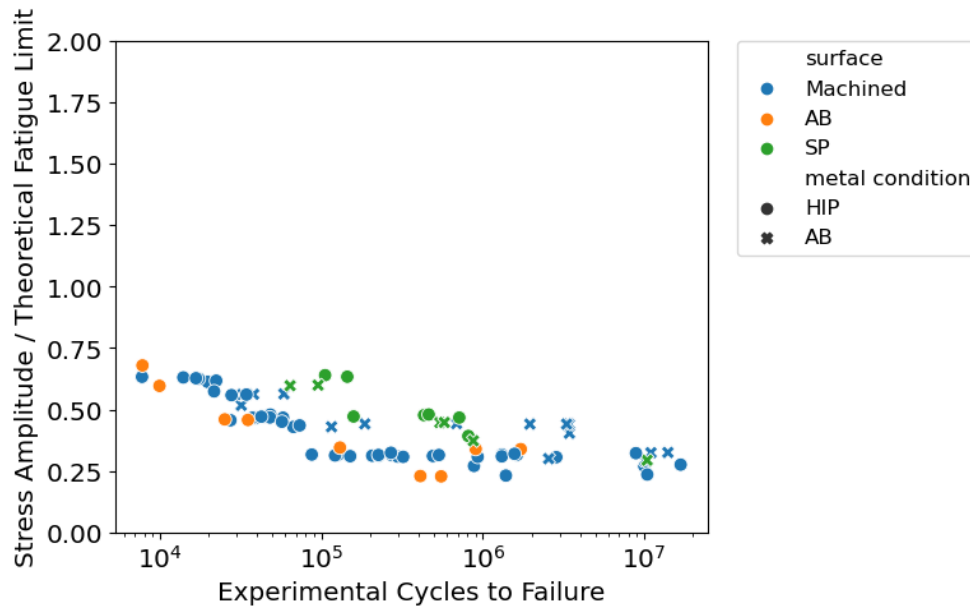


Figure 7-19: The ratio between the stress amplitude and the Theoretical Fatigue Stress versus the experimental fatigue life. The predicted values obtained using Equation 7-2.

Samples under fatigue loading are sensitive to internal defects. Therefore, an *Ideal Fatigue Limit* was determined using the critical defects, the source of crack initiation, in addition to the hardness shown in of Equation 7-3. As a result, the internal defects were considered, in addition to the bulk properties. The  $\sqrt{Area}$  parameter model was originally developed for steels and has been further adopted in evaluating the influence of defect size in Ti6Al4V<sup>256</sup>

$$\sigma_w = Y \frac{(HV+120)}{\sqrt{Area}^{\frac{1}{6}}} \quad \text{Equation 7-3}$$

where  $\sqrt{Area}$  is the equivalent defect size, and  $Y$  is 1.43 for surface defects, 1.41 for subsurface defects, and 1.56 for internal defects per Murakami et al.<sup>256</sup>. This means, internal defects result in a higher fatigue limit given the same microstructure compared to a similarly sized defect located at the surface or subsurface. The  $\sqrt{Area}$  was estimated from the size of the critical defect at the fracture origin of select samples, using the process outlined by Murakami et al.<sup>256</sup> and shown in Figure 7-17. Through incorporating hardness and the critical defect size, a more realistic cycles to failure was calculated for the samples shown in Figure 7-20 for the experimental findings in this

study. However, the fatigue behavior at the lower stresses in the as-fabricated surface were underestimated by 50%. Furthermore, the shot peened samples are overestimated using the *Ideal Fatigue Stress* of Equation 7-3.

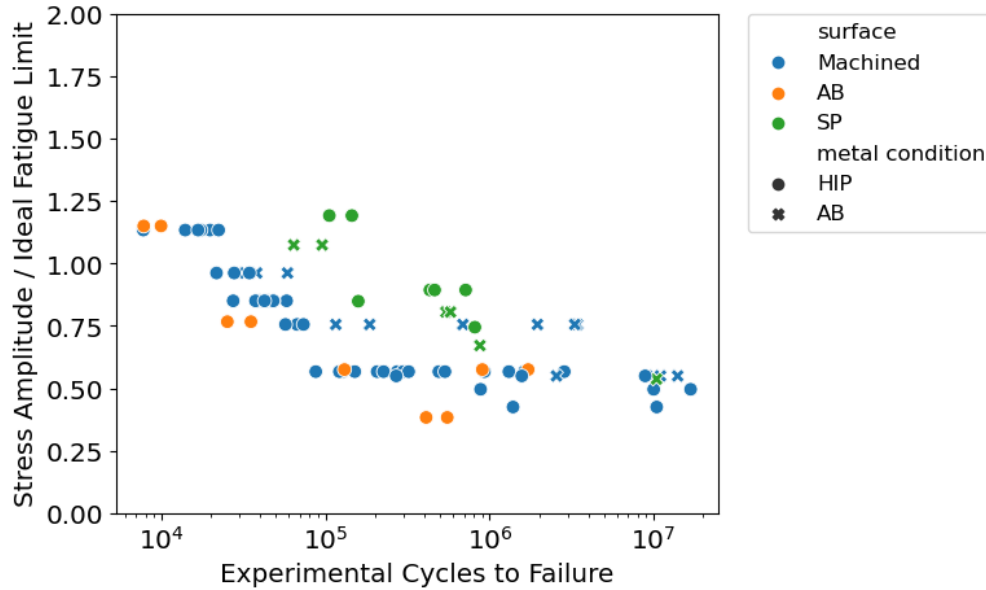


Figure 7-20: The ratio between the stress amplitude and the Ideal Fatigue Stress versus the experimental fatigue life. The predicted values are obtained using Equation 7-3.

A change in fatigue life was observed with the change in the surface treatment, where the surface roughness characteristics may play a role in the fatigue resistance. As a result, the surface roughness parameters  $R_a$ ,  $R_v$ , and  $R_z$  were plotted and compared to the cycles to failure in the as-fabricated, Machined, and shot peened condition. The experimental cycle to failure is plotted versus the average surface roughness,  $R_a$ , and the ten-point roughness  $R_z$  in the STHIP condition in Figure 7-21. While some scatter exists in the cycles to failure, there are distinct clusters of samples according to the stress level. So even though there is a wide range of  $R_a$  and  $R_z$  values reported, the average cycles to failure are similar. However, as the stress decreases to 200MPa, there is a larger variation in cycles to failure, with a 15% increase in variation in fatigue life. Additionally, as the maximum applied stress is decreased, a downward trend in roughness is observed. As the  $R_a$  and  $R_z$  decrease, the cycle to failure appears to decrease, especially at the 200MPa stress level. As the  $R_z$  value decreased below 100 $\mu$ m, samples at the 300MPa level were able to survive until 10<sup>6</sup> cycles to failure, even though similar  $R_a$  values were reported for similar samples at that stress levels which failed at 10<sup>5</sup> cycles.

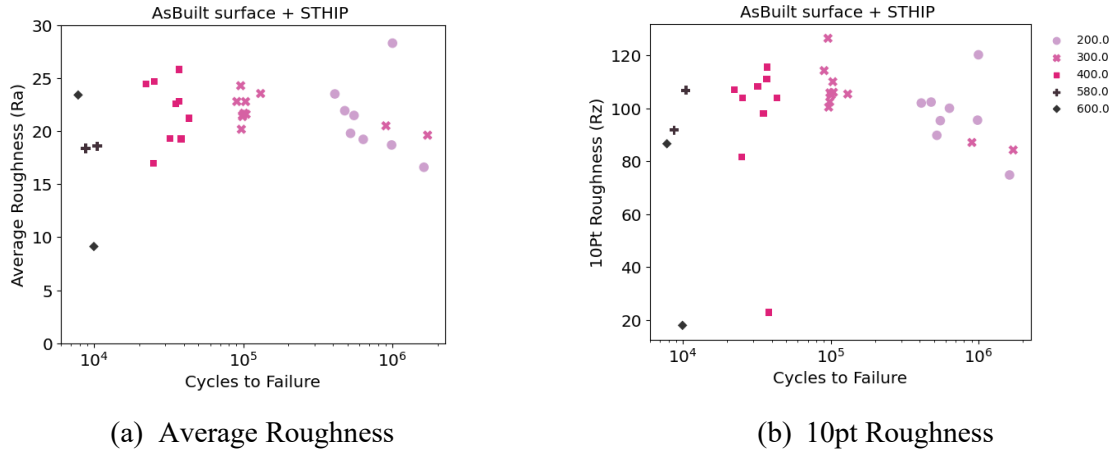


Figure 7-21: The relationship between the (a) average surface roughness ( $R_a$ ) and (b) 10-point roughness ( $R_z$ ) with respect to cycles to failure in the STHIP condition.

With a machining application, there is a significant reduction in the  $R_a$  and  $R_z$  values and the range of values shown in Figure 7-22. There is also a significant increase in the cycles to failure of up to  $10^7$  cycles, which was not observed in the STHIP condition. One key observation compared to Figure 7-21 is the increase in scatter in the cycles to failure, where there is overlap between the different stress levels. There is a notable increase in scatter (140%) in cycles to failure, as the max applied stress decreases from 600MPa to 400MPa. The samples which survived the longest appeared to have the lowest  $R_z$  values below  $4 \mu\text{m}$  at the 300-400MPa stress levels. For samples with  $R_z$  higher than  $4 \mu\text{m}$ , the samples failed prior to  $10^6$  cycles. While a large source of scatter exists in the surface roughness parameters at the higher stress levels, the cycles to failure exhibited a smaller range.

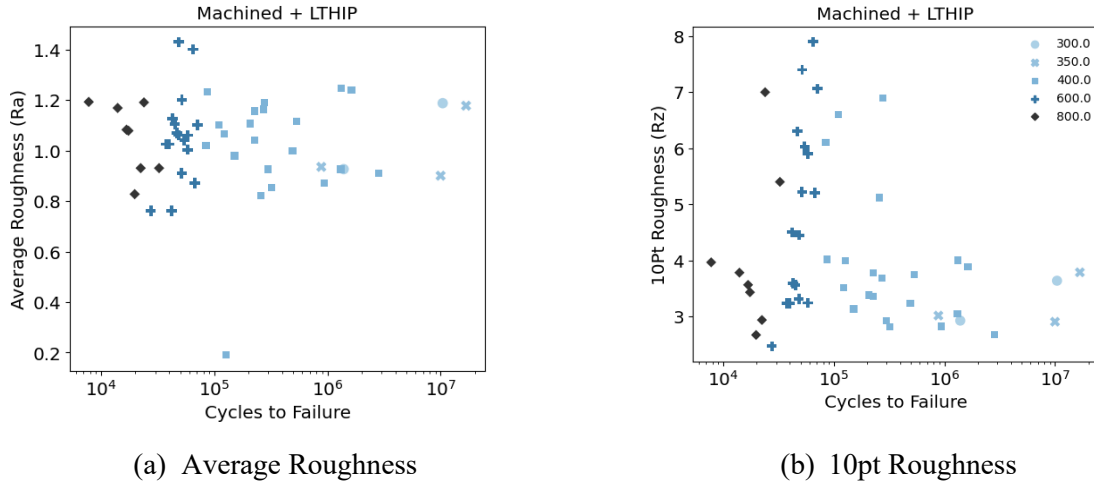


Figure 7-22: The relationship between the (a) average surface roughness ( $R_a$ ) and (b) 10-point roughness ( $R_z$ ) with respect to cycles to failure in the Machined + LTHIP condition.

Lastly, comparing the  $R_a$  and  $R_z$  to the cycles to failure in the shot peened samples in Figure 7-23. The overall range in the surface roughness  $R_a$  and  $R_z$  values decreases in the shot peened condition, compared to the machined surface, with a decrease in the overall  $R_z$  values and overall range of values reported. The samples are observed to be in distinct clusters, separated by the stress level. Overall, the shot peening application decreases the overall range of  $R_z$  values reported, with the samples surviving past  $10^6$  cycles having  $R_z$  values less than  $4 \mu\text{m}$ . This is like the trends observed in the Machined+LTHIP samples shown in Figure 7-22. Similar to the previous observations, the lowest  $R_a$  and  $R_z$  also exhibit the longest cycles to failure.

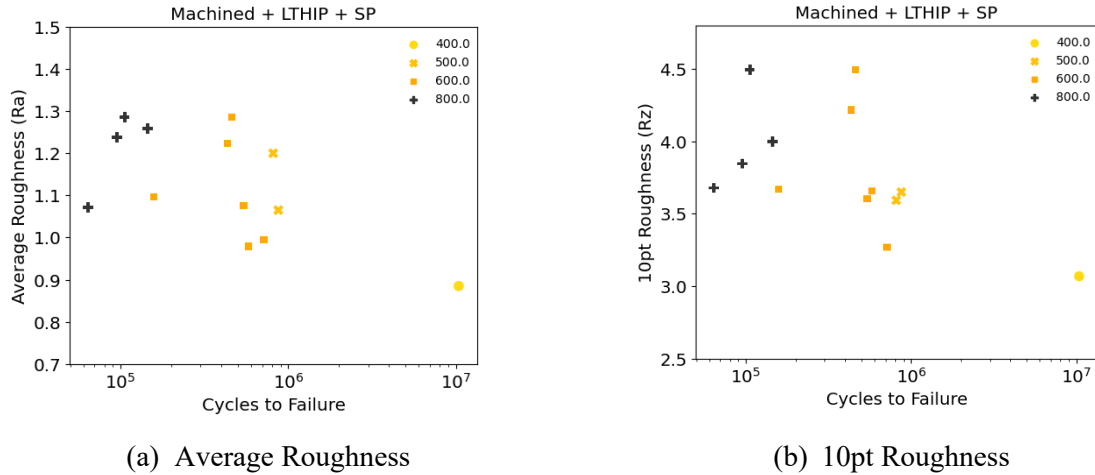


Figure 7-23: The relationship between the (a) average surface roughness ( $R_a$ ) and (b) 10-point roughness ( $R_z$ ) with respect to cycles to failure in the Machined+LTHIP+SP condition.

The cycles to failure versus the maximum valley depth ( $R_v$ ) is also provide in Figure 7-24. The samples in the STHIP condition are observed to be in distinct clusters, with a large range in  $R_v$  values reported, similar to Figure 7-21. With the machining application, there is an increase in the overall scatter in the  $R_v$  values, with significant overlap in cycles to failure in the various applied stresses. This overlap is also observed in the shot peened surfaces. The overall  $R_v$  values in the surface treated samples was below 4  $\mu\text{m}$ , with the lowest  $R_v$  values exhibiting some of the higher cycles to failure.

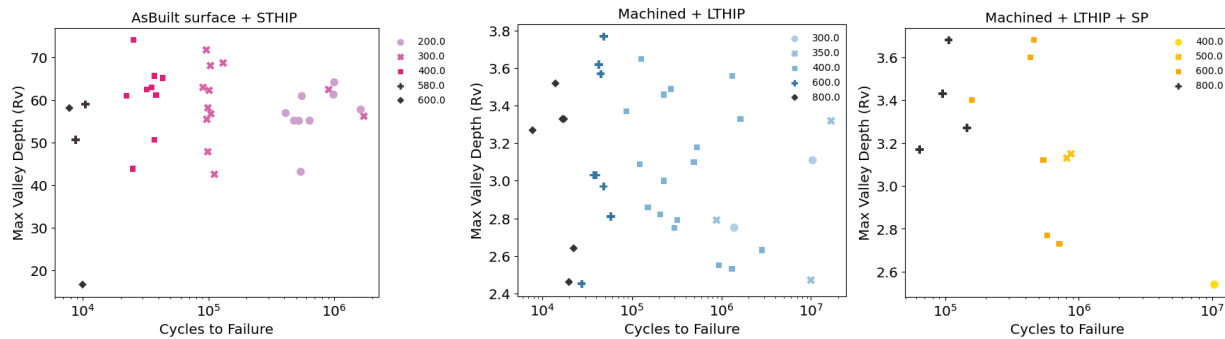


Figure 7-24: The relationship between the max valley depth ( $R_v$ ) with respect to cycles to failure.

Combining the factors which influence the fatigue limit in addition to the surface characteristics, a prediction model was obtained. Incorporating the hardness, critical defect size, and surface roughness into model resulted in a linear regression equation used predict the fatigue life of samples, with an  $R^2$  value of 0.782 and adjusted  $R^2$  of 0.762, details provided in Appendix C - HCF Regression Equations, which resulted in the following equation termed the *Regression Fatigue Life*

$$N_f = 10^{-17.525} \sigma^{-5.320} T^{2.161} HV^{11.978} \sqrt{Area}^{3.220} R_z^{3.007} R_v^{-4.297} \quad \text{Equation 7-4}$$

where  $N_f$  is the cycles to failure,  $\sigma$  is the maximum stress,  $T$  is the thickness,  $R_z$  is the ten-point height, and  $R_v$  is the maximum valley depth. Through including the surface roughness parameters for valleys and overall surface height difference, surface imperfections can be taken into consideration. Initially, the experimental fatigue behavior obtained in this study was plotted versus the fatigue life obtained from the Basquin equation in Figure 7-18. However, as it was observed, there was little correlation between the predicted and experimental fatigue behavior, using the Basquin equation alone. However, when the Basquin equation was expanded to include the metal hardness, thickness, critical defect size, and surface roughness parameter as seen in Equation 7-4, an improved correlation was obtained. Therefore, as research moves toward predicting the PBF-EB fatigue strength, it is pertinent to fully consider the process-induced attributes which influence the metal performance. Furthermore, through a holistic evaluation of the metal, we were able to obtain a prediction equation which can be used to approximate the fatigue strength of PBF-EB Ti6Al4V.

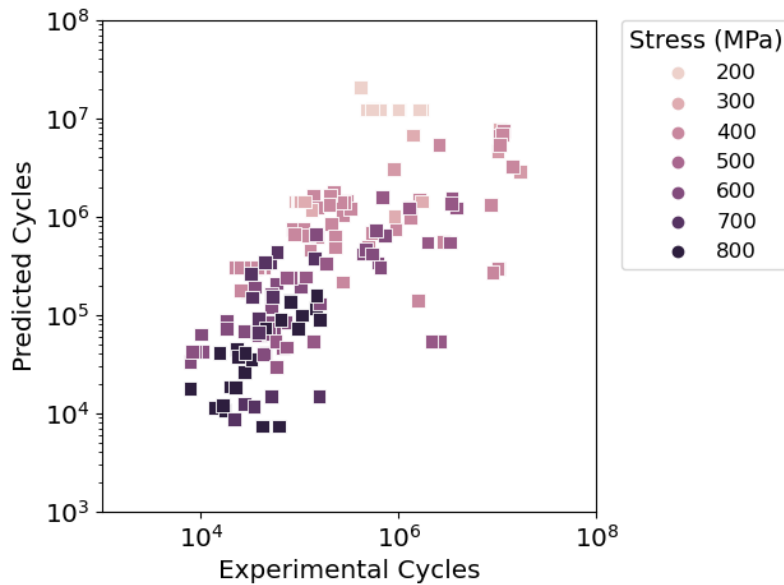


Figure 7-25: The regression equation comprised of the metal quality, surface roughness, and internal defects.

To compare which of the methods discussed can appropriately predict the endurance limit of PBF-EB Ti6Al4V, the *Theoretical, Ideal Fatigue Stress, and the Regression Fatigue Life* was

calculated using Equation 7-2, Equation 7-3, and Equation 7-4. The summary of the fatigue limit using these equations is provided in Table 7-3. The *Experimental Fatigue Limit* is the stress at which the sample achieved runout or survived up to  $10^7$  cycles without fracture, per the findings of this study. The results of Table 7-3 show the *Theoretical Fatigue* equation utilizing the hardness alone overestimates the fatigue endurance for PBF-EB Ti6Al4V and is not able to appropriately capture the influence of shot peening on fatigue life. This was also observed in Figure 7-19, where the samples in all surface conditions were overestimated. However, once hardness, the crack initiation location, and the critical defect size are considered in the *Ideal Fatigue Limit* using Equation 7-3, a more appropriate fatigue limit was obtained, especially in the as-fabricated condition. However, the Machined, Machined+LTHIP, and Machined+LTHIP+SP conditions were underestimated. Through incorporating the surface roughness characteristics, the Regression equation was able to predict a fatigue endurance limit for PBF-EB Ti6Al4V much closer to the experimental results.

Table 7-3: Experimental and theoretical fatigue limit in each condition

Condition	Experimental Fatigue Limit (MPa),	Theoretical Fatigue Limit (MPa),	Ideal Fatigue Limit (MPa),	Regression Fatigue Limit (MPa),
	From this study	Eq. 7-2	Eq. 7-3	Eq. 7-4
As-Built	< 200	454	227 - 238	~200
As-Built + STHIP	< 200	452	243	~170
Machined	400	560	324 - 345	~470
Machined + LTHIP	350	521	318 - 343	~375
Machined+LTHIP+SP	400	521	330 - 340	~425

This work encompassed samples printed systematically to evaluate the intra-build design parameters and post-processing of the fatigue life of PBF-EB Ti6Al4V. Through using a multi-factorial DOE approach, 85 samples were tested in the untreated, HIP and shot peened condition and two orientations to understand the repeatability and reliability of the metal. The post-processing treatment had the largest influence on the fatigue behavior, where shot peening reported values nearly twice those in the untreated condition and 4X the STHIP condition. While STHIP and LTHIP were successful in reducing internal porosity and defects, the subsurface defects

remained and were the source of crack initiation. Shot peening however was successful in reducing the orientation-dependent behavior and reducing scatter in the data. Additional samples and chemical analysis of the metal are recommended to better understand the remaining variation in the shot peened metal. The untreated PBF-EB Ti6Al4V alloy was promising for adoption and with the application of machining, LTHIP, and shot peening, metal comparable to annealed wrought Ti6Al4V can be achieved.

## 8 Discussion

Previous studies on the fracture-critical properties of PBF-EB Ti6Al4V have primarily examined the role of microstructure and defect characteristics on property variation. While these efforts provided valuable insights, they have not fully addressed whether the intra-build design factors influence fracture toughness and high cycle fatigue variability. Hrabe et al.<sup>22,23</sup> demonstrated that changes in size, location, and sample orientation contribute to property variability, but their assessment was limited to individual parameters, with a primary focus on the tensile properties. However, for PBF-EB Ti6Al4V to be used in damage-tolerant applications, it is crucial to understand how process-induced variability contributes to scatter in fracture-critical properties, particularly in fracture toughness and fatigue resistance. In addition to these process-driven effects, post-processing strategies play a key role in mitigating variability and enhancing mechanical properties. However, the optimization of post-processing treatment for improved durability remains limited, leaving gaps in how to best enhance the performance and reliability of PBF-EB Ti6Al4V components.

The current ASTM F2924<sup>28</sup> standard provides guidelines for HIP post-processing of metal AM Ti6Al4V to reduce internal defects and improve the mechanical properties. While this standard was foundational for metal AM, recent research has inspired optimizing HIP parameters for PBF-LB Ti6Al4V, leading to the formation of AMS7028 specification<sup>29</sup>. However, as this specification primarily addresses the PBF-LB process, its applicability to PBF-EB Ti6Al4V remains under evaluation due to the inherent differences in fabrication process. As a result, rigorous experimental evaluation necessitated further studies to ensure equivalent behavior and qualification for safety-critical applications.

Before considering the influence of post-processing, it is crucial to first examine the inherent variability in mechanical properties that arises from the PBF-EB process and build design choices. While PBF-EB Ti6Al4V has shown promise for structural applications<sup>2, 15,41</sup>, significant scatter in mechanical properties has been reported, necessitating a deeper understanding of its underlying causes. The limited number of studies on the fracture toughness result in a lack of consistency in build design strategies (e.g., specimen size, location, powder, process parameters, etc.) has led to a broad range in reported YS (730 – 1030 MPa)<sup>12, 14,115</sup>, fracture toughness (60 – 120 MPa $\sqrt{\text{m}}$ )<sup>13, 41, 94,154</sup>, and fatigue strength (100-300 MPa)<sup>26,27,171</sup>. The absence of standardized

design guidelines has further hindered the ability to directly compare results across studies, highlighting the need for a more systematic approach to understanding process-induced variability.

To systematically evaluate the fracture-critical properties, a multi-factor DOE was utilized. In addition to the common parameters of interest such as orientation, the influence and interaction of thickness and specimen location on fracture toughness and fatigue behavior were examined. Capturing the fracture-critical properties throughout the build space further provides design engineers with an understanding of the process-structure-property relationship of the PBF-EB Ti6Al4V, which is essential for verification and validation.

## 8.1 Fracture Toughness

### 8.1.1 Anisotropy

Anisotropy in mechanical properties is a well-documented characteristic of PBF-EB Ti6Al4V and has been extensively investigated<sup>23, 42, 66, 101, 112</sup>. This study demonstrated a significant relationship between orientation and mechanical properties. The vertically-built PBF-EB Ti6Al4V specimens exhibited higher tensile strength, ultimate tensile strength, and ductility compared to the horizontally-built specimens. Furthermore, build orientation contributed to ~15% difference in fracture toughness. We hypothesize that there were three factors influencing the anisotropic mechanical properties. First, the elongated prior- $\beta$  grains, aligned along the build direction, influenced the crack growth direction. The basketweave microstructure within the grains and the  $\alpha$ -enriched region along the grain boundary was observed, in line with findings by Zhai et al.<sup>14</sup>. The crack path through the microstructure thus would change based on the crack orientation, where the XZ oriented CT samples exhibited an intergranular crack path, as the crack travelled along the  $\alpha$ -GB, resulting in a more direct fracture path and reduced crack growth resistance. This aligns with the lowest fracture toughness in the XZ orientation, seen in Figure 8-1. In comparison, the XY oriented samples also exhibited a preference for intergranular crack path, however, the samples exhibited enhanced fracture resistance. In contrast to the XZ orientation, the crack path in the XY oriented samples would interact with a higher number of grain boundaries, thus increasing the energy required for the crack to grow. Unlike these two orientations, the ZX orientation exhibited a zigzag crack path through the basketweave microstructure, where the highest energy is required for crack growth, leading to the largest fracture resistance. However, the ZX orientation did not result in the highest fracture toughness.

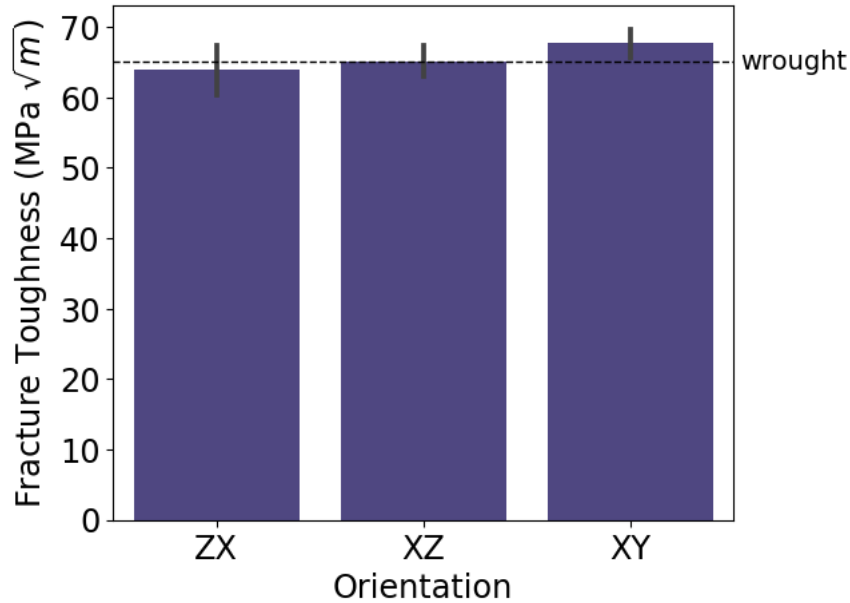


Figure 8-1: The average fracture toughness values in the ZX, XY, and XY orientation

Second, the variation in the microstructural parameters may have influenced the variation in fracture toughness due to orientation. Even though similar  $\beta$  vol.% and prior- $\beta$  grain width was reported between the three orientations, there was a significant difference in the  $\alpha$ -lath thickness shown in Figure 8-2. Notably, the XY orientations reported 30% larger  $\alpha$ -lath thickness, which was found to be significantly different from the XZ and ZX orientations. The difference in melt area also led to the orientation-dependent microstructure, where the horizontally oriented samples exhibited a coarser grain size shown in Figure 8-2. The samples oriented horizontally would exhibit a larger melt area, where a significantly larger grain size was observed in the XY oriented samples. Bruno et al. observed similar orientation dependent microstructure in PBF-EB<sup>102</sup>. Due to the larger volume of  $\alpha$ -phase in the metal, the difference in  $\alpha$ -lath could have further influenced the fracture-critical properties.

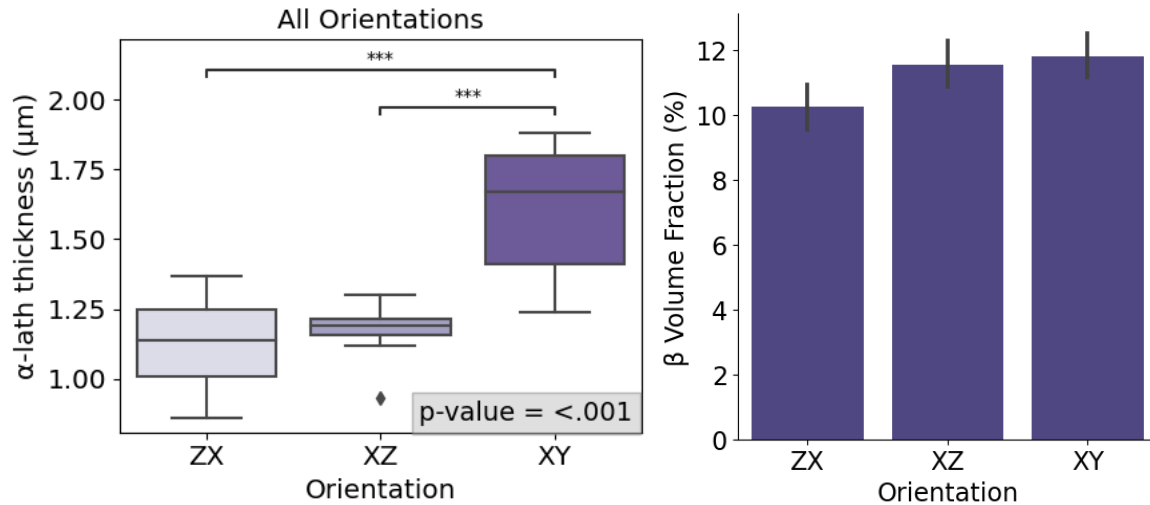


Figure 8-2: The microstructural characteristics  $\alpha$ -lath size and the  $\beta$  vol.% in the ZX, XZ, and XY. (\*\*\*) denotes statistical significance of ( $p < 0.001$ ).

Third, the LOF defects observed on the fracture surface of the untreated metal, when oriented normal to the applied load, would have the largest effect on the load carrying capacity of the specimen. While spherical pores exist within all the as-built samples, the variation in pore sphericity and size significantly affects the local stress around the defects. Consequently, the large and flat shaped LOF defects would have the most significant influence compared to gas pores, specifically in the ZX orientation, reducing fracture resistance. This aligns with our findings, where 1% of the ZX fracture surface area was comprised of defects, compared to only 0.2% in the XZ and XY orientations.

### 8.1.2 Intra-Build Variation

While most studies report specimen orientation, the broader influence of build space positioning and geometric considerations is only beginning to be explored. The absence of standardized design guidelines for additively manufactured Ti6Al6V further complicates efforts to establish reliable mechanical property database. To accurately compare available data and understand the factors driving mechanical property variation, it is essential to investigate the process-induced sources of variability, particularly those related to build design. Engineers designing metal AM components must make critical choices regarding geometry and placement within the build space, all of which can significantly influence the final material properties. While prior studies have separately examined the location<sup>24, 139, 141,257</sup> and part size<sup>210,258,259</sup>, the

combined influence of these parameters on fracture-critical properties remained largely unexplored.

Sample *height* within the build space was significant and contributed to the second largest variation in fracture toughness, following orientation. Fracture toughness is highly dependent on microstructure, making the variations in cooling rate and the temperature gradient within the PBF-EB build chamber significant. Microstructural variation induced by build design parameters could be one of main factors contributing to fracture toughness variability, seen in Figure 8-3. To understand the microstructural variability, it is important to first understand the influence of processing temperature, time, and cooling rate on microstructural characteristics, where small changes significantly influence resulting microstructure. Galarraga et al.<sup>117</sup> and Lutjering et al.<sup>30</sup> demonstrated the effect of processing temperature, time, and cooling rate on the Ti6Al4V mechanical property induced by the change in microstructure. The studies confirmed that as the processing time and temperature increase, and cooling rate decreases, the grain size of the Ti6Al4V increases.

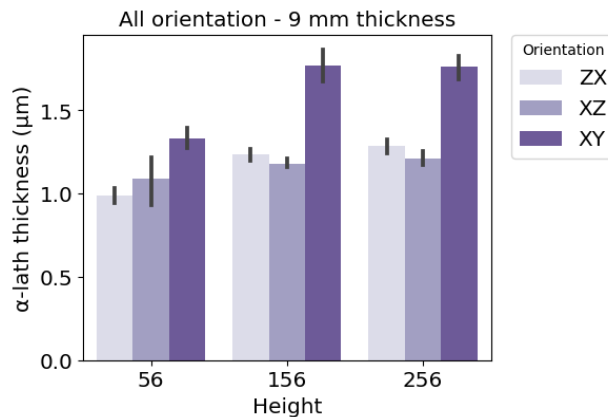


Figure 8-3:  $\alpha$ -lath variation as a function of sample height for each orientation

Due to the strong dependence of microstructure on the thermal process, there has been a growing interest in modeling and understanding the thermal complexities that develop during the PBF-EB process. As the build gets taller, the temperature in the downward direction decreases, where the higher thermal conductivity of the stainless-steel build platform acts as a heat sink<sup>260</sup>. However, the unsintered powder bed can act as an insulator<sup>261,262</sup> leading to a decrease in heat transfer, where heat accumulates as the build becomes taller. As a result, for a taller build, the temperature for a similar depth than a shorter build is found to be higher<sup>137</sup>. As a result, the heat transfer throughout the powder bed is significantly dependent on the height. As heat accumulates

and cooling rate decrease, variation in both the  $\alpha$ -phase and  $\alpha$ -lamellae would be expected, with an increasing  $\alpha$ -lamellae size. The height parameter in this study exhibited the largest contribution to microstructural variation (~20%) shown in Figure 8-4, Figure 8-5, and Figure 8-6, where a finer microstructure was observed closer to the build platform. In general agreement with this study, an increase in grain size with increase in height has also been observed in PBF-EB near-B Ti-alloy<sup>263</sup> and PBF-LB Ti6Al4<sup>264</sup>. Heat accumulation and the cooling rate are faster in samples closer to the build plate, often resulting in a finer microstructure, as seen in the Tukey pairwise comparison in Figure 5-2a. A decrease in cooling rate is observed with the addition of each layer and a larger heat gradient due to the poor powder conductivity results in the coarsening of the microstructure<sup>265</sup>. While an increase in defect size was observed with increase in height, the change in microstructure had a larger influence on the fracture toughness variation.

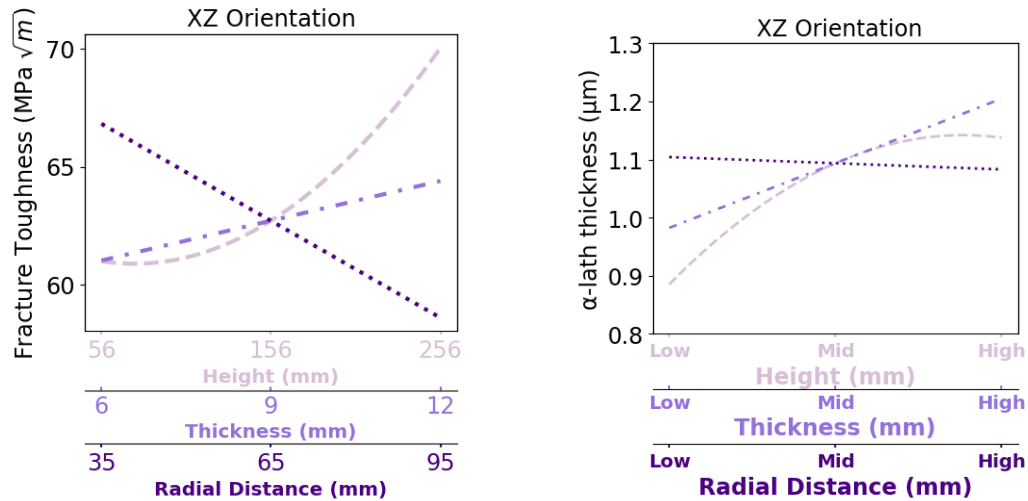


Figure 8-4: The RSM prediction curves for fracture toughness and  $\alpha$ -lath thickness, in the ZX, XZ, and XY orientation. Each factor is individually plotted while keeping the other two factors constant.

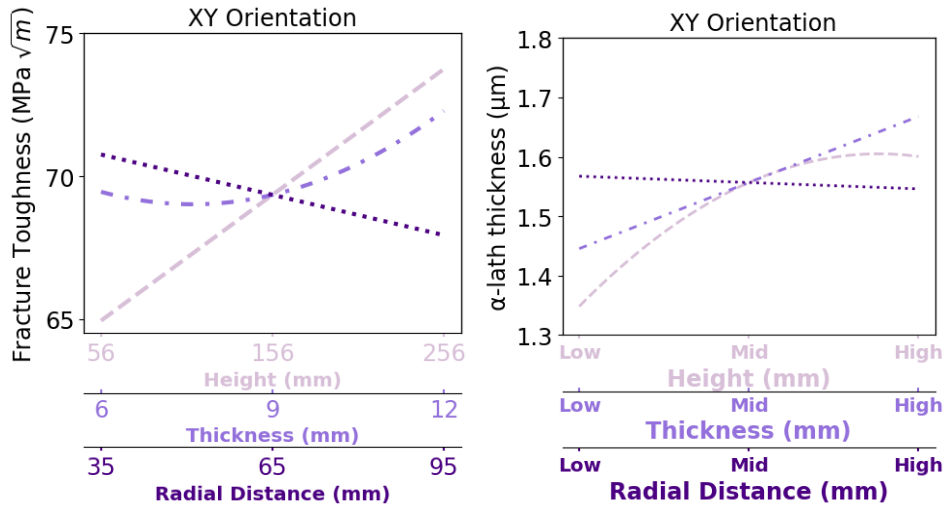


Figure 8-5: The RSM prediction curves for fracture toughness and a-lath thickness, in the ZX, XZ, and XY orientation. Each factor is individually plotted while keeping the other two factors constant.

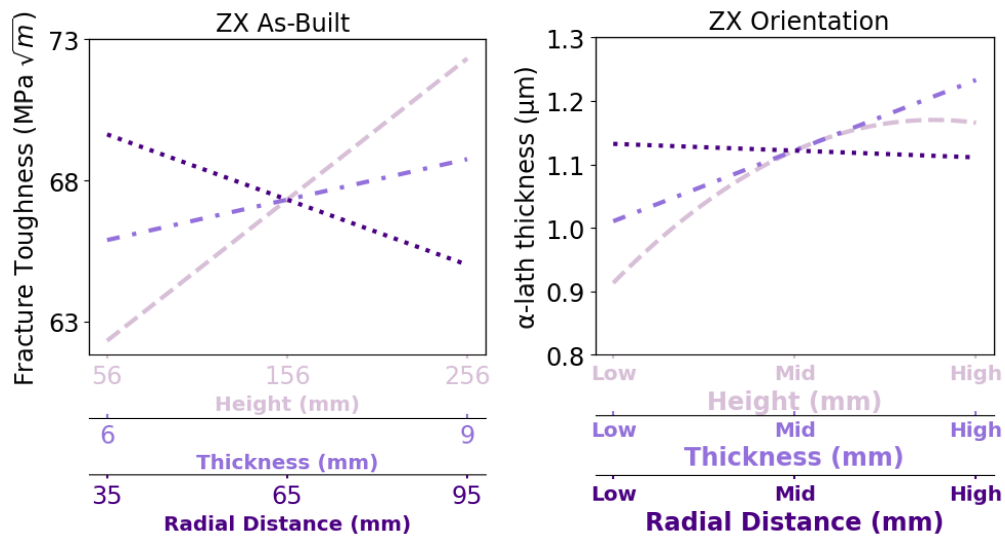
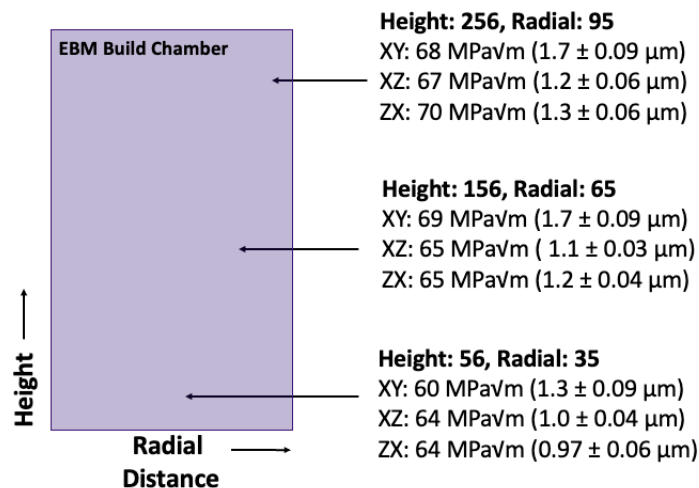


Figure 8-6: The RSM prediction curves for fracture toughness and a-lath thickness, in the ZX, XZ, and XY orientation. Each factor is individually plotted while keeping the other two factors constant.

**Radial distance**, the second spatial distribution parameter, was also found to significantly influence fracture toughness, with 6-10% decrease in fracture toughness as samples were printed from the center to the edges of the build space. A change in microstructure was also observed with the change in radial distance from the center to the edge of the build space, as seen in Figure 8-4, Figure 8-5, and Figure 8-6. This is line with Hrabec et al.'s study, where a finer microstructure in

samples located along the edges of the build plate<sup>23</sup>. Raplee et al. and Rodriguez et al. implemented thermographic imaging for in-situ monitoring, enabling layer-by-layer feedback to understand the quality of as-fabricated components<sup>266,267</sup>. While these studies provided valuable insight into the melting stage, they primarily focused on the localized heat input, rather than the global thermal evolution within the build chamber. A comprehensive investigation by Landau et al.<sup>137</sup> examined the temperature distribution within the entire PBF-EB chamber using numerical modeling. The study highlights the spatial thermal gradients, where a 70 °C temperature variation between the edges and center of the build platform was observed, leading to variable thermal histories. This finding is key when evaluating Ti6Al4V. As such, while Landau et al. did not evaluate the change in microstructure directly, the Ti6Al4V sensitivity to the temperature and cooling rate within the PBF-EB chamber would result in a microstructure that is dependent on the location within the build chamber, as seen in Figure 8-7. This would explain the significant effect of sample radial distance on the microstructure, where a lower temperature and faster cooling rate toward the edges of the powder bed would result in a finer microstructure. The decrease in grain size with increasing radial distance was also observed by<sup>24,127</sup>, where the fine alpha lath thickness contributed to the increasing YS and UTS. Further evaluation of samples located in the front and back of the chamber could provide additional information on the radial distance variations observed. While a decrease in fracture toughness did exist with the increase in radial distance, the overall difference was within 10%.



(b)

Figure 8-7: The 9mm thick fracture toughness and  $\alpha$ -lath values at three intra-build locations in the PBF-EB build chamber for each crack orientation.

The samples *thickness* was a significant parameter in the model, with an increase in fracture toughness with increasing thickness. An increase in thickness in conventional alloys leads to a decrease in fracture toughness until a plateau of plane-strain  $K_{Ic}$  values is reached to be considered a material property<sup>98</sup>. However, a small increase in fracture toughness with increasing thickness was observed in the PBF-EB fracture toughness, shown in Figure 8-6. An increase in  $\alpha$ -lath thickness was observed in Figure 8-6 with increase in thickness. Geometry-dependent microstructure has been previously observed<sup>268,269</sup>, where the increase in melt area leads to an increase in heat accumulation and decreased cooling rate leading to coarsening of microstructure. Thus, the increase in sample melt area resulting in a decrease in cooling rate, contributing to the microstructure-dependent fracture toughness. The larger sample thickness resulted in coarser grain structures, while samples position farther from the build plate exhibited an increase in grain size. These microstructural changes were consistent with findings by Razavi et al. where thermal gradient and cooling rate inherent to the PBF-EB process were linked to microstructural variation<sup>127,210</sup>. While microstructure-dependent fracture toughness was observed, it resulted in 2-8% of material property variation due to sample thickness.

These studies support our hypothesis that microstructural variation is driven by the combined effects of spatial location and geometry producing the thermal environment inherent to the PBF-EB process. This would explain the similar fracture toughness and microstructure trends observed with respect to the build design parameters (thickness, height and radial distance) provided in Figure 8-4, Figure 8-5, and Figure 8-6,. The increase in the  $\alpha$ -lath size led to an increase in slip length, causing a reduction in strength reported by Ghods et al.<sup>127</sup> with an increase in height and decrease in radial distance. Where a decrease in tensile strength was observed by Ghods et al.<sup>127</sup>, an increase in fracture toughness was observed in this study. Establishing the fundamental effects influencing microstructure allows for better understanding of the variability observed in the fracture-critical properties. Hence, the microstructure as a function of sample orientation and geometry should be the initial design consideration, as it will dictate the crack growth behavior through and along the grain and its interaction with defects.

### 8.1.3 Hot Isostatic Pressing

After considering the changes in mechanical properties due to process-induced feature, the effect of post-processing is explored. The surface condition was not a significant factor in fracture toughness variation with comparable fracture toughness in the As-Built and Machined surface conditions. However, the PBF-EB surface roughness is inherently rough, which has been shown to influence the quasi-static properties and have detrimental effects on cyclic properties<sup>15, 19, 220, 235</sup>.

The results indicate that both the standard and modified HIP treatments led to a reduction in YS, UTS, and hardness, while enhancing elongation and fracture toughness. These findings are in general agreement, where HIP treatments generally reduce internal defect and microstructure coarsening, promoting ductility at the expense of strength<sup>95</sup>. The  $\mu$ CT and fracture surface analysis confirmed the closure of internal defects after HIP. Furthermore, the increase in lamellar thickness and  $\beta$  vol.% after the LTHIP process shown in Figure 8-8 further supported the effect of HIP on the mechanical properties.

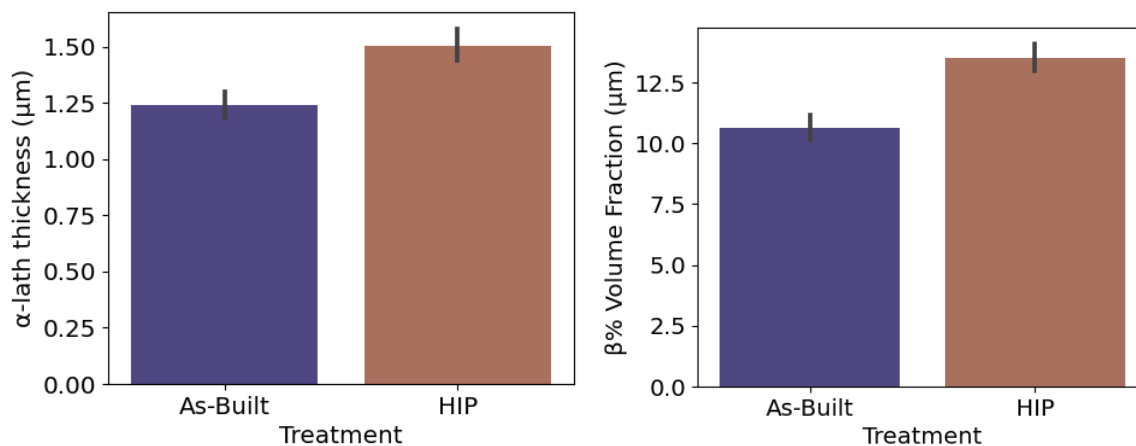


Figure 8-8: The comparison of  $\alpha$ -lath size and the  $\beta$  vol.% in the untreated and LTHIP condition.

Comparing the difference in mechanical properties after the STHIP and LTHIP provides interesting insight into the benefits of using a lower temperature HIP. The overall decrease in YS, UTS and hardness was significantly lower compared to the STHIP treatment, while a significant improvement in ductility. This is aligned with findings by Abu-Issa et al., where the lower temperature limited the microstructure coarsening<sup>149</sup>. Microstructural coarsening occurs in Ti6Al4V when heat treating down to 600 °C, where a proportional relationship exists between the lamellar thickness and the temperature<sup>30, 117</sup>. Pandian et al. similarly found a low temperature, high pressure HIP to limit grain growth size, maintain the high YS and UTS of PBF-EB Ti6Al4V<sup>150</sup>.

The typical lamellar grain size after STHIP on the PBF-EB process has been reported anywhere between 1.5 - 2.4  $\mu\text{m}$  <sup>13,150</sup>, compared to  $\sim 1.4\text{-}1.7 \mu\text{m}$  after LTHIP in this study. This further validates utilizing a low temperature HIP to limit on coarsening of the microstructure, which limits reduction in YS while increasing EF.

As tensile properties decreased with post-processing, fracture toughness values increased as seen in Figure 8-9. Similar findings by Greitemeier et al. suggested an increase in fracture toughness with STHIP treatment <sup>95</sup>. In contrast, Seifi et al. and Dzugan et al. reported a decrease in fracture toughness after STHIP <sup>13,154</sup>. The significant coarsening of the microstructure and change in texture competed with benefits of defect closure, where an increase in fracture toughness was not achieved. In contrast, the average fracture toughness of PBF-EB Ti6Al4V in this study increased from 65  $\text{MPa}\sqrt{\text{m}}$  to 74  $\text{MPa}\sqrt{\text{m}}$  after LTHIP treatment. The same features effecting the tensile behavior also played a role in the fracture toughness behavior. While there isn't a direct relationship between tensile and fracture toughness, typically an increase in toughness is observed with decreasing tensile as the materials ability to resist deformation decreases. Therefore, the combined changes in mechanical behavior, defect closure, and microstructure can be attributed to the increase in fracture resistance. The low temperature high pressure processed PBF-EB metal closed internal defects without a significant coarsening of the microstructure, making it a promising application in obtaining enhanced fracture-critical properties.

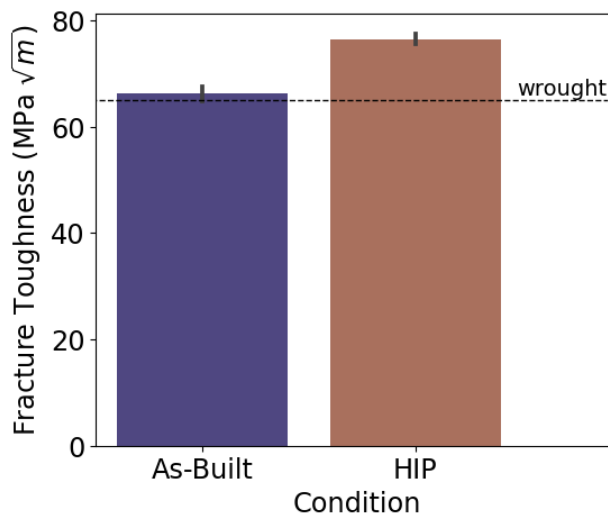


Figure 8-9: The average fracture toughness in the untreated and LTHIP condition

With the LTHIP treatment, the elongation and fracture toughness properties changed non-uniformly between the orientations. In comparison, a discrepancy in hardness between the two

orientations was not observed. The fracture toughness in the ZX orientation increased by 23% compared to ~12% in the XZ and XY orientations. Similarly, the EF increased by 76% in the vertical and 40% in the horizontal orientation. This suggests orientation-dependent values might be influenced by post-processing. The two factors influencing the anisotropic properties in the untreated state also play a role after post-processing. First, LTHIP led to removal of the large and irregular shaped LOF defects, which would have the most significant effect on improving the load-carrying capacity. With the removal of the LOF defects, the vertical tensile and ZX oriented fracture toughness samples would both benefit the most, which could explain the more significant increase in properties after post-processing.

Another possible contributor to the orientation-dependent change after post-processing is the microstructure. With post-processing, a 20% increase in the lamellar  $\alpha$  and  $\alpha$ -GB was observed, shown in Figure 8-10. Similar (17%) increase in the  $\alpha$ -lath was reported by <sup>150</sup>. The orientation-dependent microstructure similar to the untreated condition shown in Figure 8-2, is also observed in Figure 8-10, where the XY orientation is statistically different from the ZX and XZ orientations. The change in microstructure with heat treatment is attributed to the temperature the metals are processed <sup>117</sup>, where the grain size increases linearly with increase in temperature and time of treatment. The increase in the size of the lamellar grains would increase the slip length and cause a decrease in strength, as observed in our findings. This increase however would be undesired depending on the crack growth direction through the microstructure. Notably, the increase in the brittle  $\alpha$ -GB can degrade the fracture resistance and ductility in samples prone to intergranular cracking. As such, the increase in the  $\alpha$ -GB would degrade the ductility of the horizontal tensile and XY and XZ CT samples. However, an investigation of the crack growth resistance and the  $\alpha$ -GB thickness should be conducted.

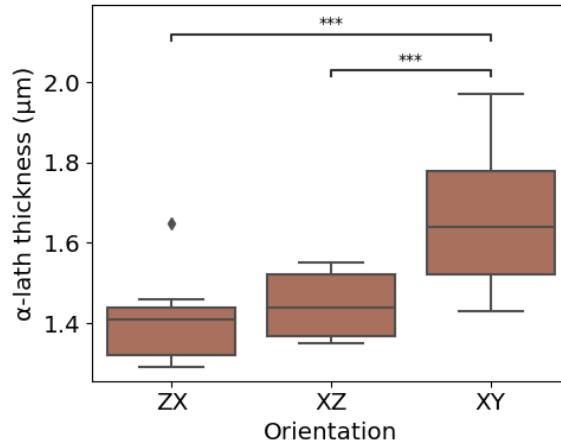


Figure 8-10: The  $\alpha$ -lath thickness of the ZX, XY, and XY in the LTHIP condition, where the XY orientation is statistically significant compared to the ZX and XZ orientations. (\*\*\*) denotes statistical significance of ( $p < 0.001$ )

The intra-build design parameters were found to significantly influence the grain size in both the untreated samples previously, <sup>43</sup>. While the low-temperature HIP treatment improved fracture resistance, the fundamental microstructure shown in Figure 8-11. The ANOVA analysis showed trends due the intra-build design parameters were similar in both the untreated and post-processed condition. In essence, while LTHIP increased the fracture toughness, the intra-build design parameters left a lasting mark on the microstructure which was not changed with LTHIP.

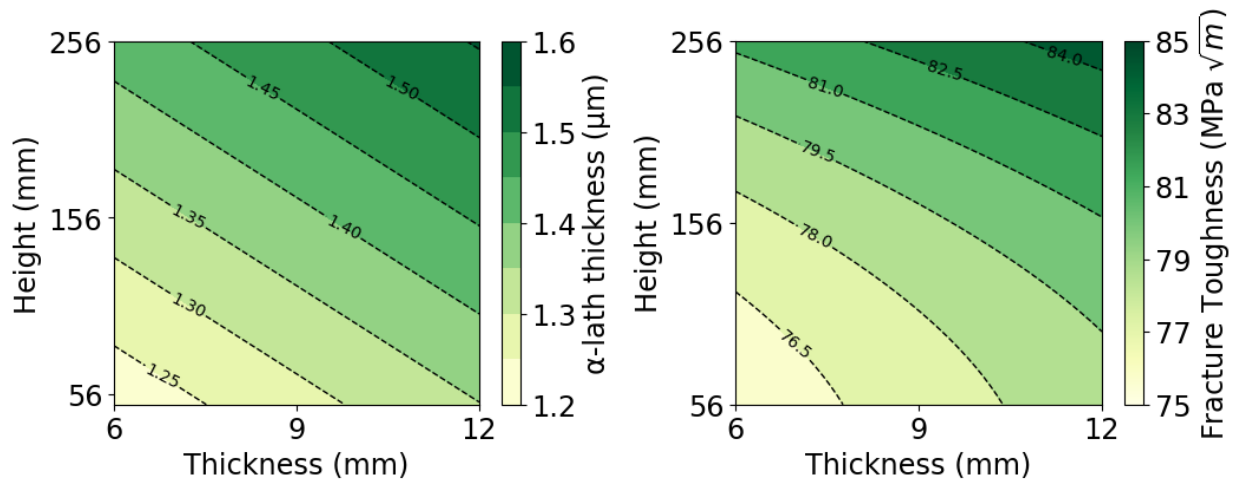


Figure 8-11: The trends in microstructure and fracture toughness as a function of sample thickness and height

As a result, while the LTHIP process was shown to be promising treatment in enhancing the fracture resistance of PBF-EB Ti6Al4V, the PBF-EB manufacturing process resulted in build

dependent fracture toughness properties. The build orientation was shown to dictate the crack growth behavior should be the initial design consideration when manufacturing for end-use production. Furthermore, the following study also shows engineers should consider the influence of geometry and build design for fabricating repeatable and reliable components.

## 8.2 High Cycle Fatigue

### 8.2.1 Anisotropy

Similar to the fracture toughness results, orientation-dependent HCF behavior was observed. Specifically, the horizontally oriented samples survived longer compared to their vertically-oriented counterparts, reported fatigue limit up to 400MPa compared to 350MPa. One of the primary observations of the fracture surface were the process-induced defects, such as the LOF defects. The orientation of the LOF defects was far more detrimental in the vertical samples, significantly reducing the load-carrying capacity. Similar behavior was observed in the fracture toughness orientation. However, samples are fatigue loading are far more sensitive to internal defects, where the horizontal orientation survived longer than the vertical orientation, with the largest difference in the untreated condition. Similar findings on the influence of internal defects were also observed in the following studies<sup>171,270</sup>. The combination of the columnar grains and the LOF defects on the anisotropic properties is in line with findings by Edwards et al. and Seifi et al.<sup>41,138</sup>.

### 8.2.2 Intra-Build Variation

The intra-build design parameters (Height, Radial Distance, and Thickness) were incorporated into a multiple linear regression used to fit the experimental data to the Basquin equation to better characterize and understand the influence of each factor on fatigue life. Figure 8-12 implies three experimental observations. First, the intra-build design parameters were found to influence the fatigue properties of the PBF-EB Ti6Al4V. **Thickness** had the largest influence on the variation in fatigue behavior, with a ~62% decrease in fatigue with decrease in thickness from 9- to 6-mm in the horizontal orientation, respectively. Zhao et al.<sup>210</sup> reported a positive correlation between fatigue life and thickness in PBF-EB Ti6Al4V fatigue behavior. As sample thickness increased from 1 to 5 mm, a more ductile microstructure and decrease in surface irregularities led to the enhanced fatigue limit. Pegues et al.<sup>132</sup> further demonstrated metal AM

fatigue properties to be more sensitive to sample volume fueled by the increase in surface and subsurface defects in smaller gauge samples, with preference in crack initiation at subsurface defects. Even with similar surface roughness values, the surface defects have a larger effect on the 6 mm samples in both metal conditions.

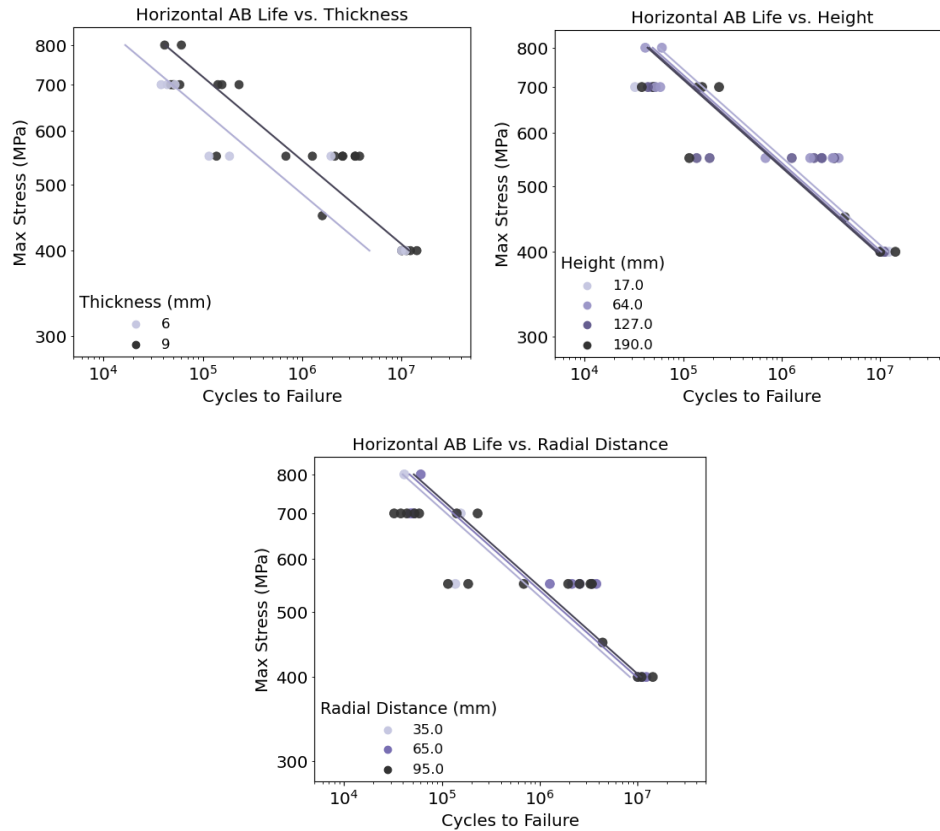


Figure 8-12: The fatigue life of as-built PBF-EB Ti6Al4V specimens in the untreated horizontal orientation

Second, the increase in *height* in Figure 8-12 contributed to the <10% decrease in fatigue properties in the Machined horizontal samples. The decrease in fatigue behavior with increase in height was attributed to the complex PBF-EB process observed in the fracture toughness samples. This decrease was not as notable than what was previously reported by Ghods et al.<sup>169</sup>, where the presence of large “rogue” defects at the highest height level may have overshadowed influence from the microstructure. The higher fatigue behavior closer to the build plate could be a result of the thermal gradient formed with the addition of each layer. With the first levels of samples built on the stainless-steel build plate undergo a faster cooling rate, while the upper levels float within the powder bed. Numerous studies have found microstructure variation in samples due to the thermal gradient within the PBF-EB build space<sup>43,127</sup>. As a result, the samples on the first level

have a finer microstructure compared to the second level. The finer microstructure is preferable in increasing the strength and fatigue resistance.

The fatigue behavior in the horizontal HCF specimens decreased ~12% with increase in *radial distance*. But in contrast to the vertical orientation, the LOF defects are oriented parallel to the applied load, having a less significant effect on fatigue behavior variation. This similar variation with *height* was not observed in the horizontally oriented samples. To build a sufficient number of samples for testing, the horizontally oriented samples were fabricated in line with each other, separated by the support structure. The difference in the build design could be contributing to the difference compared to the vertical HCF study reported by Ghods et al.<sup>169</sup>. Rahimi et al. developed a macroscale thermal model that quantified a temperature variation exceeding ~200 °C in a single layer during component fabrication<sup>265</sup>. This variation resulted from the complex interactions between the component design, previously deposited layers, and the surrounding powder bed. Notably, samples positioned directly on the build platform experience significantly higher cooling rates compared to those printed into the powder bed. Furthermore, the support structures may aid in heat dissipation through the below structures<sup>271</sup>, resulting in a different thermal gradient compared to the vertically oriented samples printed in the powder bed using floating/detached supports. As a result, the horizontally oriented samples would undergo a faster cooling rate resulting in a more uniform thermal gradient within the specimens. However, microstructural characterization of the horizontal HCF specimens is necessary to confirm this hypothesis.

### 8.2.3 Post-Processing

#### 8.2.3.1 Surface Treatment

Figure 8-13 shows the stress-life curves as a function of the crack nucleation source and sample condition. The crack initiation sources were recorded during fractography of each fractured sample. The samples reaching runout at  $10^7$  cycles are characterized by an arrow. The markers describing the three typical crack initiation locations are circle (surface), + (subsurface), and X for internal crack nucleation. Figure 8-13 implies three different observations. First, all the cracks nucleated from surface defects in the samples with as-fabricated surface due to the partially melted powder particles and irregular surface. This resulted in fatigue limit far below the ~550 MPa after STHIP reported<sup>26, 94,220</sup>. As discussed previously, the stress concentration due to surface defects

was higher than subsurface and internal defects, so while internal defects were removed after STHIP, the rough as-fabricated surface had consequential influence during cyclic loading.

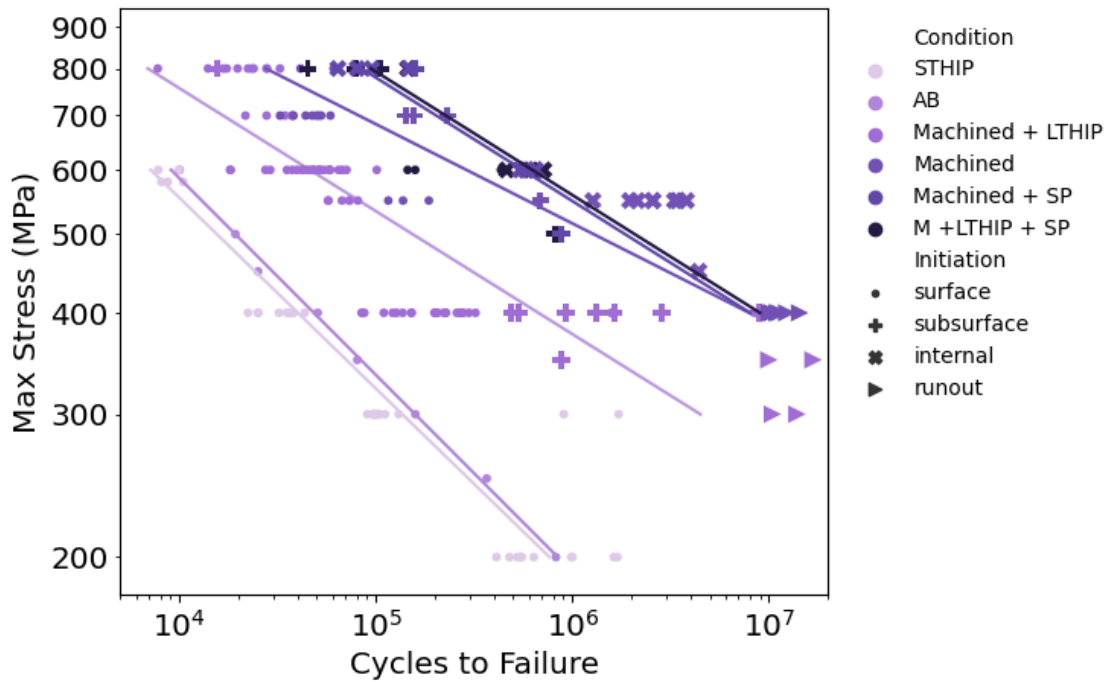


Figure 8-13: Summary of crack nucleation source of each sample, respective to the metal and surface condition.

Second, with surface finish enhancement, surface defects were no longer the main source of crack initiation. Surface roughness improved and irregular surface defects were removed with machining, where fatigue cracks nucleated from subsurface and internal defects. The increase in fatigue life of the machined PBF-EB samples was evidence that the removal of the as-built surface was necessary. Which is to say, for adoption of PBF-EB Ti6Al4V in engineering applications, treatment of the as-built surface needs to be a primary concern. Childerhouse et al.<sup>173</sup> observed an improvement in the PBF-EB surface finish with machining of 0.5 mm but only achieved enhanced cycles to failure with 1 mm of material removed. The fatigue limit doubled as a function of material removal, as a result of removal of the rough PBF-EB surface finish and subsurface defects. Therefore, machining to remove both surface and subsurface defects is vital, the two defect types that results in the highest stress concentration. Furthermore, crack nucleation was dependent on the applied load. As the maximum stress increased, the location of crack initiation shifted from internal to subsurface defects in the Machined samples. At higher loads, local plastic deformation occurs more readily at surface and subsurface defects, where there is less constraint at the surface

compared to internal defects. As the applied stress increase, it becomes easier to nucleate and propagate surface and subsurface defects.

Shot peening was performed after surface machining. The shot peened samples exhibit the higher fatigue strengths, reaching fatigue limit over 400 MPa, a factor of 2 increase compared to the As-Built samples. Shot peening application produces compressive residual stresses through striking metal shots. The process resulted in plastic deformation of the external surface of the samples, with compressive residual stresses of up to -200MPa reported on PBF-EB Ti6Al4V samples<sup>221</sup>. However, shot peening performed on the as-built surface results in fatigue strength up to 220 MPa,<sup>221,272</sup>. The as-fabricated surface is comprised of surface and subsurface defects which act as the primary source of crack nucleation. However, by machining the external surface prior to shot peening, this study was able to obtain an improved fatigue behavior, with the endurance limit reporting 425 MPa.

As a result, surface treatments are crucial in improving cycles to failure and fatigue limits comparable to cast and wrought alloys. Furthermore, the process the surface treatment operations are performed are important to consider. While shot peening the as-built surface was beneficial, to obtain the highest fatigue limit for PBF-EB Ti6Al4V, the as-fabricated surface must be removed by machining first, prior to the shot peening process.

#### *8.2.3.2 Hot Isostatic Pressing*

It is worthwhile to note that while the surface roughness had the most significant influence on the fatigue behavior, the LOF defects contributed to reduced fatigue behavior and scatter in properties. Zhang et al.<sup>273</sup> observed that even when the crack initiation sites resulted from surface defects, process-induced defects contributed to the survivability of Ti6Al4V. The large and irregularly shaped internal defects result in a larger effective stress in the specimen cross section, increasing the overall stress intensity and reducing the load-carrying capacity. Notably, the orientation of the LOF defects which form between print layers along the specimen length axis (i.e., perpendicular to the loading direction) had a more significant influence during cyclic loading.

Alternatively, the horizontally-printed Ti6Al4V samples performed 5X longer than the vertical orientation, reaching runout at 400MPa. As such, with closure of internal defects with LTHIP and STHIP process, we would expect an increase in fatigue strength. The as-fabricated surface was the main cause of the low endurance limit in the STHIP samples. However, with machining application, the LTHIP samples also did not result in enhanced survival. Figure 8-13

shows the Machined + LTHIP samples, where the majority of samples failed due to surface defects, with a portion of cracks nucleating from subsurface defects at lower stresses. In contrast, the unchanged cyclic behavior after LTHIP process correlates with the surface imperfections observed with  $\mu$ CT and valleys recorded in the surface profilometry. These notch-like defects on the surface would result in areas of high local stresses where there is less constraints, promoting premature crack nucleation and reduced fatigue life. Even though both surface and heat treatments were applied to the samples, the order in which they were performed is vital, where HIP process must occur prior to surface machining.

The intra-build design parameters (Height, Radial Distance, and Thickness) were incorporated into a multiple linear regression used to fit the experimental data to the Basquin equation to better characterize and understand the influence of each factor on cycles to failure. The intra-build design parameters were found to influence the fatigue properties of the PBF-EB Ti6Al4V, similar to the untreated metal. **Thickness** continued to have the largest influence on the variation in fatigue behavior, with a  $\sim 50\%$  decrease in fatigue with decrease in thickness from 9- to 6-mm in the LTHIP Vertical specimens, respectively.

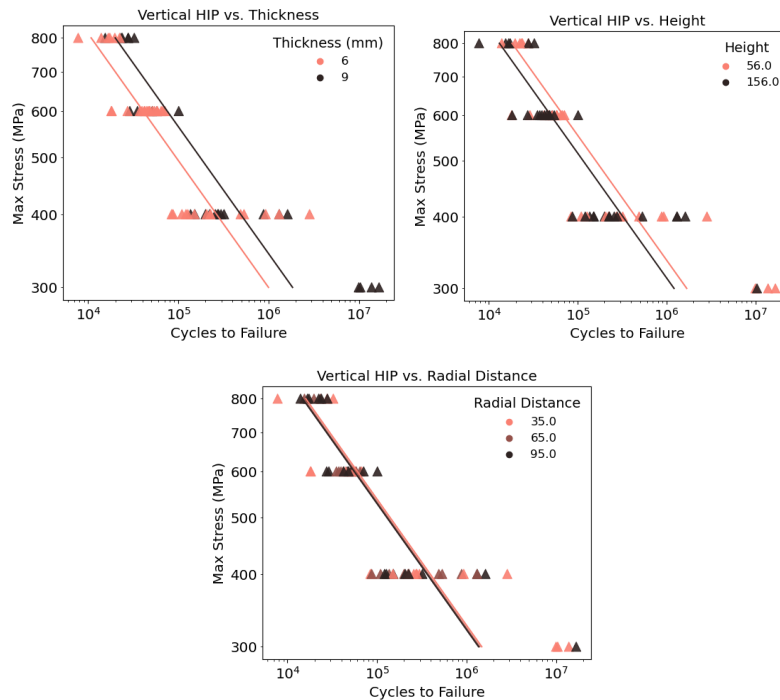


Figure 8-14: The fatigue life of as-built PBF-EB Ti6Al4V specimens in the untreated horizontal orientation (purple circle marker) and the LTHIP vertical (red triangle marker) as a function of the intra-build design parameters (thickness, height, and radial distance).

Second, the increase in *height* in Figure 8-12 contributed to the ~30% decrease in fatigue properties in the vertical LTHIP samples. Similar findings were observed in the untreated metal, which would remain due to the sub- $\beta$  transus HIP treatment. The microstructural formations which occurs during the complex PBF-EB process remained, since utilizing temperature below the  $\beta$ -transus inhibits microstructure recrystallization. Furthermore, this decrease was more notable than what was previously reported by Ghods et al, where the presence of large “rogue” defects may have overshadowed influence from the microstructure. Whereas, in the Machined+LTHIP samples, internal defects were reduced significantly, such that the crack growth behavior through the microstructure plays a more prominent role, following the surface defects. The higher fatigue life closer to the build plate could be a result of the thermal gradient formed with the addition of each layer. Numerous studies have found microstructure variation in samples due to the thermal gradient within the PBF-EB build space <sup>43,127</sup>. As a result, the samples on the first level have a finer microstructure compared to the second level. The finer microstructure is preferable in increasing the strength and fatigue resistance.

In contrast, the variation due to build height was not observed in the horizontally oriented samples. To build a sufficient number of samples for testing, the horizontally oriented samples were fabricated in line with each other, separated by the support structure. This would yield in a different thermal gradient compared to the vertically oriented samples printed the powder bed and detached from other samples.

Lastly, the LTHIP samples which did not show an effect of *radial distance*. One of the main sources of variation in the vertical orientation was the presence of LOF defects, which had a significant increase in stress concentrations. What’s more, Ghods et al.<sup>169</sup> had previously demonstrated a direct link between radial distance and pore diameter, where an increase in radial distance led to an increase in size. After the LTHIP treatment, large and irregularly shaped LOF defects were successfully removed, minimizing contribution to the fatigue variation, in addition to reducing any effects from the radial distance.

The influence of the intra-build design parameters on fracture toughness and high cycle fatigue behavior was discussed in detail. These observations highlight the critical relationship between geometry, spatial location and the thermal history in determining fracture-critical properties. However, unlike previous work that evaluated individual parameters in isolation, this study highlights the importance of also evaluating the interaction between design parameters and

their influence on mechanical properties. As a result, this study contributes a clearer understanding on the importance of build design and its influence on damage tolerance. Furthermore, this study emphasizes the need for comprehensive build design strategies to minimize variability and ensure repeatable performance. Geometry and build orientation should be carefully selected during design, paired with strategic placement of parts in the builds space to obtain repeatable fracture toughness and fatigue properties. The center column of the build space is recommended to obtain optimal PBF-EB fracture toughness properties. Coupled with adopting a “locked” build design, damage-tolerance components can be fabricated with standardized design procedures.

While the fracture toughness properties in this study were primarily driven by the microstructure, fatigue life is much more sensitive to the process-induced surface finish and internal defects. While the quasi-static properties of PBF-EB Ti6Al4V have shown to be promising for fracture-resistance components, the crack growth properties under cyclic loading need to be studied closer. However, fatigue testing requires a long time to achieve the high number of cycles needed to evaluate its fatigue limit. In addition, the randomness of the process-induced feature makes it difficult to simulate the fatigue behavior. Furthermore, modeling is further limited by the limited understanding of the influence of the build design. the powder feedstock used in this study. The generalizability of the results is limited to the recycled powder utilized in this work, where the 7-10 reuse cycles underwent an increase in oxygen content. While the oxygen content remained within the ASTM specification for Ti6Al4V, its potential effects on mechanical properties, such as reduced fatigue and fracture resistance much be considered. With an increase in oxygen content, an increase in  $\alpha$ -lath thickness is expected<sup>274</sup>, however, the similar  $\alpha$ -lath size ( $\sim 1.1 \mu\text{m}$ ) and 88%  $\alpha$ -phase volume fraction from the As-Built ZX, Machined ZX and the Machined XZ orientation do bear that influences from powder reuse were small compared to the influence of orientation and the intra-build design parameters on microstructural characteristics.

Despite this limitation, the use of the recycled powder was sufficient in addressing the primary objective in identifying sources of variability due to the build space design. Future studies should investigate the role of part-to-part variability with unused powder. Additionally, a larger sample size is recommended for evaluating the role of intra-build design parameters in the LTHIP and SP condition. Despite these limitations, this work evaluated the PBF-EB Ti6Al4V fracture-critical properties to provide a further understanding of the reliability of PBF-EB titanium alloy. Through using a multi-factor DOE approach, the influence of build design parameters on fracture

toughness and high cycles fatigue were demonstrated, paving the way in identifying the parameters of interest considered by design engineers and researchers in certifying the PBF-EB Ti6Al4V.

Future studies should explore the influence of build design parameters on mechanical properties in greater detail, focusing on microstructural characteristics, such as texture and phase fractions, and variation across the build space. This allows accurate predictive modeling and selecting in addition to comprehensive design guidelines for PBF-EB Ti6Al4V, including recommendations for geometry, optimal orientation, and necessary post-processing for specific-use cases. Furthermore, expanding the scope to other AM processes, including PBF-LB and DED, would enhance the standardization of metal AM. By addressing these avenues of research, the potential for metal AM as a reliable material for critical engineering applications can be fully realized.

## 9 Conclusion

With the advancement of metal AM in aerospace and the increasing focus on industrialization, a comprehensive understanding of fracture-critical properties is essential. One of the primary challenges in advancing metal AM adoption is the part-to-part variability in mechanical properties within builds. This experimental study addresses a key gap in the process-induced variability of PBF-EB Ti6Al4V and its contribution to mechanical property scatter. This research bridges the gap between PBF-EB process and the Ti6Al4V damage tolerance properties, such as fracture toughness and high cycles fatigue, providing critical insight into how build design parameters influence mechanical performance.

Through a design of experiments approach, this study demonstrated that build parameters—specifically orientation, thickness, and spatial location—strongly affect microstructure evolution, which in turn governs fracture toughness and fatigue behavior. The statistical approach allowed for systematic evaluation of multiple independent variables, revealing key sources of variability in mechanical properties.

### 9.1 Fracture Toughness

Intra-build variability is the spatial variation in metal quality within the build space due to inherent process-induced features in PBF-EB. This study employed a DOE framework to assess the effect of orientation, part design, and spatial location in the fracture toughness of PBF-EB Ti6Al4V, leveraging 270+ CT specimens for statistical analysis of microstructure, porosity, and mechanical properties. Using ANOVA, this study quantified the relative contribution of different intra-build design parameters to fracture toughness variations. The findings revealed:

1. The intra-build design parameters demonstrated strong effect on PBF-EB Ti6Al4V fracture toughness. Preferential crack growth direction was the dominant factor influencing fracture toughness, making up to 25% of the variation in properties. The spatial location contributed to the largest source of variation (~65%).
2. Build height had the second largest impact, with an increase in fracture toughness with increasing build height across all orientations. Radial distance from the center of the build also influenced fracture toughness, with properties decreasing at increasing

distances from the build center. This suggests the thermal gradients within the build chamber influence microstructure evolution and consequently mechanical properties.

3. Part design played a significant role in fracture resistance, as changes in microstructural features, particularly  $\alpha$ -lath thickness, reinforced the connection between geometric design and resulting fracture toughness.
4. The overall fracture toughness of PBF-EB Ti6Al4V ( $65 \text{ MPa}\sqrt{\text{m}}$ , with a spread of 10%) falls within an acceptable range, demonstrating that the process is both repeatable and reliable.
5. The application of low-temperature/high-pressure HIP led to a notable increase in fracture toughness, rising from  $65 \pm 6$  to  $74 \pm 4 \text{ MPa}\sqrt{\text{m}}$ . The modified LTHIP treatment effectively reduced the internal defects while limiting microstructural coarsening, resulting in improved work hardening, ductility, and overall fracture toughness. While LTHIP effectively improved defect distribution, the microstructural features inherent to the AM process – such as prior- $\beta$  grain structure and the basketweave structure – remained largely unchanged.

These findings confirmed the geometry and build space alone can influence the microstructure, directly leading to variation in fracture toughness. This reinforces the necessity for property verification when introducing new geometries. These findings demonstrate that while LTHIP improves the  $K_{Ic}$  fracture toughness, the underlying microstructure remains influenced by the original AM process, resulting in location- and thickness-dependent microstructure which directly influences the mechanical properties. Nonetheless the increase in fracture toughness with LTHIP emphasizes its potential for enhancing the performance of PBF-EB Ti6Al4V, making it a promising candidate for damaged-tolerant aerospace applications.

## 9.2 High Cycle Fatigue

The influence of intra-build variability on the HCF properties was evaluated. The DOE framework adopted assessed the effect of orientation, part design, and spatial location on the high cycle fatigue behavior of PBF-EB Ti6Al4V, leveraging 100 specimens for statistical analysis. Furthermore, an additional 148 samples in various post-processing conditions were evaluated to further understand the influence of HIP, Machining, and Shot peening of fatigue behavior of PBF-

EB Ti6Al4V. Using linear regression, this study quantified the relative contribution of different intra-build design parameters and post-processing treatments. The findings revealed:

1. The fatigue properties of PBF-EB Ti6Al4V were strongly influenced by surface and subsurface defects, with surface roughness contributing the largest source of variation in fatigue life. The as-built surface, characterized by defects and partially melted powder particles, promoted crack nucleation, leading to significantly reduced fatigue life.
2. Hot Isostatic Pressing effectively reduced internal defects, but only improved fatigue strength when combined with machining. However, when machining was performed prior to the LTHIP, subsurface defects deformed under high pressure, creating sharp surface notches that acted as preferential crack initiation sites.
3. A substantial increase in fatigue life was achieved through the combined post-processing, with fatigue limit exceeding cast Ti6Al4V and approaching wrought properties. The recommended post-processing order recommended per the findings of this study is the LTHIP, machining, and shot peening.
4. Despite these improvements, the intra-build design parameters, particularly thickness and height, continued to influence the scatter in HCF properties. A 50-60% reduction in fatigue life was observed as sample thickness decreased from 9 to 6 mm, which was attributed to the increased sensitivity to surface and subsurface defects in thinner specimens. Additionally, anisotropy in the fatigue behavior was evident, with the horizontally built samples outperforming the vertical counterparts.
5. While the intra-build design properties affected the fatigue behavior, the surface roughness and subsurface defects were the primary drivers to fatigue scatter, with the as-fabricated surface exhibiting significant reduction in fatigue strength.

This study has revealed that understanding the interplay that exist between build design, microstructure, and mechanical properties of PBF-EB Ti6Al4V is essential for fabrication of repeatable and reliable components. The findings emphasize that build orientation, spatial location and part design must be strategically optimized to achieve a balance between strength, ductility, and reliability in PBF-EB Ti6Al4V. Therefore, when evaluating the damage tolerance of PBF-EB Ti6Al4V, a comprehensive and systematic approach to build design must be implemented to

maintain repeatability. Strategic post-processing treatments, such as the low-temperature/high-pressure and shot peening have shown to be critical for enhancing the fracture-critical behavior of PBF-EB Ti6Al4V. Specifically, ensuring adequate material removal, optimizing post-processing treatments, and maintaining traceability of the design parameters are vital for reducing variability. This study demonstrates the potential of PBF-EB Ti6Al4V as a viable material for load-bearing applications, with fracture toughness and fatigue properties comparable to cast and wrought alloys when appropriate design and processing strategies are applied.

### 9.3 Future Work

This research has demonstrated significant insights into the fracture toughness and fatigue behavior of PBF-EB Ti6Al4V. However, several aspects remain unexplored that could provide an avenue for certification and qualification. A few potential areas of explorations include exploring tool-less surface treatments and predicting fracture toughness and fatigue behavior.

As it was demonstrated, surface finish plays a crucial role in the damage tolerance of PBF-EB Ti6Al4V. The inherent surface roughness of PBF-EB components is often detrimental to fatigue strength motivating extensive research. However, there is limited information regarding the effect of tool-less surface treatments of fracture resistance. Treatments such as shot peening can help induce compressive residual stresses, thereby improving the crack growth resistance. Through exploring the relationship between surface treatment and fracture resistance, optimized fracture toughness properties for specific applications can be developed. Furthermore, by pairing the surface treatment with an optimized HIP treatment can provide further insight into the relationship between microstructure, surface finish, and the crack growth resistance.

With an increase in machine learning models, information regarding the geometry and location-specific mechanical properties can aid in optimizing for damage tolerant designs. The fatigue and fracture toughness properties can be integrated into predictive models that design engineers can utilize when selecting for specific mechanical properties. Create models which integrate the build parameters, defect characteristics, and micro features to forecast fatigue and fracture toughness. This further promotes specific-component design for niche applications.

Future research aims to further enhance our understanding of the mechanical behavior of PBF-EB Ti6Al4V, particularly for use in safety-critical applications. Surface treatments, and machine learning are all areas of interest, when explored, could lead to more reliable and optimized

## References

- 1 Joseph A, Mahesh V, Harurasampath D. On the application of additive manufacturing methods for auxetic structures: a review. *Advances in manufacturing*. 2021;9: 342–368.
- 2 Blakey-Milner B, Gradl P, Snedden G, et al. Metal additive manufacturing in aerospace: A review. *Materials & Design*. 2021;209: 110008.
- 3 *Standardization Roadmap for Additive Manufacturing Version 3.0*.2023.
- 4 Bourell DL, Rosen DW, Leu MC. The Roadmap for Additive Manufacturing and Its Impact. <https://home.liebertpub.com/3dp>. 2014;1: 6–9.
- 5 Tian X, Wu L, Gu D, et al. Roadmap for Additive Manufacturing: Toward Intellectualization and Industrialization. *Chinese Journal of Mechanical Engineering: Additive Manufacturing Frontiers*. 2022;1: 100014.
- 6 Clark CL, Karasz EK, Melia M, et al. Machine-to-machine variability of roughness and corrosion in additively manufactured 316L stainless steel. *Journal of Manufacturing Processes*. 2023;106: 380–392.
- 7 Du Plessis A, Le Roux SG. Standardized X-ray tomography testing of additively manufactured parts: A round robin test. *Additive Manufacturing*. 2018;24: 125–136.
- 8 Gatto ML, Groppo R, Bloise N, et al. Topological, Mechanical and Biological Properties of Ti6Al4V Scaffolds for Bone Tissue Regeneration Fabricated with Reused Powders via Electron Beam Melting. *Materials*. 2021;14: 224.
- 9 Derimow N, Hrabe N. Oxidation in Reused Powder Bed Fusion Additive Manufacturing Ti-6Al-4V Feedstock: A Brief Review. *The Journal of The Minerals, Metals & Materials Society (TMS)*. 2021;73: 3618–3638.
- 10 Ghods S, Schur R, Schultz E, et al. Powder reuse and its contribution to porosity in additive manufacturing of Ti6Al4V. *Materialia*. 2021;15: 100992.
- 11 Mahtabi M, Yadollahi A, Stokes R, et al. Effect of Powder Reuse on Microstructural and Fatigue Properties of Ti-6Al-4V Fabricated via Directed Energy Deposition. In: *Solid Freeform Fabrication Symposium*. Austin: University of Texas; 2022:580–591.
- 12 Wanjara P, Backman D, Sikan F, et al. Microstructure and Mechanical Properties of Ti-6Al-4V Additively Manufactured by Electron Beam Melting with 3D Part Nesting and

- Powder Reuse Influences. *Journal of Manufacturing and Materials Processing* 2022, Vol 6, Page 21. 2022;6: 21.
- 13 Seifi M, Salem A, Satko D, Shaffer J, Lewandowski JJ. Defect distribution and microstructure heterogeneity effects on fracture resistance and fatigue behavior of EBM Ti-6Al-4V. *International Journal of Fatigue*. 2017;94: 263–287.
  - 14 Zhai Y, Galarraga H, Lados DA. Microstructure, static properties, and fatigue crack growth mechanisms in Ti-6Al-4V fabricated by additive manufacturing: LENS and EBM. *Engineering Failure Analysis*. 2016;69: 3–14.
  - 15 Lewandowski JJ, Seifi M. Metal Additive Manufacturing: A Review of Mechanical Properties. *Annual Review of Materials Research*. 2016;46: 151–186.
  - 16 DebRoy T, Wei HL, Zuback JS, et al. Additive manufacturing of metallic components – Process, structure and properties. *Progress in Materials Science*. 2018;92: 112–224.
  - 17 Anderson TL. *Fracture Mechanics: Fundamentals and Applications, Third Edition*. 4th ed. CRC Press; 2017.
  - 18 Findlay SJ, Harrison ND. Why aircraft fail. *Materials Today*. 2002;5: 18–25.
  - 19 Becker TH, Kumar P, Ramamurty U. Fracture and fatigue in additively manufactured metals. *Acta Materialia*. 2021;219: 117240.
  - 20 Khosravani MR, Berto F, Ayatollahi MR, Reinicke T. Fracture behavior of additively manufactured components: A review. *Theoretical and Applied Fracture Mechanics*. 2020;109: 102763.
  - 21 Elambasseril J, Rogers J, Wallbrink C, Munk D, Leary M, Qian M. Laser powder bed fusion additive manufacturing (LPBF-AM): the influence of design features and LPBF variables on surface topography and effect on fatigue properties. *Critical Reviews in Solid State and Materials Sciences*. 2023;48: 132–168.
  - 22 Hrabec N, Quinn T. Effects of processing on microstructure and mechanical properties of a titanium alloy (Ti-6Al-4V) fabricated using electron beam melting (EBM), part 1: Distance from build plate and part size. *Materials Science & Engineering A*. 2013;573: 264–270.
  - 23 Hrabec N, Quinn T. Effects of processing on microstructure and mechanical properties of a titanium alloy (Ti-6Al-4V) fabricated using electron beam melting (EBM), Part 2: Energy input, orientation, and location. *Materials Science and Engineering A*. 2013;573: 271–277.

- 24 Tiferet E, Ganor M, Zolotaryov D, et al. Mapping the Tray of Electron Beam Melting of Ti-6Al-4V: Properties and Microstructure. *Materials 2019, Vol 12, Page 1470*. 2019;12: 1470.
- 25 Li P, Warner DH, Fatemi A, Phan N. Critical assessment of the fatigue performance of additively manufactured Ti-6Al-4V and perspective for future research. *International Journal of Fatigue*. 2016;85: 130–143.
- 26 Chern AH, Nandwana P, Yuan T, et al. A review on the fatigue behavior of Ti-6Al-4V fabricated by electron beam melting additive manufacturing. *International Journal of Fatigue*. 2019;119: 173–184.
- 27 Vayssette B, Saintier N, Brugger C, Elmay M, Pessard E. Surface roughness of Ti-6Al-4V parts obtained by SLM and EBM: Effect on the High Cycle Fatigue life. In: *Procedia Engineering*. Vol 213. Elsevier Ltd; 2018:89–97.
- 28 ASTM International. *ASTM F2924-14, Standard Specification for Additive Manufacturing Titanium-6 Aluminum-4 Vanadium with Powder Bed Fusion*. ASTM International; 2014.
- 29 SAE International. *AMS7028: Titanium Alloy, Ti-6Al-4V, Hot Isostatically Pressed (Low Temperature, High Pressure), Produced by Laser Powder Bed Fusion*. 400 Commonwealth Drive, Warrendale, PA, United States: SAE International; 2024.
- 30 Lütjering G. Influence of processing on microstructure and mechanical properties of ( $\alpha$ + $\beta$ ) titanium alloys. *Materials Science and Engineering: A*. 1998;243: 32–45.
- 31 Nguyen HD, Pramanik A, Basak AK, et al. A critical review on additive manufacturing of Ti-6Al-4V alloy: microstructure and mechanical properties. *Journal of Materials Research and Technology*. 2022;18: 4641–4661.
- 32 Joshi S, Martukanitz RP, Nassar AR, Michaleris P. Metal Additive Manufacturing Processes – Laser and Electron Beam Powder Bed Fusion. *Additive Manufacturing with Metals*. 2023: 59–109.
- 33 Frazier WE. Metal additive manufacturing: A review. *Journal of Materials Engineering and Performance*. 2014;23: 1917–1928.
- 34 Yi HJ, Kim JW, Kim YL, Shin S. Effects of Cooling Rate on the Microstructure and Tensile Properties of Wire-Arc Additive Manufactured Ti-6Al-4V Alloy. *Metals and Materials International*. 2020;26: 1235–1246.
- 35 Gong X, Anderson T, Chou K. Review on powder-based electron beam additive manufacturing technology. *Manufacturing Review*. 2014;1.

- 36 Tshephe TS, Akinwamide SO, Olevsky E, Olubambi PA. Additive manufacturing of titanium-based alloys- A review of methods, properties, challenges, and prospects. *Heliyon*. 2022;8: e09041.
- 37 Damon J, Dietrich S, Vollert F, Gibmeier J, Schulze V. Process dependent porosity and the influence of shot peening on porosity morphology regarding selective laser melted AlSi10Mg parts. *Additive Manufacturing*. 2018;20: 77–89.
- 38 Körner C. Additive manufacturing of metallic components by selective electron beam melting - A review. *International Materials Reviews*. 2016;61: 361–377.
- 39 Tepylo N, Huang X, Patnaik PC. Laser-Based Additive Manufacturing Technologies for Aerospace Applications. *Advanced Engineering Materials*. 2019;21: 1900617.
- 40 Zhang W, Chabok A, Kooi BJ, Pei Y. Additive manufactured high entropy alloys: A review of the microstructure and properties. *Materials & Design*. 2022;220: 110875.
- 41 Edwards P, O’Conner A, Ramulu M. Electron beam additive manufacturing of titanium components: Properties and performance. *Journal of Manufacturing Science and Engineering, Transactions of the ASME*. 2013;135: 061016.
- 42 Schur R, Ghods S, Wisdom C, et al. Mechanical anisotropy and its evolution with powder reuse in Electron Beam Melting AM of Ti6Al4V. *Materials & Design*. 2021;200: 109450.
- 43 Mojib NM, Fero K, Atmadja N, Arola D, Chen X, Ramulu M. Effect of intra-build design parameters on the fracture toughness properties of Electron Beam Melted Ti6Al4V. *Fatigue & Fracture of Engineering Materials & Structures*. 2024;47: 3894–3909.
- 44 Longhitano GA, García IM, Arenas MA, de Damborenea JJ, Maciel Filho R, Conde A. Effect of designed pore size on electrochemical, wear, and tribocorrosion behavior of additively manufactured Ti-6Al-4V lattice structures. *Additive Manufacturing*. 2024;79: 103931.
- 45 Soria SR, Soul H, Bergant M, Yawny A. Fretting wear behaviour of biomedical grade Ti6Al4V produced by electron beam powder bed fusion. *Additive Manufacturing*. 2024;86: 104217.
- 46 Van Hooreweder B, Apers Y, Lietaert K, Kruth JP. Improving the fatigue performance of porous metallic biomaterials produced by Selective Laser Melting. *Acta Biomaterialia*. 2017;47: 193–202.

- 47 Edwards P, Ramulu M. Fatigue performance evaluation of selective laser melted Ti-6Al-4V. *Materials Science and Engineering A*. 2014;598: 327–337.
- 48 Cain V, Thijs L, Van Humbeeck J, Van Hooreweder B, Knutsen R. Crack propagation and fracture toughness of Ti6Al4V alloy produced by selective laser melting. *Additive Manufacturing*. 2015;5: 68–76.
- 49 Van Hooreweder B, Moens D, Boonen R, Kruth J-P, Sas P. Analysis of Fracture Toughness and Crack Propagation of Ti6Al4V Produced by Selective Laser Melting. *Advanced Engineering Materials*. 2012;14: 92–97.
- 50 Zhang J, Wang X, Paddea S, Zhang X. Fatigue crack propagation behaviour in wire+arc additive manufactured Ti-6Al-4V: Effects of microstructure and residual stress. *Materials & Design*. 2016;90: 551–561.
- 51 Akbari P, Zamani M, Mostafaei A. Machine learning prediction of mechanical properties in metal additive manufacturing. *Additive Manufacturing*. 2024;91: 104320.
- 52 Svetlizky D, Das M, Zheng B, et al. Directed energy deposition (DED) additive manufacturing: Physical characteristics, defects, challenges and applications. *Materials Today*. 2021;49: 271–295.
- 53 Ahn DG. Directed Energy Deposition (DED) Process: State of the Art. *International Journal of Precision Engineering and Manufacturing-Green Technology 2021 8:2*. 2021;8: 703–742.
- 54 Xu T, Jing C, Xu H, et al. Parallel multi arc directed energy deposition: New way to achieve efficient manufacturing of large-size lattice sandwich structure. *Additive Manufacturing*. 2024;90: 104322.
- 55 Stenberg K, Dittrick S, Bose S, Bandyopadhyay A. Influence of simultaneous addition of carbon nanotubes and calcium phosphate on wear resistance of 3D-printed Ti6Al4V. *Journal of Materials Research*. 2018;33: 2077–2086.
- 56 Maizza G, Caporale A, Polley C, Seitz H. Micro-Macro Relationship between Microstructure, Porosity, Mechanical Properties, and Build Mode Parameters of a Selective-Electron-Beam-Melted Ti-6Al-4V Alloy. *Metals*. 2019;9: 786.
- 57 Puebla K. The Influence of Build Parameters on the Microstructure during Electron Beam Melting of Ti6Al4V. May 2012.

- 58 Jeffs S, Lancaster R, Davies G, et al. Effect of Process Parameters and Build Orientation on Microstructure and Impact Energy of Electron Beam Powder Bed Fused Ti-6Al-4V. *Materials* 2021, Vol 14, Page 5376. 2021;14: 5376.
- 59 Tammam-Williams S, Withers PJ, Todd I, Prangnell PB. The Influence of Porosity on Fatigue Crack Initiation in Additively Manufactured Titanium Components. *Scientific Reports*. 2017;7.
- 60 Zhao Y, Aoyagi K, Yamanaka K, Chiba A. Role of operating and environmental conditions in determining molten pool dynamics during electron beam melting and selective laser melting. *Additive Manufacturing*. 2020;36.
- 61 Zhao Y, Koizumi Y, Aoyagi K, Wei D, Yamanaka K, Chiba A. Molten pool behavior and effect of fluid flow on solidification conditions in selective electron beam melting (SEBM) of a biomedical Co-Cr-Mo alloy. *Additive Manufacturing*. 2019;26: 202–214.
- 62 Gockel J, Sheridan L, Koerper B, Whip B. The influence of additive manufacturing processing parameters on surface roughness and fatigue life. *International Journal of Fatigue*. 2019;124: 380–388.
- 63 Whip B, Sheridan L, Gockel J. The effect of primary processing parameters on surface roughness in laser powder bed additive manufacturing. *International Journal of Advanced Manufacturing Technology*. 2019;103: 4411–4422.
- 64 Safdar A, He HZ, Wei LY, Snis A, Chavez De Paz LE. Effect of process parameters settings and thickness on surface roughness of EBM produced Ti-6Al-4V. *Rapid Prototyping Journal*. 2012;18: 401–408.
- 65 Bin Abdullah MS, Bol E, Kelley G, et al. Microstructure and microhardness of electron beam melted Ti-6Al-4V components with differential thickness in initial deposition layers. *Journal of Materials Research and Technology*. 2023;26: 6493–6507.
- 66 Wang J, Tang HP, Yang K, Liu N, Jia L, Qian M. Selective Electron Beam Manufacturing of Ti-6Al-4V Strips: Effect of Build Orientation, Columnar Grain Orientation, and Hot Isostatic Pressing on Tensile Properties. *JOM*. 2018;70: 638–643.
- 67 Guzanová A, Ižaríková G, Brezinová J, Živčák J, Draganovská D, Hudák R. Influence of build orientation, heat treatment, and laser power on the hardness of Ti6Al4V manufactured using the DMLS process. *Metals*. 2017;7.

- 68 Alsalla HH, Smith C, Hao L. The effect of different build orientations on the consolidation, tensile and fracture toughness properties of direct metal laser sintering Ti-6Al-4V. *Rapid Prototyping Journal*. 2018;24: 276–284.
- 69 Kumar P, Prakash O, Ramamurty U. Micro-and meso-structures and their influence on mechanical properties of selectively laser melted Ti-6Al-4V. *Acta Materialia*. 2018;154: 246–260.
- 70 Liu P, Wang Z, Xiao Y, Horstemeyer MF, Cui X, Chen L. Insight into the mechanisms of columnar to equiaxed grain transition during metallic additive manufacturing. *Additive Manufacturing*. 2019;26: 22–29.
- 71 de Formanoir C, Michotte S, Rigo O, Germain L, Godet S. Electron beam melted Ti-6Al-4V: Microstructure, texture and mechanical behavior of the as-built and heat-treated material. *Materials Science and Engineering: A*. 2016;652: 105–119.
- 72 Drstvenšek I, Zupanič F, Bončina T, Brajljih T, Pal S. Influence of local heat flow variations on geometrical deflections, microstructure, and tensile properties of Ti-6Al-4 V products in powder bed fusion systems. *Journal of Manufacturing Processes*. 2021;65: 382–396.
- 73 Gaunt P, Christian JW. The crystallography of the  $\beta$ - $\alpha$  transformation in zirconium and in two titanium-molybdenum alloys. *Acta Metallurgica*. 1959;7: 534–543.
- 74 Zhang M, Ng CH, Dehghan-Manshadi A, Hall C, Bermingham MJ, Dargusch MS. Towards isotropic behaviour in Ti-6Al-4V fabricated with laser powder bed fusion and super transus hot isostatic pressing. *Materials Science and Engineering: A*. 2023;874: 145094.
- 75 Laleh M, Sadeghi E, Revilla RI, et al. Heat treatment for metal additive manufacturing. *Progress in Materials Science*. 2023;133: 101051.
- 76 Wang S, Ning J, Zhu L, et al. Role of porosity defects in metal 3D printing: Formation mechanisms, impacts on properties and mitigation strategies. *Materials Today*. 2022;59: 133–160.
- 77 Reddy T, Ngo A, Miner JP, et al. Fatigue-based process window for laser beam powder bed fusion additive manufacturing. *International Journal of Fatigue*. 2024;187: 108428.
- 78 Galarraga H, Lados DA, Dehoff RR, Kirka MM, Nandwana P. Effects of the microstructure and porosity on properties of Ti-6Al-4V ELI alloy fabricated by electron beam melting (EBM). *Additive Manufacturing*. 2016;10: 47–57.

- 79 Murakami Y, Masuo H, Tanaka Y, Nakatani M. Defect Analysis for Additively Manufactured Materials in Fatigue from the Viewpoint of Quality Control and Statistics of Extremes. *Procedia Structural Integrity*. 2019;19: 113–122.
- 80 Muro-Barrios R, Cui Y, Lambros J, Chew HB. Dual-scale porosity effects on crack growth in additively manufactured metals: 3D ductile fracture models. *Journal of the Mechanics and Physics of Solids*. 2022;159: 104727.
- 81 Serrano-Munoz I, Buffiere J-Y, Mokso R, Verdu C, Nadot Y. Location, location & size: defects close to surfaces dominate fatigue crack initiation. *Nature Publishing Group*. 2017;7: 1–9.
- 82 Nandwana P, Kirka MM, Paquit VC, Yoder S, Dehoff RR. Correlations Between Powder Feedstock Quality, In Situ Porosity Detection, and Fatigue Behavior of Ti-6Al-4V Fabricated by Powder Bed Electron Beam Melting: A Step Towards Qualification. *JOM*. 2018;70: 1686–1691.
- 83 Carpenter K, Tabei A. On Residual Stress Development, Prevention, and Compensation in Metal Additive Manufacturing. *Materials*. 2020;13: 1–38.
- 84 Mishurova T, Cabeza S, Artzt K, et al. An Assessment of Subsurface Residual Stress Analysis in SLM Ti-6Al-4V. *Materials 2017, Vol 10, Page 348*. 2017;10: 348.
- 85 Yadroitsev I, Yadroitsava I. Evaluation of residual stress in stainless steel 316L and Ti6Al4V samples produced by selective laser melting. *Virtual and Physical Prototyping*. 2015;10: 67–76.
- 86 Araújo LC, Gabriel AHG, da Fonseca EB, et al. Effects of build orientation and heat treatments on the tensile and fracture toughness properties of additively manufactured AlSi10Mg. *International Journal of Mechanical Sciences*. 2022;213: 106868.
- 87 Teixeira Ó, Silva FJG, Ferreira LP, Atzeni E. A Review of Heat Treatments on Improving the Quality and Residual Stresses of the Ti-6Al-4V Parts Produced by Additive Manufacturing. *Metals 2020, Vol 10, Page 1006*. 2020;10: 1006.
- 88 Ali H, Ghadbeigi H, Mumtaz K. Effect of scanning strategies on residual stress and mechanical properties of Selective Laser Melted Ti6Al4V. *Materials Science and Engineering: A*. 2018;712: 175–187.
- 89 Ali H, Ma L, Ghadbeigi H, Mumtaz K. In-situ residual stress reduction, martensitic decomposition and mechanical properties enhancement through high temperature powder

- bed pre-heating of Selective Laser Melted Ti6Al4V. *Materials Science and Engineering: A*. 2017;695: 211–220.
- 90 Scheerer M, Stelzer N, Scheerer M, et al. Mechanical properties of surface engineered metallic parts prepared by additive manufacturing. In: *The European Conference on Spacecraft Structures, Materials and Environmental Testing*. ESTEC; 2018.
- 91 Rogers J, Elambasseril J, Wallbrink C, et al. The impact of surface orientation on surface roughness and fatigue life of laser-based powder bed fusion Ti-6Al-4V. *Additive Manufacturing*. 2024;85: 104149.
- 92 Chen Z, Yan X, Yin S, et al. Influence of the pore size and porosity of selective laser melted Ti6Al4V ELI porous scaffold on cell proliferation, osteogenesis and bone ingrowth. *Materials Science and Engineering C*. 2020;106: 110289.
- 93 Goto M, Matsumine A, Yamaguchi S, et al. Osteoconductivity of bioactive Ti-6Al-4V implants with lattice-shaped interconnected large pores fabricated by electron beam melting. *Journal of Biomaterials Applications*. 2020;0: 1–15.
- 94 Greitemeier D, Palm F, Syassen F, Melz T. Fatigue performance of additive manufactured TiAl6V4 using electron and laser beam melting. *International Journal of Fatigue*. 2017;94: 211–217.
- 95 Greitemeier D, Dalle Donne C, Syassen F, Eufinger J, Melz T. Effect of surface roughness on fatigue performance of additive manufactured Ti-6Al-4V. *Materials Science and Technology (United Kingdom)*. 2016;32: 629–634.
- 96 Junet A, Messenger A, Boulnat X, et al. Fabrication of artificial defects to study internal fatigue crack propagation in metals. *Scripta Materialia*. 2019;171: 87–91.
- 97 Andreau O, Pessard E, Koutiri I, et al. A competition between the contour and hatching zones on the high cycle fatigue behaviour of a 316L stainless steel: Analyzed using X-ray computed tomography. *Materials Science and Engineering: A*. 2019;757: 146–159.
- 98 ASM Handbook. *Fatigue and Fracture*. Vol 19. ASM International; 1996.
- 99 Collins JA. *Failure of Materials in Mechanical Design: Analysis, Prediction, Prevention*. 2nd ed. Wiley; 1993.
- 100 Lütjering G, Williams JC. *Titanium*. 2nd ed. Berlin, Heidelberg: Springer Berlin Heidelberg; 2007.

- 101 Chern AH, Nandwana P, McDaniels R, et al. Build orientation, surface roughness, and scan path influence on the microstructure, mechanical properties, and flexural fatigue behavior of Ti-6Al-4V fabricated by electron beam melting. *Materials Science and Engineering: A*. 2020;772: 138740.
- 102 Bruno J, Rochman A, Cassar G. Effect of Build Orientation of Electron Beam Melting on Microstructure and Mechanical Properties of Ti-6Al-4V. *Journal of Materials Engineering and Performance*. 2017;26: 692–703.
- 103 Bobbert FSL, Lietaert K, Eftekhari AA, et al. Additively manufactured metallic porous biomaterials based on minimal surfaces: A unique combination of topological, mechanical, and mass transport properties. *Acta Biomaterialia*. 2017;53: 572–584.
- 104 Damon J, Czink S, Schüßler P, et al. Mechanical surface treatment of EBM Ti6Al4V components: Effects of the resulting surface layer state on fatigue mechanisms and service life. *Materials Science and Engineering: A*. 2022;849: 143422.
- 105 Chastand V, Quaegebeur P, Maia W, Charkaluk E. Comparative study of fatigue properties of Ti-6Al-4V specimens built by electron beam melting (EBM) and selective laser melting (SLM). *Materials Characterization*. 2018;143: 76–81.
- 106 Rafi HK, Karthik N V., Gong H, Starr TL, Stucker BE. Microstructures and mechanical properties of Ti6Al4V parts fabricated by selective laser melting and electron beam melting. *Journal of Materials Engineering and Performance*. 2013;22: 3872–3883.
- 107 Pei C, Yuan H. Microstructural characteristics and its correlation to mechanical properties of additively manufactured nickel-base superalloy upon heat treatments. *Fatigue and Fracture of Engineering Materials and Structures*. 2023;46: 987–1006.
- 108 Sharma H, Parfitt D, Syed AK, et al. A critical evaluation of the microstructural gradient along the build direction in electron beam melted Ti-6Al-4V alloy. *Materials Science and Engineering: A*. 2019;744: 182–194.
- 109 Choi G, Choi WS, Han J, Choi PP. Additive manufacturing of titanium-base alloys with equiaxed microstructures using powder blends. *Additive Manufacturing*. 2020;36: 101467.
- 110 Wang M, Li HQ, Lou DJ, et al. Microstructure anisotropy and its implication in mechanical properties of biomedical titanium alloy processed by electron beam melting. *Materials Science and Engineering: A*. 2019;743: 123–137.

- 111 Carroll BE, Palmer TA, Beese AM. Anisotropic tensile behavior of Ti–6Al–4V components fabricated with directed energy deposition additive manufacturing. *Acta Materialia*. 2015;87: 309–320.
- 112 Kok Y, Tan XP, Wang P, et al. Anisotropy and heterogeneity of microstructure and mechanical properties in metal additive manufacturing: A critical review. *Materials & Design*. 2018;139: 565–586.
- 113 Lu SL, Tang HP, Ning YP, Liu N, Stjohn DH, Qian M. Microstructure and Mechanical Properties of Long Ti-6Al-4V Rods Additively Manufactured by Selective Electron Beam Melting Out of a Deep Powder Bed and the Effect of Subsequent Hot Isostatic Pressing. *Metallurgical and Materials Transactions A*. 2015;46A: 3824–3824.
- 114 Tan X, Kok Y, Tan YJ, et al. Graded microstructure and mechanical properties of additive manufactured Ti–6Al–4V via electron beam melting. *Acta Materialia*. 2015;97: 1–16.
- 115 Schur R, Ghods S, Schultz E, et al. A Fractographic Analysis of Additively Manufactured Ti6Al4V by Electron Beam Melting: Effects of Powder Reuse. *Journal of Failure Analysis and Prevention*. 2020;20: 794–803.
- 116 Zhai Y, Galarraga H, Lados DA. Microstructure, static properties, and fatigue crack growth mechanisms in Ti-6Al-4V fabricated by additive manufacturing: LENS and EBM. *Engineering Failure Analysis*. 2016;69: 3–14.
- 117 Galarraga H, Warren RJ, Lados DA, Dehoff RR, Kirka MM, Nandwana P. Effects of heat treatments on microstructure and properties of Ti-6Al-4V ELI alloy fabricated by electron beam melting (EBM). *Materials Science and Engineering: A*. 2017;685: 417–428.
- 118 Zhao X, Li S, Zhang M, et al. Comparison of the microstructures and mechanical properties of Ti–6Al–4V fabricated by selective laser melting and electron beam melting. *Materials & Design*. 2016;95: 21–31.
- 119 Qiu C, Ravi GA, Dance C, Ranson A, Dilworth S, Attallah MM. Fabrication of large Ti–6Al–4V structures by direct laser deposition. *Journal of Alloys and Compounds*. 2015;629: 351–361.
- 120 Keist JS, Nayir S, Palmer TA. Impact of hot isostatic pressing on the mechanical and microstructural properties of additively manufactured Ti–6Al–4V fabricated using directed energy deposition. *Materials Science and Engineering: A*. 2020;787: 139454.

- 121 Donachie MJ. Titanium: A Technical Guide, 2nd Edition | Introduction to Selection of Titanium Alloys. *ASM International*. 2000;180: 5–11.
- 122 Kobryn PA,. *WL-TR-96-4066 Casting of Titanium Alloys*. OH; 1995.
- 123 Da Rocha SS, Adabo GL, Henriques GEP, Nóbilo MADA. Vickers hardness of cast commercially pure titanium and Ti-6Al-4V alloy submitted to heat treatments. *Brazilian dental journal*. 2006;17: 126–129.
- 124 Persenot T, Martin G, Dendievel R, Buffière JY, Maire E. Enhancing the tensile properties of EBM as-built thin parts: Effect of HIP and chemical etching. *Materials Characterization*. 2018;143: 82–93.
- 125 Gupta A, Bennett CJ, Sun W. The role of defects and characterisation of tensile behaviour of EBM Additive manufactured Ti-6Al-4V: An experimental study at elevated temperature. *Engineering Failure Analysis*. 2021;120: 105115.
- 126 Pirozzi C, Franchitti S, Borrelli R, Caiazzo F, Alfieri V, Argenio P. Study on the Factors Affecting the Mechanical Behavior of Electron Beam Melted Ti6Al4V. *Journal of Materials Engineering and Performance*. 2017;26: 4491–4499.
- 127 Ghods S, Schur R, Schleusener R, et al. Contributions of intra-build design parameters to mechanical properties in electron beam additive manufacturing of Ti6Al4V. *Materials Today Communications*. 2022;30: 103190.
- 128 du Plessis A, Yadroitsava I, Yadroitsev I. Effects of defects on mechanical properties in metal additive manufacturing: A review focusing on X-ray tomography insights. *Materials & Design*. 2020;187: 108385.
- 129 Gabilondo M, Cearsolo X, Arrue M, Castro F. Influence of Build Orientation, Chamber Temperature and Infill Pattern on Mechanical Properties of 316L Parts Manufactured by Bound Metal Deposition. *Materials 2022, Vol 15, Page 1183*. 2022;15: 1183.
- 130 Karimi P, Sadeghi E, Åkerfeldt P, Ålgårdh J, Andersson J. Influence of successive thermal cycling on microstructure evolution of EBM-manufactured alloy 718 in track-by-track and layer-by-layer design. *Materials and Design*. 2018;160: 427–441.
- 131 Yadollahi A, Shamsaei N, Thompson SM, Seely DW. Effects of process time interval and heat treatment on the mechanical and microstructural properties of direct laser deposited 316L stainless steel. *Materials Science and Engineering: A*. 2015;644: 171–183.

- 132 Pegues J, Roach M, Williamson RS, Shamsaei N. Volume Effects on the Fatigue Behavior of Additively Manufactured Ti-6Al-4V Parts. In: *Solid Freeform Fabrication Symposium*. Austin: University of Texas; 2018:1373–1381.
- 133 Pessard E, Laviaille M, Laheurte P, Didier P, Brochu M. High-cycle fatigue behavior of a laser powder bed fusion additive manufactured Ti-6Al-4V titanium: Effect of pores and tested volume size. *International Journal of Fatigue*. 2021;149: 106206.
- 134 Wang X, Chou K. Effect of support structures on Ti-6Al-4V overhang parts fabricated by powder bed fusion electron beam additive manufacturing. *Journal of Materials Processing Technology*. 2018;257: 65–78.
- 135 Kok Y, Tan X, Tor SB, Chua CK. Fabrication and microstructural characterisation of additive manufactured Ti-6Al-4V parts by electron beam melting: This paper reports that the microstructure and micro-hardness of an EBM part is thickness dependent. *Virtual and Physical Prototyping*. 2015;10: 13–21.
- 136 Keist JS, Palmer TA. Development of strength-hardness relationships in additively manufactured titanium alloys. *Materials Science and Engineering: A*. 2017;693: 214–224.
- 137 Landau E, Tiferet E, Ganor YI, et al. Thermal characterization of the build chamber in electron beam melting. *Additive Manufacturing*. 2020;36: 101535.
- 138 Seifi M, Dahar M, Aman R, Harrysson O, Beuth J, Lewandowski JJ. Evaluation of Orientation Dependence of Fracture Toughness and Fatigue Crack Propagation Behavior of As-Deposited ARCAM EBM Ti-6Al-4V. *JOM*. 2015;67: 597–607.
- 139 Derimow N, Romero A, Rubio A, et al. Assessment of intra-build variations in tensile strength in electron beam powder-bed fusion Ti-6AL-4V part 1: Effects of build height. *Materials Science and Engineering: A*. 2022;849.
- 140 Hitzler L, Janousch C, Schanz J, et al. Direction and location dependency of selective laser melted AlSi10Mg specimens. *Journal of Materials Processing Technology*. 2017;243: 48–61.
- 141 Narra SP, Cunningham R, Beuth J, Rollett AD. Location specific solidification microstructure control in electron beam melting of Ti-6Al-4V. *Additive Manufacturing*. 2018;19: 160–166.
- 142 Lulu-Bitton N, Navi NU, Haroush S, et al. The Effects of Hot Isostatic Pressing (HIP) and Heat Treatment on the Microstructure and Mechanical Behavior of Electron Beam-Melted

- (EBM) Ti-6Al-4V Alloy and Its Susceptibility to Hydrogen. *Materials* 2024, Vol 17, Page 2846. 2024;17: 2846.
- 143 Vrancken B, Thijs L, Kruth JP, Van Humbeeck J. Heat treatment of Ti6Al4V produced by Selective Laser Melting: Microstructure and mechanical properties. *Journal of Alloys and Compounds*. 2012;541: 177–185.
- 144 Jin X, Lan L, Gao S, He B, Rong Y. Effects of laser shock peening on microstructure and fatigue behavior of Ti-6Al-4V alloy fabricated via electron beam melting. *Materials Science and Engineering A*. 2020;780.
- 145 Soyama H, Okura Y. The use of various peening methods to improve the fatigue strength of titanium alloy Ti6Al4V manufactured by electron beam melting. *AIMS Materials Science*. 2018;5: 1000–1015.
- 146 Galarraga H, Warren RJ, Lados DA, Dehoff RR, Kirka MM. Fatigue crack growth mechanisms at the microstructure scale in as-fabricated and heat treated Ti-6Al-4V ELI manufactured by electron beam melting (EBM). *Engineering Fracture Mechanics*. 2017;176: 263–280.
- 147 Ter Haar GM, Becker TH. Selective Laser Melting Produced Ti-6Al-4V: Post-Process Heat Treatments to Achieve Superior Tensile Properties. *Materials* 2018, Vol 11, Page 146. 2018;11: 146.
- 148 Atkinson H V., Davies S. Fundamental aspects of hot isostatic pressing: An overview. *Metallurgical and Materials Transactions A: Physical Metallurgy and Materials Science*. 2000;31: 2981–3000.
- 149 Abu-Issa A, Lopez M, Pickett C, et al. Effects of altered hot isostatic pressing treatments on the microstructures and mechanical performance of electron beam melted Ti-6Al-4V. *Journal of Materials Research and Technology*. 2020;9: 8735–8743.
- 150 Thalavai Pandian K, Neikter M, Bahbou F, Hansson T, Pederson R. Elevated-Temperature Tensile Properties of Low-Temperature HIP-Treated EBM-Built Ti-6Al-4V. *Materials* 2022, Vol 15, Page 3624. 2022;15: 3624.
- 151 Ahlfors M, Bahbou F, Ackelid U. *Optimizing HIP and Printing Parameters for EBM Ti-6Al-4V*. 2018.
- 152 Quénard O, Dorival O, Guy P, Votié A, Brethome K. Measurement of fracture toughness of metallic materials produced by additive manufacturing. *CEAS Space Journal*. 2018;10.

- 153 Kumar P, Ramamurty U. Microstructural optimization through heat treatment for enhancing the fracture toughness and fatigue crack growth resistance of selective laser melted Ti-6Al-4V alloy. *Acta Materialia*. 2019;169: 45–59.
- 154 Dzugan J, Seifi M, Rzepa S, et al. The effects of post-processing on the local fracture toughness properties of electron beam powder bed fusion Ti-6Al-4V alloy. *Engineering Fracture Mechanics*. 2022;273: 108697.
- 155 Romero C, Yang F, Bolzoni L. Fatigue and fracture properties of Ti alloys from powder-based processes – A review. *International Journal of Fatigue*. 2018;117: 407–419.
- 156 Svensson M, Thundal S. Ti6Al4V manufactured with Electron Beam Melting (EBM): Mechanical and Chemical properties. In: *Materials & Processes for Medical Devices Conference*. Novelty, OH: ASM International; 2009:189–194.
- 157 Paul MJ, Liu Q, Best JP, et al. Fracture resistance of AlSi10Mg fabricated by laser powder bed fusion. *Acta Materialia*. 2021;211.
- 158 Dhansay NM, Tait R, Becker T. Fatigue and fracture toughness of Ti-6Al-4V titanium alloy manufactured by selective laser melting. In: *Advanced Materials Research*. Vol 1019. Trans Tech Publications Ltd; 2014:248–253.
- 159 Li C, Wang C, Yang G, Qin L, Ren Y. Effect of heat treatment on microstructure and fracture toughness of Ti-6Al-4V alloy by forging-additive hybrid manufacturing. *Journal of Materials Research*. 2022;37: 2406–2416.
- 160 Conway KM, Kunka C, White BC, Pataky GJ, Boyce BL. Increasing fracture toughness via architected porosity. *Materials & Design*. 2021;205: 109696.
- 161 Zhang H, Dong D, Su S, Chen A. Experimental study of effect of post processing on fracture toughness and fatigue crack growth performance of selective laser melting Ti-6Al-4V. *Chinese Journal of Aeronautics*. 2019;32: 2383–2393.
- 162 Becker TH, Beck M, Scheffer C. Microstructure and mechanical properties of direct metal laser sintered Ti-6Al-4V. *South African Journal of Industrial Engineering*. 2015;26: 1–10.
- 163 Hasib MT, Liu Q, Ostergaard HE, Li X, Kruzic JJ. Fracture toughness anisotropy of commercially pure titanium produced by laser powder bed fusion additive manufacturing. *International Journal of Fracture*. 2022;235: 99–115.

- 164 Verma R, Kumar P, Jayaganthan R, Pathak H. Extended finite element simulation on Tensile, fracture toughness and fatigue crack growth behaviour of additively manufactured Ti6Al4V alloy. *Theoretical and Applied Fracture Mechanics*. 2022;117: 103163.
- 165 Pan J, Song C. Prediction of fracture toughness using small specimens based on machine learning. *Theoretical and Applied Fracture Mechanics*. 2024;132.
- 166 Jones R, Rans C, Iliopoulos AP, Michopoulos JG, Phan N, Peng D. Modelling the Variability and the Anisotropic Behaviour of Crack Growth in SLM Ti-6Al-4V. *Materials* 2021, Vol 14, Page 1400. 2021;14: 1400.
- 167 Watring DS, Benzing JT, Kafka OL, et al. Evaluation of a modified void descriptor function to uniquely characterize pore networks and predict fracture-related properties in additively manufactured metals. *Acta Materialia*. 2022;223: 117464.
- 168 Kumar S, Singh I V., Mishra BK, Sharma K, Khan IA. A homogenized multigrid XFEM to predict the crack growth behavior of ductile material in the presence of microstructural defects. *Engineering Fracture Mechanics*. 2019;205: 577–602.
- 169 Ghods S, Schur R, Montelione A, Schleusener R, Arola DD, Ramulu M. Importance of Build Design Parameters to the Fatigue Strength of Ti6Al4V in Electron Beam Melting Additive Manufacturing. *materials*. 2022;15: 5617.
- 170 Persenot T, Buffiere JY, Maire E, Dendievel R, Martin G. Fatigue properties of EBM as-built and chemically etched thin parts. In: *3rd International Symposium on Fatigue Design and Materials Defects*. Vol 7. Lecco: Elsevier B.V.; 2017:158–165.
- 171 Nicoletto G, Konečná R, Frkání M, Riva E. Surface roughness and directional fatigue behavior of as-built EBM and DMLS Ti6Al4V. *International Journal of Fatigue*. 2018;116: 140–148.
- 172 Solberg K, Berto F. Notch-defect interaction in additively manufactured Inconel 718. *International Journal of Fatigue*. 2019;122: 35–45.
- 173 Childerhouse T, Hernandez-Nava E, M'Saoubi R, Tapoglou N, Jackson M. Surface and sub-surface integrity of Ti-6Al-4V components produced by selective electron beam melting with post-build finish machining. In: *Procedia CIRP*. Vol 87. Elsevier B.V.; 2020:309–314.

- 174 Witkin DB, Patel DN, Helvajian H, Steffaney L, Diaz A. Surface Treatment of Powder-Bed Fusion Additive Manufactured Metals for Improved Fatigue Life. *Journal of Materials Engineering and Performance*. 2019;28: 681–692.
- 175 Sun YY, Lu SL, Gulizia S, et al. Fatigue Performance of Additively Manufactured Ti-6Al-4V: Surface Condition vs. Internal Defects. *JOM*. 2020;72: 1022–1030.
- 176 Le VD, Pessard E, Morel F, Prigent S. Fatigue behaviour of additively manufactured Ti-6Al-4V alloy: The role of defects on scatter and statistical size effect. *International Journal of Fatigue*. 2020;140: 105811.
- 177 Naab B, Celikin M. The role of microstructural evolution on the fatigue behavior of additively manufactured Ti-6Al-4V alloy. *Materials Science and Engineering: A*. 2022;859: 144232.
- 178 Günther J, Krewerth D, Lippmann T, et al. Fatigue life of additively manufactured Ti-6Al-4V in the very high cycle fatigue regime. *International Journal of Fatigue*. 2017;94: 236–245.
- 179 Hrabe N, Gnäupel-Herold T, Quinn T. Fatigue properties of a titanium alloy (Ti-6Al-4V) fabricated via electron beam melting (EBM): Effects of internal defects and residual stress. *International Journal of Fatigue*. 2017;94: 202–210.
- 180 Li C, Liu ZY, Fang XY, Guo YB. Residual Stress in Metal Additive Manufacturing. *Procedia CIRP*. 2018;71: 348–353.
- 181 Leuders S, Lieneke T, Lammers S, Tröster T, Niendorf T. On the fatigue properties of metals manufactured by selective laser melting - The role of ductility. *Journal of Materials Research*. 2014;29: 1911–1919.
- 182 Teixeira Ó, Silva FJG, Ferreira LP, Atzeni E. A review of heat treatments on improving the quality and residual stresses of the Ti-6Al-4V parts produced by additive manufacturing. *Metals*. 2020;10: 1–24.
- 183 Schneller W, Leitner M, Pomberger S, Springer S, Beter F, Grün F. Effect of Post Treatment on the Microstructure, Surface Roughness and Residual Stress Regarding the Fatigue Strength of Selectively Laser Melted AlSi10Mg Structures. *Journal of Manufacturing and Materials Processing*. 2019;3: 89.

- 184 Moran TP, Carrion PE, Lee S, Shamsaei N, Phan N, Warner DH. Hot Isostatic Pressing for Fatigue Critical Additively Manufactured Ti-6Al-4V. *Materials* 2022, Vol 15, Page 2051. 2022;15: 2051.
- 185 Mussatto A, Groarke R, Vijayaraghavan RK, et al. Assessing dependency of part properties on the printing location in laser-powder bed fusion metal additive manufacturing. *Materials Today Communications*. 2022;30: 103209.
- 186 Vayssette B, Saintier N, Brugger C, May M El. Surface roughness effect of SLM and EBM Ti-6Al-4V on multiaxial high cycle fatigue. *Theoretical and Applied Fracture Mechanics*. 2020;108: 102581.
- 187 Kaletsch A, Qin S, Herzog S, Broeckmann C. Influence of high initial porosity introduced by laser powder bed fusion on the fatigue strength of Inconel 718 after post-processing with hot isostatic pressing. *Additive Manufacturing*. 2021;47: 102331.
- 188 VanSickle R, Foehring D, Chew HB, Lambros J. Microstructure effects on fatigue crack growth in additively manufactured Ti-6Al-4V. *Materials Science and Engineering: A*. 2020;795: 139993.
- 189 Sanaei N, Fatemi A. Defect-based fatigue life prediction of L-PBF additive manufactured metals. *Engineering Fracture Mechanics*. 2021;244: 107541.
- 190 Zhang Z, Teng X, Hu X, et al. Fatigue life affected by various defects of a selective laser-manufactured Titanium alloy. *Materials Science and Technology*. 2023;39: 412–422.
- 191 Le V-D, Pessard E, Morel F, Prigent S. Fatigue behaviour of additively manufactured Ti-6Al-4V alloy: The role of defects on scatter and statistical size effect. 2020.
- 192 Varney TC, Quammen RN, Telesz N, Balk TJ, Wessman A, Rottmann PF. Effects of Pore Geometry on the Fatigue Properties of Electron Beam Melted Titanium-6Al-4V. *Metallurgical and Materials Transactions A: Physical Metallurgy and Materials Science*. 2021;52: 1836–1849.
- 193 Gong H, Rafi K, Starr T, Stucker B. Effect of Defects on Fatigue Tests of As-Built Ti-6Al-4V Parts Fabricated by Selective Laser Melting. In: *Internal Solid Freeform Fabrication Symposium*. University of Texas; 2012.
- 194 Murakami Y, Takagi T, Wada K, Matsunaga H. Essential structure of S-N curve: Prediction of fatigue life and fatigue limit of defective materials and nature of scatter. *International Journal of Fatigue*. 2021;146: 106138.

- 195 Sarkar S, Kumar CS, Nath AK. Effects of different surface modifications on the fatigue life of selective laser melted 15–5 PH stainless steel. *Materials Science and Engineering: A*. 2019;762: 138109.
- 196 Masuo H, Tanaka Y, Morokoshi S, et al. Influence of defects, surface roughness and HIP on the fatigue strength of Ti-6Al-4V manufactured by additive manufacturing. *International Journal of Fatigue*. 2018;117: 163–179.
- 197 Yadollahi A, Mahmoudi M, Elwany A, Doude H, Bian L, Newman JC. Fatigue-life prediction of additively manufactured material: Effects of heat treatment and build orientation. *Fatigue and Fracture of Engineering Materials and Structures*. 2020;43: 831–844.
- 198 Yadollahi A, Shamsaei N. Additive manufacturing of fatigue resistant materials: Challenges and opportunities. *International Journal of Fatigue*. 2017;98: 14–31.
- 199 Fleishel R, Ferrell W, TerMaath S. Fatigue-Damage Initiation at Process Introduced Internal Defects in Electron-Beam-Melted Ti-6Al-4V. *Metals 2023, Vol 13, Page 350*. 2023;13: 350.
- 200 Roirand H, Hor A, Malard B, Saintier N. Effect of laser-scan strategy on microstructure and fatigue properties of 316L additively manufactured stainless steel. *Fatigue and Fracture of Engineering Materials and Structures*. 2023;46: 32–48.
- 201 Nezhadfar PD, Thompson S, Saharan A, Phan N, Shamsaei N. Structural integrity of additively manufactured aluminum alloys: Effects of build orientation on microstructure, porosity, and fatigue behavior. *Additive Manufacturing*. 2021;47: 102292.
- 202 Pegues J, Roach M, Williamson RS, Shamsaei N. Effect of Specimen Surface Area Size on Fatigue Strength of Additively Manufactured Ti-6Al-4V Parts. In: *Solid Freeform Fabrication Symposium*. University of Texas; 2017.
- 203 Shrestha R, Simsiriwong J, Shamsaei N, Thompson SM, Bian L. Effect of Build Orientation on the Fatigue Behavior of Stainless Steel 316L Manufactured via a Laser-Powder Bed Fusion Process. In: *Solid Freeform Fabrication Symposium*. University of Texas; 2016:605–616.
- 204 Leuders S, Thöne M, Riemer A, et al. On the mechanical behaviour of titanium alloy TiAl6V4 manufactured by selective laser melting: Fatigue resistance and crack growth performance. *International Journal of Fatigue*. 2013;48: 300–307.

- 205 Molaei R, Fatemi A. Crack paths in additive manufactured metallic materials subjected to multiaxial cyclic loads including surface roughness, HIP, and notch effects. *International Journal of Fatigue*. 2019;124: 558–570.
- 206 Razavi SMJ, Berto F. Directed Energy Deposition versus Wrought Ti-6Al-4V: A Comparison of Microstructure, Fatigue Behavior, and Notch Sensitivity. *Advanced Engineering Materials*. 2019;21: 1900220.
- 207 Xu ZW, Liu A, Wang XS. The influence of building direction on the fatigue crack propagation behavior of Ti6Al4V alloy produced by selective laser melting. *Materials Science and Engineering: A*. 2019;767: 138409.
- 208 Torries B, Shamsaei N. Fatigue Behavior and Modeling of Additively Manufactured Ti-6Al-4V Including Interlayer Time Interval Effects. *JOM*. 2017;69: 2698–2705.
- 209 Shrestha R, Nezhadfar PD, Masoomi M, Simisiriwong J, Phan N, Shamsaei N. Effects of Design Parameters on Thermal History and Mechanical Behavior of Additively Manufactured 17-4 PH Stainless Steel. In: *Solid Freeform Fabrication Symposium*. Austin: University of Texas at Austin; 2018:1277–1289.
- 210 Razavi SMJ, Van Hooreweder B, Berto F. Effect of build thickness and geometry on quasi-static and fatigue behavior of Ti-6Al-4V produced by Electron Beam Melting. *Additive Manufacturing*. 2020;36: 101426.
- 211 Soltani-Tehrani A, Pegues J, Shamsaei N. Fatigue behavior of additively manufactured 17-4 PH stainless steel: The effects of part location and powder re-use. *Additive Manufacturing*. 2020;36.
- 212 Shui X, Yamanaka K, Mori M, Nagata Y, Kurita K, Chiba A. Effects of post-processing on cyclic fatigue response of a titanium alloy additively manufactured by electron beam melting. *Materials Science and Engineering A*. 2017;680: 239–248.
- 213 Sanaei N, Fatemi A, Phan N. Defect characteristics and analysis of their variability in metal L-PBF additive manufacturing. *Materials & Design*. 2019;182: 108091.
- 214 Li P, Warner DH, Pegues JW, Roach MD, Shamsaei N, Phan N. Investigation of the mechanisms by which hot isostatic pressing improves the fatigue performance of powder bed fused Ti-6Al-4V. *International Journal of Fatigue*. 2019;120: 342–352.
- 215 Butt MM, Laieghi H, Kvvssn V, et al. Fatigue performance in additively manufactured metal alloys. *Progress in Additive Manufacturing*. August 2024.

- 216 Javidrad H, Koc B, Bayraktar H, Simsek U, Gunaydin K. Fatigue performance of metal additive manufacturing: a comprehensive overview. *Virtual and Physical Prototyping*. 2024;19.
- 217 Persenot T, Burr A, Plancher E, Buffière J-Y, Dendievel R, Martin G. Effect of ultrasonic shot peening on the surface defects of thin struts built by electron beam melting: Consequences on fatigue resistance. *Additive Manufacturing*. 2019;28: 821–830.
- 218 Kahlin M, Ansell H, Basu D, et al. Improved fatigue strength of additively manufactured Ti6Al4V by surface post processing. *International Journal of Fatigue*. 2020;134: 105497.
- 219 Sanaei N, Fatemi A. Defects in additive manufactured metals and their effect on fatigue performance: A state-of-the-art review. *Progress in Materials Science*. 2020;117: 100724.
- 220 Franchitti S, Pirozzi C, Borrelli R. Influence of hot isostatic pressing and surface finish on the mechanical behaviour of Ti6Al4V processed by electron beam melting. *Fatigue & Fracture of Engineering Materials & Structures*. 2020;43: 2828–2841.
- 221 Soyama H, Takeo F. Effect of various peening methods on the fatigue properties of Titanium alloy Ti6Al4V manufactured by direct metal laser sintering and electron beam melting. *Materials*. 2020;13.
- 222 Soyama H, Sanders D. Use of an Abrasive Water Cavitating Jet and Peening Process to Improve the Fatigue Strength of Titanium Alloy 6Al-4V Manufactured by the Electron Beam Powder Bed Melting (EBPB) Additive Manufacturing Method. *JOM*. 2019;71: 4311–4318.
- 223 Denti L, Bassoli E, Gatto A, Santecchia E, Mengucci P. Fatigue life and microstructure of additive manufactured Ti6Al4V after different finishing processes. *Materials Science and Engineering A*. 2019;755: 1–9.
- 224 Derrick C, Fatemi A. Correlations of fatigue strength of additively manufactured metals with hardness and defect size. *International Journal of Fatigue*. 2022;162: 106920.
- 225 Mian MJ, Razmi J, Ladani L. Defect analysis and fatigue strength prediction of as-built Ti6Al4V parts, produced using electron beam melting (EBM) AM technology. *Materialia*. 2021;16: 101041.
- 226 Lee S, Rasoolian B, Silva DF, Pegues JW, Shamsaei N. Surface roughness parameter and modeling for fatigue behavior of additive manufactured parts: A non-destructive data-driven approach. *Additive Manufacturing*. 2021;46: 102094.

- 227 Montelione A, Ghods S, Schur R, Wisdom C, Arola D, Ramulu M. Powder Reuse in Electron Beam Melting Additive Manufacturing of Ti6Al4V: Particle Microstructure, Oxygen Content and Mechanical Properties. *Additive Manufacturing*. 2020;35: 101216.
- 228 *ASTM E399-20: Standard Test Method for Linear-Elastic Plane-Strain Fracture Toughness of Metallic Materials*. West Conshohocken, PA; 2020.
- 229 Searles T, Tiley J, Tanner A, et al. Rapid characterization of titanium microstructural features for specific modelling of mechanical properties. *Measurement Science and Technology*. 2004;16: 60.
- 230 *ASTM E466-21: Standard Practice for Conducting Force Controlled Constant Amplitude Axial Fatigue Tests of Metallic Materials*. West Conshohocken, PA; 2021.
- 231 *ASTM E8/E8M – 16a Standard Test Methods for Tension Testing of Metallic Materials*. West Conshohocken, PA; 2016.
- 232 *ASTM E92 - Standard Test Methods for Vickers Hardness and Knoop Hardness of Metallic Materials*. West Conshohocken, PA; 2017.
- 233 Dzugan J, Seifi M, Prochazka R, et al. Effects of thickness and orientation on the small scale fracture behaviour of additively manufactured Ti-6Al-4V. *Materials Characterization*. 2018;143: 94–109.
- 234 Bertsch KM, Voisin T, Forien JB, et al. Critical differences between electron beam melted and selective laser melted Ti-6Al-4 V. *Materials & Design*. 2022;216: 110533.
- 235 Karakaş Ö, Kardeş FB, Foti P, Berto F. An overview of factors affecting high-cycle fatigue of additive manufacturing metals. *Fatigue and Fracture of Engineering Materials and Structures*. 2023;46: 1649–1668.
- 236 Edwards P, Ramulu M. Effect of build direction on the fracture toughness and fatigue crack growth in selective laser melted Ti-6Al-4 V. *Fatigue & Fracture of Engineering Materials & Structures*. 2015;38: 1228–1236.
- 237 Boyer R, Welsch G, Collings EW. *Materials Properties Handbook: Titanium Alloys*. ASM International; 1994.
- 238 Yu X, Lin X, Liu F, et al. Influence of post-heat-treatment on the microstructure and fracture toughness properties of Inconel 718 fabricated with laser directed energy deposition additive manufacturing. *Materials Science and Engineering: A*. 2020;798: 140092.

- 239 Molaei R, Fatemi A, Razavi SMJ, Berto F. Fatigue and Fracture of Additively Manufactured Metallic Materials. *Comprehensive Structural Integrity*. 2023;2: 186–214.
- 240 Liu C, Mai Z, Yan D, et al. Effect of Hot Isostatic Pressing on Microstructures and Mechanical Properties of Ti6Al4V Fabricated by Electron Beam Melting. *Metals* 2020, Vol 10, Page 593. 2020;10: 593.
- 241 Raghavan S, Nai MLS, Wang P, Sin WJ, Li T, Wei J. Heat treatment of electron beam melted (EBM) Ti-6Al-4V: microstructure to mechanical property correlations. *Rapid Prototyping Journal*. 2018;24: 774–783.
- 242 Li S, Li S, Liu H, et al. Microstructure and mechanical properties of large Ti6Al4V components by electron beam powder bed fusion. *Materials Science and Engineering: A*. 2024;913: 147023.
- 243 Soundarapandiyan G, Khan R, Johnston C, Chen B, Fitzpatrick M. Effect of postprocessing thermal treatments on electron-beam powder bed–fused Ti6Al4V. *Material Design & Processing Communications*. 2021;3: e168.
- 244 Chen F, Gu Y, Xu G, Cui Y, Chang H, Zhou L. Improved fracture toughness by microalloying of Fe in Ti-6Al-4V. *Materials and Design*. 2020;185: 108251.
- 245 Jaber H, Kónya J, Kulcsár K, Kovács T. Effects of Annealing and Solution Treatments on the Microstructure and Mechanical Properties of Ti6Al4V Manufactured by Selective Laser Melting. *Materials*. 2022;15.
- 246 Katarov I, Malinov S, Sha W. Finite element modeling of the morphology of  $\beta$  to  $\alpha$  phase transformation in Ti-6Al-4V alloy. *Metallurgical and Materials Transactions A: Physical Metallurgy and Materials Science*. 2002;33: 1027–1040.
- 247 Takajo S, Tomida T, Caspi EN, Pesach A, Tiferet E, Vogel SC. Property improvement of additively manufactured Ti64 by heat treatment characterized by in situ high temperature EBSD and neutron diffraction. *Metals*. 2021;11: 2–19.
- 248 Tammis-Williams S, Zhao H, Léonard F, Derguti F, Todd I, Prangnell PB. XCT analysis of the influence of melt strategies on defect population in Ti-6Al-4V components manufactured by Selective Electron Beam Melting. *Materials Characterization*. 2015;102: 47–61.

- 249 Laursen CM, DeJong SA, Dickens SM, Exil AN, Susan DF, Carroll JD. Relationship between ductility and the porosity of additively manufactured AlSi10Mg. *Materials Science and Engineering: A*. 2020;795: 139922.
- 250 Hansen N. Hall-Petch relation and boundary strengthening. *Scripta Materialia*. 2004;51: 801–806.
- 251 Tahri C, Chauveau T, Hocini A, Dirras G, Bacroix B. Impact of hot isostatic pressing treatments on the mechanical performance of EBMed Ti-6Al-4V alloy. *Materials Characterization*. 2023;201: 112962.
- 252 Boyer RR, Briggs RD. The use of  $\beta$  titanium alloys in the aerospace industry. In: *Journal of Materials Engineering and Performance*. Vol 14. ; 2005:681–685.
- 253 Arola D, Williams CL. Estimating the fatigue stress concentration factor of machined surfaces. *International Journal of Fatigue*. 2002;24: 923–930.
- 254 Mojib M, Pahuja R, Ramulu M, Arola D. High Cycle Fatigue Behavior of Recycled Additive Manufactured Electron Beam Melted Titanium Ti6Al4V. In: *International Mechanical Engineering Congress and Exposition IMECE2020*. Portland: ASME; 2020:24194.
- 255 Facchini L, Magalini E, Robotti P, Molinari A. Microstructure and mechanical properties of Ti-6Al-4V produced by electron beam melting of pre-alloyed powders. *Rapid Prototyping Journal*. 2009;15: 171–178.
- 256 Murakami Y (Yukitaka). *Metal Fatigue: Effects of Small Defects and Nonmetallic Inclusions*. 2nd ed. Elsevier Ltd.; 2019.
- 257 Goel S, Olsson J, Ahlfors M, Klement U, Joshi S. The effect of location and post-treatment on the microstructure of EBM-built Alloy 718. In: *Proceedings of the 9th International Symposium on Superalloy 718 & Derivatives: Energy, Aerospace, and Industrial Applications*. Springer Nature; 2018:115–129.
- 258 Barba D, Alabort C, Tang YT, Viscasillas MJ, Reed RC, Alabort E. On the size and orientation effect in additive manufactured Ti-6Al-4V. *Materials and Design*. 2020;186: 108235.
- 259 Mertová K, Džugan J, Roudnická M, et al. Build Size and Orientation Influence on Mechanical Properties of Powder Bed Fusion Deposited Titanium Parts. *Metals 2020, Vol 10, Page 1340*. 2020;10: 1340.

- 260 William James Sames V. Additive Manufacturing of Inconel 718 using Electron Beam Melting: Processing, Post-Processing, & Mechanical Properties. January 2015.
- 261 Zhou L, Deng H, Qiu W, et al. Influence of thermal effects via powder bed fusion on the graded microstructure and mechanical properties of near- $\beta$  Ti-5Al-5Mo-5V-3Cr-1Zr alloy. *Materials Science and Engineering: A*. 2023;877: 145194.
- 262 Wang P, Tan X, Nai MLS, Tor SB, Wei J. Spatial and geometrical-based characterization of microstructure and microhardness for an electron beam melted Ti-6Al-4V component. *Materials & Design*. 2016;95: 287–295.
- 263 Zhou L, Deng H, Qiu W, et al. Influence of thermal effects via powder bed fusion on the graded microstructure and mechanical properties of near- $\beta$  Ti-5Al-5Mo-5V-3Cr-1Zr alloy. *Materials Science and Engineering: A*. 2023;877: 145194.
- 264 Palanivel S, Dutt AK, Faierson EJ, Mishra RS. Spatially dependent properties in a laser additive manufactured Ti-6Al-4V component. *Materials Science and Engineering: A*. 2016;654: 39–52.
- 265 Rahimi F, Pourabdollah P, Farhang Mehr F, Cockcroft S, Maijer D. A macroscale heat transfer analysis of the build chamber in a commercial electron beam powder bed fusion (EB-PBF) additive manufacturing system during component fabrication. *Additive Manufacturing*. 2023;78: 103831.
- 266 Raplee J, Plotkowski A, Kirka MM, et al. Thermographic Microstructure Monitoring in Electron Beam Additive Manufacturing. *Scientific Reports 2017 7:1*. 2017;7: 1–16.
- 267 Rodriguez E, Medina F, Espalin D, et al. Integration of a Thermal Imaging Feedback Control System in Electron Beam Melting. In: *Solid Freeform Fabrication Symposium*. Austin: University of Texas; 2012:945–961.
- 268 Antonysamy AA, Meyer J, Prangnell PB. Effect of build geometry on the  $\beta$ -grain structure and texture in additive manufacture of Ti6Al4V by selective electron beam melting. *Materials Characterization*. 2013;84: 153–168.
- 269 Algardh JK, Horn T, West H, et al. Thickness dependency of mechanical properties for thin-walled titanium parts manufactured by Electron Beam Melting (EBM)®. *Additive Manufacturing*. 2016;12: 45–50.

- 270 Sun YY, Gulizia S, Oh CH, et al. The Influence of As-Built Surface Conditions on Mechanical Properties of Ti-6Al-4V Additively Manufactured by Selective Electron Beam Melting. *JOM*. 2016;68: 791–798.
- 271 Wang X, Chou K. Effect of support structures on Ti-6Al-4V overhang parts fabricated by powder bed fusion electron beam additive manufacturing. *Journal of Materials Processing Technology*. 2018;257: 65–78.
- 272 Mojib M, Soyama H, Sanders D, Arola D, Ramulu M. The High Cycle Fatigue Behavior of Surface Treated Electron Beam Melted Titanium Ti6Al4V. In: *International Mechanical Engineering Congress and Exposition IMECE2021*. American Society of Mechanical Engineers Digital Collection; 2021:71975.
- 273 Zhang JS, Tang YT, Jin R, et al. On the size-dependent fatigue behaviour of laser powder bed fusion Ti-6Al-4V. *Additive Manufacturing*. 2024;79: 103922.
- 274 Ghods S, Schultz E, Wisdom C, et al. Electron beam additive manufacturing of Ti6Al4V: Evolution of powder morphology and part microstructure with powder reuse. *Materialia*. 2020;9: 100631.

# Appendix

## A- Experimental Properties

### *Hardness*

Condition	Surface	Orientation	Thickness	Height	Radial	Hardness
HIP	Machined	ZX	9	256	95	337
HIP	Machined	ZX	9	256	95	322
HIP	Machined	ZX	9	256	95	324
HIP	Machined	ZX	9	256	95	327
HIP	Machined	ZX	9	256	95	318
HIP	Machined	ZX	9	256	95	340
HIP	Machined	ZX	9	256	95	312
HIP	Machined	ZX	9	156	65	331
HIP	Machined	ZX	9	156	65	333
HIP	Machined	ZX	9	156	65	320
HIP	Machined	ZX	9	156	65	327
HIP	Machined	ZX	9	156	65	314
HIP	Machined	ZX	9	156	65	333
HIP	Machined	ZX	9	156	65	316
HIP	Machined	ZX	9	56	35	331
HIP	Machined	ZX	9	56	35	334
HIP	Machined	ZX	9	56	35	311
HIP	Machined	ZX	9	56	35	320
HIP	Machined	ZX	9	56	35	327
HIP	Machined	ZX	9	56	35	348
HIP	Machined	ZX	9	56	35	338
HIP	Machined	XY	9	56	35	316
HIP	Machined	XY	9	56	35	333
HIP	Machined	XY	9	56	35	354
HIP	Machined	XY	9	56	35	322
HIP	Machined	XY	9	56	35	352
HIP	Machined	XY	9	56	35	331
HIP	Machined	XY	9	56	35	388
HIP	Machined	XY	9	156	65	342

HIP	Machined	XY	9	156	65	305
HIP	Machined	XY	9	156	65	326
HIP	Machined	XY	9	156	65	305
HIP	Machined	XY	9	156	65	301
HIP	Machined	XY	9	156	65	313
HIP	Machined	XY	9	156	65	326
HIP	Machined	XY	9	156	35	284
HIP	Machined	XY	9	156	35	300
HIP	Machined	XY	9	156	35	322
HIP	Machined	XY	9	156	35	386
HIP	Machined	XY	9	156	35	316
HIP	Machined	XY	9	156	35	312
HIP	Machined	XY	9	156	35	308
As-Built	Machined	XY	9	256	95	352
As-Built	Machined	XY	9	256	95	332
As-Built	Machined	XY	9	256	95	352
As-Built	Machined	XY	9	256	95	346
As-Built	Machined	XY	9	256	95	369
As-Built	Machined	XY	9	256	95	379
As-Built	Machined	XY	9	256	95	390
As-Built	Machined	XY	9	156	65	406
As-Built	Machined	XY	9	156	65	322
As-Built	Machined	XY	9	156	65	300
As-Built	Machined	XY	9	156	65	364
As-Built	Machined	XY	9	156	65	349
As-Built	Machined	XY	9	156	65	329
As-Built	Machined	XY	9	156	65	285
As-Built	Machined	XY	9	56	35	334
As-Built	Machined	XY	9	56	35	403
As-Built	Machined	XY	9	56	35	336
As-Built	Machined	XY	9	56	35	348
As-Built	Machined	XY	9	56	35	354
As-Built	Machined	XY	9	56	35	350

<b>As-Built</b>	Machined	XY	9	56	35	338
<b>As-Built</b>	Machined	ZX	6	256	35	379
<b>As-Built</b>	Machined	ZX	6	256	35	335
<b>As-Built</b>	Machined	ZX	6	256	35	334
<b>As-Built</b>	Machined	ZX	6	256	35	347
<b>As-Built</b>	Machined	ZX	6	256	35	361
<b>As-Built</b>	Machined	ZX	6	256	35	324
<b>As-Built</b>	Machined	ZX	6	256	35	362
<b>As-Built</b>	Machined	ZX	3	256	95	349
<b>As-Built</b>	Machined	ZX	3	256	95	344
<b>As-Built</b>	Machined	ZX	3	256	95	339
<b>As-Built</b>	Machined	ZX	3	256	95	334
<b>As-Built</b>	Machined	ZX	3	256	95	352
<b>As-Built</b>	Machined	ZX	3	256	95	346
<b>As-Built</b>	Machined	ZX	3	256	95	344
<b>As-Built</b>	Machined	ZX	6	256	95	290
<b>As-Built</b>	Machined	ZX	6	256	95	338
<b>As-Built</b>	Machined	ZX	6	256	95	350
<b>As-Built</b>	Machined	ZX	6	256	95	338
<b>As-Built</b>	Machined	ZX	6	256	95	334
<b>As-Built</b>	Machined	ZX	6	256	95	346
<b>As-Built</b>	Machined	ZX	6	256	95	354
<b>As-Built</b>	Machined	ZX	6	156	35	334
<b>As-Built</b>	Machined	ZX	6	156	35	341
<b>As-Built</b>	Machined	ZX	6	156	35	355
<b>As-Built</b>	Machined	ZX	6	156	35	363
<b>As-Built</b>	Machined	ZX	6	156	35	329
<b>As-Built</b>	Machined	ZX	6	156	35	371
<b>As-Built</b>	Machined	ZX	6	156	35	363
<b>As-Built</b>	Machined	ZX	6	56	35	357
<b>As-Built</b>	Machined	ZX	6	56	35	346
<b>As-Built</b>	Machined	ZX	6	56	35	357
<b>As-Built</b>	Machined	ZX	6	56	35	354

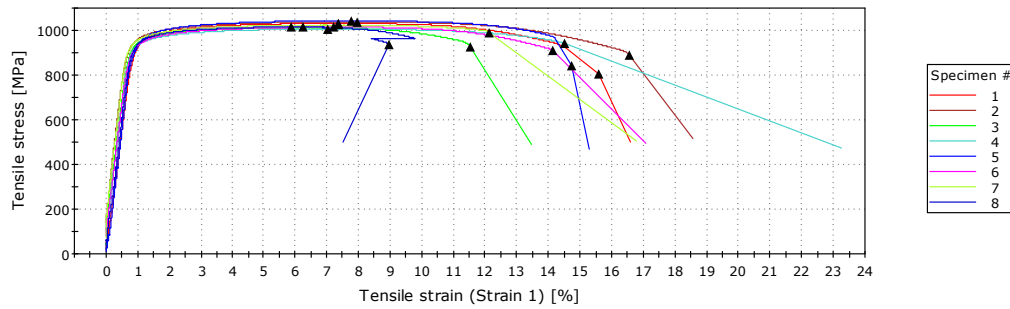
<b>As-Built</b>	Machined	ZX	6	56	35	361
<b>As-Built</b>	Machined	ZX	6	56	35	357
<b>As-Built</b>	Machined	ZX	6	56	35	375
<b>As-Built</b>	Machined	ZX	3	56	35	345
<b>As-Built</b>	Machined	ZX	3	56	35	364
<b>As-Built</b>	Machined	ZX	3	56	35	334
<b>As-Built</b>	Machined	ZX	3	56	35	359
<b>As-Built</b>	Machined	ZX	3	56	35	354
<b>As-Built</b>	Machined	ZX	3	56	35	359
<b>As-Built</b>	Machined	ZX	3	56	35	364
<b>As-Built</b>	As-Built	ZX	9	256	65	317
<b>As-Built</b>	As-Built	ZX	9	256	65	351
<b>As-Built</b>	As-Built	ZX	9	256	65	331
<b>As-Built</b>	As-Built	ZX	9	256	65	339
<b>As-Built</b>	As-Built	ZX	9	256	65	331
<b>As-Built</b>	As-Built	ZX	9	256	65	344
<b>As-Built</b>	As-Built	ZX	9	256	65	349
<b>As-Built</b>	As-Built	ZX	6	56	35	361
<b>As-Built</b>	As-Built	ZX	6	56	35	336
<b>As-Built</b>	As-Built	ZX	6	56	35	325
<b>As-Built</b>	As-Built	ZX	6	56	35	385
<b>As-Built</b>	As-Built	ZX	6	56	35	364
<b>As-Built</b>	As-Built	ZX	6	56	35	341
<b>As-Built</b>	As-Built	ZX	6	56	35	379
<b>As-Built</b>	As-Built	ZX	9	156	65	298
<b>As-Built</b>	As-Built	ZX	9	156	65	314
<b>As-Built</b>	As-Built	ZX	9	156	65	342
<b>As-Built</b>	As-Built	ZX	9	156	65	330
<b>As-Built</b>	As-Built	ZX	9	156	65	334
<b>As-Built</b>	As-Built	ZX	9	156	65	322
<b>As-Built</b>	As-Built	ZX	9	156	65	319
<b>As-Built</b>	As-Built	ZX	9	56	95	350
<b>As-Built</b>	As-Built	ZX	9	56	95	366

<b>As-Built</b>	As-Built	ZX	9	56	95	355
<b>As-Built</b>	As-Built	ZX	9	56	95	329
<b>As-Built</b>	As-Built	ZX	9	56	95	346
<b>As-Built</b>	As-Built	ZX	9	56	95	356
<b>As-Built</b>	As-Built	ZX	9	56	95	340
<b>As-Built</b>	As-Built	ZX	9	56	35	362
<b>As-Built</b>	As-Built	ZX	9	56	35	379
<b>As-Built</b>	As-Built	ZX	9	56	35	369
<b>As-Built</b>	As-Built	ZX	9	56	35	380
<b>As-Built</b>	As-Built	ZX	9	56	35	361
<b>As-Built</b>	As-Built	ZX	9	56	35	372
<b>As-Built</b>	As-Built	ZX	9	56	35	351
<b>As-Built</b>	Machined	ZX	9	156	95	362
<b>As-Built</b>	Machined	ZX	9	156	95	356
<b>As-Built</b>	Machined	ZX	9	156	95	362
<b>As-Built</b>	Machined	ZX	9	156	95	362
<b>As-Built</b>	Machined	ZX	9	156	95	355
<b>As-Built</b>	Machined	ZX	9	156	95	364
<b>As-Built</b>	Machined	ZX	9	156	95	345
<b>As-Built</b>	Machined	ZX	9	156	35	370
<b>As-Built</b>	Machined	ZX	9	156	35	356
<b>As-Built</b>	Machined	ZX	9	156	35	357
<b>As-Built</b>	Machined	ZX	9	156	35	353
<b>As-Built</b>	Machined	ZX	9	156	35	383
<b>As-Built</b>	Machined	ZX	9	156	35	348
<b>As-Built</b>	Machined	ZX	9	156	35	354
<b>HT</b>	Machined	ZX	9	156	95	365
<b>HT</b>	Machined	ZX	9	156	95	367
<b>HT</b>	Machined	ZX	9	156	95	366
<b>HT</b>	Machined	ZX	9	156	95	380
<b>HT</b>	Machined	ZX	9	156	95	370
<b>HT</b>	Machined	ZX	9	156	95	373
<b>HT</b>	Machined	ZX	9	156	95	

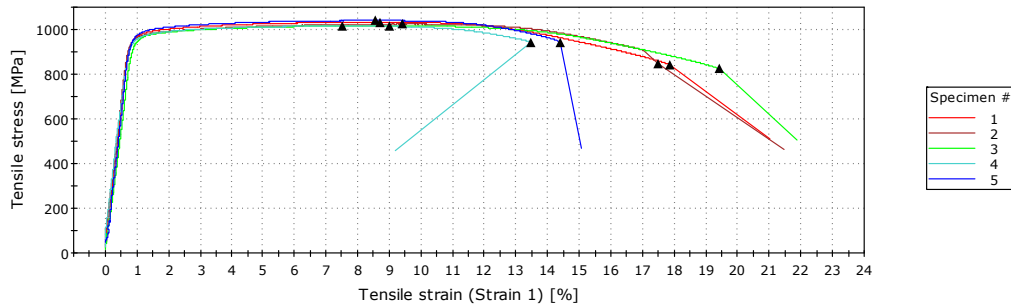
HT	Machined	ZX	9	156	35	393
HT	Machined	ZX	9	156	35	361
HT	Machined	ZX	9	156	35	377
HT	Machined	ZX	9	156	35	384
HT	Machined	ZX	9	156	35	361
HT	Machined	ZX	9	156	35	375
HT	Machined	ZX	9	156	35	359
HT	Machined	ZX	9	256	95	357
HT	Machined	ZX	9	256	95	361
HT	Machined	ZX	9	256	95	373
HT	Machined	ZX	9	256	95	356
HT	Machined	ZX	9	256	95	357
HT	Machined	ZX	9	256	95	361
HT	Machined	ZX	9	256	65	327
HT	Machined	ZX	9	256	65	367
HT	Machined	ZX	9	256	65	361
HT	Machined	ZX	9	256	65	367
HT	Machined	ZX	9	256	65	356
HT	Machined	ZX	9	256	65	385
HT	Machined	ZX	9	256	65	363
HT	Machined	ZX	9	56	35	372
HT	Machined	ZX	9	56	35	366
HT	Machined	ZX	9	56	35	377
HT	Machined	ZX	9	56	35	374
HT	Machined	ZX	9	56	35	391
HT	Machined	ZX	9	56	35	378
HT	Machined	ZX	9	56	35	375
HT	Machined	ZX	9	56	35	379
HT	Machined	ZX	9	56	35	373
HT	Machined	ZX	9	56	35	386
HT	Machined	ZX	9	56	35	374
HT	Machined	ZX	9	256	95	428
HT	Machined	ZX	9	256	95	379

<b>HT</b>	Machined	ZX	9	256	95	407
<b>HT</b>	Machined	ZX	9	256	95	413
<b>HT</b>	Machined	ZX	9	256	95	398
<b>HT</b>	Machined	ZX	9	256	95	423
<b>HT</b>	Machined	ZX	9	256	95	384

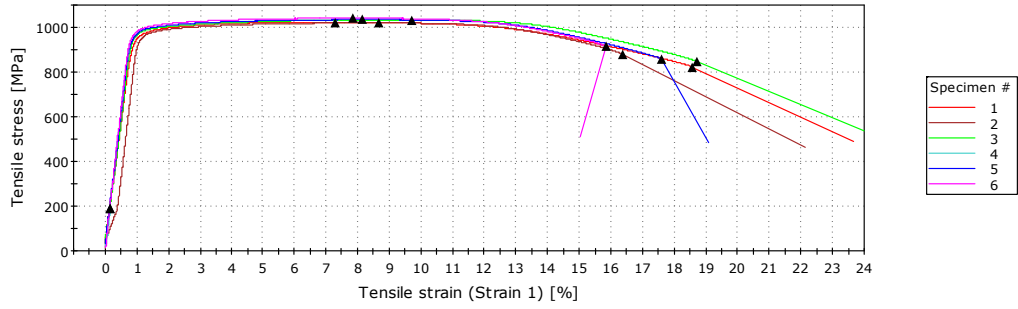
## Tensile Properties



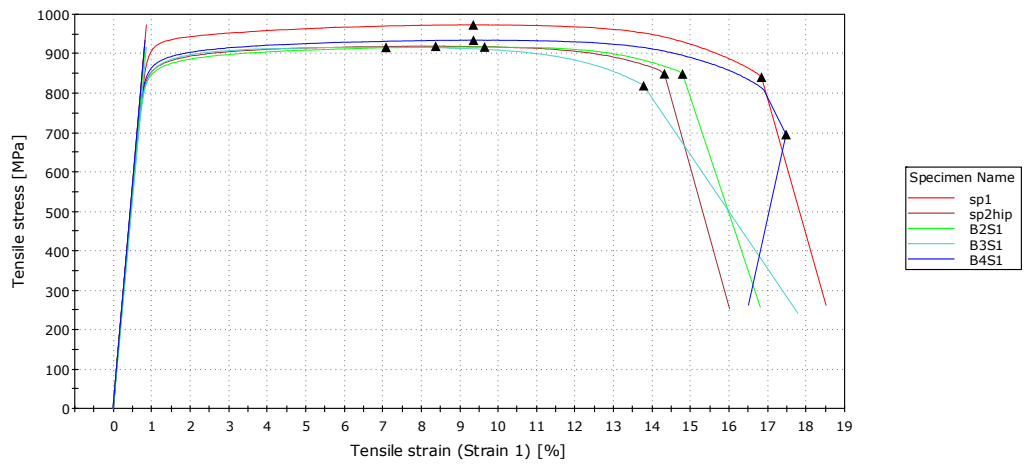
	Specimen label	Maximum Load [N]	Ultimate Tensile Stress [MPa]	Modulus [GPa]	Yield stress (Offset 0.2 %) [MPa]	% Elongation at break [%]
1	156-65-1	29470.90	1031.68	113.13	933.63	15.59
2	156-65-3	26973.71	1038.65	147.05	906.73	16.55
3	156-65-2	28077.73	1013.38	130.30	914.53	11.55
4	56-95-1	30960.70	1006.95	134.82	902.28	14.51
5	56-95-2	31571.45	1043.24	129.39	922.25	14.73
6	156-65-4	28610.56	1014.99	116.58	918.09	14.13
7	56-65-1	29629.12	1023.74	144.80	915.02	12.14
8	56-65-2	23722.27	1014.86	117.56	933.89	8.99



	Specimen label	Maximum Load [N]	Ultimate Tensile Stress [MPa]	Modulus [GPa]	Yield stress (Offset 0.2 %) [MPa]	% Elongation at break [%]
1	ZAA-1	29100.86	1033.12	119.36	966.40	17.88
2	ZAA-2	30576.86	1024.04	122.37	957.37	17.50
3	ZAB-1	31361.00	1016.81	113.49	953.13	19.42
4	ZAB-2	31196.02	1015.30	121.71	945.45	13.47
5	ZAB-3	30785.44	1040.40	154.52	943.63	14.41



	Specimen label	Maximum Load [N]	Ultimate Tensile Stress [MPa]	Modulus [GPa]	Yield stress (Offset 0.2 %) [MPa]	% Elongation at break [%]
1	ZAB-4	32095.62	1022.87	103.68	958.18	18.59
2	ZAB-5	30401.35	1020.00	98.73	971.98	16.37
3	ZAB-6	30971.80	1034.06	105.18	975.96	18.70
X 4	ZAB-7	5137.74	187.24	-----	-----	0.15
5	ZAB-7	28399.78	1034.98	134.06	951.81	17.61
6	ZAB-10	30863.42	1041.10	175.76	899.19	15.87



	Specimen label	Maximum Load [N]	Ultimate Tensile Stress [MPa]	Modulus [MPa]	Yield stress (Offset 0.2 %) [MPa]	% Elongation at break [%]
1	sp1	29668.78	973.27	111657.22	908.88	16.82
2	sp2hip	30050.28	919.69	113171.72	848.72	14.30
3	B2S1	30544.54	917.66	109595.86	843.05	14.78
4	B3S1	30235.88	916.82	106782.81	853.64	13.77
5	B4S1	30636.57	934.73	112422.19	859.92	17.46

### *Fracture Toughness Data*

<b>Metal</b>	<b>Surface</b>	<b>Orientation</b>	<b>Thickness</b>	<b>Radial Distance</b>	<b>height</b>	<b>Crack Length</b>	<b>Kq</b>	<b>Kic</b>	<b>Kr Curve</b>
As-Built	As-Built	ZX	3	35	56	10.8	62		75
As-Built	As-Built	ZX	3	35	156	8.6	67		
As-Built	As-Built	ZX	3	35	156	9.3	60		100
As-Built	As-Built	ZX	3	35	256	9.7	78		
As-Built	As-Built	ZX	3	35	256	10.8	65		107
As-Built	As-Built	ZX	3	65	56	9.5	83		11
As-Built	As-Built	ZX	3	65	56	11.8	61		85
As-Built	As-Built	ZX	3	65	156	8.1	65		6
As-Built	As-Built	ZX	3	65	156	10.8	60		95
As-Built	As-Built	ZX	3	65	256	6.9	62		2
As-Built	As-Built	ZX	3	65	256	11.9	74		94
As-Built	As-Built	ZX	3	95	56	8.1	56		
As-Built	As-Built	ZX	3	95	56	10.4	60		92
As-Built	As-Built	ZX	3	95	156	9.0	59		
As-Built	As-Built	ZX	3	95	156	11.7	60		87
As-Built	As-Built	ZX	3	95	256	9.7	66		
As-Built	As-Built	ZX	3	95	256	11.0	53		95
As-Built	As-Built	ZX	6	35	56	7.6		61	
As-Built	As-Built	ZX	6	35	56	10.7		64	
As-Built	As-Built	ZX	6	35	156	6.9	64		
As-Built	As-Built	ZX	6	35	156	9.5	64		
As-Built	As-Built	ZX	6	35	256	7.5		75	
As-Built	As-Built	ZX	6	35	256	9.9	74		
As-Built	As-Built	ZX	6	65	56	7.7		61	
As-Built	As-Built	ZX	6	65	56	10.2	58		
As-Built	As-Built	ZX	6	65	156	7.7		66	
As-Built	As-Built	ZX	6	65	156	9.3		72	
As-Built	As-Built	ZX	6	65	256	7.3		75	
As-Built	As-Built	ZX	6	65	256	8.9		69	
As-Built	As-Built	ZX	6	95	56	7.7	54		

<b>As-Built</b>	As-Built	ZX	6	95	56	9.8	58
<b>As-Built</b>	As-Built	ZX	6	95	156	10.4	64
<b>As-Built</b>	As-Built	ZX	6	95	156	10.8	60
<b>As-Built</b>	As-Built	ZX	6	95	256	8.1	71
<b>As-Built</b>	As-Built	ZX	6	95	256	9.3	72
<b>As-Built</b>	As-Built	ZX	9	35	56	11.6	67
<b>As-Built</b>	As-Built	ZX	9	35	56	12.7	64
<b>As-Built</b>	As-Built	ZX	9	35	156	10.0	73
<b>As-Built</b>	As-Built	ZX	9	35	256	11.5	87
<b>As-Built</b>	As-Built	ZX	9	35	256	12.1	72
<b>As-Built</b>	As-Built	ZX	9	65	56	13.2	67
<b>As-Built</b>	As-Built	ZX	9	65	156	8.5	64
<b>As-Built</b>	As-Built	ZX	9	65	156	13.8	66
<b>As-Built</b>	As-Built	ZX	9	65	256	10.2	75
<b>As-Built</b>	As-Built	ZX	9	65	256	12.7	71
<b>As-Built</b>	As-Built	ZX	9	95	56	11.7	66
<b>As-Built</b>	As-Built	ZX	9	95	156	10.0	58
<b>As-Built</b>	As-Built	ZX	9	95	256	12.1	70
<b>As-Built</b>	As-Built	ZX	9	95	256	13.0	70
<b>As-Built</b>	Machined	XY	6	35	56	12.0	66
<b>As-Built</b>	Machined	XY	6	35	156	11.2	67
<b>As-Built</b>	Machined	XY	6	35	256	11.1	35
<b>As-Built</b>	Machined	XY	6	35	256	11.2	35
<b>As-Built</b>	Machined	XY	6	65	56	10.2	60
<b>As-Built</b>	Machined	XY	6	65	56	12.6	65
<b>As-Built</b>	Machined	XY	6	65	156	10.3	65
<b>As-Built</b>	Machined	XY	6	65	156	10.6	65
<b>As-Built</b>	Machined	XY	6	65	256	9.8	65
<b>As-Built</b>	Machined	XY	6	65	256	9.9	65
<b>As-Built</b>	Machined	XY	6	95	56	11.1	95
<b>As-Built</b>	Machined	XY	6	95	56	11.4	95
<b>As-Built</b>	Machined	XY	6	95	156	11.3	95
<b>As-Built</b>	Machined	XY	6	95	156	11.5	95

As-Built	Machined	XY	6	95	256	11.3	
As-Built	Machined	XY	9	35	56	10.9	61
As-Built	Machined	XY	9	35	56	11.4	58
As-Built	Machined	XY	9	35	156	11.2	35
As-Built	Machined	XY	9	35	256	9.9	77
As-Built	Machined	XY	9	35	256	13.9	35
As-Built	Machined	XY	9	65	56	9.8	52
As-Built	Machined	XY	9	65	56	10.9	65
As-Built	Machined	XY	9	65	156	10.9	65
As-Built	Machined	XY	9	65	156	11.7	65
As-Built	Machined	XY	9	65	256	10.0	65
As-Built	Machined	XY	9	65	256	12.1	69
As-Built	Machined	XY	9	95	56	14.6	58
As-Built	Machined	XY	9	95	156	11.7	95
As-Built	Machined	XY	9	95	156	13.0	70
As-Built	Machined	XY	9	95	256	11.3	95
As-Built	Machined	XY	12	35	56	11.0	35
As-Built	Machined	XY	12	35	156	10.3	35
As-Built	Machined	XY	12	35	156	13.2	35
As-Built	Machined	XY	12	35	256	11.4	35
As-Built	Machined	XY	12	65	56	11.1	65
As-Built	Machined	XY	12	65	56	11.3	65
As-Built	Machined	XY	12	65	156	11.6	65
As-Built	Machined	XY	12	65	256	10.6	65
As-Built	Machined	XY	12	65	256	10.7	65
As-Built	Machined	XY	12	95	56	10.8	95
As-Built	Machined	XY	12	95	156	10.0	95
As-Built	Machined	XY	12	95	156	11.8	95
As-Built	Machined	XY	12	95	256	12.5	72
As-Built	Machined	XZ	6	35	56	10.6	64
As-Built	Machined	XZ	6	35	156	10.8	64
As-Built	Machined	XZ	6	35	256	10.4	75
As-Built	Machined	XZ	6	65	156	11.2	57

As-Built	Machined	XZ	6	95	56	11.8	55	
As-Built	Machined	XZ	6	95	256	10.3	64	
As-Built	Machined	XZ	9	35	56	11.3	66	
As-Built	Machined	XZ	9	35	56	12.8	63	
As-Built	Machined	XZ	9	35	156	11.5	69	
As-Built	Machined	XZ	9	35	156	12.3	68	
As-Built	Machined	XZ	9	35	256	11.7	74	
As-Built	Machined	XZ	9	35	256	11.8	72	
As-Built	Machined	XZ	9	65	56	9.4	58	
As-Built	Machined	XZ	9	65	56	11.7	64	
As-Built	Machined	XZ	9	65	156	10.1	64	
As-Built	Machined	XZ	9	65	156	11.0	66	
As-Built	Machined	XZ	9	65	256	11.4	72	
As-Built	Machined	XZ	9	65	256	13.1	70	
As-Built	Machined	XZ	9	95	56	11.6	58	
As-Built	Machined	XZ	9	95	56	12.2	57	
As-Built	Machined	XZ	9	95	156	11.9	60	
As-Built	Machined	XZ	9	95	156	14.1	61	
As-Built	Machined	XZ	9	95	256	10.6	66	
As-Built	Machined	XZ	9	95	256	12.8	68	
As-Built	Machined	XZ	12	35	56	10.1	69	
As-Built	Machined	XZ	12	35	256	11.6	75	
As-Built	Machined	XZ	12	65	56	12.9	61	
As-Built	Machined	XZ	12	65	156	10.1	65	
As-Built	Machined	XZ	12	95	56	10.2	56	
As-Built	Machined	XZ	12	95	156	9.9	61	
As-Built	Machined	XZ	12	95	256	10.3	65	
As-Built	Machined	ZX	3	35	56	12.0	70	104
As-Built	Machined	ZX	3	35	156	12.4	75	108
As-Built	Machined	ZX	3	35	256	12.0	85	128
As-Built	Machined	ZX	3	65	56	11.9	76	98
As-Built	Machined	ZX	3	65	156	12.0	71	98
As-Built	Machined	ZX	3	65	256	12.5	79	116

As-Built	Machined	ZX	3	95	56	12.2	68	85
As-Built	Machined	ZX	3	95	156	12.3	64	92
As-Built	Machined	ZX	3	95	256	12.0	71	113
As-Built	Machined	ZX	6	35	56	13.0	56	56
As-Built	Machined	ZX	6	35	156	12.6	67	67
As-Built	Machined	ZX	6	35	256	13.6	75	
As-Built	Machined	ZX	6	65	56	11.0	57	57
As-Built	Machined	ZX	6	65	156	11.7	64	64
As-Built	Machined	ZX	6	65	256	13.2	73	
As-Built	Machined	ZX	6	95	56	12.3	50	
As-Built	Machined	ZX	6	95	156	10.7	55	
As-Built	Machined	ZX	6	95	256	12.6	70	70
As-Built	Machined	ZX	9	35	56	10.5	66	66
As-Built	Machined	ZX	9	35	156	12.8	68	68
As-Built	Machined	ZX	9	35	256	12.0	77	
As-Built	Machined	ZX	9	65	56	10.8	66	66
As-Built	Machined	ZX	9	65	156	12.3	61	61
As-Built	Machined	ZX	9	95	56	10.6	57	57
As-Built	Machined	ZX	9	95	156	11.7	60	60
As-Built	Machined	ZX	9	95	256	11.4	68	68
HIP	Machined	XY	6	35	56	10.3	78	
HIP	Machined	XY	6	35	156	10.1	78	
HIP	Machined	XY	6	65	56	9.8	75	75
HIP	Machined	XY	6	65	156	10.0	78	
HIP	Machined	XY	6	95	56	9.5	75	75
HIP	Machined	XY	6	95	156	9.5	73	73
HIP	Machined	XY	6	95	156	9.9	72	72
HIP	Machined	XY	9	35	56	11.1	79	
HIP	Machined	XY	9	35	56	11.8	82	
HIP	Machined	XY	9	35	256	11.2	71	71
HIP	Machined	XY	9	35	256	11.7	69	69
HIP	Machined	XY	9	65	56	11.6	84	
HIP	Machined	XY	9	65	56	11.7	79	

HIP	Machined	XY	9	65	256	11.2	71
HIP	Machined	XY	9	65	256	11.5	69
HIP	Machined	XY	9	95	56	11.2	76
HIP	Machined	XY	9	95	56	13.8	78
HIP	Machined	XY	9	95	256	11.9	70 70
HIP	Machined	XY	12	35	156	10.1	77
HIP	Machined	XY	12	35	156	10.9	75
HIP	Machined	XY	12	35	256	9.7	88
HIP	Machined	XY	12	35	256	10.4	87
HIP	Machined	XY	12	65	156	11.2	78
HIP	Machined	XY	12	65	256	9.5	86
HIP	Machined	XY	12	65	256	10.6	85
HIP	Machined	XY	12	95	156	10.2	76 76
HIP	Machined	XY	12	95	256	9.7	81
HIP	Machined	XY	12	95	256	10.1	77
HIP	Machined	XZ	6	35	56	10.9	71 71
HIP	Machined	XZ	6	35	56	11.1	74
HIP	Machined	XZ	6	65	56	10.4	70 70
HIP	Machined	XZ	6	95	56	10.5	67 67
HIP	Machined	XZ	6	95	56	11.1	68 68
HIP	Machined	XZ	9	35	56	11.8	75
HIP	Machined	XZ	9	35	56	13.3	73
HIP	Machined	XZ	9	65	56	12.1	69
HIP	Machined	XZ	9	65	56	12.1	73
HIP	Machined	XZ	9	95	56	12.5	67 67
HIP	Machined	XZ	9	95	56	12.8	66 66
HIP	Machined	XZ	12	35	56	9.9	66 66
HIP	Machined	XZ	12	35	56	11.4	70 70
HIP	Machined	XZ	12	65	56	11.0	70 70
HIP	Machined	XZ	12	65	56	11.0	69 69
HIP	Machined	XZ	12	95	56	10.3	60 60
HIP	Machined	XZ	12	95	56	10.5	72 72
HIP	Machined	ZX	6	35	56	10.7	76

HIP	Machined	ZX	6	35	156	10.9	78
HIP	Machined	ZX	6	35	256	10.8	85
HIP	Machined	ZX	6	65	56	11.1	75
HIP	Machined	ZX	6	65	56	11.1	82
HIP	Machined	ZX	6	65	156	12.0	81
HIP	Machined	ZX	6	65	256	10.6	85
HIP	Machined	ZX	6	65	256	11.5	80
HIP	Machined	ZX	6	95	56	11.0	78
HIP	Machined	ZX	6	95	156	10.5	80
HIP	Machined	ZX	6	95	156	10.8	74 74
HIP	Machined	ZX	6	95	256	11.2	80
HIP	Machined	ZX	6	95	256	11.3	82
HIP	Machined	ZX	9	35	56	10.0	82
HIP	Machined	ZX	9	35	156	14.5	80
HIP	Machined	ZX	9	35	156	14.8	81
HIP	Machined	ZX	9	35	256	12.3	82
HIP	Machined	ZX	9	65	56	10.4	82
HIP	Machined	ZX	9	65	56	11.5	83
HIP	Machined	ZX	9	65	156	11.9	80
HIP	Machined	ZX	9	65	256	9.5	80
HIP	Machined	ZX	9	65	256	11.4	84
HIP	Machined	ZX	9	95	56	9.9	76 76
HIP	Machined	ZX	9	95	56	10.1	73
HIP	Machined	ZX	9	95	56	12.3	72
HIP	Machined	ZX	9	95	156	9.3	73 73
HIP	Machined	ZX	9	95	156	12.1	76
HIP	Machined	ZX	9	95	156	12.2	72
HIP	Machined	ZX	9	95	256	9.7	78
HIP	Machined	ZX	9	95	256	11.8	74
HIP	Machined	ZX	9	95	256	14.7	76

### Fracture Toughness Shear Lip Area

Condition	Orientation	Thickness	Height	Radial	%Shear Lip Area
HIP	XY	6	56	95	19.6%
HIP	XY	6	156	35	18.7%
HIP	XY	6	156	95	22.0%
HIP	XY	9	56	65	14.6%
HIP	XY	9	156	35	16.2%
HIP	XY	9	156	95	15.2%
HIP	XY	12	56	65	15.3%
HIP	XY	12	156	35	11.9%
HIP	XY	12	156	65	15.2%
HIP	XZ	6	56	35	21.8%
HIP	XZ	6	56	65	27.6%
HIP	XZ	6	56	95	26.7%
HIP	XZ	9	56	35	17.6%
HIP	XZ	9	56	65	19.1%
HIP	XZ	9	56	95	18.1%
HIP	XZ	12	56	35	17.7%
HIP	XZ	12	56	65	12.5%
HIP	XZ	12	56	95	16.1%
HIP	ZX	6	56	65	23.6%
HIP	ZX	6	156	95	23.5%
HIP	ZX	6	256	65	30.3%
HIP	ZX	9	56	95	19.2%
HIP	ZX	9	256	35	20.2%
As-Built	ZX	6	56	95	0.205
As-Built	ZX	6	156	35	0.285
As-Built	ZX	6	156	95	0.222
As-Built	ZX	9	56	35	0.123
As-Built	ZX	9	56	65	0.238
As-Built	ZX	9	256	95	0.198
As-Built	XZ	6	56	35	0.19
As-Built	XZ	6	156	65	0.163

<b>As-Built</b>	XZ	6	256	95	0.193
<b>As-Built</b>	XZ	9	56	35	0.1875
<b>As-Built</b>	XZ	9	156	65	0.135
<b>As-Built</b>	XZ	9	256	95	0.168
<b>As-Built</b>	XZ	12	56	35	0.126
<b>As-Built</b>	XZ	12	156	95	0.126
<b>As-Built</b>	XZ	12	256	65	0.09
<b>As-Built</b>	XY	6	56	35	0.085
<b>As-Built</b>	XY	6	156	65	0.111
<b>As-Built</b>	XY	6	256	95	0.21
<b>As-Built</b>	XY	9	56	35	0.092
<b>As-Built</b>	XY	9	156	65	0.082
<b>As-Built</b>	XY	9	256	95	0.088
<b>As-Built</b>	XY	12	56	35	0.085
<b>As-Built</b>	XY	12	156	95	0.103
<b>As-Built</b>	XY	12	256	95	0.091

## B – Statistical Analysis

### *As-Built Fracture Toughness DOE Tables and ANOVA Results*

#### **As-Built ZX Fracture Toughness RSM**

<b>Run</b>	<b>Factor 1</b> A:thickness	<b>Factor 2</b> B:height	<b>Factor 3</b> C:radial	<b>Response 1</b> ZX_AB_FT
1	6	56	95	54
2	9	256	65	75
3	9	156	35	73
4	6	256	65	69
5	9	156	95	58
6	6	156	65	66
7	6	56	35	64
8	6	156	95	60
9	6	156	65	72
10	9	156	65	65
11	6	56	35	61
12	6	56	65	61
13	9	56	95	65
14	6	256	35	75
15	6	156	35	64
16	9	56	35	65
17	6	256	65	75
18	6	256	95	72
19	9	256	65	71
20	6	156	95	64
21	9	56	65	67
22	9	256	95	70
23	9	256	95	69

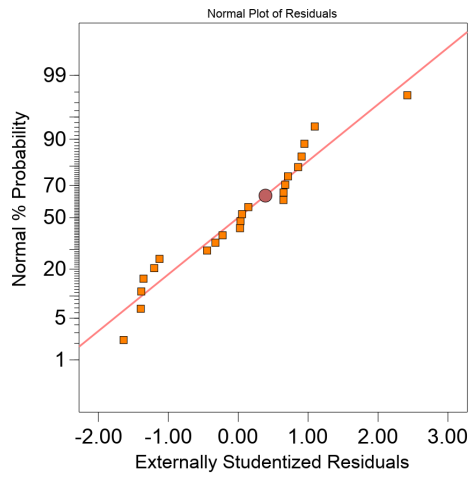
<b>Source</b>	<b>Sum of Squares</b>	<b>df</b>	<b>Mean Square</b>	<b>F-value</b>	<b>p-value</b>	
<b>Model</b>	491.27	4	122.82	13.98	< 0.0001	significant
<i>A-thickness</i>	42.53	1	42.53	4.84	0.0419	
<i>B-height</i>	358.70	1	358.70	40.84	< 0.0001	
<i>C-radial</i>	66.35	1	66.35	7.55	0.0137	
<i>AB</i>	38.92	1	38.92	4.43	0.0505	
<b>Residual</b>	149.32	17	8.78			
<i>Lack of Fit</i>	92.32	11	8.39	0.8835	0.5948	not significant
<i>Pure Error</i>	57.00	6	9.50			
<b>Cor Total</b>	640.59	21				

**Std. Dev.** 2.96      **R<sup>2</sup>** 0.7669

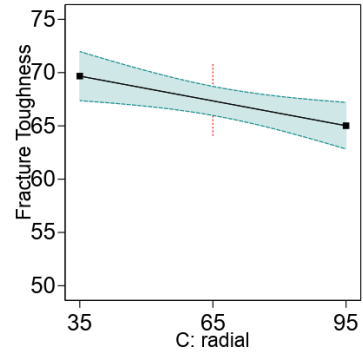
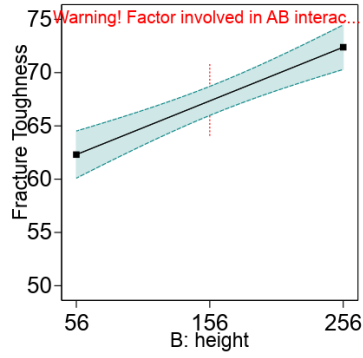
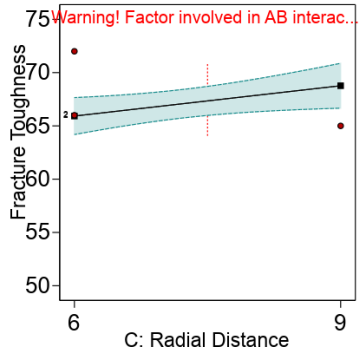
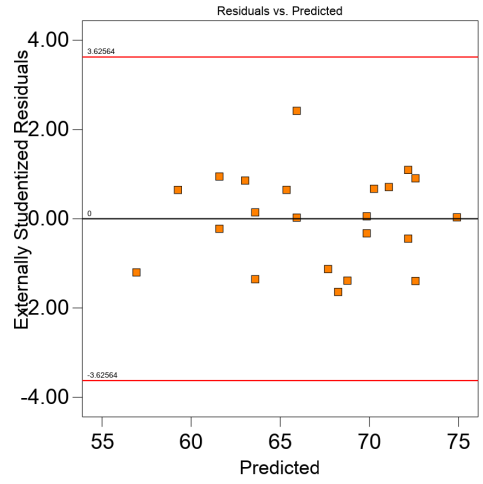
<b>Mean</b>	67.14	<b>Adjusted R<sup>2</sup></b>	0.7121
<b>C.V. %</b>	4.41	<b>Predicted R<sup>2</sup></b>	0.6398
		<b>Adeq Precision</b>	12.7307

**Equation** ZX\_AB\_FT=44.72+ 2.64 thickness +0.13173 height- 0.0775 radial - 0.0108 thickness  
\* height

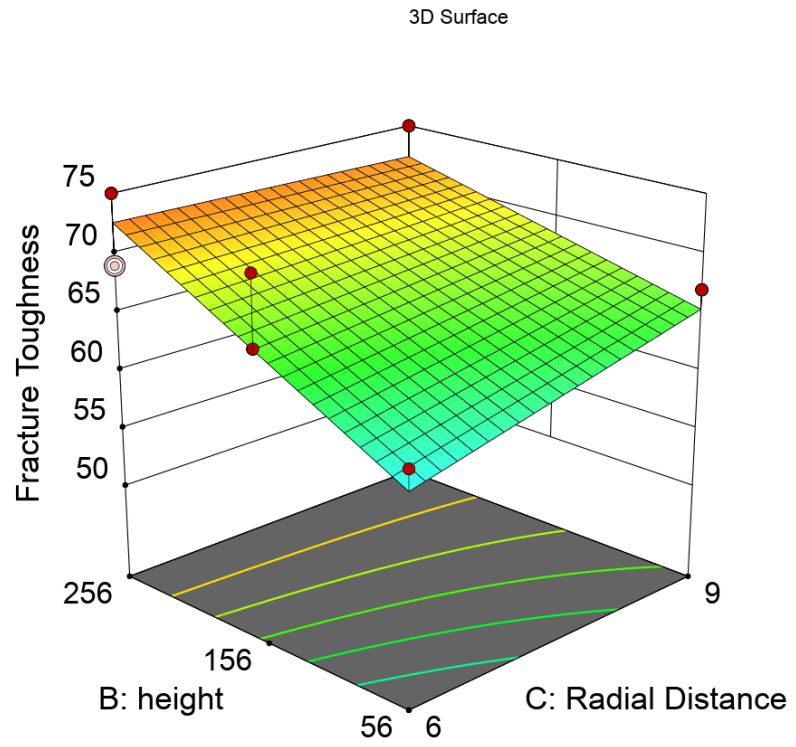
Response: ZX\_AB\_FT



Response: ZX\_AB\_FT



Factor Coding: Actual  
Response: ZX\_AB\_FT  
Design Points:  
● Above Surface  
○ Below Surface  
S1 75  
ZX\_AB\_FT = 69  
Std # 12 Run # 4  
Actual Factor:  
C = 65



*Intra-Build Fracture Toughness RSM ANOVA*

	<b>Factor 1</b>	<b>Factor 2</b>	<b>Factor 3</b>	<b>Factor 4</b>	<b>Response 1</b>
<b>Run</b>	A:thickness	B:height	C:radial distance	D:Orientation	toughness
1	9	56	95	ZX	56.7
2	6	156	65	ZX	63.7
3	12	56	65	XZ	61
4	6	56	95	XZ	54.8
5	9	156	35	ZX	68.3
6	9	256	95	XY	70
7	6	56	35	XY	66
8	12	56	35	XY	68
9	9	56	35	ZX	66
10	6	56	65	ZX	56.5
11	12	156	95	XZ	61
12	6	256	35	XY	71
13	9	256	65	XZ	71
14	9	256	65	XZ	69
15	6	256	95	ZX	69.6
17	6	156	35	XZ	63.8
18	9	156	65	XY	67
19	12	56	95	XY	64
20	9	156	65	XY	70
21	6	256	35	XZ	75
22	6	56	95	XY	63
23	6	156	95	XY	64
24	9	156	65	ZX	61.4
25	12	256	35	XY	74
26	9	156	65	XY	69
	9	156	95	XZ	60

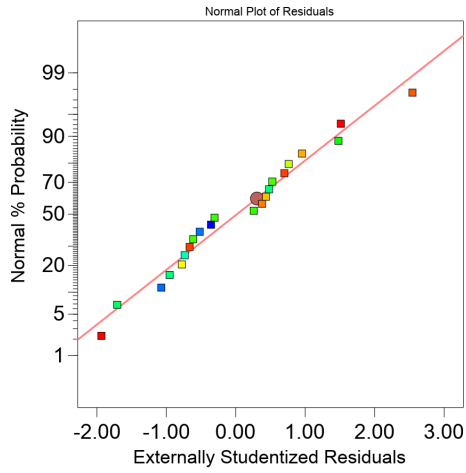
<i>Source</i>	<b>Sum of Squares</b>	<b>% Contribution</b>	<b>df</b>	<b>Mean Square</b>	<b>F-value</b>	<b>p-value</b>
<i>Model</i>	615.79		7	87.97	19.03	< 0.0001
<i>Thickness</i>	18.43	3.2	1	18.43	3.99	0.0612
<i>Height</i>	336.31	58.6	1	336.31	72.75	< 0.0001
<i>Radial distance</i>	98.50	17.2	1	98.50	21.31	<0.001
<i>Orientation</i>	88.35	15.4	2	44.18	9.56	<0.05

$ZX FT = 58.029 + 0.395 * T + 0.059 * H - 0.0838 * R$   
 $XX FT = 56.273 + 0.395 * T + 0.624 * H - 0.0838 * R$   
 $XY FT = 65.148 + 0.395 * T + 0.031 * H - 0.0838 * R$

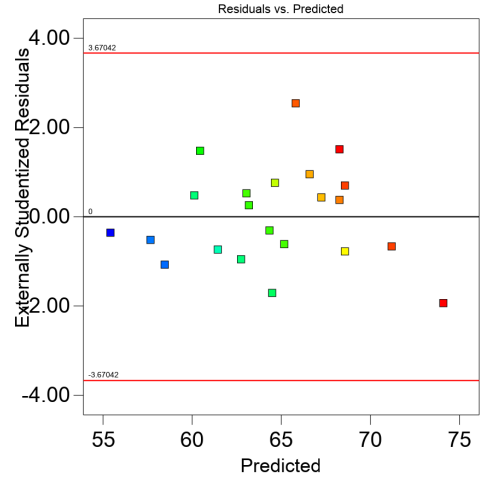
**Std. Dev. 2.14 R<sup>2</sup> 0.8547**

<b>Mean</b>	64.54	<b>Adjusted R<sup>2</sup></b>	0.8093
<b>C.V. %</b>	3.31	<b>Predicted R<sup>2</sup></b>	0.7146
		<b>Adeq Precision</b>	16.7327

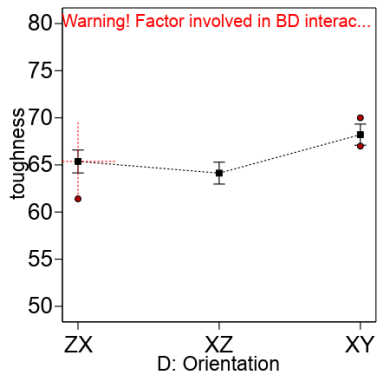
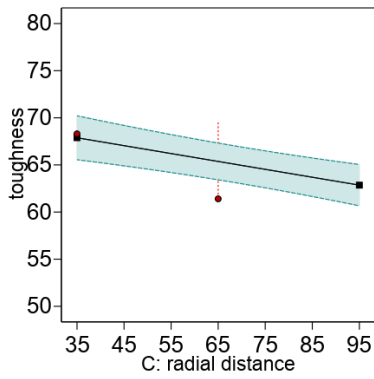
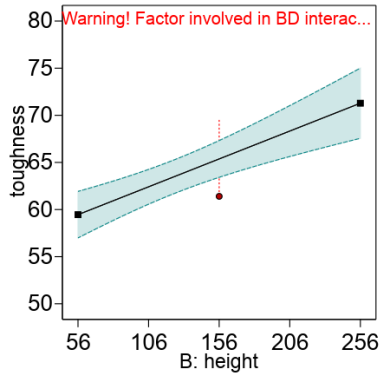
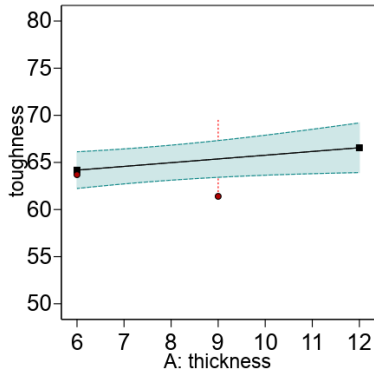
Response: toughness  
 Color points by value:  
 toughness:  
 54.8 71



Response: toughness  
 Color points by value:  
 toughness:  
 54.8 71



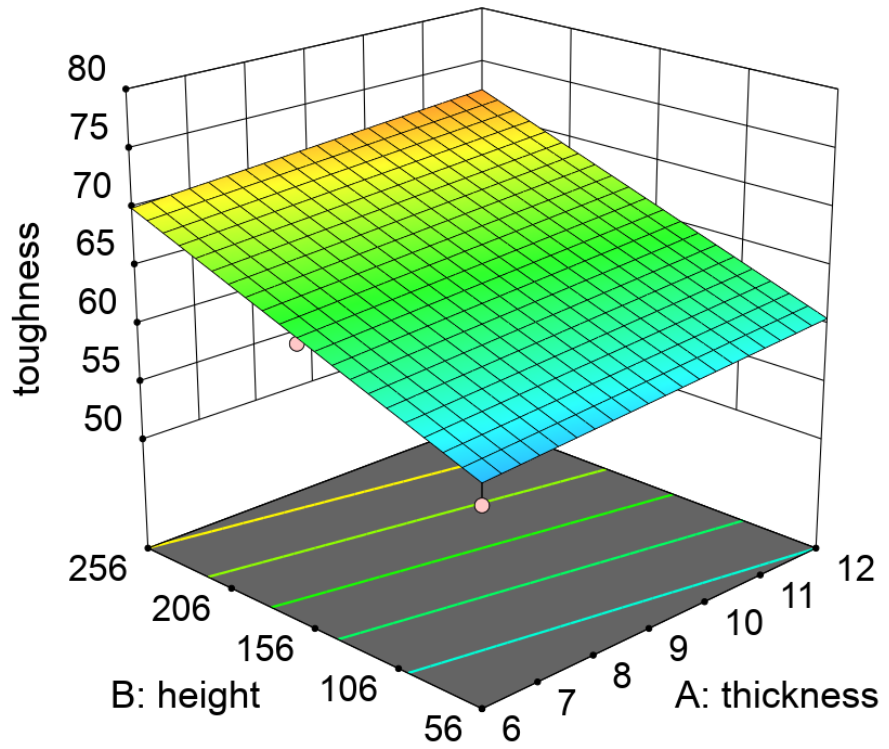
Factor Coding: Actual  
 Response: toughness  
 ● Design Points  
 Actual Factors:  
 A = 9  
 B = 156  
 C = 65  
 D = ZX



Factor Coding: Actual  
Response: toughness  
● Design Points  
54.8 75

Actual Factors:  
C = 65  
D = ZX

3D Surface



### *HIP Fracture Toughness ANOVA*

	<b>Factor 1</b>	<b>Factor 2</b>	<b>Factor 3</b>	<b>Factor 4</b>	<b>Response 1</b>
<b>Run</b>	A:Thick	B:Radial	C:Height	D:Orientation	Kic
<b>1</b>	12	35	256	ZX	84.3
<b>2</b>	6	95	56	ZX	73.8
<b>3</b>	6	65	56	ZX	74.73
<b>4</b>	6	35	256	XZ	74.23
<b>5</b>	6	35	256	XZ	74.94
<b>6</b>	6	65	56	XZ	69.22
<b>7</b>	9	35	256	XY	79.67
<b>8</b>	12	95	56	XZ	72.62
<b>9</b>	6	95	156	XZ	69.33
<b>10</b>	9	35	56	ZX	78.6
<b>11</b>	6	35	56	XY	71.97
<b>12</b>	6	95	256	XY	77.87
<b>13</b>	12	65	56	XY	75.4
<b>14</b>	9	35	256	XY	81.53
<b>15</b>	6	35	56	ZX	75.95
<b>16</b>	12	95	56	XZ	70.45
<b>17</b>	9	35	56	XZ	70.82
<b>18</b>	12	95	156	ZX	80.83
<b>19</b>	6	65	156	XY	74.71
<b>20</b>	12	95	256	XY	81.98
<b>21</b>	6	35	56	XY	73.59
<b>22</b>	6	95	256	ZX	82.11
<b>23</b>	6	35	156	ZX	78.13
<b>24</b>	9	95	56	XY	73.93
<b>25</b>	12	35	256	ZX	85.23
<b>26</b>	9	65	256	XZ	74.54
<b>27</b>	12	35	56	ZX	79.34
<b>28</b>	12	35	156	XZ	73.85

Source	Sum of Squares	df	Mean Square	F-value	p-value	
<b>Model</b>	509.54	6	84.92	117.63	< 0.0001	significant
<i>A-Thick</i>	62.41	1	62.41	86.45	< 0.0001	
<i>B-Radial</i>	3.51	1	3.51	4.86	0.0388	
<i>C-Height</i>	185.61	1	185.61	257.10	< 0.0001	
<i>D-Orientation</i>	246.24	2	123.12	170.54	< 0.0001	
<i>C<sup>2</sup></i>	3.44	1	3.44	4.76	0.0406	
<b>Residual</b>	15.16	21	0.7219			
<i>Lack of Fit</i>	9.08	16	0.5675	0.4666	0.8874	not significant
<i>Pure Error</i>	6.08	5	1.22			
<b>Cor Total</b>	524.70	27				

**Std. Dev. 0.8497      R<sup>2</sup>                      0.9711**

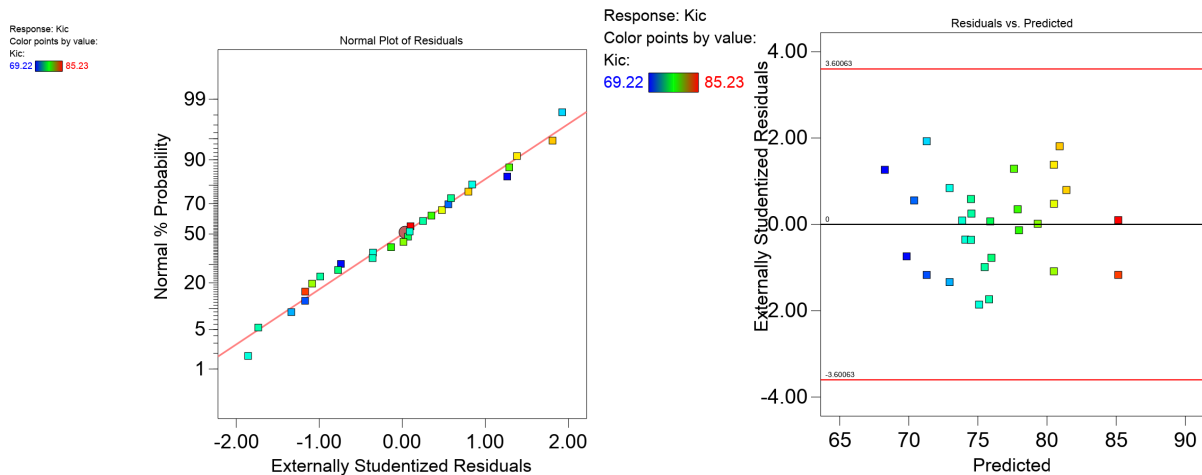
<b>Mean</b>	76.20	<b>Adjusted R<sup>2</sup></b>	0.9629
<b>C.V. %</b>	1.12	<b>Predicted R<sup>2</sup></b>	0.9499
		<b>Adeq Precision</b>	39.7483

### Equations:

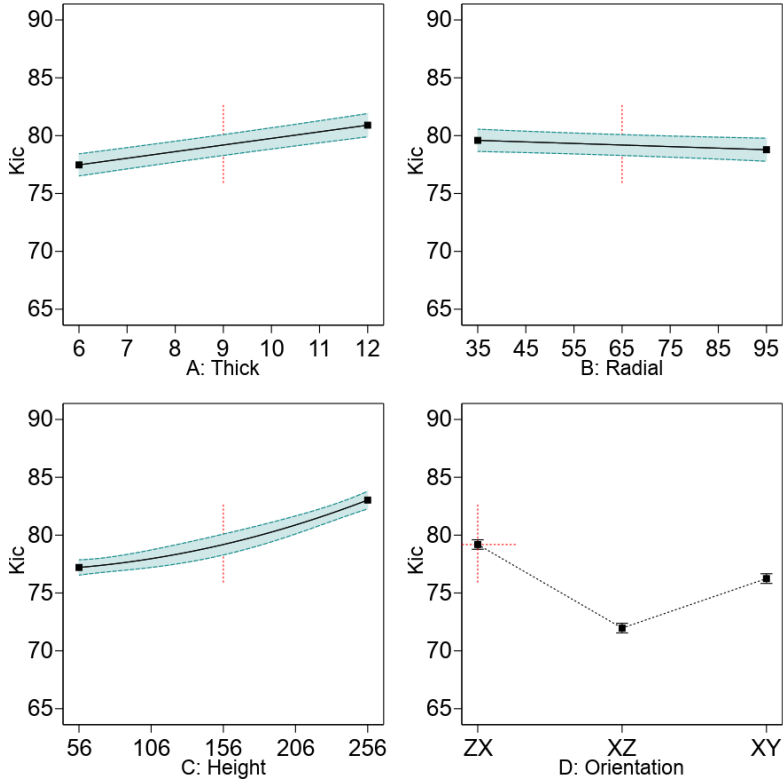
$$ZX \text{ Kic} = 72.637 + 0.572 \text{ Thick} - 0.0134 \text{ Radial} + 0.00011 \text{ Height} + 9.300e-05 \text{ Height}^2$$

$$XZ \text{ Kic} = 65.415 + 0.572 \text{ Thick} - 0.0134 \text{ Radial} + 0.00011 \text{ Height} + 9.300e-05 \text{ Height}^2$$

$$XY \text{ Kic} = 69.695 + 0.572 \text{ Thick} - 0.0134 \text{ Radial} + 0.00011 \text{ Height} + 9.300e-05 \text{ Height}^2$$

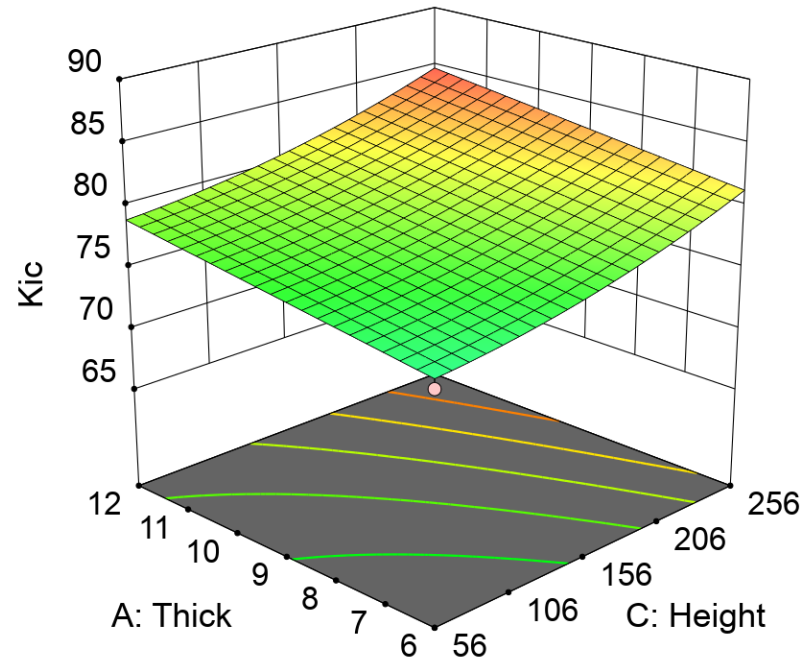


Factor Coding: Actual  
 Response: Kic  
 Actual Factors:  
 A = 9  
 B = 65  
 C = 156  
 D = ZX



Factor Coding: Actual  
 Response: Kic  
 Design Points  
 69.22 85.23  
 Actual Factors:  
 B = 65  
 D = ZX

3D Surface



### Tukey Ad-Hoc Results

As-Built Fracture Toughness

#### Multiple Comparisons

Dependent Variable: Kic

Tukey HSD

(I) Orientation	(J) Orientation	Mean Difference (I- J)	Std. Error	Sig.	95% Confidence Interval	
					Lower Bound	Upper Bound
XY	XZ	3.67*	.952	.002	1.32	6.02
	ZX	2.45*	.934	.036	.14	4.76
XZ	XY	-3.67*	.952	.002	-6.02	-1.32
	ZX	-1.22	.943	.411	-3.55	1.11
ZX	XY	-2.45*	.934	.036	-4.76	-.14
	XZ	1.22	.943	.411	-1.11	3.55

Based on observed means.

The error term is Mean Square(Error) = 11.997.

\*. The mean difference is significant at the 0.05 level.

#### Multiple Comparisons

Dependent Variable: Kic

Tukey HSD

(I) Thickness	(J) Thickness	Mean Difference (I- J)	Std. Error	Sig.	95% Confidence Interval	
					Lower Bound	Upper Bound
6	9	2.07	.853	.055	-.04	4.18
	12	-1.02	1.084	.621	-3.69	1.66
9	6	-2.07	.853	.055	-4.18	.04
	12	-3.09*	1.074	.020	-5.74	-.44
12	6	1.02	1.084	.621	-1.66	3.69
	9	3.09*	1.074	.020	.44	5.74

Based on observed means.

The error term is Mean Square(Error) = 11.997.

\*. The mean difference is significant at the 0.05 level.

### Multiple Comparisons

Dependent Variable: Kic

Tukey HSD

(I) Height	(J) Height	Mean	Std. Error	Sig.	95% Confidence Interval	
		Difference (I-J)			Lower Bound	Upper Bound
56	156	-3.16*	.860	.003	-5.28	-1.04
	256	-8.60*	1.050	<.001	-11.19	-6.00
156	56	3.16*	.860	.003	1.04	5.28
	256	-5.43*	1.066	<.001	-8.07	-2.80
256	56	8.60*	1.050	<.001	6.00	11.19
	156	5.43*	1.066	<.001	2.80	8.07

Based on observed means.

The error term is Mean Square(Error) = 11.997.

\*. The mean difference is significant at the 0.05 level.

### Multiple Comparisons

Dependent Variable: Kic

Tukey HSD

(I) Radial	(J) Radial	Mean Difference	Std. Error	Sig.	95% Confidence Interval	
		(I-J)			Lower Bound	Upper Bound
35	65	.81	.966	.681	-1.57	3.20
	95	3.90*	.987	.001	1.47	6.34
65	35	-.81	.966	.681	-3.20	1.57
	95	3.09*	.903	.005	.86	5.32
95	35	-3.90*	.987	.001	-6.34	-1.47
	65	-3.09*	.903	.005	-5.32	-.86

Based on observed means.

The error term is Mean Square(Error) = 11.997.

\*. The mean difference is significant at the 0.05 level.

## HIP Fracture Toughness

### Multiple Comparisons

Dependent Variable: Kq

Tukey HSD

(I) Orientation	(J) Orientation	Mean Difference (I- J)	Std. Error	Sig.	95% Confidence Interval	
					Lower Bound	Upper Bound
XY	XZ	8.18*	1.073	<.001	5.54	10.82
	ZX	-1.24	.910	.374	-3.47	1.00
XZ	XY	-8.18*	1.073	<.001	-10.82	-5.54
	ZX	-9.42*	1.053	<.001	-12.01	-6.83
ZX	XY	1.24	.910	.374	-1.00	3.47
	XZ	9.42*	1.053	<.001	6.83	12.01

Based on observed means.

The error term is Mean Square(Error) = 12.170.

\*. The mean difference is significant at the 0.05 level.

### Multiple Comparisons

Dependent Variable: Kq

Tukey HSD

(I) Thickness	(J) Thickness	Mean Difference (I- J)	Std. Error	Sig.	95% Confidence Interval	
					Lower Bound	Upper Bound
6	9	-.05	.914	.998	-2.30	2.19
	12	-.12	1.117	.993	-2.87	2.63
9	6	.05	.914	.998	-2.19	2.30
	12	-.07	1.053	.998	-2.66	2.52
12	6	.12	1.117	.993	-2.63	2.87
	9	.07	1.053	.998	-2.52	2.66

Based on observed means.

The error term is Mean Square(Error) = 12.170.

### Multiple Comparisons

Dependent Variable: Kq

Tukey HSD

(I) Height	(J) Height	Mean			95% Confidence Interval	
		Difference (I-J)	Std. Error	Sig.	Lower Bound	Upper Bound
56	156	-6.82*	.883	<.001	-8.99	-4.64
	256	-8.86*	1.191	<.001	-11.79	-5.93
156	56	6.82*	.883	<.001	4.64	8.99
	256	-2.04	1.255	.249	-5.13	1.04
256	56	8.86*	1.191	<.001	5.93	11.79
	156	2.04	1.255	.249	-1.04	5.13

Based on observed means.

The error term is Mean Square(Error) = 12.170.

\*. The mean difference is significant at the 0.05 level.

### Multiple Comparisons

Dependent Variable: Kq

Tukey HSD

(I) Radial	(J) Radial	Mean			95% Confidence Interval	
		Difference (I-J)	Std. Error	Sig.	Lower Bound	Upper Bound
35	65	.26	1.018	.964	-2.24	2.77
	95	3.03*	.974	.011	.64	5.43
65	35	-.26	1.018	.964	-2.77	2.24
	95	2.77*	.963	.019	.40	5.14
95	35	-3.03*	.974	.011	-5.43	-.64
	65	-2.77*	.963	.019	-5.14	-.40

Based on observed means.

The error term is Mean Square(Error) = 12.170.

\*. The mean difference is significant at the 0.05 level.

## C - High Cycle Fatigue Data

thickness	radial	height	surface	orientation	metal condition	S	N
9	35	56	Machined	V	HIP	400	273455
9	35	56	Machined	V	HIP	600	51566
9	35	56	Machined	V	HIP	800	27769
9	35	56	Machined	V	HIP	400	297362
9	35	56	Machined	V	HIP	300	1389905
9	35	56	Machined	V	HIP	350	10000000
9	65	56	Machined	V	HIP	600	57971
9	65	56	Machined	V	HIP	800	23282
9	65	56	Machined	V	HIP	400	222169
9	65	56	Machined	V	HIP	350	881832
9	95	56	Machined	V	HIP	600	29007
9	95	56	Machined	V	HIP	800	23879
9	95	56	Machined	V	HIP	400	321234
9	95	56	Machined	V	HIP	350	16789140
9	35	156	Machined	V	HIP	400	278555
9	35	156	Machined	V	HIP	600	51483
9	35	156	Machined	V	HIP	800	32490
9	35	156	Machined	V	HIP	400	257832
9	35	156	Machined	V	HIP	300	10432280
9	65	156	Machined	V	HIP	800	15470
9	65	156	Machined	V	HIP	600	35237
9	65	156	Machined	V	HIP	400	200808
9	65	156	Machined	V	HIP	400	136769
9	95	156	Machined	V	HIP	800	27917
9	95	156	Machined	V	HIP	600	101059
9	95	156	Machined	V	HIP	400	1627730
9	95	156	Machined	V	HIP	400	1314813
9	95	156	Machined	V	HIP	400	152239
6	35	56	Machined	V	HIP	400	2852092
6	35	56	Machined	V	HIP	400	930000

6	35	56	Machined	V	HIP	600	67363
6	35	56	Machined	V	HIP	600	58019
6	35	56	Machined	V	HIP	600	18090
6	35	56	Machined	V	HIP	400	84453
6	65	56	Machined	V	HIP	800	19777
6	65	56	Machined	V	HIP	400	109688
6	65	56	Machined	V	HIP	600	41911
6	65	56	Machined	V	HIP	600	64558
6	65	56	Machined	V	HIP	600	58468
6	65	56	Machined	V	HIP	400	490654
6	95	56	Machined	V	HIP	400	127388
6	95	56	Machined	V	HIP	800	22341
6	95	56	Machined	V	HIP	600	70927
6	95	56	Machined	V	HIP	600	51632
6	95	56	Machined	V	HIP	600	46558
6	95	56	Machined	V	HIP	400	206463
6	95	56	Machined	V	HIP	800	13983
6	35	156	Machined	V	HIP	800	7761
6	35	156	Machined	V	HIP	400	227246
6	35	156	Machined	V	HIP	600	54417
6	35	156	Machined	V	HIP	600	18261
6	35	156	Machined	V	HIP	600	44770
6	35	156	Machined	V	HIP	400	150899
6	65	156	Machined	V	HIP	400	87274
6	65	156	Machined	V	HIP	400	1311433
6	65	156	Machined	V	HIP	600	39591
6	65	156	Machined	V	HIP	600	37466
6	65	156	Machined	V	HIP	600	48352
6	65	156	Machined	V	HIP	400	534735
6	95	156	Machined	V	HIP	400	121579
6	95	156	Machined	V	HIP	800	17415
6	95	156	Machined	V	HIP	600	48091
6	95	156	Machined	V	HIP	600	42518

6	95	156	Machined	V	HIP	600	27388
6	95	156	Machined	V	HIP	400	225850
6	95	156	Machined	V	HIP	800	16746
6			AB	V	HIP	600	9954
6			AB	V	HIP	600	7809
6			AB	V	HIP	400	35139
6			AB	V	HIP	400	25241
6			AB	V	HIP	200	410680
6			AB	V	HIP	200	552139
6			AB	V	HIP	300	130540
6			AB	V	HIP	300	903500
6			AB	V	HIP	300	1718251
6			AB	V	HIP	580	10460
6			AB	V	HIP	400	37195
6			AB	V	HIP	400	43348
6			AB	V	HIP	400	38254
6			AB	V	HIP	300	104399
6			AB	V	HIP	300	98846
6			AB	V	HIP	200	523284
6			AB	V	HIP	200	478665
6			AB	V	HIP	300	90382
6			AB	V	HIP	580	8737
6			AB	V	HIP	400	22358
6			AB	V	HIP	400	25039
6			AB	V	HIP	300	95975
6			AB	V	HIP	300	96998
6			AB	V	HIP	200	636428
6			AB	V	HIP	200	1000000
6			AB	V	HIP	300	98659
6			AB	V	HIP	200	1694095
6			AB	V	HIP	580	8106
6			AB	V	HIP	400	32113
6			AB	V	HIP	400	36988

6			AB	V	HIP	300	103467
6			AB	V	HIP	300	101003
6			AB	V	HIP	200	986103
6			AB	V	HIP	200	1623521
6			AB	V	HIP	200	541159
6			AB	V	HIP	300	111279
9	35	56	Machined	H	AB	400	10066553
9	35	56	Machined	H	AB	800	41326
9	35	56	Machined	H	AB	400	10081474
9	35	156	Machined	H	AB	550	137387
9	35	156	Machined	H	AB	700	156048
9	65	56	Machined	H	AB	550	2572613
9	65	56	Machined	H	AB	800	60915
9	65	56	Machined	H	AB	400	10030000
9	65	156	Machined	H	AB	550	2140446
9	65	156	Machined	H	AB	700	51209
9	65	156	Machined	H	AB	550	3436587
9	65	56	Machined	H	AB	400	10339128
9	65	56	Machined	H	AB	550	3802823
9	65	56	Machined	H	AB	700	47428
9	65	156	Machined	H	AB	550	1271042
9	65	156	Machined	H	AB	700	49778
9	95	56	Machined	H	AB	550	687701
9	95	56	Machined	H	AB	700	58676
9	95	156	Machined	H	AB	550	3423174
9	95	156	Machined	H	AB	700	141937
9	95	156	Machined	H	AB	400	11347166
9	95	156	Machined	H	AB	400	2556625
9	95	156	Machined	H	AB	700	31959
9	95	156	Machined	H	AB		
6	95	56	Machined	H	AB	700	32536
6	95	56	Machined	H	AB	550	3303424
6	95	56	Machined	H	AB	700	52667

6	95	56	Machined	H	AB	550	1957079
6	95	56	Machined	H	AB	400	11000000
6	95	156	Machined	H	AB	700	43915
6	95	156	Machined	H	AB	550	186000
6	95	156	Machined	H	AB	700	38081
6	95	156	Machined	H	AB	550	115620
6	95	156	Machined	H	AB	400	14000000
9	65	56	SP	V	HIP	600	145040
9	65	156	SP	V	HIP	800	78836
9	95	56	SP	V	HIP	500	813481
9	95	56	SP	V	HIP	600	614010
9	95	56	SP	V	HIP	800	45046
9	35	156	SP	V	HIP	600	432629
9	65	156	SP	V	HIP	600	714965
9	65	156	SP	V	HIP	800	105534
9	95	156	SP	V	HIP	600	462594
9	95	156	SP	V	HIP	800	144841
9	35	111	SP	H	HIP	600	158429
9	35	48	SP	H	AB	600	651296
9	35	206	SP	H	AB	800	64094
9	65	17	SP	H	AB	600	542236
9	65	111	SP	H	AB	800	157808
9	65	206	SP	H	AB	500	873517
9	95	17	SP	H	AB	800	95469
9	95	111	SP	H	AB	600	577906
9	95	17	SP	H	AB	600	583044
9	95	48	SP	H	AB	800	147354
9	95	80	SP	H	AB	400	10406139
9	95	111	SP	H	AB	800	80283
9	35	17	Machined	H	HIP	400	198366
9	35	48	Machined	H	HIP	550	80959
9	35	80	Machined	H	HIP	700	37267
9	35	143	Machined	H	HIP	550	73156

9	35	174	Machined	H	HIP	700	37777
9	35	206	Machined	H	HIP	400	8439724
6	35	9	Machined	H	HIP	400	8873569
6	35	30	Machined	H	HIP	550	57379
6	35	51	Machined	H	HIP	700	27793
6	35	72	Machined	H	HIP	400	269934
6	35	93	Machined	H	HIP	550	67135
6	35	114	Machined	H	HIP	700	34380
6	35	135	Machined	H	HIP	400	1571448
6	35	156	Machined	H	HIP	700	21685
6	35	177	Machined	H	HIP	550	57036
6	35	198	Machined	H	HIP	550	73437

*HCF Regression Equations*

**Model Summary**

Model	R	R Square	Adjusted R Square	Std. Error of the Estimate
1	.884 <sup>a</sup>	.782	.762	.43623

a. Predictors: (Constant), LogRv, LogT, LogStress, LogHV, LogrootArea, LogRz10

**ANOVA<sup>a</sup>**

Model		Sum of Squares	df	Mean Square	F	Sig.
1	Regression	46.327	6	7.721	40.574	<.001 <sup>b</sup>
	Residual	12.940	68	.190		
	Total	59.267	74			

a. Dependent Variable: LogCycles

b. Predictors: (Constant), LogRv, LogT, LogStress, LogHV, LogrootArea, LogRz10

**Coefficients<sup>a</sup>**

Model		Unstandardized Coefficients		Standardized Coefficients	t	Sig.
		B	Std. Error	Beta		
1	(Constant)	-17.525	11.367		-1.542	.128
	LogStress	-5.320	.441	-.836	-12.061	<.001
	LogT	2.161	.712	.204	3.034	.003
	LogHV	11.978	4.555	.348	2.630	.011
	LogrootArea	3.220	1.119	.377	2.879	.005
	LogRz10	3.007	1.318	1.514	2.282	.026
	LogRv	-4.297	1.611	-1.954	-2.668	.010

a. Dependent Variable: LogCycles

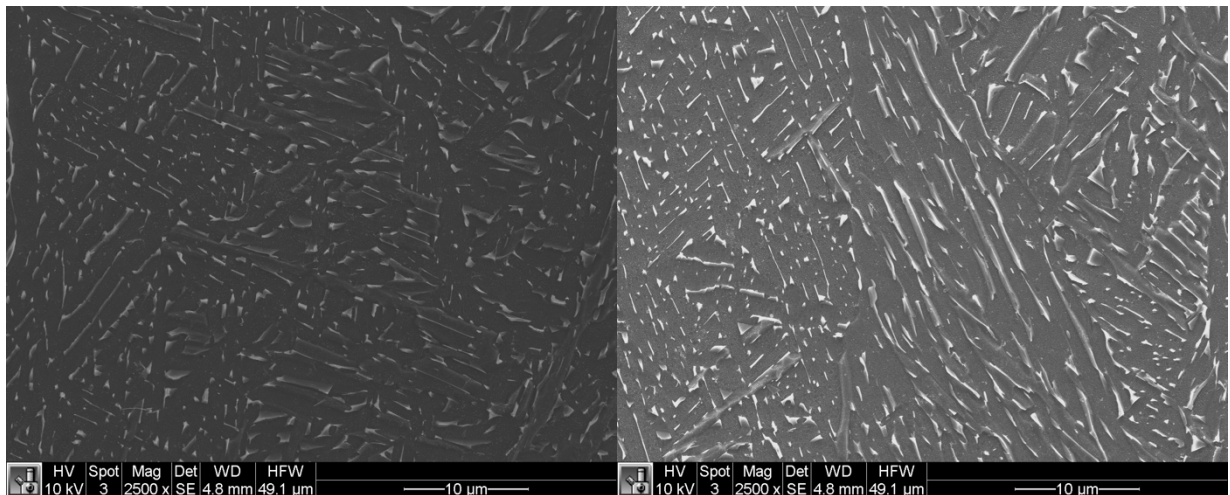
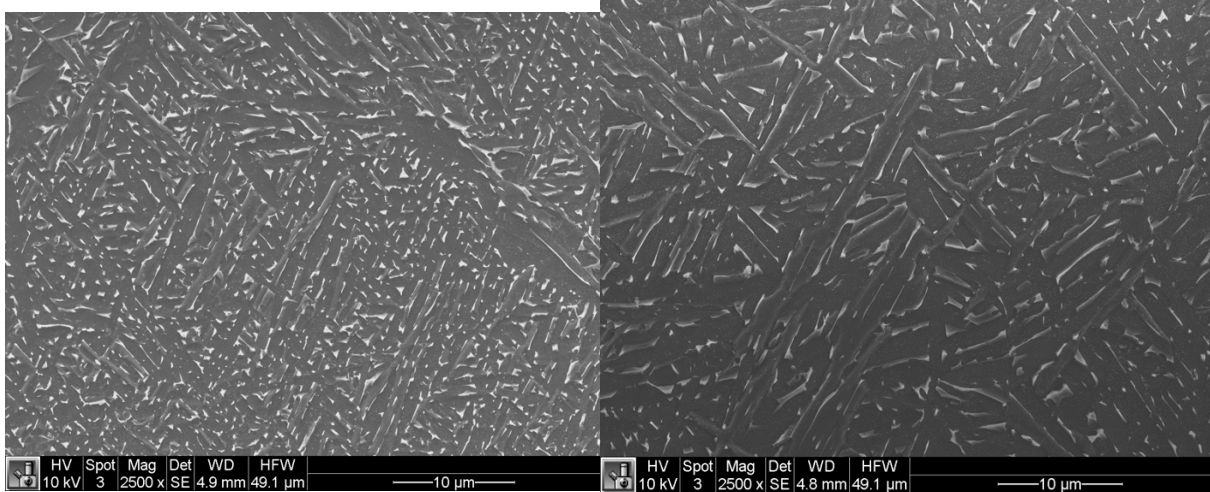
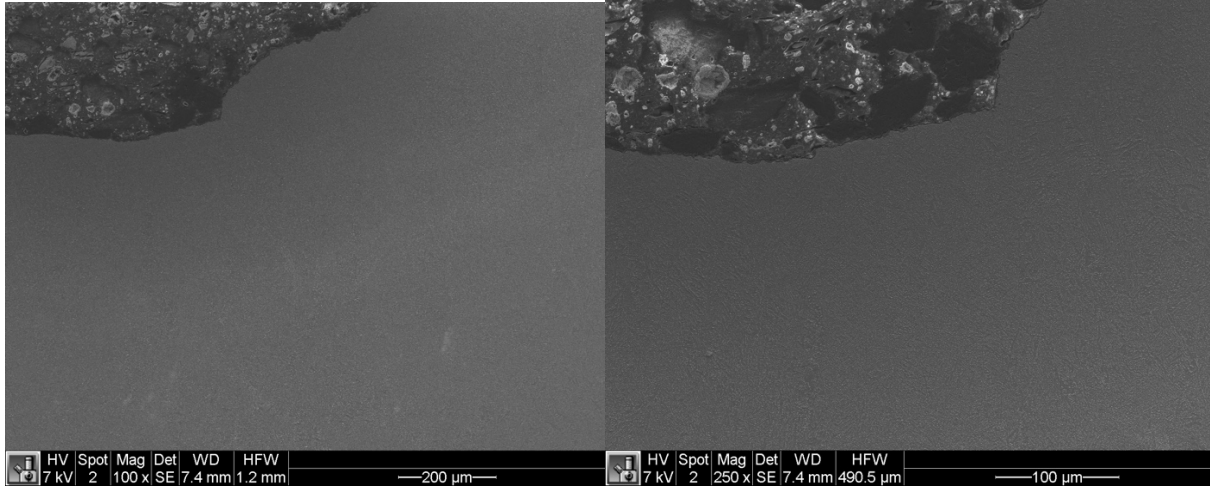
### *Murakami Defect Area*

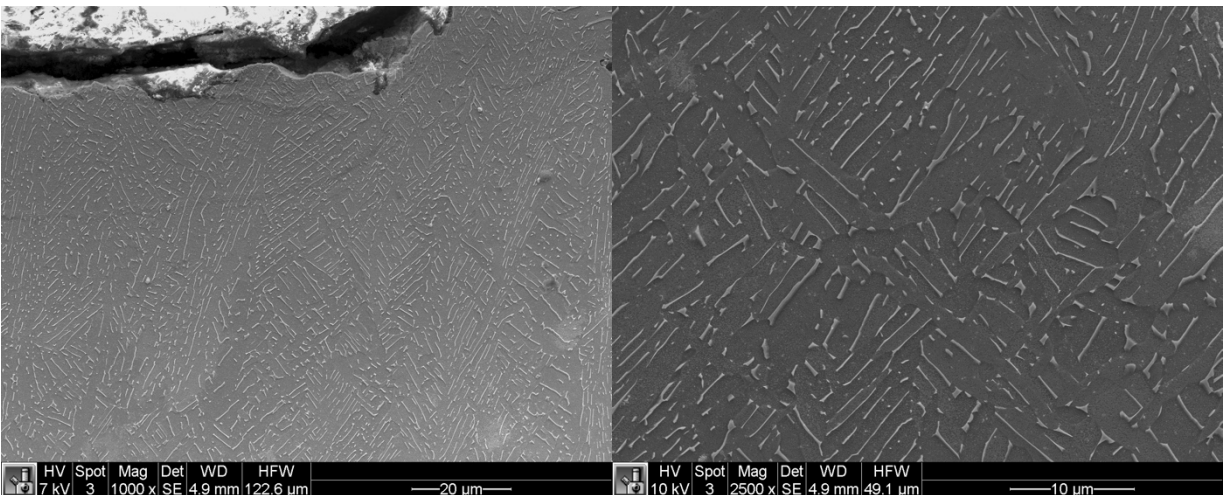
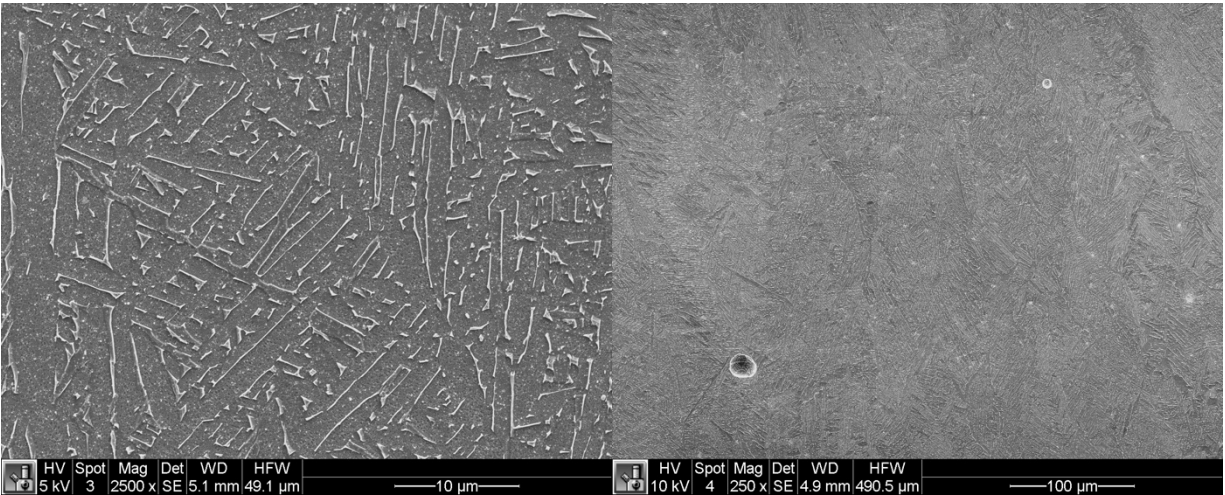
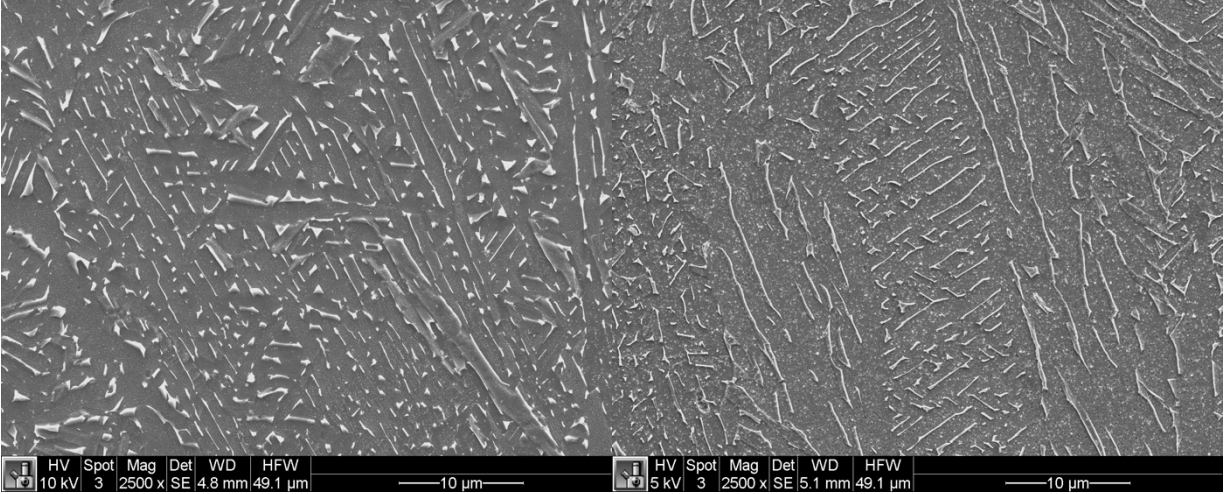
Label	$\sqrt{\text{Area}}$
A3_3.TIF	41.5616049
A3_3.TIF	13.3003383
A3_3.TIF	37.619051
C1_1.TIF	63.887127
C5_3.TIF	65.8355527
C5_4.TIF	53.2403982
C5_1.TIF	33.4142634
C6_1.TIF	67.8310106
C6_3.TIF	44.5190296
C6_12.TIF	43.8900217
B9	77.5826591
B9	76.2689321
B9	65.1053608
B9	56.1553203
F2_14.TIF	79.6886127
F2_14.TIF	91.5257778
F3_2.TIF	79.1305314
F3_1.TIF	52.1717644
A7_1.TIF	88.6428508
D2_5.TIF	65.0667965
E2	0
AP7_2.TIF	227.190973
S6_218_6.TIF	199.34874
s15_1.TIF	261.577826
B2S9_10.TIF	178.94087

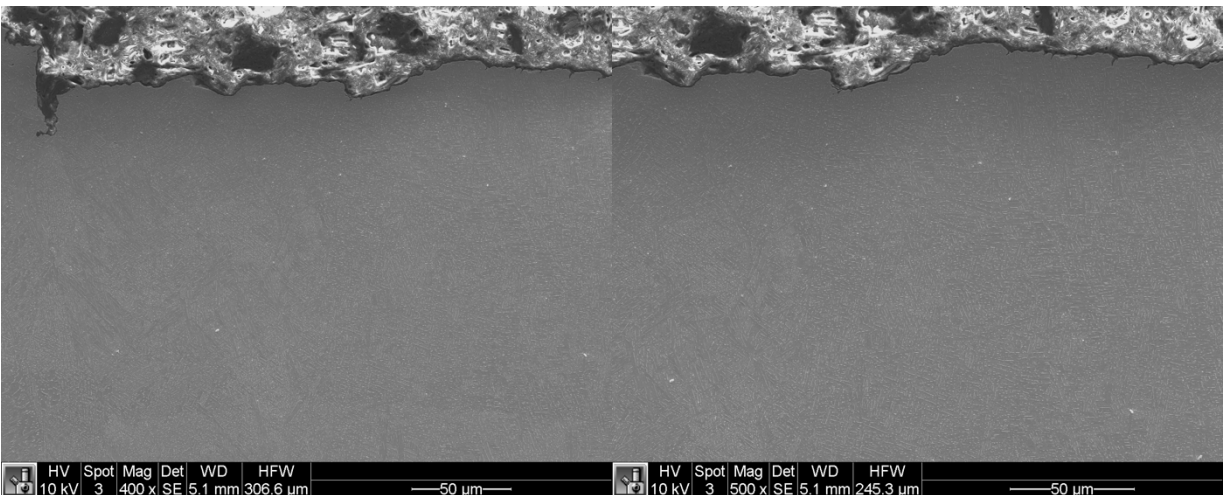
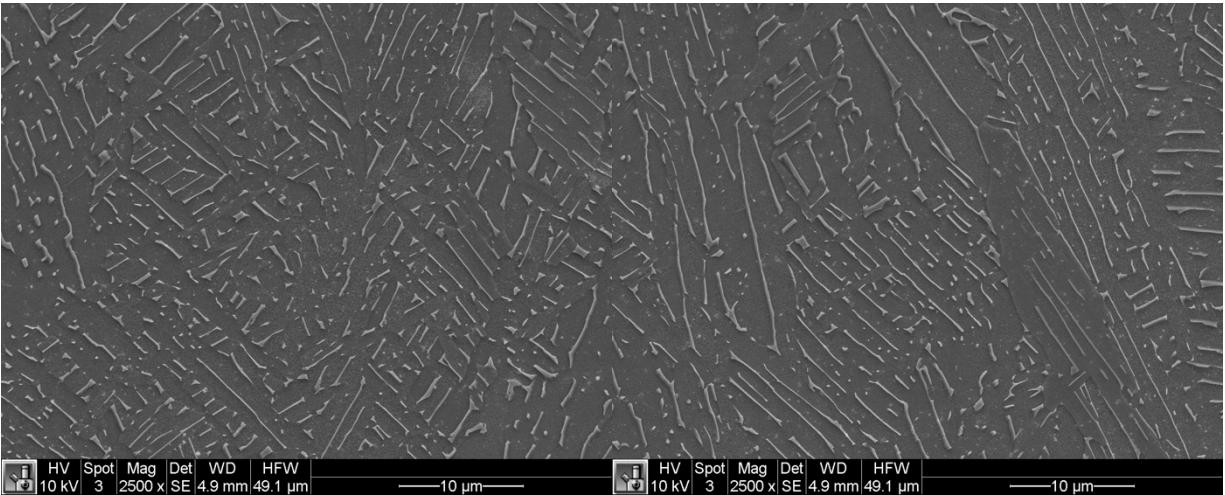
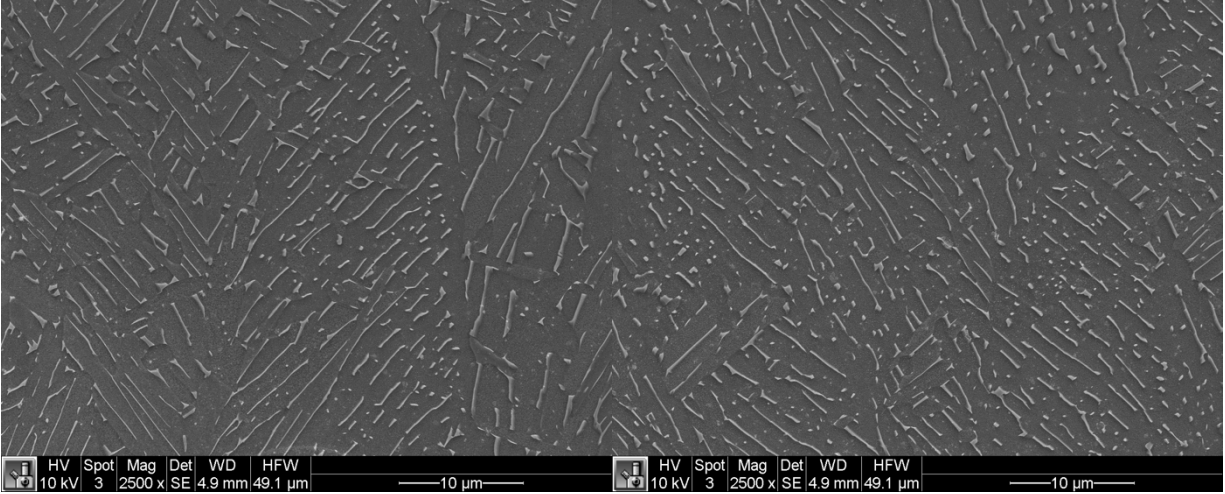
# D – Microstructure

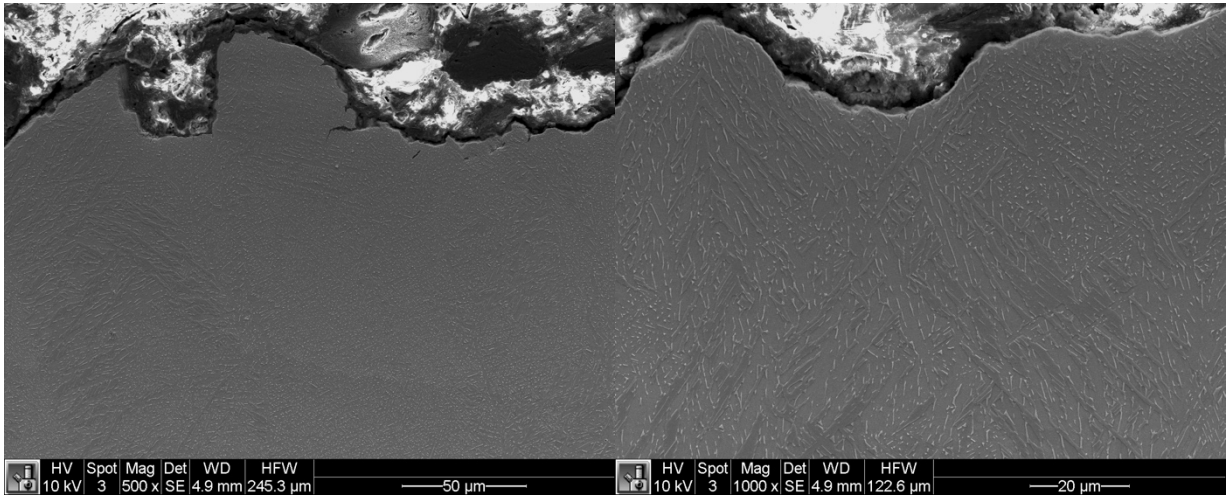
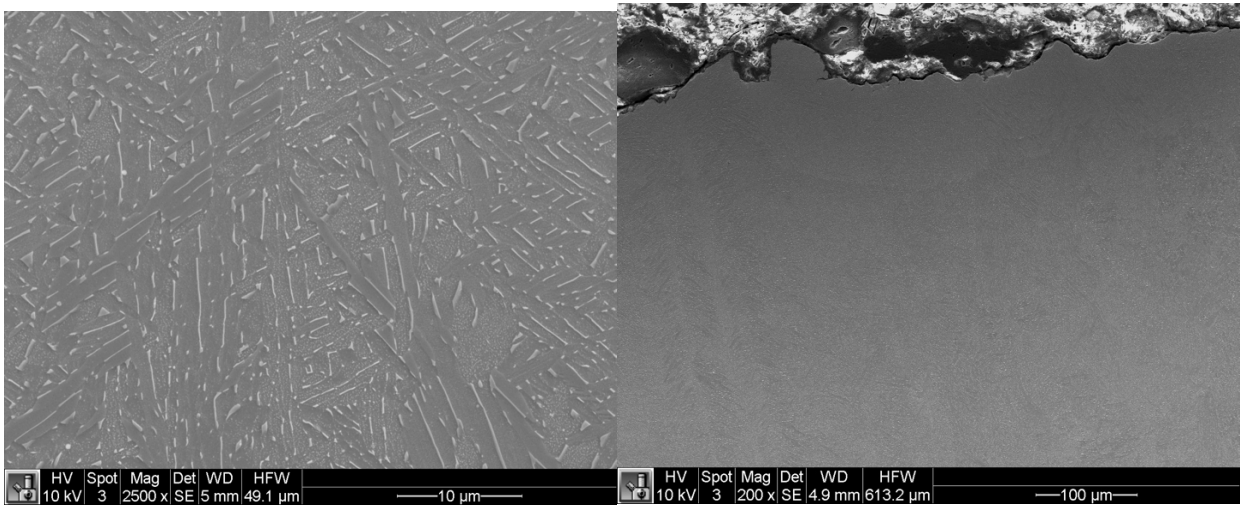
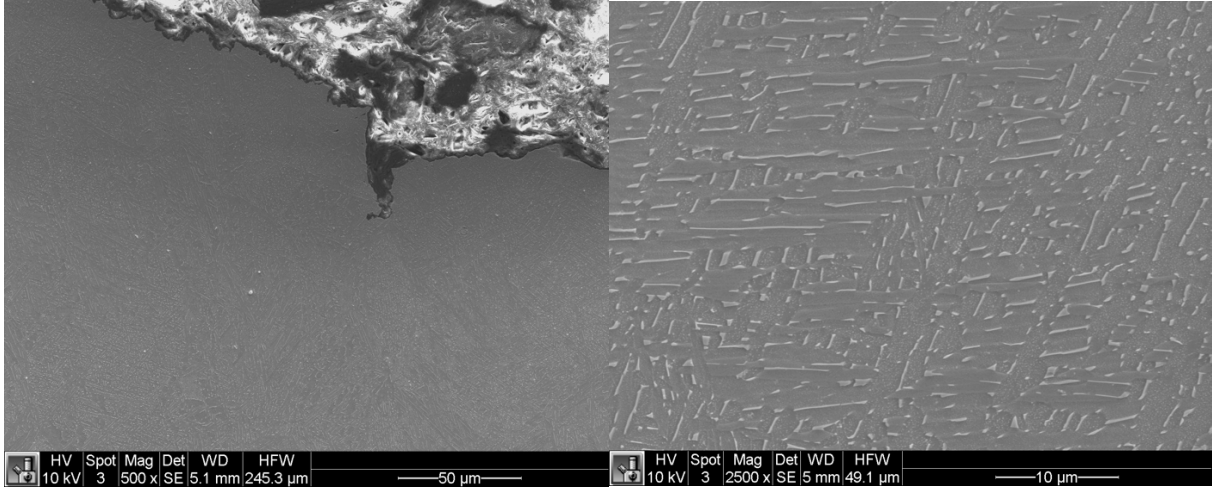
## SEM Micrographs

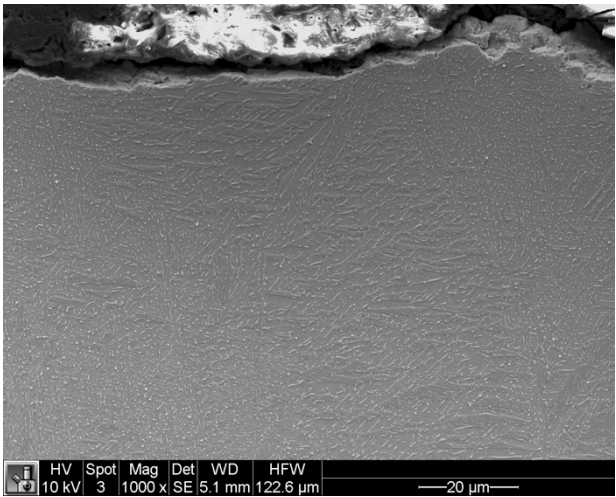
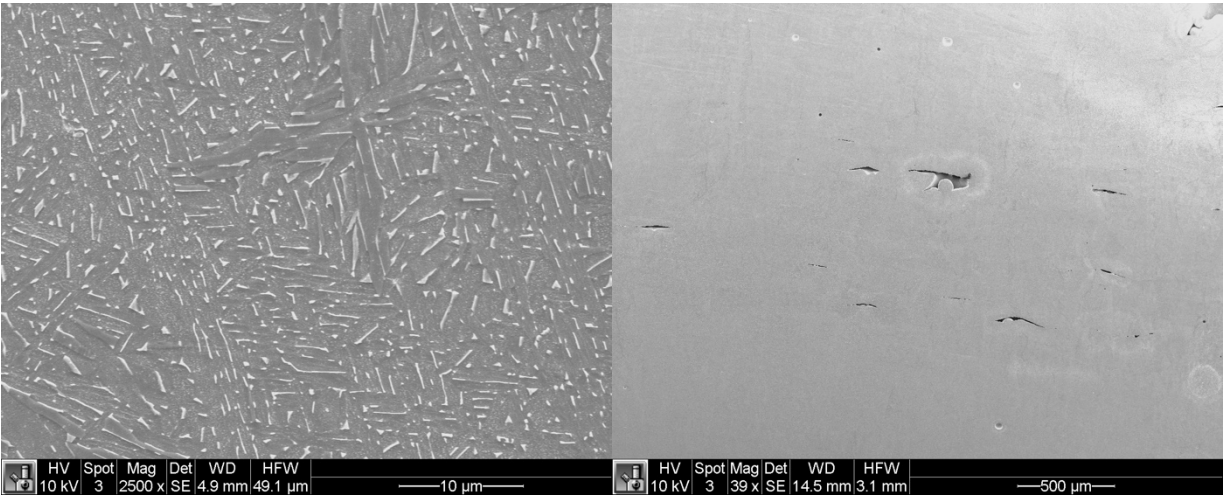
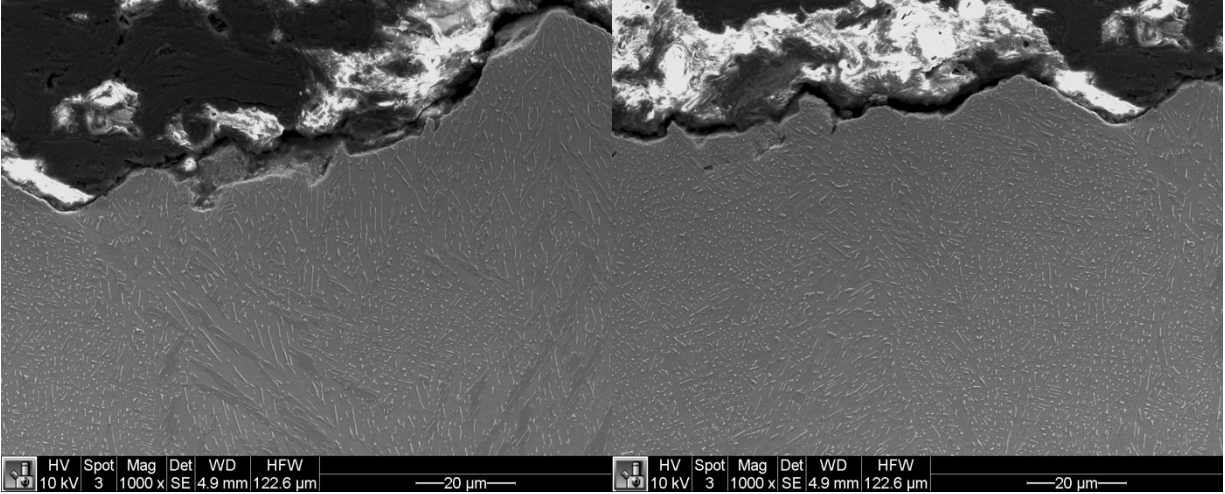
### ZX As-Built



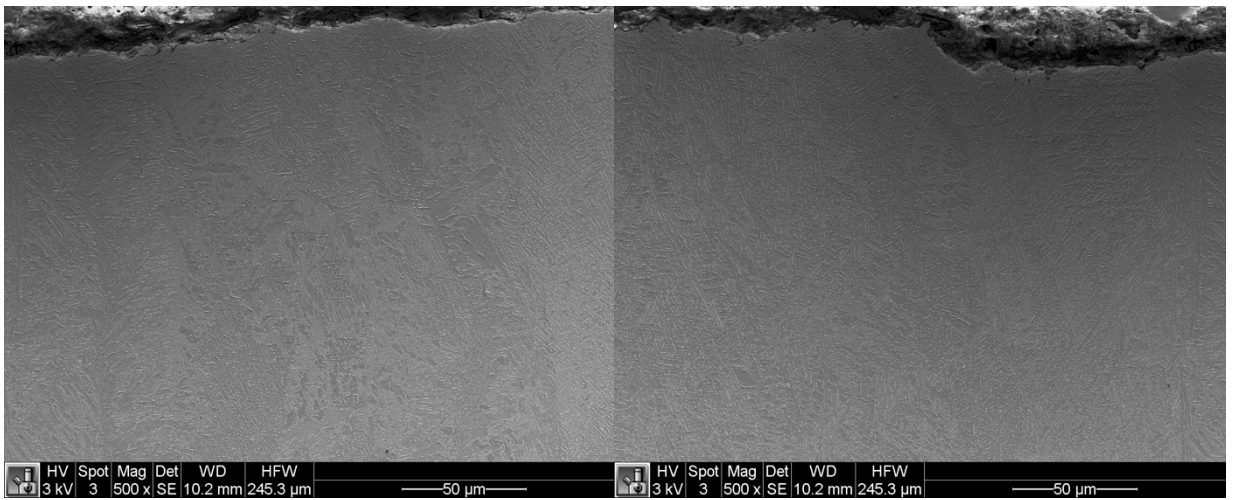
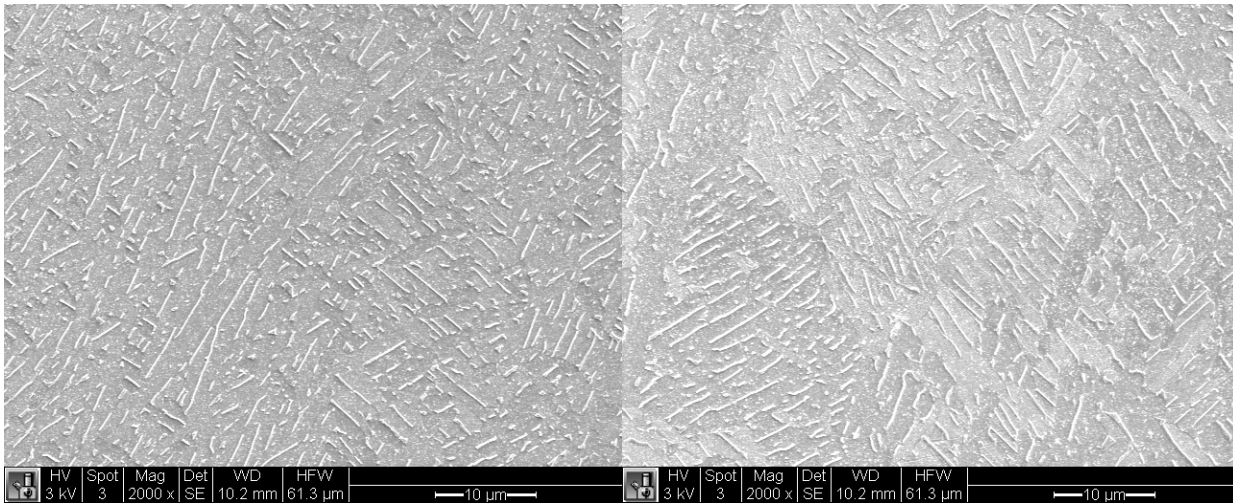
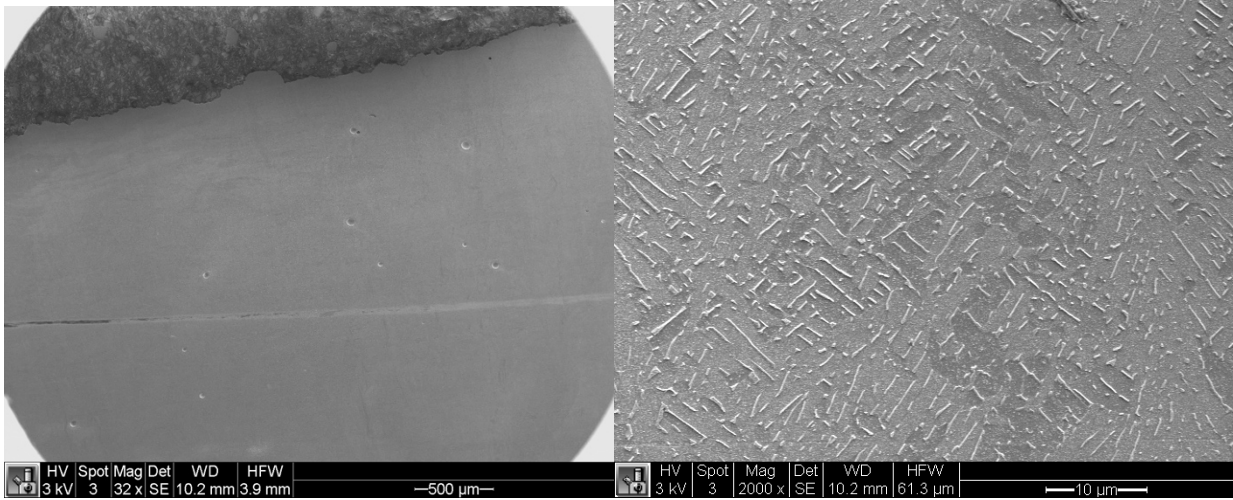


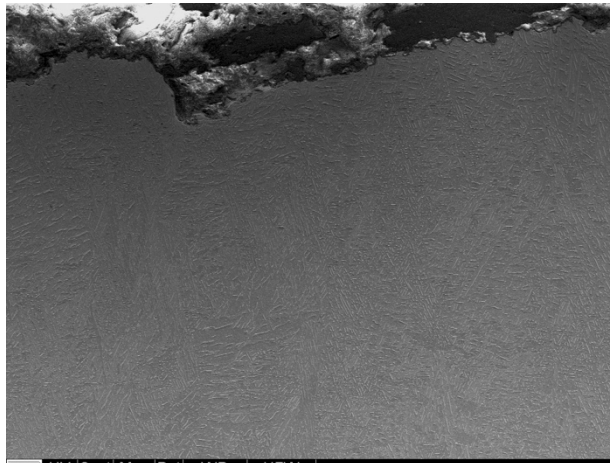






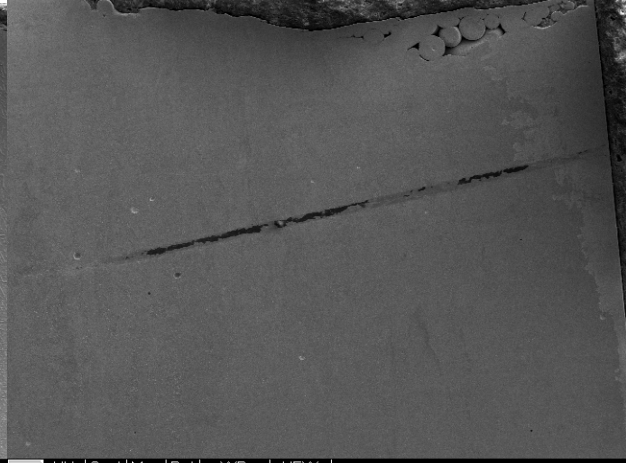
# ZX Machined





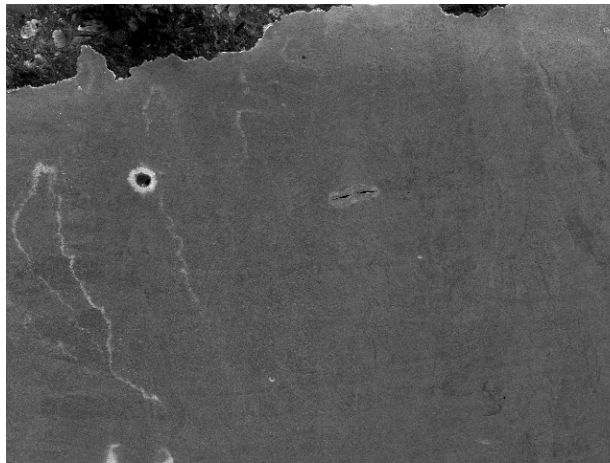
HV	Spot	Mag	Det	WD	HFW
3 kV	3	500 x	SE	10.2 mm	245.3 μm

50 μm



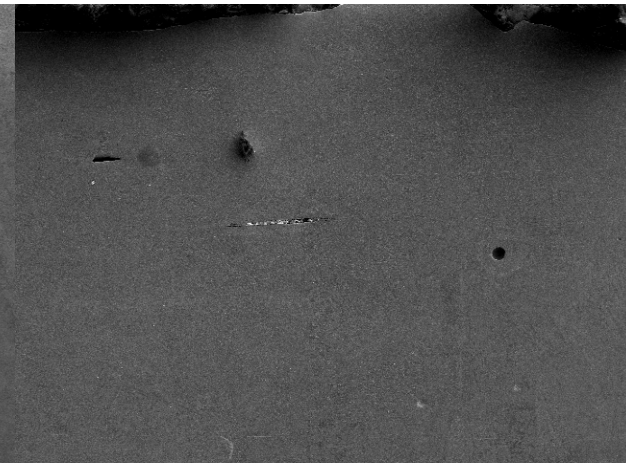
HV	Spot	Mag	Det	WD	HFW
3 kV	3	59 x	SE	13.4 mm	2.1 mm

500 μm



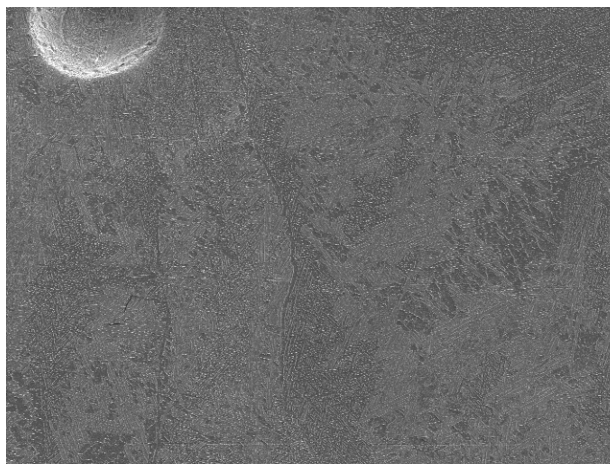
HV	Spot	Mag	Det	WD	HFW
2 kV	3	59 x	SE	13.7 mm	2.1 mm

500 μm



HV	Spot	Mag	Det	WD	HFW
2 kV	3	127 x	SE	10.4 mm	968.5 μm

200 μm



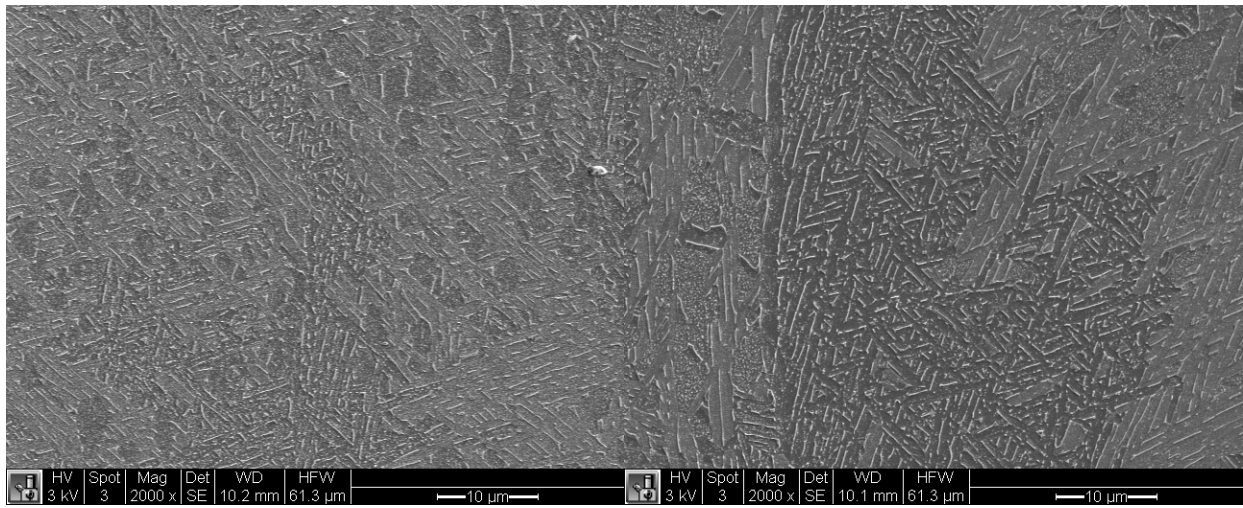
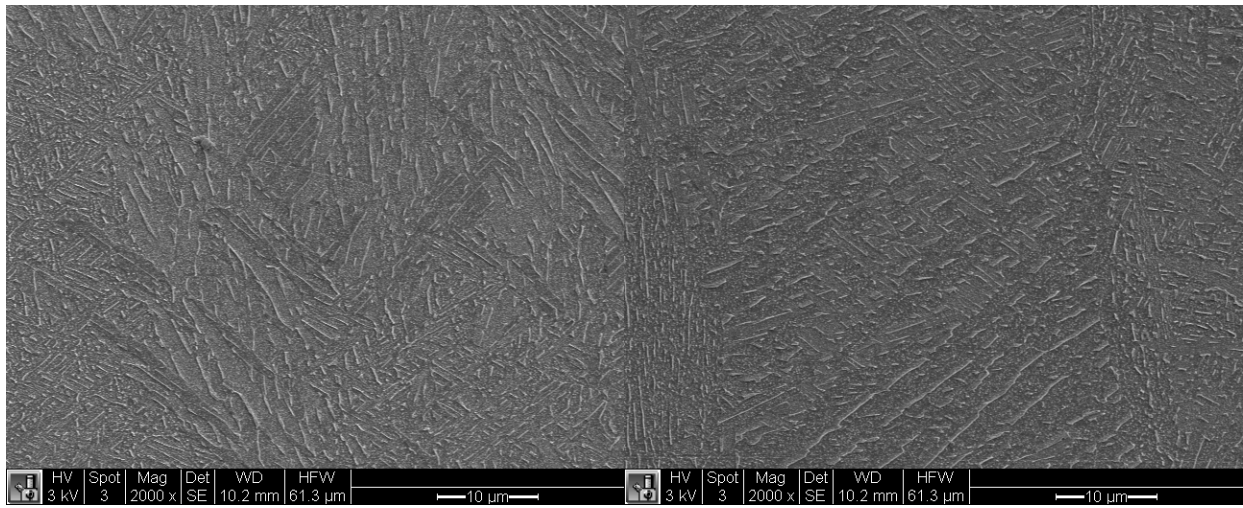
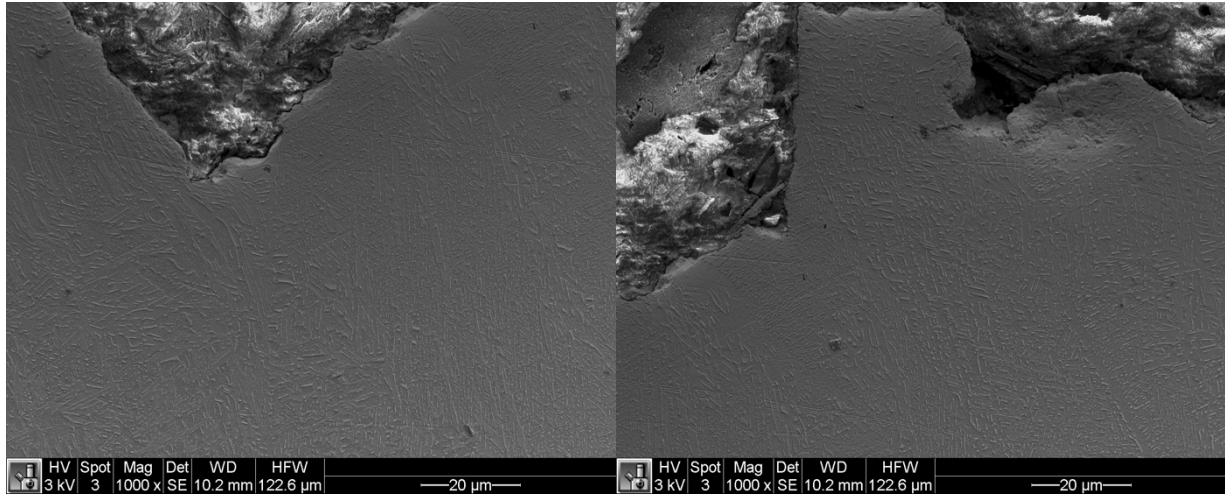
HV	Spot	Mag	Det	WD	HFW
3 kV	3	500 x	SE	10.1 mm	245.3 μm

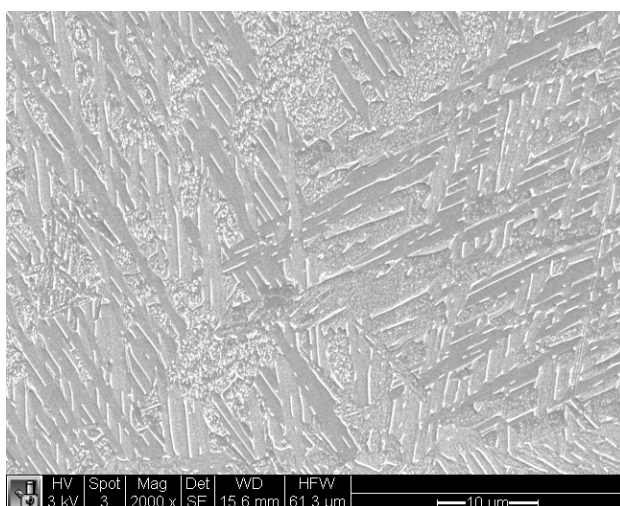
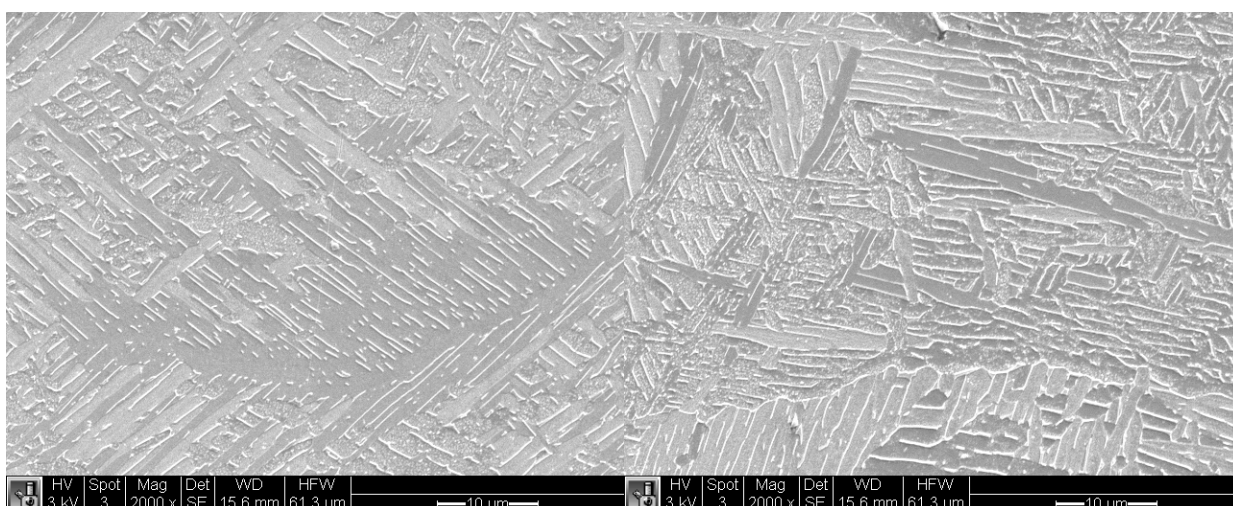
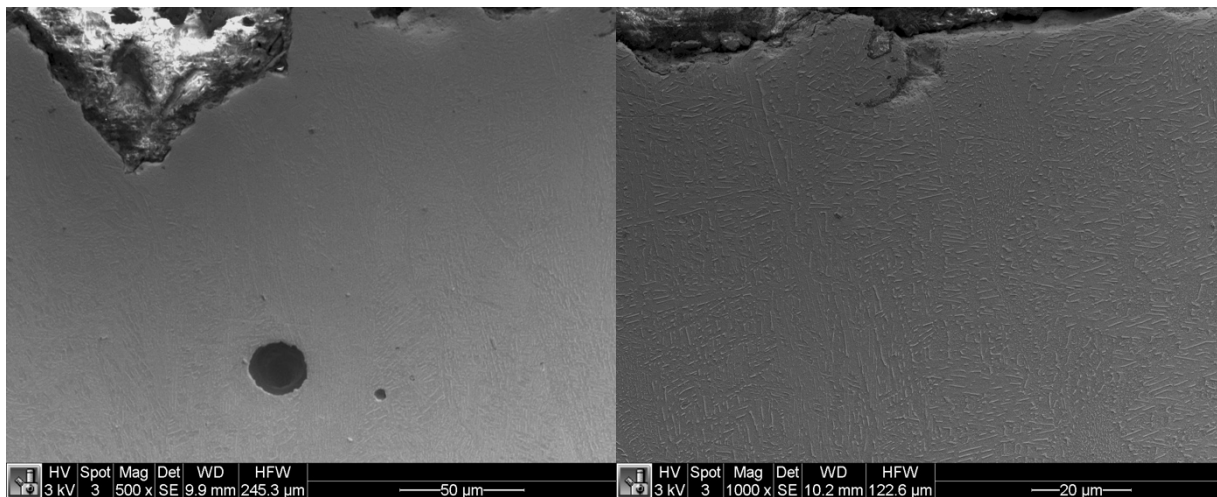
50 μm



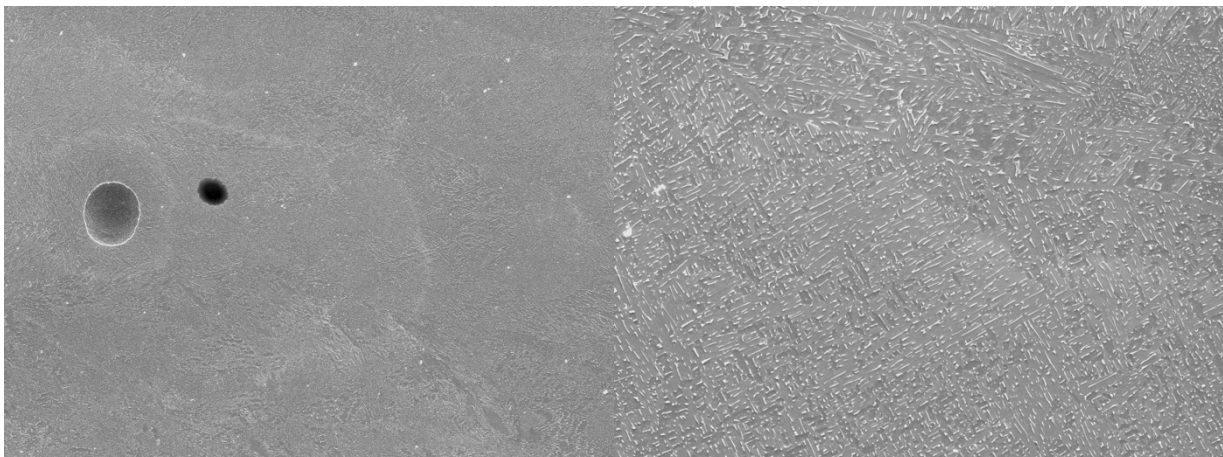
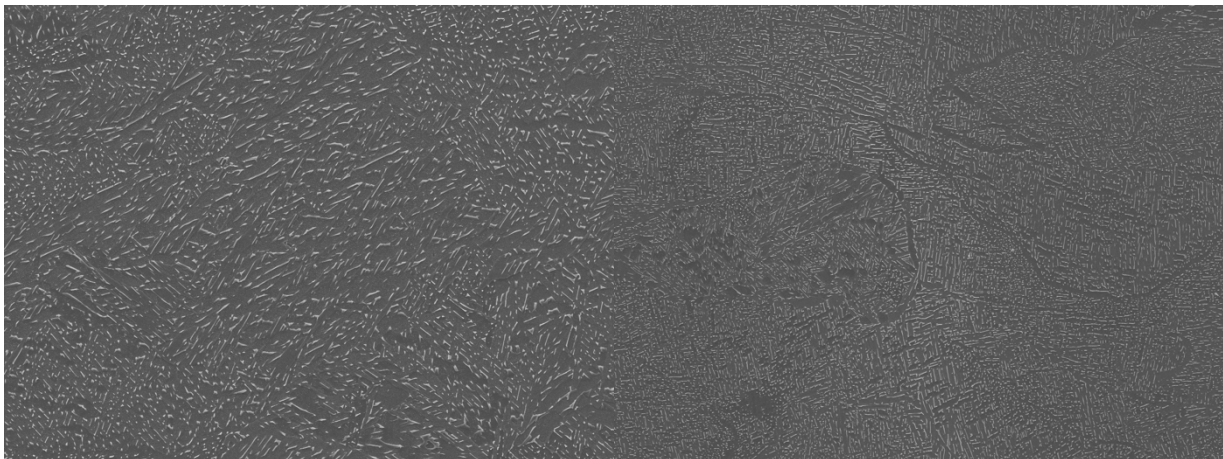
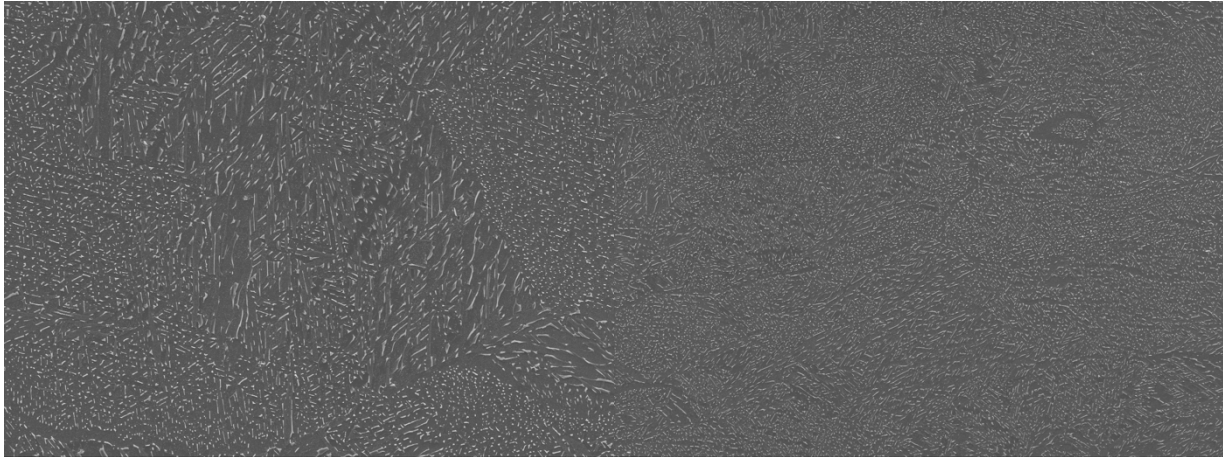
HV	Spot	Mag	Det	WD	HFW
2 kV	2	506 x	SE	10.2 mm	242.1 μm

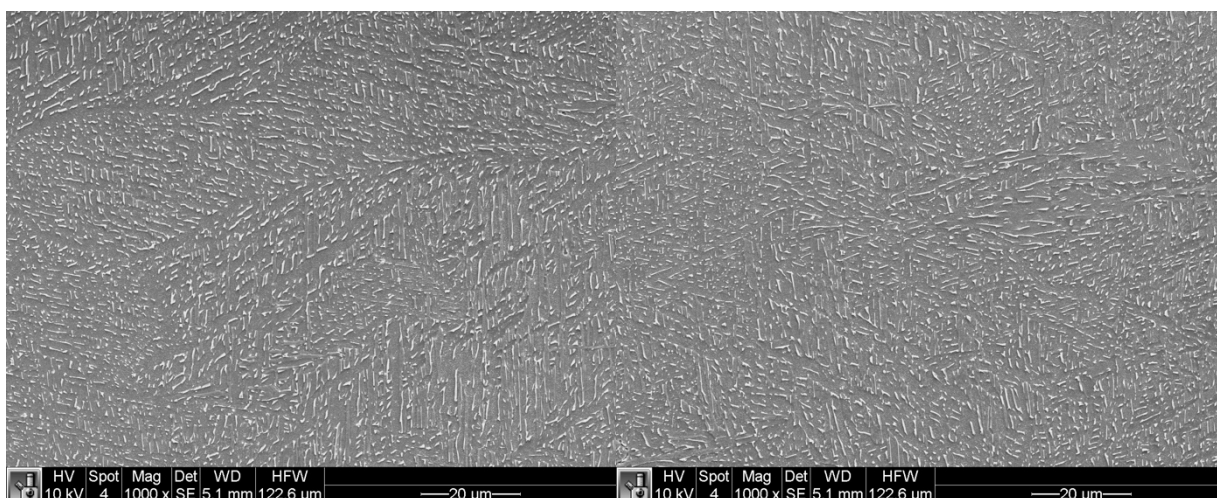
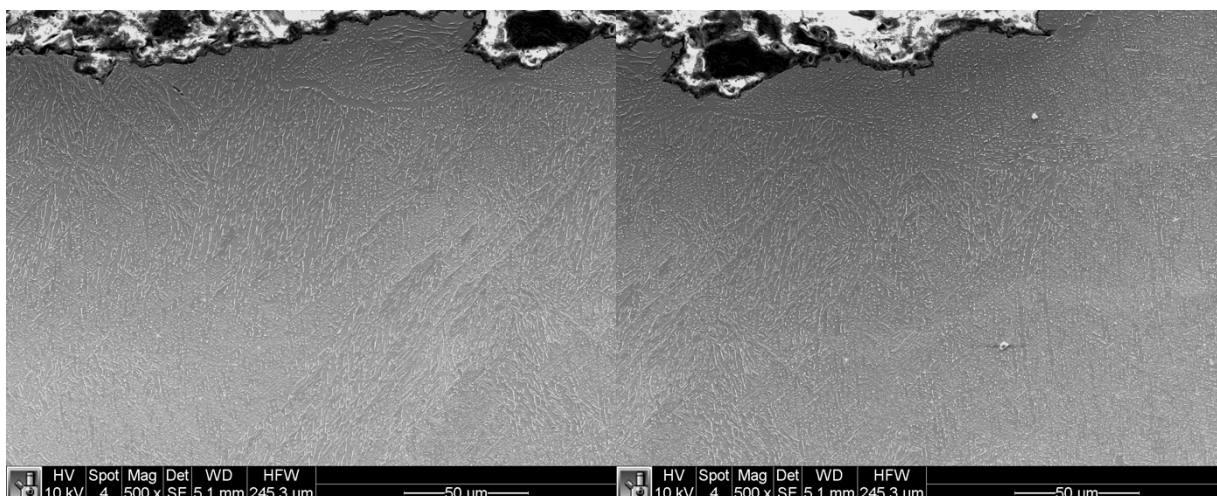
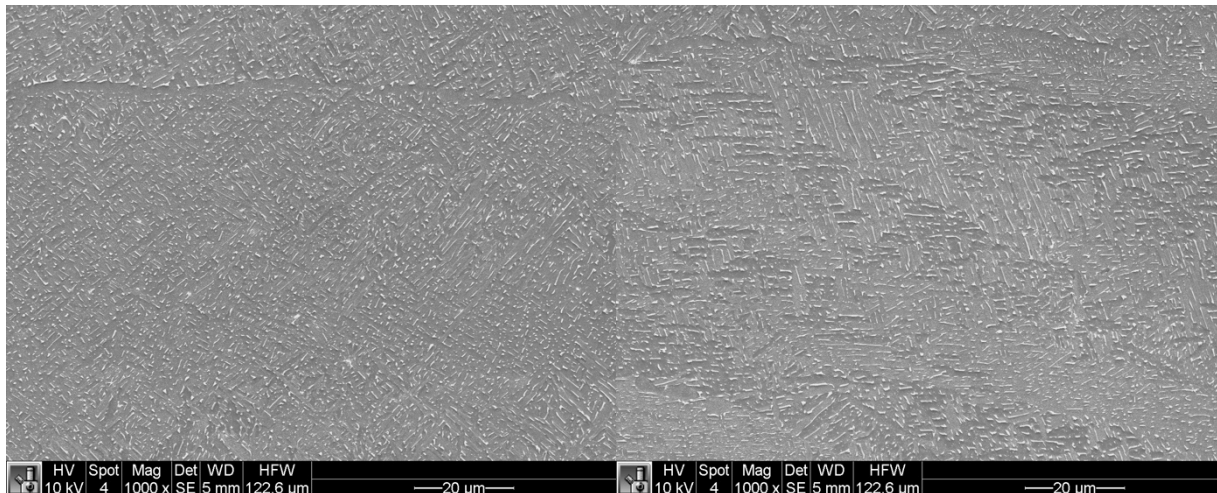
50 μm

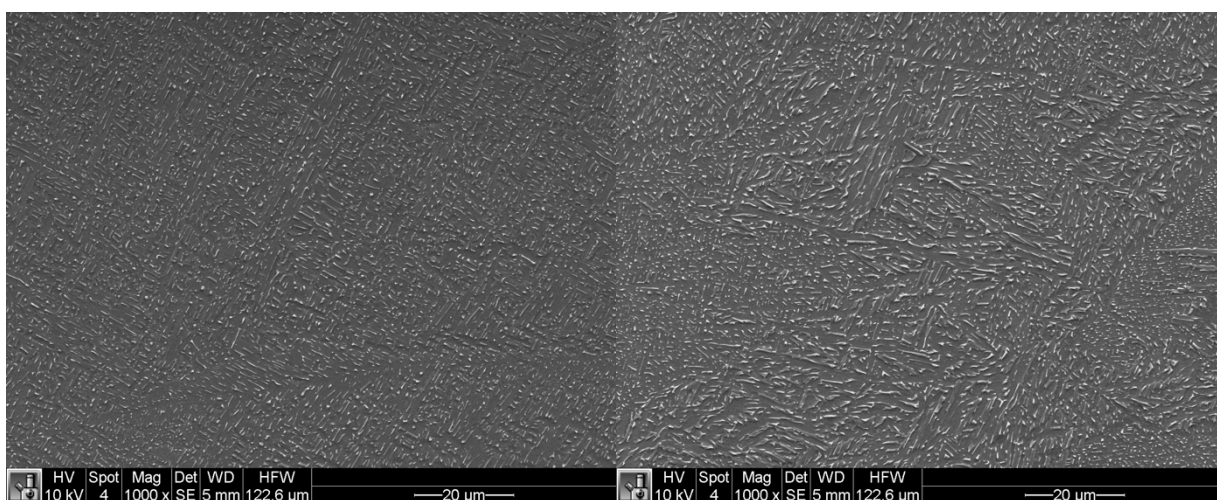
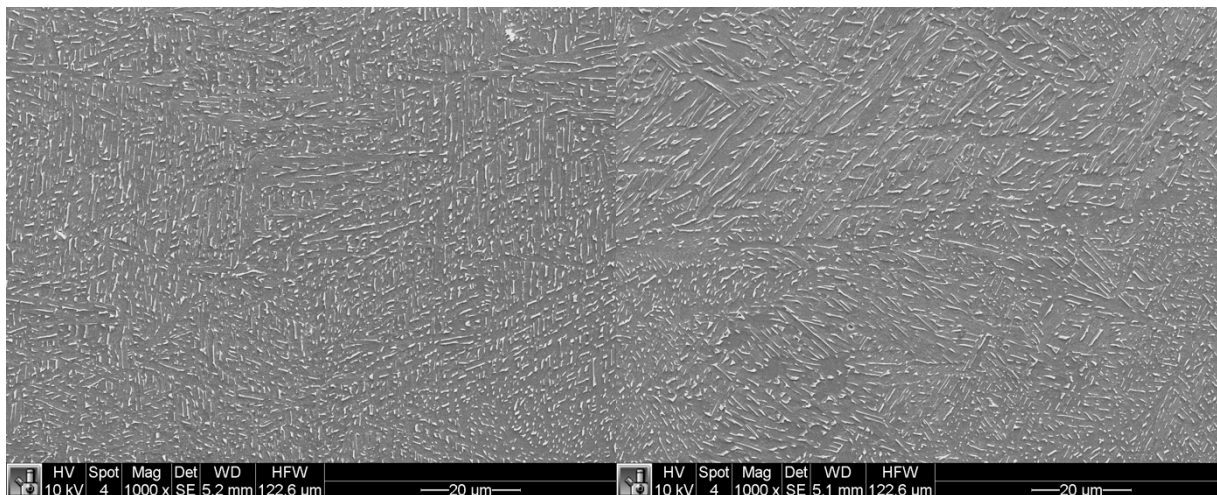


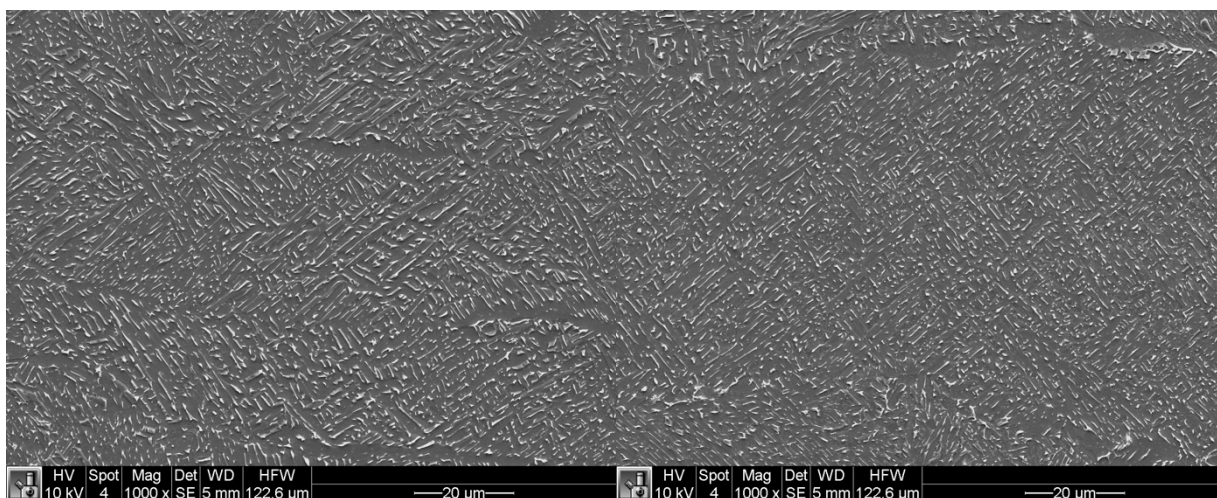
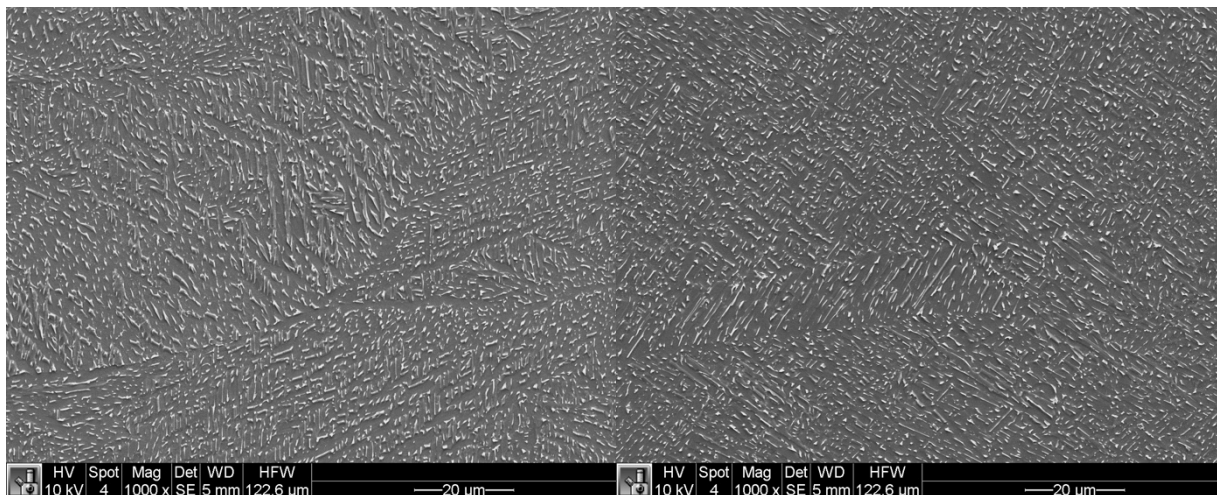


# XZ Machined

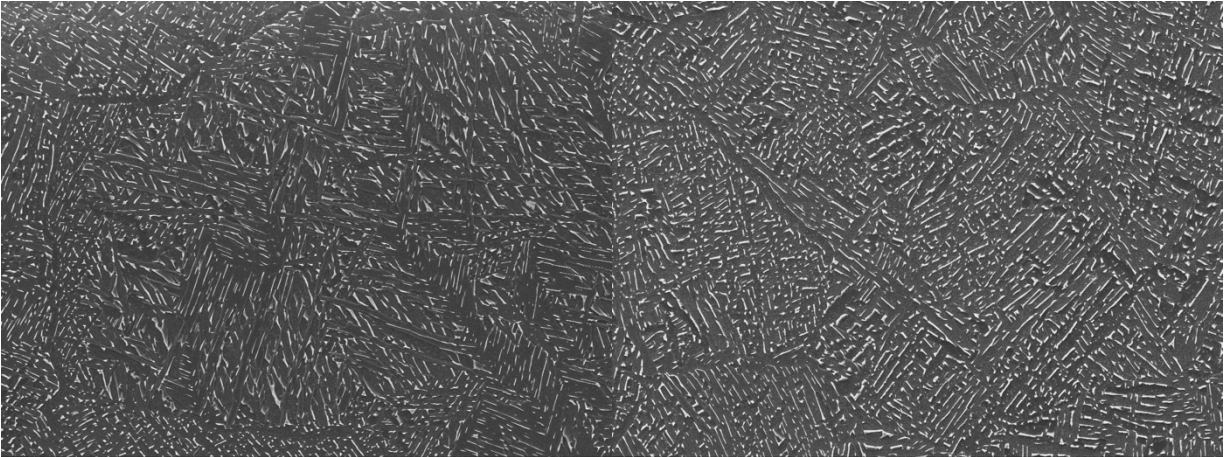






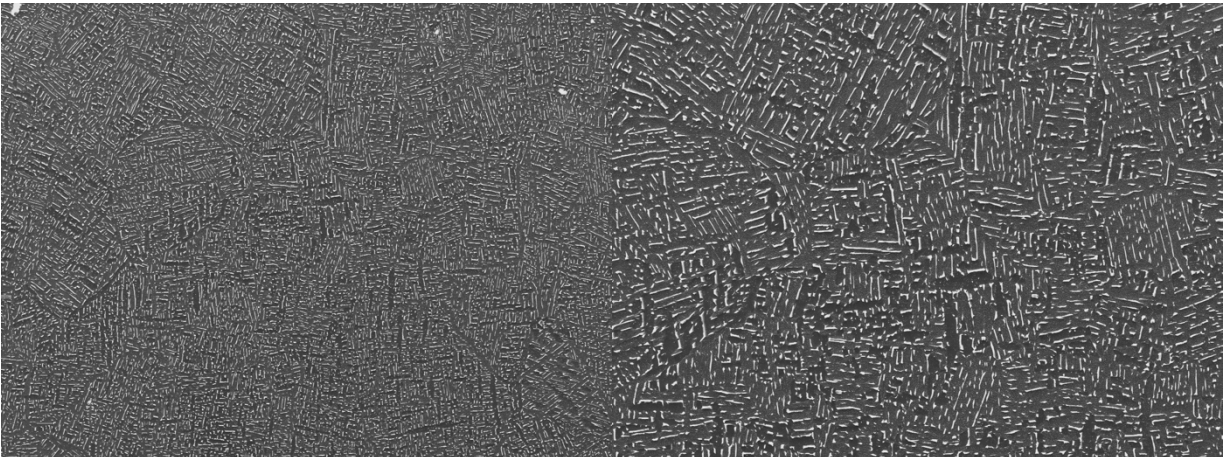


# XY Machined



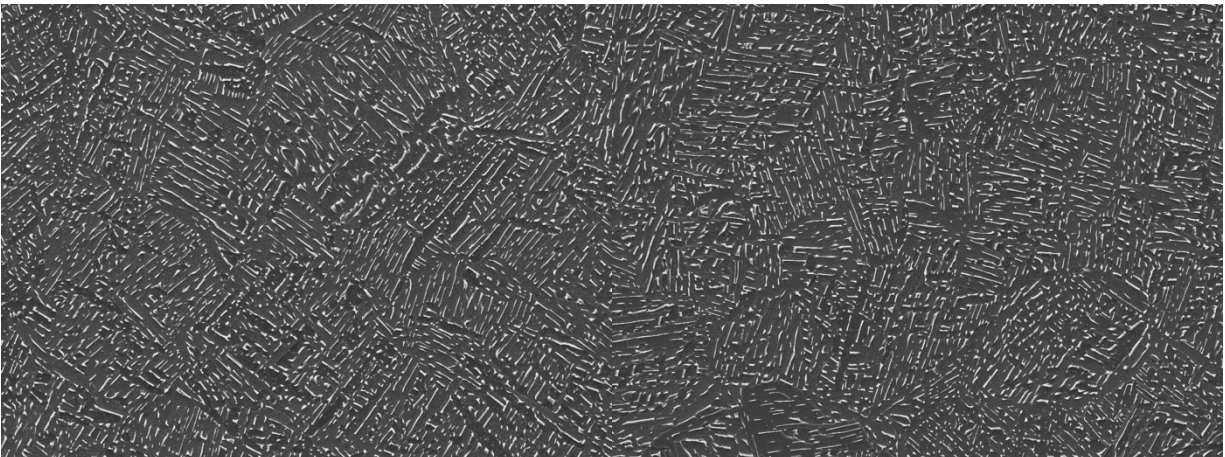
	HV	Spot	Mag	Det	WD	HFWD	
10 kV	4	1000 x	SE	5 mm	122.6 μm		—20 μm—

	HV	Spot	Mag	Det	WD	HFWD	
10 kV	4	1000 x	SE	5 mm	122.6 μm		—20 μm—



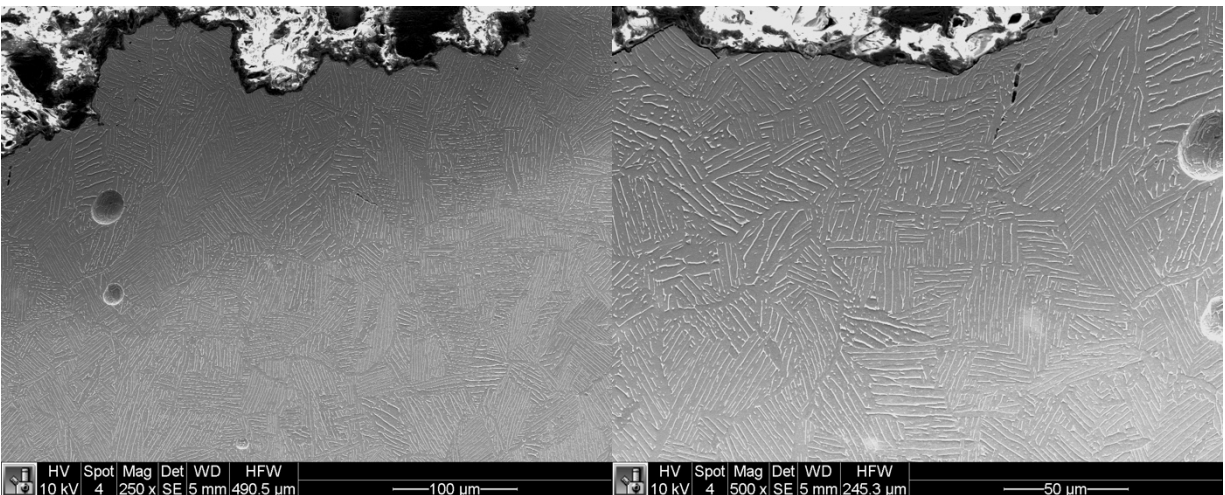
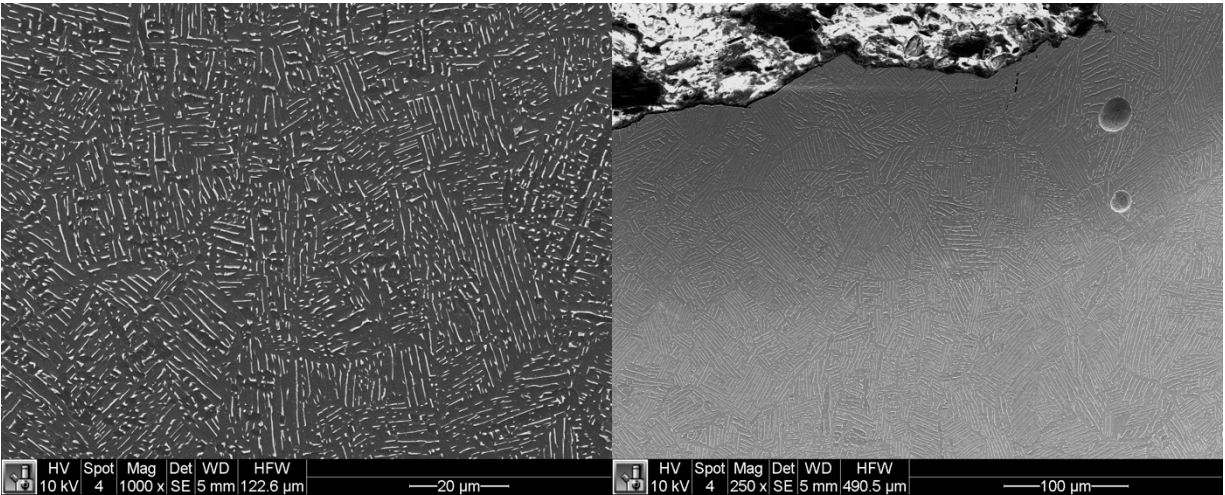
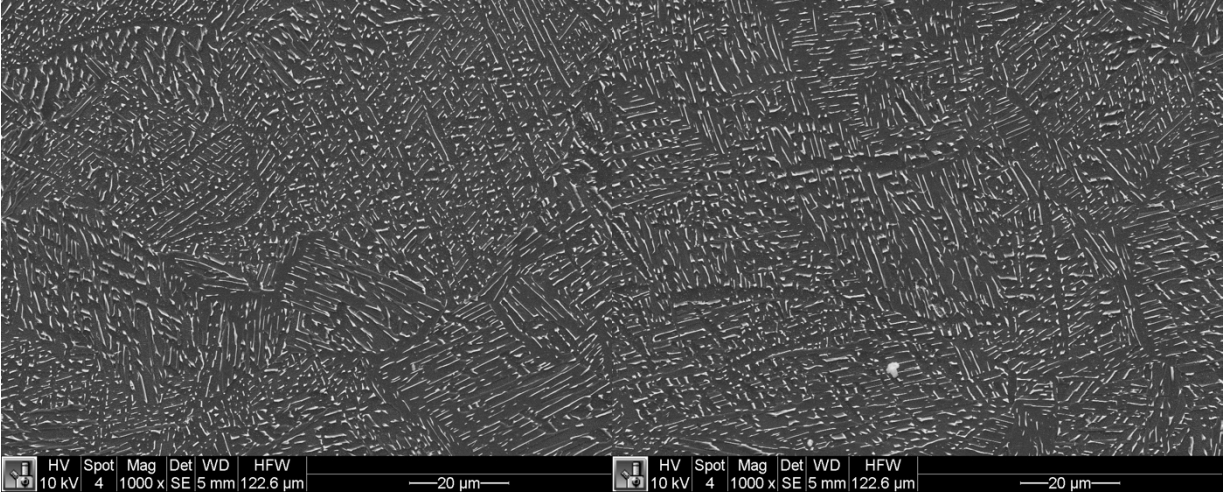
	HV	Spot	Mag	Det	WD	HFWD	
10 kV	4	500 x	SE	5 mm	245.3 μm		—50 μm—

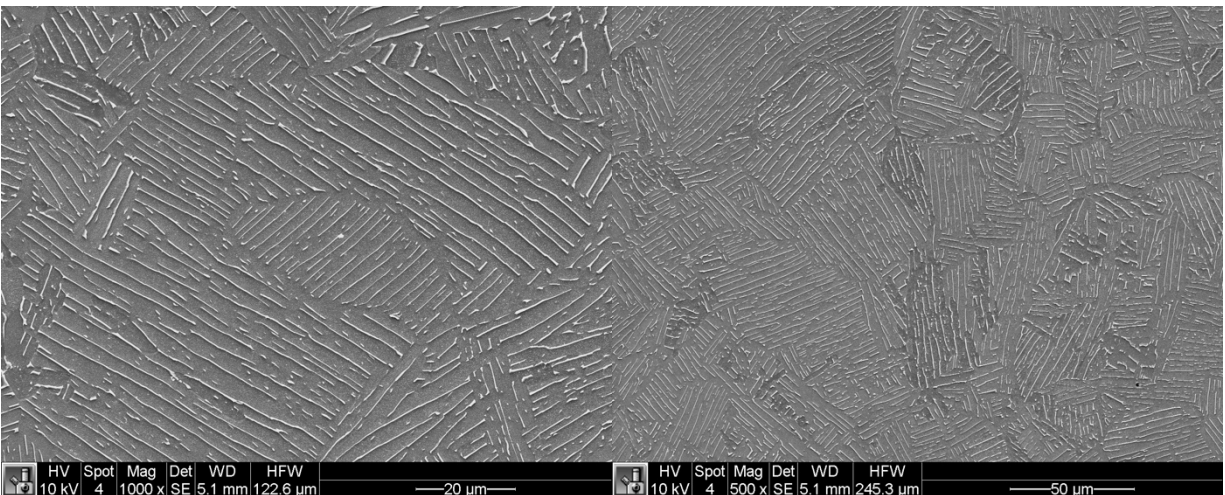
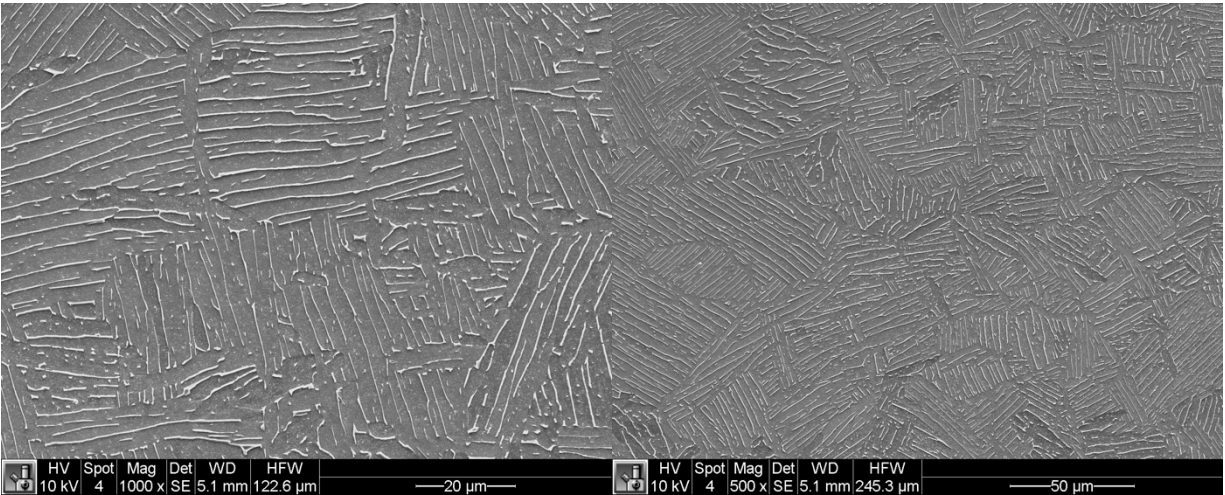
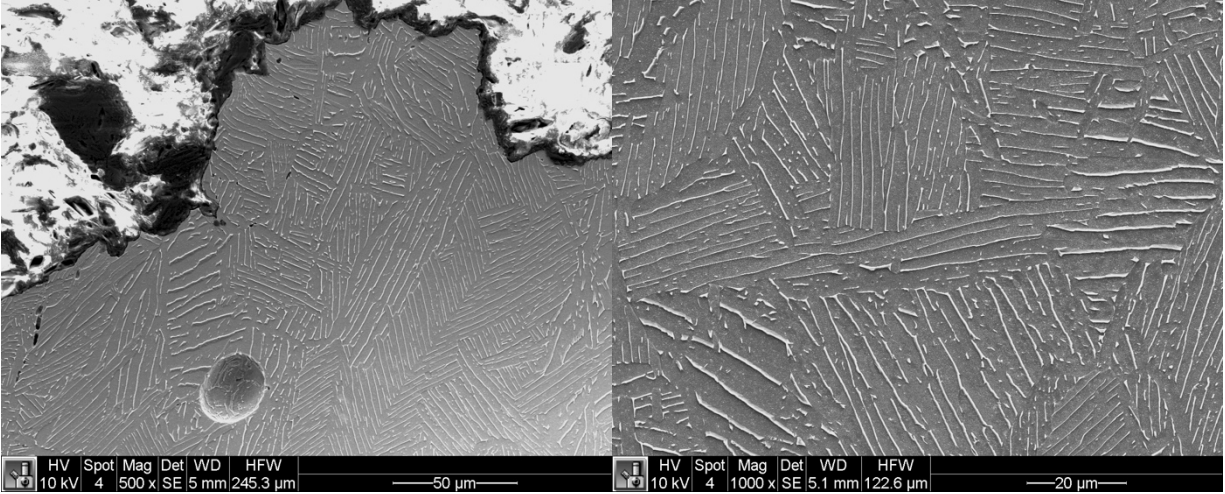
	HV	Spot	Mag	Det	WD	HFWD	
10 kV	4	1000 x	SE	5 mm	122.6 μm		—20 μm—

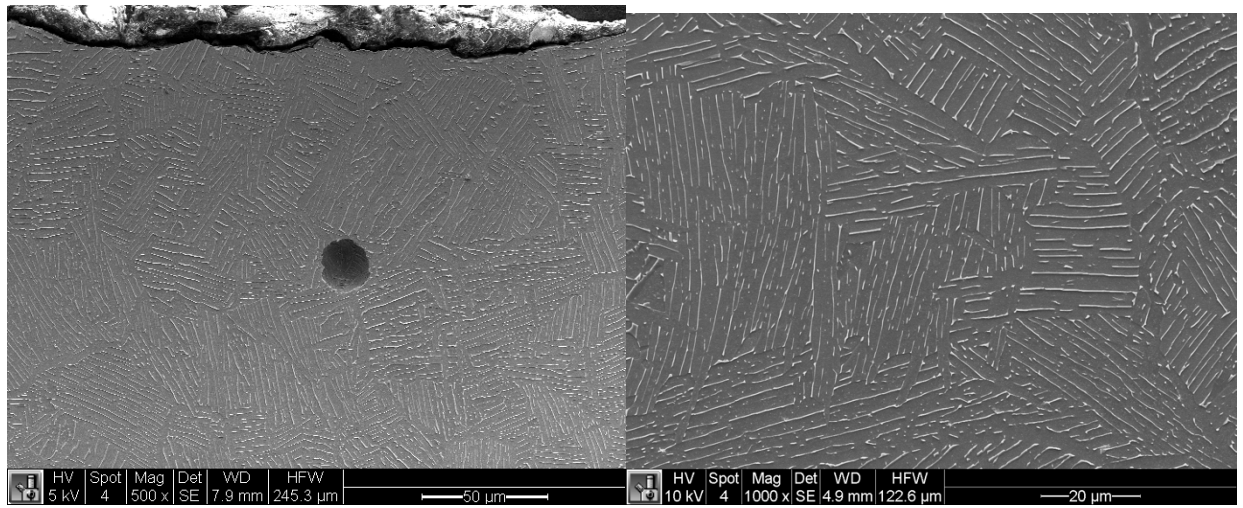
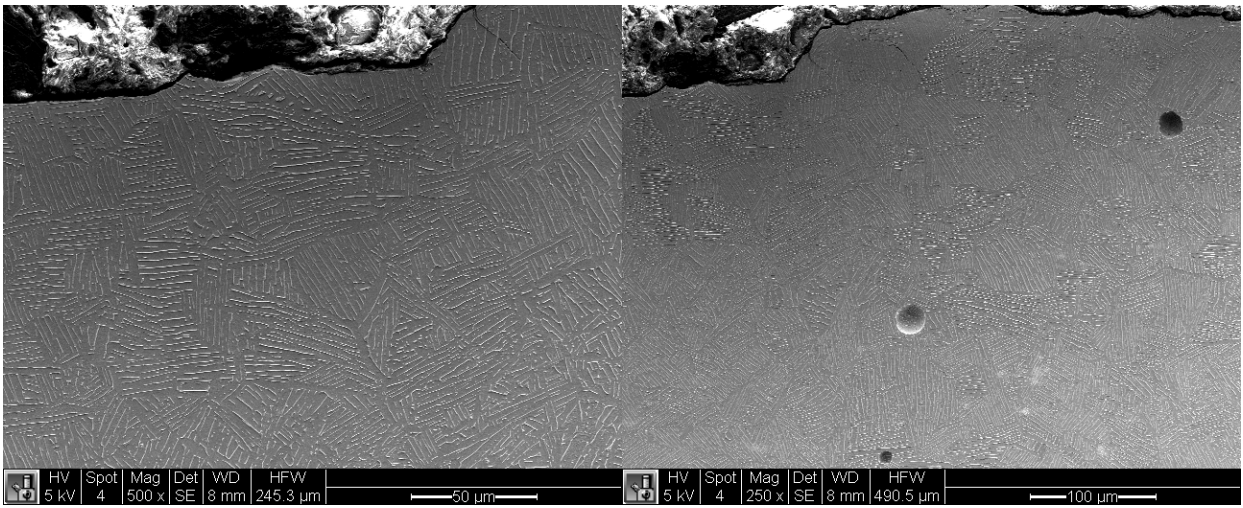
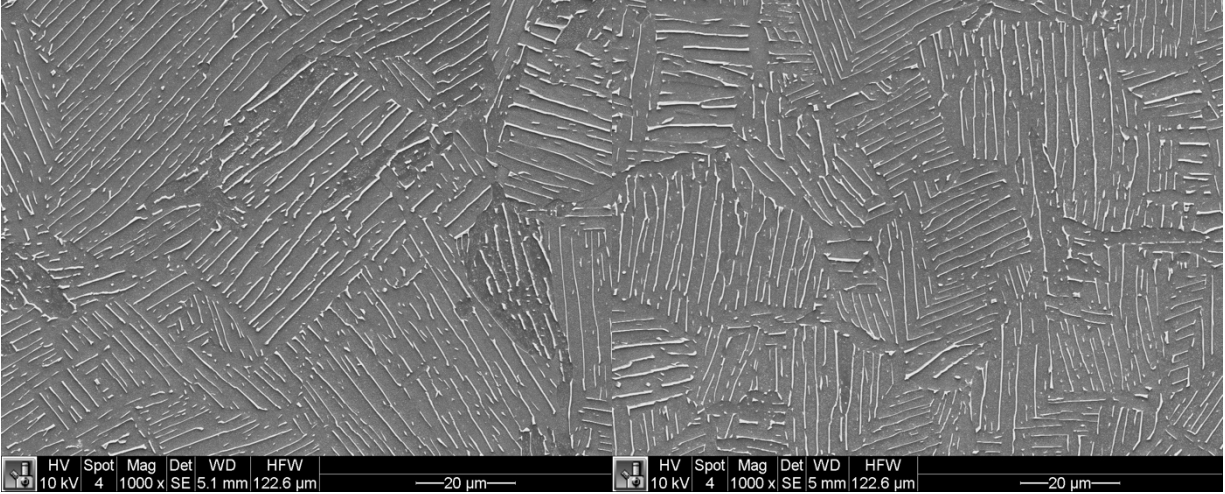


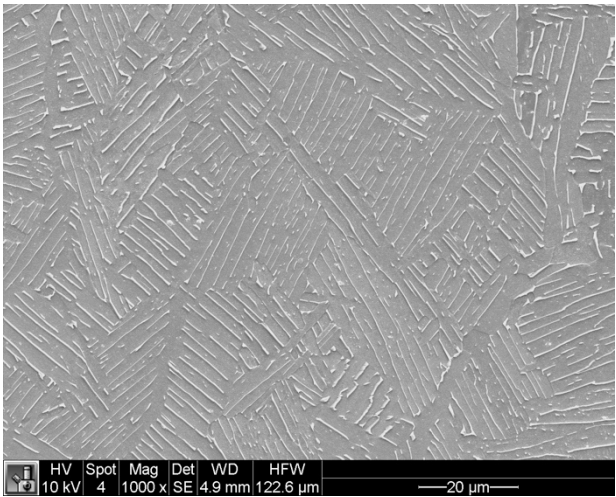
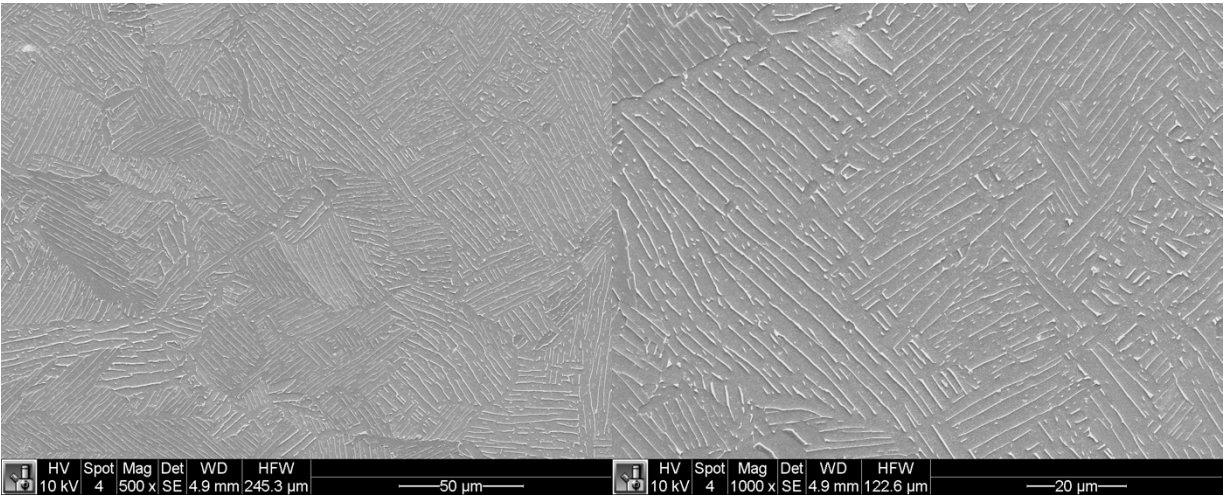
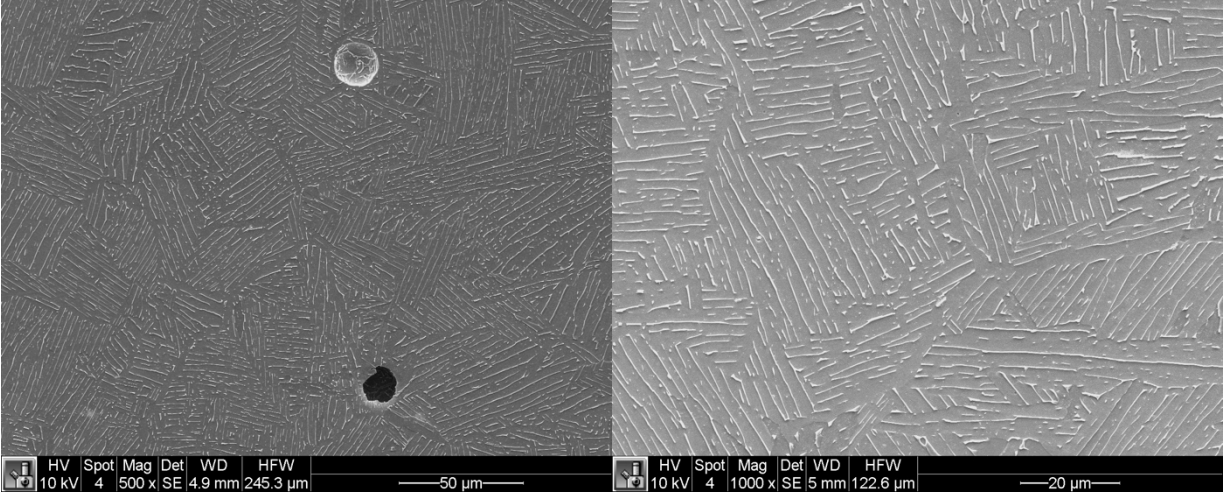
	HV	Spot	Mag	Det	WD	HFWD	
10 kV	4	1000 x	SE	5 mm	122.6 μm		—20 μm—

	HV	Spot	Mag	Det	WD	HFWD	
10 kV	4	1000 x	SE	5 mm	122.6 μm		—20 μm—

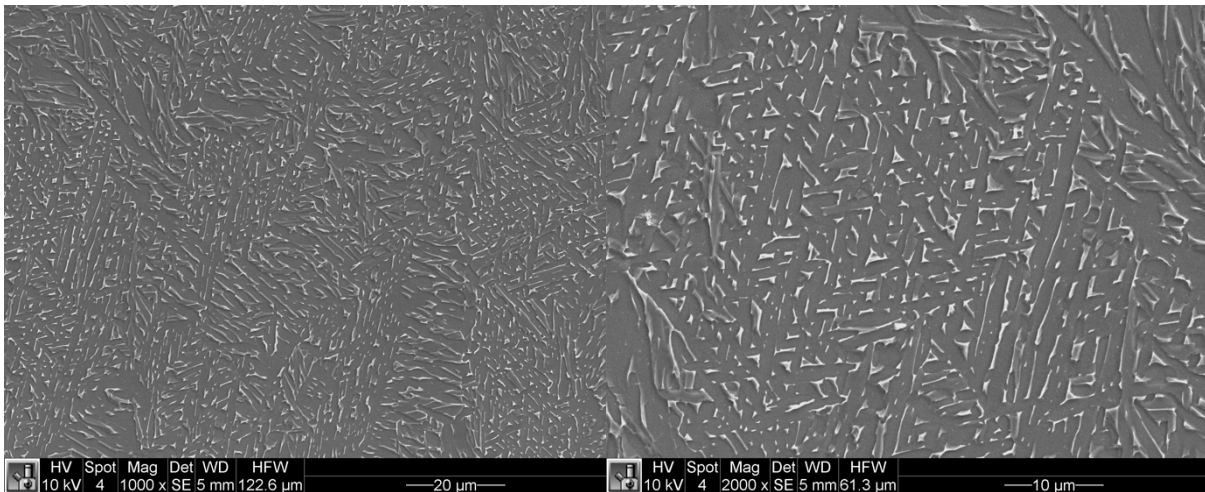
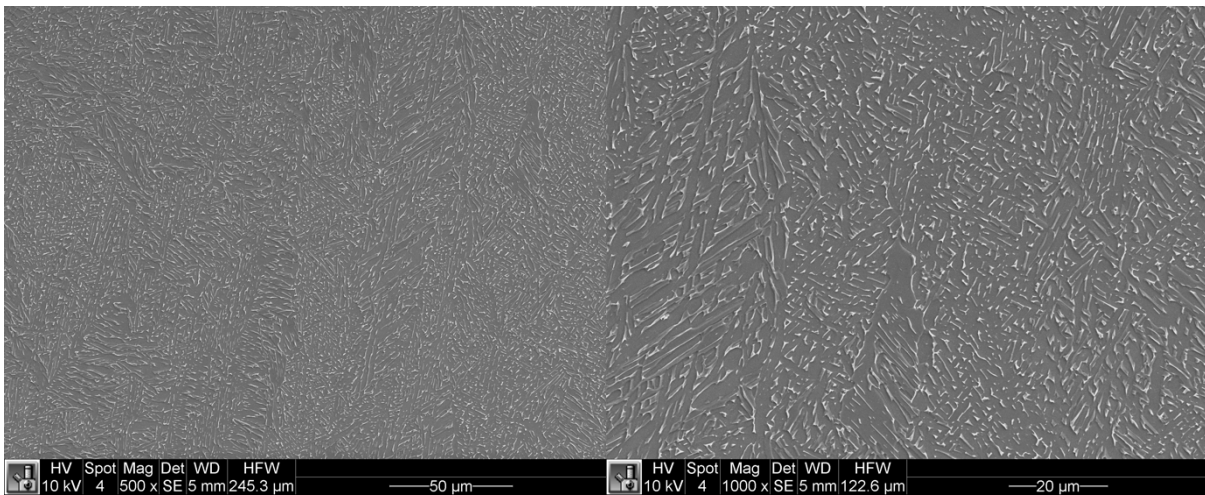
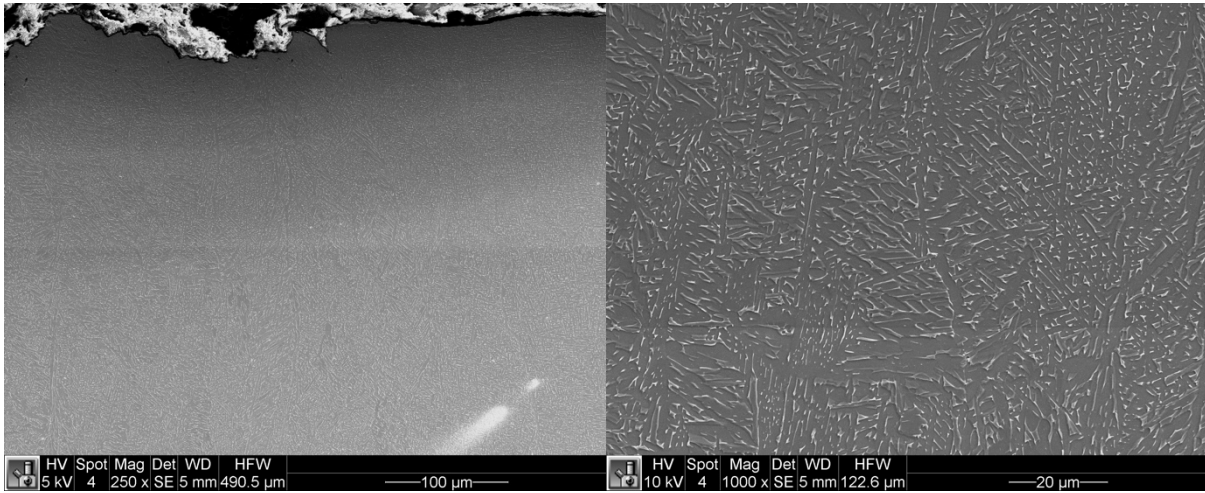


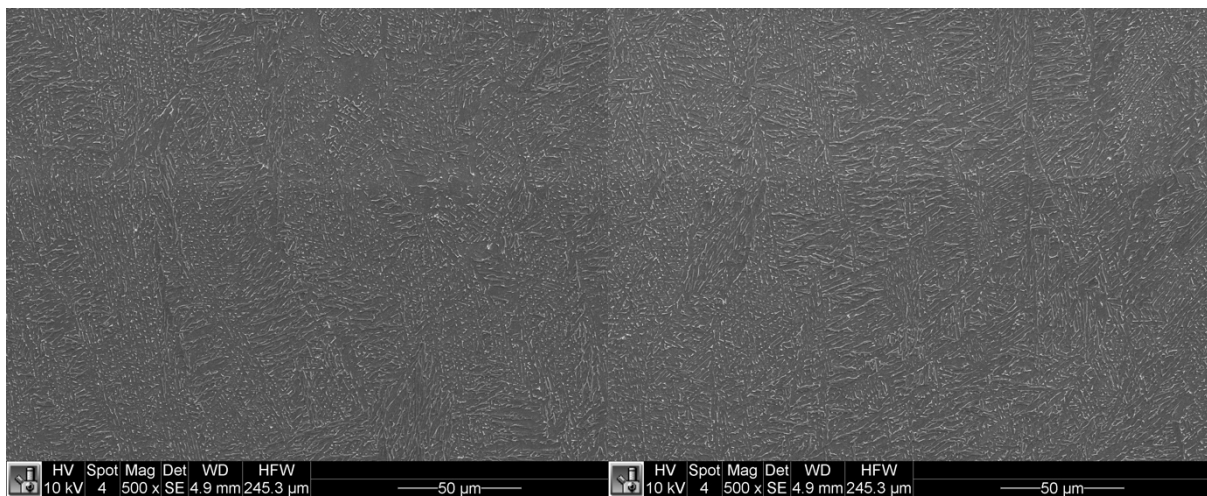
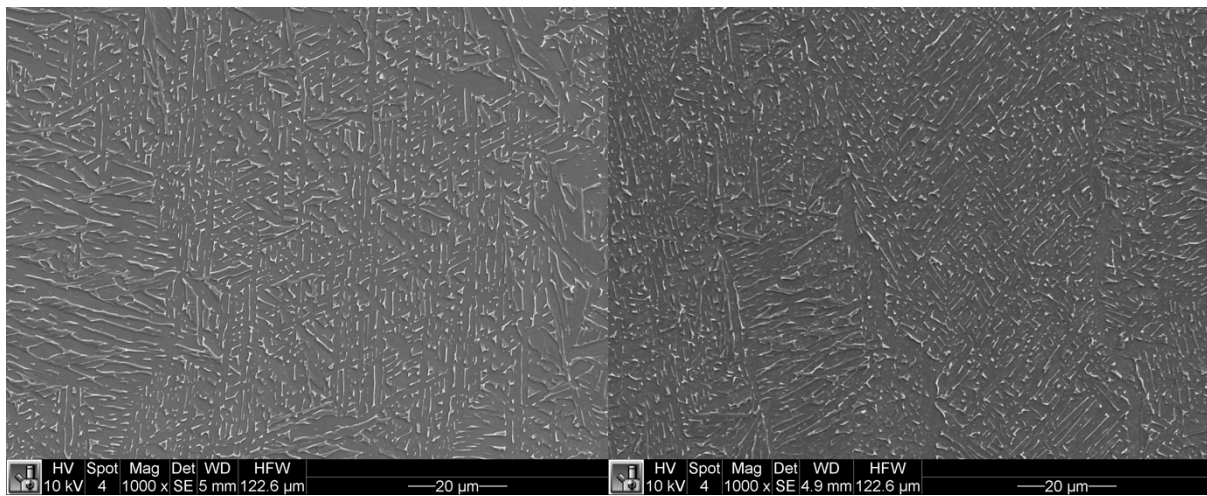
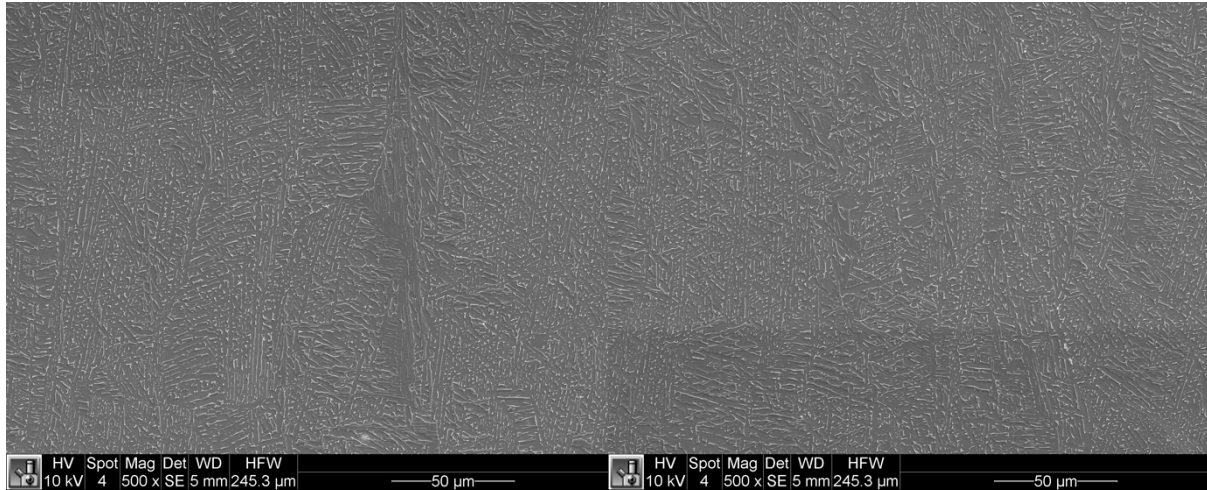


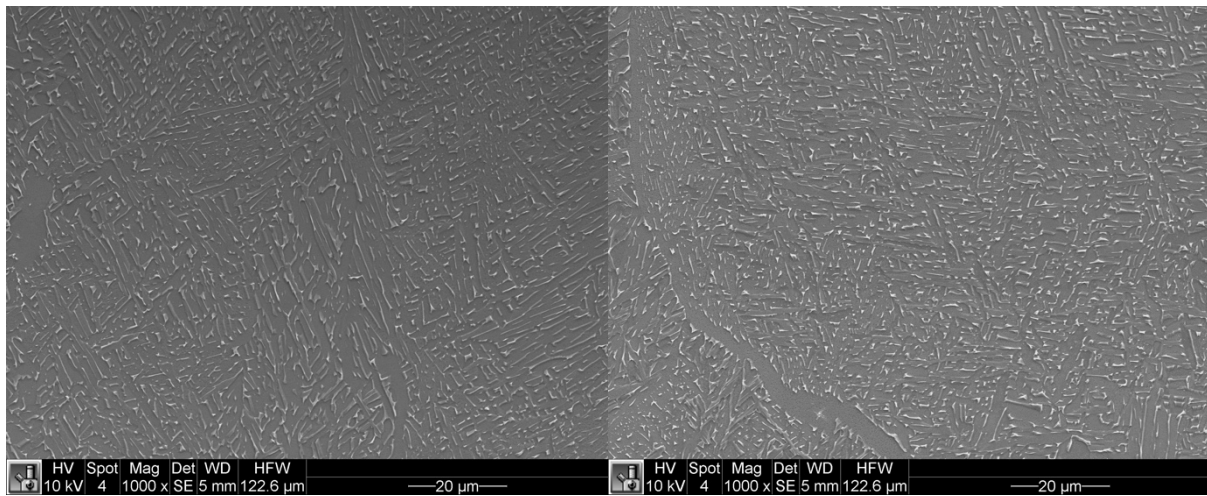
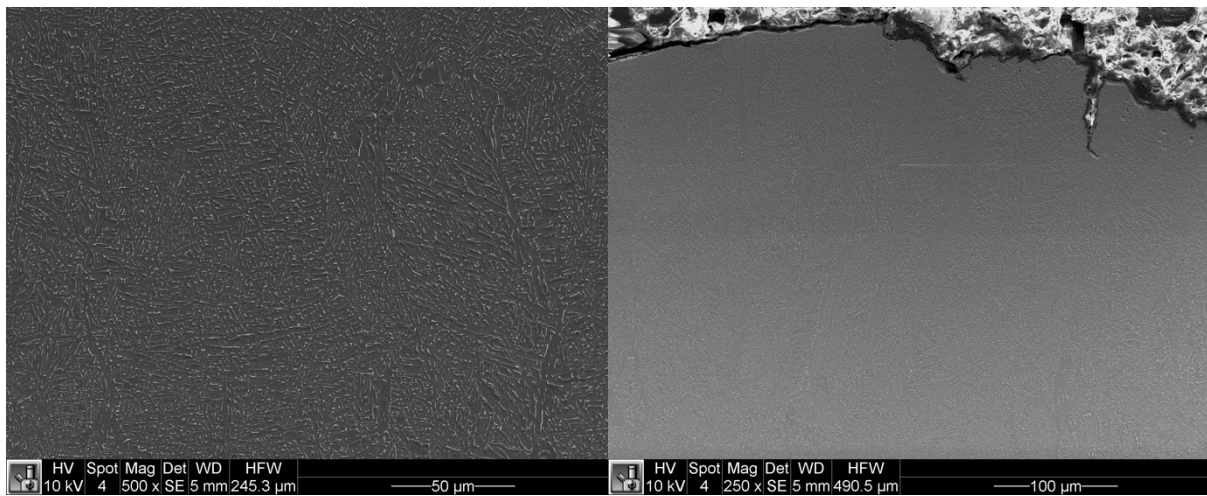
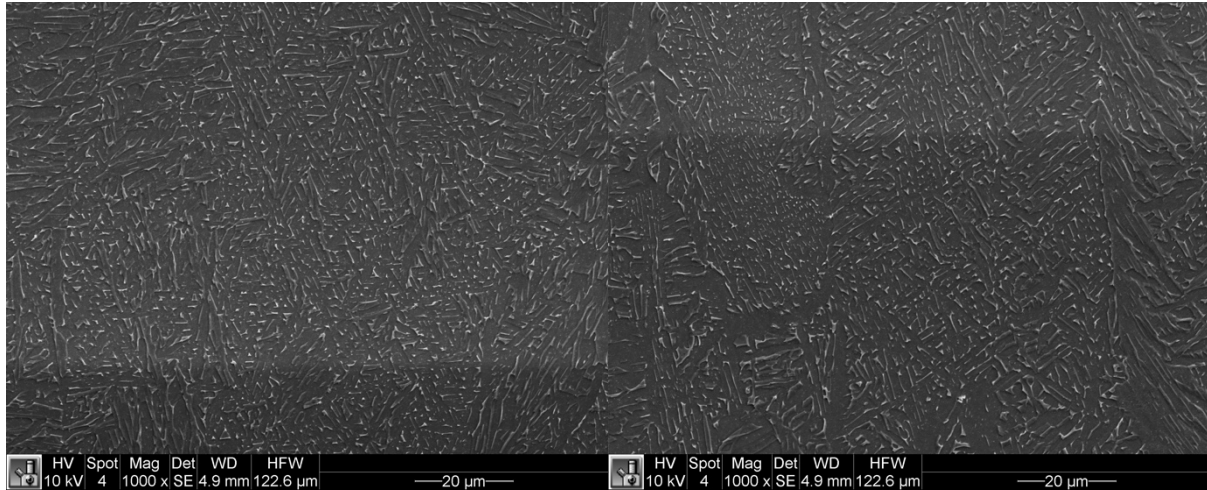


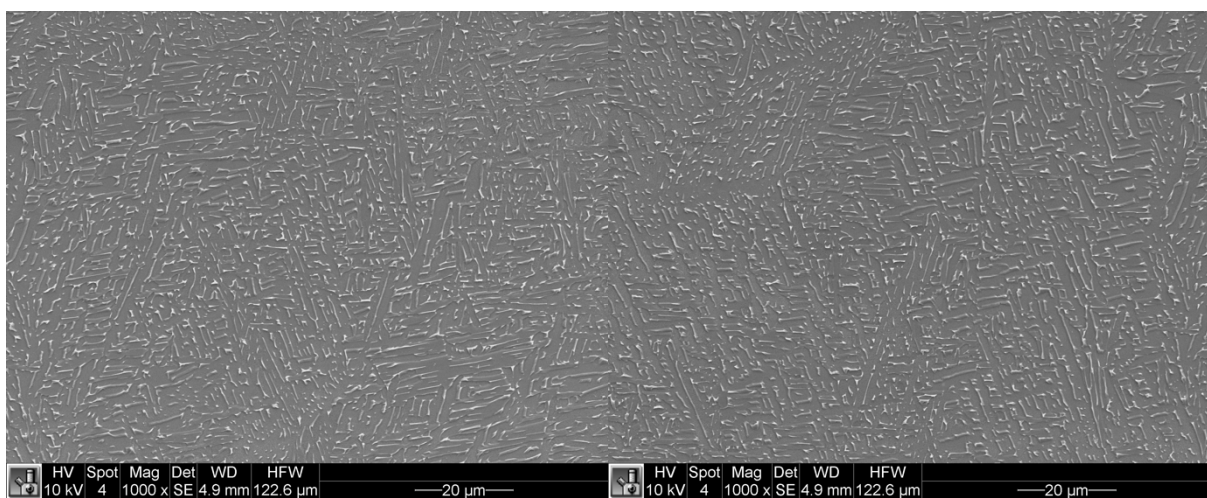
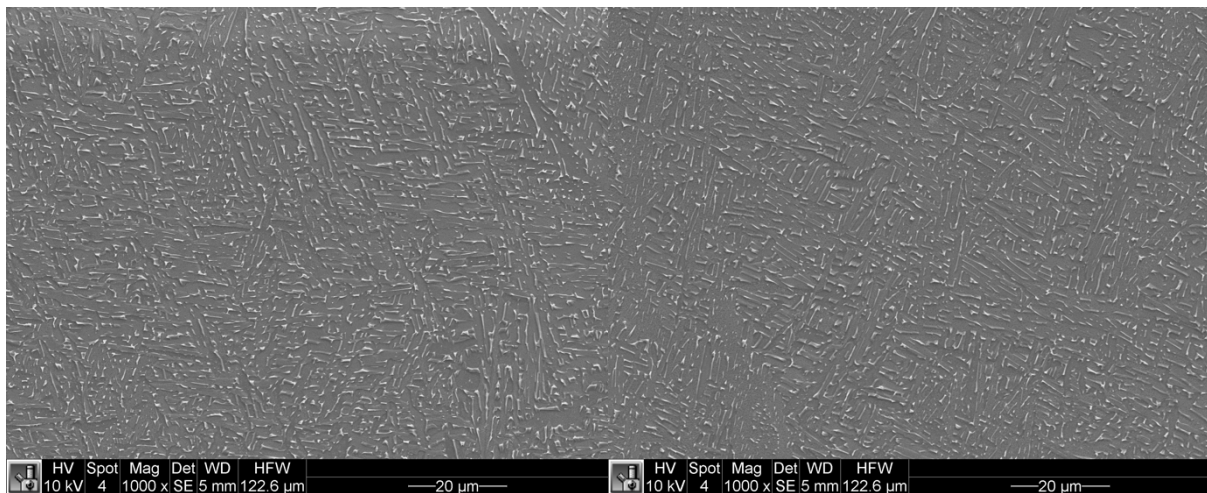


# ZX HIP

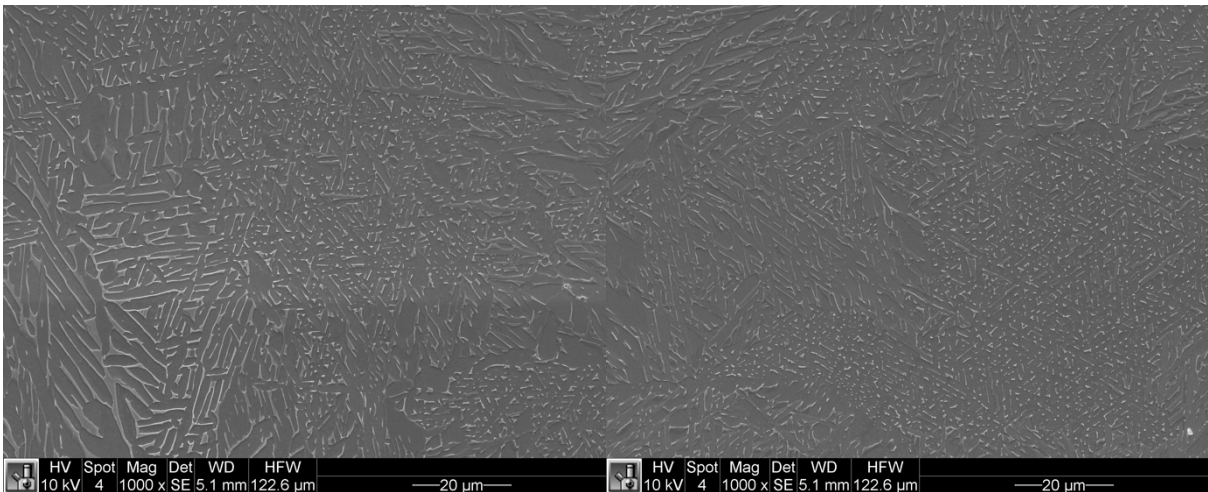
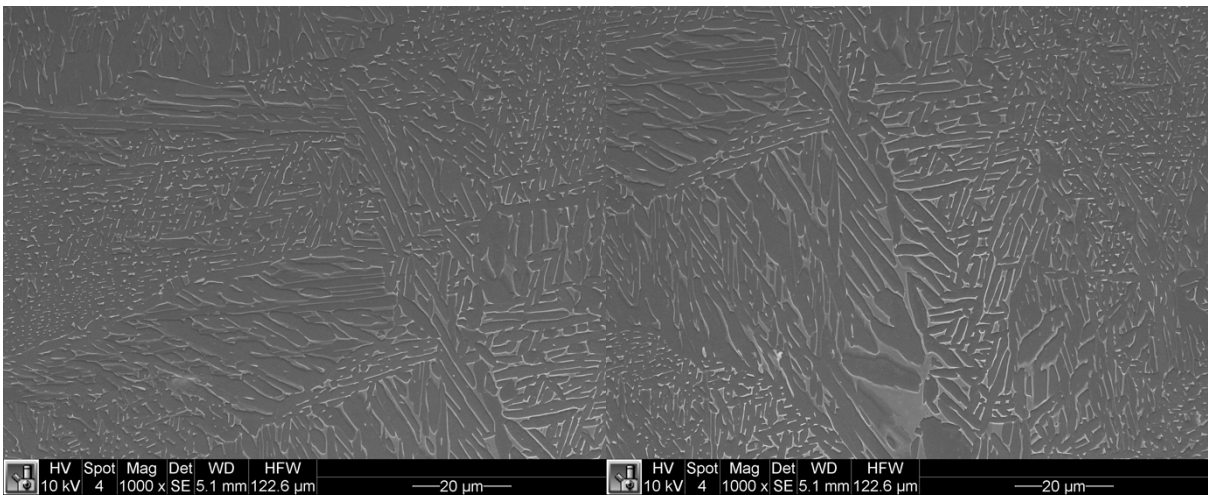
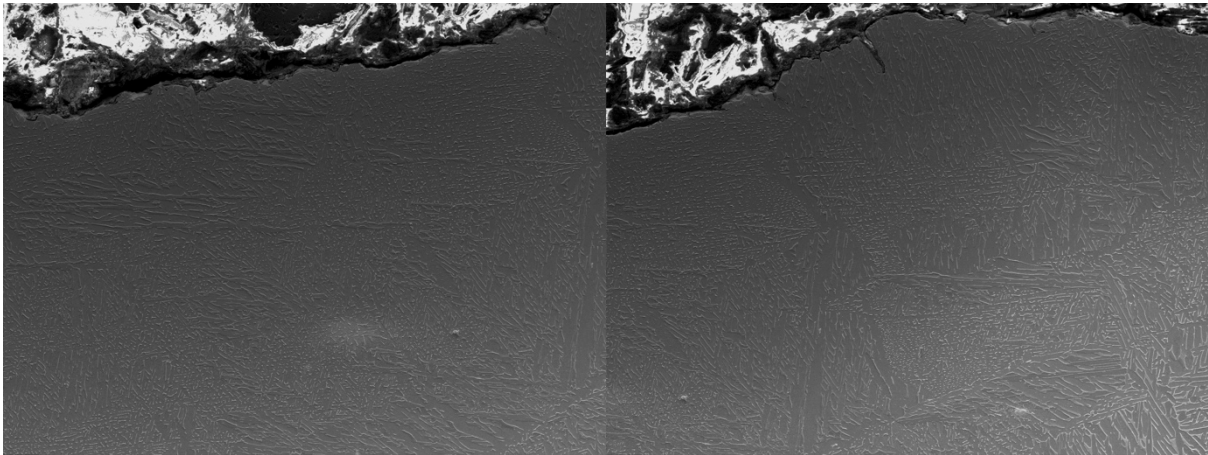


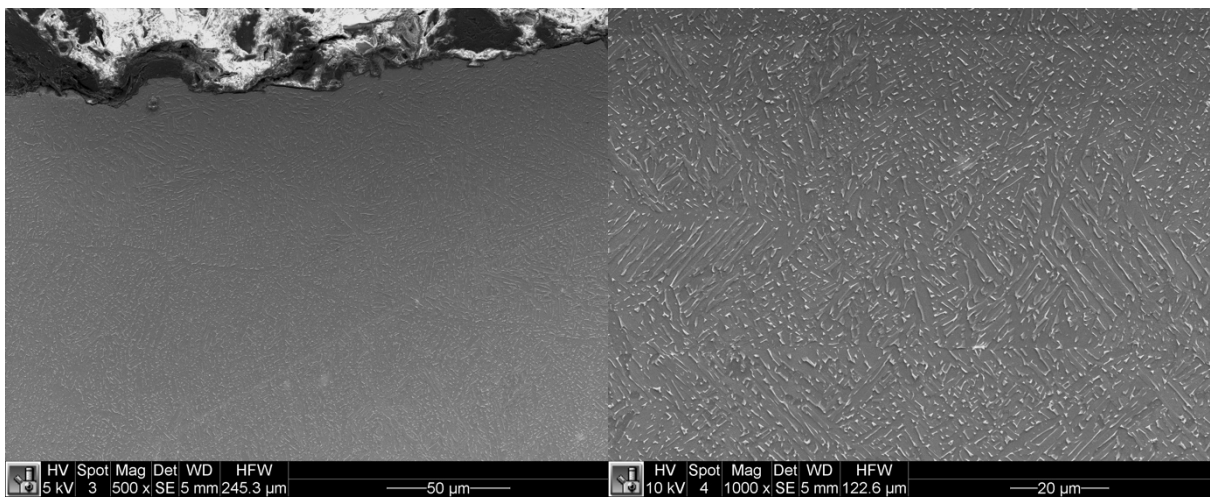
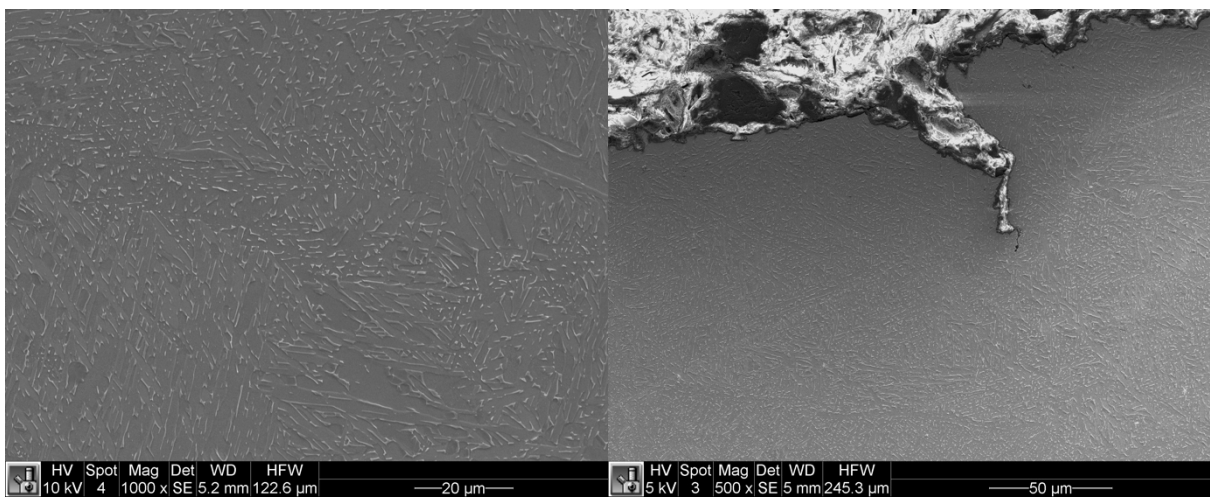
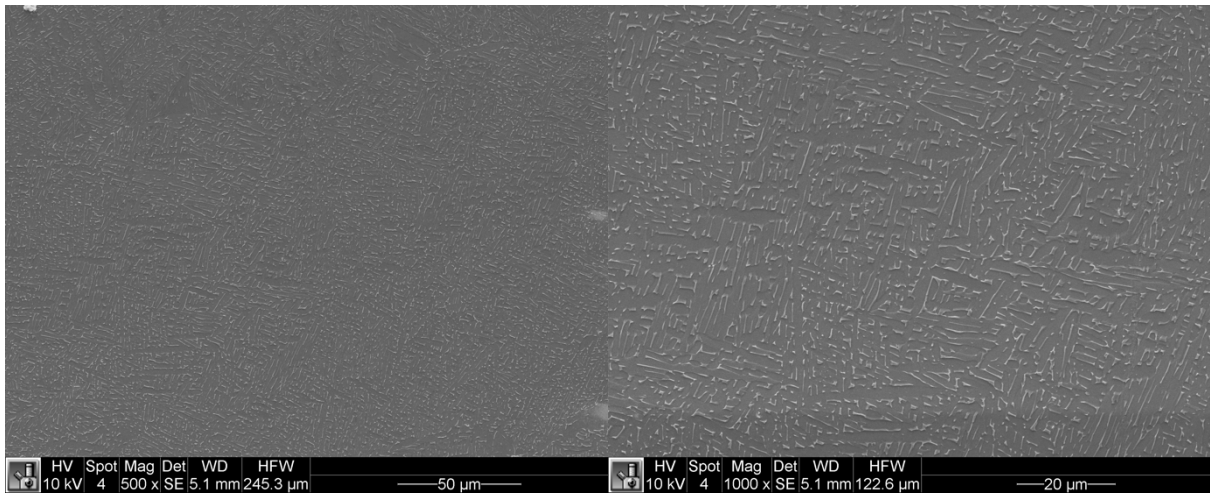


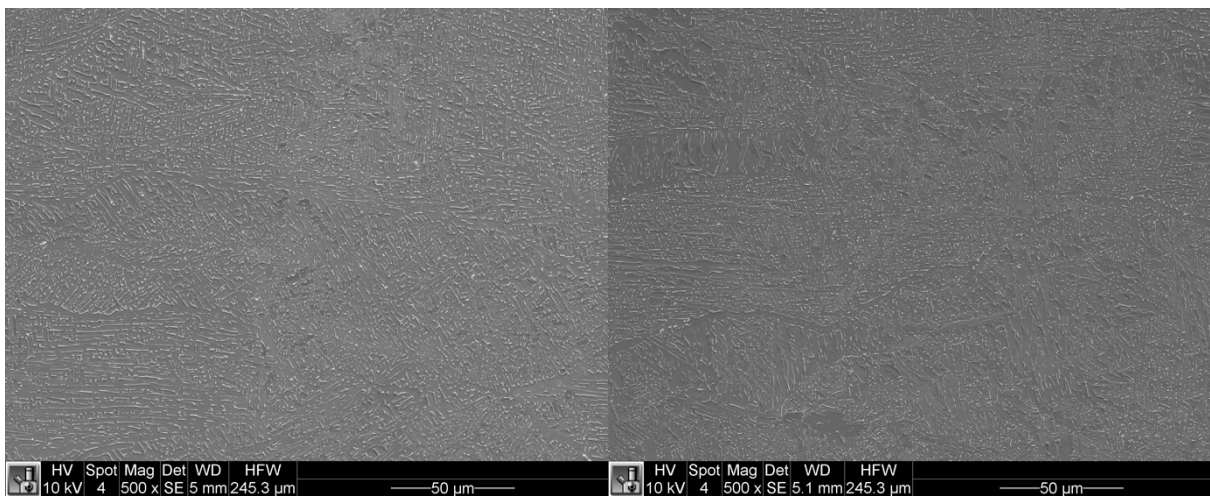
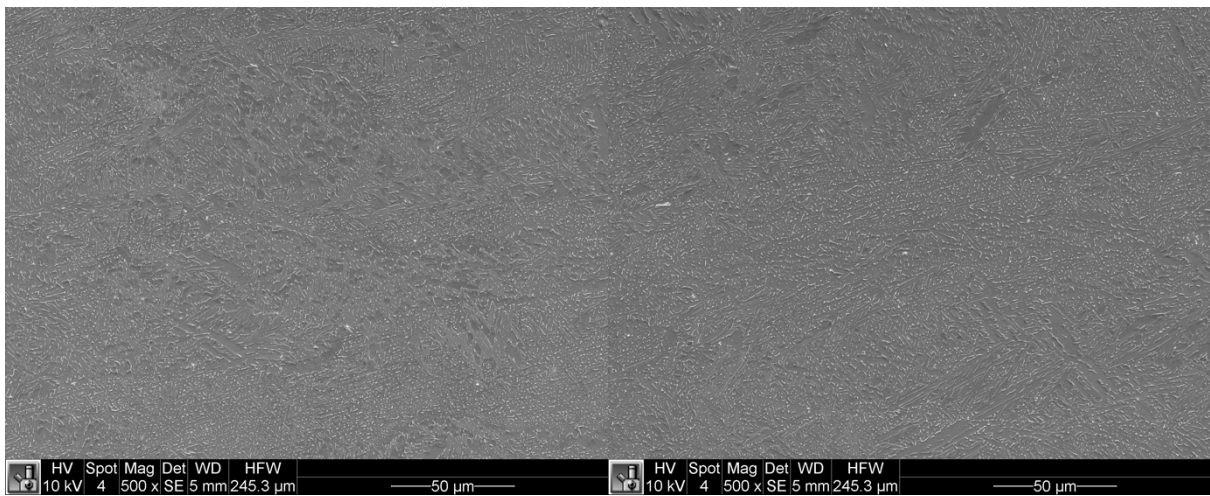
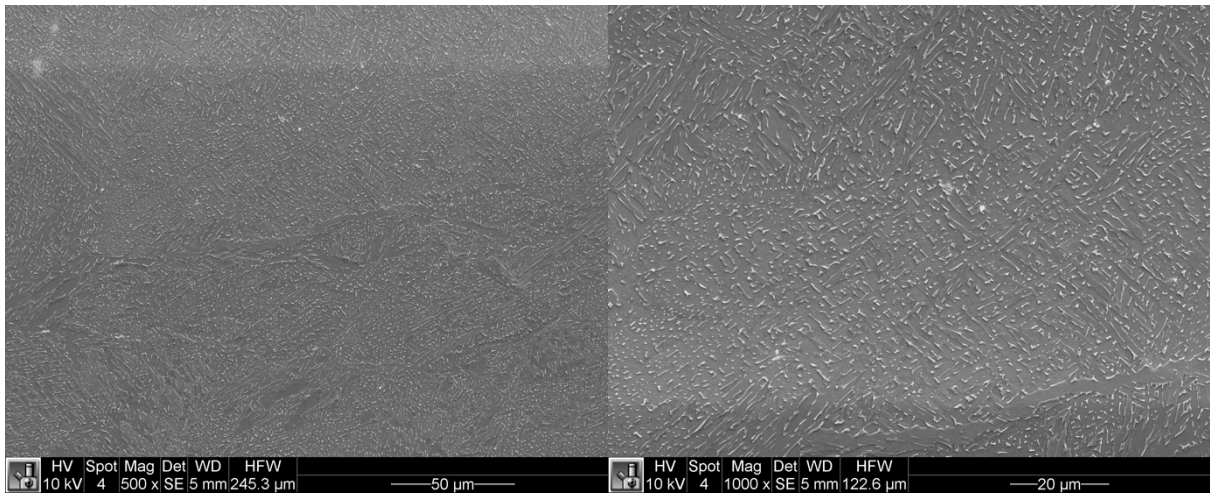




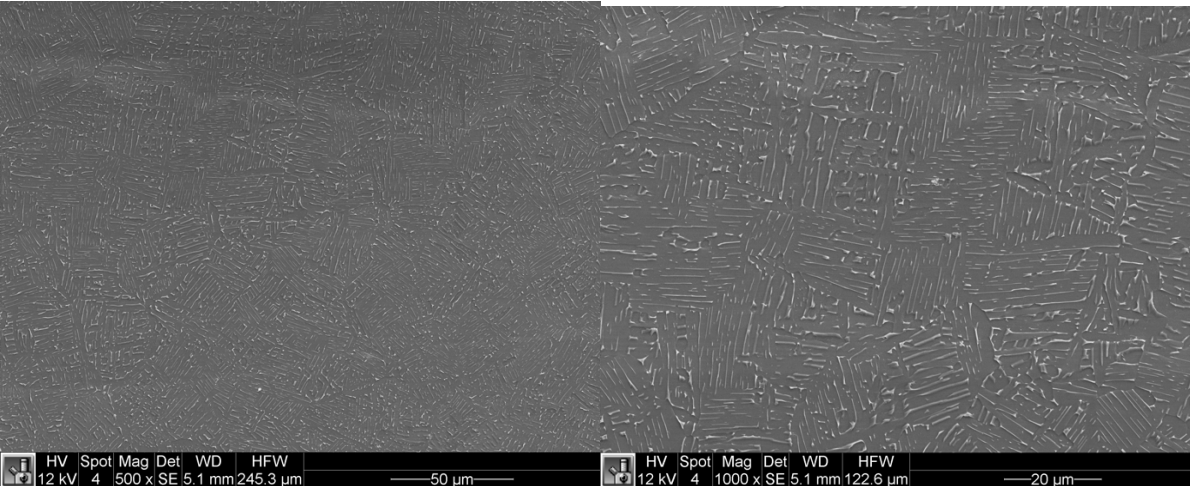
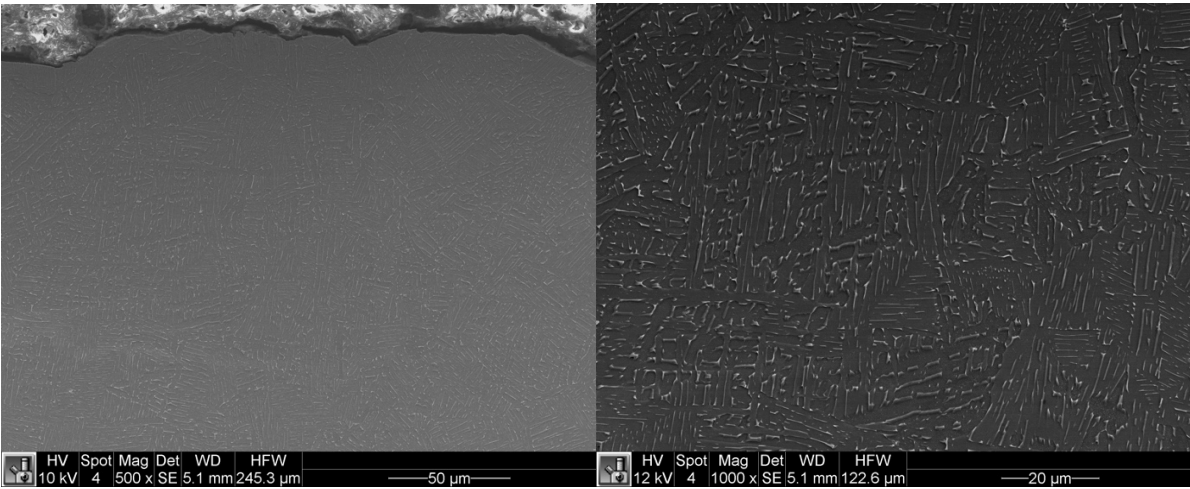
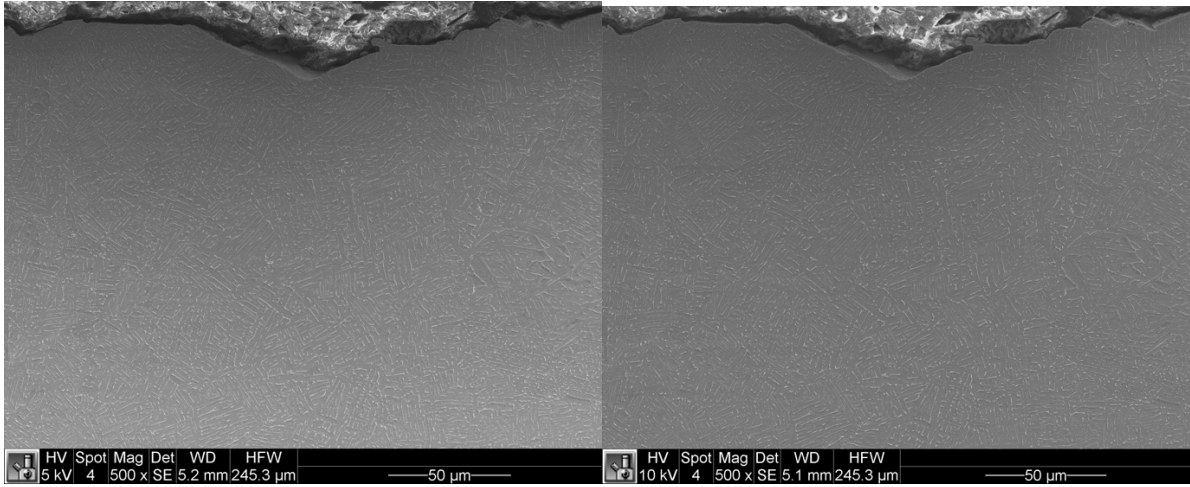
# XZ HIP

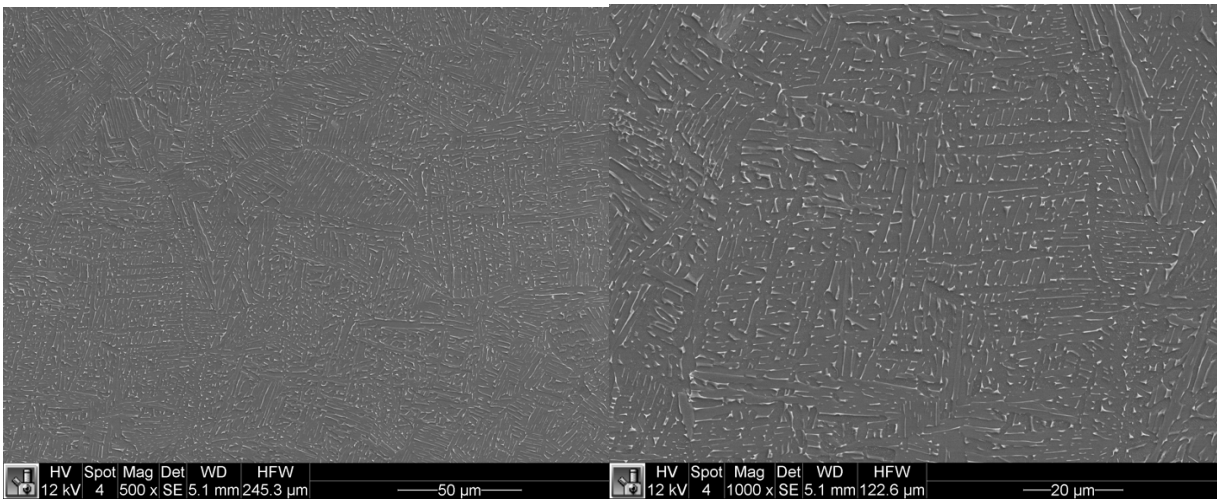
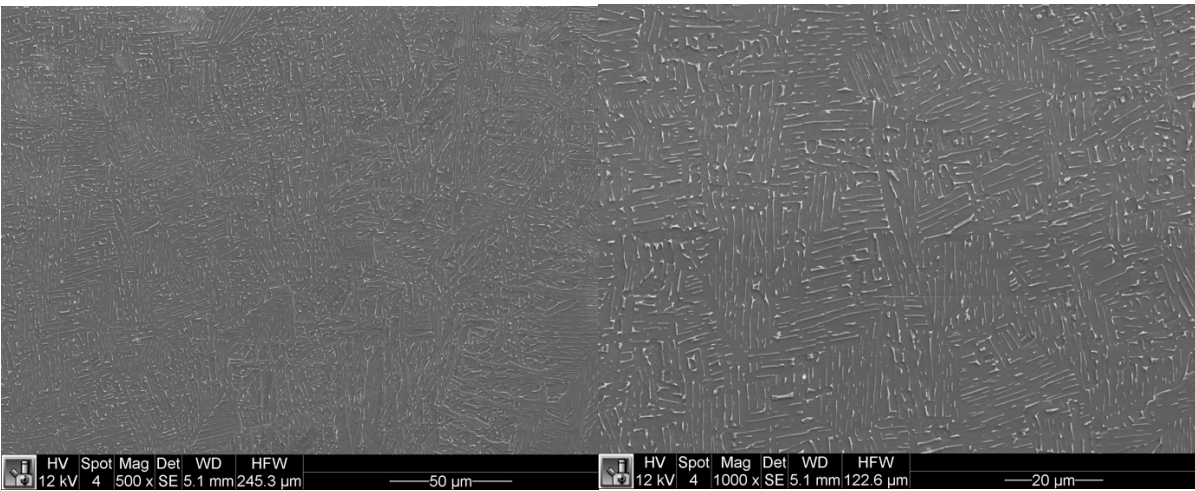
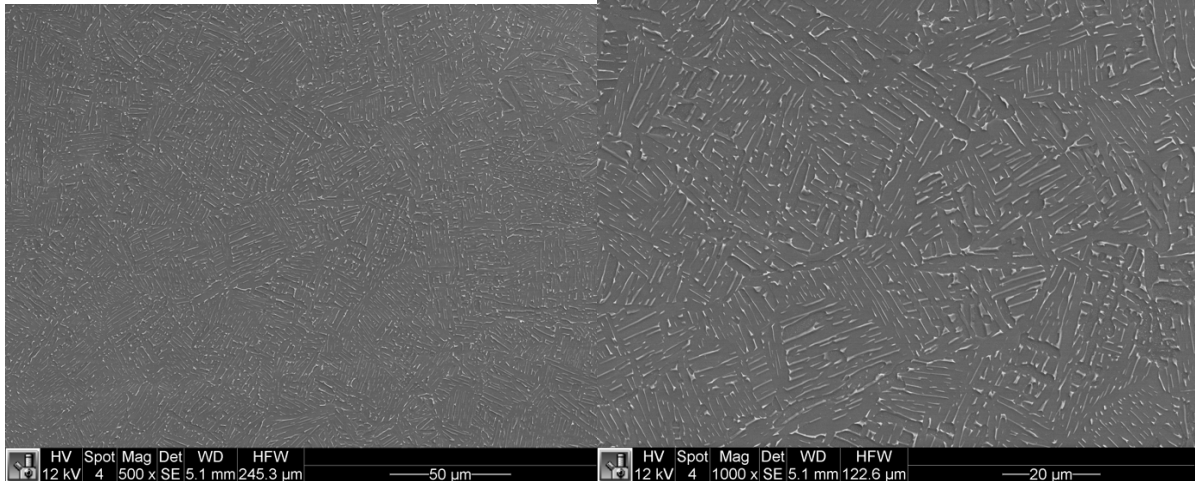


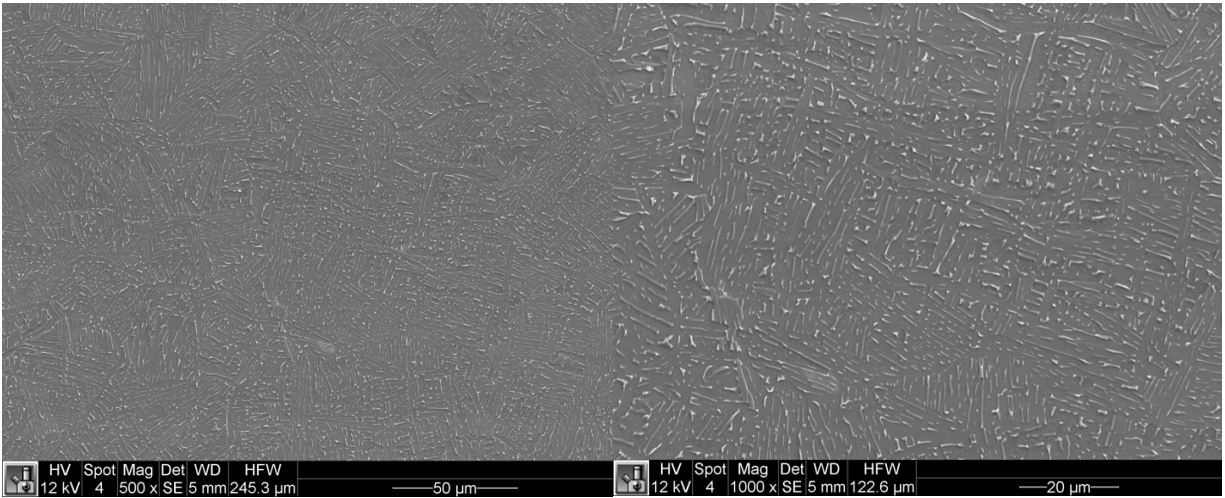
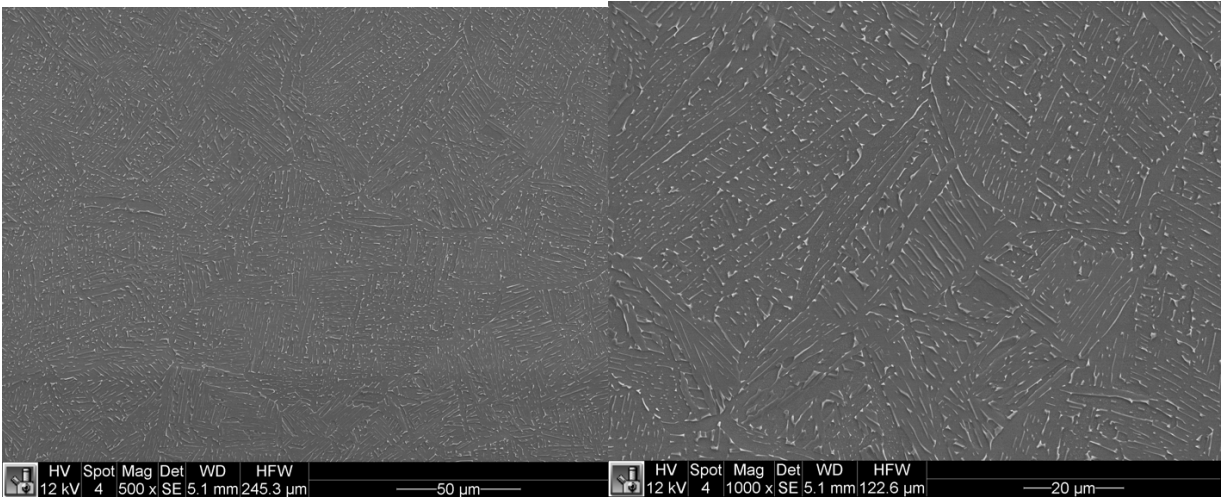
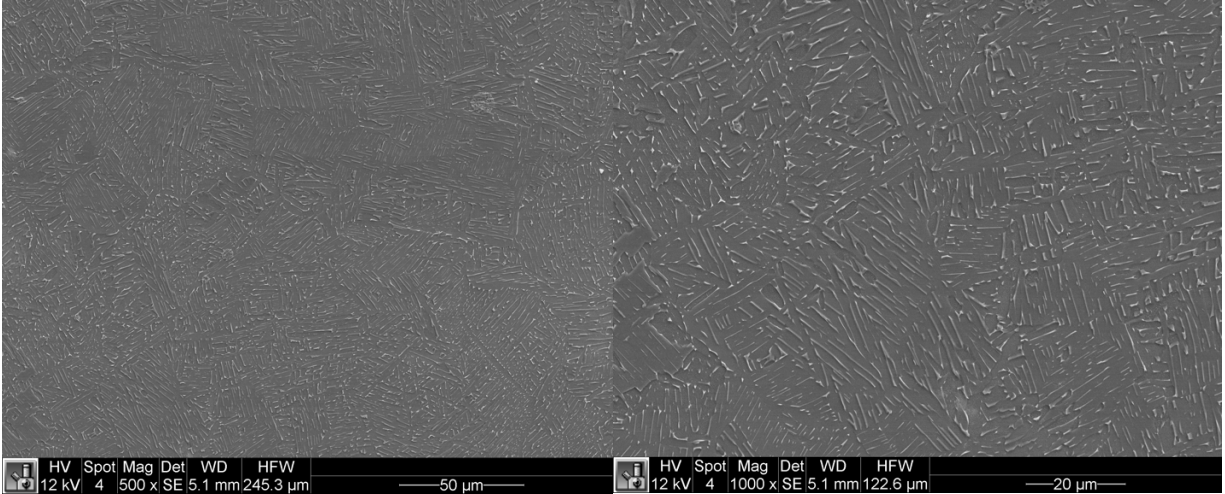


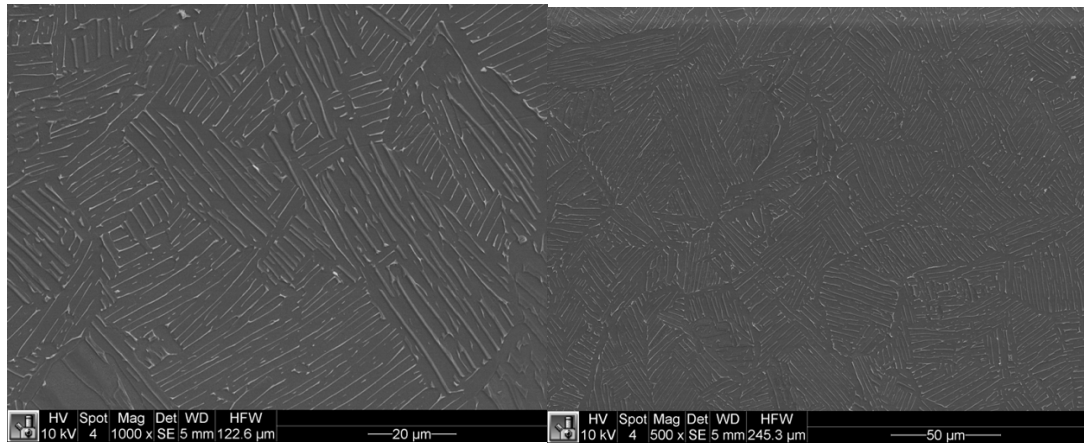
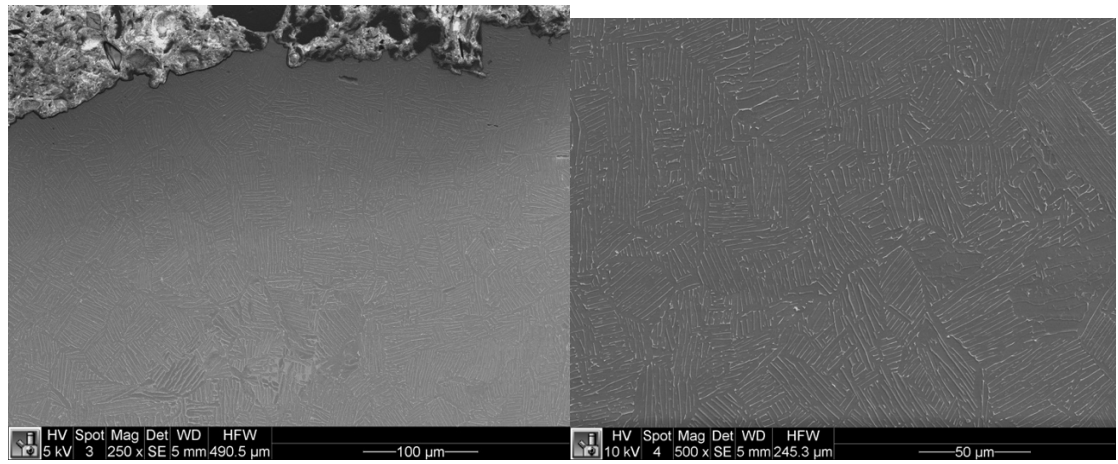
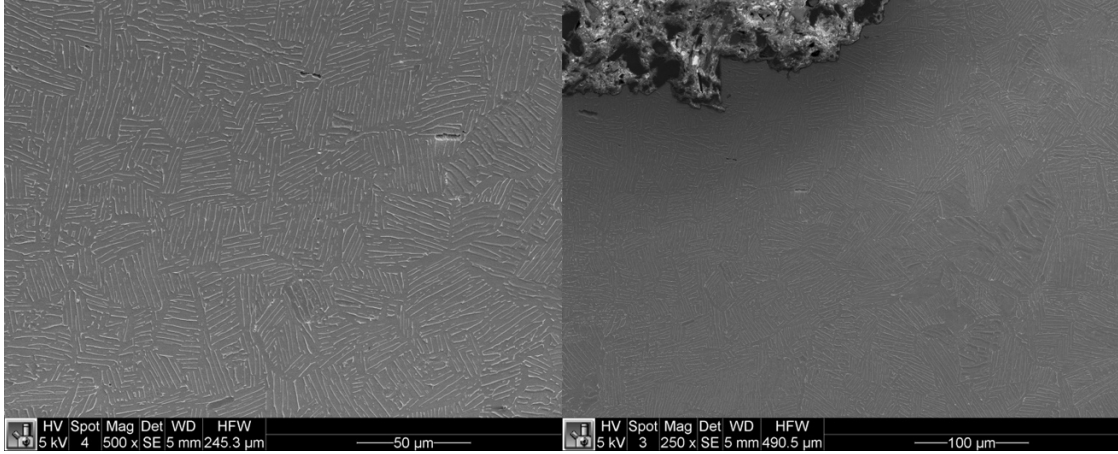


# XY HIP









**a-lath grain size**

Type	Condition	Orientation	Thickness	Height	Radial Distance	a-lath
AB	AB	ZX	6	56	35	1.1
AB	AB	ZX	6	56	35	1.07
AB	AB	ZX	6	56	35	0.9
AB	AB	ZX	6	156	95	1.16
AB	AB	ZX	6	156	95	0.938
AB	AB	ZX	6	156	95	1.18
AB	AB	ZX	6	156	95	0.948
AB	AB	ZX	6	156	95	1.3
AB	AB	ZX	9	56	35	1.06
AB	AB	ZX	9	56	35	1
AB	AB	ZX	9	56	95	1.01
AB	AB	ZX	9	56	95	1.01
AB	AB	ZX	9	56	95	0.97
AB	AB	ZX	9	56	95	0.89
AB	AB	ZX	9	156	65	1.23
AB	AB	ZX	9	156	65	1.28
AB	AB	ZX	9	156	65	1.26
AB	AB	ZX	9	156	65	1.18
AB	AB	ZX	9	256	35	1.32
AB	AB	ZX	9	256	35	1.18
AB	AB	ZX	9	256	35	1.28
AB	AB	ZX	9	256	95	1.37
AB	AB	ZX	9	256	95	1.34
AB	AB	ZX	9	256	95	1.25
AB	AB	ZX	9	256	95	1.23
AB	AB	ZX	9	256	95	1.3
Machined	AB	ZX	3	256	95	0.94
Machined	AB	ZX	3	256	95	1.04
Machined	AB	ZX	3	256	95	0.86
Machined	AB	ZX	3	256	95	1.14

<b>Machined</b>	AB	ZX	3	256	95	0.96
<b>Machined</b>	AB	ZX	6	56	35	1.03
<b>Machined</b>	AB	ZX	6	56	35	1.1
<b>Machined</b>	AB	ZX	6	156	35	1.23
<b>Machined</b>	AB	ZX	6	156	35	1.18
<b>Machined</b>	AB	ZX	6	156	35	1.13
<b>Machined</b>	AB	ZX	6	156	35	0.86
<b>Machined</b>	AB	ZX	6	256	35	1.07
<b>Machined</b>	AB	ZX	6	256	35	1.14
<b>Machined</b>	AB	ZX	6	256	35	1.18
<b>Machined</b>	AB	ZX	6	256	95	1.36
<b>Machined</b>	AB	ZX	6	256	95	1
<b>Machined</b>	AB	ZX	6	256	95	1.33
<b>Machined</b>	AB	ZX	6	256	95	1.23
<b>Machined</b>	AB	ZX	6	256	95	1.25
<b>Machined</b>	AB	XZ	9	56	35	0.93
<b>Machined</b>	AB	XZ	9	56	35	1.22
<b>Machined</b>	AB	XZ	9	56	35	1.12
<b>Machined</b>	AB	XZ	9	156	65	1.16
<b>Machined</b>	AB	XZ	9	156	65	1.21
<b>Machined</b>	AB	XZ	9	156	65	1.16
<b>Machined</b>	AB	XZ	9	256	95	1.19
<b>Machined</b>	AB	XZ	9	256	95	1.19
<b>Machined</b>	AB	XZ	9	256	95	1.15
<b>Machined</b>	AB	XZ	9	256	95	1.3
<b>Machined</b>	AB	XZ	9	256	95	1.23
<b>Machined</b>	AB	XY	9	56	35	1.44
<b>Machined</b>	AB	XY	9	56	35	1.24
<b>Machined</b>	AB	XY	9	56	35	1.28
<b>Machined</b>	AB	XY	9	56	35	1.38
<b>Machined</b>	AB	XY	9	56	35	1.32
<b>Machined</b>	AB	XY	9	156	65	1.79
<b>Machined</b>	AB	XY	9	156	65	1.88

<b>Machined</b>	AB	XY	9	156	65	1.88
<b>Machined</b>	AB	XY	9	156	65	1.67
<b>Machined</b>	AB	XY	9	156	65	1.62
<b>Machined</b>	AB	XY	9	256	95	1.81
<b>Machined</b>	AB	XY	9	256	95	1.74
<b>Machined</b>	AB	XY	9	256	95	1.87
<b>Machined</b>	AB	XY	9	256	95	1.62
<b>Machined</b>	AB	XY	9	256	95	1.76
<b>HT</b>	HT	ZX	3	56	35	1.13
<b>HT</b>	HT	ZX	3	56	35	1.33
<b>HT</b>	HT	ZX	3	56	35	1.26
<b>HIP</b>	HIP	ZX	9	56	35	1.42
<b>HIP</b>	HIP	ZX	9	56	35	1.35
<b>HIP</b>	HIP	ZX	9	56	35	1.32
<b>HIP</b>	HIP	ZX	9	56	35	1.31
<b>HIP</b>	HIP	ZX	9	156	65	1.39
<b>HIP</b>	HIP	ZX	9	156	65	1.65
<b>HIP</b>	HIP	ZX	9	156	65	1.3
<b>HIP</b>	HIP	ZX	9	156	65	1.41
<b>HIP</b>	HIP	ZX	9	156	65	1.29
<b>HIP</b>	HIP	ZX	9	256	95	1.42
<b>HIP</b>	HIP	ZX	9	256	95	1.45
<b>HIP</b>	HIP	ZX	9	256	95	1.42
<b>HIP</b>	HIP	ZX	9	256	95	1.44
<b>HIP</b>	HIP	ZX	9	256	95	1.46
<b>HIP</b>	HIP	XZ	9	56	35	1.55
<b>HIP</b>	HIP	XZ	9	56	35	1.54
<b>HIP</b>	HIP	XZ	9	56	35	1.46
<b>HIP</b>	HIP	XZ	9	56	95	1.35
<b>HIP</b>	HIP	XZ	9	56	95	1.42
<b>HIP</b>	HIP	XZ	9	56	95	1.35
<b>HIP</b>	HIP	XY	9	56	35	1.43
<b>HIP</b>	HIP	XY	9	56	35	1.51

<b>HIP</b>	HIP	XY	9	56	35	1.56
<b>HIP</b>	HIP	XY	9	56	35	1.43
<b>HIP</b>	HIP	XY	9	56	35	1.59
<b>HIP</b>	HIP	XY	9	156	65	1.69
<b>HIP</b>	HIP	XY	9	156	65	1.97
<b>HIP</b>	HIP	XY	9	156	65	1.78
<b>HIP</b>	HIP	XY	9	156	65	1.78
<b>HIP</b>	HIP	XY	9	156	65	1.97

**B-vol.% fraction**

Type	Condition	Orientation	Thickness	Height	Radial	B vol.%
HIP	HIP	XY	9	156	65	11.253
HIP	HIP	XY	9	156	65	10.955
HIP	HIP	ZX	9	56	35	12.591
HIP	HIP	ZX	9	56	35	16.328
HIP	HIP	ZX	9	56	35	14.368
HIP	HIP	ZX	9	56	35	15.524
HIP	HIP	ZX	9	56	35	11.875
HIP	HIP	ZX	9	156	65	12.544
HIP	HIP	ZX	9	156	65	13.645
HIP	HIP	ZX	9	156	65	13.54
HIP	HIP	ZX	9	256	95	14.235
HIP	HIP	ZX	9	256	95	15.627
HIP	HIP	ZX	9	256	95	14.898
HIP	HIP	XZ	9	56	35	13.7
HIP	HIP	XZ	9	56	35	14.8
HIP	HIP	XZ	9	56	35	14.8
HIP	HIP	XZ	9	56	35	12
HIP	HIP	XZ	9	56	95	12.564
HIP	HIP	XZ	9	56	95	11.728
HIP	HIP	XZ	9	56	95	12.788
HIP	HIP	XZ	9	56	95	14.8
HIP	HIP	XZ	9	56	95	15.6
HIP	HIP	XZ	9	56	95	13.478
HIP	HIP	XZ	9	56	95	13.116
HIP	HIP	XZ	9	56	95	15.3
HIP	HIP	XZ	9	56	95	14
HIP	HIP	XY	9	56	35	12.3
HIP	HIP	XY	9	56	35	13.3
HIP	HIP	XY	9	56	35	11.7
HIP	HIP	XY	9	56	35	12.9
HIP	HIP	XY	9	56	35	11.5

HIP	HIP	XY	9	56	35	11.785
HIP	HIP	XY	9	156	65	10.798
HIP	HIP	XY	9	156	65	15.3
HIP	HIP	XY	9	156	65	12.44
HIP	HIP	XY	9	156	65	11.898
HIP	HIP	XY	9	156	65	11.176
HIP	HIP	XY	9	156	65	12.993
HIP	HIP	XY	9	156	65	10.999
Machined	As-Built	ZX	3	256	95	14.623
Machined	As-Built	ZX	3	256	95	13.586
Machined	As-Built	ZX	3	256	95	13.787
Machined	As-Built	ZX	3	256	95	17.958
AsBuilt	As-Built	ZX	9	56	35	9.676
AsBuilt	As-Built	ZX	9	256	35	14.684
AsBuilt	As-Built	ZX	9	56	95	13.15
AsBuilt	As-Built	ZX	6	56	35	7.148
AsBuilt	As-Built	ZX	6	56	35	8.184
AsBuilt	As-Built	ZX	9	56	35	9.759
AsBuilt	As-Built	ZX	9	56	35	9.262
AsBuilt	As-Built	ZX	9	56	35	9.554
AsBuilt	As-Built	ZX	9	56	35	10.002
AsBuilt	As-Built	ZX	9	56	35	8.595
Machined	As-Built	ZX	6	156	35	4.974
Machined	As-Built	ZX	6	156	35	6.491
Machined	As-Built	ZX	6	156	35	6.37
Machined	As-Built	ZX	6	56	35	6.605
Machined	As-Built	ZX	6	56	35	8.145
Machined	As-Built	ZX	6	56	35	6.13
Machined	As-Built	ZX	6	56	35	7.705
Machined	As-Built	ZX	3	56	35	9.849
Machined	As-Built	ZX	3	56	35	8.651
Machined	As-Built	ZX	3	56	35	12.139
Machined	As-Built	ZX	3	56	35	7.335

<b>Machined</b>	As-Built	ZX	6	56	35	7.87
<b>Machined</b>	As-Built	ZX	6	56	35	10.846
<b>Machined</b>	As-Built	ZX	6	56	35	8.362
<b>Machined</b>	As-Built	ZX	6	56	35	9.906
<b>Machined</b>	As-Built	ZX	6	56	35	9.417
<b>Machined</b>	As-Built	ZX	6	56	35	17.825
<b>Machined</b>	As-Built	ZX	6	56	35	14.342
<b>Machined</b>	As-Built	ZX	6	56	35	11.215
<b>Machined</b>	As-Built	ZX	6	56	35	12.601
<b>Machined</b>	As-Built	ZX	6	156	35	7.814
<b>AsBuilt</b>	As-Built	ZX	9	56	35	8.166
<b>AsBuilt</b>	As-Built	ZX	9	56	95	11.419
<b>AsBuilt</b>	As-Built	ZX	9	56	95	13.994
<b>AsBuilt</b>	As-Built	ZX	9	56	95	10.128
<b>AsBuilt</b>	As-Built	ZX	9	156	65	6.843
<b>AsBuilt</b>	As-Built	ZX	9	156	65	10.016
<b>AsBuilt</b>	As-Built	ZX	9	256	65	7.805
<b>AsBuilt</b>	As-Built	ZX	9	256	65	8.896
<b>AsBuilt</b>	As-Built	ZX	9	256	65	8.911
<b>AsBuilt</b>	As-Built	ZX	9	256	65	8.697
<b>Machined</b>	As-Built	ZX	9	56	35	12.43
<b>Machined</b>	As-Built	ZX	9	56	35	10.722
<b>Machined</b>	As-Built	ZX	9	56	35	8.522
<b>Machined</b>	As-Built	ZX	9	56	35	10.264
<b>Machined</b>	As-Built	ZX	9	56	35	10.656
<b>Machined</b>	As-Built	ZX	6	256	35	16.962
<b>Machined</b>	As-Built	ZX	6	256	35	11.803
<b>Machined</b>	As-Built	ZX	6	256	35	9.946
<b>Machined</b>	As-Built	ZX	6	256	35	13.079
<b>Machined</b>	As-Built	ZX	9	56	35	7.903
<b>Machined</b>	As-Built	ZX	9	56	35	7.594
<b>Machined</b>	As-Built	ZX	9	56	35	7.3
<b>Machined</b>	As-Built	ZX	3	256	95	11.182

<b>Machined</b>	As-Built	ZX	6	256	35	10.853
<b>Machined</b>	As-Built	ZX	3	256	95	9.878
<b>Machined</b>	As-Built	ZX	3	256	95	9.662
<b>AsBuilt</b>	As-Built	ZX	9	156	65	8.779
<b>AsBuilt</b>	As-Built	ZX	9	256	65	7.683
<b>AsBuilt</b>	As-Built	ZX	9	256	65	7.684
<b>Machined</b>	As-Built	ZX	3	56	35	19.452
<b>Machined</b>	As-Built	XZ	9	56	35	10.798
<b>Machined</b>	As-Built	XZ	9	156	65	11.407
<b>Machined</b>	As-Built	XZ	9	256	95	10.38
<b>Machined</b>	As-Built	XZ	9	256	95	11.834
<b>Machined</b>	As-Built	XZ	9	256	95	12.436
<b>Machined</b>	As-Built	XY	9	156	65	13.108
<b>Machined</b>	As-Built	XY	9	156	65	13.392
<b>Machined</b>	As-Built	XY	9	256	95	9.485
<b>Machined</b>	As-Built	XY	9	56	35	12.106
<b>Machined</b>	As-Built	XY	9	56	35	14.662
<b>Machined</b>	As-Built	XY	9	56	35	12.071
<b>Machined</b>	As-Built	XY	9	56	35	11.921
<b>Machined</b>	As-Built	XY	9	156	65	12.167
<b>Machined</b>	As-Built	XY	9	156	65	10.725
<b>Machined</b>	As-Built	XY	9	156	65	10.433
<b>Machined</b>	As-Built	XY	9	156	65	11.428
<b>Machined</b>	As-Built	XY	9	156	65	10.604
<b>Machined</b>	As-Built	XY	9	156	65	12.772
<b>Machined</b>	As-Built	XY	9	256	95	12.226
<b>Machined</b>	As-Built	XY	9	256	95	12.032
<b>Machined</b>	As-Built	XY	9	256	95	9.646
<b>Machined</b>	As-Built	XZ	9	56	35	10.582
<b>Machined</b>	As-Built	XZ	9	56	35	9.619
<b>Machined</b>	As-Built	XZ	9	156	65	12.202
<b>Machined</b>	As-Built	XZ	9	156	65	12.736
<b>Machined</b>	As-Built	XZ	9	256	95	13.336

<b>HIP</b>	HIP	ZX	9	256	65	18.424
<b>HIP</b>	HIP	ZX	9	256	65	14.785
<b>HIP</b>	HIP	ZX	9	256	65	18.735
<b>Machined</b>	As-Built	ZX	9	156	65	11.243
<b>Machined</b>	As-Built	ZX	9	156	65	10.319
<b>Machined</b>	As-Built	ZX	9	156	65	12.538

### Prior B grain Width

Type	Condition	Orientation	Thickness	Height	Radial	B-width
Machined	AB	XY	9	156	65	46.79
Machined	AB	XY	9	156	65	41.63
Machined	AB	XY	9	156	65	42.26
Machined	AB	XY	9	156	65	17.81
Machined	AB	XY	9	156	65	28.86
Machined	AB	XY	9	156	65	33.77
Machined	AB	XY	9	156	65	32.07
Machined	AB	XY	9	156	65	42.70
Machined	AB	XY	9	156	65	26.79
Machined	AB	XY	9	156	65	69.09
Machined	AB	XY	9	156	65	35.05
Machined	AB	XY	9	156	65	34.72
Machined	AB	XY	9	156	65	50
Machined	AB	XY	9	156	65	59.9
Machined	AB	XY	9	256	95	29.57
Machined	AB	XY	9	256	95	33.20
Machined	AB	XY	9	256	95	57.44
Machined	AB	XY	9	256	95	25.6
Machined	AB	XY	9	256	95	38.2
Machined	AB	XY	9	256	95	45.40
Machined	AB	XY	9	256	95	39.04
Machined	AB	XY	9	256	95	48.06
Machined	AB	XY	9	256	95	45.5
Machined	AB	XY	9	256	95	23.97
Machined	AB	XY	9	256	95	43.77
Machined	AB	XY	9	256	95	21.45
Machined	AB	XY	9	256	95	45.24
Machined	AB	XY	9	256	95	35.59
Machined	AB	XY	9	256	95	50.03
Machined	AB	XY	9	256	95	45.04
Machined	AB	XY	9	56	35	36.
Machined	AB	XY	9	56	35	42.89
Machined	AB	XY	9	56	35	29.51

<b>Machined</b>	AB	XY	9	56	35	24.89
<b>Machined</b>	AB	XY	9	56	35	31.05
<b>Machined</b>	AB	XY	9	56	35	39.73
<b>Machined</b>	AB	XY	9	56	35	34.91
<b>Machined</b>	AB	XY	9	56	35	40.64
<b>Machined</b>	AB	XY	9	56	35	41.49
<b>Machined</b>	AB	XY	9	56	35	51.34
<b>Machined</b>	AB	XY	9	56	35	37.08
<b>HIP</b>	HIP	XY	9	56	35	30.5
<b>HIP</b>	HIP	XY	9	56	35	55.38
<b>HIP</b>	HIP	XY	9	56	35	30.37
<b>HIP</b>	HIP	XY	9	56	35	45.17
<b>HIP</b>	HIP	XY	9	56	35	13.13
<b>HIP</b>	HIP	XY	9	56	35	38.19
<b>HIP</b>	HIP	XY	9	56	35	42.78
<b>HIP</b>	HIP	XY	9	56	35	25.36
<b>HIP</b>	HIP	XY	9	56	35	57.18
<b>HIP</b>	HIP	XY	9	56	35	26.76
<b>HIP</b>	HIP	XY	9	56	35	31.97
<b>HIP</b>	HIP	XY	9	56	35	46.66
<b>HIP</b>	HIP	XY	9	56	35	26.06
<b>HIP</b>	HIP	XY	9	56	35	53.47
<b>HIP</b>	HIP	XY	9	56	35	21.40
<b>HIP</b>	HIP	XY	9	156	65	66.32
<b>HIP</b>	HIP	XY	9	156	65	24.37
<b>HIP</b>	HIP	XY	9	156	65	57.25
<b>HIP</b>	HIP	XY	9	156	65	79.15
<b>HIP</b>	HIP	XY	9	156	65	40.30
<b>HIP</b>	HIP	XY	9	156	65	40.62
<b>HIP</b>	HIP	XY	9	156	65	103.63
<b>HIP</b>	HIP	XY	9	156	65	23.87
<b>HIP</b>	HIP	XZ	9	56	35	57.58
<b>HIP</b>	HIP	XZ	9	56	35	41.69
<b>HIP</b>	HIP	XZ	9	56	35	52.92
<b>HIP</b>	HIP	XZ	9	56	35	70.74

HIP	HIP	XZ	9	56	35	42.42
HIP	HIP	XZ	9	56	35	33.93
HIP	HIP	XZ	9	56	35	46.43
HIP	HIP	XZ	9	56	35	30.73
HIP	HIP	XZ	9	56	35	43.49
HIP	HIP	XZ	9	56	95	69.58
HIP	HIP	XZ	9	56	95	42.14
HIP	HIP	XZ	9	56	95	76.14
HIP	HIP	XZ	9	56	95	50.01
HIP	HIP	XZ	9	56	95	30.98
HIP	HIP	XZ	9	56	95	27.68
HIP	HIP	XZ	9	56	95	68.79
HIP	HIP	XZ	9	56	95	59.65
Machined	AB	XZ	9	56	35	38.68
Machined	AB	XZ	9	56	35	39.55
Machined	AB	XZ	9	56	35	30.94
Machined	AB	XZ	9	56	35	30.18
Machined	AB	XZ	9	56	35	33.96
Machined	AB	XZ	9	56	35	25.96
Machined	AB	XZ	9	56	35	44.93
Machined	AB	XZ	9	56	35	51.33
Machined	AB	XZ	9	56	35	51.14
Machined	AB	XZ	9	56	35	42.76
Machined	AB	XZ	9	56	35	39.39
Machined	AB	XZ	9	56	35	59.62
Machined	AB	XZ	9	56	35	44.42
Machined	AB	XZ	9	56	35	32.92
Machined	AB	XZ	9	56	35	32.55
Machined	AB	XZ	9	56	35	52
Machined	AB	XZ	9	56	35	49
Machined	AB	XZ	9	56	35	36
Machined	AB	XZ	9	56	35	44
Machined	AB	XZ	9	56	35	34.10
Machined	AB	XZ	9	256	95	39.77
Machined	AB	XZ	9	256	95	48.50

<b>Machined</b>	AB	XZ	9	256	95	45.10
<b>Machined</b>	AB	XZ	9	256	95	31.08
<b>Machined</b>	AB	XZ	9	256	95	28.03
<b>Machined</b>	AB	XZ	9	256	95	27.36
<b>Machined</b>	AB	XZ	9	256	95	50.09
<b>Machined</b>	AB	XZ	9	256	95	40.26
<b>Machined</b>	AB	XZ	9	156	65	46.21
<b>Machined</b>	AB	XZ	9	156	65	40
<b>Machined</b>	AB	XZ	9	156	65	28
<b>Machined</b>	AB	XZ	9	156	65	55
<b>Machined</b>	AB	XZ	9	156	65	16
<b>Machined</b>	AB	XZ	9	156	65	56.8
<b>Machined</b>	AB	XZ	9	156	65	49.2
<b>Machined</b>	AB	XZ	9	156	65	41.9
<b>Machined</b>	AB	XZ	9	156	65	36.114
<b>Machined</b>	AB	XZ	9	256	95	44.737
<b>Machined</b>	AB	XZ	9	256	95	33.712
<b>Machined</b>	AB	XZ	9	256	95	38
<b>Machined</b>	AB	XZ	9	256	95	21.604
<b>Machined</b>	AB	XZ	9	256	95	24.245
<b>Machined</b>	AB	XZ	9	256	95	54.179
<b>Machined</b>	AB	XZ	9	256	95	35.855
<b>Machined</b>	AB	XZ	9	256	95	30.194
<b>Machined</b>	AB	XZ	9	256	95	17.496
<b>Machined</b>	AB	XZ	9	256	95	29.246
<b>AsBuilt</b>	AB	ZX	9	56	35	77.612
<b>AsBuilt</b>	AB	ZX	9	56	35	69.765
<b>AsBuilt</b>	AB	ZX	9	56	35	48
<b>AsBuilt</b>	AB	ZX	9	56	35	74.627
<b>AsBuilt</b>	AB	ZX	9	56	35	75.74
<b>AsBuilt</b>	AB	ZX	9	56	35	20
<b>AsBuilt</b>	AB	ZX	9	56	35	49
<b>AsBuilt</b>	AB	ZX	9	56	35	31
<b>AsBuilt</b>	AB	ZX	9	56	35	77.029
<b>Machined</b>	AB	ZX	3	56	35	41

<b>Machined</b>	AB	ZX	3	56	35	49
<b>Machined</b>	AB	ZX	3	56	35	34.835
<b>Machined</b>	AB	ZX	3	56	35	61
<b>Machined</b>	AB	ZX	3	56	35	36.979
<b>Machined</b>	AB	ZX	3	56	35	30.569
<b>Machined</b>	AB	ZX	3	56	35	55
<b>Machined</b>	AB	ZX	3	56	35	58
<b>Machined</b>	AB	ZX	3	56	35	47
<b>Machined</b>	AB	ZX	3	56	35	69
<b>Machined</b>	AB	ZX	3	56	35	55
<b>Machined</b>	AB	ZX	3	56	35	71
<b>Machined</b>	AB	ZX	3	56	35	32
<b>Machined</b>	AB	ZX	3	56	35	62
<b>Machined</b>	AB	ZX	6	56	35	40.783
<b>Machined</b>	AB	ZX	6	56	35	46
<b>Machined</b>	AB	ZX	6	56	35	27.966
<b>Machined</b>	AB	ZX	6	56	35	39.81
<b>Machined</b>	AB	ZX	6	56	35	66.286
<b>Machined</b>	AB	ZX	6	56	35	70.095
<b>Machined</b>	AB	ZX	6	56	35	66
<b>Machined</b>	AB	ZX	6	56	35	34.47
<b>Machined</b>	AB	ZX	6	56	35	62
<b>Machined</b>	AB	ZX	6	56	35	39.802
<b>Machined</b>	AB	ZX	6	56	35	40.911
<b>Machined</b>	AB	ZX	6	56	35	38.258
<b>Machined</b>	AB	ZX	6	56	35	51
<b>Machined</b>	AB	ZX	6	56	35	57
<b>Machined</b>	AB	ZX	6	56	35	37
<b>Machined</b>	AB	ZX	6	56	35	28.053
<b>Machined</b>	AB	ZX	6	56	35	63
<b>Machined</b>	AB	ZX	3	256	95	23.884
<b>Machined</b>	AB	ZX	3	256	95	18.466
<b>Machined</b>	AB	ZX	3	256	95	28.571
<b>Machined</b>	AB	ZX	3	256	95	13.716
<b>Machined</b>	AB	ZX	3	256	95	23.429

<b>Machined</b>	AB	ZX	3	256	95	17.524
<b>Machined</b>	AB	ZX	3	256	95	13.396
<b>Machined</b>	AB	ZX	3	256	95	13.396
<b>Machined</b>	AB	ZX	3	256	95	28.303
<b>Machined</b>	AB	ZX	3	256	95	25.101
<b>Machined</b>	AB	ZX	3	256	95	25.663
<b>AsBuilt</b>	AB	ZX	6	56	35	55.435
<b>AsBuilt</b>	AB	ZX	6	56	35	47.613
<b>AsBuilt</b>	AB	ZX	9	56	95	41.667
<b>AsBuilt</b>	AB	ZX	9	56	95	22.348
<b>AsBuilt</b>	AB	ZX	9	56	95	23.867
<b>AsBuilt</b>	AB	ZX	9	56	95	31.063
<b>AsBuilt</b>	AB	ZX	9	56	95	39.396
<b>AsBuilt</b>	AB	ZX	9	56	95	22.666
<b>AsBuilt</b>	AB	ZX	9	56	95	49.816
<b>AsBuilt</b>	AB	ZX	9	56	95	47.334
<b>AsBuilt</b>	AB	ZX	9	56	95	24.001
<b>AsBuilt</b>	AB	ZX	9	256	35	40.916
<b>AsBuilt</b>	AB	ZX	9	256	35	43.183
<b>AsBuilt</b>	AB	ZX	9	256	35	48.864
<b>AsBuilt</b>	AB	ZX	9	256	35	40
<b>AsBuilt</b>	AB	ZX	9	256	35	28
<b>AsBuilt</b>	AB	ZX	9	256	35	26
<b>AsBuilt</b>	AB	ZX	9	256	35	13.258
<b>AsBuilt</b>	AB	ZX	9	256	35	47.159
<b>AsBuilt</b>	AB	ZX	9	256	35	22.166
<b>AsBuilt</b>	AB	ZX	9	256	35	89.018
<b>AsBuilt</b>	AB	ZX	9	256	35	41.099
<b>AsBuilt</b>	AB	ZX	9	256	65	40.803
<b>AsBuilt</b>	AB	ZX	9	256	65	20.295
<b>AsBuilt</b>	AB	ZX	9	256	65	16.511
<b>AsBuilt</b>	AB	ZX	9	256	65	30.197
<b>AsBuilt</b>	AB	ZX	9	256	65	21.699
<b>AsBuilt</b>	AB	ZX	9	256	65	36.104
<b>AsBuilt</b>	AB	ZX	9	256	65	47

<b>AsBuilt</b>	AB	ZX	9	256	65	32.555
<b>AsBuilt</b>	AB	ZX	9	256	65	34.454
<b>HIP</b>	HIP	ZX	9	56	35	38.491
<b>HIP</b>	HIP	ZX	9	56	35	67.17
<b>HIP</b>	HIP	ZX	9	56	35	33.019
<b>HIP</b>	HIP	ZX	9	56	35	21.483
<b>HIP</b>	HIP	ZX	9	56	35	34.824
<b>HIP</b>	HIP	ZX	9	56	35	47.148
<b>HIP</b>	HIP	ZX	9	56	35	29.81
<b>HIP</b>	HIP	ZX	9	56	35	69.715
<b>HIP</b>	HIP	ZX	9	56	35	62.954
<b>HIP</b>	HIP	ZX	9	56	35	43.189
<b>HIP</b>	HIP	ZX	9	156	65	53.206
<b>HIP</b>	HIP	ZX	9	156	65	49.772
<b>HIP</b>	HIP	ZX	9	156	65	28.431
<b>HIP</b>	HIP	ZX	9	156	65	48.576
<b>HIP</b>	HIP	ZX	9	156	65	49.071
<b>HIP</b>	HIP	ZX	9	256	95	55.315
<b>HIP</b>	HIP	ZX	9	256	95	30.305
<b>HIP</b>	HIP	ZX	9	256	95	36.372
<b>HIP</b>	HIP	ZX	9	256	95	49.248
<b>HIP</b>	HIP	ZX	9	256	95	15.572
<b>HIP</b>	HIP	ZX	9	256	95	27.654
<b>HIP</b>	HIP	ZX	9	256	95	45.835
<b>HIP</b>	HIP	ZX	9	256	95	40.909
<b>HIP</b>	HIP	ZX	9	256	95	48.326
<b>HIP</b>	HIP	ZX	9	256	95	16.918
<b>HIP</b>	HIP	ZX	9	256	95	24.659
<b>HIP</b>	HIP	ZX	9	256	95	28.384
<b>HIP</b>	HIP	ZX	9	256	95	56.542
<b>Machined</b>	AB	ZX	9	56	35	37.126
<b>Machined</b>	AB	ZX	9	56	35	34.091
<b>Machined</b>	AB	ZX	9	56	35	30.687
<b>Machined</b>	AB	ZX	9	56	35	37.69
<b>Machined</b>	AB	ZX	9	56	35	34.091

<b>Machined</b>	AB	ZX	6	256	95	53.435
<b>Machined</b>	AB	ZX	6	256	95	46.566
<b>Machined</b>	AB	ZX	6	256	95	55.345
<b>Machined</b>	AB	ZX	6	256	95	46.197
<b>AsBuilt</b>	AB	ZX	6	156	95	43
<b>AsBuilt</b>	AB	ZX	6	156	95	49
<b>AsBuilt</b>	AB	ZX	6	156	95	54
<b>AsBuilt</b>	AB	ZX	6	156	95	51
<b>AsBuilt</b>	AB	ZX	6	156	95	49
<b>AsBuilt</b>	AB	ZX	6	156	95	29
<b>AsBuilt</b>	AB	ZX	6	156	95	76
<b>AsBuilt</b>	AB	ZX	6	156	95	56
<b>AsBuilt</b>	AB	ZX	6	156	95	48
<b>Machined</b>	AB	ZX	6	256	35	68
<b>Machined</b>	AB	ZX	6	256	35	42
<b>Machined</b>	AB	ZX	6	256	35	39
<b>Machined</b>	AB	ZX	6	256	35	23
<b>Machined</b>	AB	ZX	6	256	35	47
<b>Machined</b>	AB	ZX	6	256	35	54
<b>Machined</b>	AB	ZX	6	256	35	26
<b>Machined</b>	AB	ZX	6	156	35	49
<b>Machined</b>	AB	ZX	6	156	35	62
<b>Machined</b>	AB	ZX	6	156	35	46
<b>Machined</b>	AB	ZX	6	156	35	60
<b>Machined</b>	AB	ZX	6	156	35	55
<b>Machined</b>	AB	ZX	6	156	35	26
<b>Machined</b>	AB	ZX	6	156	35	26
<b>Machined</b>	AB	ZX	6	156	35	29
<b>Machined</b>	AB	ZX	6	156	35	42
<b>Machined</b>	AB	ZX	6	156	35	38

## Statistics

### Microstructure 4-way ANOVA

	<b>Factor 1</b>	<b>Factor 2</b>	<b>Factor 3</b>	<b>Factor 4</b>	<b>Response 1</b>
<b>Sample</b>	A: Thickness	B: Height	C: Radial Distance	D: Orientation	a-lath thickness (um)
<b>1</b>	12	156	65	ZX	1.23
<b>2</b>	6	256	95	ZX	0.988
<b>3</b>	12	56	95	ZX	0.97
<b>4</b>	12	156	65	XZ	1.17
<b>5</b>	9	156	95	ZX	1.1
<b>6</b>	12	156	35	XY	1.76
<b>7</b>	12	56	35	XY	1.33
<b>8</b>	12	256	95	XZ	1.21
<b>9</b>	12	256	35	ZX	1.26
<b>10</b>	9	156	35	ZX	1.1
<b>11</b>	12	56	35	ZX	1.03
<b>12</b>	12	256	95	ZX	1.29
<b>13</b>	9	56	35	ZX	1.05
<b>14</b>	9	256	35	ZX	1.13
<b>15</b>	12	256	95	XY	1.76
<b>16</b>	9	256	95	ZX	1.23
<b>17</b>	12	56	35	XZ	1.07

### ANOVA Table

<b>Source</b>	<b>Sum of Squares</b>	<b>% Contribution</b>	<b>df</b>	<b>Mean Square</b>	<b>F-value</b>	<b>p-value</b>
<b>Model</b>	0.7782		6	0.1297	19.38	< 0.0001
<b>Thickness</b>	0.0530	8.2	1	0.0530	7.92	< 0.05
<b>Height</b>	0.1336	20.7	1	0.1336	19.97	< 0.05
<b>Radial Distance</b>	0.0013	0.2	1	0.0013	0.1959	0.6675
<b>Orient</b>	0.4346	67.3	2	0.2173	32.48	< 0.0001
<b>H<sup>2</sup></b>	0.0235	3.6	1	0.0235	3.51	0.0904

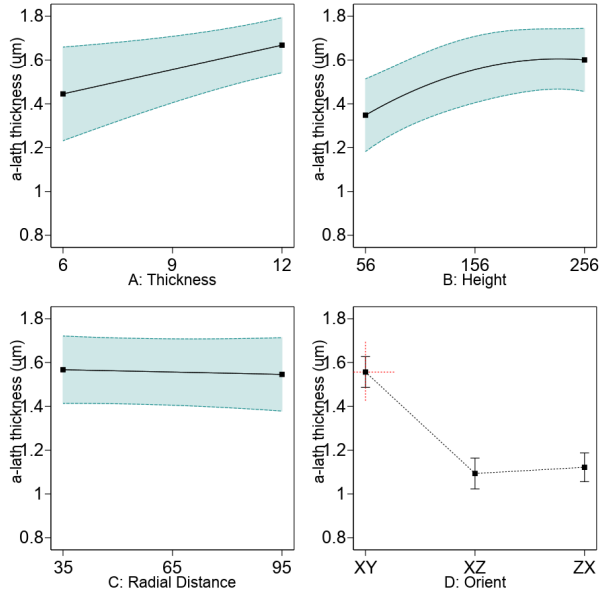
**Equation:** ZX a-lath = 0.4138+ 0.0370\*B +.00383\*H – 0.000355\*R -.0000082\*H<sup>2</sup>

XY a-lath = 0.385 + 0.0370\*B +.00383\*H – 0.000355\*R -.0000082\*H<sup>2</sup>

XY a-lath = 0.848 + 0.0370\*B +.00383\*H – 0.000355\*R -.0000082\*H<sup>2</sup>

Factor Coding: Actual  
Response: a-lath thickness (μm)

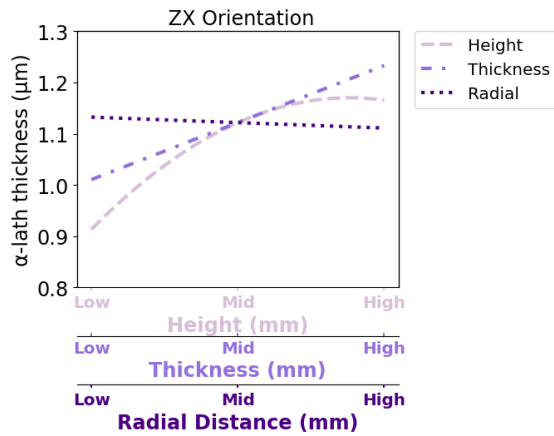
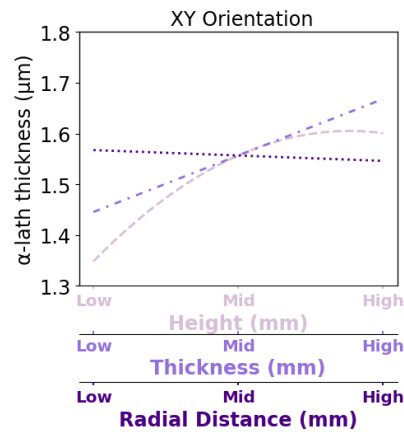
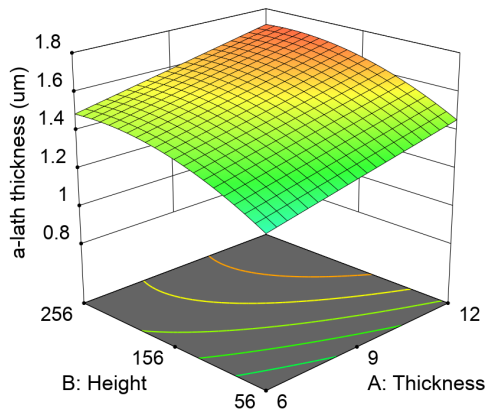
Actual Factors:  
A = 9  
B = 156  
C = 65  
D = XY



Factor Coding: Actual  
Response: a-lath thickness (μm)

Actual Factors:  
C = 65  
D = XY

3D Surface



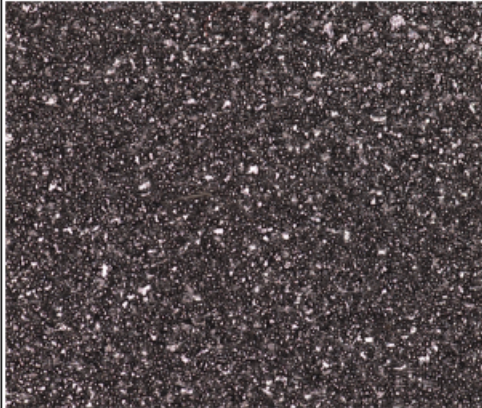
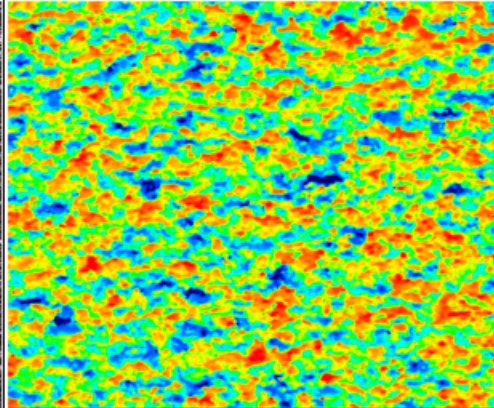
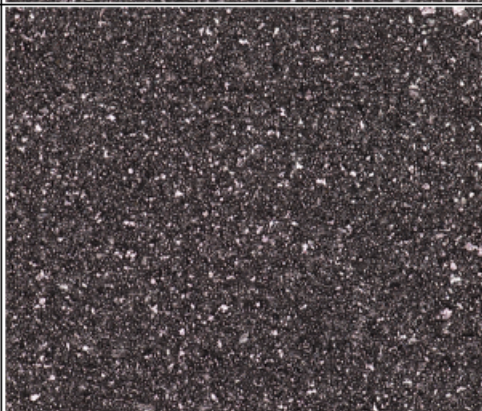
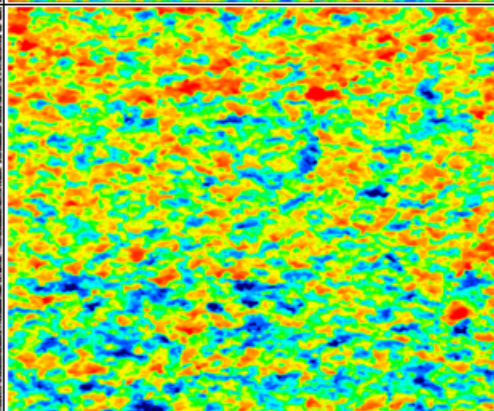
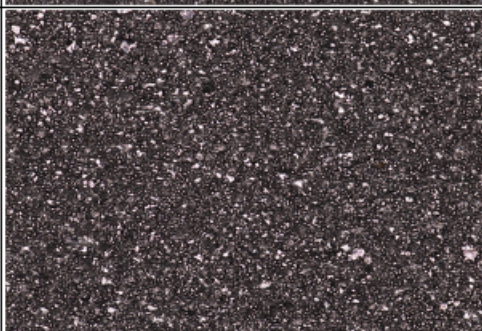
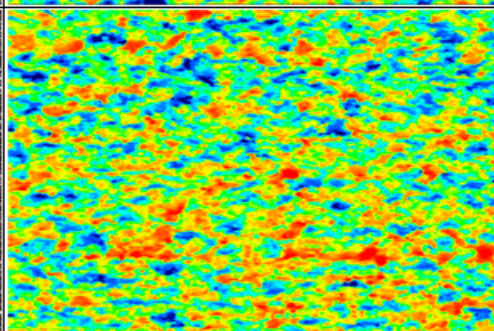
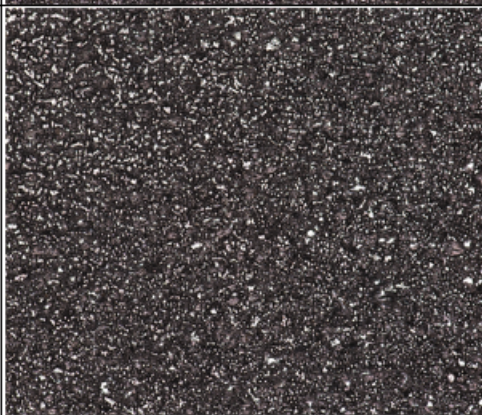
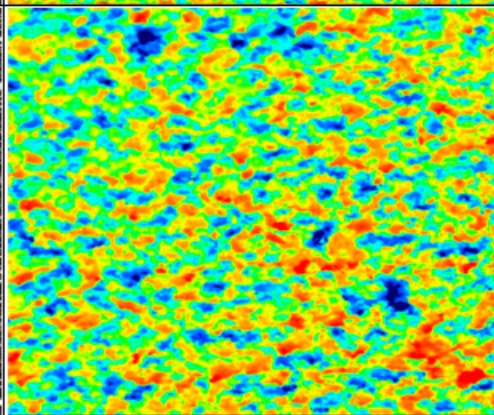
## E - Surface Roughness

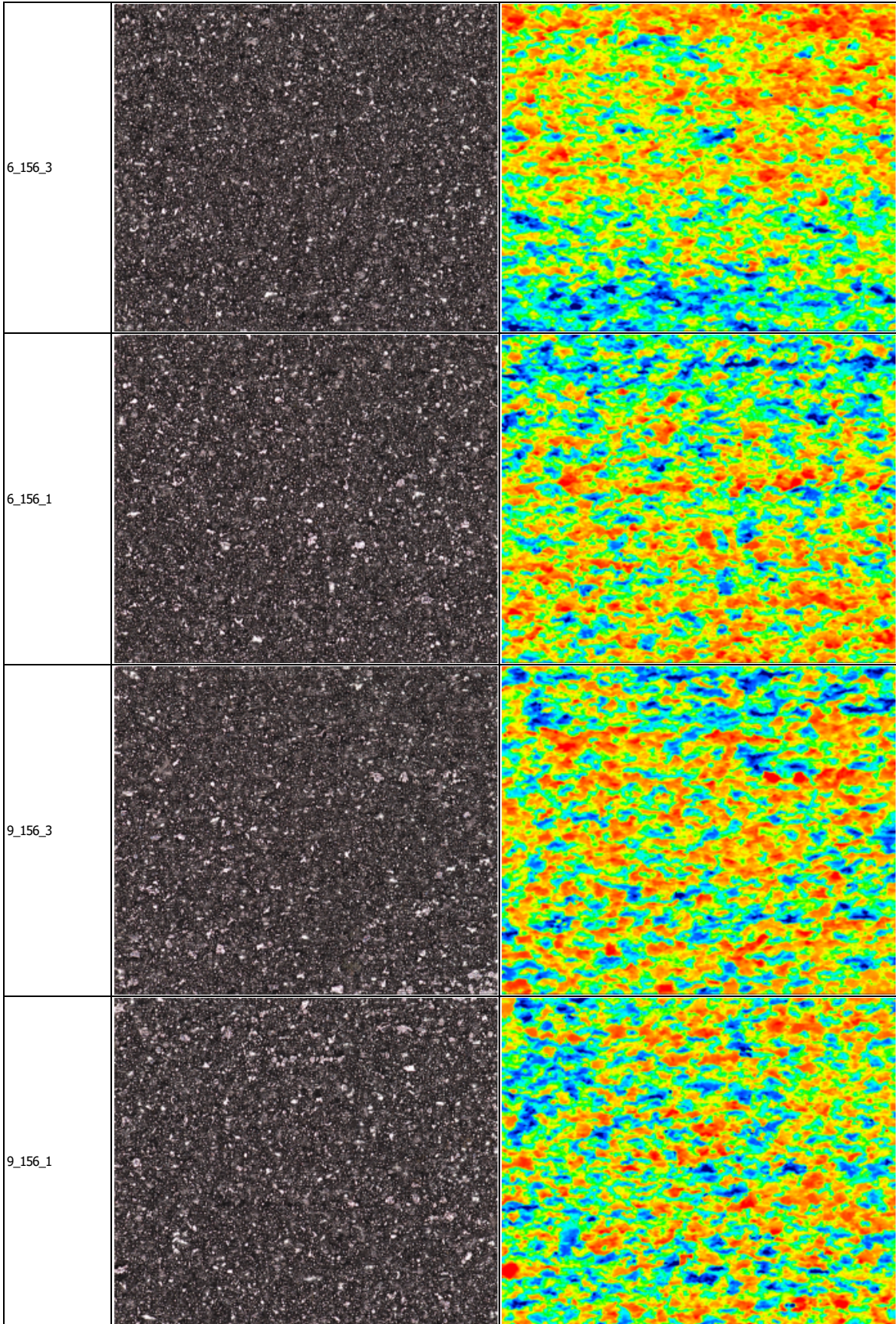
Thick	Orientation	Condition	Surface	Ra	Rz10	Rz	Rt	Rv	Rsk
9	V	HIP	Machined	1.163	3.685	6.8753	10.6194	3.49	-0.0766
9	V	HIP	Machined	0.926	2.9239	5.3301	8.6198	2.7538	-0.0758
9	V	HIP	Machined						
9	V	HIP	Machined	0.8995	2.904	5.3449	8.8165	2.47	0.1885
9	V	HIP	Machined	1.003	3.241	5.7986	8.7385	2.8118	0.0649
9	V	HIP	Machined	0.9354	3.014	5.4821	8.6464	2.786	-0.087
9	V	HIP	Machined	0.8519	2.8134	5.0649			
9	V	HIP	Machined	1.177	3.786	6.604	10.908	3.323	-0.0344
9	V	HIP	Machined	1.1869	3.6355	6.069	8.698	3.111	-0.085
9	V	HIP	Machined	1.24	3.889	7.828	12.103	3.3256	0.3995
9	V	HIP	Machined	1.245	4	7.31	12.78	3.557	0.49
9	H	AB	Machined	0.9338	3.0136	5.241	7.2826	2.51	0.0722
9	H	AB	Machined	1.104	3.536	5.928	7.625	2.955	0.0016
9	H	AB	Machined	1.723	9.145	11.2194	11.2194	5.4249	0.1134
9	H	AB	Machined	1.5107	8.553	10.536	10.5361	5.3544	-0.0006
9	H	AB	Machined	0.973	3.1705	5.4859	7.7545	2.809	-0.0588
9	H	AB	Machined	1.296	3.941	6.9095	9.288	3.362	0.0703
9	H	AB	Machined	1.0045	3.268	5.841	8.7418	2.983	-0.0595
9	H	AB	Machined	1.355	4.136	7.143	10.301	3.66	-0.0789
9	V	HIP	SP	1.2	3.593	6.4549	9.056	3.132	0.07
9	V	HIP	SP	1.12	3.89	6.853	9.893	3.571	-0.152
9	V	HIP	SP	1.224	4.216	6.93	9.38	3.6	-0.0817
9	V	HIP	SP	0.994	3.269	5.49	7.464	2.729	0.0001
9	V	HIP	SP	1.285	4.493	7.204	9.839	3.675	-0.0749
9	V	HIP	SP	1.2591	3.9979	6.504	8.58	3.265	-0.0151
9	H	HIP	SP	1.097	3.668	6.4762	9.593	3.398	-0.1274
9	H	AB	SP	1.072	3.679	6.13	8.187	3.174	-0.1165
9	H	AB	SP	1.075	3.604	5.95	7.922	3.116	-0.0773
9	H	AB	SP	1.0646	3.6504	6.145	8.7172	3.152	-0.0427
9	H	AB	SP	1.238	3.846	6.576	8.931	3.43	-0.0994
9	H	AB	SP	0.9787	3.656	5.445	7.372	2.769	-0.0472
9	H	AB	SP	0.8852	3.0691	5.1118	6.8929	2.538	0.0032
6	V	HIP	Machined	0.9097	2.668	5.221	7.8295	2.6267	-0.0584
6	V	HIP	Machined	0.8712	2.8219	5.261	9.8038	2.5509	0.0588
6	V	HIP	Machined	0.8265	2.668	5.1215	8.9194	2.457	0.1562
6	V	HIP	Machined	0.998	3.23	6.22	11.16	3.1	-0.0037

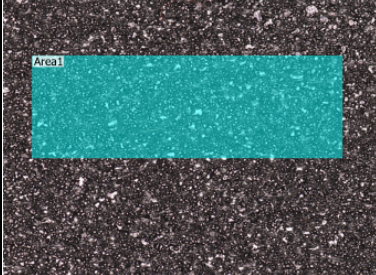
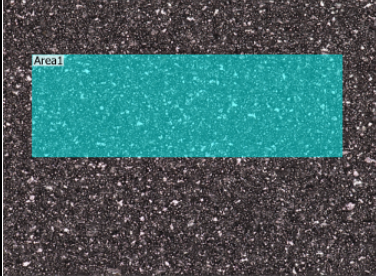
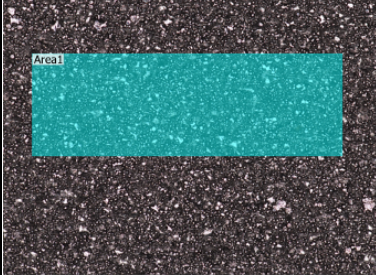
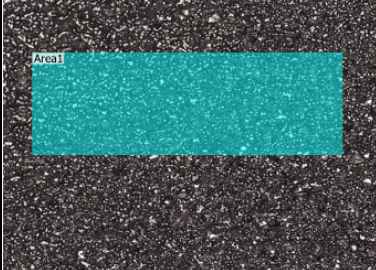
6	V	HIP	Machined	0.19	3.99	7.048	12.54	3.646	-0.0872
6	V	HIP	Machined	0.93	2.935	5.403	8.792	2.644	0.0966
6	V	HIP	Machined	1.106	3.38	5.813	8.356	2.8214	0.1389
6	V	HIP	Machined	1.168	3.78	6.576	9.7035	3.52	-0.167
6	V	HIP	Machined	1.192	3.9637	6.922	10.838	3.27	0.1326
6	V	HIP	Machined	1.042	3.351	6.0387	9.592	3	0.0171
6	V	HIP	Machined	1.103	3.555	7.0653	13.907	3.573	0.0498
6	V	HIP	Machined	0.9787	3.1321	5.651	9.39	2.86	-0.0795
6	V	HIP	Machined	1.232	4.0161	7.4075	11.553	3.373	0.1884
6	V	HIP	Machined	0.9256	3.041	5.1986	7.805	2.53	0.0667
6	V	HIP	Machined	1.025	3.231	6.107	10.3079	3.03	0.0195
6	V	HIP	Machined	1.429	4.45	7.9	11.7609	3.766	0.167
6	V	HIP	Machined	1.116	3.747	6.521	9.898	3.1784	0.0787
6	V	HIP	Machined	1.066	3.513	6.292	9.8145	3.09	0.07
6	V	HIP	Machined	1.0778	3.4297	6.3051	10.412	3.326	-0.2099
6	V	HIP	Machined	1.06	3.315	5.924	8.436	2.966	0.0138
6	V	HIP	Machined	1.127	3.5889	6.653	10.879	3.62	-0.206
6	V	HIP	Machined	0.76	2.4669	4.596	7.72	2.453	-0.2018
6	V	HIP	Machined	1.156	3.771	6.883	11.596	3.46	-0.023
6	V	HIP	Machined	1.082	3.562	6.328	10.202	3.33	-0.1095
6	H	HIP	Machined	1.533	4.974	9.02	16.2739	4.181	0.2258
6	H	HIP	Machined	1.53	4.6386	8.9256	14.803	4.49	-0.0493
6	H	HIP	Machined	1.435	4.3776	7.982	13.113	3.93	-0.0144
6	H	HIP	Machined	1.759	5.295	10.306	16.7456	4.61	0.699
6	H	HIP	Machined	1.062	3.366	6.675	11.975	3.235	0.0617
6	H	HIP	Machined	1.469	4.596	8.7917	13.925	4.1056	0.1689
6	H	HIP	Machined	1.44	4.49	9.47	17.6478	4.541	0.134
6	H	HIP	Machined	1.902	6.053	10.908	15.95	5.362	0.1396
6	H	HIP	Machined	1.906	5.946	10.501	16.718	4.661	0.328
6	H	HIP	Machined	1.297	3.993	7.514	12.406	3.636	0.115
6	H	HIP	Machined	1.471	8.71	10.8	10.8	5.478	-0.0166
6	H	HIP	Machined	1.482	8.664	10.686	10.686	5.45	0.0056
6	H	AB	Machined	1.655	10.01	13.017	15.3986	4.98	0.18
6	H	AB	Machined	1.509	8.86	11.456	18.16	6.227	-0.037
6	H	AB	Machined	1.988	6.3914	10.664	16.442	5.323	-0.0167
6	H	AB	Machined	1.6435	10.372	13.5661	17.5662	6.0796	0.04
6	V	HIP	AB	9.1283	18.0356	35.1578	56.1548	16.7219	0.1856
6	V	HIP	AB	23.4134	86.5887	119.3343	119.3343	58.1451	-0.0359
6	V	HIP	AB	22.5582	97.958	127.0614	127.0614	63.0263	0.1076

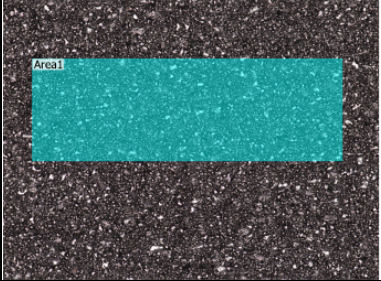
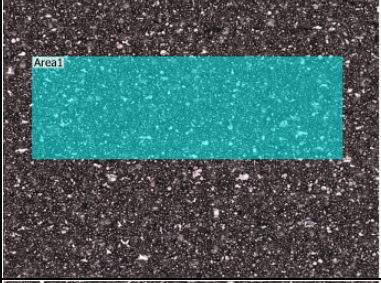
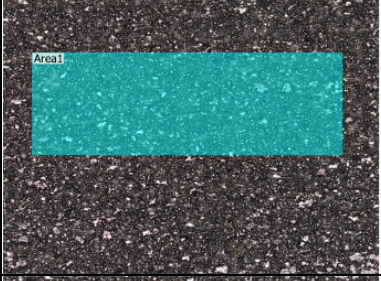
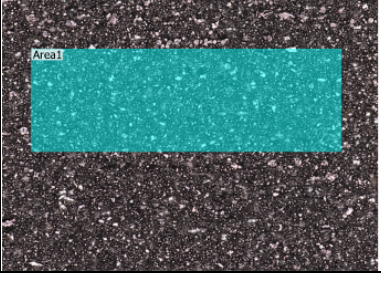
6	V	HIP	AB	24.6637	104.0107	149.4763	149.4763	74.091	0.0691
6	V	HIP	AB	23.5108	101.9635	129.2111	129.2111	56.9794	0.4974
6	V	HIP	AB	21.4848	95.3106	119.1047	119.1047	60.9724	0.037
6	V	HIP	AB	23.5531	105.3528	144.6605	144.6605	68.7442	0.2532
6	V	HIP	AB	20.5075	87.0798	128.3176	128.3176	62.4761	0.1092
6	V	HIP	AB	19.6243	84.2498	103.5835	103.5835	56.2352	-0.1984
6	V	AB	AB	18.6204	51.7929	91.554	133.2404	46.4355	-0.0228
6	V	AB	AB	18.795	88.88	112.35	114.33	50.83	-0.24
6	V	AB	AB	20.66	96.19	112.87	125	46.59	0.28
6	V	AB	AB	16.73	86.902	107.49	111.13	50.48	-0.22
6	V	AB	AB	17.157	81.669	97.39	107.36	45.61	-0.35
6	V	AB	AB	16.477	83.01	105.18	105.18	49.5	-0.41
6	V	AB	AB	16.934	89.61	132.26	132.26	51.41	0.18
6	V	HIP	AB	19.952	61.33	85	128.796	48.66	-0.1447

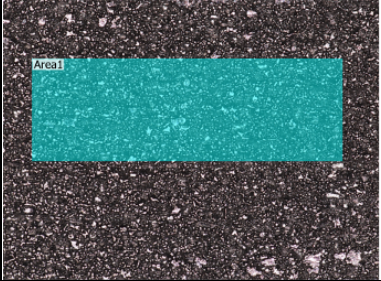
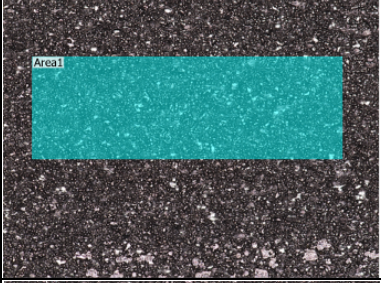
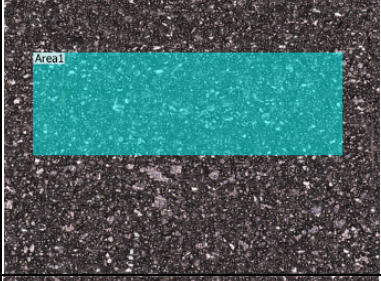
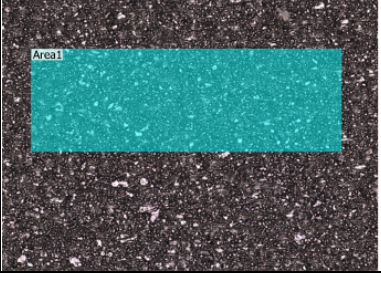
### Keyence Surface Profilometry – As-Built

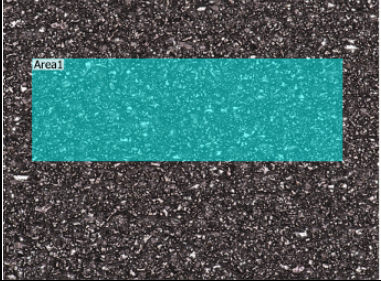
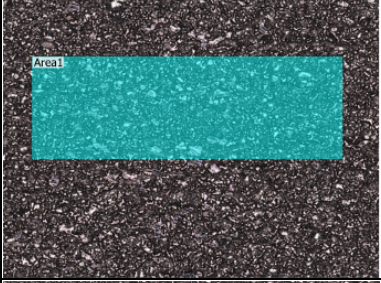
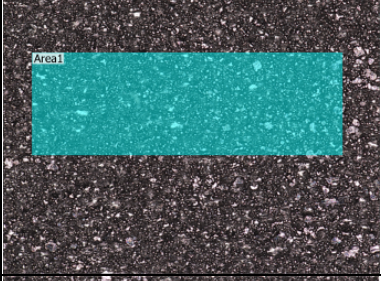
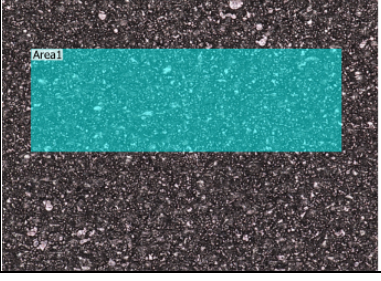
Measurement data name	Main image	Main image2
	Optical	Height
3_156_2		
3_156_3		
3_156_1		
6_156_2		

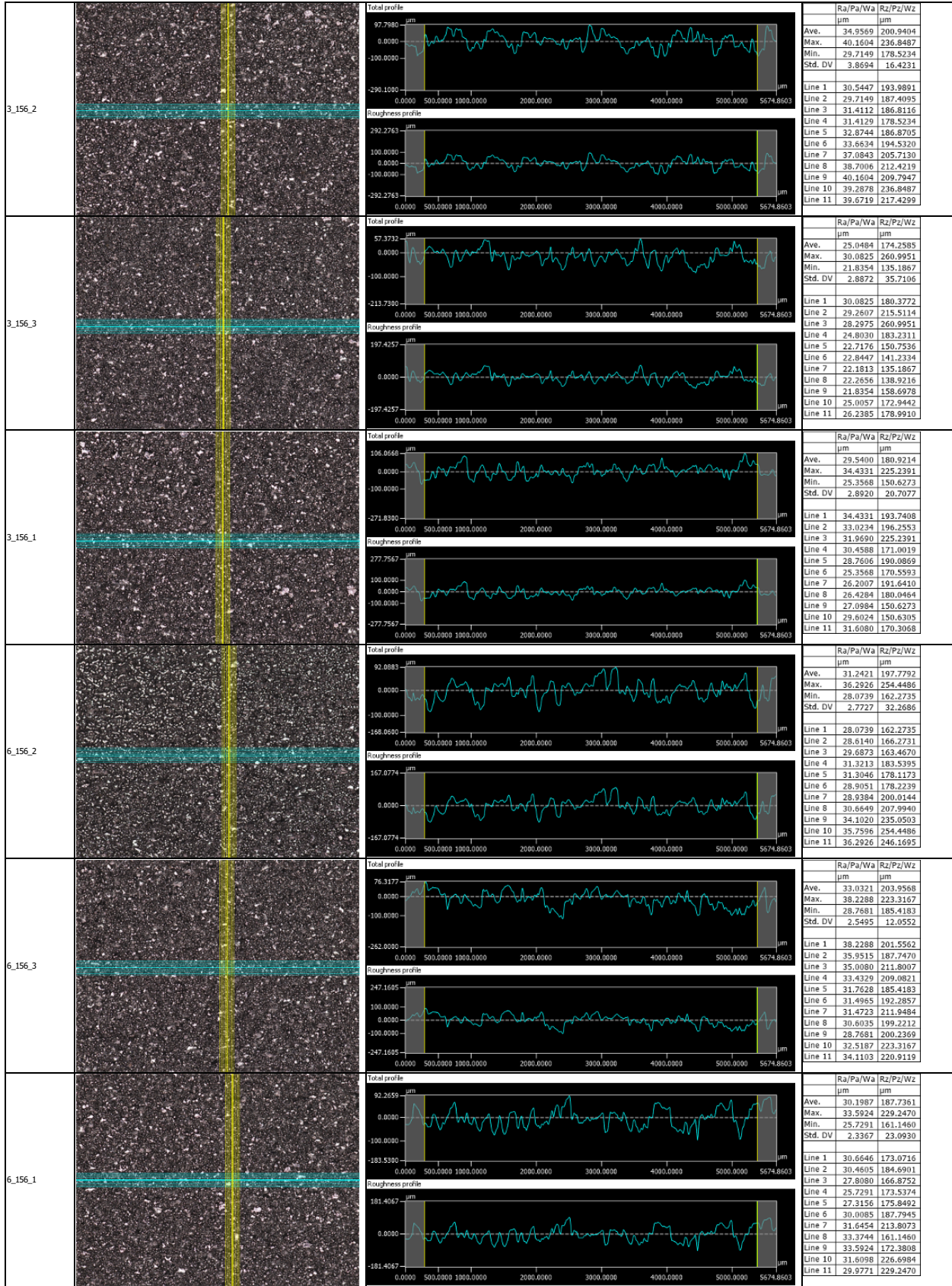


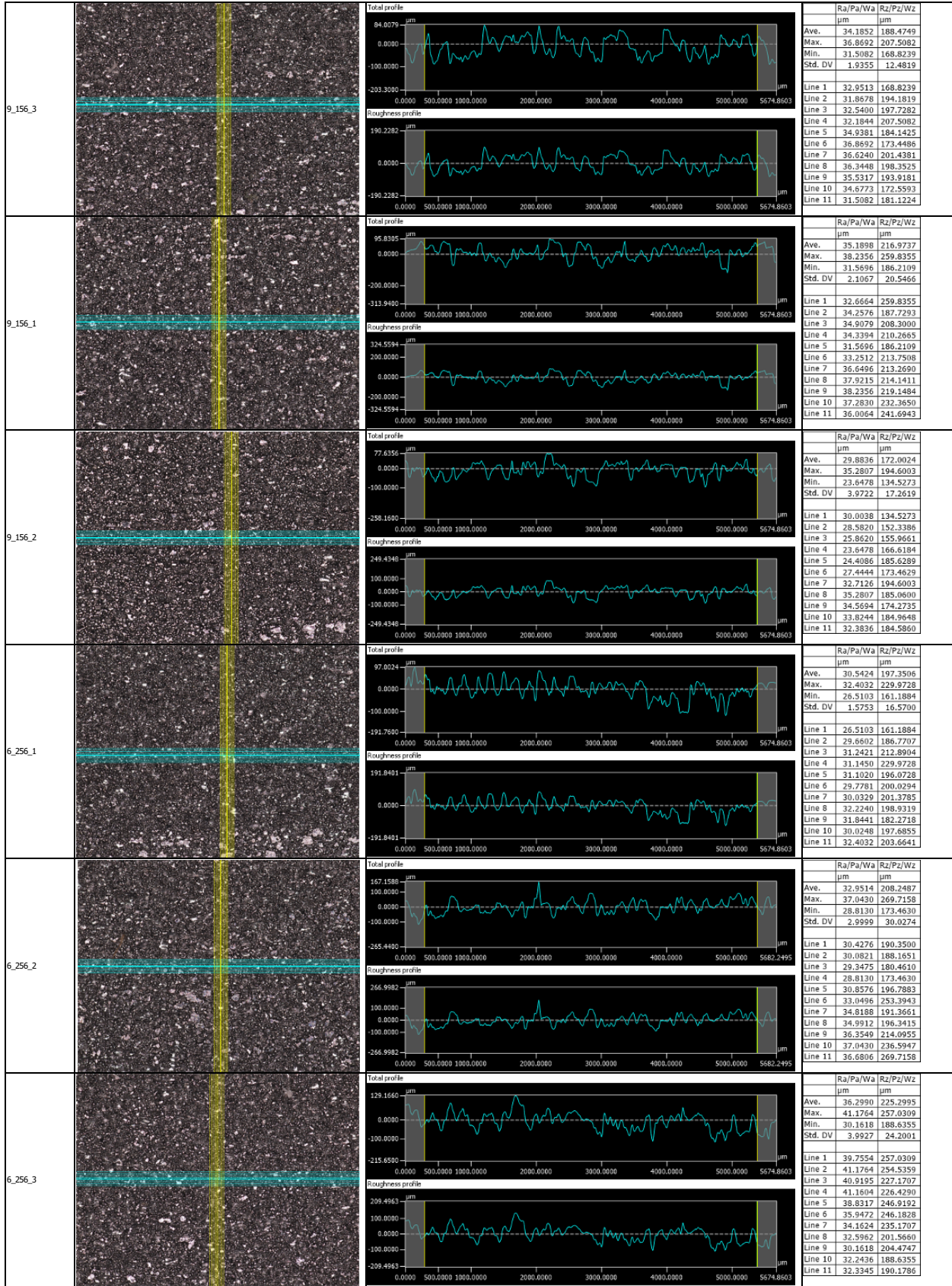
Measurement data name	Original surface		Surface roughness					Area1																													
	Optical	Measured values	Sa	Sz	Sq	Sp	Sv	Sa	Sz	Sq	Sp	Sv																									
			μm	μm	μm	μm	μm	μm	μm	μm	μm	μm	μm																								
3_156_2		<table border="1"> <tr><td>Max.</td><td>26.6755</td><td>294.7634</td><td>33.1988</td><td>151.6086</td><td>143.1547</td></tr> <tr><td>Min.</td><td>26.6755</td><td>294.7634</td><td>33.1988</td><td>151.6086</td><td>143.1547</td></tr> <tr><td>Ave.</td><td>26.6755</td><td>294.7634</td><td>33.1988</td><td>151.6086</td><td>143.1547</td></tr> <tr><td>Std. DV</td><td>0.0000</td><td>0.0000</td><td>0.0000</td><td>0.0000</td><td>0.0000</td></tr> <tr><td>Area1</td><td>26.6755</td><td>294.7634</td><td>33.1988</td><td>151.6086</td><td>143.1547</td></tr> </table>	Max.	26.6755	294.7634	33.1988	151.6086	143.1547	Min.	26.6755	294.7634	33.1988	151.6086	143.1547	Ave.	26.6755	294.7634	33.1988	151.6086	143.1547	Std. DV	0.0000	0.0000	0.0000	0.0000	0.0000	Area1	26.6755	294.7634	33.1988	151.6086	143.1547	26.6755	294.7634	33.1988	151.6086	143.1547
Max.	26.6755	294.7634	33.1988	151.6086	143.1547																																
Min.	26.6755	294.7634	33.1988	151.6086	143.1547																																
Ave.	26.6755	294.7634	33.1988	151.6086	143.1547																																
Std. DV	0.0000	0.0000	0.0000	0.0000	0.0000																																
Area1	26.6755	294.7634	33.1988	151.6086	143.1547																																
3_156_3		<table border="1"> <tr><td>Max.</td><td>20.7664</td><td>248.4134</td><td>26.1728</td><td>92.7598</td><td>155.6536</td></tr> <tr><td>Min.</td><td>20.7664</td><td>248.4134</td><td>26.1728</td><td>92.7598</td><td>155.6536</td></tr> <tr><td>Ave.</td><td>20.7664</td><td>248.4134</td><td>26.1728</td><td>92.7598</td><td>155.6536</td></tr> <tr><td>Std. DV</td><td>0.0000</td><td>0.0000</td><td>0.0000</td><td>0.0000</td><td>0.0000</td></tr> <tr><td>Area1</td><td>20.7664</td><td>248.4134</td><td>26.1728</td><td>92.7598</td><td>155.6536</td></tr> </table>	Max.	20.7664	248.4134	26.1728	92.7598	155.6536	Min.	20.7664	248.4134	26.1728	92.7598	155.6536	Ave.	20.7664	248.4134	26.1728	92.7598	155.6536	Std. DV	0.0000	0.0000	0.0000	0.0000	0.0000	Area1	20.7664	248.4134	26.1728	92.7598	155.6536	20.7664	248.4134	26.1728	92.7598	155.6536
Max.	20.7664	248.4134	26.1728	92.7598	155.6536																																
Min.	20.7664	248.4134	26.1728	92.7598	155.6536																																
Ave.	20.7664	248.4134	26.1728	92.7598	155.6536																																
Std. DV	0.0000	0.0000	0.0000	0.0000	0.0000																																
Area1	20.7664	248.4134	26.1728	92.7598	155.6536																																
3_156_1		<table border="1"> <tr><td>Max.</td><td>25.3579</td><td>292.9000</td><td>31.5312</td><td>113.6462</td><td>179.2538</td></tr> <tr><td>Min.</td><td>25.3579</td><td>292.9000</td><td>31.5312</td><td>113.6462</td><td>179.2538</td></tr> <tr><td>Ave.</td><td>25.3579</td><td>292.9000</td><td>31.5312</td><td>113.6462</td><td>179.2538</td></tr> <tr><td>Std. DV</td><td>0.0000</td><td>0.0000</td><td>0.0000</td><td>0.0000</td><td>0.0000</td></tr> <tr><td>Area1</td><td>25.3579</td><td>292.9000</td><td>31.5312</td><td>113.6462</td><td>179.2538</td></tr> </table>	Max.	25.3579	292.9000	31.5312	113.6462	179.2538	Min.	25.3579	292.9000	31.5312	113.6462	179.2538	Ave.	25.3579	292.9000	31.5312	113.6462	179.2538	Std. DV	0.0000	0.0000	0.0000	0.0000	0.0000	Area1	25.3579	292.9000	31.5312	113.6462	179.2538	25.3579	292.9000	31.5312	113.6462	179.2538
Max.	25.3579	292.9000	31.5312	113.6462	179.2538																																
Min.	25.3579	292.9000	31.5312	113.6462	179.2538																																
Ave.	25.3579	292.9000	31.5312	113.6462	179.2538																																
Std. DV	0.0000	0.0000	0.0000	0.0000	0.0000																																
Area1	25.3579	292.9000	31.5312	113.6462	179.2538																																
6_156_2		<table border="1"> <tr><td>Max.</td><td>24.8593</td><td>210.6510</td><td>30.6993</td><td>115.4558</td><td>95.1952</td></tr> <tr><td>Min.</td><td>24.8593</td><td>210.6510</td><td>30.6993</td><td>115.4558</td><td>95.1952</td></tr> <tr><td>Ave.</td><td>24.8593</td><td>210.6510</td><td>30.6993</td><td>115.4558</td><td>95.1952</td></tr> <tr><td>Std. DV</td><td>0.0000</td><td>0.0000</td><td>0.0000</td><td>0.0000</td><td>0.0000</td></tr> <tr><td>Area1</td><td>24.8593</td><td>210.6510</td><td>30.6993</td><td>115.4558</td><td>95.1952</td></tr> </table>	Max.	24.8593	210.6510	30.6993	115.4558	95.1952	Min.	24.8593	210.6510	30.6993	115.4558	95.1952	Ave.	24.8593	210.6510	30.6993	115.4558	95.1952	Std. DV	0.0000	0.0000	0.0000	0.0000	0.0000	Area1	24.8593	210.6510	30.6993	115.4558	95.1952	24.8593	210.6510	30.6993	115.4558	95.1952
Max.	24.8593	210.6510	30.6993	115.4558	95.1952																																
Min.	24.8593	210.6510	30.6993	115.4558	95.1952																																
Ave.	24.8593	210.6510	30.6993	115.4558	95.1952																																
Std. DV	0.0000	0.0000	0.0000	0.0000	0.0000																																
Area1	24.8593	210.6510	30.6993	115.4558	95.1952																																

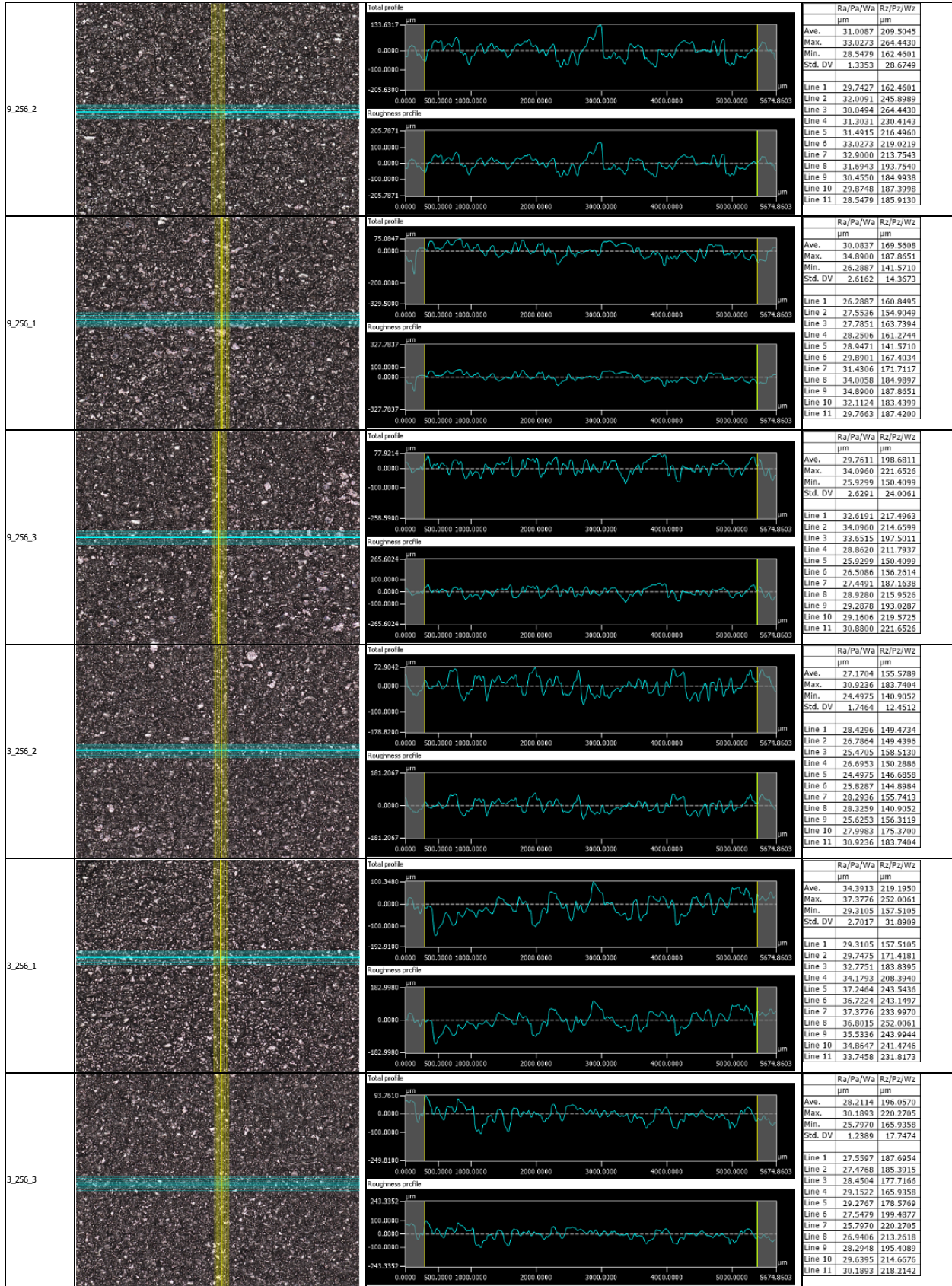
6_156_3		<table border="1"> <thead> <tr> <th></th> <th>Sa</th> <th>Sz</th> <th>Sq</th> <th>Sp</th> <th>Sv</th> </tr> <tr> <th></th> <th>µm</th> <th>µm</th> <th>µm</th> <th>µm</th> <th>µm</th> </tr> </thead> <tbody> <tr> <td>Max.</td> <td>23.6987</td> <td>371.4445</td> <td>29.9168</td> <td>149.5027</td> <td>221.9418</td> </tr> <tr> <td>Min.</td> <td>23.6987</td> <td>371.4445</td> <td>29.9168</td> <td>149.5027</td> <td>221.9418</td> </tr> <tr> <td>Ave.</td> <td>23.6987</td> <td>371.4445</td> <td>29.9168</td> <td>149.5027</td> <td>221.9418</td> </tr> <tr> <td>Std. DV</td> <td>0.0000</td> <td>0.0000</td> <td>0.0000</td> <td>0.0000</td> <td>0.0000</td> </tr> <tr> <td>Area1</td> <td>23.6987</td> <td>371.4445</td> <td>29.9168</td> <td>149.5027</td> <td>221.9418</td> </tr> </tbody> </table>		Sa	Sz	Sq	Sp	Sv		µm	µm	µm	µm	µm	Max.	23.6987	371.4445	29.9168	149.5027	221.9418	Min.	23.6987	371.4445	29.9168	149.5027	221.9418	Ave.	23.6987	371.4445	29.9168	149.5027	221.9418	Std. DV	0.0000	0.0000	0.0000	0.0000	0.0000	Area1	23.6987	371.4445	29.9168	149.5027	221.9418	23.6987	371.4445	29.9168	149.5027	221.9418
	Sa	Sz	Sq	Sp	Sv																																												
	µm	µm	µm	µm	µm																																												
Max.	23.6987	371.4445	29.9168	149.5027	221.9418																																												
Min.	23.6987	371.4445	29.9168	149.5027	221.9418																																												
Ave.	23.6987	371.4445	29.9168	149.5027	221.9418																																												
Std. DV	0.0000	0.0000	0.0000	0.0000	0.0000																																												
Area1	23.6987	371.4445	29.9168	149.5027	221.9418																																												
6_156_1		<table border="1"> <thead> <tr> <th></th> <th>Sa</th> <th>Sz</th> <th>Sq</th> <th>Sp</th> <th>Sv</th> </tr> <tr> <th></th> <th>µm</th> <th>µm</th> <th>µm</th> <th>µm</th> <th>µm</th> </tr> </thead> <tbody> <tr> <td>Max.</td> <td>23.8377</td> <td>244.8426</td> <td>29.8632</td> <td>96.2497</td> <td>148.5929</td> </tr> <tr> <td>Min.</td> <td>23.8377</td> <td>244.8426</td> <td>29.8632</td> <td>96.2497</td> <td>148.5929</td> </tr> <tr> <td>Ave.</td> <td>23.8377</td> <td>244.8426</td> <td>29.8632</td> <td>96.2497</td> <td>148.5929</td> </tr> <tr> <td>Std. DV</td> <td>0.0000</td> <td>0.0000</td> <td>0.0000</td> <td>0.0000</td> <td>0.0000</td> </tr> <tr> <td>Area1</td> <td>23.8377</td> <td>244.8426</td> <td>29.8632</td> <td>96.2497</td> <td>148.5929</td> </tr> </tbody> </table>		Sa	Sz	Sq	Sp	Sv		µm	µm	µm	µm	µm	Max.	23.8377	244.8426	29.8632	96.2497	148.5929	Min.	23.8377	244.8426	29.8632	96.2497	148.5929	Ave.	23.8377	244.8426	29.8632	96.2497	148.5929	Std. DV	0.0000	0.0000	0.0000	0.0000	0.0000	Area1	23.8377	244.8426	29.8632	96.2497	148.5929	23.8377	244.8426	29.8632	96.2497	148.5929
	Sa	Sz	Sq	Sp	Sv																																												
	µm	µm	µm	µm	µm																																												
Max.	23.8377	244.8426	29.8632	96.2497	148.5929																																												
Min.	23.8377	244.8426	29.8632	96.2497	148.5929																																												
Ave.	23.8377	244.8426	29.8632	96.2497	148.5929																																												
Std. DV	0.0000	0.0000	0.0000	0.0000	0.0000																																												
Area1	23.8377	244.8426	29.8632	96.2497	148.5929																																												
9_156_3		<table border="1"> <thead> <tr> <th></th> <th>Sa</th> <th>Sz</th> <th>Sq</th> <th>Sp</th> <th>Sv</th> </tr> <tr> <th></th> <th>µm</th> <th>µm</th> <th>µm</th> <th>µm</th> <th>µm</th> </tr> </thead> <tbody> <tr> <td>Max.</td> <td>25.7722</td> <td>213.8586</td> <td>31.9092</td> <td>113.6602</td> <td>100.1985</td> </tr> <tr> <td>Min.</td> <td>25.7722</td> <td>213.8586</td> <td>31.9092</td> <td>113.6602</td> <td>100.1985</td> </tr> <tr> <td>Ave.</td> <td>25.7722</td> <td>213.8586</td> <td>31.9092</td> <td>113.6602</td> <td>100.1985</td> </tr> <tr> <td>Std. DV</td> <td>0.0000</td> <td>0.0000</td> <td>0.0000</td> <td>0.0000</td> <td>0.0000</td> </tr> <tr> <td>Area1</td> <td>25.7722</td> <td>213.8586</td> <td>31.9092</td> <td>113.6602</td> <td>100.1985</td> </tr> </tbody> </table>		Sa	Sz	Sq	Sp	Sv		µm	µm	µm	µm	µm	Max.	25.7722	213.8586	31.9092	113.6602	100.1985	Min.	25.7722	213.8586	31.9092	113.6602	100.1985	Ave.	25.7722	213.8586	31.9092	113.6602	100.1985	Std. DV	0.0000	0.0000	0.0000	0.0000	0.0000	Area1	25.7722	213.8586	31.9092	113.6602	100.1985	25.7722	213.8586	31.9092	113.6602	100.1985
	Sa	Sz	Sq	Sp	Sv																																												
	µm	µm	µm	µm	µm																																												
Max.	25.7722	213.8586	31.9092	113.6602	100.1985																																												
Min.	25.7722	213.8586	31.9092	113.6602	100.1985																																												
Ave.	25.7722	213.8586	31.9092	113.6602	100.1985																																												
Std. DV	0.0000	0.0000	0.0000	0.0000	0.0000																																												
Area1	25.7722	213.8586	31.9092	113.6602	100.1985																																												
9_156_1		<table border="1"> <thead> <tr> <th></th> <th>Sa</th> <th>Sz</th> <th>Sq</th> <th>Sp</th> <th>Sv</th> </tr> <tr> <th></th> <th>µm</th> <th>µm</th> <th>µm</th> <th>µm</th> <th>µm</th> </tr> </thead> <tbody> <tr> <td>Max.</td> <td>26.4505</td> <td>280.4033</td> <td>32.6576</td> <td>118.8094</td> <td>161.5938</td> </tr> <tr> <td>Min.</td> <td>26.4505</td> <td>280.4033</td> <td>32.6576</td> <td>118.8094</td> <td>161.5938</td> </tr> <tr> <td>Ave.</td> <td>26.4505</td> <td>280.4033</td> <td>32.6576</td> <td>118.8094</td> <td>161.5938</td> </tr> <tr> <td>Std. DV</td> <td>0.0000</td> <td>0.0000</td> <td>0.0000</td> <td>0.0000</td> <td>0.0000</td> </tr> <tr> <td>Area1</td> <td>26.4505</td> <td>280.4033</td> <td>32.6576</td> <td>118.8094</td> <td>161.5938</td> </tr> </tbody> </table>		Sa	Sz	Sq	Sp	Sv		µm	µm	µm	µm	µm	Max.	26.4505	280.4033	32.6576	118.8094	161.5938	Min.	26.4505	280.4033	32.6576	118.8094	161.5938	Ave.	26.4505	280.4033	32.6576	118.8094	161.5938	Std. DV	0.0000	0.0000	0.0000	0.0000	0.0000	Area1	26.4505	280.4033	32.6576	118.8094	161.5938	26.4505	280.4033	32.6576	118.8094	161.5938
	Sa	Sz	Sq	Sp	Sv																																												
	µm	µm	µm	µm	µm																																												
Max.	26.4505	280.4033	32.6576	118.8094	161.5938																																												
Min.	26.4505	280.4033	32.6576	118.8094	161.5938																																												
Ave.	26.4505	280.4033	32.6576	118.8094	161.5938																																												
Std. DV	0.0000	0.0000	0.0000	0.0000	0.0000																																												
Area1	26.4505	280.4033	32.6576	118.8094	161.5938																																												

9_156_2		<table border="1"> <thead> <tr> <th></th> <th>Sa</th> <th>Sz</th> <th>Sq</th> <th>Sp</th> <th>Sv</th> </tr> <tr> <th></th> <th>μm</th> <th>μm</th> <th>μm</th> <th>μm</th> <th>μm</th> </tr> </thead> <tbody> <tr> <td>Max.</td> <td>23.2561</td> <td>258.1228</td> <td>29.5107</td> <td>113.8671</td> <td>144.2557</td> </tr> <tr> <td>Min.</td> <td>23.2561</td> <td>258.1228</td> <td>29.5107</td> <td>113.8671</td> <td>144.2557</td> </tr> <tr> <td>Ave.</td> <td>23.2561</td> <td>258.1228</td> <td>29.5107</td> <td>113.8671</td> <td>144.2557</td> </tr> <tr> <td>Std. DV</td> <td>0.0000</td> <td>0.0000</td> <td>0.0000</td> <td>0.0000</td> <td>0.0000</td> </tr> <tr> <td>Area1</td> <td>23.2561</td> <td>258.1228</td> <td>29.5107</td> <td>113.8671</td> <td>144.2557</td> </tr> </tbody> </table>		Sa	Sz	Sq	Sp	Sv		μm	μm	μm	μm	μm	Max.	23.2561	258.1228	29.5107	113.8671	144.2557	Min.	23.2561	258.1228	29.5107	113.8671	144.2557	Ave.	23.2561	258.1228	29.5107	113.8671	144.2557	Std. DV	0.0000	0.0000	0.0000	0.0000	0.0000	Area1	23.2561	258.1228	29.5107	113.8671	144.2557	23.2561	258.1228	29.5107	113.8671	144.2557
	Sa	Sz	Sq	Sp	Sv																																												
	μm	μm	μm	μm	μm																																												
Max.	23.2561	258.1228	29.5107	113.8671	144.2557																																												
Min.	23.2561	258.1228	29.5107	113.8671	144.2557																																												
Ave.	23.2561	258.1228	29.5107	113.8671	144.2557																																												
Std. DV	0.0000	0.0000	0.0000	0.0000	0.0000																																												
Area1	23.2561	258.1228	29.5107	113.8671	144.2557																																												
6_256_1		<table border="1"> <thead> <tr> <th></th> <th>Sa</th> <th>Sz</th> <th>Sq</th> <th>Sp</th> <th>Sv</th> </tr> <tr> <th></th> <th>μm</th> <th>μm</th> <th>μm</th> <th>μm</th> <th>μm</th> </tr> </thead> <tbody> <tr> <td>Max.</td> <td>25.6397</td> <td>247.6244</td> <td>31.9918</td> <td>117.4163</td> <td>130.2080</td> </tr> <tr> <td>Min.</td> <td>25.6397</td> <td>247.6244</td> <td>31.9918</td> <td>117.4163</td> <td>130.2080</td> </tr> <tr> <td>Ave.</td> <td>25.6397</td> <td>247.6244</td> <td>31.9918</td> <td>117.4163</td> <td>130.2080</td> </tr> <tr> <td>Std. DV</td> <td>0.0000</td> <td>0.0000</td> <td>0.0000</td> <td>0.0000</td> <td>0.0000</td> </tr> <tr> <td>Area1</td> <td>25.6397</td> <td>247.6244</td> <td>31.9918</td> <td>117.4163</td> <td>130.2080</td> </tr> </tbody> </table>		Sa	Sz	Sq	Sp	Sv		μm	μm	μm	μm	μm	Max.	25.6397	247.6244	31.9918	117.4163	130.2080	Min.	25.6397	247.6244	31.9918	117.4163	130.2080	Ave.	25.6397	247.6244	31.9918	117.4163	130.2080	Std. DV	0.0000	0.0000	0.0000	0.0000	0.0000	Area1	25.6397	247.6244	31.9918	117.4163	130.2080	25.6397	247.6244	31.9918	117.4163	130.2080
	Sa	Sz	Sq	Sp	Sv																																												
	μm	μm	μm	μm	μm																																												
Max.	25.6397	247.6244	31.9918	117.4163	130.2080																																												
Min.	25.6397	247.6244	31.9918	117.4163	130.2080																																												
Ave.	25.6397	247.6244	31.9918	117.4163	130.2080																																												
Std. DV	0.0000	0.0000	0.0000	0.0000	0.0000																																												
Area1	25.6397	247.6244	31.9918	117.4163	130.2080																																												
6_256_2		<table border="1"> <thead> <tr> <th></th> <th>Sa</th> <th>Sz</th> <th>Sq</th> <th>Sp</th> <th>Sv</th> </tr> <tr> <th></th> <th>μm</th> <th>μm</th> <th>μm</th> <th>μm</th> <th>μm</th> </tr> </thead> <tbody> <tr> <td>Max.</td> <td>26.2514</td> <td>414.8461</td> <td>32.7521</td> <td>164.5467</td> <td>250.2994</td> </tr> <tr> <td>Min.</td> <td>26.2514</td> <td>414.8461</td> <td>32.7521</td> <td>164.5467</td> <td>250.2994</td> </tr> <tr> <td>Ave.</td> <td>26.2514</td> <td>414.8461</td> <td>32.7521</td> <td>164.5467</td> <td>250.2994</td> </tr> <tr> <td>Std. DV</td> <td>0.0000</td> <td>0.0000</td> <td>0.0000</td> <td>0.0000</td> <td>0.0000</td> </tr> <tr> <td>Area1</td> <td>26.2514</td> <td>414.8461</td> <td>32.7521</td> <td>164.5467</td> <td>250.2994</td> </tr> </tbody> </table>		Sa	Sz	Sq	Sp	Sv		μm	μm	μm	μm	μm	Max.	26.2514	414.8461	32.7521	164.5467	250.2994	Min.	26.2514	414.8461	32.7521	164.5467	250.2994	Ave.	26.2514	414.8461	32.7521	164.5467	250.2994	Std. DV	0.0000	0.0000	0.0000	0.0000	0.0000	Area1	26.2514	414.8461	32.7521	164.5467	250.2994	26.2514	414.8461	32.7521	164.5467	250.2994
	Sa	Sz	Sq	Sp	Sv																																												
	μm	μm	μm	μm	μm																																												
Max.	26.2514	414.8461	32.7521	164.5467	250.2994																																												
Min.	26.2514	414.8461	32.7521	164.5467	250.2994																																												
Ave.	26.2514	414.8461	32.7521	164.5467	250.2994																																												
Std. DV	0.0000	0.0000	0.0000	0.0000	0.0000																																												
Area1	26.2514	414.8461	32.7521	164.5467	250.2994																																												
6_256_3		<table border="1"> <thead> <tr> <th></th> <th>Sa</th> <th>Sz</th> <th>Sq</th> <th>Sp</th> <th>Sv</th> </tr> <tr> <th></th> <th>μm</th> <th>μm</th> <th>μm</th> <th>μm</th> <th>μm</th> </tr> </thead> <tbody> <tr> <td>Max.</td> <td>28.0428</td> <td>278.6556</td> <td>34.7888</td> <td>127.6550</td> <td>151.0005</td> </tr> <tr> <td>Min.</td> <td>28.0428</td> <td>278.6556</td> <td>34.7888</td> <td>127.6550</td> <td>151.0005</td> </tr> <tr> <td>Ave.</td> <td>28.0428</td> <td>278.6556</td> <td>34.7888</td> <td>127.6550</td> <td>151.0005</td> </tr> <tr> <td>Std. DV</td> <td>0.0000</td> <td>0.0000</td> <td>0.0000</td> <td>0.0000</td> <td>0.0000</td> </tr> <tr> <td>Area1</td> <td>28.0428</td> <td>278.6556</td> <td>34.7888</td> <td>127.6550</td> <td>151.0005</td> </tr> </tbody> </table>		Sa	Sz	Sq	Sp	Sv		μm	μm	μm	μm	μm	Max.	28.0428	278.6556	34.7888	127.6550	151.0005	Min.	28.0428	278.6556	34.7888	127.6550	151.0005	Ave.	28.0428	278.6556	34.7888	127.6550	151.0005	Std. DV	0.0000	0.0000	0.0000	0.0000	0.0000	Area1	28.0428	278.6556	34.7888	127.6550	151.0005	28.0428	278.6556	34.7888	127.6550	151.0005
	Sa	Sz	Sq	Sp	Sv																																												
	μm	μm	μm	μm	μm																																												
Max.	28.0428	278.6556	34.7888	127.6550	151.0005																																												
Min.	28.0428	278.6556	34.7888	127.6550	151.0005																																												
Ave.	28.0428	278.6556	34.7888	127.6550	151.0005																																												
Std. DV	0.0000	0.0000	0.0000	0.0000	0.0000																																												
Area1	28.0428	278.6556	34.7888	127.6550	151.0005																																												

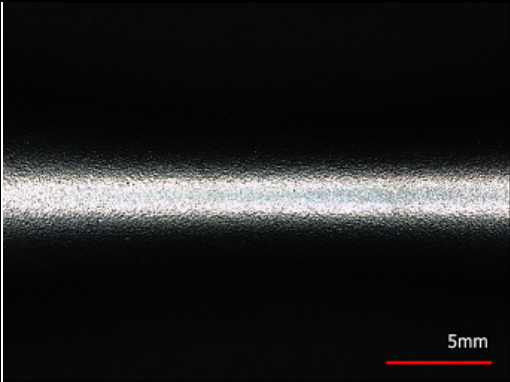
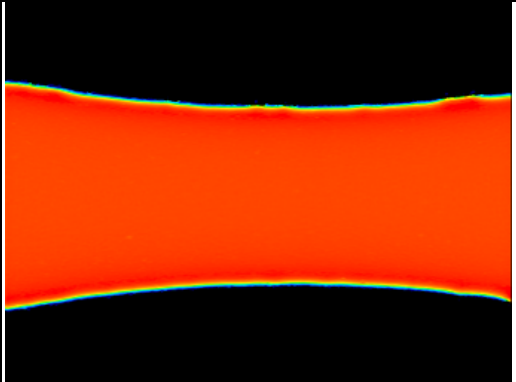
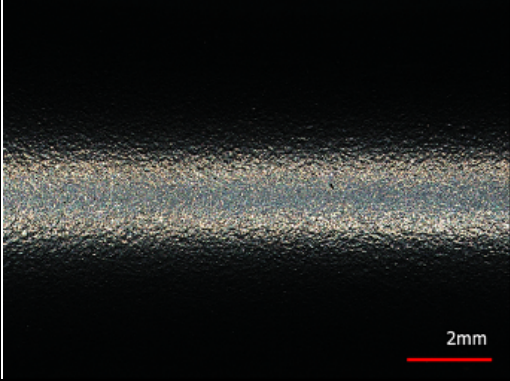
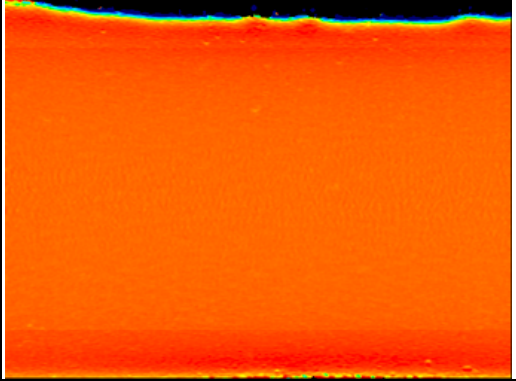
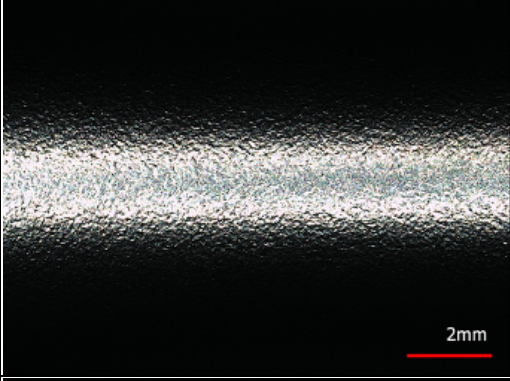
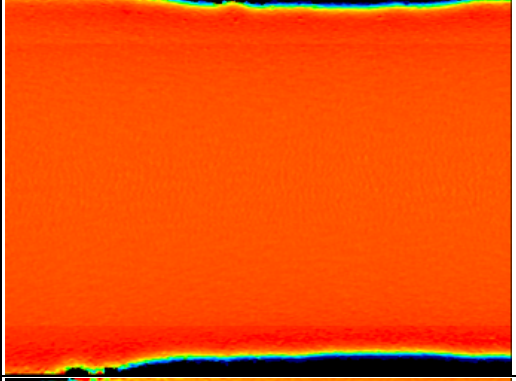
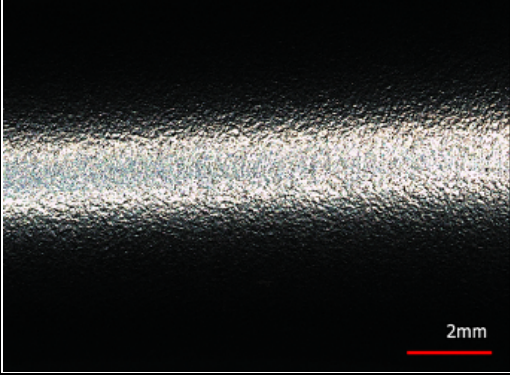
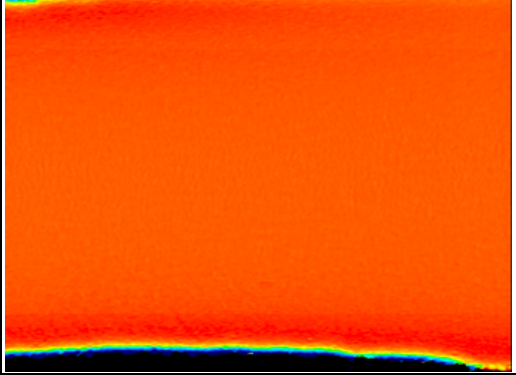
9_256_2		<table border="1"> <thead> <tr> <th></th> <th>Sa</th> <th>Sz</th> <th>Sq</th> <th>Sp</th> <th>Sv</th> </tr> <tr> <th></th> <th>µm</th> <th>µm</th> <th>µm</th> <th>µm</th> <th>µm</th> </tr> </thead> <tbody> <tr> <td>Max.</td> <td>24.8574</td> <td>354.7231</td> <td>30.6000</td> <td>173.1792</td> <td>181.5439</td> </tr> <tr> <td>Min.</td> <td>24.8574</td> <td>354.7231</td> <td>30.6000</td> <td>173.1792</td> <td>181.5439</td> </tr> <tr> <td>Ave.</td> <td>24.8574</td> <td>354.7231</td> <td>30.6000</td> <td>173.1792</td> <td>181.5439</td> </tr> <tr> <td>Std. DV</td> <td>0.0000</td> <td>0.0000</td> <td>0.0000</td> <td>0.0000</td> <td>0.0000</td> </tr> <tr> <td>Area1</td> <td>24.8574</td> <td>354.7231</td> <td>30.6000</td> <td>173.1792</td> <td>181.5439</td> </tr> </tbody> </table>		Sa	Sz	Sq	Sp	Sv		µm	µm	µm	µm	µm	Max.	24.8574	354.7231	30.6000	173.1792	181.5439	Min.	24.8574	354.7231	30.6000	173.1792	181.5439	Ave.	24.8574	354.7231	30.6000	173.1792	181.5439	Std. DV	0.0000	0.0000	0.0000	0.0000	0.0000	Area1	24.8574	354.7231	30.6000	173.1792	181.5439	24.8574	354.7231	30.6000	173.1792	181.5439
	Sa	Sz	Sq	Sp	Sv																																												
	µm	µm	µm	µm	µm																																												
Max.	24.8574	354.7231	30.6000	173.1792	181.5439																																												
Min.	24.8574	354.7231	30.6000	173.1792	181.5439																																												
Ave.	24.8574	354.7231	30.6000	173.1792	181.5439																																												
Std. DV	0.0000	0.0000	0.0000	0.0000	0.0000																																												
Area1	24.8574	354.7231	30.6000	173.1792	181.5439																																												
9_256_1		<table border="1"> <thead> <tr> <th></th> <th>Sa</th> <th>Sz</th> <th>Sq</th> <th>Sp</th> <th>Sv</th> </tr> <tr> <th></th> <th>µm</th> <th>µm</th> <th>µm</th> <th>µm</th> <th>µm</th> </tr> </thead> <tbody> <tr> <td>Max.</td> <td>24.3069</td> <td>271.5735</td> <td>29.7602</td> <td>96.3467</td> <td>175.2268</td> </tr> <tr> <td>Min.</td> <td>24.3069</td> <td>271.5735</td> <td>29.7602</td> <td>96.3467</td> <td>175.2268</td> </tr> <tr> <td>Ave.</td> <td>24.3069</td> <td>271.5735</td> <td>29.7602</td> <td>96.3467</td> <td>175.2268</td> </tr> <tr> <td>Std. DV</td> <td>0.0000</td> <td>0.0000</td> <td>0.0000</td> <td>0.0000</td> <td>0.0000</td> </tr> <tr> <td>Area1</td> <td>24.3069</td> <td>271.5735</td> <td>29.7602</td> <td>96.3467</td> <td>175.2268</td> </tr> </tbody> </table>		Sa	Sz	Sq	Sp	Sv		µm	µm	µm	µm	µm	Max.	24.3069	271.5735	29.7602	96.3467	175.2268	Min.	24.3069	271.5735	29.7602	96.3467	175.2268	Ave.	24.3069	271.5735	29.7602	96.3467	175.2268	Std. DV	0.0000	0.0000	0.0000	0.0000	0.0000	Area1	24.3069	271.5735	29.7602	96.3467	175.2268	24.3069	271.5735	29.7602	96.3467	175.2268
	Sa	Sz	Sq	Sp	Sv																																												
	µm	µm	µm	µm	µm																																												
Max.	24.3069	271.5735	29.7602	96.3467	175.2268																																												
Min.	24.3069	271.5735	29.7602	96.3467	175.2268																																												
Ave.	24.3069	271.5735	29.7602	96.3467	175.2268																																												
Std. DV	0.0000	0.0000	0.0000	0.0000	0.0000																																												
Area1	24.3069	271.5735	29.7602	96.3467	175.2268																																												
9_256_3		<table border="1"> <thead> <tr> <th></th> <th>Sa</th> <th>Sz</th> <th>Sq</th> <th>Sp</th> <th>Sv</th> </tr> <tr> <th></th> <th>µm</th> <th>µm</th> <th>µm</th> <th>µm</th> <th>µm</th> </tr> </thead> <tbody> <tr> <td>Max.</td> <td>27.4643</td> <td>251.3152</td> <td>33.6451</td> <td>106.7631</td> <td>144.5521</td> </tr> <tr> <td>Min.</td> <td>27.4643</td> <td>251.3152</td> <td>33.6451</td> <td>106.7631</td> <td>144.5521</td> </tr> <tr> <td>Ave.</td> <td>27.4643</td> <td>251.3152</td> <td>33.6451</td> <td>106.7631</td> <td>144.5521</td> </tr> <tr> <td>Std. DV</td> <td>0.0000</td> <td>0.0000</td> <td>0.0000</td> <td>0.0000</td> <td>0.0000</td> </tr> <tr> <td>Area1</td> <td>27.4643</td> <td>251.3152</td> <td>33.6451</td> <td>106.7631</td> <td>144.5521</td> </tr> </tbody> </table>		Sa	Sz	Sq	Sp	Sv		µm	µm	µm	µm	µm	Max.	27.4643	251.3152	33.6451	106.7631	144.5521	Min.	27.4643	251.3152	33.6451	106.7631	144.5521	Ave.	27.4643	251.3152	33.6451	106.7631	144.5521	Std. DV	0.0000	0.0000	0.0000	0.0000	0.0000	Area1	27.4643	251.3152	33.6451	106.7631	144.5521	27.4643	251.3152	33.6451	106.7631	144.5521
	Sa	Sz	Sq	Sp	Sv																																												
	µm	µm	µm	µm	µm																																												
Max.	27.4643	251.3152	33.6451	106.7631	144.5521																																												
Min.	27.4643	251.3152	33.6451	106.7631	144.5521																																												
Ave.	27.4643	251.3152	33.6451	106.7631	144.5521																																												
Std. DV	0.0000	0.0000	0.0000	0.0000	0.0000																																												
Area1	27.4643	251.3152	33.6451	106.7631	144.5521																																												
3_256_2		<table border="1"> <thead> <tr> <th></th> <th>Sa</th> <th>Sz</th> <th>Sq</th> <th>Sp</th> <th>Sv</th> </tr> <tr> <th></th> <th>µm</th> <th>µm</th> <th>µm</th> <th>µm</th> <th>µm</th> </tr> </thead> <tbody> <tr> <td>Max.</td> <td>24.8341</td> <td>238.2002</td> <td>30.5806</td> <td>122.1689</td> <td>116.0312</td> </tr> <tr> <td>Min.</td> <td>24.8341</td> <td>238.2002</td> <td>30.5806</td> <td>122.1689</td> <td>116.0312</td> </tr> <tr> <td>Ave.</td> <td>24.8341</td> <td>238.2002</td> <td>30.5806</td> <td>122.1689</td> <td>116.0312</td> </tr> <tr> <td>Std. DV</td> <td>0.0000</td> <td>0.0000</td> <td>0.0000</td> <td>0.0000</td> <td>0.0000</td> </tr> <tr> <td>Area1</td> <td>24.8341</td> <td>238.2002</td> <td>30.5806</td> <td>122.1689</td> <td>116.0312</td> </tr> </tbody> </table>		Sa	Sz	Sq	Sp	Sv		µm	µm	µm	µm	µm	Max.	24.8341	238.2002	30.5806	122.1689	116.0312	Min.	24.8341	238.2002	30.5806	122.1689	116.0312	Ave.	24.8341	238.2002	30.5806	122.1689	116.0312	Std. DV	0.0000	0.0000	0.0000	0.0000	0.0000	Area1	24.8341	238.2002	30.5806	122.1689	116.0312	24.8341	238.2002	30.5806	122.1689	116.0312
	Sa	Sz	Sq	Sp	Sv																																												
	µm	µm	µm	µm	µm																																												
Max.	24.8341	238.2002	30.5806	122.1689	116.0312																																												
Min.	24.8341	238.2002	30.5806	122.1689	116.0312																																												
Ave.	24.8341	238.2002	30.5806	122.1689	116.0312																																												
Std. DV	0.0000	0.0000	0.0000	0.0000	0.0000																																												
Area1	24.8341	238.2002	30.5806	122.1689	116.0312																																												

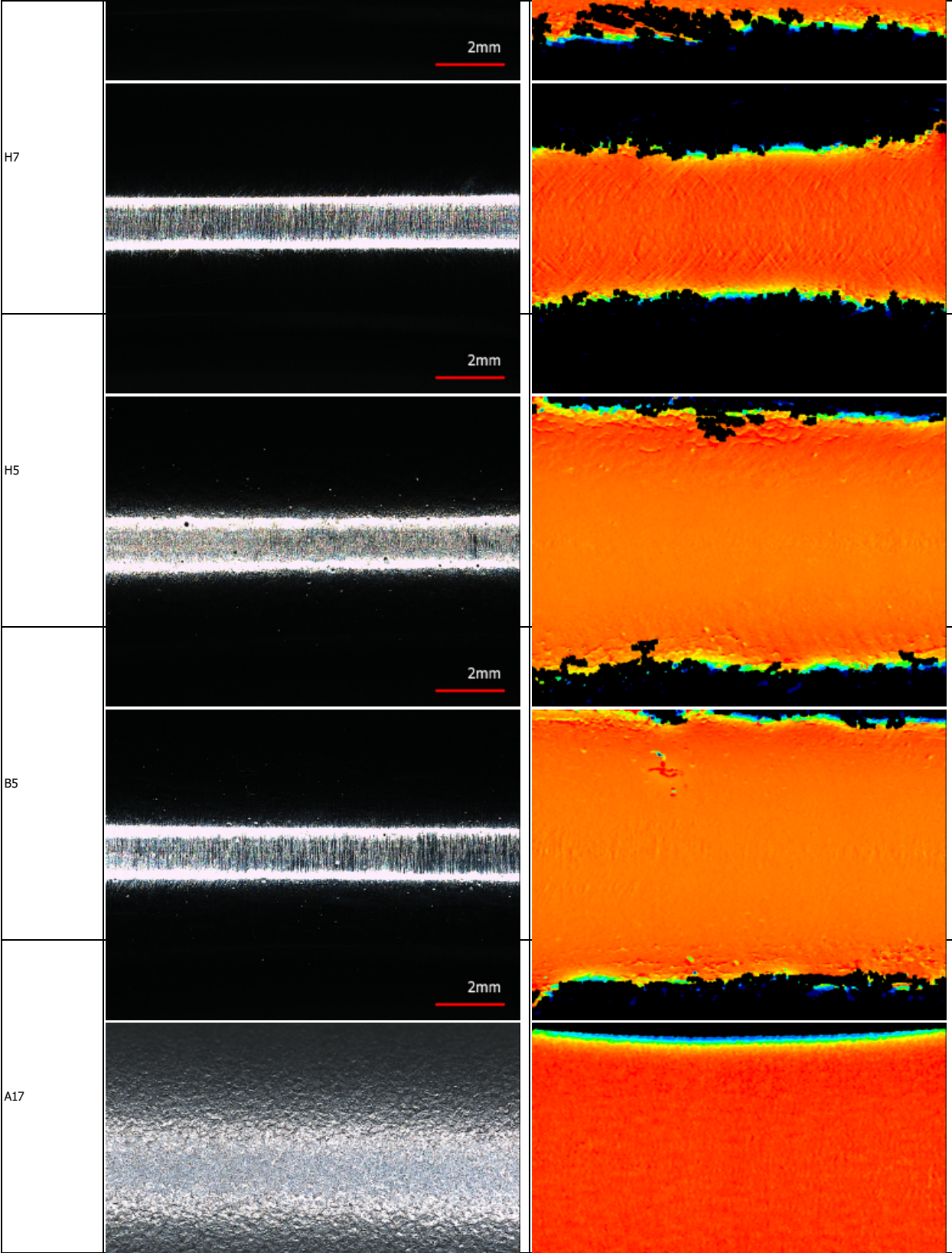


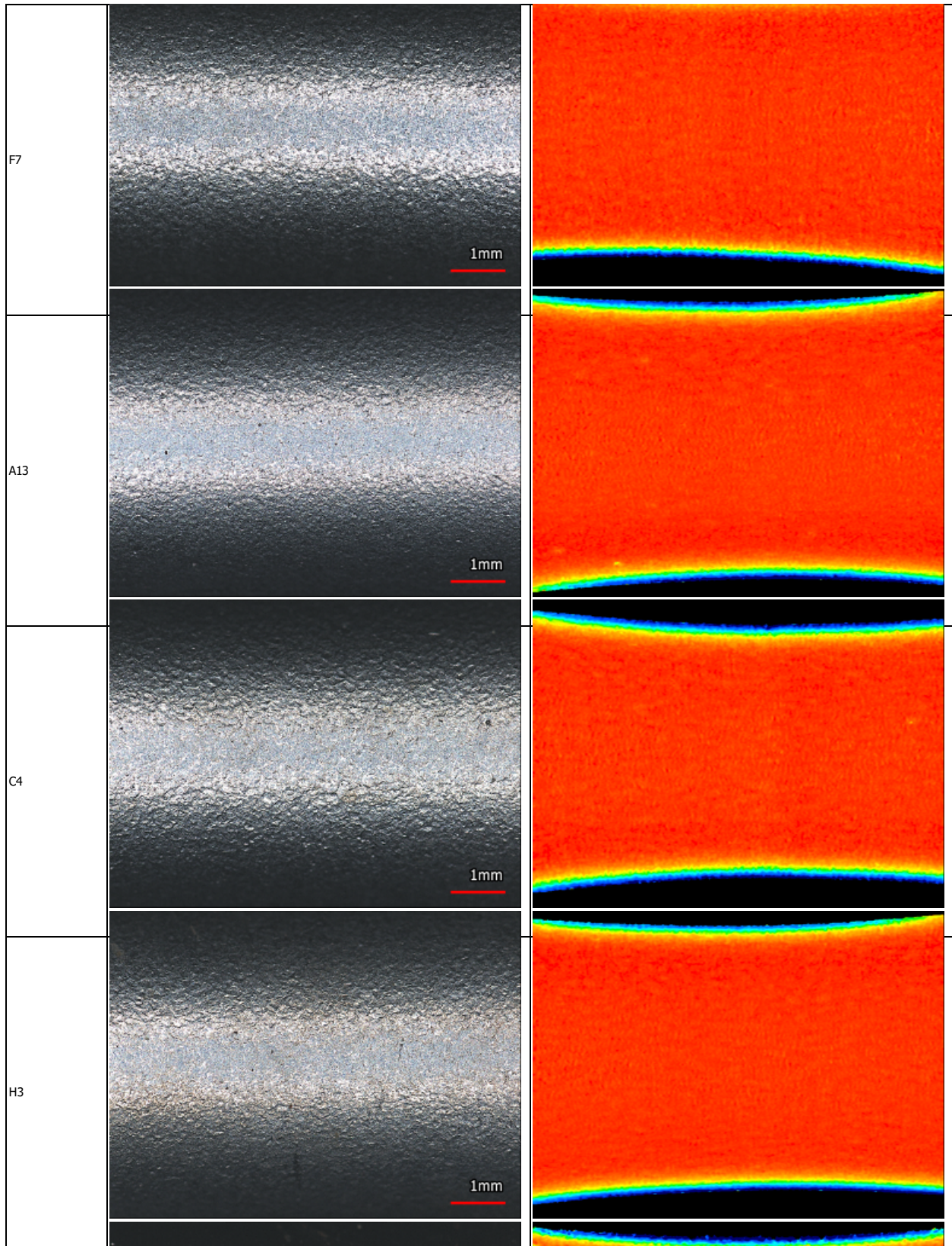


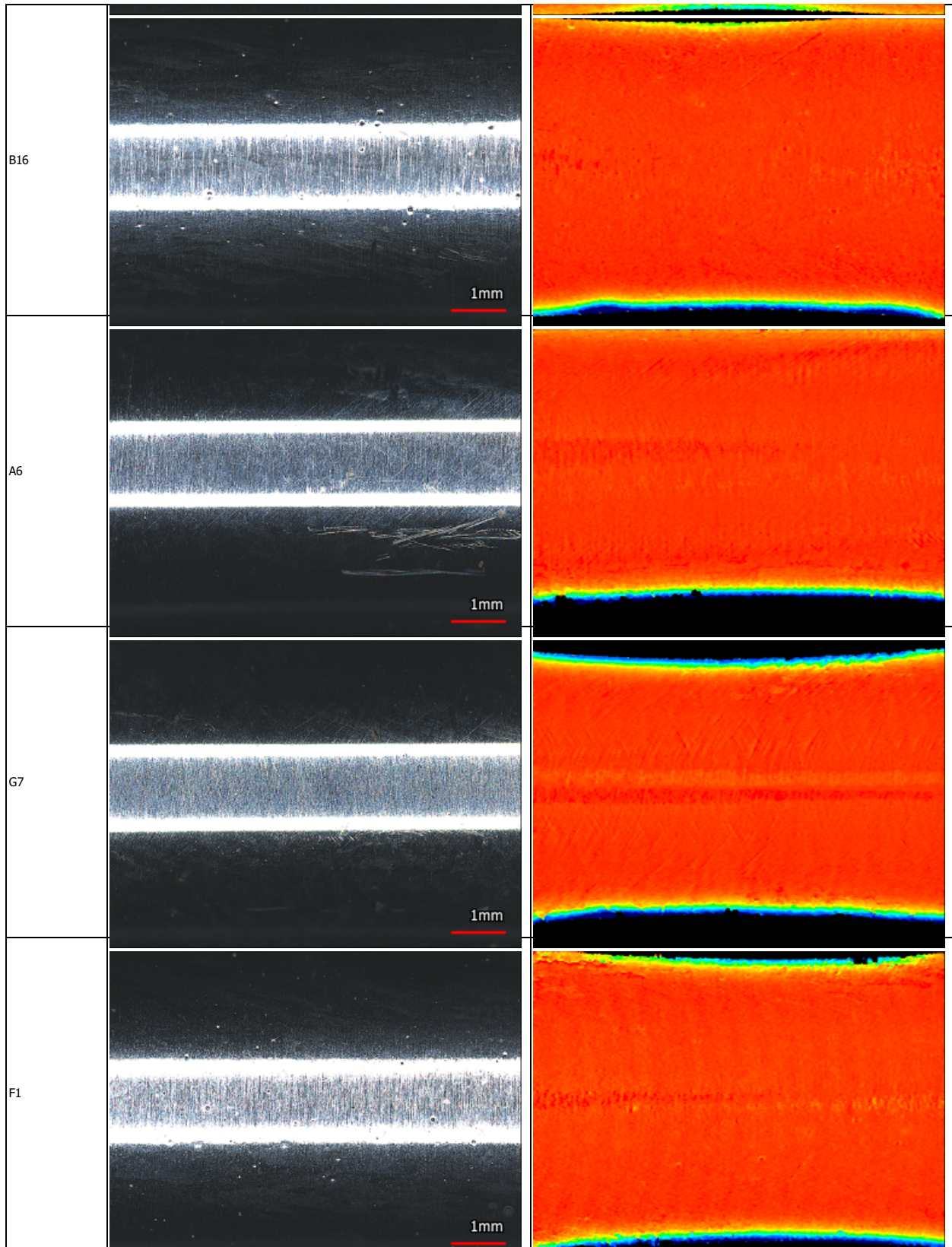


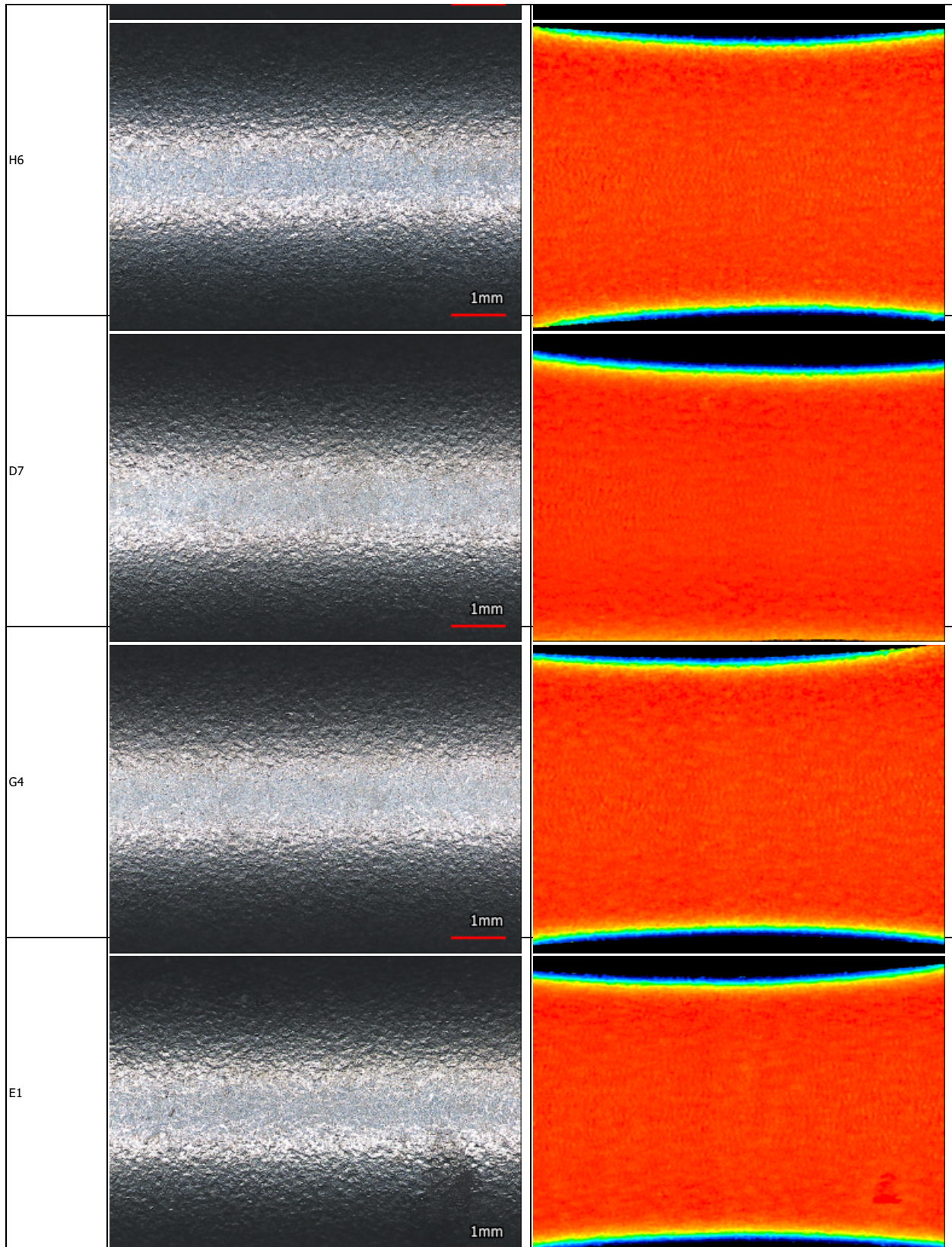
### Keyence Surface Profilometry – Surface Treated

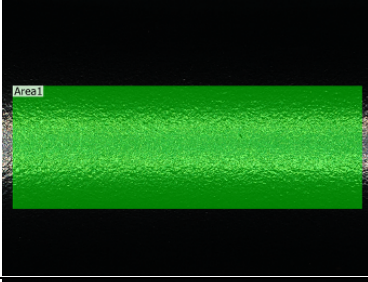
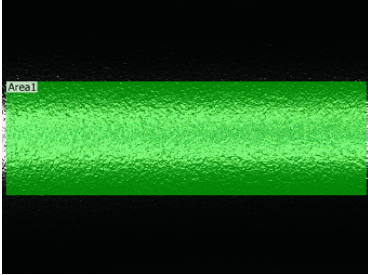
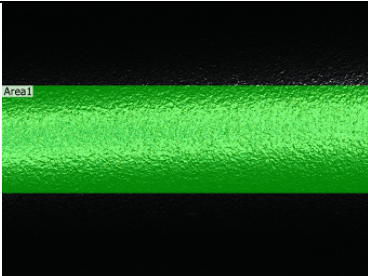

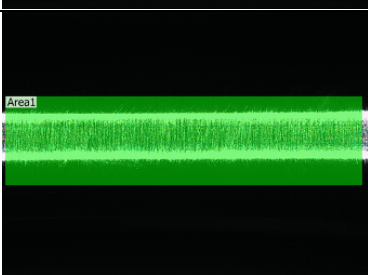
Measurement data name	Main image	Main image2
	Optical	Height
A13 - low mag		
A13 - high Mag		
B17		
G1		





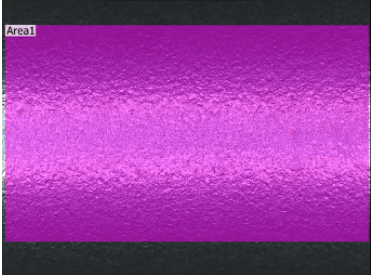
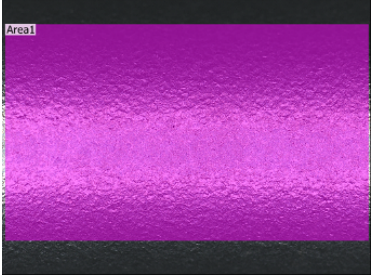






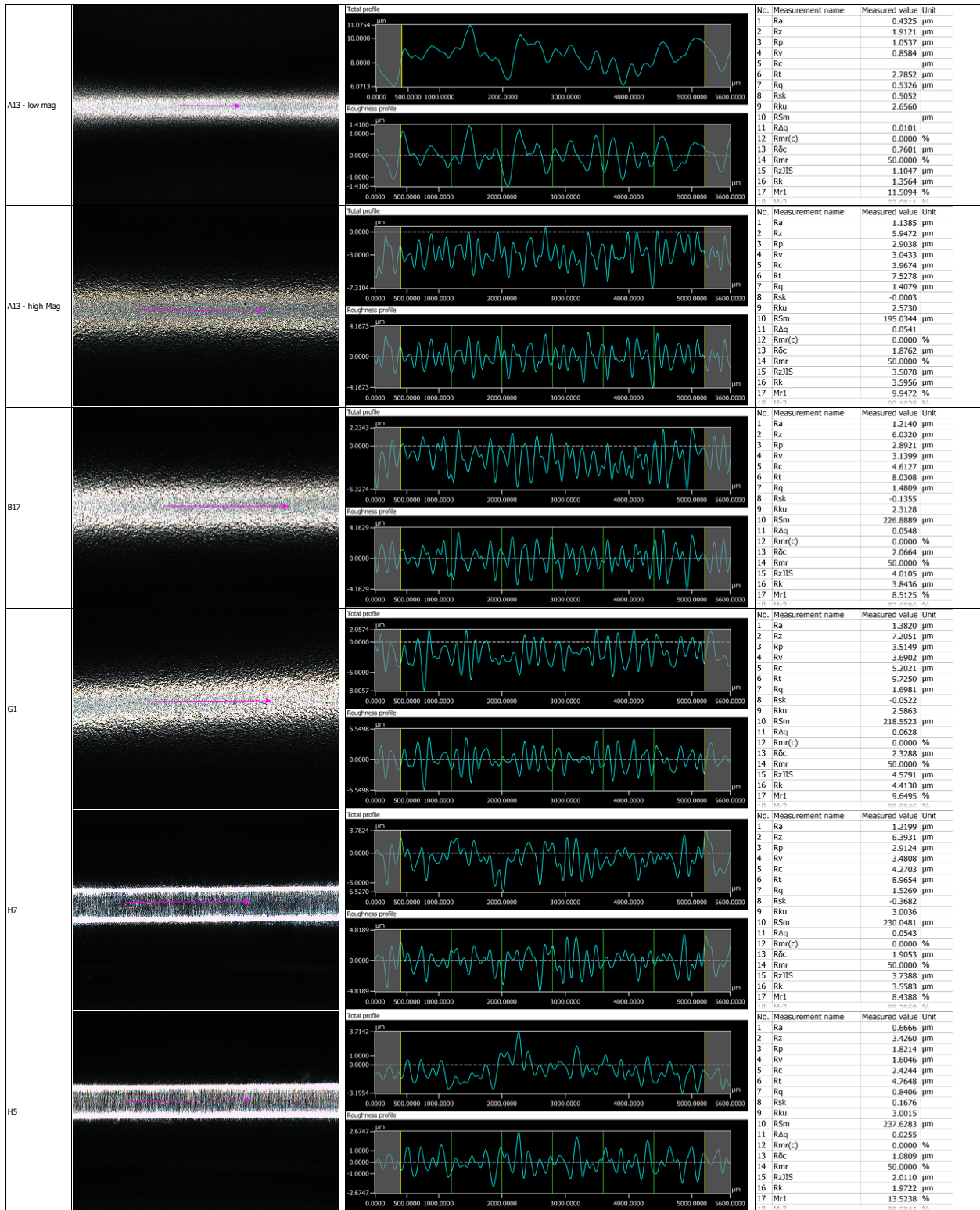


A13 - high Mag		<table border="1"> <thead> <tr> <th></th> <th>Sa</th> <th>Sz</th> <th>Str</th> <th>Spc</th> <th>Sdr</th> <th>Sq</th> <th>Ssk</th> </tr> <tr> <th></th> <th>µm</th> <th>µm</th> <th>1/mm</th> <th></th> <th></th> <th>µm</th> <th></th> </tr> </thead> <tbody> <tr> <td>Max.</td> <td>1.3340</td> <td>17.7400</td> <td>0.659</td> <td>3.9357</td> <td>0.0023641</td> <td>1.6893</td> <td>-0.2030</td> </tr> <tr> <td>Min.</td> <td>1.3340</td> <td>17.7400</td> <td>0.659</td> <td>3.9357</td> <td>0.0023641</td> <td>1.6893</td> <td>-0.2030</td> </tr> <tr> <td>Ave.</td> <td>1.3340</td> <td>17.7400</td> <td>0.659</td> <td>3.9357</td> <td>0.0023641</td> <td>1.6893</td> <td>-0.2030</td> </tr> <tr> <td>Std. DV</td> <td>0.0000</td> <td>0.0000</td> <td>0.000</td> <td>0.0000</td> <td>0.0000000</td> <td>0.0000</td> <td>0.0000</td> </tr> <tr> <td>Area1</td> <td>1.3340</td> <td>17.7400</td> <td>0.659</td> <td>3.9357</td> <td>0.0023641</td> <td>1.6893</td> <td>-0.2030</td> </tr> </tbody> </table>		Sa	Sz	Str	Spc	Sdr	Sq	Ssk		µm	µm	1/mm			µm		Max.	1.3340	17.7400	0.659	3.9357	0.0023641	1.6893	-0.2030	Min.	1.3340	17.7400	0.659	3.9357	0.0023641	1.6893	-0.2030	Ave.	1.3340	17.7400	0.659	3.9357	0.0023641	1.6893	-0.2030	Std. DV	0.0000	0.0000	0.000	0.0000	0.0000000	0.0000	0.0000	Area1	1.3340	17.7400	0.659	3.9357	0.0023641	1.6893	-0.2030	1.3340	17.7400	0.659	1.6893	7.2601	10.4799
	Sa	Sz	Str	Spc	Sdr	Sq	Ssk																																																									
	µm	µm	1/mm			µm																																																										
Max.	1.3340	17.7400	0.659	3.9357	0.0023641	1.6893	-0.2030																																																									
Min.	1.3340	17.7400	0.659	3.9357	0.0023641	1.6893	-0.2030																																																									
Ave.	1.3340	17.7400	0.659	3.9357	0.0023641	1.6893	-0.2030																																																									
Std. DV	0.0000	0.0000	0.000	0.0000	0.0000000	0.0000	0.0000																																																									
Area1	1.3340	17.7400	0.659	3.9357	0.0023641	1.6893	-0.2030																																																									
B17		<table border="1"> <thead> <tr> <th></th> <th>Sa</th> <th>Sz</th> <th>Str</th> <th>Spc</th> <th>Sdr</th> <th>Sq</th> <th>Ssk</th> </tr> <tr> <th></th> <th>µm</th> <th>µm</th> <th>1/mm</th> <th></th> <th></th> <th>µm</th> <th></th> </tr> </thead> <tbody> <tr> <td>Max.</td> <td>1.3167</td> <td>18.3800</td> <td>0.623</td> <td>3.9358</td> <td>0.0024121</td> <td>1.6718</td> <td>-0.2470</td> </tr> <tr> <td>Min.</td> <td>1.3167</td> <td>18.3800</td> <td>0.623</td> <td>3.9358</td> <td>0.0024121</td> <td>1.6718</td> <td>-0.2470</td> </tr> <tr> <td>Ave.</td> <td>1.3167</td> <td>18.3800</td> <td>0.623</td> <td>3.9358</td> <td>0.0024121</td> <td>1.6718</td> <td>-0.2470</td> </tr> <tr> <td>Std. DV</td> <td>0.0000</td> <td>0.0000</td> <td>0.000</td> <td>0.0000</td> <td>0.0000000</td> <td>0.0000</td> <td>0.0000</td> </tr> <tr> <td>Area1</td> <td>1.3167</td> <td>18.3800</td> <td>0.623</td> <td>3.9358</td> <td>0.0024121</td> <td>1.6718</td> <td>-0.2470</td> </tr> </tbody> </table>		Sa	Sz	Str	Spc	Sdr	Sq	Ssk		µm	µm	1/mm			µm		Max.	1.3167	18.3800	0.623	3.9358	0.0024121	1.6718	-0.2470	Min.	1.3167	18.3800	0.623	3.9358	0.0024121	1.6718	-0.2470	Ave.	1.3167	18.3800	0.623	3.9358	0.0024121	1.6718	-0.2470	Std. DV	0.0000	0.0000	0.000	0.0000	0.0000000	0.0000	0.0000	Area1	1.3167	18.3800	0.623	3.9358	0.0024121	1.6718	-0.2470	1.3167	18.3800	0.623	1.6718	7.7409	10.6391
	Sa	Sz	Str	Spc	Sdr	Sq	Ssk																																																									
	µm	µm	1/mm			µm																																																										
Max.	1.3167	18.3800	0.623	3.9358	0.0024121	1.6718	-0.2470																																																									
Min.	1.3167	18.3800	0.623	3.9358	0.0024121	1.6718	-0.2470																																																									
Ave.	1.3167	18.3800	0.623	3.9358	0.0024121	1.6718	-0.2470																																																									
Std. DV	0.0000	0.0000	0.000	0.0000	0.0000000	0.0000	0.0000																																																									
Area1	1.3167	18.3800	0.623	3.9358	0.0024121	1.6718	-0.2470																																																									
G1		<table border="1"> <thead> <tr> <th></th> <th>Sa</th> <th>Sz</th> <th>Str</th> <th>Spc</th> <th>Sdr</th> <th>Sq</th> <th>Ssk</th> </tr> <tr> <th></th> <th>µm</th> <th>µm</th> <th>1/mm</th> <th></th> <th></th> <th>µm</th> <th></th> </tr> </thead> <tbody> <tr> <td>Max.</td> <td>1.4396</td> <td>17.0600</td> <td>0.554</td> <td>4.0800</td> <td>0.0026464</td> <td>1.8113</td> <td>-0.1080</td> </tr> <tr> <td>Min.</td> <td>1.4396</td> <td>17.0600</td> <td>0.554</td> <td>4.0800</td> <td>0.0026464</td> <td>1.8113</td> <td>-0.1080</td> </tr> <tr> <td>Ave.</td> <td>1.4396</td> <td>17.0600</td> <td>0.554</td> <td>4.0800</td> <td>0.0026464</td> <td>1.8113</td> <td>-0.1080</td> </tr> <tr> <td>Std. DV</td> <td>0.0000</td> <td>0.0000</td> <td>0.000</td> <td>0.0000</td> <td>0.0000000</td> <td>0.0000</td> <td>0.0000</td> </tr> <tr> <td>Area1</td> <td>1.4396</td> <td>17.0600</td> <td>0.554</td> <td>4.0800</td> <td>0.0026464</td> <td>1.8113</td> <td>-0.1080</td> </tr> </tbody> </table>		Sa	Sz	Str	Spc	Sdr	Sq	Ssk		µm	µm	1/mm			µm		Max.	1.4396	17.0600	0.554	4.0800	0.0026464	1.8113	-0.1080	Min.	1.4396	17.0600	0.554	4.0800	0.0026464	1.8113	-0.1080	Ave.	1.4396	17.0600	0.554	4.0800	0.0026464	1.8113	-0.1080	Std. DV	0.0000	0.0000	0.000	0.0000	0.0000000	0.0000	0.0000	Area1	1.4396	17.0600	0.554	4.0800	0.0026464	1.8113	-0.1080	1.4396	17.0600	0.554	1.8113	7.6867	9.3733
	Sa	Sz	Str	Spc	Sdr	Sq	Ssk																																																									
	µm	µm	1/mm			µm																																																										
Max.	1.4396	17.0600	0.554	4.0800	0.0026464	1.8113	-0.1080																																																									
Min.	1.4396	17.0600	0.554	4.0800	0.0026464	1.8113	-0.1080																																																									
Ave.	1.4396	17.0600	0.554	4.0800	0.0026464	1.8113	-0.1080																																																									
Std. DV	0.0000	0.0000	0.000	0.0000	0.0000000	0.0000	0.0000																																																									
Area1	1.4396	17.0600	0.554	4.0800	0.0026464	1.8113	-0.1080																																																									
H7		<table border="1"> <thead> <tr> <th></th> <th>Sa</th> <th>Sz</th> <th>Str</th> <th>Spc</th> <th>Sdr</th> <th>Sq</th> <th>Ssk</th> </tr> <tr> <th></th> <th>µm</th> <th>µm</th> <th>1/mm</th> <th></th> <th></th> <th>µm</th> <th></th> </tr> </thead> <tbody> <tr> <td>Max.</td> <td>1.6297</td> <td>23.4100</td> <td>0.436</td> <td>4.4872</td> <td>0.0032639</td> <td>2.0916</td> <td>-0.1010</td> </tr> <tr> <td>Min.</td> <td>1.6297</td> <td>23.4100</td> <td>0.436</td> <td>4.4872</td> <td>0.0032639</td> <td>2.0916</td> <td>-0.1010</td> </tr> <tr> <td>Ave.</td> <td>1.6297</td> <td>23.4100</td> <td>0.436</td> <td>4.4872</td> <td>0.0032639</td> <td>2.0916</td> <td>-0.1010</td> </tr> <tr> <td>Std. DV</td> <td>0.0000</td> <td>0.0000</td> <td>0.000</td> <td>0.0000</td> <td>0.0000000</td> <td>0.0000</td> <td>0.0000</td> </tr> <tr> <td>Area1</td> <td>1.6297</td> <td>23.4100</td> <td>0.436</td> <td>4.4872</td> <td>0.0032639</td> <td>2.0916</td> <td>-0.1010</td> </tr> </tbody> </table>		Sa	Sz	Str	Spc	Sdr	Sq	Ssk		µm	µm	1/mm			µm		Max.	1.6297	23.4100	0.436	4.4872	0.0032639	2.0916	-0.1010	Min.	1.6297	23.4100	0.436	4.4872	0.0032639	2.0916	-0.1010	Ave.	1.6297	23.4100	0.436	4.4872	0.0032639	2.0916	-0.1010	Std. DV	0.0000	0.0000	0.000	0.0000	0.0000000	0.0000	0.0000	Area1	1.6297	23.4100	0.436	4.4872	0.0032639	2.0916	-0.1010	1.6297	23.4100	0.436	2.0916	11.7993	11.6107
	Sa	Sz	Str	Spc	Sdr	Sq	Ssk																																																									
	µm	µm	1/mm			µm																																																										
Max.	1.6297	23.4100	0.436	4.4872	0.0032639	2.0916	-0.1010																																																									
Min.	1.6297	23.4100	0.436	4.4872	0.0032639	2.0916	-0.1010																																																									
Ave.	1.6297	23.4100	0.436	4.4872	0.0032639	2.0916	-0.1010																																																									
Std. DV	0.0000	0.0000	0.000	0.0000	0.0000000	0.0000	0.0000																																																									
Area1	1.6297	23.4100	0.436	4.4872	0.0032639	2.0916	-0.1010																																																									
H5		<table border="1"> <thead> <tr> <th></th> <th>Sa</th> <th>Sz</th> <th>Str</th> <th>Spc</th> <th>Sdr</th> <th>Sq</th> <th>Ssk</th> </tr> <tr> <th></th> <th>µm</th> <th>µm</th> <th>1/mm</th> <th></th> <th></th> <th>µm</th> <th></th> </tr> </thead> <tbody> <tr> <td>Max.</td> <td>1.8362</td> <td>25.8900</td> <td>0.409</td> <td>4.9261</td> <td>0.0041799</td> <td>2.4014</td> <td>0.1624</td> </tr> <tr> <td>Min.</td> <td>1.8362</td> <td>25.8900</td> <td>0.409</td> <td>4.9261</td> <td>0.0041799</td> <td>2.4014</td> <td>0.1624</td> </tr> <tr> <td>Ave.</td> <td>1.8362</td> <td>25.8900</td> <td>0.409</td> <td>4.9261</td> <td>0.0041799</td> <td>2.4014</td> <td>0.1624</td> </tr> <tr> <td>Std. DV</td> <td>0.0000</td> <td>0.0000</td> <td>0.000</td> <td>0.0000</td> <td>0.0000000</td> <td>0.0000</td> <td>0.0000</td> </tr> <tr> <td>Area1</td> <td>1.8362</td> <td>25.8900</td> <td>0.409</td> <td>4.9261</td> <td>0.0041799</td> <td>2.4014</td> <td>0.1624</td> </tr> </tbody> </table>		Sa	Sz	Str	Spc	Sdr	Sq	Ssk		µm	µm	1/mm			µm		Max.	1.8362	25.8900	0.409	4.9261	0.0041799	2.4014	0.1624	Min.	1.8362	25.8900	0.409	4.9261	0.0041799	2.4014	0.1624	Ave.	1.8362	25.8900	0.409	4.9261	0.0041799	2.4014	0.1624	Std. DV	0.0000	0.0000	0.000	0.0000	0.0000000	0.0000	0.0000	Area1	1.8362	25.8900	0.409	4.9261	0.0041799	2.4014	0.1624	1.8362	25.8900	0.409	2.4014	14.3401	11.5499
	Sa	Sz	Str	Spc	Sdr	Sq	Ssk																																																									
	µm	µm	1/mm			µm																																																										
Max.	1.8362	25.8900	0.409	4.9261	0.0041799	2.4014	0.1624																																																									
Min.	1.8362	25.8900	0.409	4.9261	0.0041799	2.4014	0.1624																																																									
Ave.	1.8362	25.8900	0.409	4.9261	0.0041799	2.4014	0.1624																																																									
Std. DV	0.0000	0.0000	0.000	0.0000	0.0000000	0.0000	0.0000																																																									
Area1	1.8362	25.8900	0.409	4.9261	0.0041799	2.4014	0.1624																																																									

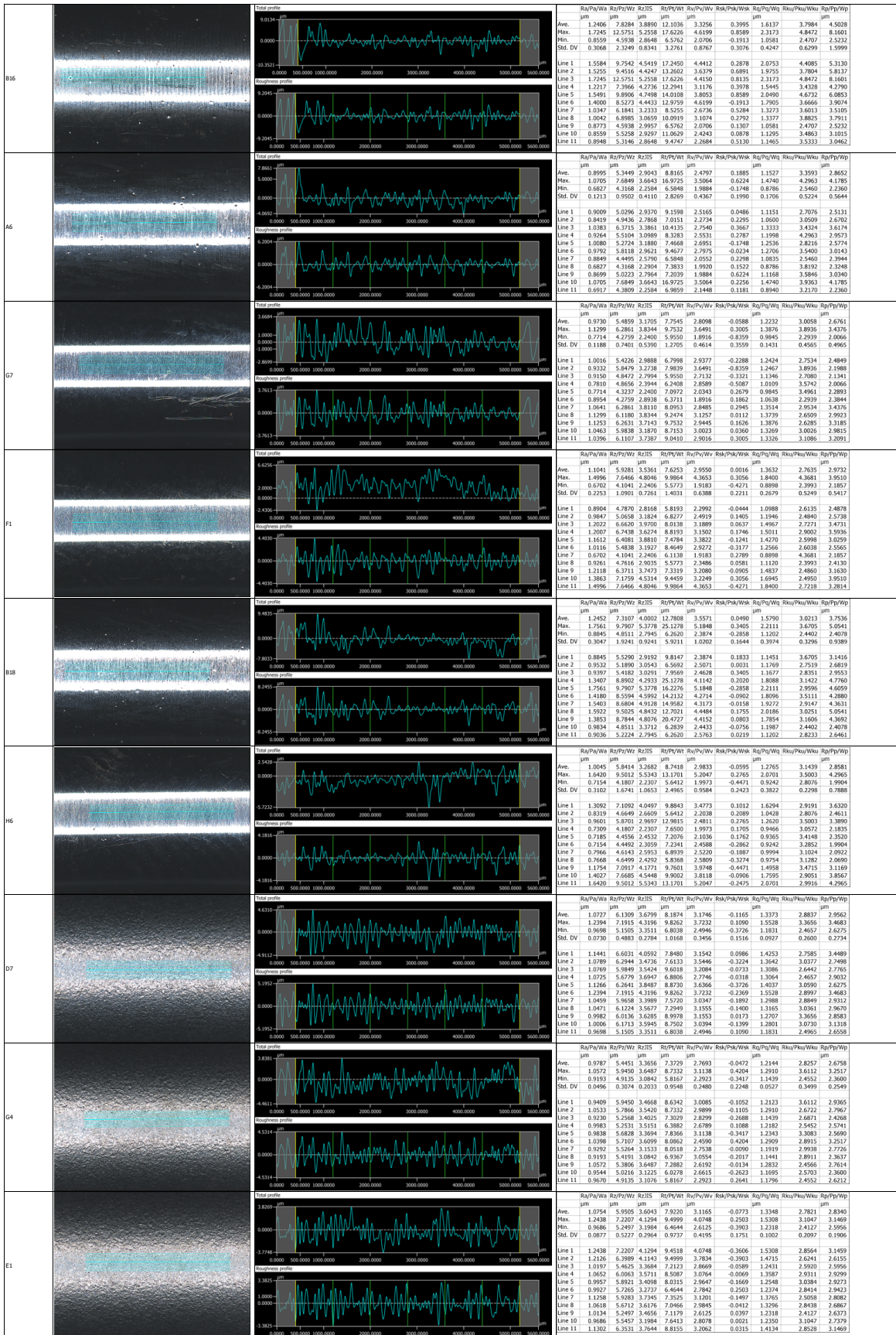
B5		<table border="1"> <thead> <tr> <th>Sa</th> <th>Sz</th> <th>Str</th> <th>Spc</th> <th>Sdr</th> <th>Sq</th> <th>Ssk</th> </tr> <tr> <th><math>\mu\text{m}</math></th> <th><math>\mu\text{m}</math></th> <th>1/mm</th> <th></th> <th></th> <th><math>\mu\text{m}</math></th> <th></th> </tr> </thead> <tbody> <tr> <td>Max. 1.5639</td> <td>25.9300</td> <td>0.083</td> <td>3.9204</td> <td>0.0023087</td> <td>2.0339</td> <td>-0.2000</td> </tr> <tr> <td>Min. 1.5639</td> <td>25.9300</td> <td>0.083</td> <td>3.9204</td> <td>0.0023087</td> <td>2.0339</td> <td>-0.2000</td> </tr> <tr> <td>Ave. 1.5639</td> <td>25.9300</td> <td>0.083</td> <td>3.9204</td> <td>0.0023087</td> <td>2.0339</td> <td>-0.2000</td> </tr> <tr> <td>Std. DV 0.0000</td> <td>0.0000</td> <td>0.000</td> <td>0.0000</td> <td>0.0000000</td> <td>0.0000</td> <td>0.0000</td> </tr> <tr> <td>Area1 1.5639</td> <td>25.9300</td> <td>0.083</td> <td>3.9204</td> <td>0.0023087</td> <td>2.0339</td> <td>-0.2000</td> </tr> </tbody> </table>	Sa	Sz	Str	Spc	Sdr	Sq	Ssk	$\mu\text{m}$	$\mu\text{m}$	1/mm			$\mu\text{m}$		Max. 1.5639	25.9300	0.083	3.9204	0.0023087	2.0339	-0.2000	Min. 1.5639	25.9300	0.083	3.9204	0.0023087	2.0339	-0.2000	Ave. 1.5639	25.9300	0.083	3.9204	0.0023087	2.0339	-0.2000	Std. DV 0.0000	0.0000	0.000	0.0000	0.0000000	0.0000	0.0000	Area1 1.5639	25.9300	0.083	3.9204	0.0023087	2.0339	-0.2000	1.5639	25.9300	0.083	2.0339	12.9026	13.0274
Sa	Sz	Str	Spc	Sdr	Sq	Ssk																																																			
$\mu\text{m}$	$\mu\text{m}$	1/mm			$\mu\text{m}$																																																				
Max. 1.5639	25.9300	0.083	3.9204	0.0023087	2.0339	-0.2000																																																			
Min. 1.5639	25.9300	0.083	3.9204	0.0023087	2.0339	-0.2000																																																			
Ave. 1.5639	25.9300	0.083	3.9204	0.0023087	2.0339	-0.2000																																																			
Std. DV 0.0000	0.0000	0.000	0.0000	0.0000000	0.0000	0.0000																																																			
Area1 1.5639	25.9300	0.083	3.9204	0.0023087	2.0339	-0.2000																																																			
A17		<table border="1"> <thead> <tr> <th>Sa</th> <th>Sz</th> <th>Str</th> <th>Spc</th> <th>Sdr</th> <th>Sq</th> <th>Ssk</th> </tr> <tr> <th><math>\mu\text{m}</math></th> <th><math>\mu\text{m}</math></th> <th>1/mm</th> <th></th> <th></th> <th><math>\mu\text{m}</math></th> <th></th> </tr> </thead> <tbody> <tr> <td>Max. 1.3246</td> <td>33.4200</td> <td>0.316</td> <td>3.8700</td> <td>0.0024373</td> <td>1.7947</td> <td>-0.3760</td> </tr> <tr> <td>Min. 1.3246</td> <td>33.4200</td> <td>0.316</td> <td>3.8700</td> <td>0.0024373</td> <td>1.7947</td> <td>-0.3760</td> </tr> <tr> <td>Ave. 1.3246</td> <td>33.4200</td> <td>0.316</td> <td>3.8700</td> <td>0.0024373</td> <td>1.7947</td> <td>-0.3760</td> </tr> <tr> <td>Std. DV 0.0000</td> <td>0.0000</td> <td>0.000</td> <td>0.0000</td> <td>0.0000000</td> <td>0.0000</td> <td>0.0000</td> </tr> <tr> <td>Area1 1.3246</td> <td>33.4200</td> <td>0.316</td> <td>3.8700</td> <td>0.0024373</td> <td>1.7947</td> <td>-0.3760</td> </tr> </tbody> </table>	Sa	Sz	Str	Spc	Sdr	Sq	Ssk	$\mu\text{m}$	$\mu\text{m}$	1/mm			$\mu\text{m}$		Max. 1.3246	33.4200	0.316	3.8700	0.0024373	1.7947	-0.3760	Min. 1.3246	33.4200	0.316	3.8700	0.0024373	1.7947	-0.3760	Ave. 1.3246	33.4200	0.316	3.8700	0.0024373	1.7947	-0.3760	Std. DV 0.0000	0.0000	0.000	0.0000	0.0000000	0.0000	0.0000	Area1 1.3246	33.4200	0.316	3.8700	0.0024373	1.7947	-0.3760	1.3246	33.4200	0.316	1.7947	15.2030	18.2170
Sa	Sz	Str	Spc	Sdr	Sq	Ssk																																																			
$\mu\text{m}$	$\mu\text{m}$	1/mm			$\mu\text{m}$																																																				
Max. 1.3246	33.4200	0.316	3.8700	0.0024373	1.7947	-0.3760																																																			
Min. 1.3246	33.4200	0.316	3.8700	0.0024373	1.7947	-0.3760																																																			
Ave. 1.3246	33.4200	0.316	3.8700	0.0024373	1.7947	-0.3760																																																			
Std. DV 0.0000	0.0000	0.000	0.0000	0.0000000	0.0000	0.0000																																																			
Area1 1.3246	33.4200	0.316	3.8700	0.0024373	1.7947	-0.3760																																																			
F7		<table border="1"> <thead> <tr> <th>Sa</th> <th>Sz</th> <th>Str</th> <th>Spc</th> <th>Sdr</th> <th>Sq</th> <th>Ssk</th> </tr> <tr> <th><math>\mu\text{m}</math></th> <th><math>\mu\text{m}</math></th> <th>1/mm</th> <th></th> <th></th> <th><math>\mu\text{m}</math></th> <th></th> </tr> </thead> <tbody> <tr> <td>Max. 2.0727</td> <td>50.0800</td> <td>0.053</td> <td>9.3054</td> <td>0.0054202</td> <td>3.8179</td> <td>-4.3590</td> </tr> <tr> <td>Min. 2.0727</td> <td>50.0800</td> <td>0.053</td> <td>9.3054</td> <td>0.0054202</td> <td>3.8179</td> <td>-4.3590</td> </tr> <tr> <td>Ave. 2.0727</td> <td>50.0800</td> <td>0.053</td> <td>9.3054</td> <td>0.0054202</td> <td>3.8179</td> <td>-4.3590</td> </tr> <tr> <td>Std. DV 0.0000</td> <td>0.0000</td> <td>0.000</td> <td>0.0000</td> <td>0.0000000</td> <td>0.0000</td> <td>0.0000</td> </tr> <tr> <td>Area1 2.0727</td> <td>50.0800</td> <td>0.053</td> <td>9.3054</td> <td>0.0054202</td> <td>3.8179</td> <td>-4.3590</td> </tr> </tbody> </table>	Sa	Sz	Str	Spc	Sdr	Sq	Ssk	$\mu\text{m}$	$\mu\text{m}$	1/mm			$\mu\text{m}$		Max. 2.0727	50.0800	0.053	9.3054	0.0054202	3.8179	-4.3590	Min. 2.0727	50.0800	0.053	9.3054	0.0054202	3.8179	-4.3590	Ave. 2.0727	50.0800	0.053	9.3054	0.0054202	3.8179	-4.3590	Std. DV 0.0000	0.0000	0.000	0.0000	0.0000000	0.0000	0.0000	Area1 2.0727	50.0800	0.053	9.3054	0.0054202	3.8179	-4.3590	2.0727	50.0800	0.053	3.8179	9.7580	40.3220
Sa	Sz	Str	Spc	Sdr	Sq	Ssk																																																			
$\mu\text{m}$	$\mu\text{m}$	1/mm			$\mu\text{m}$																																																				
Max. 2.0727	50.0800	0.053	9.3054	0.0054202	3.8179	-4.3590																																																			
Min. 2.0727	50.0800	0.053	9.3054	0.0054202	3.8179	-4.3590																																																			
Ave. 2.0727	50.0800	0.053	9.3054	0.0054202	3.8179	-4.3590																																																			
Std. DV 0.0000	0.0000	0.000	0.0000	0.0000000	0.0000	0.0000																																																			
Area1 2.0727	50.0800	0.053	9.3054	0.0054202	3.8179	-4.3590																																																			
A13		<table border="1"> <thead> <tr> <th>Sa</th> <th>Sz</th> <th>Str</th> <th>Spc</th> <th>Sdr</th> <th>Sq</th> <th>Ssk</th> </tr> <tr> <th><math>\mu\text{m}</math></th> <th><math>\mu\text{m}</math></th> <th>1/mm</th> <th></th> <th></th> <th><math>\mu\text{m}</math></th> <th></th> </tr> </thead> <tbody> <tr> <td>Max. 1.5819</td> <td>29.7400</td> <td>0.049</td> <td>8.3484</td> <td>0.0038322</td> <td>2.3693</td> <td>-2.3331</td> </tr> <tr> <td>Min. 1.5819</td> <td>29.7400</td> <td>0.049</td> <td>8.3484</td> <td>0.0038322</td> <td>2.3693</td> <td>-2.3331</td> </tr> <tr> <td>Ave. 1.5819</td> <td>29.7400</td> <td>0.049</td> <td>8.3484</td> <td>0.0038322</td> <td>2.3693</td> <td>-2.3331</td> </tr> <tr> <td>Std. DV 0.0000</td> <td>0.0000</td> <td>0.000</td> <td>0.0000</td> <td>0.0000000</td> <td>0.0000</td> <td>0.0000</td> </tr> <tr> <td>Area1 1.5819</td> <td>29.7400</td> <td>0.049</td> <td>8.3484</td> <td>0.0038322</td> <td>2.3693</td> <td>-2.3331</td> </tr> </tbody> </table>	Sa	Sz	Str	Spc	Sdr	Sq	Ssk	$\mu\text{m}$	$\mu\text{m}$	1/mm			$\mu\text{m}$		Max. 1.5819	29.7400	0.049	8.3484	0.0038322	2.3693	-2.3331	Min. 1.5819	29.7400	0.049	8.3484	0.0038322	2.3693	-2.3331	Ave. 1.5819	29.7400	0.049	8.3484	0.0038322	2.3693	-2.3331	Std. DV 0.0000	0.0000	0.000	0.0000	0.0000000	0.0000	0.0000	Area1 1.5819	29.7400	0.049	8.3484	0.0038322	2.3693	-2.3331	1.5819	29.7400	0.049	2.3693	7.6523	22.0877
Sa	Sz	Str	Spc	Sdr	Sq	Ssk																																																			
$\mu\text{m}$	$\mu\text{m}$	1/mm			$\mu\text{m}$																																																				
Max. 1.5819	29.7400	0.049	8.3484	0.0038322	2.3693	-2.3331																																																			
Min. 1.5819	29.7400	0.049	8.3484	0.0038322	2.3693	-2.3331																																																			
Ave. 1.5819	29.7400	0.049	8.3484	0.0038322	2.3693	-2.3331																																																			
Std. DV 0.0000	0.0000	0.000	0.0000	0.0000000	0.0000	0.0000																																																			
Area1 1.5819	29.7400	0.049	8.3484	0.0038322	2.3693	-2.3331																																																			
C4		<table border="1"> <thead> <tr> <th>Sa</th> <th>Sz</th> <th>Str</th> <th>Spc</th> <th>Sdr</th> <th>Sq</th> <th>Ssk</th> </tr> <tr> <th><math>\mu\text{m}</math></th> <th><math>\mu\text{m}</math></th> <th>1/mm</th> <th></th> <th></th> <th><math>\mu\text{m}</math></th> <th></th> </tr> </thead> <tbody> <tr> <td>Max. 4.8596</td> <td>93.2800</td> <td>0.086</td> <td>8.8658</td> <td>0.0062699</td> <td>8.9803</td> <td>-3.7870</td> </tr> <tr> <td>Min. 4.8596</td> <td>93.2800</td> <td>0.086</td> <td>8.8658</td> <td>0.0062699</td> <td>8.9803</td> <td>-3.7870</td> </tr> <tr> <td>Ave. 4.8596</td> <td>93.2800</td> <td>0.086</td> <td>8.8658</td> <td>0.0062699</td> <td>8.9803</td> <td>-3.7870</td> </tr> <tr> <td>Std. DV 0.0000</td> <td>0.0000</td> <td>0.000</td> <td>0.0000</td> <td>0.0000000</td> <td>0.0000</td> <td>0.0000</td> </tr> <tr> <td>Area1 4.8596</td> <td>93.2800</td> <td>0.086</td> <td>8.8658</td> <td>0.0062699</td> <td>8.9803</td> <td>-3.7870</td> </tr> </tbody> </table>	Sa	Sz	Str	Spc	Sdr	Sq	Ssk	$\mu\text{m}$	$\mu\text{m}$	1/mm			$\mu\text{m}$		Max. 4.8596	93.2800	0.086	8.8658	0.0062699	8.9803	-3.7870	Min. 4.8596	93.2800	0.086	8.8658	0.0062699	8.9803	-3.7870	Ave. 4.8596	93.2800	0.086	8.8658	0.0062699	8.9803	-3.7870	Std. DV 0.0000	0.0000	0.000	0.0000	0.0000000	0.0000	0.0000	Area1 4.8596	93.2800	0.086	8.8658	0.0062699	8.9803	-3.7870	4.8596	93.2800	0.086	8.9803	11.6288	81.6512
Sa	Sz	Str	Spc	Sdr	Sq	Ssk																																																			
$\mu\text{m}$	$\mu\text{m}$	1/mm			$\mu\text{m}$																																																				
Max. 4.8596	93.2800	0.086	8.8658	0.0062699	8.9803	-3.7870																																																			
Min. 4.8596	93.2800	0.086	8.8658	0.0062699	8.9803	-3.7870																																																			
Ave. 4.8596	93.2800	0.086	8.8658	0.0062699	8.9803	-3.7870																																																			
Std. DV 0.0000	0.0000	0.000	0.0000	0.0000000	0.0000	0.0000																																																			
Area1 4.8596	93.2800	0.086	8.8658	0.0062699	8.9803	-3.7870																																																			
H3		<table border="1"> <thead> <tr> <th>Sa</th> <th>Sz</th> <th>Str</th> <th>Spc</th> <th>Sdr</th> <th>Sq</th> <th>Ssk</th> </tr> <tr> <th><math>\mu\text{m}</math></th> <th><math>\mu\text{m}</math></th> <th>1/mm</th> <th></th> <th></th> <th><math>\mu\text{m}</math></th> <th></th> </tr> </thead> <tbody> <tr> <td>Max. 1.8841</td> <td>43.5800</td> <td>0.055</td> <td>7.7625</td> <td>0.0036507</td> <td>3.4753</td> <td>-4.1210</td> </tr> <tr> <td>Min. 1.8841</td> <td>43.5800</td> <td>0.055</td> <td>7.7625</td> <td>0.0036507</td> <td>3.4753</td> <td>-4.1210</td> </tr> <tr> <td>Ave. 1.8841</td> <td>43.5800</td> <td>0.055</td> <td>7.7625</td> <td>0.0036507</td> <td>3.4753</td> <td>-4.1210</td> </tr> <tr> <td>Std. DV 0.0000</td> <td>0.0000</td> <td>0.000</td> <td>0.0000</td> <td>0.0000000</td> <td>0.0000</td> <td>0.0000</td> </tr> <tr> <td>Area1 1.8841</td> <td>43.5800</td> <td>0.055</td> <td>7.7625</td> <td>0.0036507</td> <td>3.4753</td> <td>-4.1210</td> </tr> </tbody> </table>	Sa	Sz	Str	Spc	Sdr	Sq	Ssk	$\mu\text{m}$	$\mu\text{m}$	1/mm			$\mu\text{m}$		Max. 1.8841	43.5800	0.055	7.7625	0.0036507	3.4753	-4.1210	Min. 1.8841	43.5800	0.055	7.7625	0.0036507	3.4753	-4.1210	Ave. 1.8841	43.5800	0.055	7.7625	0.0036507	3.4753	-4.1210	Std. DV 0.0000	0.0000	0.000	0.0000	0.0000000	0.0000	0.0000	Area1 1.8841	43.5800	0.055	7.7625	0.0036507	3.4753	-4.1210	1.8841	43.5800	0.055	3.4753	8.0732	35.5068
Sa	Sz	Str	Spc	Sdr	Sq	Ssk																																																			
$\mu\text{m}$	$\mu\text{m}$	1/mm			$\mu\text{m}$																																																				
Max. 1.8841	43.5800	0.055	7.7625	0.0036507	3.4753	-4.1210																																																			
Min. 1.8841	43.5800	0.055	7.7625	0.0036507	3.4753	-4.1210																																																			
Ave. 1.8841	43.5800	0.055	7.7625	0.0036507	3.4753	-4.1210																																																			
Std. DV 0.0000	0.0000	0.000	0.0000	0.0000000	0.0000	0.0000																																																			
Area1 1.8841	43.5800	0.055	7.7625	0.0036507	3.4753	-4.1210																																																			

B16		<table border="1"> <thead> <tr> <th>Sa</th> <th>Sz</th> <th>Str</th> <th>Spc</th> <th>Sdr</th> <th>Sq</th> <th>Ssk</th> </tr> <tr> <th>µm</th> <th>µm</th> <th>1/mm</th> <th>µm</th> <th>µm</th> <th>µm</th> <th></th> </tr> </thead> <tbody> <tr> <td>Max. 1.4041</td> <td>61.9900</td> <td>0.030</td> <td>8.5045</td> <td>0.0040597</td> <td>2.2648</td> <td>-3.2033</td> </tr> <tr> <td>Min. 1.4041</td> <td>61.9900</td> <td>0.030</td> <td>8.5045</td> <td>0.0040597</td> <td>2.2648</td> <td>-3.2033</td> </tr> <tr> <td>Ave. 1.4041</td> <td>61.9900</td> <td>0.030</td> <td>8.5045</td> <td>0.0040597</td> <td>2.2648</td> <td>-3.2033</td> </tr> <tr> <td>Std. DV 0.0000</td> <td>0.0000</td> <td>0.000</td> <td>0.0000</td> <td>0.0000000</td> <td>0.0000</td> <td>0.0000</td> </tr> <tr> <td>Area1 1.4041</td> <td>61.9900</td> <td>0.030</td> <td>8.5045</td> <td>0.0040597</td> <td>2.2648</td> <td>-3.2033</td> </tr> </tbody> </table>	Sa	Sz	Str	Spc	Sdr	Sq	Ssk	µm	µm	1/mm	µm	µm	µm		Max. 1.4041	61.9900	0.030	8.5045	0.0040597	2.2648	-3.2033	Min. 1.4041	61.9900	0.030	8.5045	0.0040597	2.2648	-3.2033	Ave. 1.4041	61.9900	0.030	8.5045	0.0040597	2.2648	-3.2033	Std. DV 0.0000	0.0000	0.000	0.0000	0.0000000	0.0000	0.0000	Area1 1.4041	61.9900	0.030	8.5045	0.0040597	2.2648	-3.2033	1.4041	61.9900	0.030	2.2648	13.3213	48.6687
Sa	Sz	Str	Spc	Sdr	Sq	Ssk																																																			
µm	µm	1/mm	µm	µm	µm																																																				
Max. 1.4041	61.9900	0.030	8.5045	0.0040597	2.2648	-3.2033																																																			
Min. 1.4041	61.9900	0.030	8.5045	0.0040597	2.2648	-3.2033																																																			
Ave. 1.4041	61.9900	0.030	8.5045	0.0040597	2.2648	-3.2033																																																			
Std. DV 0.0000	0.0000	0.000	0.0000	0.0000000	0.0000	0.0000																																																			
Area1 1.4041	61.9900	0.030	8.5045	0.0040597	2.2648	-3.2033																																																			
A6		<table border="1"> <thead> <tr> <th>Sa</th> <th>Sz</th> <th>Str</th> <th>Spc</th> <th>Sdr</th> <th>Sq</th> <th>Ssk</th> </tr> <tr> <th>µm</th> <th>µm</th> <th>1/mm</th> <th>µm</th> <th>µm</th> <th>µm</th> <th></th> </tr> </thead> <tbody> <tr> <td>Max. 1.2186</td> <td>33.4100</td> <td>0.087</td> <td>8.4406</td> <td>0.0037252</td> <td>1.5795</td> <td>-0.0333</td> </tr> <tr> <td>Min. 1.2186</td> <td>33.4100</td> <td>0.087</td> <td>8.4406</td> <td>0.0037252</td> <td>1.5795</td> <td>-0.0333</td> </tr> <tr> <td>Ave. 1.2186</td> <td>33.4100</td> <td>0.087</td> <td>8.4406</td> <td>0.0037252</td> <td>1.5795</td> <td>-0.0333</td> </tr> <tr> <td>Std. DV 0.0000</td> <td>0.0000</td> <td>0.000</td> <td>0.0000</td> <td>0.0000000</td> <td>0.0000</td> <td>0.0000</td> </tr> <tr> <td>Area1 1.2186</td> <td>33.4100</td> <td>0.087</td> <td>8.4406</td> <td>0.0037252</td> <td>1.5795</td> <td>-0.0333</td> </tr> </tbody> </table>	Sa	Sz	Str	Spc	Sdr	Sq	Ssk	µm	µm	1/mm	µm	µm	µm		Max. 1.2186	33.4100	0.087	8.4406	0.0037252	1.5795	-0.0333	Min. 1.2186	33.4100	0.087	8.4406	0.0037252	1.5795	-0.0333	Ave. 1.2186	33.4100	0.087	8.4406	0.0037252	1.5795	-0.0333	Std. DV 0.0000	0.0000	0.000	0.0000	0.0000000	0.0000	0.0000	Area1 1.2186	33.4100	0.087	8.4406	0.0037252	1.5795	-0.0333	1.2186	33.4100	0.087	1.5795	18.7294	14.6806
Sa	Sz	Str	Spc	Sdr	Sq	Ssk																																																			
µm	µm	1/mm	µm	µm	µm																																																				
Max. 1.2186	33.4100	0.087	8.4406	0.0037252	1.5795	-0.0333																																																			
Min. 1.2186	33.4100	0.087	8.4406	0.0037252	1.5795	-0.0333																																																			
Ave. 1.2186	33.4100	0.087	8.4406	0.0037252	1.5795	-0.0333																																																			
Std. DV 0.0000	0.0000	0.000	0.0000	0.0000000	0.0000	0.0000																																																			
Area1 1.2186	33.4100	0.087	8.4406	0.0037252	1.5795	-0.0333																																																			
G7		<table border="1"> <thead> <tr> <th>Sa</th> <th>Sz</th> <th>Str</th> <th>Spc</th> <th>Sdr</th> <th>Sq</th> <th>Ssk</th> </tr> <tr> <th>µm</th> <th>µm</th> <th>1/mm</th> <th>µm</th> <th>µm</th> <th>µm</th> <th></th> </tr> </thead> <tbody> <tr> <td>Max. 5.5864</td> <td>111.7500</td> <td>0.055</td> <td>12.2841</td> <td>0.0108724</td> <td>12.0202</td> <td>-4.4661</td> </tr> <tr> <td>Min. 5.5864</td> <td>111.7500</td> <td>0.055</td> <td>12.2841</td> <td>0.0108724</td> <td>12.0202</td> <td>-4.4661</td> </tr> <tr> <td>Ave. 5.5864</td> <td>111.7500</td> <td>0.055</td> <td>12.2841</td> <td>0.0108724</td> <td>12.0202</td> <td>-4.4661</td> </tr> <tr> <td>Std. DV 0.0000</td> <td>0.0000</td> <td>0.000</td> <td>0.0000</td> <td>0.0000000</td> <td>0.0000</td> <td>0.0000</td> </tr> <tr> <td>Area1 5.5864</td> <td>111.7500</td> <td>0.055</td> <td>12.2841</td> <td>0.0108724</td> <td>12.0202</td> <td>-4.4661</td> </tr> </tbody> </table>	Sa	Sz	Str	Spc	Sdr	Sq	Ssk	µm	µm	1/mm	µm	µm	µm		Max. 5.5864	111.7500	0.055	12.2841	0.0108724	12.0202	-4.4661	Min. 5.5864	111.7500	0.055	12.2841	0.0108724	12.0202	-4.4661	Ave. 5.5864	111.7500	0.055	12.2841	0.0108724	12.0202	-4.4661	Std. DV 0.0000	0.0000	0.000	0.0000	0.0000000	0.0000	0.0000	Area1 5.5864	111.7500	0.055	12.2841	0.0108724	12.0202	-4.4661	5.5864	#####	0.055	12.0202	18.0830	93.6670
Sa	Sz	Str	Spc	Sdr	Sq	Ssk																																																			
µm	µm	1/mm	µm	µm	µm																																																				
Max. 5.5864	111.7500	0.055	12.2841	0.0108724	12.0202	-4.4661																																																			
Min. 5.5864	111.7500	0.055	12.2841	0.0108724	12.0202	-4.4661																																																			
Ave. 5.5864	111.7500	0.055	12.2841	0.0108724	12.0202	-4.4661																																																			
Std. DV 0.0000	0.0000	0.000	0.0000	0.0000000	0.0000	0.0000																																																			
Area1 5.5864	111.7500	0.055	12.2841	0.0108724	12.0202	-4.4661																																																			
F1		<table border="1"> <thead> <tr> <th>Sa</th> <th>Sz</th> <th>Str</th> <th>Spc</th> <th>Sdr</th> <th>Sq</th> <th>Ssk</th> </tr> <tr> <th>µm</th> <th>µm</th> <th>1/mm</th> <th>µm</th> <th>µm</th> <th>µm</th> <th></th> </tr> </thead> <tbody> <tr> <td>Max. 3.4667</td> <td>77.0200</td> <td>0.065</td> <td>9.3344</td> <td>0.0061565</td> <td>6.7520</td> <td>-4.3500</td> </tr> <tr> <td>Min. 3.4667</td> <td>77.0200</td> <td>0.065</td> <td>9.3344</td> <td>0.0061565</td> <td>6.7520</td> <td>-4.3500</td> </tr> <tr> <td>Ave. 3.4667</td> <td>77.0200</td> <td>0.065</td> <td>9.3344</td> <td>0.0061565</td> <td>6.7520</td> <td>-4.3500</td> </tr> <tr> <td>Std. DV 0.0000</td> <td>0.0000</td> <td>0.000</td> <td>0.0000</td> <td>0.0000000</td> <td>0.0000</td> <td>0.0000</td> </tr> <tr> <td>Area1 3.4667</td> <td>77.0200</td> <td>0.065</td> <td>9.3344</td> <td>0.0061565</td> <td>6.7520</td> <td>-4.3500</td> </tr> </tbody> </table>	Sa	Sz	Str	Spc	Sdr	Sq	Ssk	µm	µm	1/mm	µm	µm	µm		Max. 3.4667	77.0200	0.065	9.3344	0.0061565	6.7520	-4.3500	Min. 3.4667	77.0200	0.065	9.3344	0.0061565	6.7520	-4.3500	Ave. 3.4667	77.0200	0.065	9.3344	0.0061565	6.7520	-4.3500	Std. DV 0.0000	0.0000	0.000	0.0000	0.0000000	0.0000	0.0000	Area1 3.4667	77.0200	0.065	9.3344	0.0061565	6.7520	-4.3500	3.4667	77.0200	0.065	6.7520	14.4279	62.5921
Sa	Sz	Str	Spc	Sdr	Sq	Ssk																																																			
µm	µm	1/mm	µm	µm	µm																																																				
Max. 3.4667	77.0200	0.065	9.3344	0.0061565	6.7520	-4.3500																																																			
Min. 3.4667	77.0200	0.065	9.3344	0.0061565	6.7520	-4.3500																																																			
Ave. 3.4667	77.0200	0.065	9.3344	0.0061565	6.7520	-4.3500																																																			
Std. DV 0.0000	0.0000	0.000	0.0000	0.0000000	0.0000	0.0000																																																			
Area1 3.4667	77.0200	0.065	9.3344	0.0061565	6.7520	-4.3500																																																			
B18		<table border="1"> <thead> <tr> <th>Sa</th> <th>Sz</th> <th>Str</th> <th>Spc</th> <th>Sdr</th> <th>Sq</th> <th>Ssk</th> </tr> <tr> <th>µm</th> <th>µm</th> <th>1/mm</th> <th>µm</th> <th>µm</th> <th>µm</th> <th></th> </tr> </thead> <tbody> <tr> <td>Max. 1.2442</td> <td>28.8300</td> <td>0.091</td> <td>8.9179</td> <td>0.0042410</td> <td>1.6685</td> <td>-0.4661</td> </tr> <tr> <td>Min. 1.2442</td> <td>28.8300</td> <td>0.091</td> <td>8.9179</td> <td>0.0042410</td> <td>1.6685</td> <td>-0.4661</td> </tr> <tr> <td>Ave. 1.2442</td> <td>28.8300</td> <td>0.091</td> <td>8.9179</td> <td>0.0042410</td> <td>1.6685</td> <td>-0.4661</td> </tr> <tr> <td>Std. DV 0.0000</td> <td>0.0000</td> <td>0.000</td> <td>0.0000</td> <td>0.0000000</td> <td>0.0000</td> <td>0.0000</td> </tr> <tr> <td>Area1 1.2442</td> <td>28.8300</td> <td>0.091</td> <td>8.9179</td> <td>0.0042410</td> <td>1.6685</td> <td>-0.4661</td> </tr> </tbody> </table>	Sa	Sz	Str	Spc	Sdr	Sq	Ssk	µm	µm	1/mm	µm	µm	µm		Max. 1.2442	28.8300	0.091	8.9179	0.0042410	1.6685	-0.4661	Min. 1.2442	28.8300	0.091	8.9179	0.0042410	1.6685	-0.4661	Ave. 1.2442	28.8300	0.091	8.9179	0.0042410	1.6685	-0.4661	Std. DV 0.0000	0.0000	0.000	0.0000	0.0000000	0.0000	0.0000	Area1 1.2442	28.8300	0.091	8.9179	0.0042410	1.6685	-0.4661	1.2442	28.8300	0.091	1.6685	12.1288	16.7012
Sa	Sz	Str	Spc	Sdr	Sq	Ssk																																																			
µm	µm	1/mm	µm	µm	µm																																																				
Max. 1.2442	28.8300	0.091	8.9179	0.0042410	1.6685	-0.4661																																																			
Min. 1.2442	28.8300	0.091	8.9179	0.0042410	1.6685	-0.4661																																																			
Ave. 1.2442	28.8300	0.091	8.9179	0.0042410	1.6685	-0.4661																																																			
Std. DV 0.0000	0.0000	0.000	0.0000	0.0000000	0.0000	0.0000																																																			
Area1 1.2442	28.8300	0.091	8.9179	0.0042410	1.6685	-0.4661																																																			
H6		<table border="1"> <thead> <tr> <th>Sa</th> <th>Sz</th> <th>Str</th> <th>Spc</th> <th>Sdr</th> <th>Sq</th> <th>Ssk</th> </tr> <tr> <th>µm</th> <th>µm</th> <th>1/mm</th> <th>µm</th> <th>µm</th> <th>µm</th> <th></th> </tr> </thead> <tbody> <tr> <td>Max. 2.8302</td> <td>95.5400</td> <td>0.043</td> <td>12.5590</td> <td>0.0079448</td> <td>6.0924</td> <td>-5.1661</td> </tr> <tr> <td>Min. 2.8302</td> <td>95.5400</td> <td>0.043</td> <td>12.5590</td> <td>0.0079448</td> <td>6.0924</td> <td>-5.1661</td> </tr> <tr> <td>Ave. 2.8302</td> <td>95.5400</td> <td>0.043</td> <td>12.5590</td> <td>0.0079448</td> <td>6.0924</td> <td>-5.1661</td> </tr> <tr> <td>Std. DV 0.0000</td> <td>0.0000</td> <td>0.000</td> <td>0.0000</td> <td>0.0000000</td> <td>0.0000</td> <td>0.0000</td> </tr> <tr> <td>Area1 2.8302</td> <td>95.5400</td> <td>0.043</td> <td>12.5590</td> <td>0.0079448</td> <td>6.0924</td> <td>-5.1661</td> </tr> </tbody> </table>	Sa	Sz	Str	Spc	Sdr	Sq	Ssk	µm	µm	1/mm	µm	µm	µm		Max. 2.8302	95.5400	0.043	12.5590	0.0079448	6.0924	-5.1661	Min. 2.8302	95.5400	0.043	12.5590	0.0079448	6.0924	-5.1661	Ave. 2.8302	95.5400	0.043	12.5590	0.0079448	6.0924	-5.1661	Std. DV 0.0000	0.0000	0.000	0.0000	0.0000000	0.0000	0.0000	Area1 2.8302	95.5400	0.043	12.5590	0.0079448	6.0924	-5.1661	2.8302	95.5400	0.043	6.0924	19.6806	75.8594
Sa	Sz	Str	Spc	Sdr	Sq	Ssk																																																			
µm	µm	1/mm	µm	µm	µm																																																				
Max. 2.8302	95.5400	0.043	12.5590	0.0079448	6.0924	-5.1661																																																			
Min. 2.8302	95.5400	0.043	12.5590	0.0079448	6.0924	-5.1661																																																			
Ave. 2.8302	95.5400	0.043	12.5590	0.0079448	6.0924	-5.1661																																																			
Std. DV 0.0000	0.0000	0.000	0.0000	0.0000000	0.0000	0.0000																																																			
Area1 2.8302	95.5400	0.043	12.5590	0.0079448	6.0924	-5.1661																																																			

D7		<table border="1"> <thead> <tr> <th>Sa</th> <th>Sz</th> <th>Str</th> <th>Spc</th> <th>Sdr</th> <th>Sq</th> <th>Ssk</th> </tr> <tr> <th><math>\mu\text{m}</math></th> <th><math>\mu\text{m}</math></th> <th>1/mm</th> <th></th> <th></th> <th><math>\mu\text{m}</math></th> <th></th> </tr> </thead> <tbody> <tr> <td>Max. 1.4705</td> <td>28.8400</td> <td>0.032</td> <td>8.6133</td> <td>0.0043880</td> <td>2.0105</td> <td>-1.0890</td> </tr> <tr> <td>Min. 1.4705</td> <td>28.8400</td> <td>0.032</td> <td>8.6133</td> <td>0.0043880</td> <td>2.0105</td> <td>-1.0890</td> </tr> <tr> <td>Ave. 1.4705</td> <td>28.8400</td> <td>0.032</td> <td>8.6133</td> <td>0.0043880</td> <td>2.0105</td> <td>-1.0890</td> </tr> <tr> <td>Std. DV 0.0000</td> <td>0.0000</td> <td>0.000</td> <td>0.0000</td> <td>0.0000000</td> <td>0.0000</td> <td>0.0000</td> </tr> <tr> <td>Area1 1.4705</td> <td>28.8400</td> <td>0.032</td> <td>8.6133</td> <td>0.0043880</td> <td>2.0105</td> <td>-1.0890</td> </tr> </tbody> </table>	Sa	Sz	Str	Spc	Sdr	Sq	Ssk	$\mu\text{m}$	$\mu\text{m}$	1/mm			$\mu\text{m}$		Max. 1.4705	28.8400	0.032	8.6133	0.0043880	2.0105	-1.0890	Min. 1.4705	28.8400	0.032	8.6133	0.0043880	2.0105	-1.0890	Ave. 1.4705	28.8400	0.032	8.6133	0.0043880	2.0105	-1.0890	Std. DV 0.0000	0.0000	0.000	0.0000	0.0000000	0.0000	0.0000	Area1 1.4705	28.8400	0.032	8.6133	0.0043880	2.0105	-1.0890	1.4705	28.8400	0.032	2.0105	8.6604	20.1796
Sa	Sz	Str	Spc	Sdr	Sq	Ssk																																																			
$\mu\text{m}$	$\mu\text{m}$	1/mm			$\mu\text{m}$																																																				
Max. 1.4705	28.8400	0.032	8.6133	0.0043880	2.0105	-1.0890																																																			
Min. 1.4705	28.8400	0.032	8.6133	0.0043880	2.0105	-1.0890																																																			
Ave. 1.4705	28.8400	0.032	8.6133	0.0043880	2.0105	-1.0890																																																			
Std. DV 0.0000	0.0000	0.000	0.0000	0.0000000	0.0000	0.0000																																																			
Area1 1.4705	28.8400	0.032	8.6133	0.0043880	2.0105	-1.0890																																																			
G4		<table border="1"> <thead> <tr> <th>Sa</th> <th>Sz</th> <th>Str</th> <th>Spc</th> <th>Sdr</th> <th>Sq</th> <th>Ssk</th> </tr> <tr> <th><math>\mu\text{m}</math></th> <th><math>\mu\text{m}</math></th> <th>1/mm</th> <th></th> <th></th> <th><math>\mu\text{m}</math></th> <th></th> </tr> </thead> <tbody> <tr> <td>Max. 6.8825</td> <td>104.7200</td> <td>0.061</td> <td>9.4673</td> <td>0.0087471</td> <td>14.3020</td> <td>-4.2400</td> </tr> <tr> <td>Min. 6.8825</td> <td>104.7200</td> <td>0.061</td> <td>9.4673</td> <td>0.0087471</td> <td>14.3020</td> <td>-4.2400</td> </tr> <tr> <td>Ave. 6.8825</td> <td>104.7200</td> <td>0.061</td> <td>9.4673</td> <td>0.0087471</td> <td>14.3020</td> <td>-4.2400</td> </tr> <tr> <td>Std. DV 0.0000</td> <td>0.0000</td> <td>0.000</td> <td>0.0000</td> <td>0.0000000</td> <td>0.0000</td> <td>0.0000</td> </tr> <tr> <td>Area1 6.8825</td> <td>104.7200</td> <td>0.061</td> <td>9.4673</td> <td>0.0087471</td> <td>14.3020</td> <td>-4.2400</td> </tr> </tbody> </table>	Sa	Sz	Str	Spc	Sdr	Sq	Ssk	$\mu\text{m}$	$\mu\text{m}$	1/mm			$\mu\text{m}$		Max. 6.8825	104.7200	0.061	9.4673	0.0087471	14.3020	-4.2400	Min. 6.8825	104.7200	0.061	9.4673	0.0087471	14.3020	-4.2400	Ave. 6.8825	104.7200	0.061	9.4673	0.0087471	14.3020	-4.2400	Std. DV 0.0000	0.0000	0.000	0.0000	0.0000000	0.0000	0.0000	Area1 6.8825	104.7200	0.061	9.4673	0.0087471	14.3020	-4.2400	6.8825	#####	0.061	14.3020	11.6918	93.0282
Sa	Sz	Str	Spc	Sdr	Sq	Ssk																																																			
$\mu\text{m}$	$\mu\text{m}$	1/mm			$\mu\text{m}$																																																				
Max. 6.8825	104.7200	0.061	9.4673	0.0087471	14.3020	-4.2400																																																			
Min. 6.8825	104.7200	0.061	9.4673	0.0087471	14.3020	-4.2400																																																			
Ave. 6.8825	104.7200	0.061	9.4673	0.0087471	14.3020	-4.2400																																																			
Std. DV 0.0000	0.0000	0.000	0.0000	0.0000000	0.0000	0.0000																																																			
Area1 6.8825	104.7200	0.061	9.4673	0.0087471	14.3020	-4.2400																																																			
E1		<table border="1"> <thead> <tr> <th>Sa</th> <th>Sz</th> <th>Str</th> <th>Spc</th> <th>Sdr</th> <th>Sq</th> <th>Ssk</th> </tr> <tr> <th><math>\mu\text{m}</math></th> <th><math>\mu\text{m}</math></th> <th>1/mm</th> <th></th> <th></th> <th><math>\mu\text{m}</math></th> <th></th> </tr> </thead> <tbody> <tr> <td>Max. 1.4709</td> <td>22.7300</td> <td>0.038</td> <td>8.6310</td> <td>0.0041463</td> <td>1.9585</td> <td>-0.7230</td> </tr> <tr> <td>Min. 1.4709</td> <td>22.7300</td> <td>0.038</td> <td>8.6310</td> <td>0.0041463</td> <td>1.9585</td> <td>-0.7230</td> </tr> <tr> <td>Ave. 1.4709</td> <td>22.7300</td> <td>0.038</td> <td>8.6310</td> <td>0.0041463</td> <td>1.9585</td> <td>-0.7230</td> </tr> <tr> <td>Std. DV 0.0000</td> <td>0.0000</td> <td>0.000</td> <td>0.0000</td> <td>0.0000000</td> <td>0.0000</td> <td>0.0000</td> </tr> <tr> <td>Area1 1.4709</td> <td>22.7300</td> <td>0.038</td> <td>8.6310</td> <td>0.0041463</td> <td>1.9585</td> <td>-0.7230</td> </tr> </tbody> </table>	Sa	Sz	Str	Spc	Sdr	Sq	Ssk	$\mu\text{m}$	$\mu\text{m}$	1/mm			$\mu\text{m}$		Max. 1.4709	22.7300	0.038	8.6310	0.0041463	1.9585	-0.7230	Min. 1.4709	22.7300	0.038	8.6310	0.0041463	1.9585	-0.7230	Ave. 1.4709	22.7300	0.038	8.6310	0.0041463	1.9585	-0.7230	Std. DV 0.0000	0.0000	0.000	0.0000	0.0000000	0.0000	0.0000	Area1 1.4709	22.7300	0.038	8.6310	0.0041463	1.9585	-0.7230	1.4709	22.7300	0.038	1.9585	7.8767	14.8533
Sa	Sz	Str	Spc	Sdr	Sq	Ssk																																																			
$\mu\text{m}$	$\mu\text{m}$	1/mm			$\mu\text{m}$																																																				
Max. 1.4709	22.7300	0.038	8.6310	0.0041463	1.9585	-0.7230																																																			
Min. 1.4709	22.7300	0.038	8.6310	0.0041463	1.9585	-0.7230																																																			
Ave. 1.4709	22.7300	0.038	8.6310	0.0041463	1.9585	-0.7230																																																			
Std. DV 0.0000	0.0000	0.000	0.0000	0.0000000	0.0000	0.0000																																																			
Area1 1.4709	22.7300	0.038	8.6310	0.0041463	1.9585	-0.7230																																																			
B11		<table border="1"> <thead> <tr> <th>Sa</th> <th>Sz</th> <th>Str</th> <th>Spc</th> <th>Sdr</th> <th>Sq</th> <th>Ssk</th> </tr> <tr> <th><math>\mu\text{m}</math></th> <th><math>\mu\text{m}</math></th> <th>1/mm</th> <th></th> <th></th> <th><math>\mu\text{m}</math></th> <th></th> </tr> </thead> <tbody> <tr> <td>Max. 2.2470</td> <td>108.8400</td> <td>0.054</td> <td>8.2485</td> <td>0.0049295</td> <td>4.4368</td> <td>-3.0740</td> </tr> <tr> <td>Min. 2.2470</td> <td>108.8400</td> <td>0.054</td> <td>8.2485</td> <td>0.0049295</td> <td>4.4368</td> <td>-3.0740</td> </tr> <tr> <td>Ave. 2.2470</td> <td>108.8400</td> <td>0.054</td> <td>8.2485</td> <td>0.0049295</td> <td>4.4368</td> <td>-3.0740</td> </tr> <tr> <td>Std. DV 0.0000</td> <td>0.0000</td> <td>0.000</td> <td>0.0000</td> <td>0.0000000</td> <td>0.0000</td> <td>0.0000</td> </tr> <tr> <td>Area1 2.2470</td> <td>108.8400</td> <td>0.054</td> <td>8.2485</td> <td>0.0049295</td> <td>4.4368</td> <td>-3.0740</td> </tr> </tbody> </table>	Sa	Sz	Str	Spc	Sdr	Sq	Ssk	$\mu\text{m}$	$\mu\text{m}$	1/mm			$\mu\text{m}$		Max. 2.2470	108.8400	0.054	8.2485	0.0049295	4.4368	-3.0740	Min. 2.2470	108.8400	0.054	8.2485	0.0049295	4.4368	-3.0740	Ave. 2.2470	108.8400	0.054	8.2485	0.0049295	4.4368	-3.0740	Std. DV 0.0000	0.0000	0.000	0.0000	0.0000000	0.0000	0.0000	Area1 2.2470	108.8400	0.054	8.2485	0.0049295	4.4368	-3.0740	2.2470	#####	0.054	4.4368	63.6426	45.1974
Sa	Sz	Str	Spc	Sdr	Sq	Ssk																																																			
$\mu\text{m}$	$\mu\text{m}$	1/mm			$\mu\text{m}$																																																				
Max. 2.2470	108.8400	0.054	8.2485	0.0049295	4.4368	-3.0740																																																			
Min. 2.2470	108.8400	0.054	8.2485	0.0049295	4.4368	-3.0740																																																			
Ave. 2.2470	108.8400	0.054	8.2485	0.0049295	4.4368	-3.0740																																																			
Std. DV 0.0000	0.0000	0.000	0.0000	0.0000000	0.0000	0.0000																																																			
Area1 2.2470	108.8400	0.054	8.2485	0.0049295	4.4368	-3.0740																																																			
A18		<table border="1"> <thead> <tr> <th>Sa</th> <th>Sz</th> <th>Str</th> <th>Spc</th> <th>Sdr</th> <th>Sq</th> <th>Ssk</th> </tr> <tr> <th><math>\mu\text{m}</math></th> <th><math>\mu\text{m}</math></th> <th>1/mm</th> <th></th> <th></th> <th><math>\mu\text{m}</math></th> <th></th> </tr> </thead> <tbody> <tr> <td>Max. 1.7033</td> <td>36.1500</td> <td>0.045</td> <td>8.5476</td> <td>0.0045959</td> <td>2.4810</td> <td>-1.9870</td> </tr> <tr> <td>Min. 1.7033</td> <td>36.1500</td> <td>0.045</td> <td>8.5476</td> <td>0.0045959</td> <td>2.4810</td> <td>-1.9870</td> </tr> <tr> <td>Ave. 1.7033</td> <td>36.1500</td> <td>0.045</td> <td>8.5476</td> <td>0.0045959</td> <td>2.4810</td> <td>-1.9870</td> </tr> <tr> <td>Std. DV 0.0000</td> <td>0.0000</td> <td>0.000</td> <td>0.0000</td> <td>0.0000000</td> <td>0.0000</td> <td>0.0000</td> </tr> <tr> <td>Area1 1.7033</td> <td>36.1500</td> <td>0.045</td> <td>8.5476</td> <td>0.0045959</td> <td>2.4810</td> <td>-1.9870</td> </tr> </tbody> </table>	Sa	Sz	Str	Spc	Sdr	Sq	Ssk	$\mu\text{m}$	$\mu\text{m}$	1/mm			$\mu\text{m}$		Max. 1.7033	36.1500	0.045	8.5476	0.0045959	2.4810	-1.9870	Min. 1.7033	36.1500	0.045	8.5476	0.0045959	2.4810	-1.9870	Ave. 1.7033	36.1500	0.045	8.5476	0.0045959	2.4810	-1.9870	Std. DV 0.0000	0.0000	0.000	0.0000	0.0000000	0.0000	0.0000	Area1 1.7033	36.1500	0.045	8.5476	0.0045959	2.4810	-1.9870	1.7033	36.1500	0.045	2.4810	10.9978	25.1522
Sa	Sz	Str	Spc	Sdr	Sq	Ssk																																																			
$\mu\text{m}$	$\mu\text{m}$	1/mm			$\mu\text{m}$																																																				
Max. 1.7033	36.1500	0.045	8.5476	0.0045959	2.4810	-1.9870																																																			
Min. 1.7033	36.1500	0.045	8.5476	0.0045959	2.4810	-1.9870																																																			
Ave. 1.7033	36.1500	0.045	8.5476	0.0045959	2.4810	-1.9870																																																			
Std. DV 0.0000	0.0000	0.000	0.0000	0.0000000	0.0000	0.0000																																																			
Area1 1.7033	36.1500	0.045	8.5476	0.0045959	2.4810	-1.9870																																																			
B12		<table border="1"> <thead> <tr> <th>Sa</th> <th>Sz</th> <th>Str</th> <th>Spc</th> <th>Sdr</th> <th>Sq</th> <th>Ssk</th> </tr> <tr> <th><math>\mu\text{m}</math></th> <th><math>\mu\text{m}</math></th> <th>1/mm</th> <th></th> <th></th> <th><math>\mu\text{m}</math></th> <th></th> </tr> </thead> <tbody> <tr> <td>Max. 3.1601</td> <td>76.1100</td> <td>0.051</td> <td>8.7284</td> <td>0.0054194</td> <td>6.7416</td> <td>-4.8440</td> </tr> <tr> <td>Min. 3.1601</td> <td>76.1100</td> <td>0.051</td> <td>8.7284</td> <td>0.0054194</td> <td>6.7416</td> <td>-4.8440</td> </tr> <tr> <td>Ave. 3.1601</td> <td>76.1100</td> <td>0.051</td> <td>8.7284</td> <td>0.0054194</td> <td>6.7416</td> <td>-4.8440</td> </tr> <tr> <td>Std. DV 0.0000</td> <td>0.0000</td> <td>0.000</td> <td>0.0000</td> <td>0.0000000</td> <td>0.0000</td> <td>0.0000</td> </tr> <tr> <td>Area1 3.1601</td> <td>76.1100</td> <td>0.051</td> <td>8.7284</td> <td>0.0054194</td> <td>6.7416</td> <td>-4.8440</td> </tr> </tbody> </table>	Sa	Sz	Str	Spc	Sdr	Sq	Ssk	$\mu\text{m}$	$\mu\text{m}$	1/mm			$\mu\text{m}$		Max. 3.1601	76.1100	0.051	8.7284	0.0054194	6.7416	-4.8440	Min. 3.1601	76.1100	0.051	8.7284	0.0054194	6.7416	-4.8440	Ave. 3.1601	76.1100	0.051	8.7284	0.0054194	6.7416	-4.8440	Std. DV 0.0000	0.0000	0.000	0.0000	0.0000000	0.0000	0.0000	Area1 3.1601	76.1100	0.051	8.7284	0.0054194	6.7416	-4.8440	3.1601	76.1100	0.051	6.7416	10.5946	65.5154
Sa	Sz	Str	Spc	Sdr	Sq	Ssk																																																			
$\mu\text{m}$	$\mu\text{m}$	1/mm			$\mu\text{m}$																																																				
Max. 3.1601	76.1100	0.051	8.7284	0.0054194	6.7416	-4.8440																																																			
Min. 3.1601	76.1100	0.051	8.7284	0.0054194	6.7416	-4.8440																																																			
Ave. 3.1601	76.1100	0.051	8.7284	0.0054194	6.7416	-4.8440																																																			
Std. DV 0.0000	0.0000	0.000	0.0000	0.0000000	0.0000	0.0000																																																			
Area1 3.1601	76.1100	0.051	8.7284	0.0054194	6.7416	-4.8440																																																			





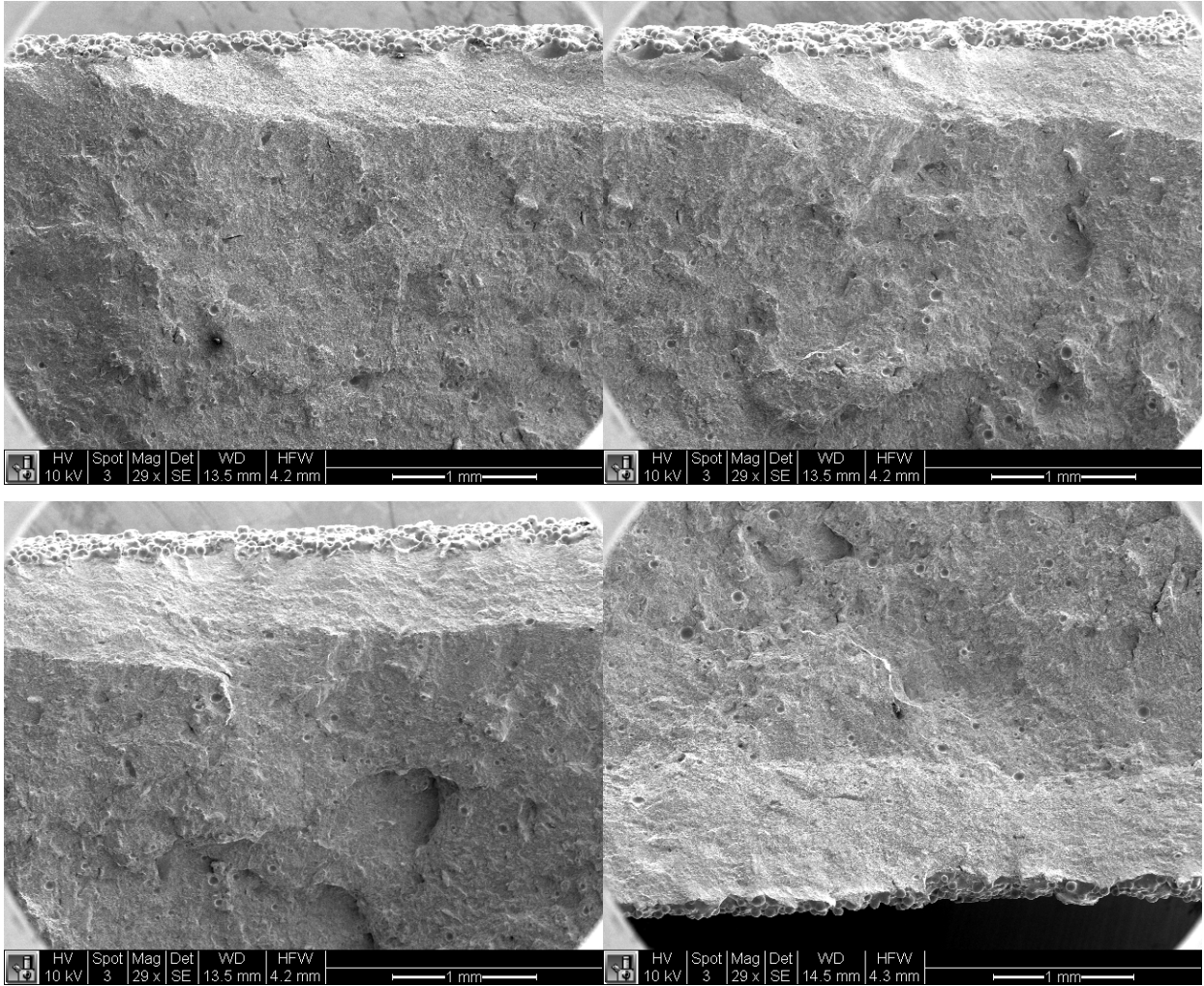


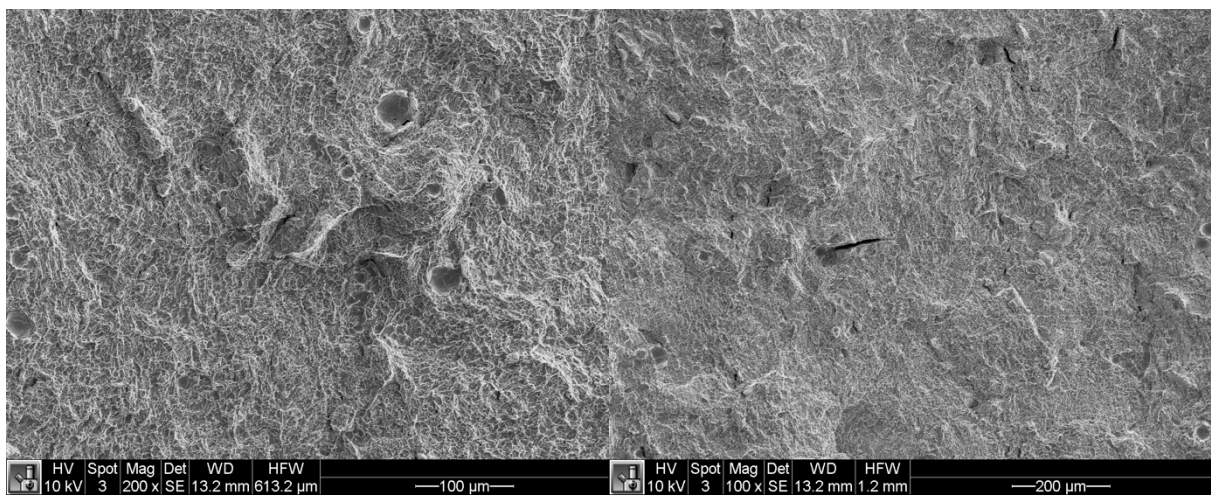
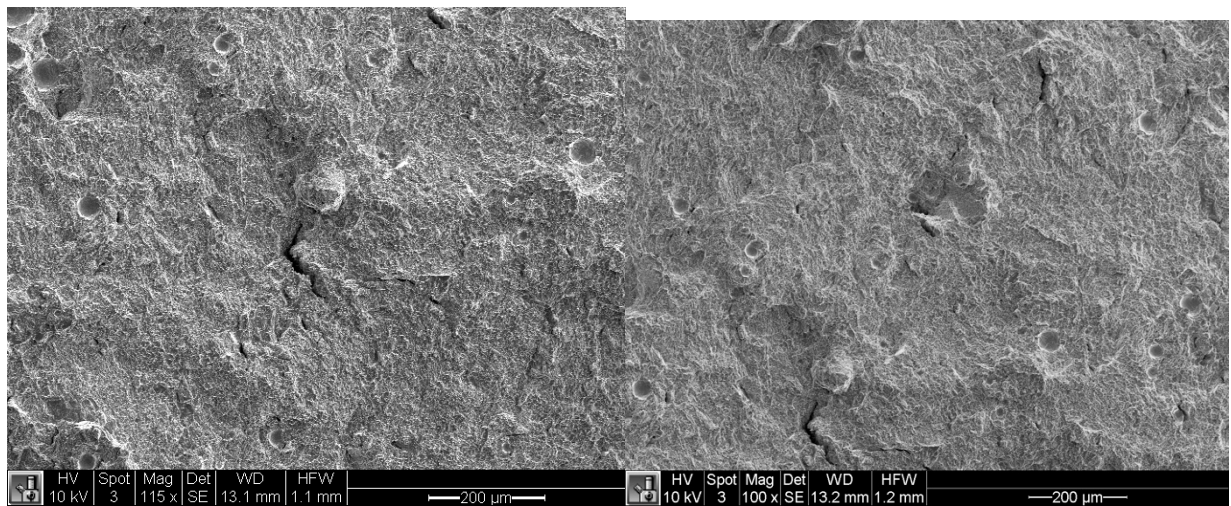
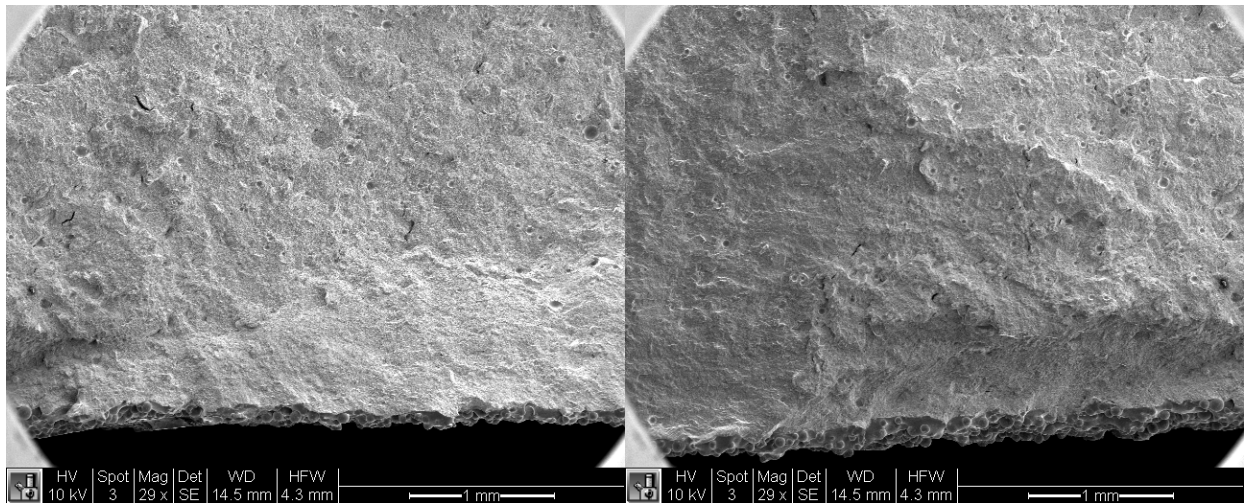


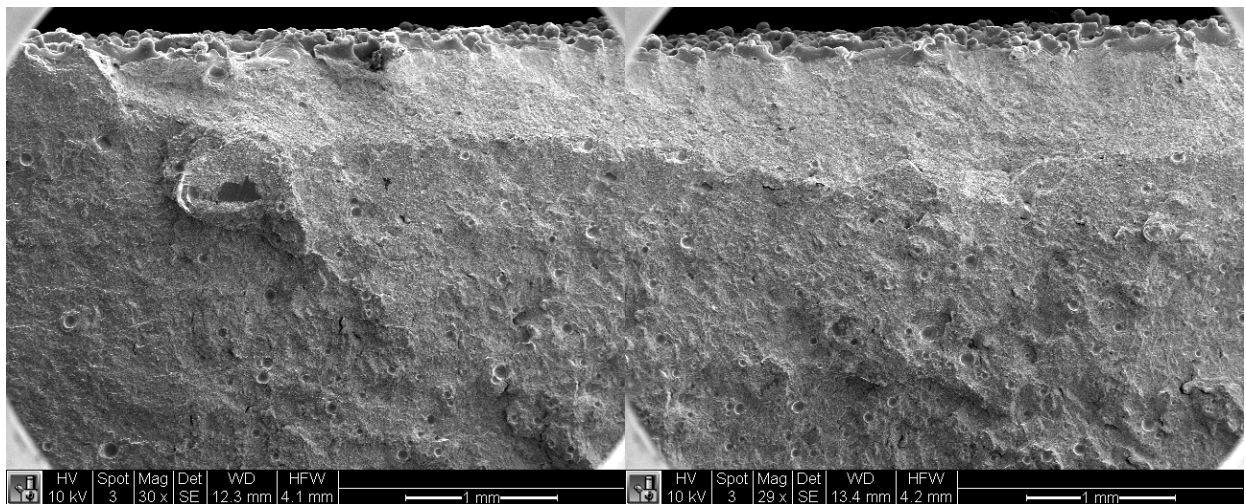
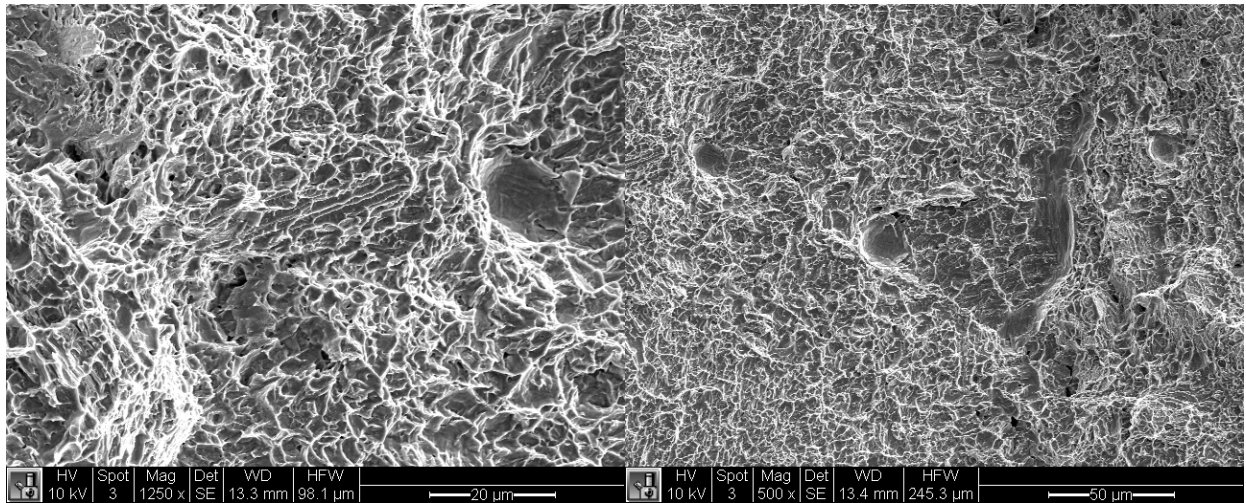
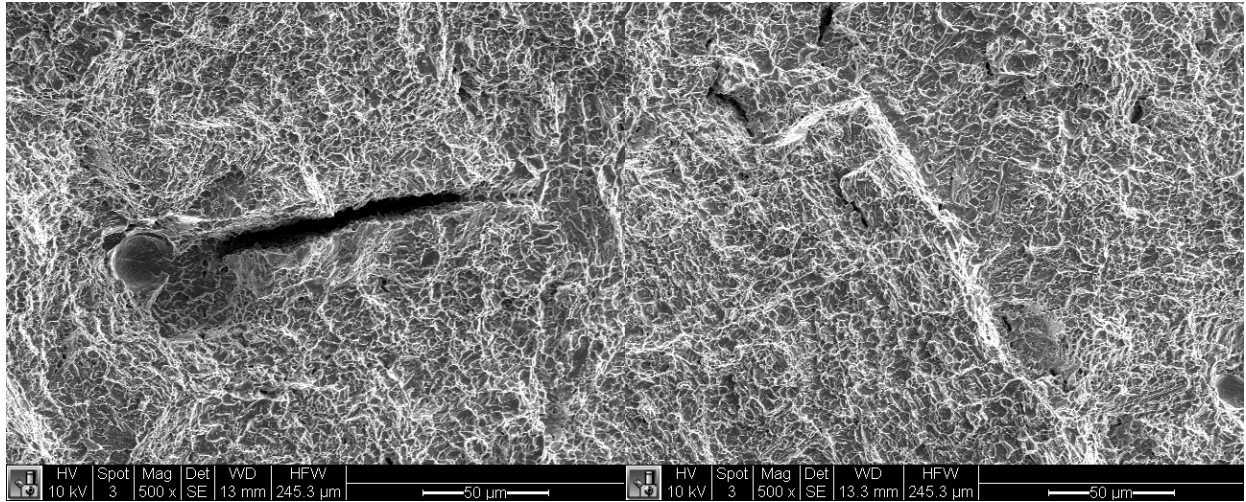
# F - Fractography

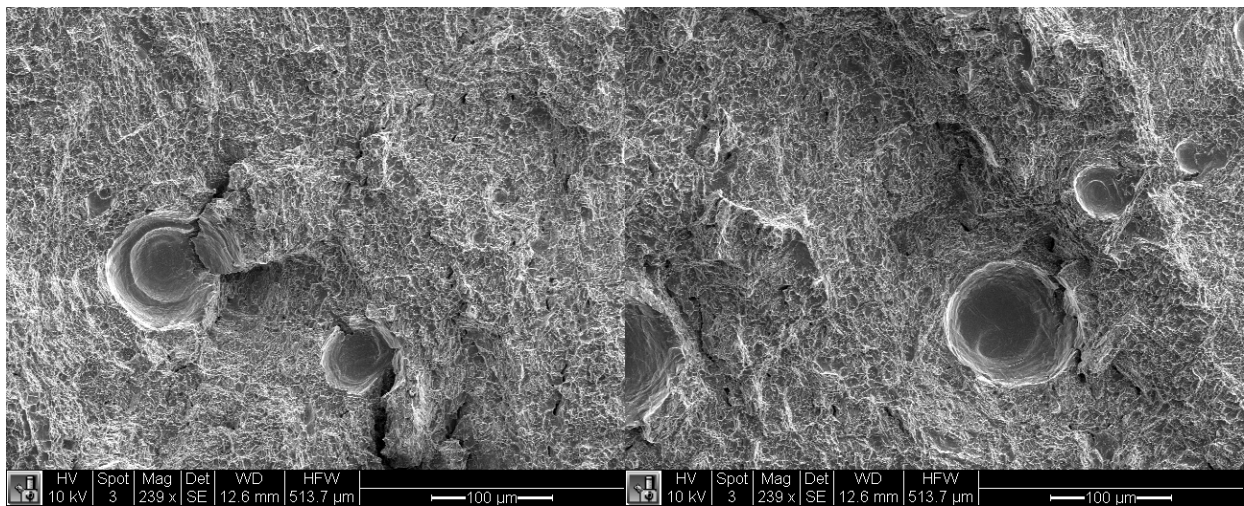
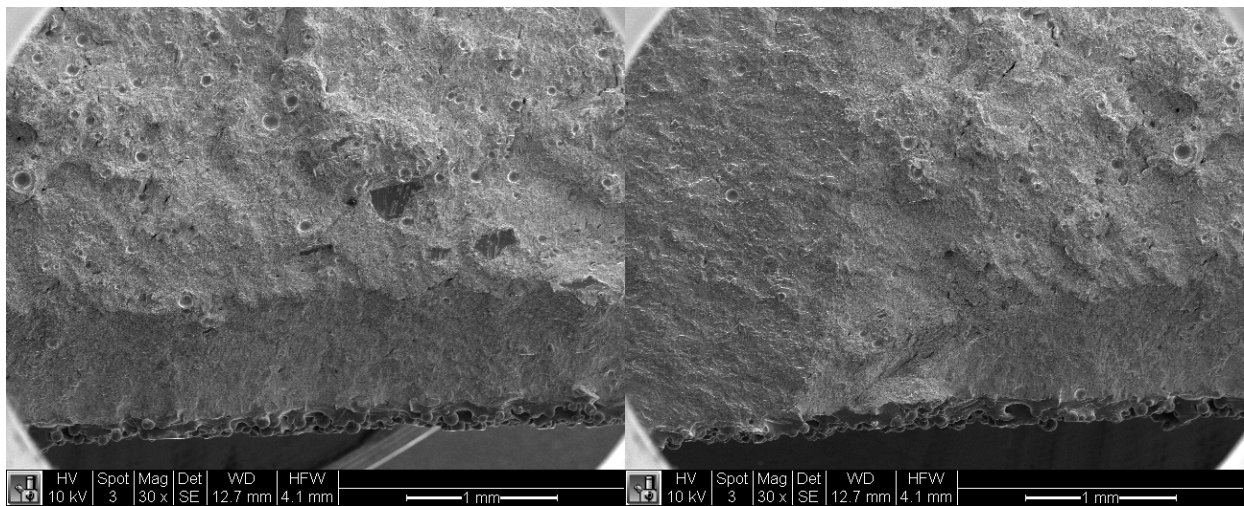
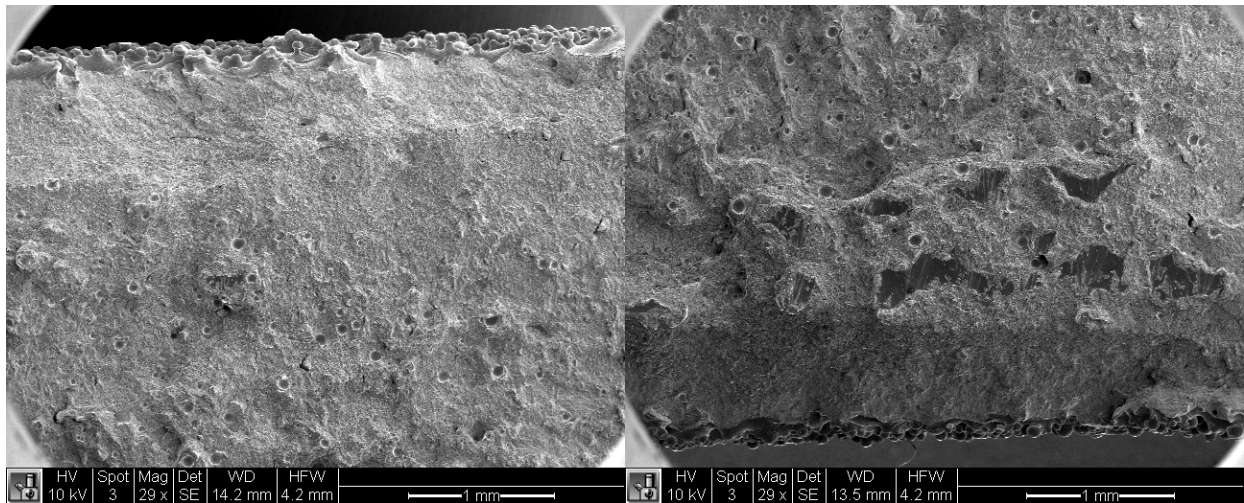
## Fracture Toughness

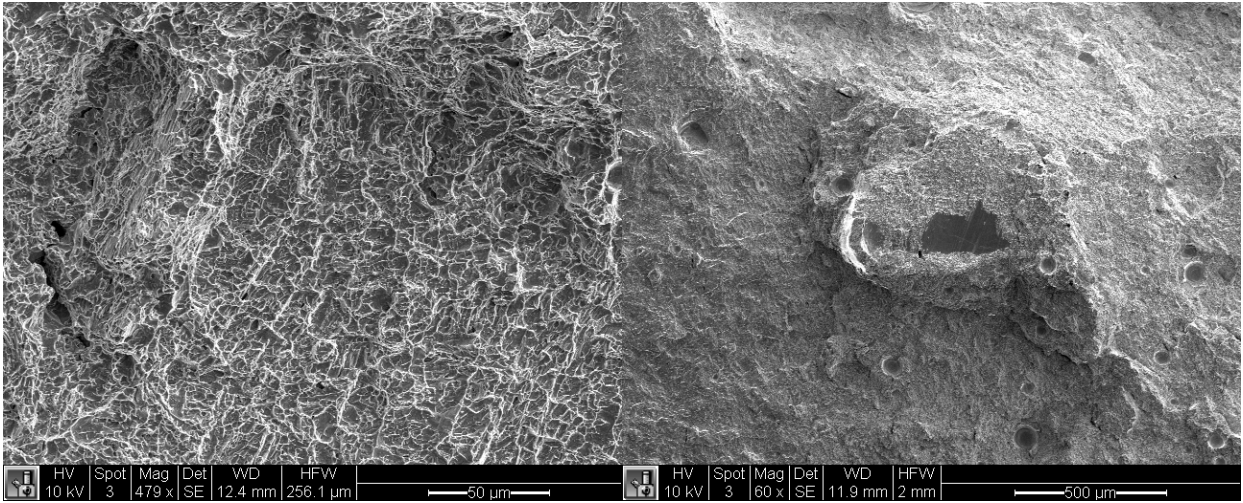
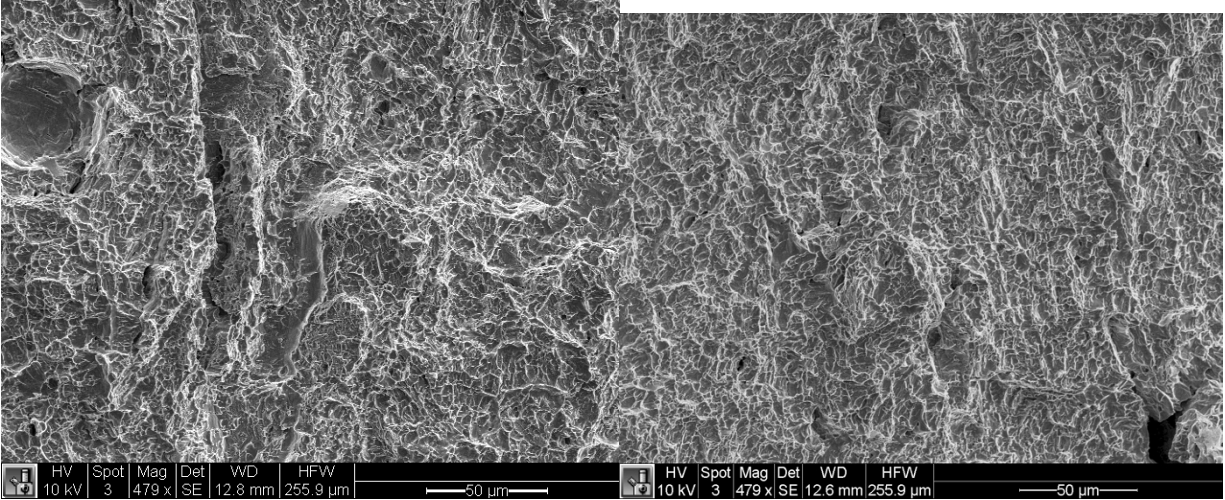
### ZX As-Built

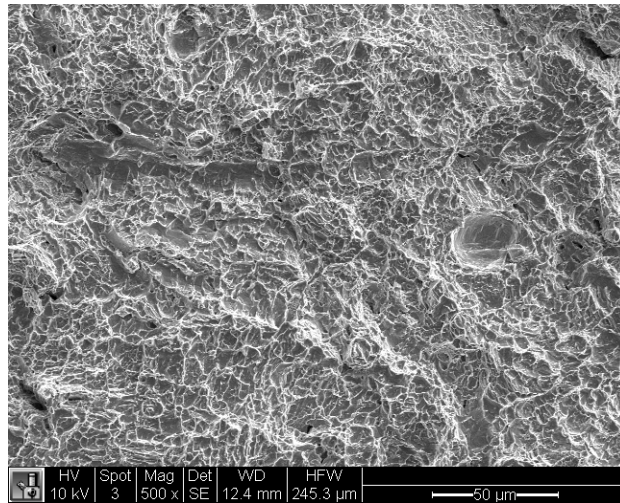
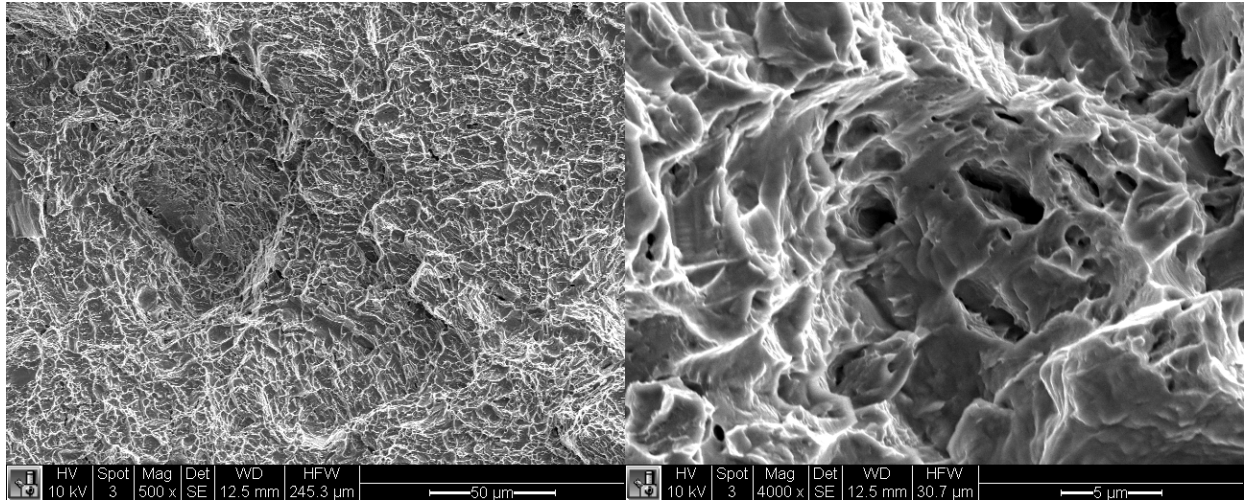




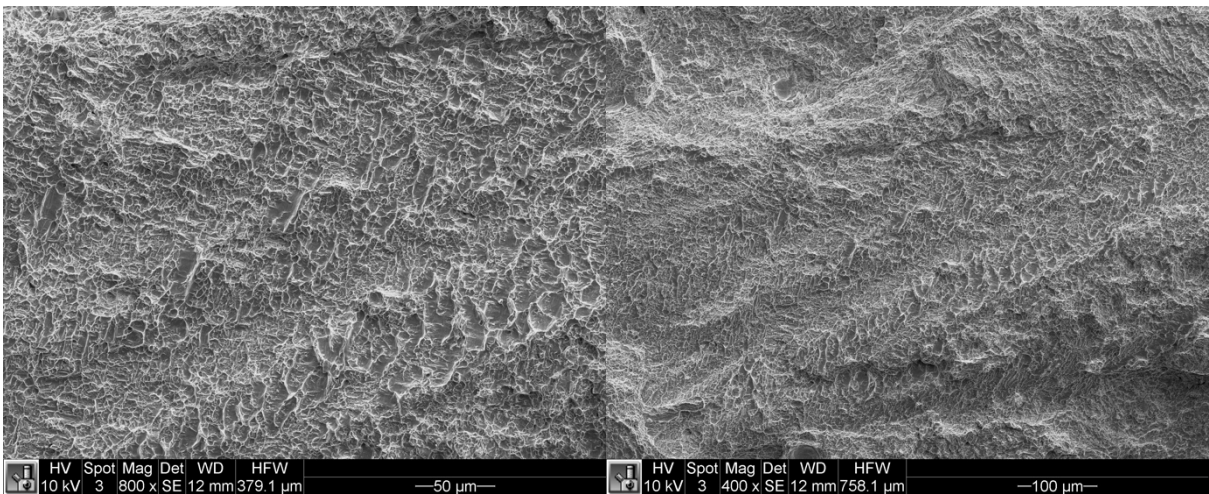
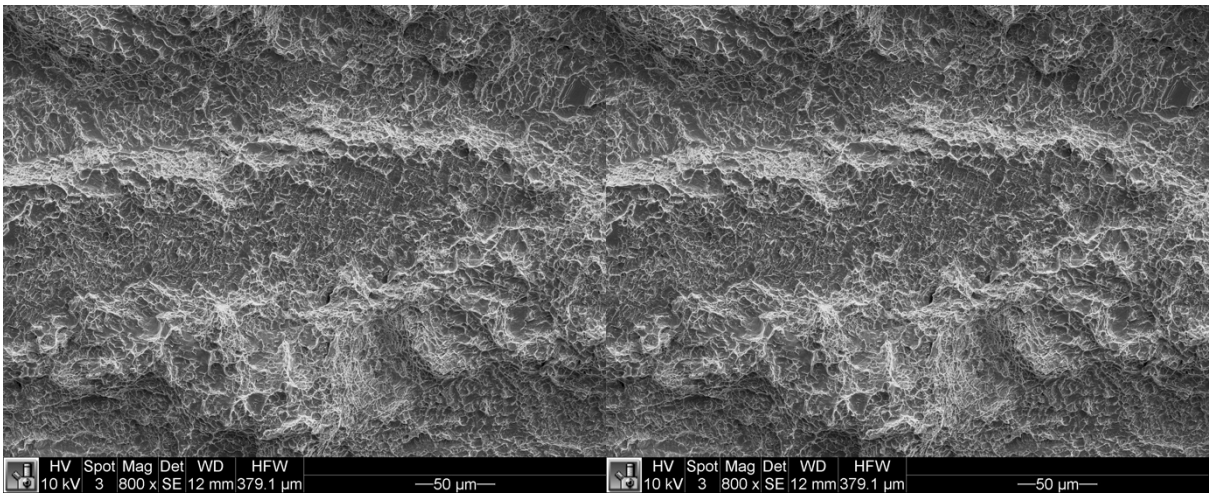
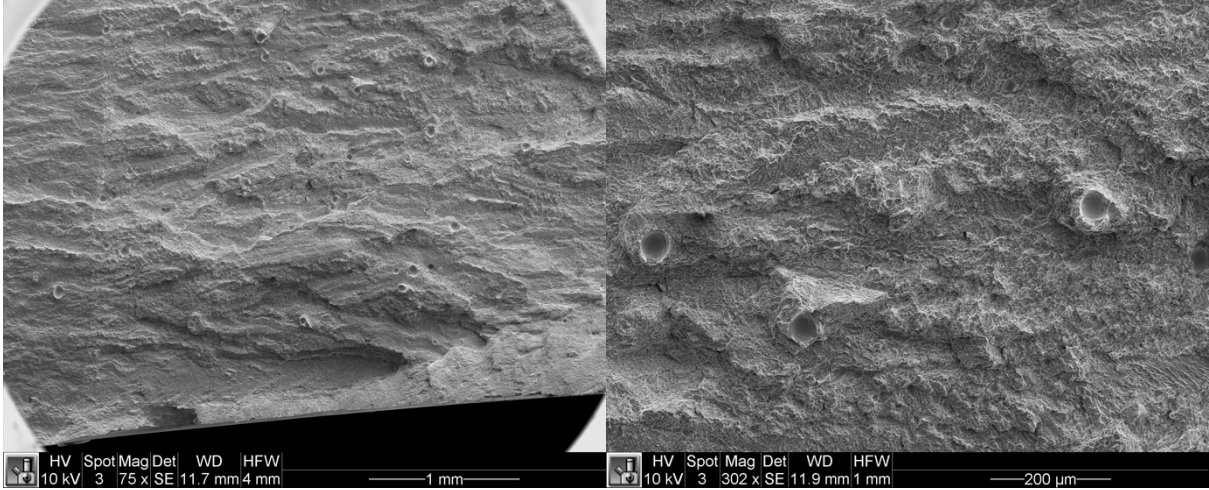


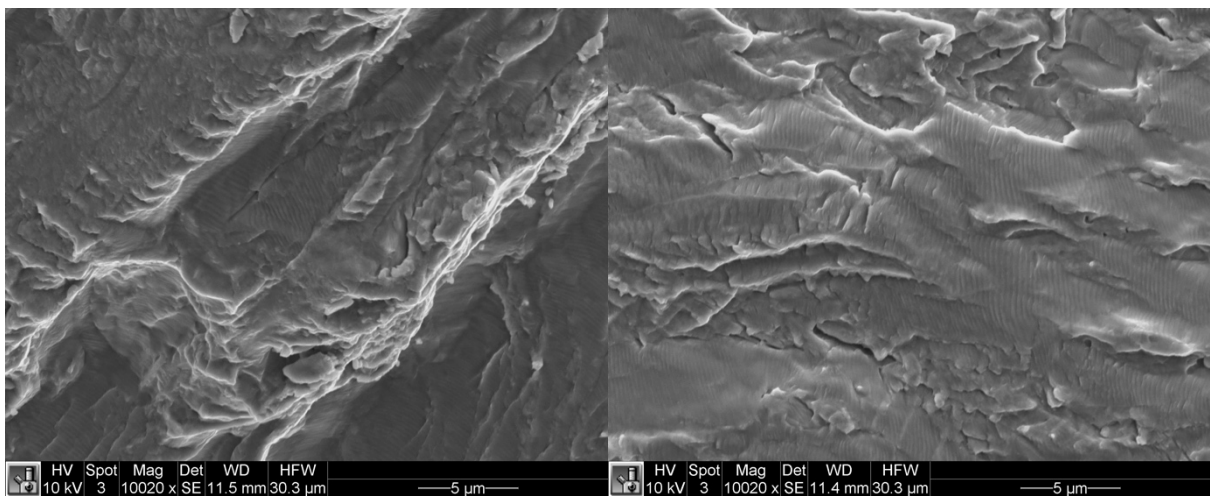
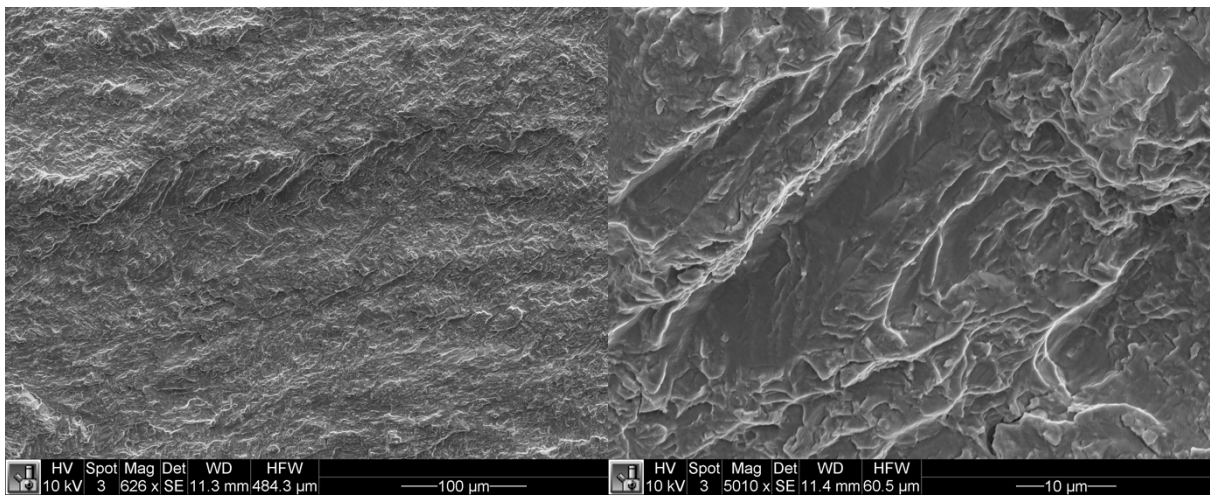
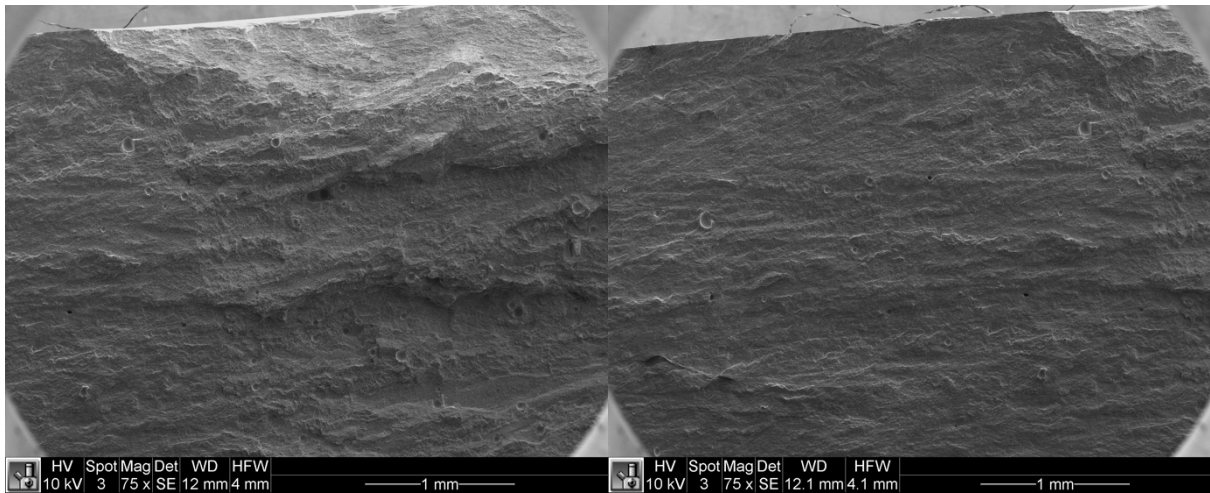


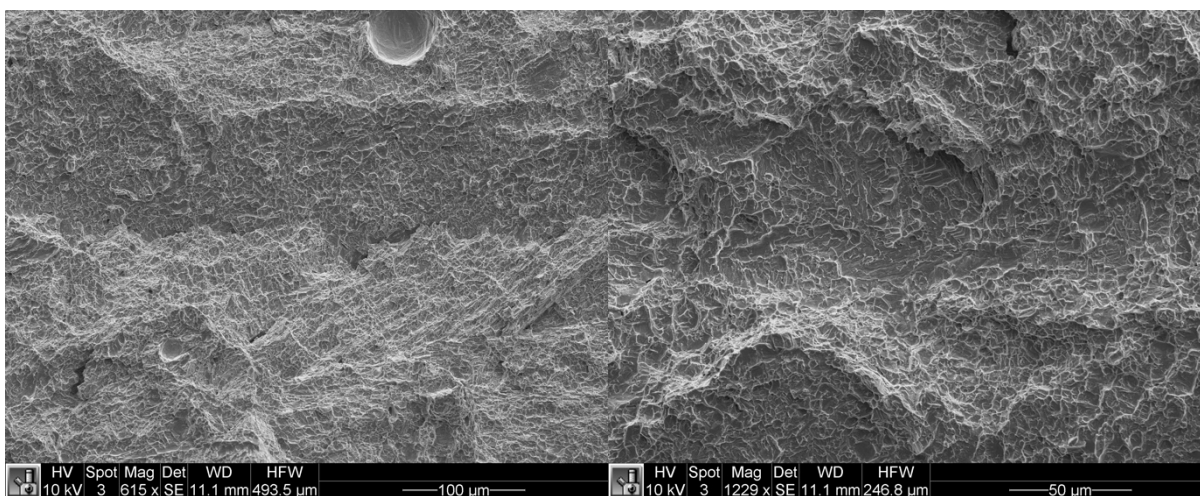
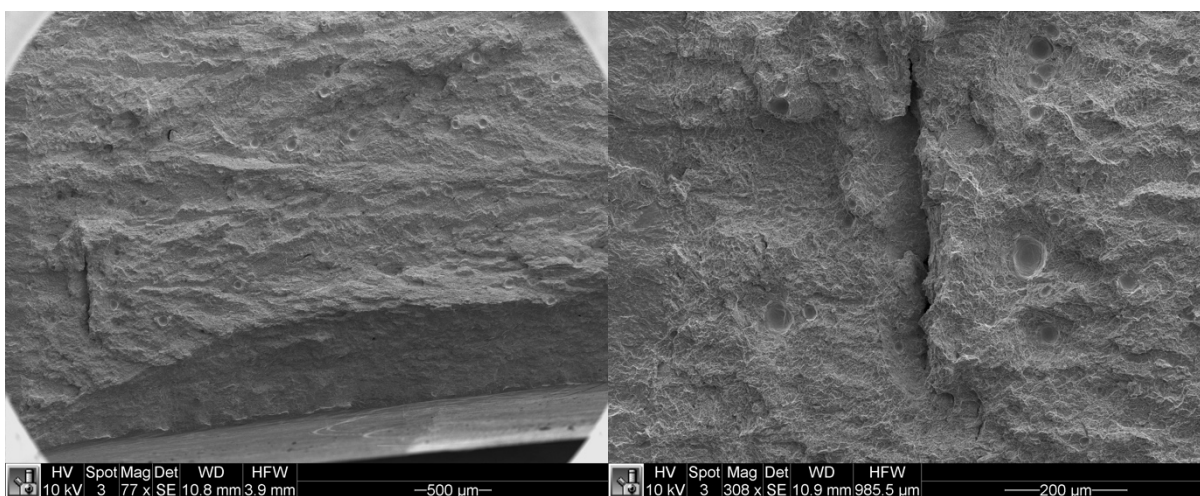
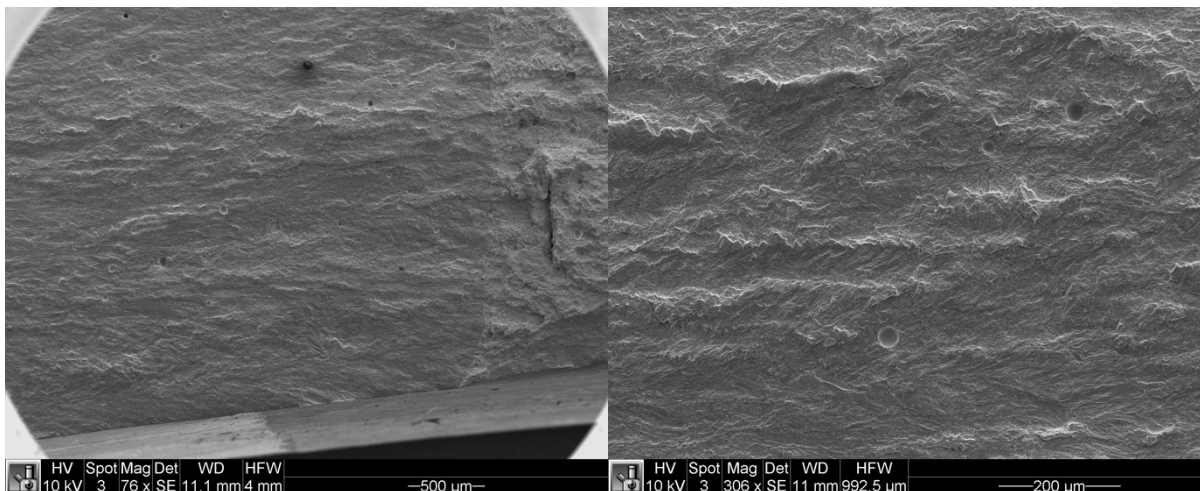


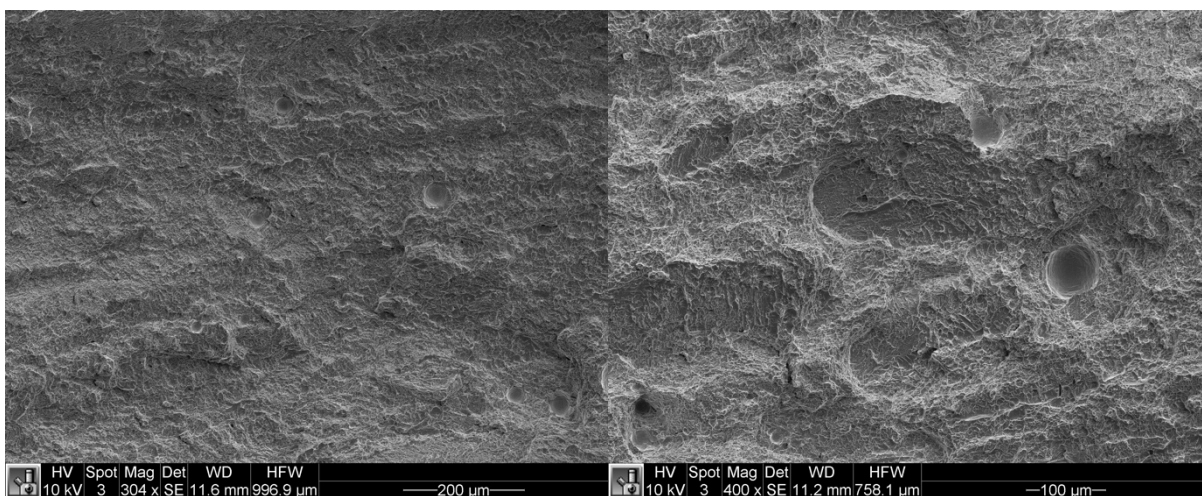
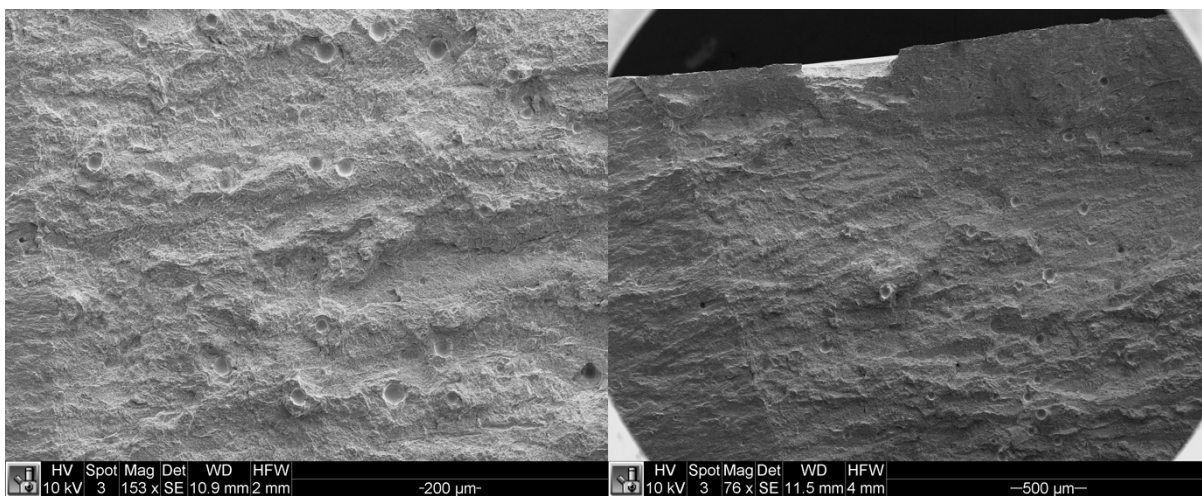
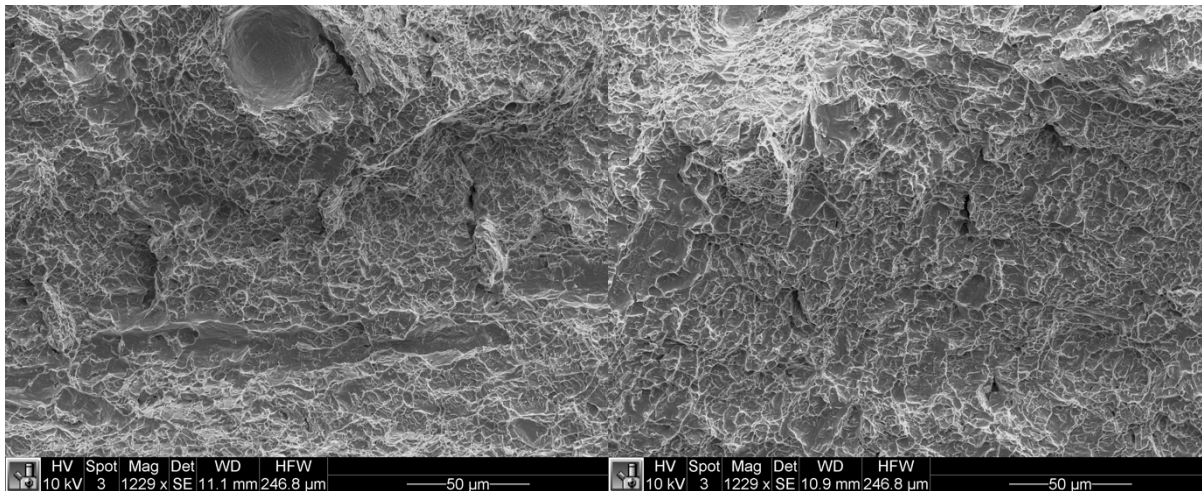


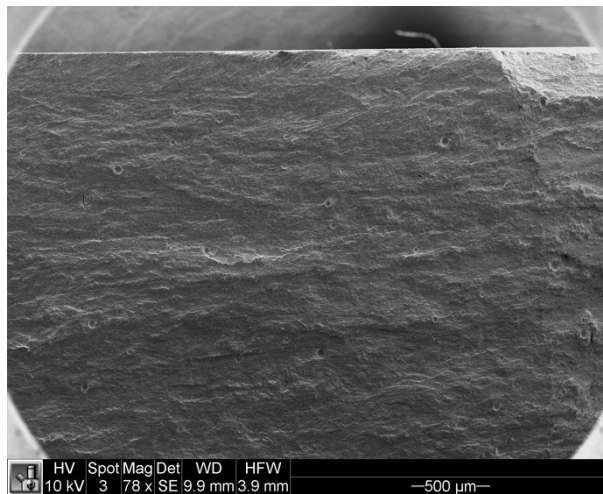
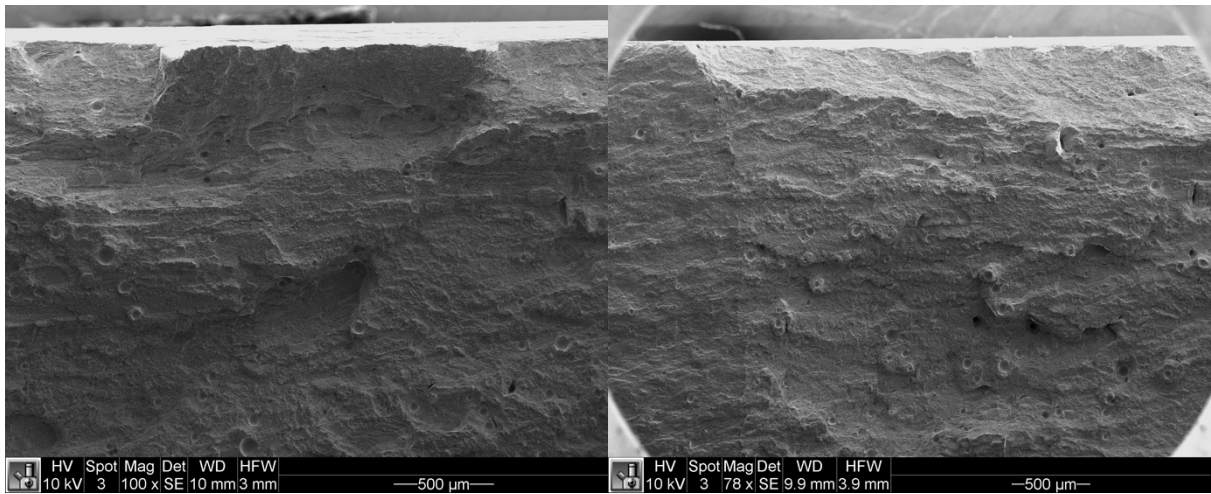
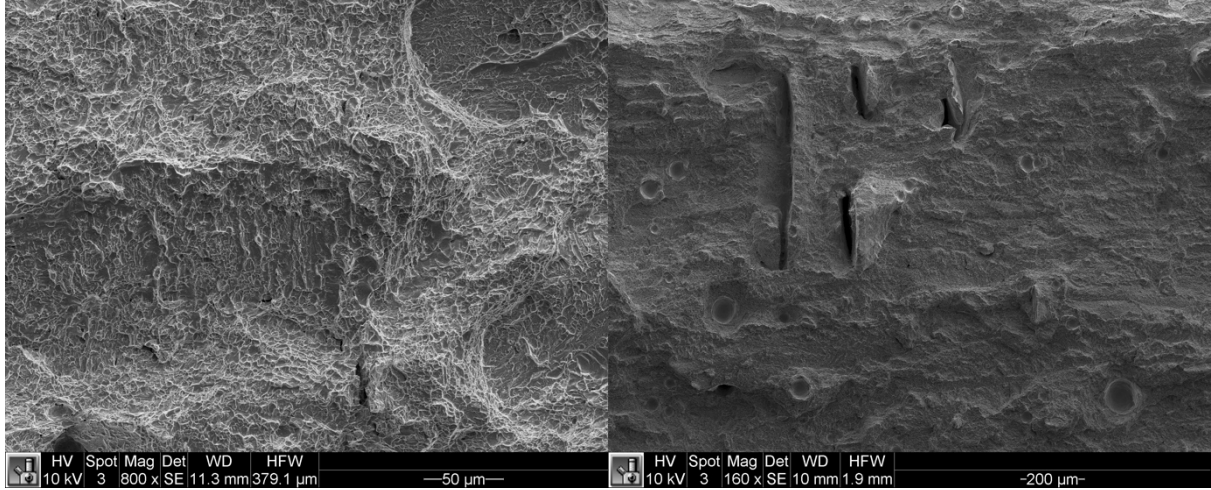
**XZ As-Built**



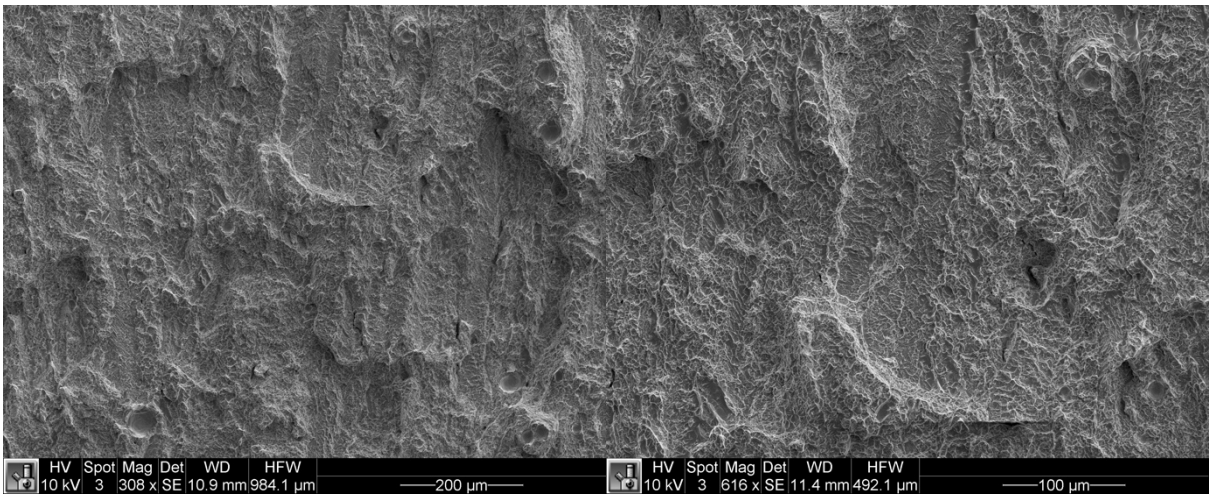
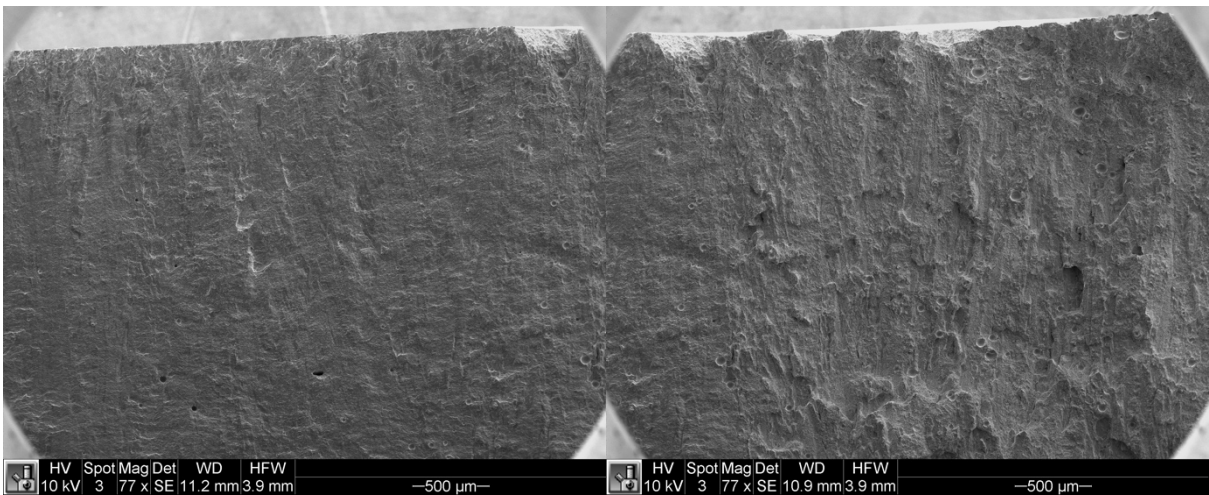
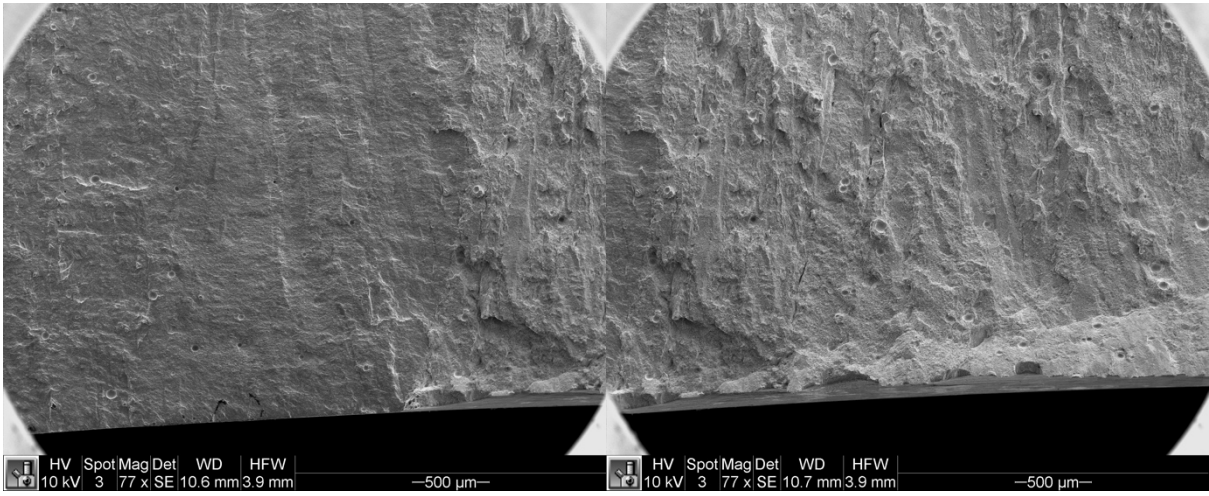


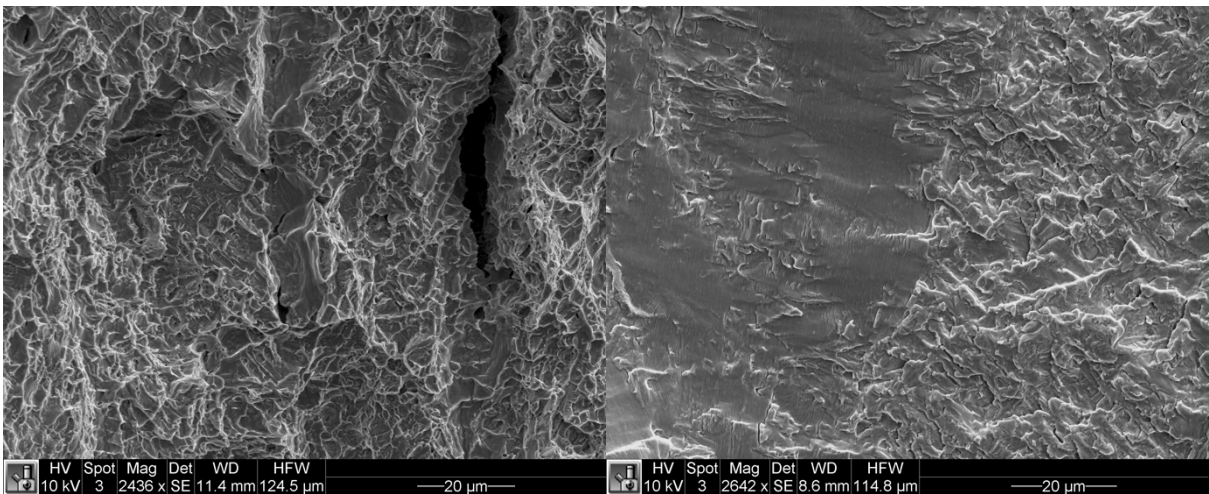
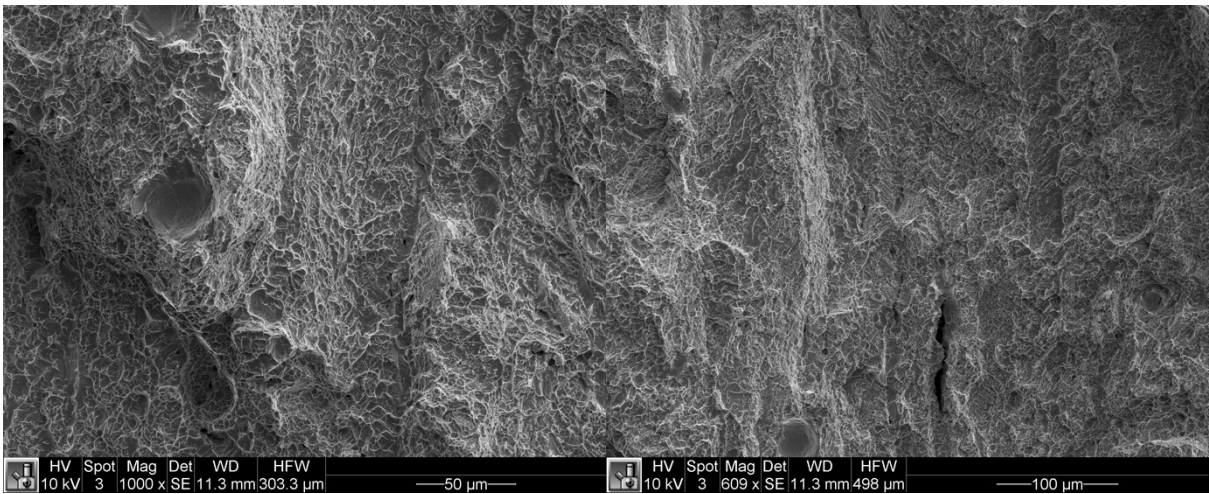
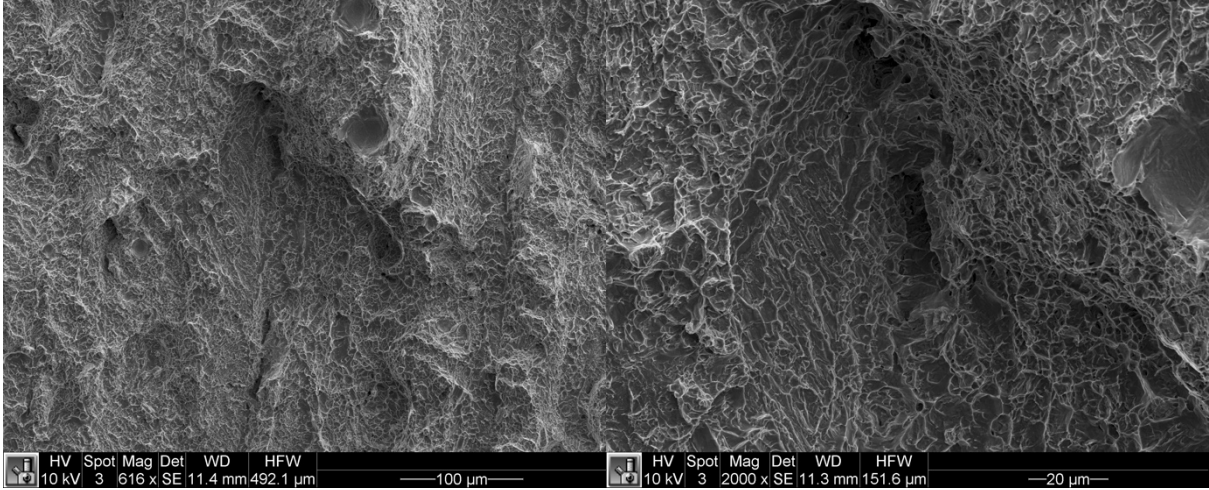


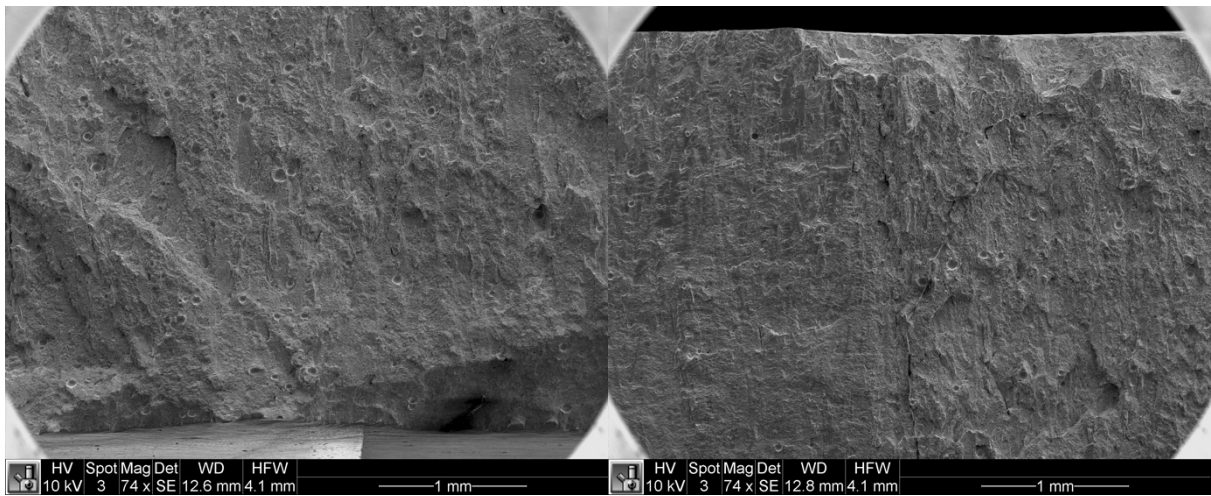
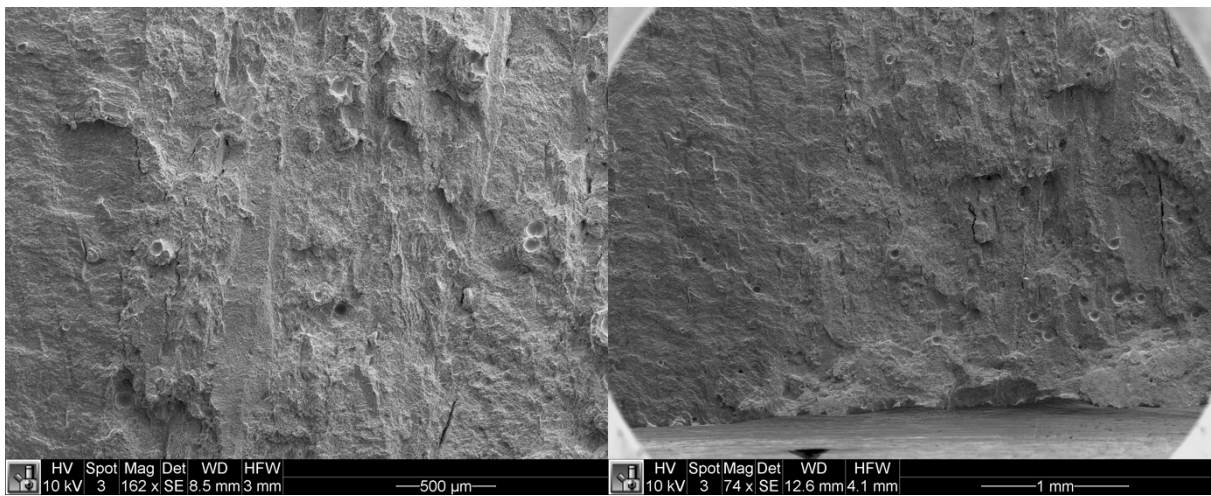
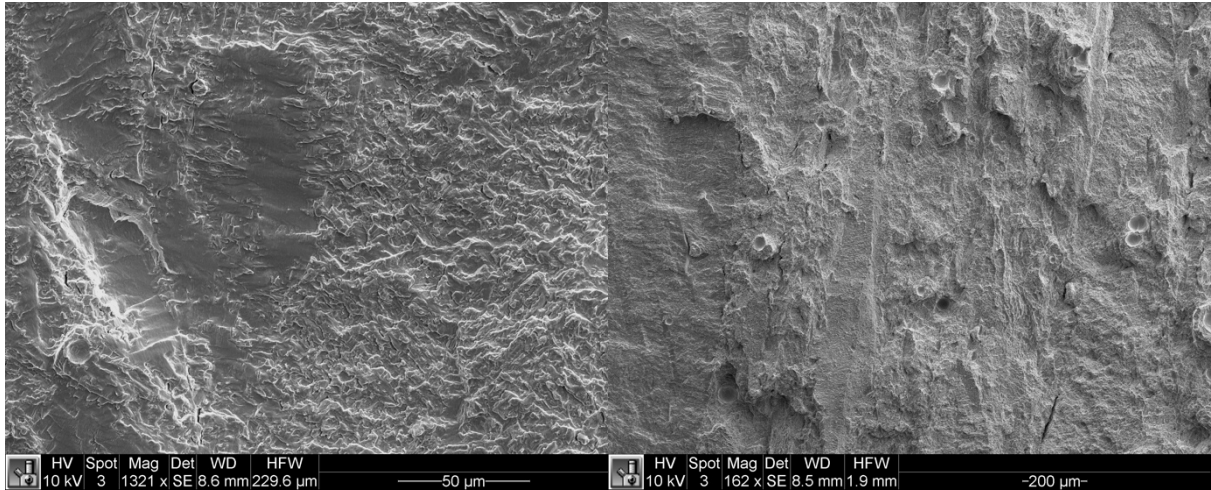


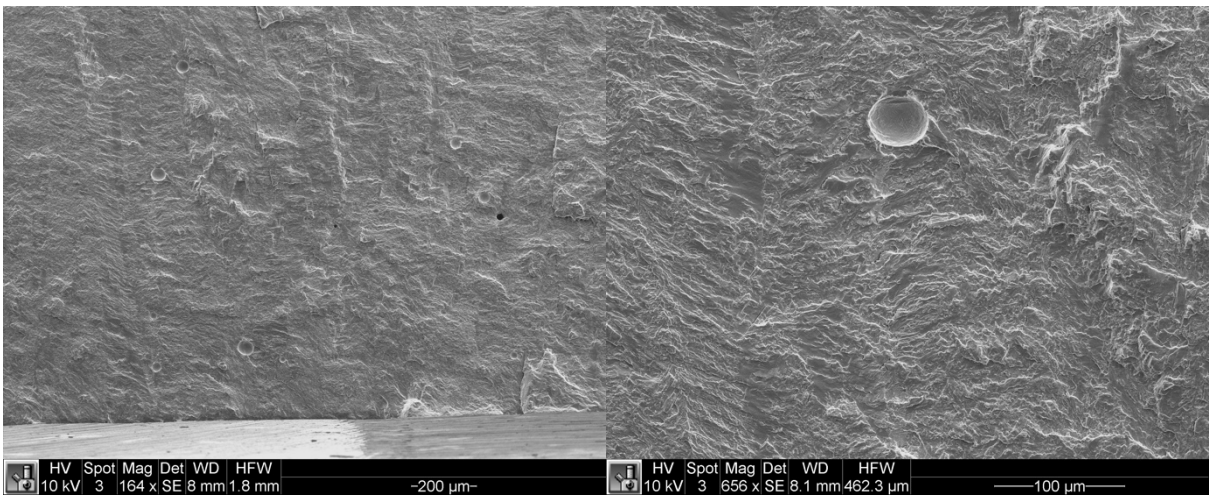
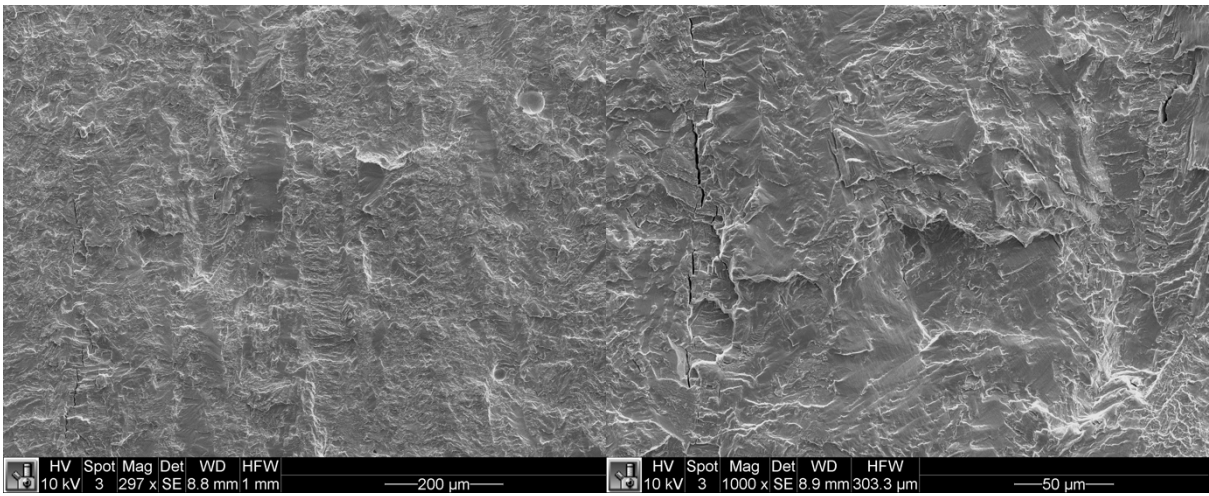
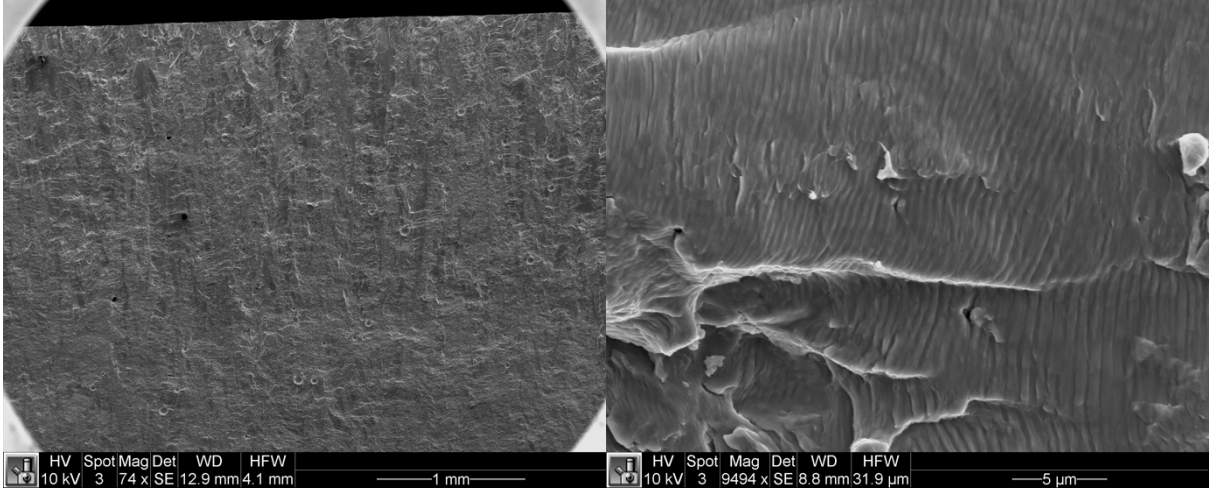


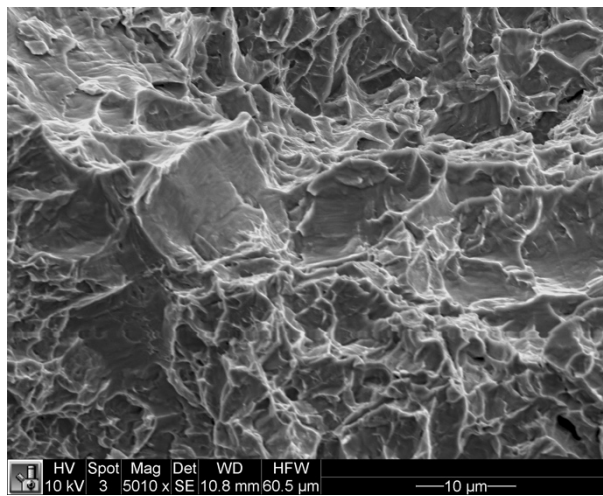
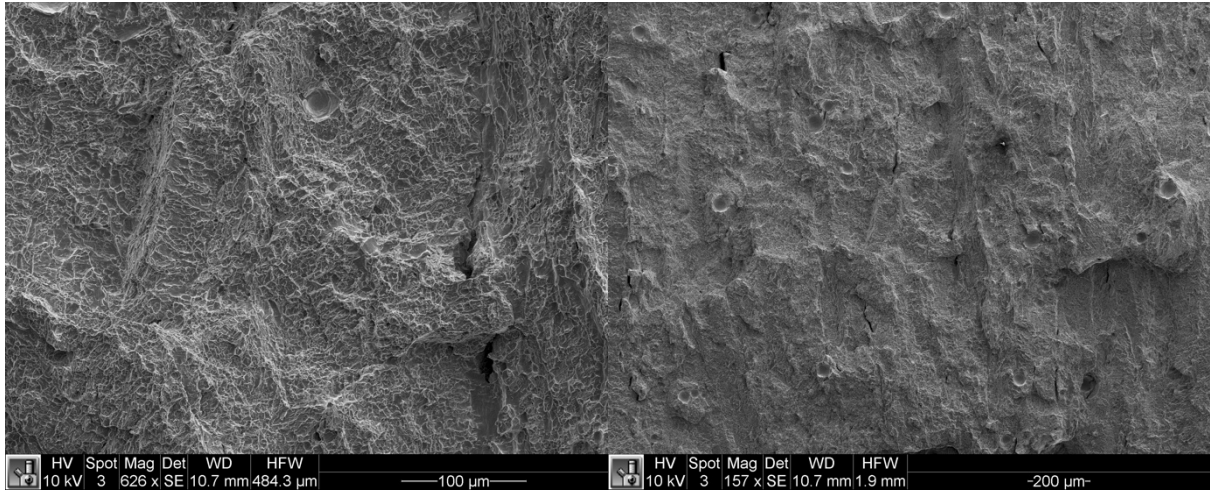
# XY As-Built



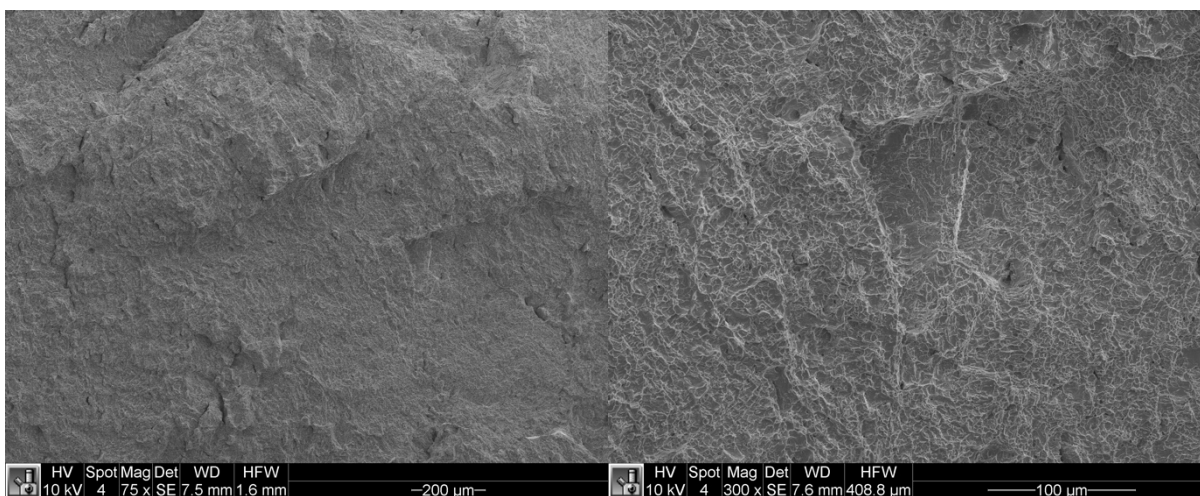
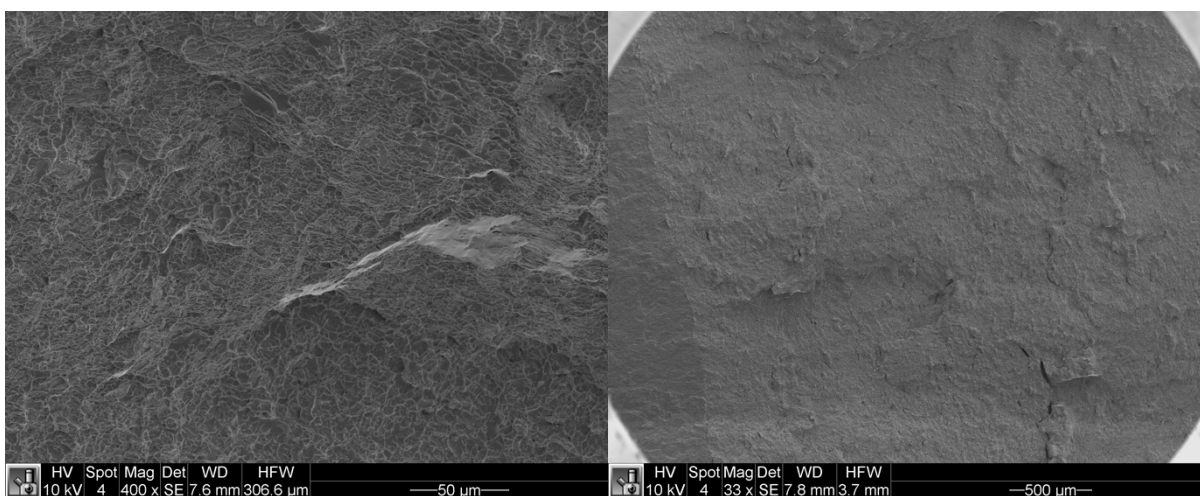
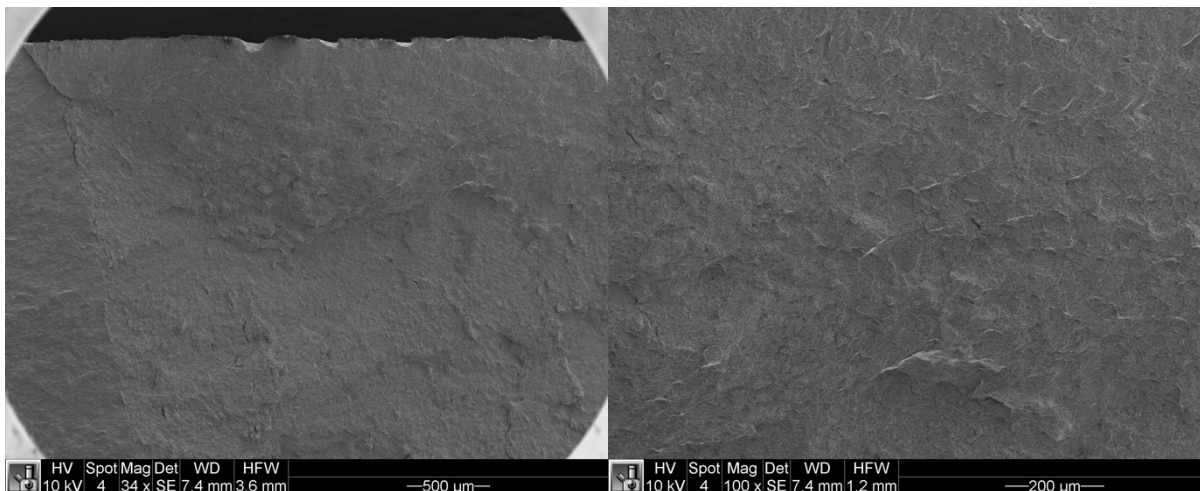


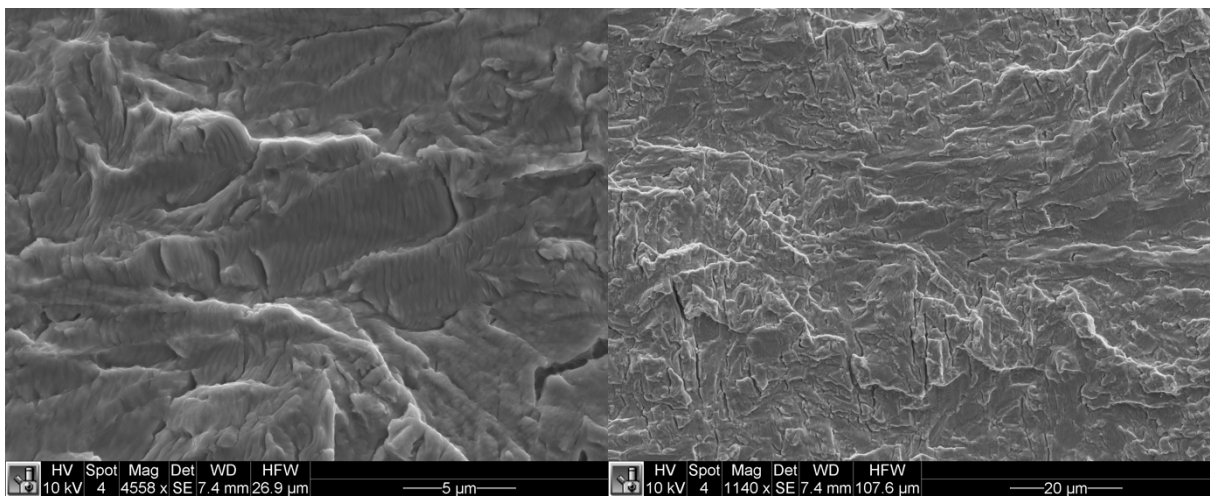
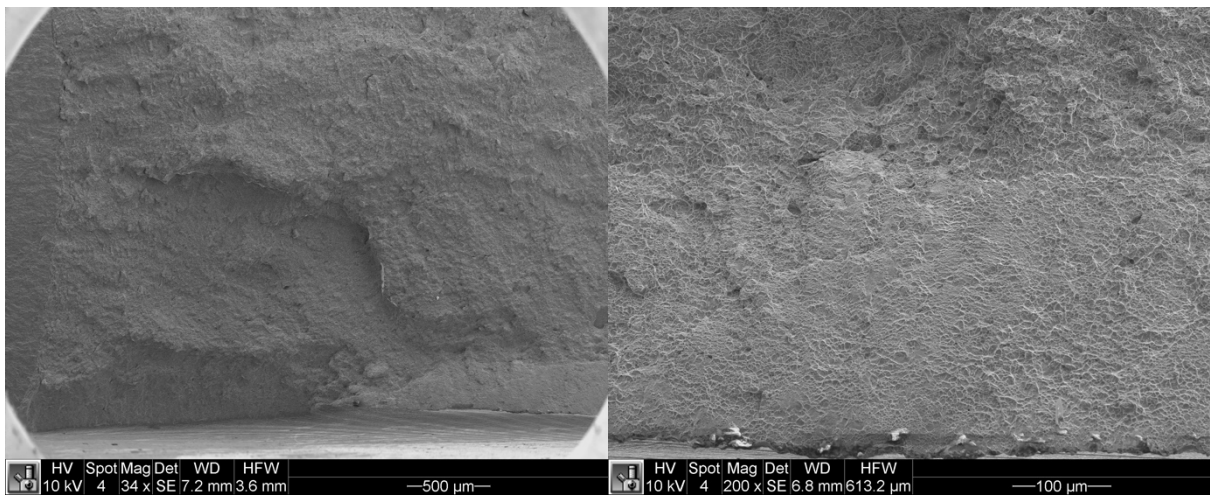
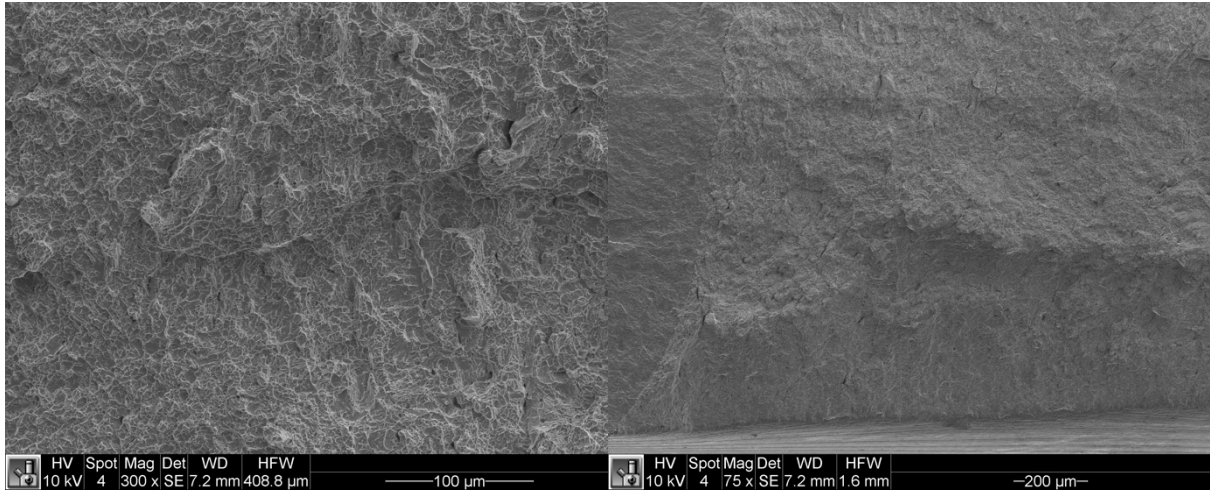


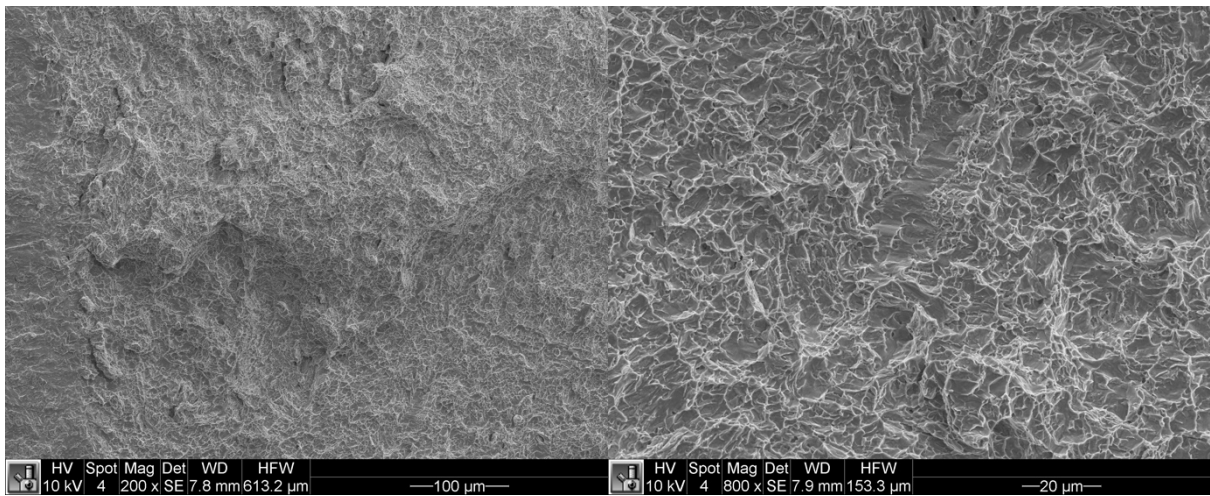
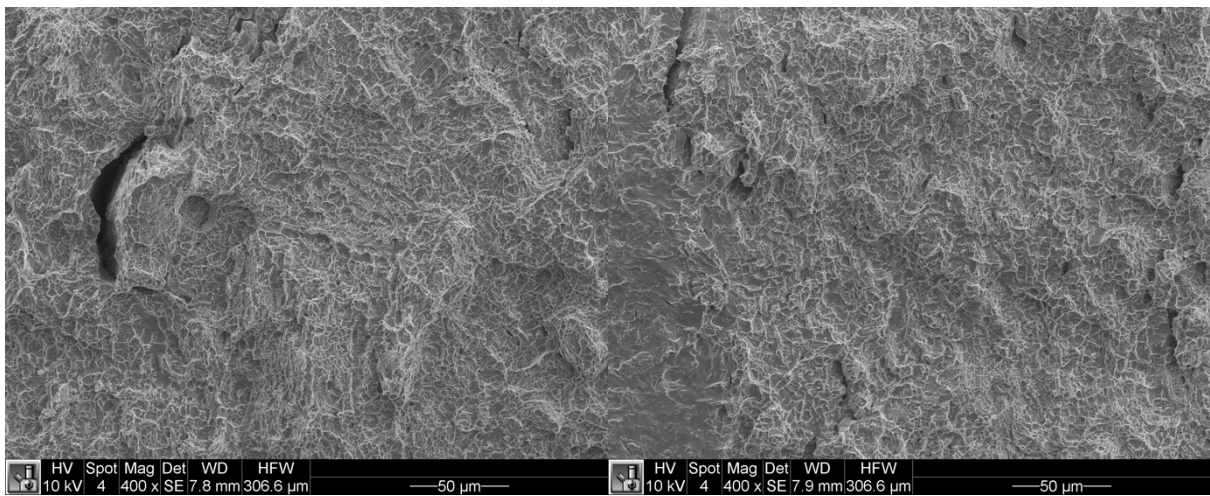
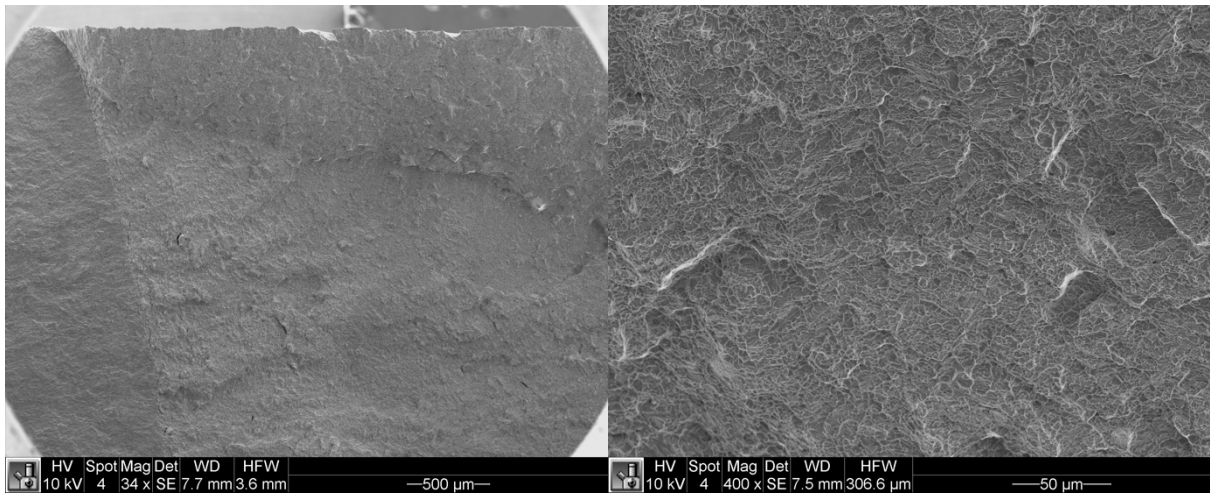


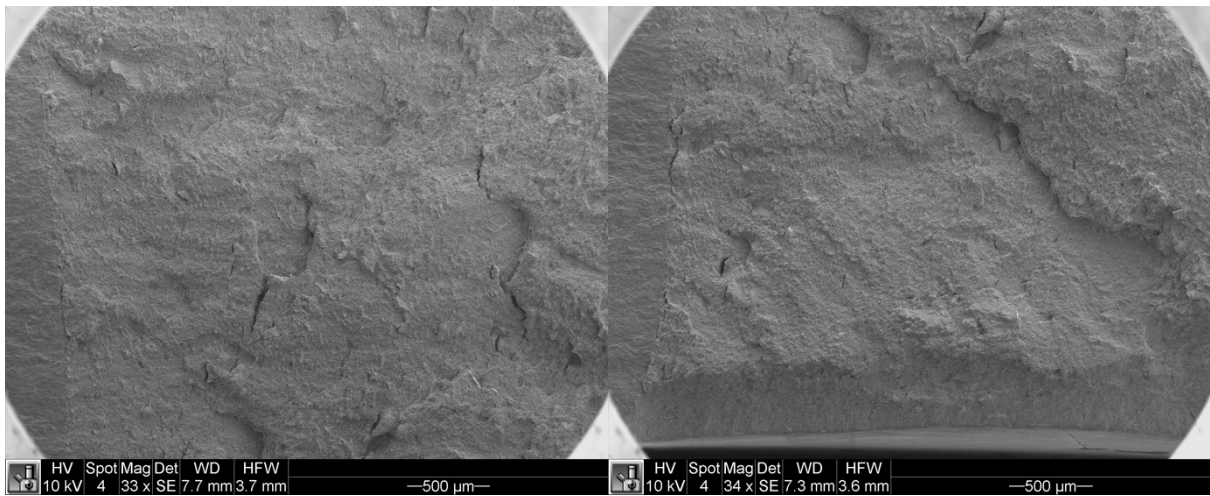
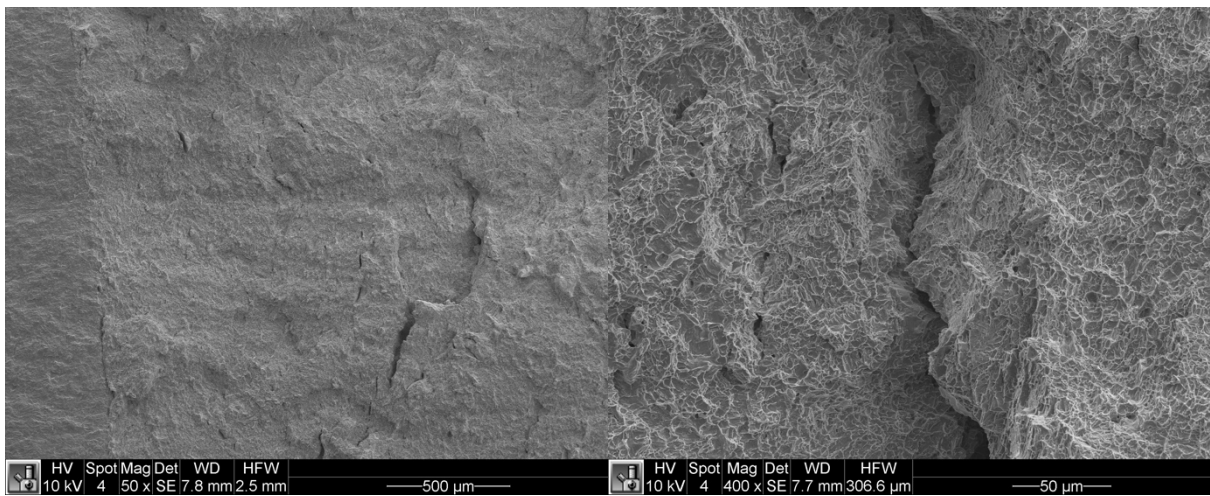
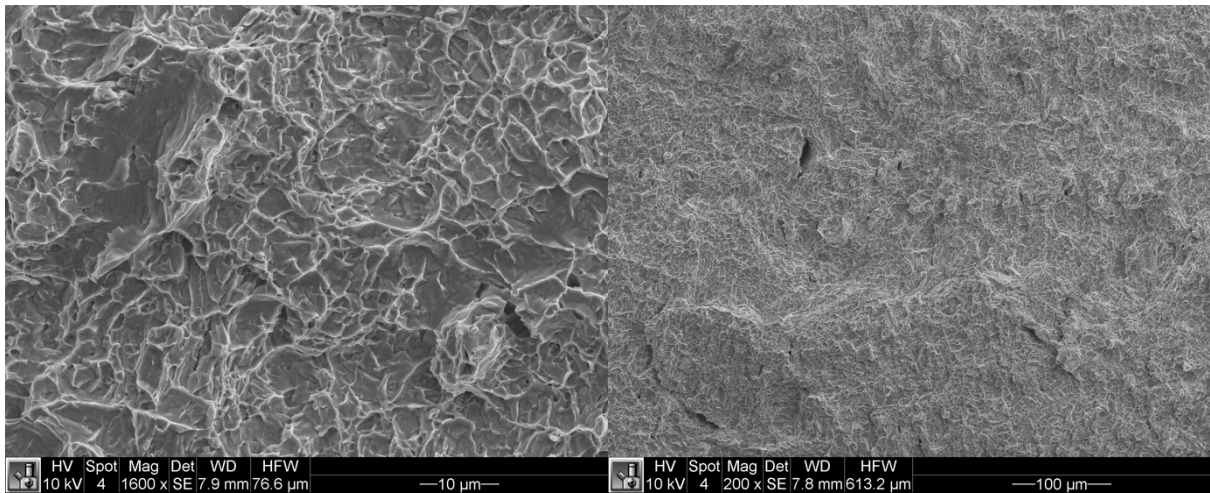


**ZX HIP**

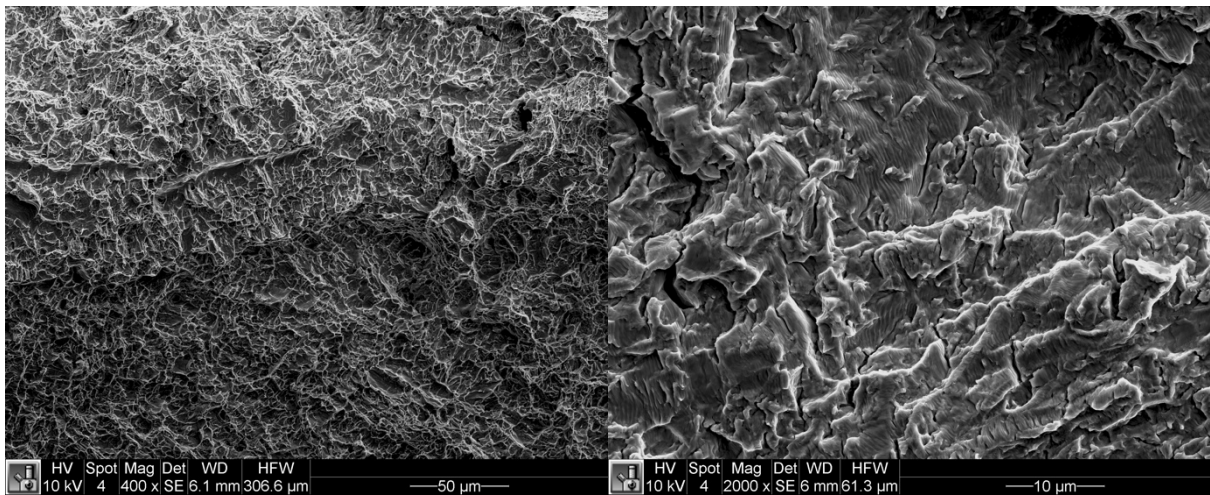
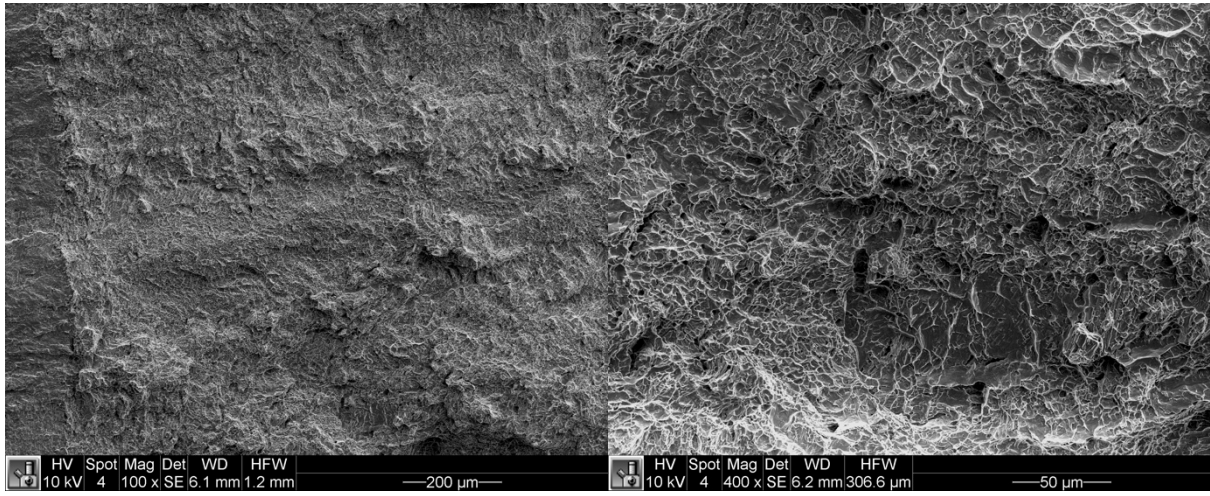


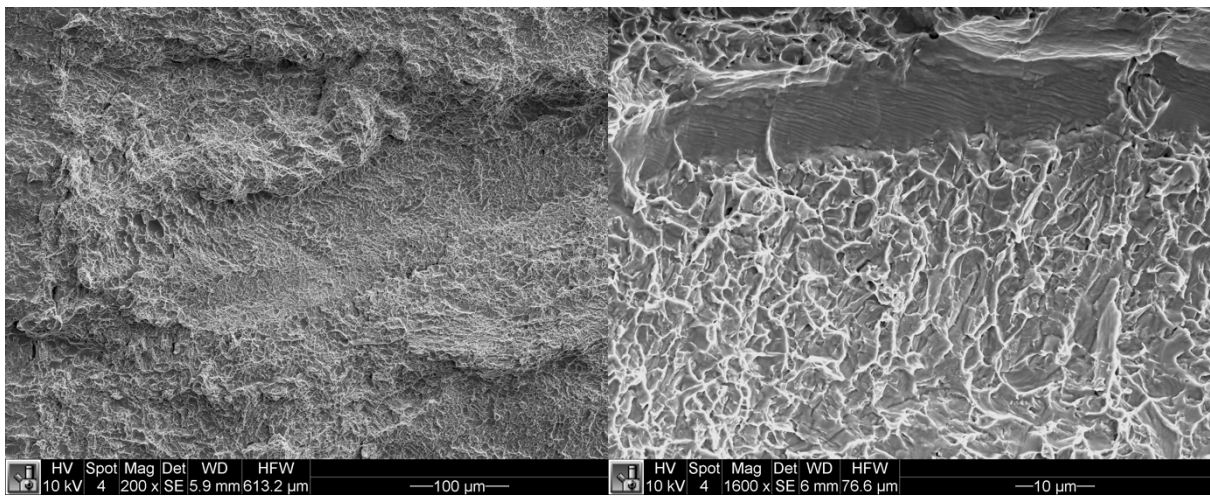
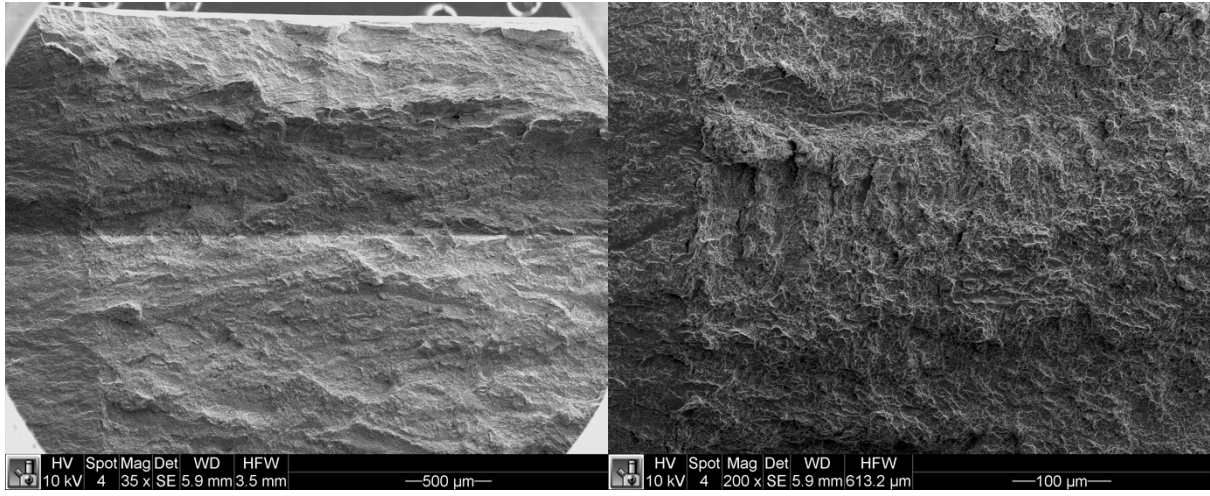




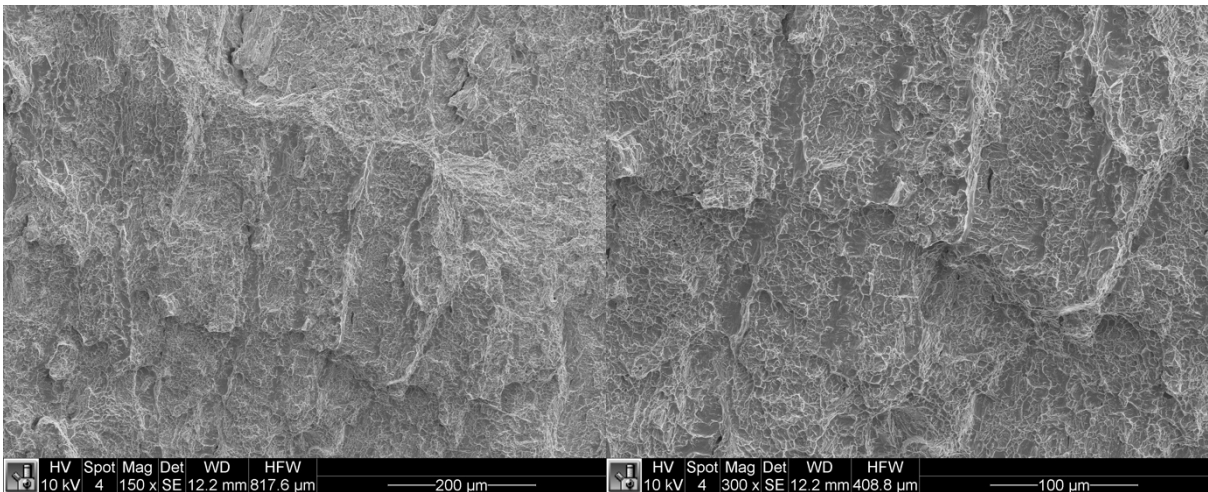
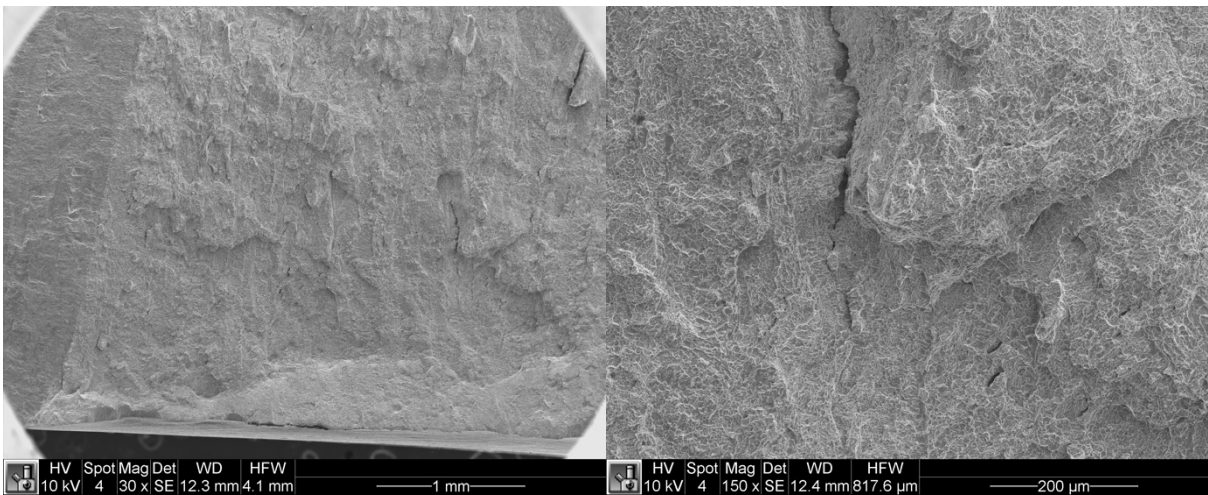
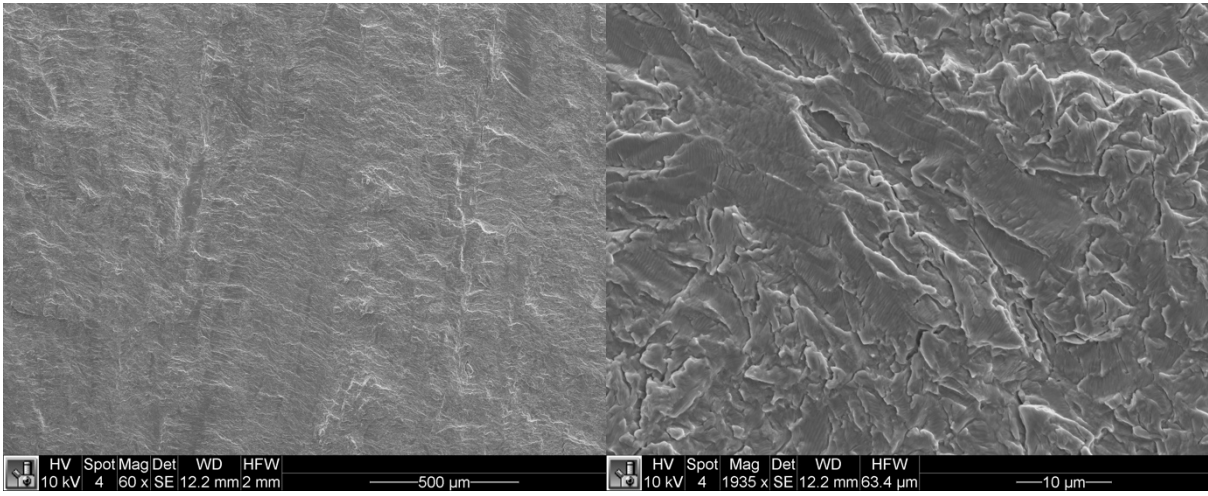


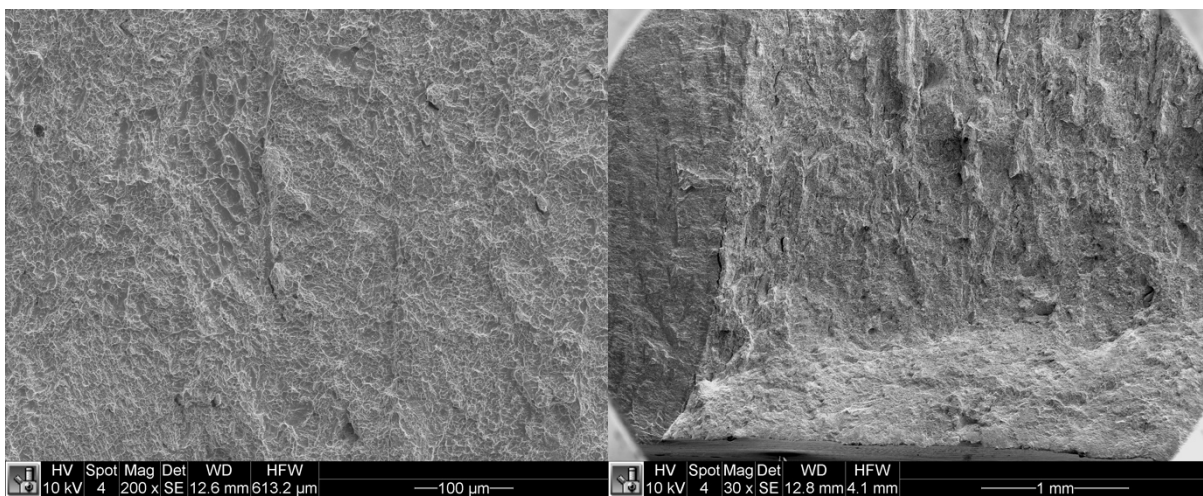
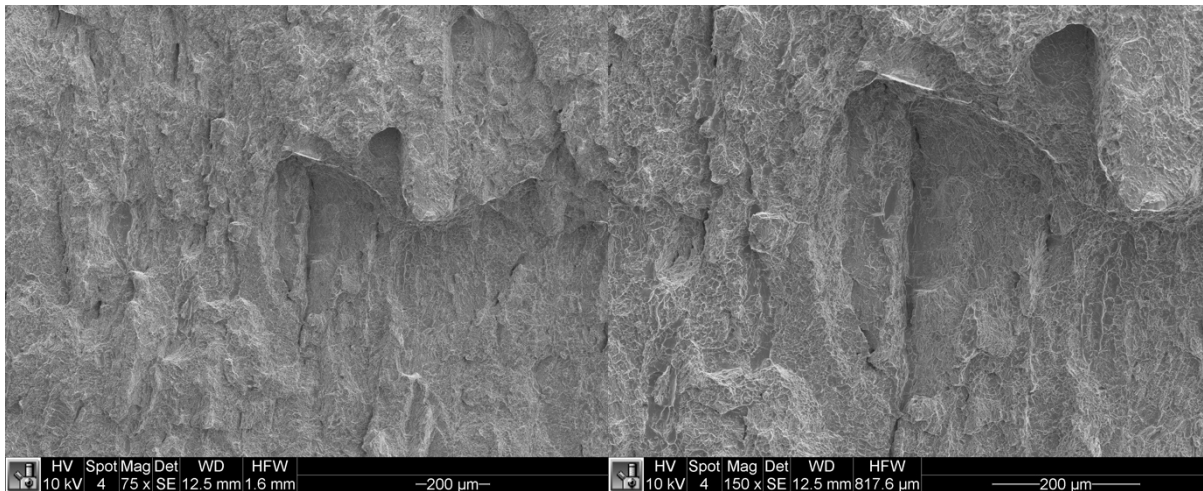
# XZ HIP

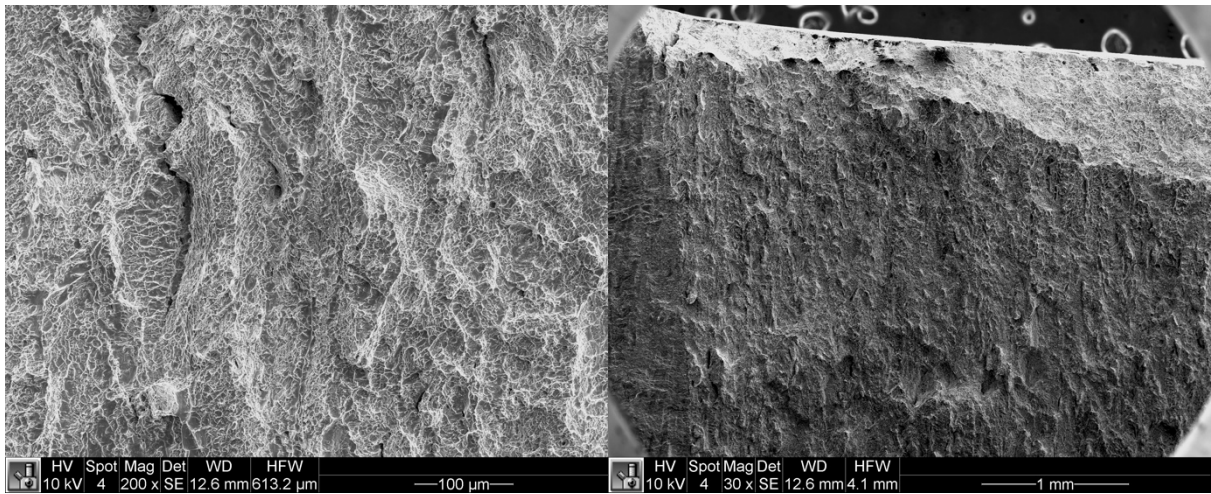
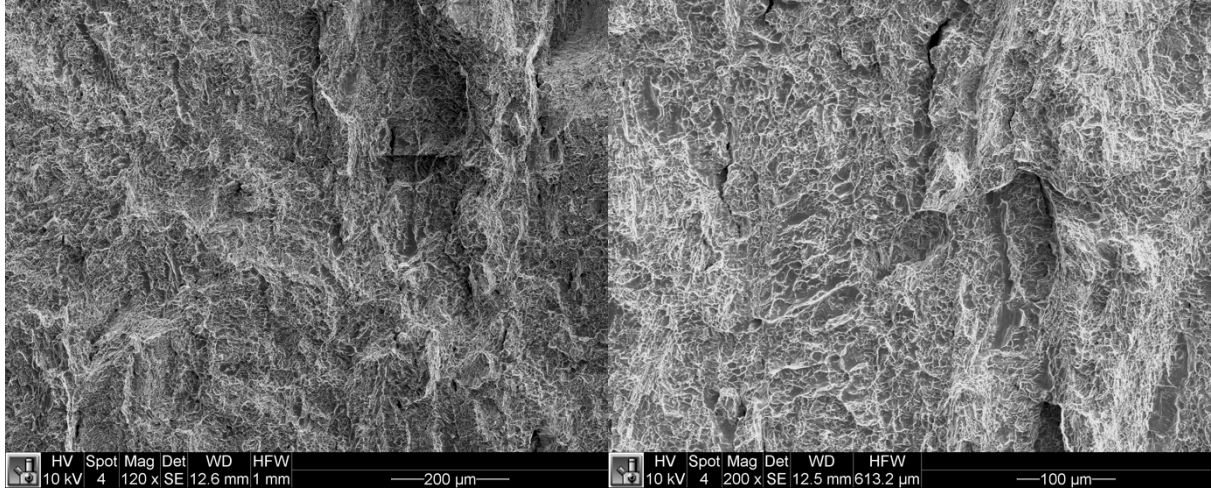




# XY HIP

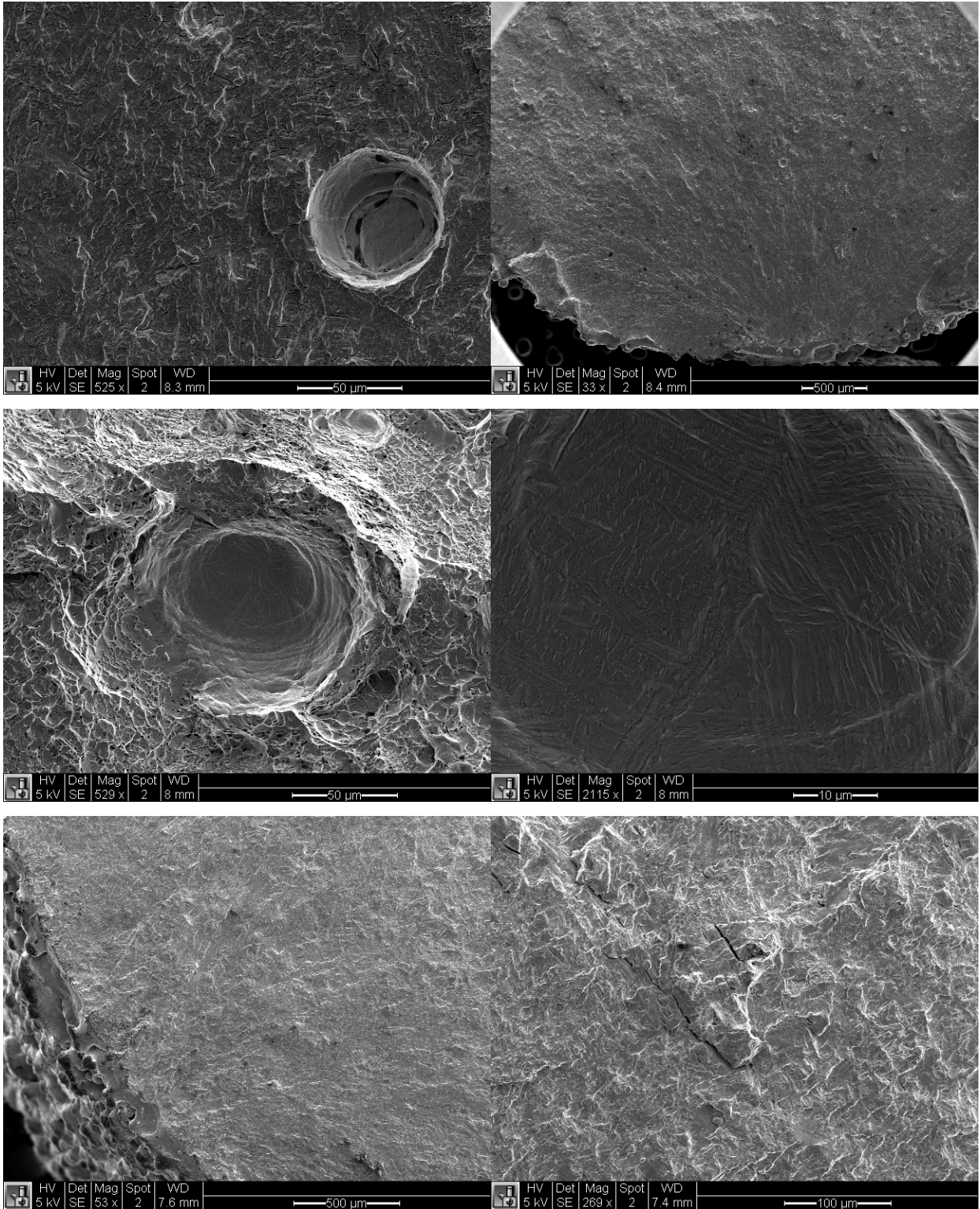


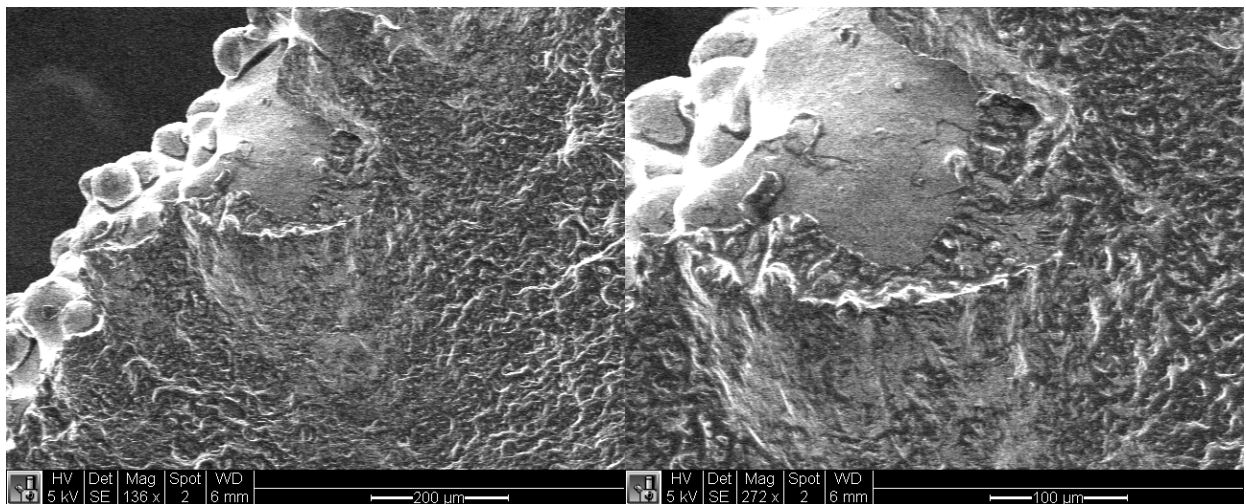
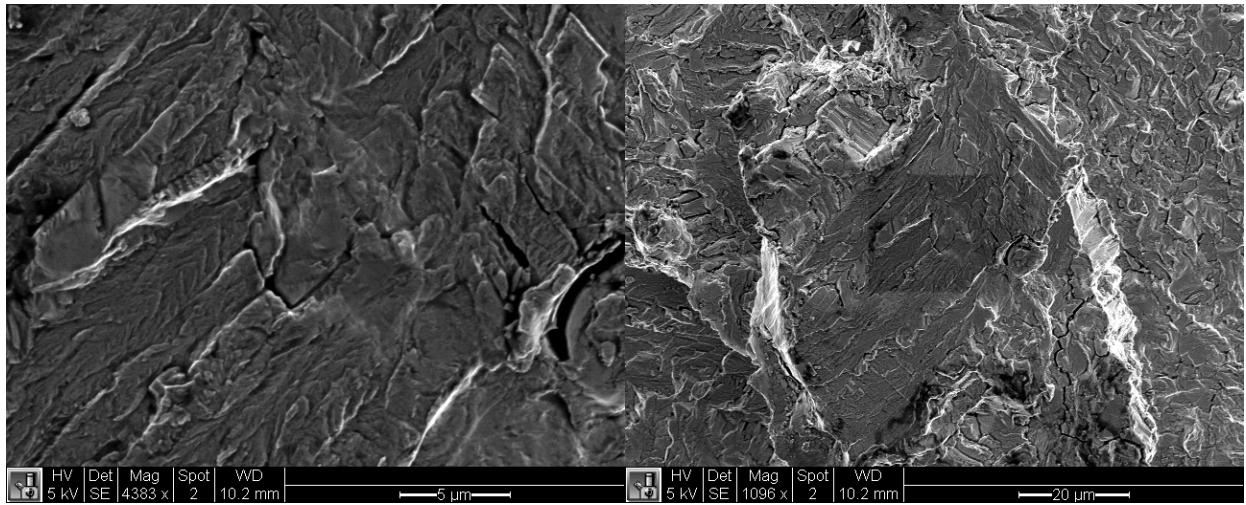
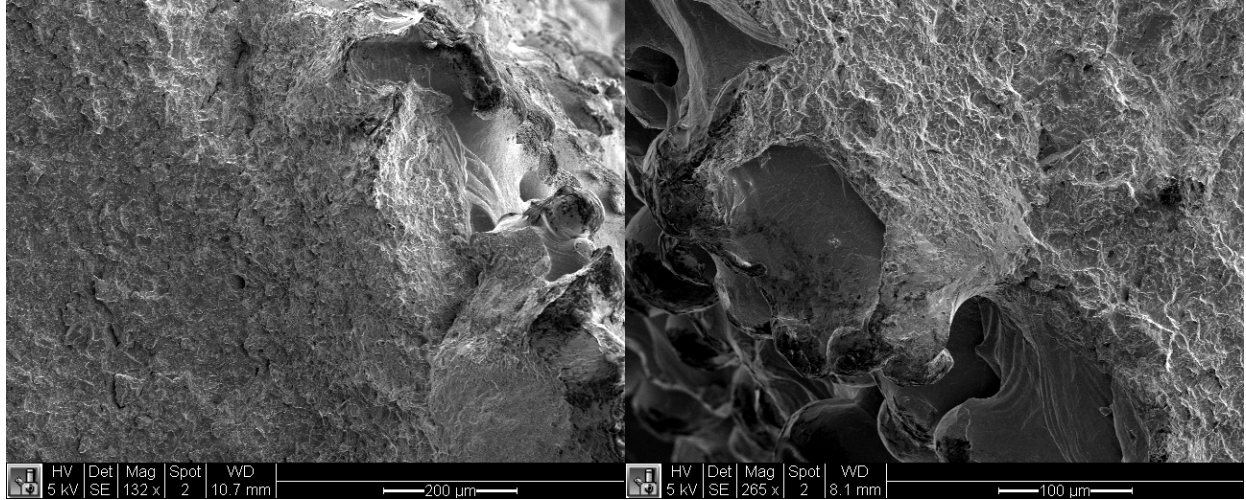


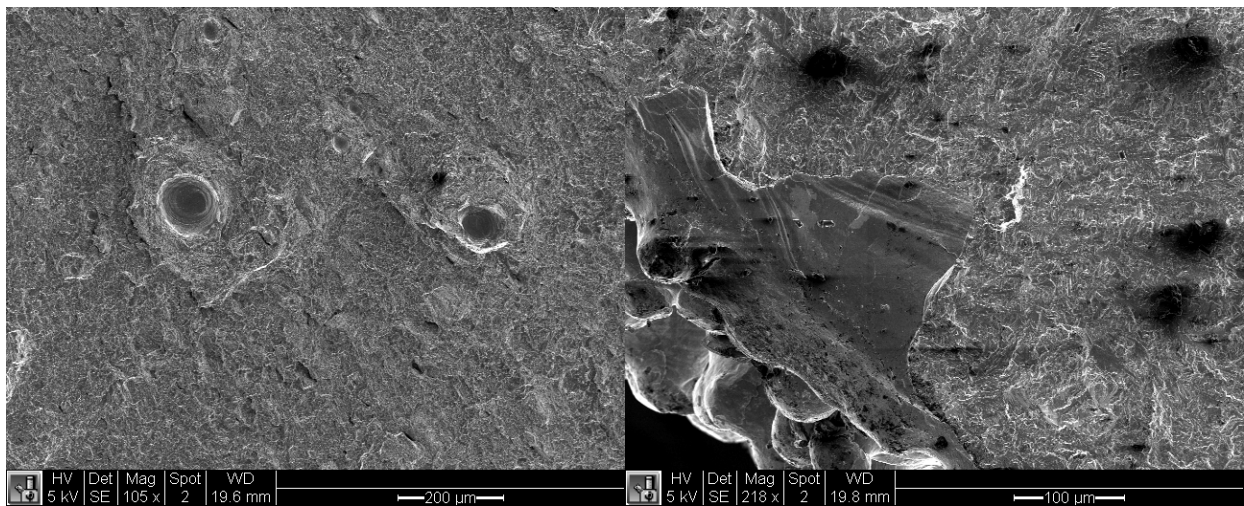
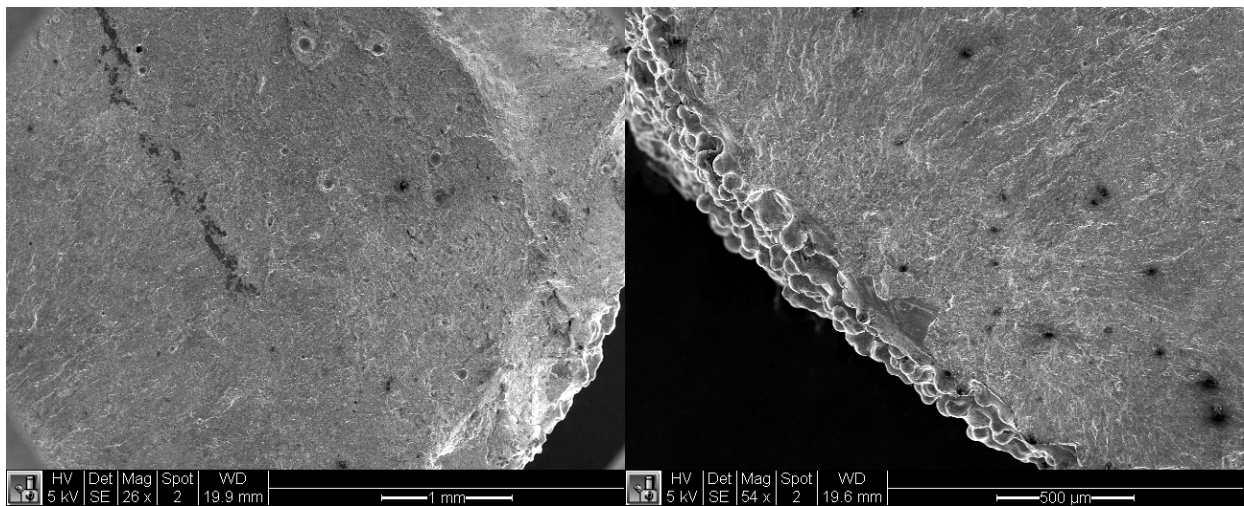
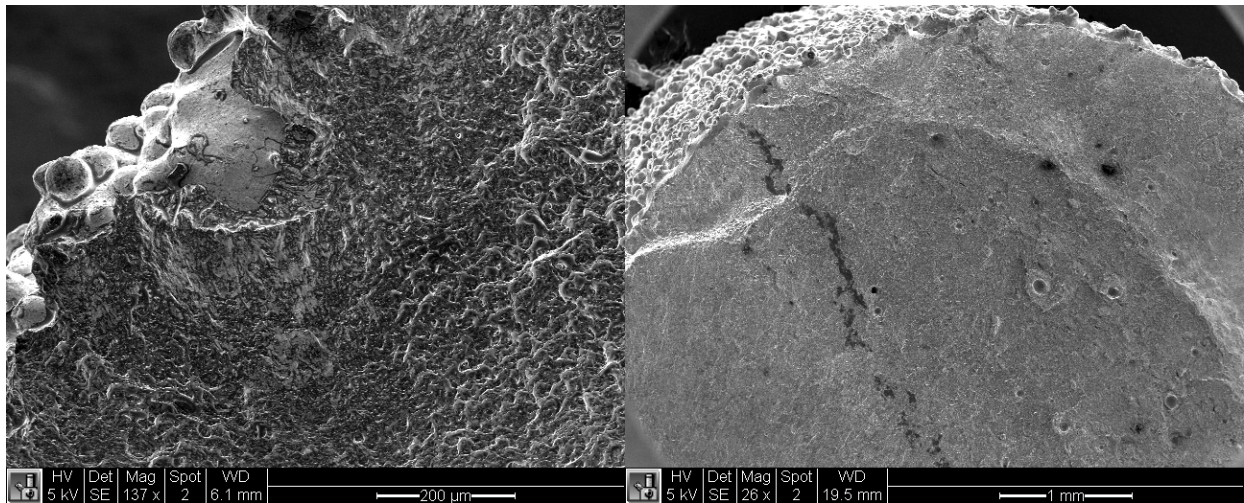


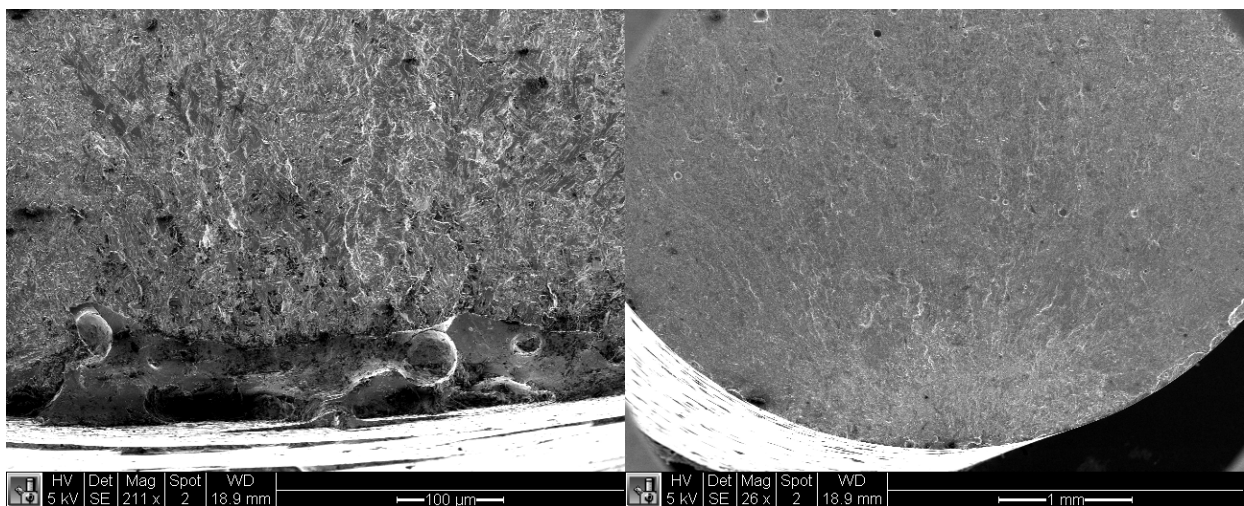
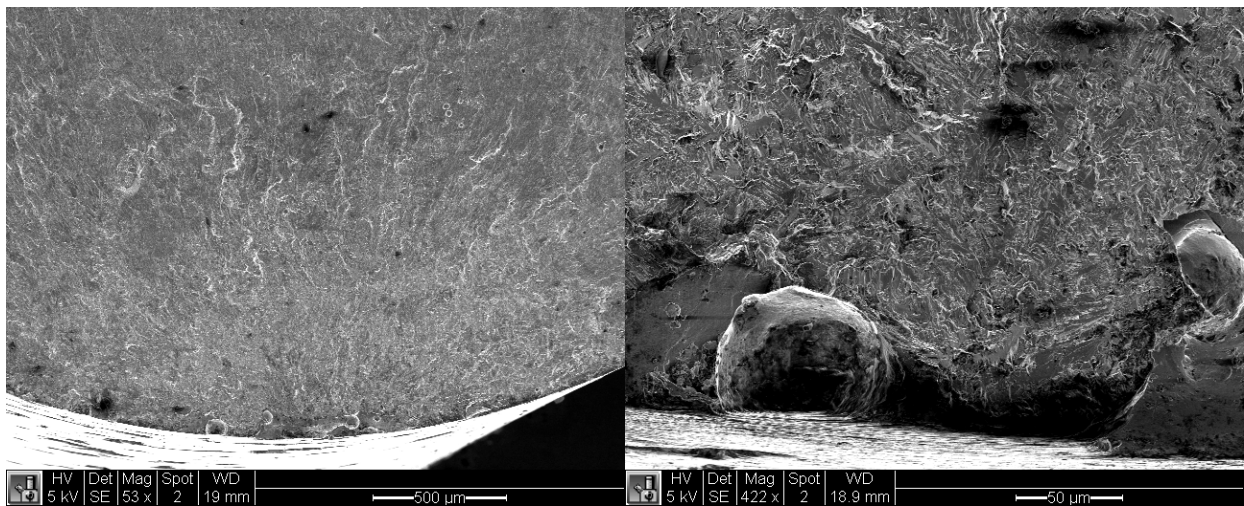
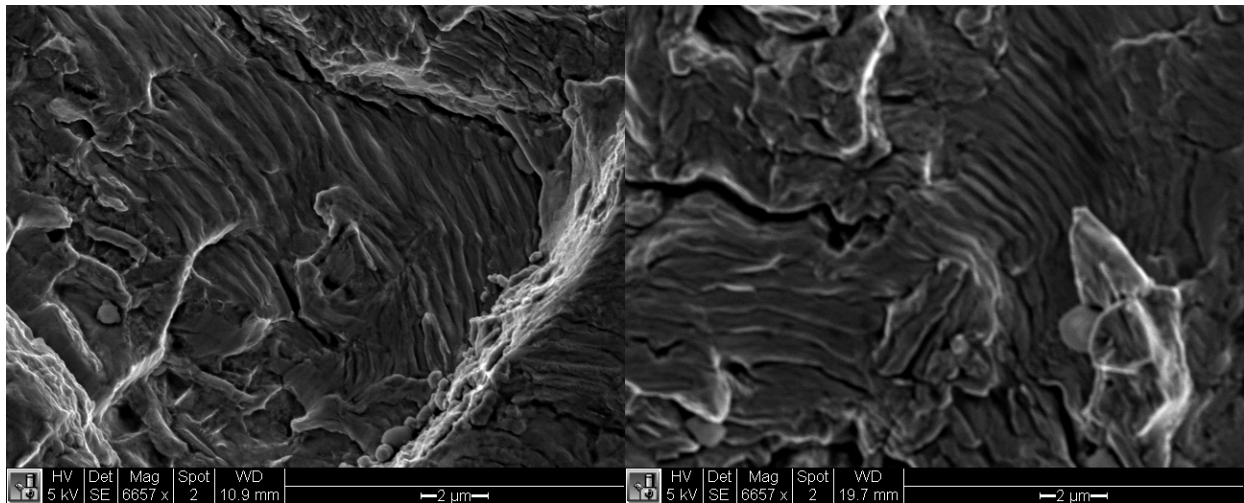
# High Cycle Fatigue

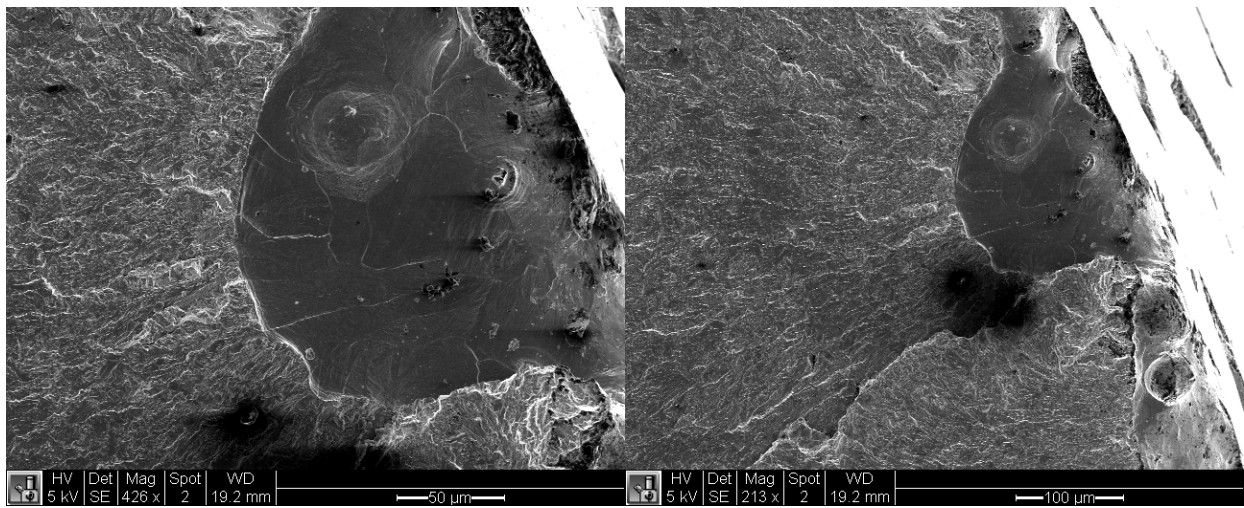
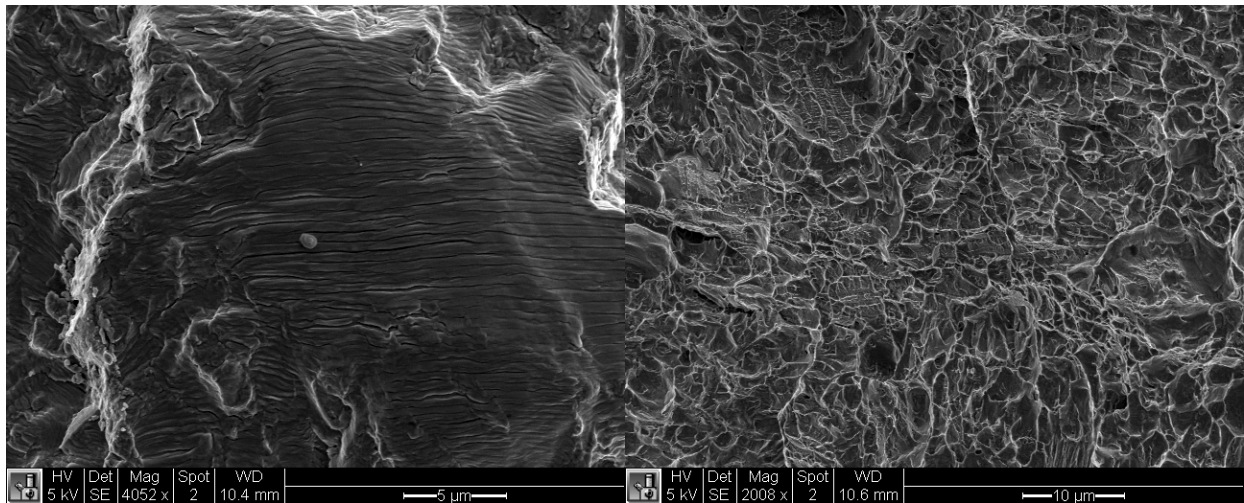
## As-Built + STHIP



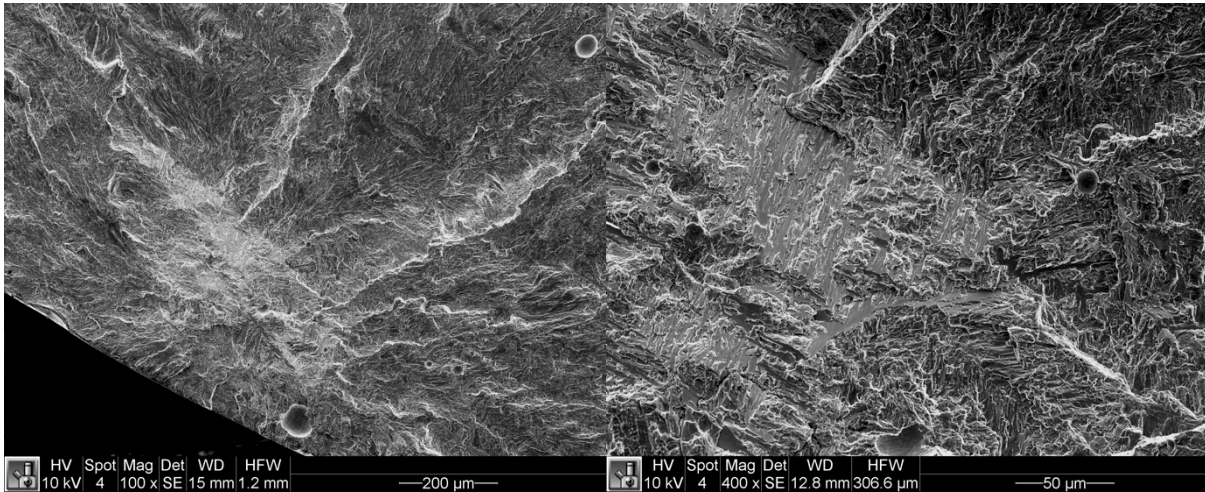
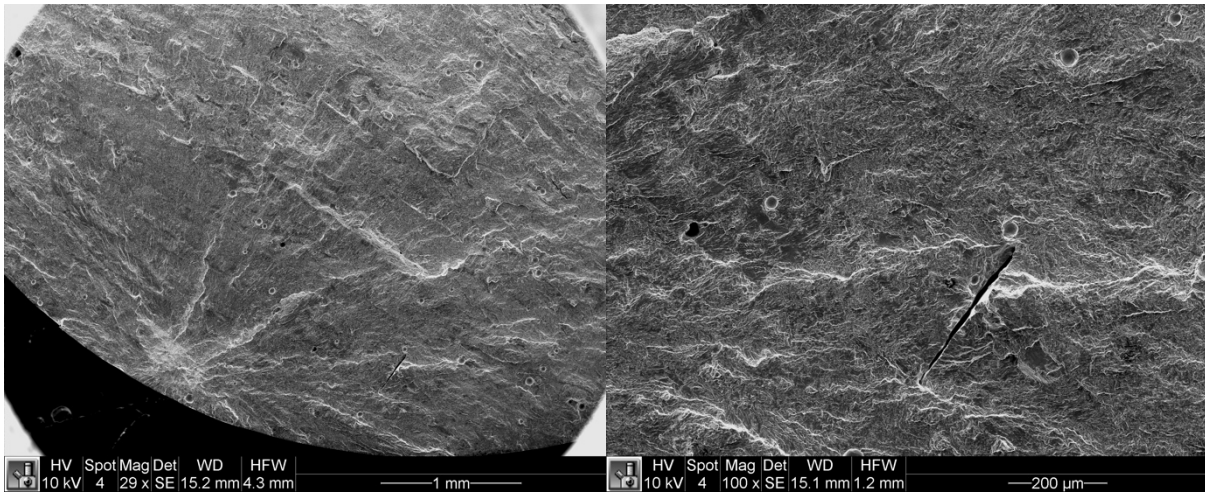
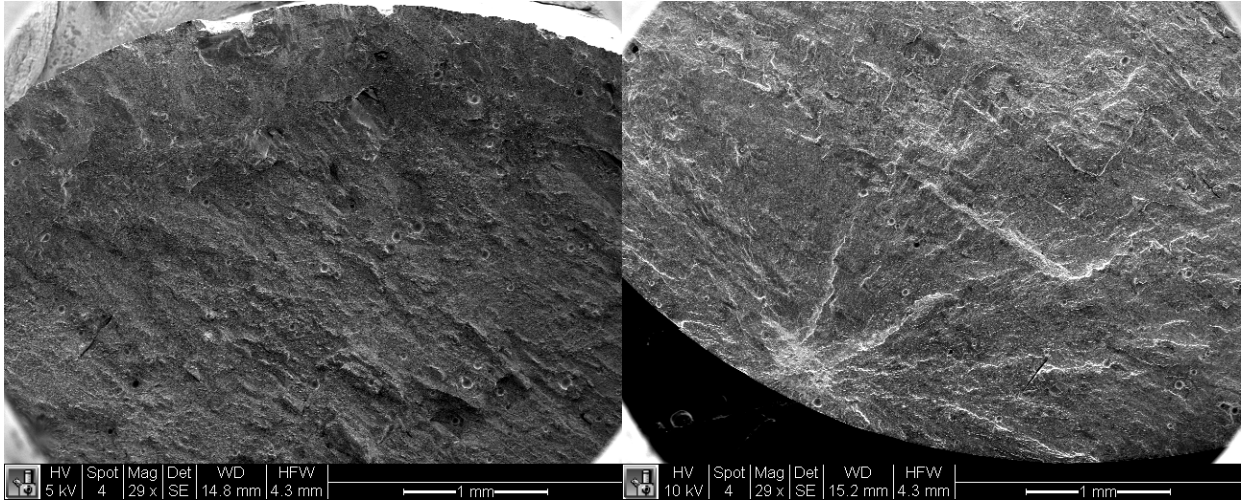


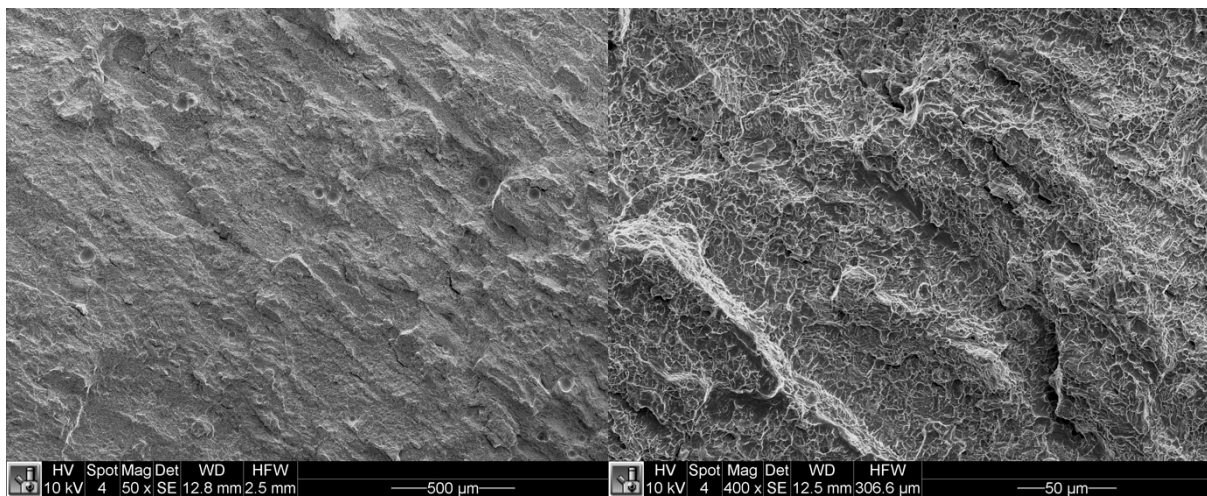
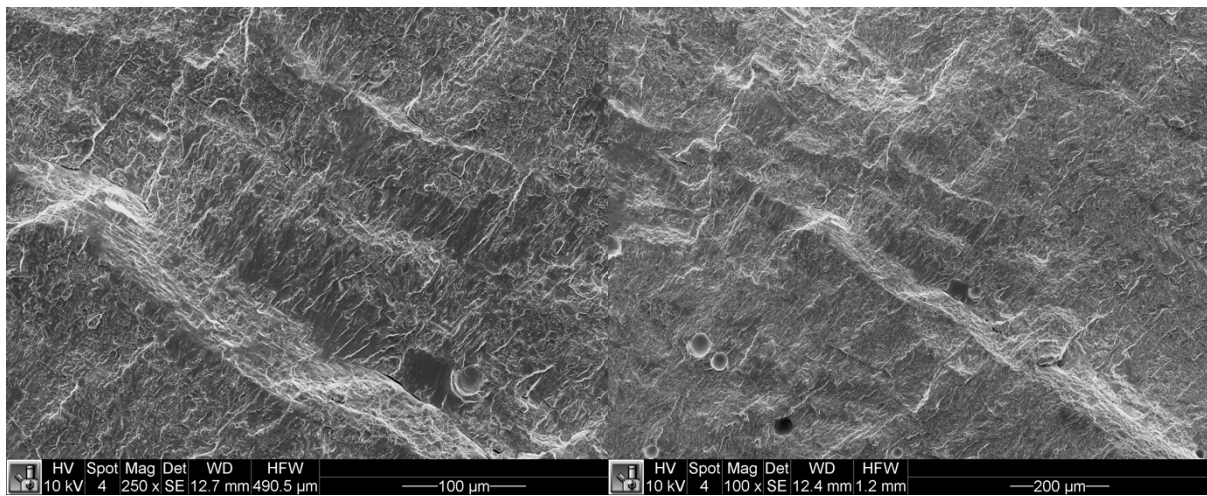
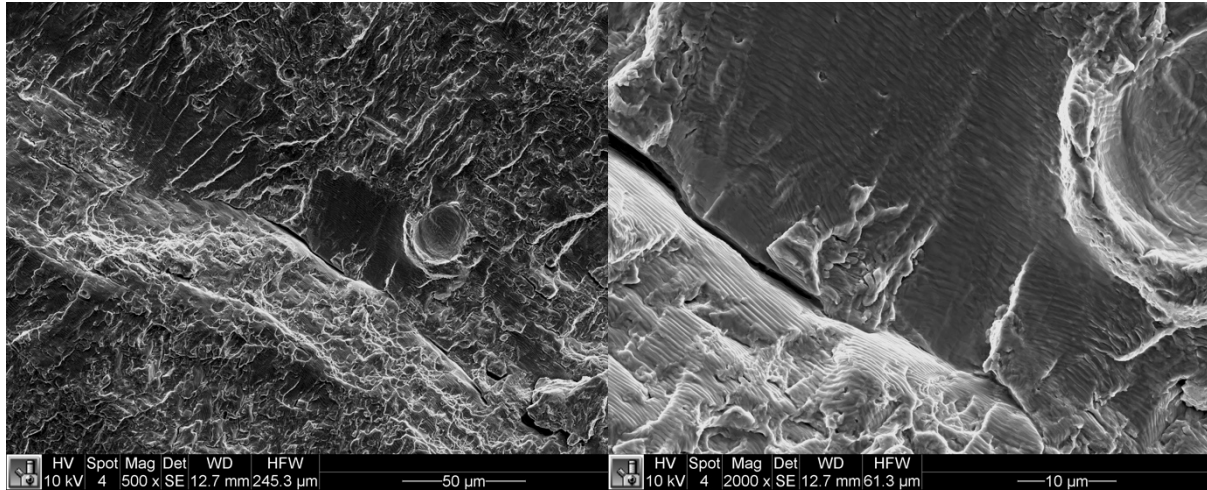


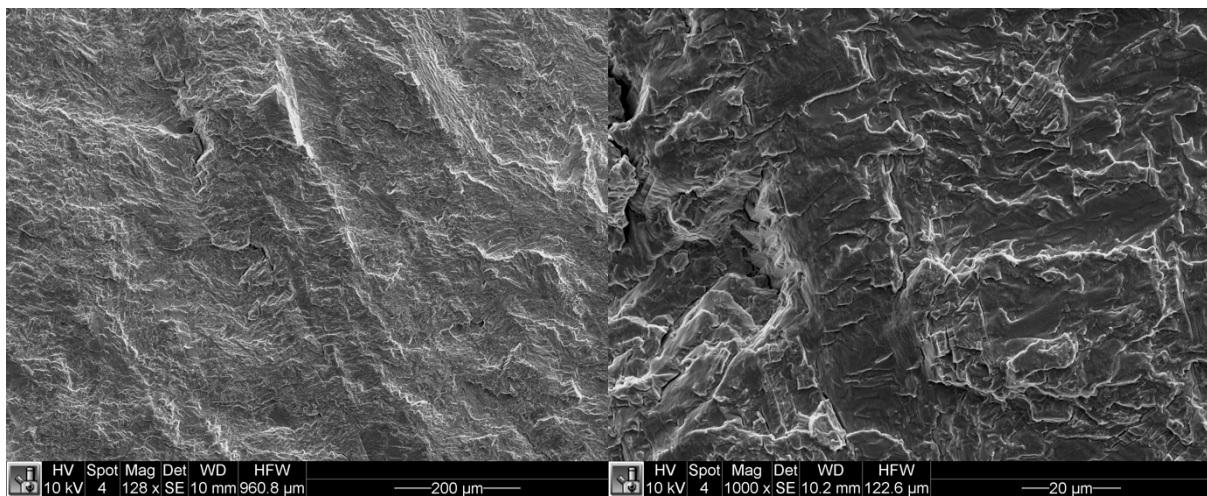
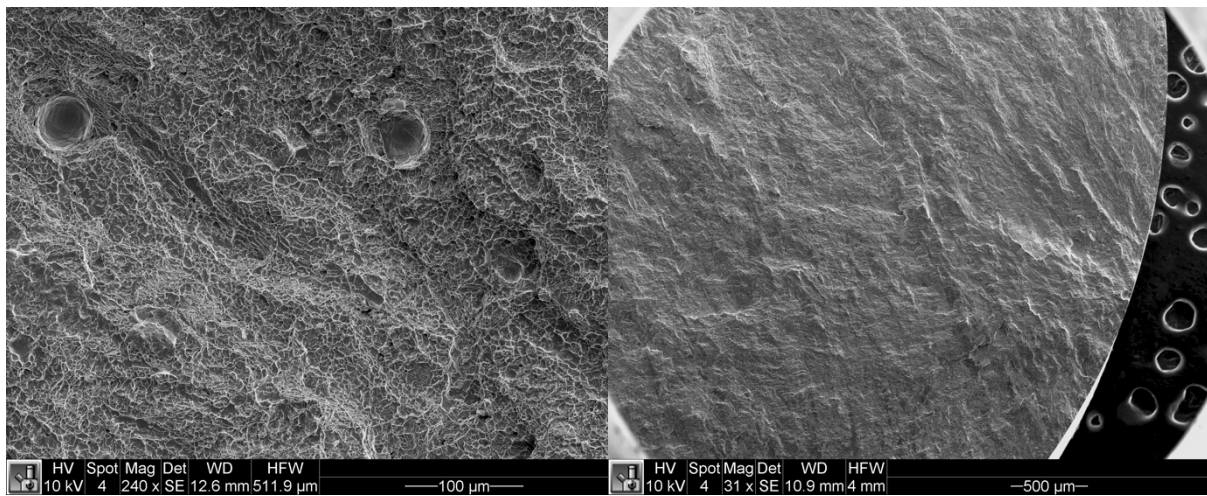
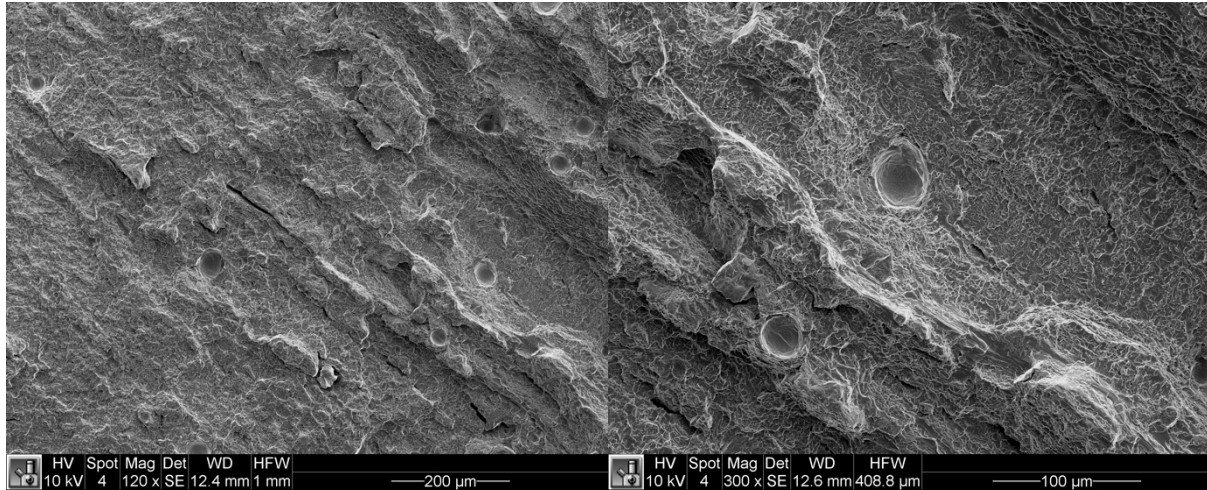


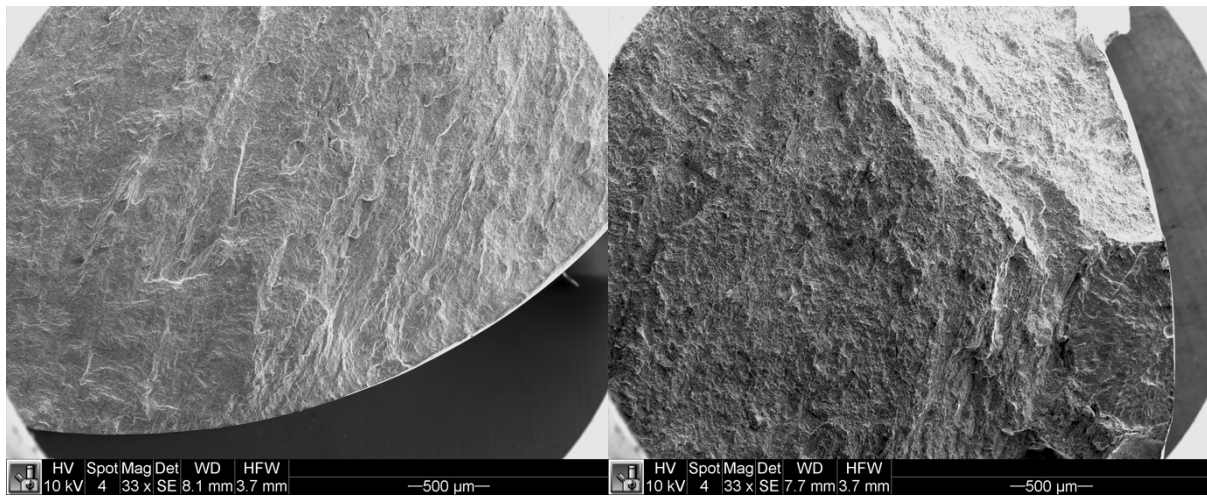
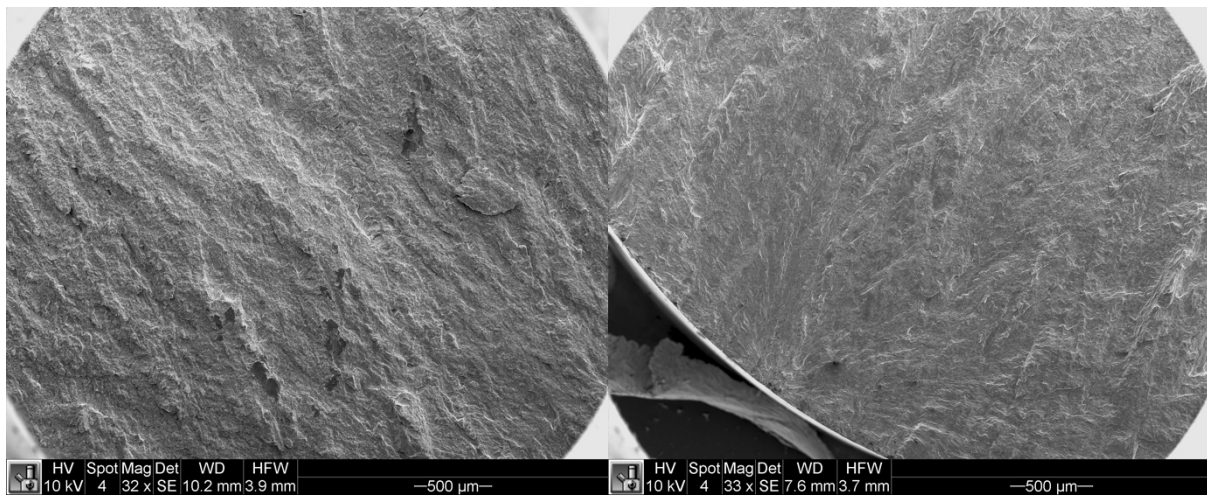
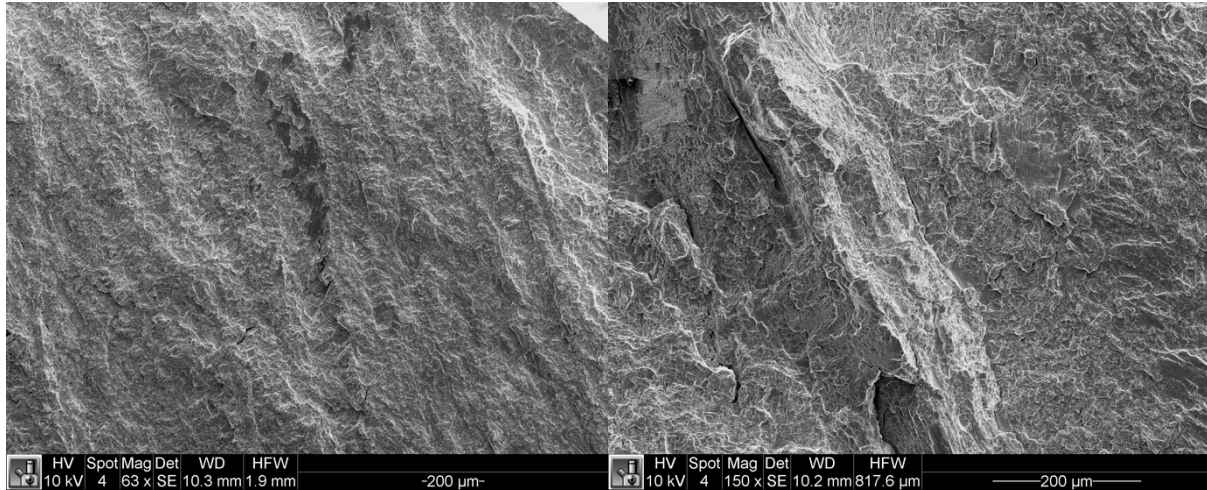


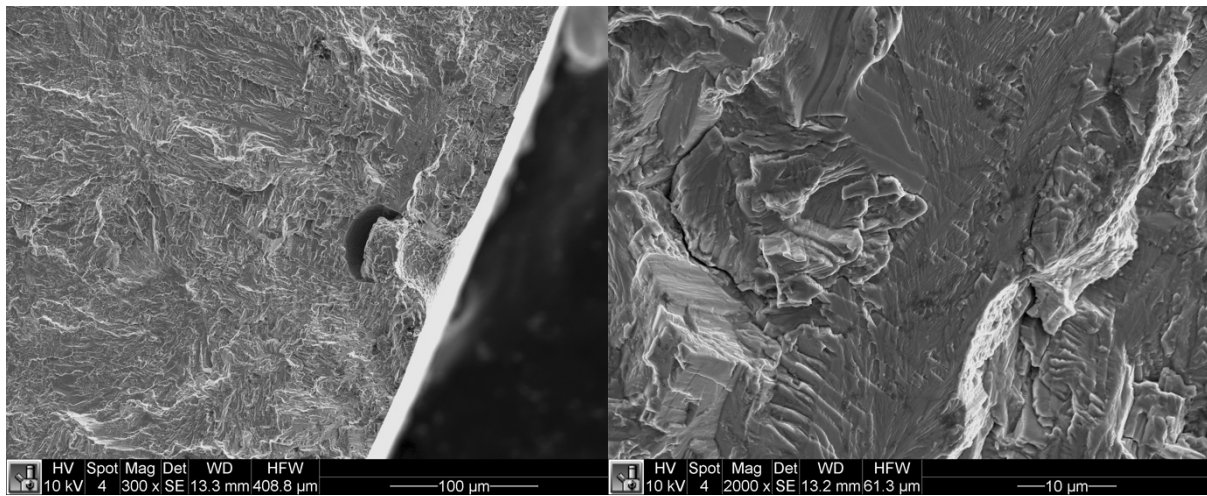
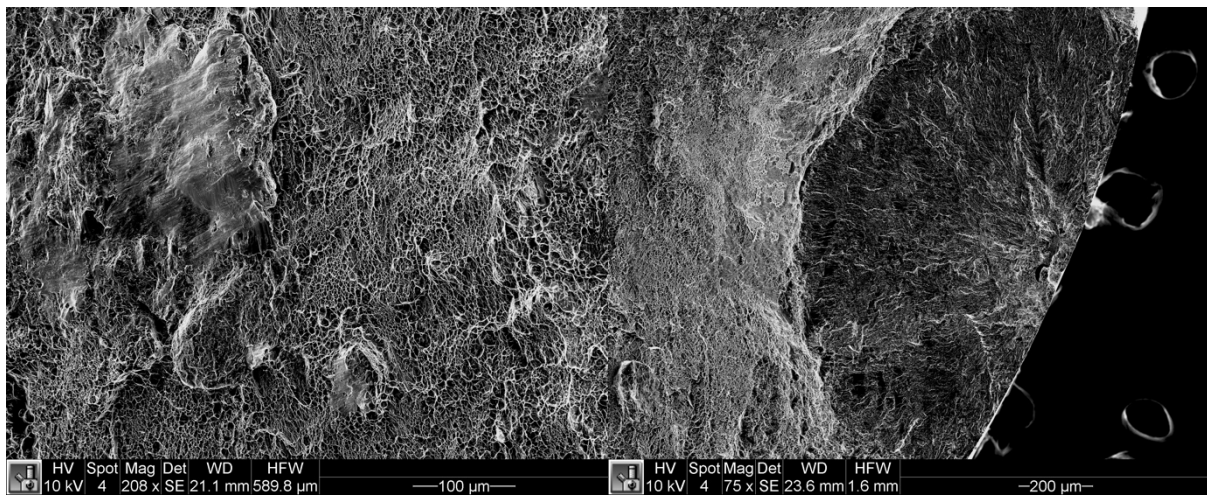
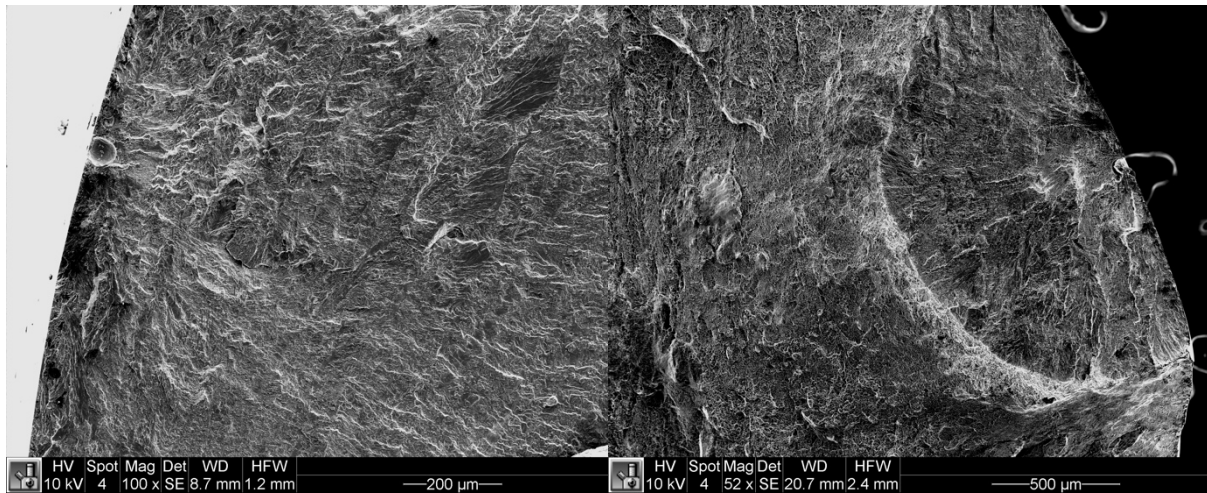
# BARC DOE

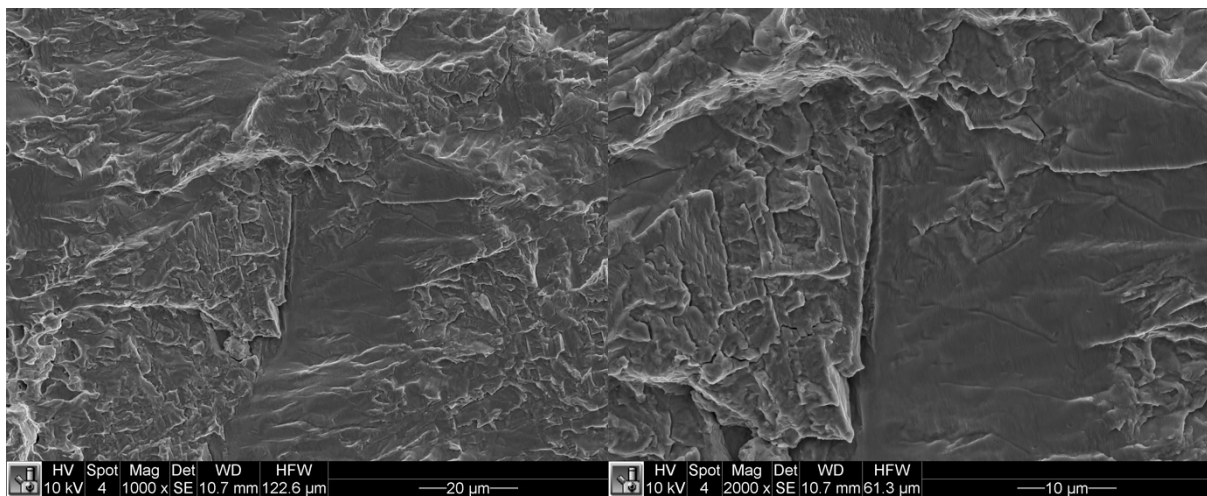
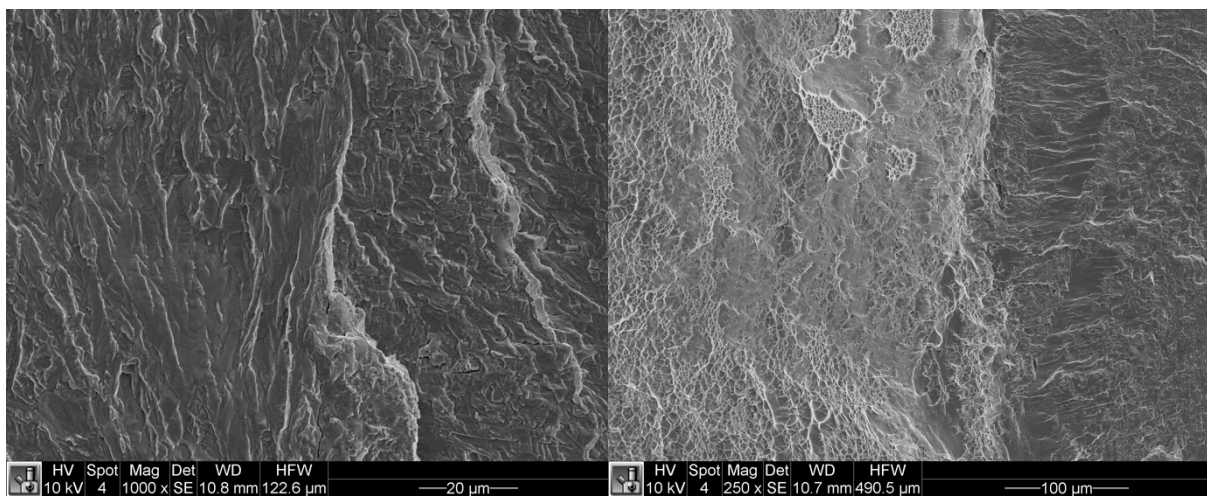
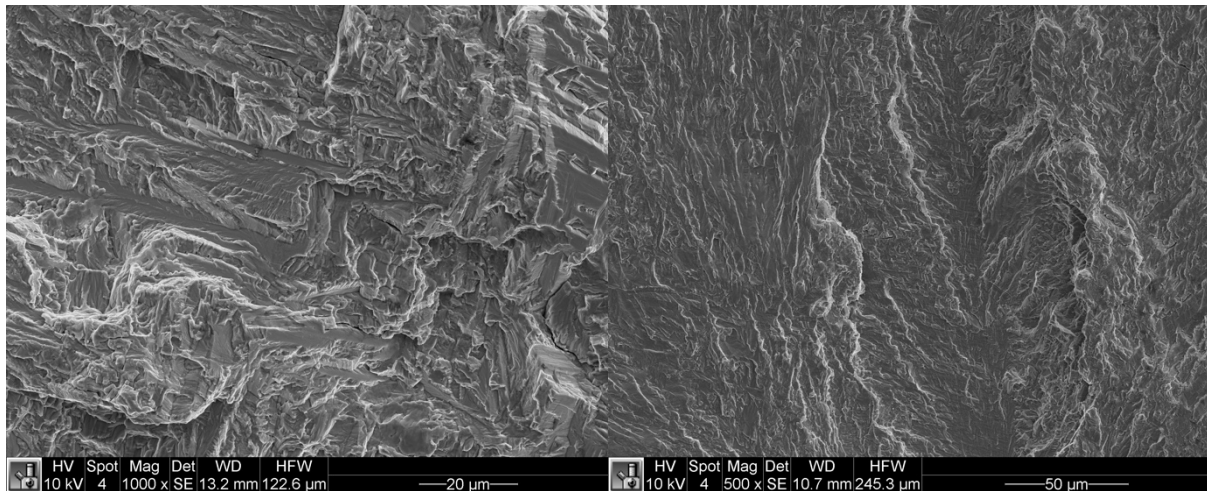


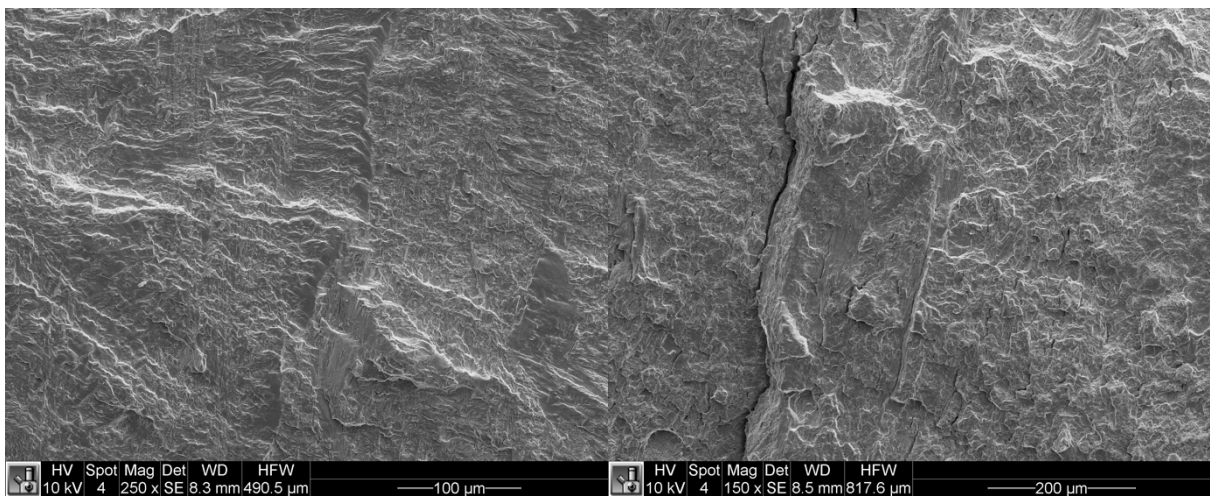
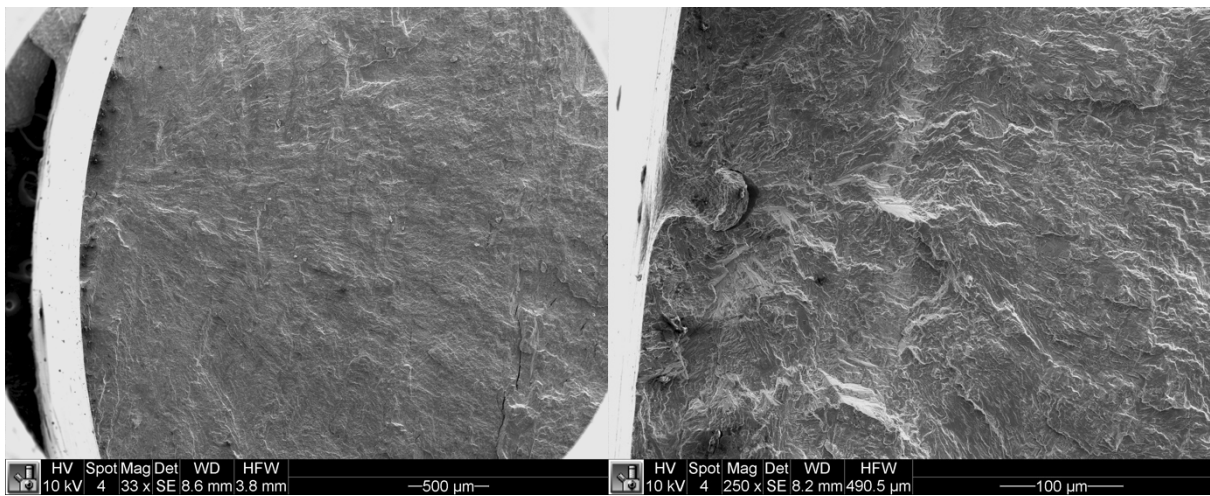
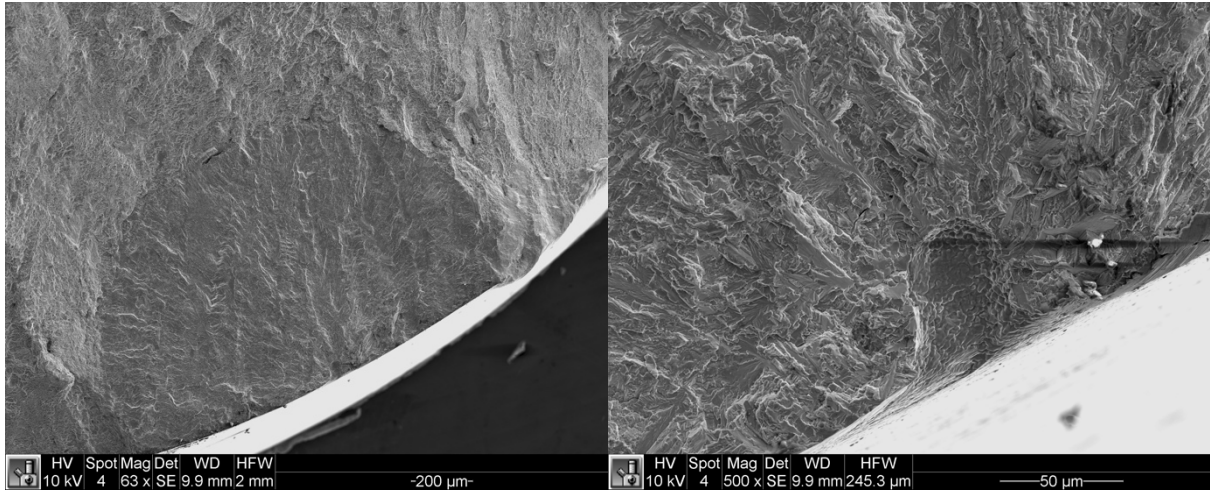


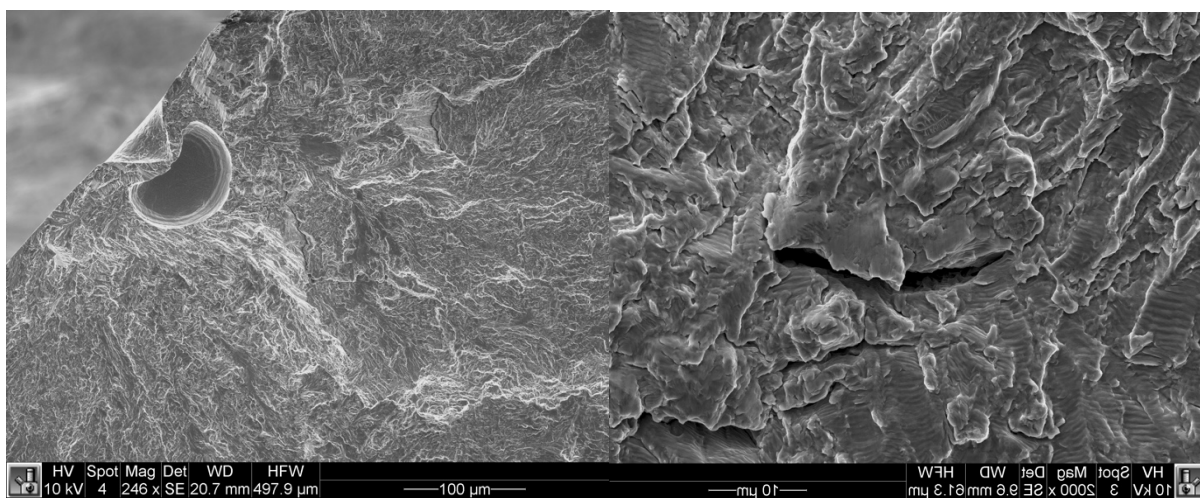
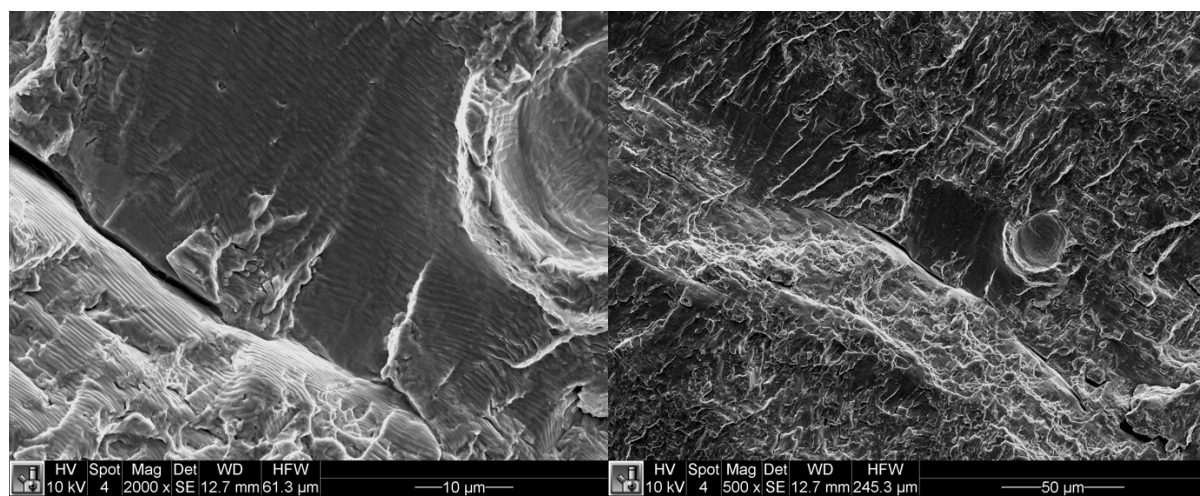
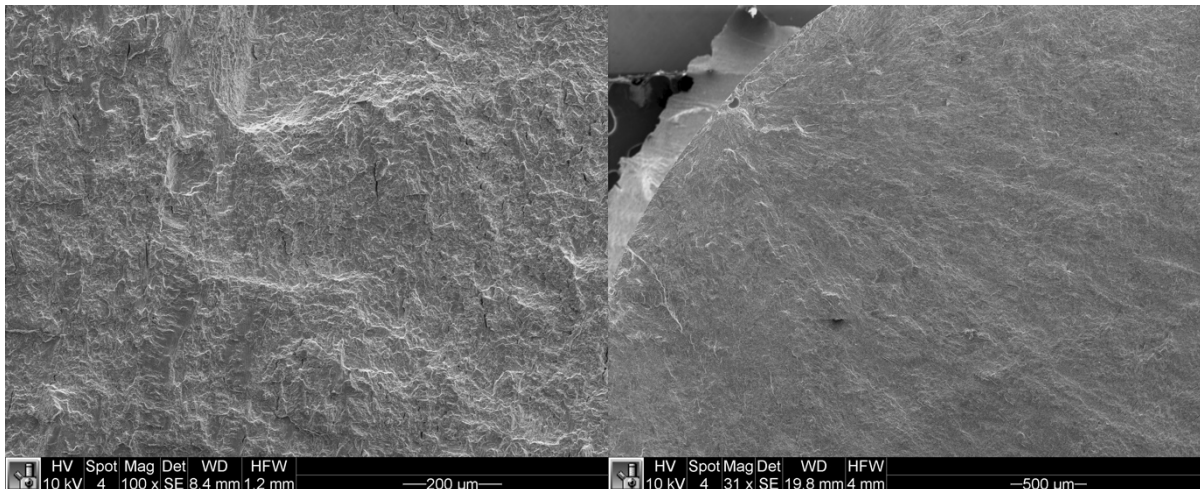












# Curriculum Vitae (CV)

## **Education:**

### **Ph.D., University of Washington, Seattle, WA 2019-2026**

Doctor of Philosophy in Mechanical Engineering

Dissertation: Evaluation of Intra-Build Interactions on Fracture-Critical Properties of PBF-EB Ti6Al4V

### **M.S., University of Washington, Seattle, WA 2019-2022**

Master of Science in Mechanical Engineering

### **B.S., California State University, Northridge, CA 2011-2016**

Bachelor of Science in Mechanical Engineering

## **Publications:**

- [1] **Mojib NM**, Fero K, Atmadja N, Arola D, Chen X, Ramulu M. Effect of intra-build design parameters on the fracture toughness properties of Electron Beam Melted Ti6Al4V. *Fatigue & Fracture of Engineering Materials & Structures*. 2024;47: 3894–3909.
- [2] **Mojib NM**, Ramulu M, Arola D. Low-Temperature Hot Isostatic Pressing Effects on Microstructure, Defects, and Fracture Resistance of Electron Beam Powder Bed Fusion Ti6Al4V. To be submitted to *Materials Science & Engineers A*. 2025
- [3] Bin Abdullah MS, **Mojib NM**, Atmadja N, Ramulu M. Machinability of Electron Beam Powder Bed Fused Ti-6Al-4V in Face Milling with Coated Carbide End Mill. In Press at *Journal of Materials Engineering and Performance*.
- [4] Bin Abdullah MS, Bol E, Kelley G, Doyle C, Schleusener R, **Mojib M**, Chen X, Arola, D, Ramulu M. Microstructure and microhardness of electron beam melted Ti-6Al-4V components with differential thickness in initial deposition layers. *Journal of Materials Research and Technology*. 2023;26: 6493–6507.
- [5] **Mojib M**, Pahuja R, Ramulu M, Arola D. High Cycle Fatigue Behavior of Recycled Additive Manufactured Electron Beam Melted Titanium Ti6Al4V. In: *International Mechanical Engineering Congress and Exposition IMECE2020*. Portland: ASME; 2020:24194.
- [6] **Mojib M**, Soyama H, Sanders D, Arola D, Ramulu M. The High Cycle Fatigue Behavior of Surface Treated Electron Beam Melted Titanium Ti6Al4V. In: *International Mechanical*

*Engineering Congress and Exposition IMECE2021*. American Society of Mechanical Engineers Digital Collection; 2021:71975.